UCID-19609

SYNFUELS FROM FUSION - USING THE TANDEM MIRROR REACTOR AND A THERMOCHEMICAL CYCLE TO PRODUCE HYDROGEN

Edited by: Richard W. Werner

November 1, 1982

UCID--19609

DE83 005216

A Collaborative Study by:

Lawrence Livermore National Laboratory, P. O. Box 808, Livermore, CA 94550:

Richard W. Werner (Principal Investigator)
Edward N. C. Dalder
David W. Dorn
Robert G. Hickman
Gary L. Johnson
Oscar H. Krikorian
R. Carroll Maninger

U. C. Davis, Department of Mechanical Engineering, Davis, CA 95616:

Myron A. Hoffman

University of Washington, Nuclear Engineering Department, Seattle, WA 98195:

Fred L. Ribe (Principal Investigator)
Gene L. Woodruff
M. E. Abhold
A. L. Babb
Mike Lloid
J. Oelund
T. H. Zerguini

Rowe & Associates, 14400 Bellevue Redmond Rd. Suite 208, Bellevue, WA 98007:

Don S. Rowe

General Atomic Co., P. O. Box 81608, San Diego, CA 92138:

Lloyd C. Brown
John H. Norman

Work Performed for:
Office of Fusion Energy
U. S. Department of Energy

U. S. Department of Energy Contracts: W-7405-Eng-48 at the Lawrence Livermore National Laboratory; DE-AMOG-76RL 0222S and TA-DE AT06-76ET 52047 at the University of Washington.

PREFACE

Our study on synfuels is intended to focus primarily on the engineering aspects of coupling a tandem mirror fusion reactor (TMR) to a thermochemical cycle for the express purpose of producing hydrogen. The hydrogen is then to be used:

- As a portable fuel
- As a feedstock to synthesize other fuels such as gasoline or methanol
- To produce other useful hydrocarbons, NH_3, etc.

The detailed "how to" of hydrogen utilization is beyond the scope of this report. We have concentrated solely on the thermochemistry of the hydrogen production process, although a brief Section 12 discusses "Synfuels Beyond Hydrogen."

The physics data are supportive to the study and are based on the most recent plasma theory and experiment. The model used is that of the tandem mirror reactor and the physics parameters of MARS.

TABLE OF CONTENTS

SECTION 1

EXECUTIVE SUMMARY

Contributor:

R. W. Werner

TABLE OF CONTENTS

TABLE OF CONTENTS

LIST OF TABLES

LIST OF FIGURES

LIST OF FIGURES

1.0 EXECUTIVE SUMMARY

1.1 INTRODUCTION

This is the third annual report in a series by Lawrence Livermore National Laboratory/University of Washington on the application of fusion energy for the production of synthetic fuel. The fusion driver is the Tandem Mirror Reactor (TMR) of the Lawrence Livermore National Laboratory. The thermochemical process is based on the General Atomic sulfur-iodine cycle. The product is hydrogen. Our estimated costs for producing the hydrogen are $12-$15/G.J.

The main body of the report essentially presents this year's work, but builds naturally on the two prior years' progress. In this Executive Summary, we will first highlight some of the major findings, new concepts introduced, progress made and conclusions arrived at over the course of the three-year study. This will then be followed by design specifics of this year's work.

1.2 HIGHLIGHTS

- Our major conclusion is that the concept of Fusion/Synfuels via the Tandem Mirror Reactor (TMR) and thermochemical cycles has positive potential and should continue to be an integral part of the national fusion program.

  The positive advantage of Fusion/Synfuels to the U.S. and its energy economy is that it is a replacement process. Synfuels can replace oil and natural gas as a source of energy or be used in conjunction with a plentiful coal resource to convert it to a more useful form in an efficient way.

  Since the exhaustibles--coal, oil and natural gas--have a bank account already fixed in geologic time and we continue to draw on

this bank account in ever increasing amount, it is important to begin to reverse this process. The reversal may be accomplished in two ways that are complementary:

Making use of Fusion/Electric, which reduces the demand on the exhaustibles

and

Utilizing Fusion/Synfuels, which adds to the bank account.

- The production of hydrogen using thermochemical cycles continues to have a demonstrated experimental base at the laboratory level with positive progress. Production rates of 100 liters/hour have been achieved. Production rates of 10,000 liters/hour will occur in CY82 or by mid CY83 at Ispra, Italy, in the Christina project.

- A thermochemical cycle for hydrogen production is a process in which water is used as the feedstock along with a non-fossil high temperature heat source to produce H_2 and O_2 as product gases. Three cycles of about 25 cycles proposed worldwide continue to dominate the production of H_2 from water. These cycles are:

  1. The General Atomic Sulfure Iodine cycle (our design base)

  2. The Westinghouse cycle

  3. The Ispra cycle (our international collaboration backup).

- Potential drivers for these thermochemical cycles that can provide a viable energy source are limited. There are only three:

  1. The fusion reactor

  2. The HGTR or VHTR

  3. Solar.

- Of the three drivers, the fusion reactor and the HGTR continue to have an edge over solar concentrators due to the diurnal nature of solar and the need for thermochemical plants to be run on a continuous basis.

- Assuming that an economically competitive fusion reactor can be created, the reasons for using a fusion reactor in preference to the HGTR as an energy source for synfuel production were not addressed within the context of this study. Either could do the job. Both may be appropriate.

- The TMR has some advantage over the Tokamak for synfuels, due principally to its relatively simple central cell topology. When further progress is made in increasing the Q of the TMR, it will have the additional advantage over both the Tokamak and the HGTR of directly supplying electricity for the bulk of the high temperature SO_3 decomposition process step rather than supplying high temperature via thermal energy. This will allow the reactor blanket to run substantially cooler.

- The design of a synfuel plant remains extremely complicated. It is large--like an oil refinery--and has many units to design. In working on the design of the individual parts rather than the total complex we were justifiably encouraged, through our conceptual design results, to find that the components perceived to be the most difficult--the SO_3 decomposer, the H_2SO_4 boiler and the fusion reactor blanket--all had potentially good design solutions and also a credible materials base.

- The Fusion Reactor/Synfuel total plant complex is substantially more difficult to analyze than a Fusion Reactor/Electrical Plant. In this area of analysis we have done some significant work and made substantial contributions in developing standardized procedures for flow sheeting and for matching plant load lines and

temperatures to the energy source. The procedures will be useful for all combinations of energy sources and thermochemical plants.

- The key engineering problem in the reactor area is the design of the blanket. We have accomplished, by our own choice, conceptual designs for two basically different types or approaches. The selection of one over the other is both philosophical and sensitive to future technological progress. The first design is a modest temperature blanket operating as low as 825 K to as high as 950 K exit gas temperature. This design relies on electrical heating (a process we call Joule Boosting) to do the high temperature SO_3 decomposition step in the chemical process. The second design is for a high temperature blanket operating at 1150-1200 K maximum exit gas temperature wherein the decomposition step is done thermally. The efficiency of the process using the modest temperature blanket is about 38%. Not too surprisingly the efficiency of the process using the high temperature blanket is approximately 43%. The philosophical choice is based on whether one is more comfortable at lesser efficiency with presently available materials or at higher efficiency with a material that is yet to be developed. One must bear in mind that the LWR, at an efficiency of 32%, is economically competitive.

1.3 THE TANDEM MIRROR REACTOR DRIVER

Our study on synfuels focused primarily on the engineering aspects of coupling a Tandem Mirror Fusion Reactor (TMR) to a thermochemical cycle for the express purpose of producing hydrogen from water. The hydrogen is then to be used:

- As a portable fuel
- As a feedstock to synthesize other fuels such as gasoline or methanol

- To produce other useful chemicals such as NH_3.

The fusion reactor physics had a very strong bearing on our engineering design and was an integral part of our study. This energy source uses the D-T reaction, producing an energetic neutron and an alpha particle.

$$D + T \rightarrow n\ (14.1\ MeV) + \alpha\ (3.5\ MeV)$$

An artist's view of a TMR is shown in Fig. 1.1.

The Tandem Mirror Reactor in this year's report has a MARS[1,2] (Mirror Advanced Reactor Study) axicell design (Fig. 1.2). MARS is a linear magnetic mirror fusion device which uses electrostatic end plugs to confine a steady-state fusion plasma in a long solenoid called the central cell. The central cell plasma is self-sustained by alpha particle heating (ignition). Continuous injection of neutral beams and ECRH (Electron Cyclotron Resonance Heating) are both required to maintain the end plug electrostatic potential that confines the plasma and to pump out (by charge exchange) the ions which get trapped into the negative potential of the thermal barrier. Maintaining the thermal barrier significantly reduces the plug injection power requirements.

The central cell is the heart of the reactor, producing energy in the form of 14.1 MeV neutrons and 3.5 MeV alpha particles. The kinetic energy of the neutrons is recovered in a blanket surrounding the central cell plasma. The charged particle energy is recovered in the direct convertor. The principal design parameters used for the reactor in this year's study are shown in Table 1.1. A typical reactor energy balance for our reference design is shown in Fig. 1.3.

1.4 THE THERMOCHEMICAL PLANT PROCESS

The thermochemical process uses General Atomic's sulfur-iodine cycle. The net result of this cycle, as Fig. 1.4 illustrates, is the thermochemical decomposition of water to make hydrogen and oxygen using only water as the feedstock. It is a pure thermochemical cycle (without electrolysis) and is

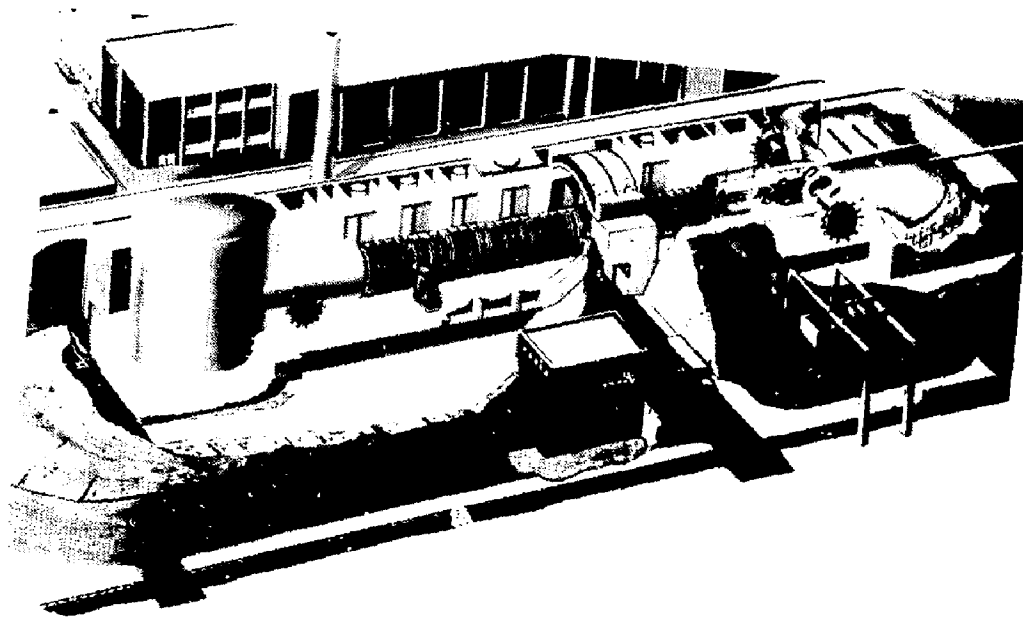

Fig. 1.1 The Tandem Mirror Reactor

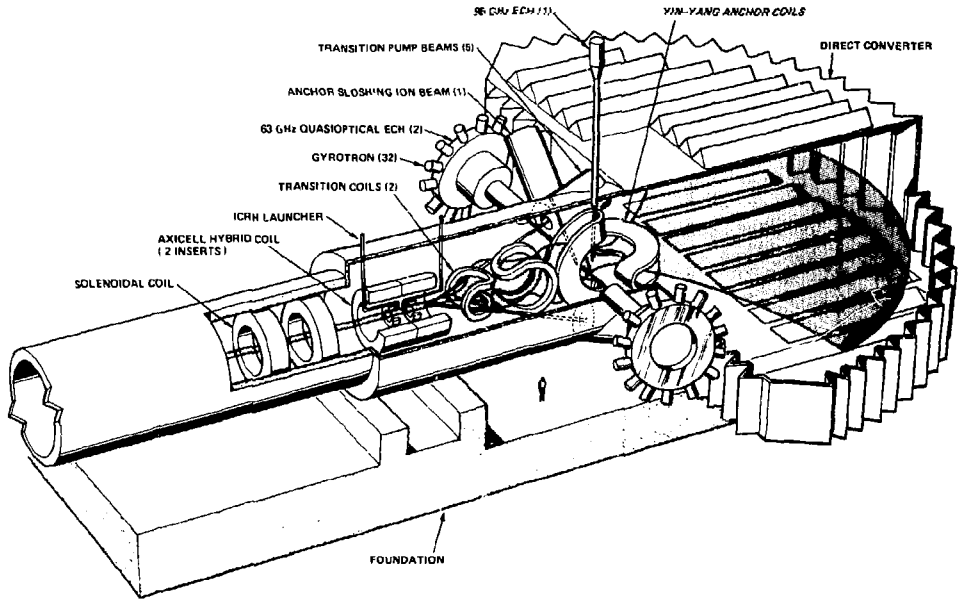

Fig. 1.2 Tandem Mirror Reactor (MARS)

Table 1.1 Design parameters for the Tandem Mirror Reactor as a driver for the thermochemical plant

Fusion power	3500 MW
Neutron power	2800 MW
Blanket energy multip., M	1.2
Blanket thermal power	3360 MW
First wall loading (ave.)	2.0 MW/m^2
Reactor Q	25.
Central cell length	150 m
Direct convertor power (from alpha particles)	700 MW
Direct convertor power (from injector power)	140 MW

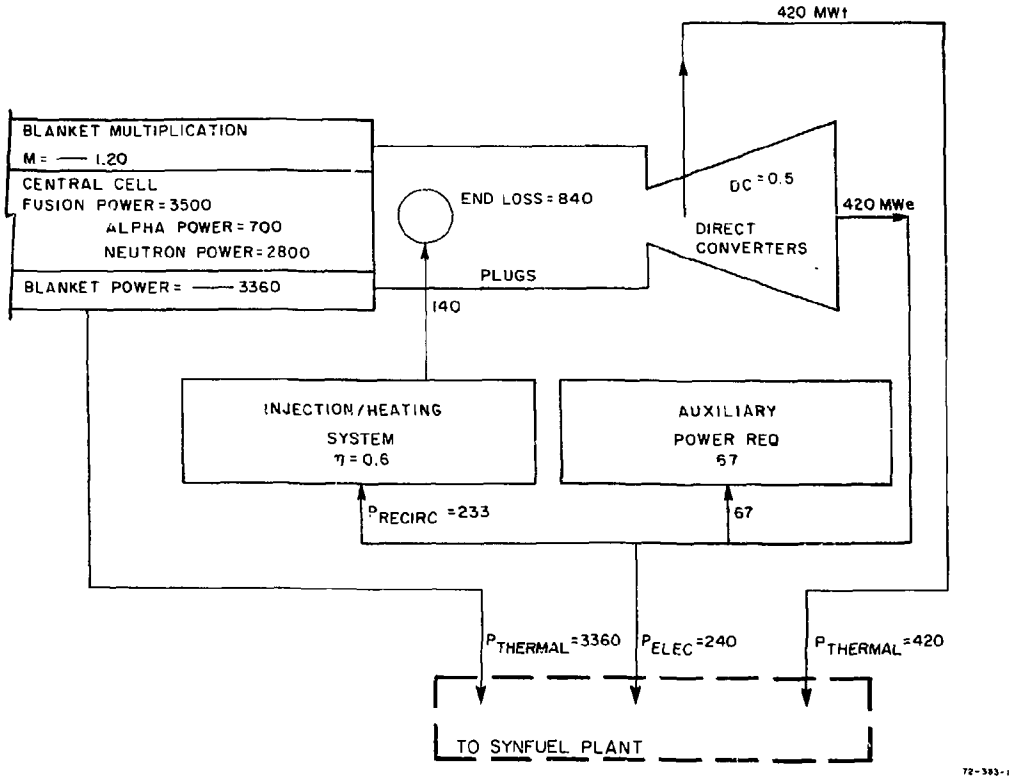

Fig. 1.3 Power balance of a Tandem Mirror Reactor used for producing synfuels, Q = 25.0 and M = 1.20

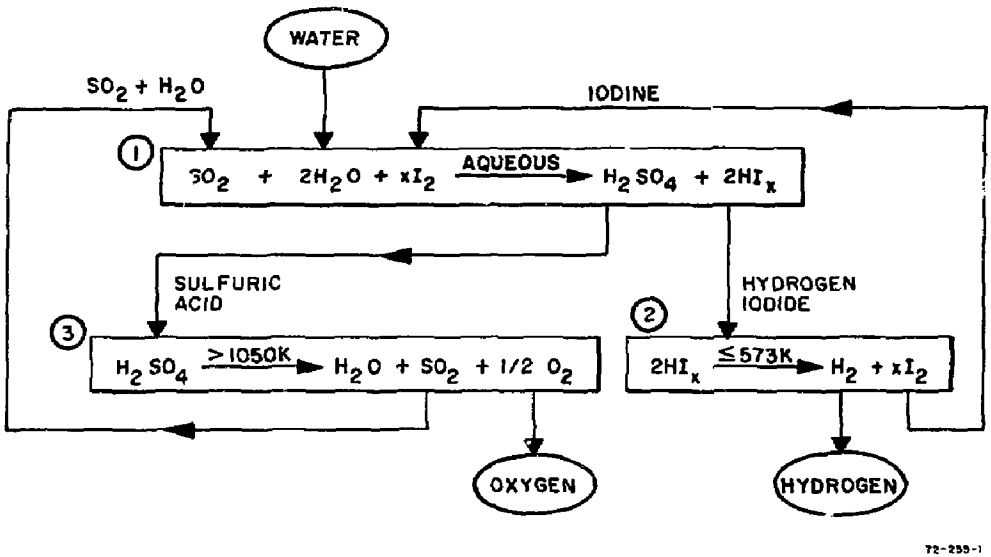

Fig. 1.4 The General Atomic sulfur-iodine cycle

described by the major reaction steps shown in Fig. 1.4. Major parts of the process are associated with separation and purification of the reaction products. For example, a critical aspect for the successful operation of the process is in the separation of the aqueous reaction products in reaction (1). Researchers at the General Atomic Company have solved this problem by using an excess of I_2, which leads to separation of the products into a lower density liquid phase, containing H_2SO_4 and H_2O, and a higher density liquid phase containing HI, I_2 and H_2O.

Reaction (2) shows the catalytic decomposition of HI, which is in the purified liquid form (50 atm). Pure H_2 is obtained by scrubbing out I_2 with H_2O.

The equilibrium for reaction (3) lies to the right at temperatures above 1000 K, but catalysts or higher temperatures are needed to attain sufficiently rapid decomposition rates below 1250 K. Catalysts are available for this process, but careful consideration needs to be given to their costs versus effectiveness.

1.5 REACTOR BLANKET DESIGN, THE CANISTER BLANKET WITH THE JOULE-BOOSTED DECOMPOSER - OUR OPTION

This Canister blanket (Fig. 1.5) is one of two complementary blanket designs we have studied for Synfuel applications which go with two decomposer concepts. The Canister blanket as used here can be characterized as a medium temperature blanket when used with the Joule-Boosted decomposer (JBD). By joule-boosting we refer to the utilization of electrically heated, commercial SiC furnace elements in place of using a heat exchanger to transfer process heat to the highest temperature step of the thermochemical process. The General Atomic Sulfur-Iodine Thermochemical Cycle has, as its highest temperature step (1100-1200 K), the thermal decomposition of SO_3 to SO_2 and O_2 (Step 3).

The most important advantage of this Joule-Boosted approach from the TMR

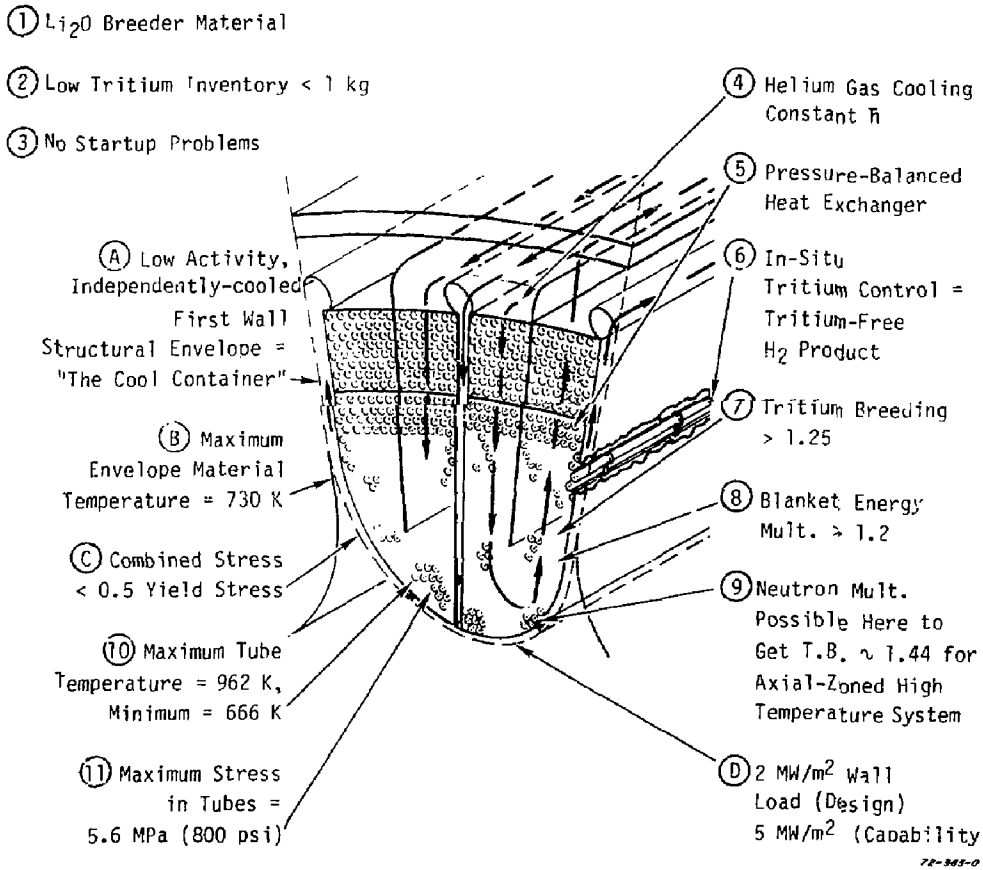

Fig. 1.5 Cross section through the Canister blanket showing its main features

Blanket standpoint is that the temperature requirements of the blanket can be reduced dramatically. The exit temperature of the coolant from the Canister blanket is as low as 825 K as compared with ~ 1200 K exit temperature for our alternate design.

In this particular Canister blanket we have elected to use a combination of solid lithium oxide as the moderator and helium as the coolant in the belief that gas-cooled "dry" blankets offer distinct advantages of simplicity, safety and ease of startup and shutdown over those blankets using some combination of water, liquid metals and/or molten salts. We also use "in situ" tritium control rather than slip stream processing to assure that our hydrogen product is tritium free. In situ tritium control isolates the tritium from the main helium flow. Recovery of the tritium is by an independent purge circuit.

The four candidate structural materials we examined were 316 SS, 2-1/4 Cr - 1 Mo, Inconel 800H and Tenelon. The structural material selected for the blanket is Tenelon (an Fe-Mn-Cr austenitic stainless steel), chosen for its low residual radioactivity. The waste disposal rating (WDR)* of Tenelon is 0.40, a very low value which is desirable. This means that surface disposal of spent blankets is acceptable and deep burial is not required. By comparison the 2-1/4 Cr-Mo has a WDR of 15. Tenelon also has very attractive neutronic performance and structural properties.

The summary and conclusions on this blanket are divided into two principal areas of design; (a) those having to do with the Canister structural envelope followed by (b) the Canister moderating volume and hot shield, both shown in Fig. 1.5. Succeeding Figs. 1.6, 1.7 and 1.8 illustrate the overall assembly.

---

* The WDR is a measure of how much an activated material has to be diluted with inert material to provide for disposal.

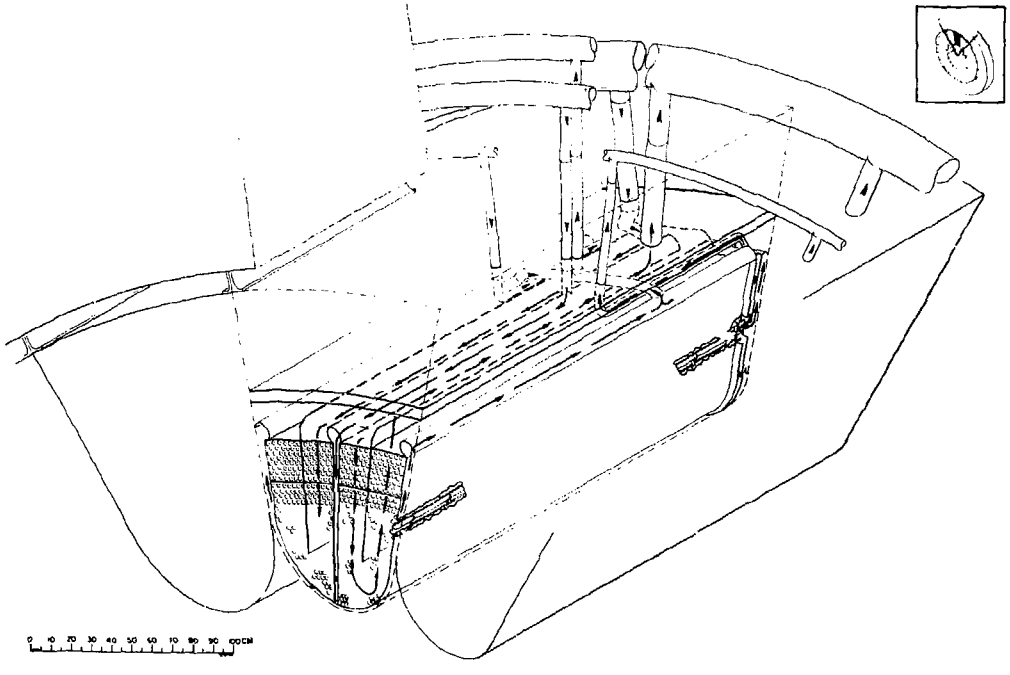

72-297-011

Fig. 1.6 Manifolding to ring headers is offset for assembly

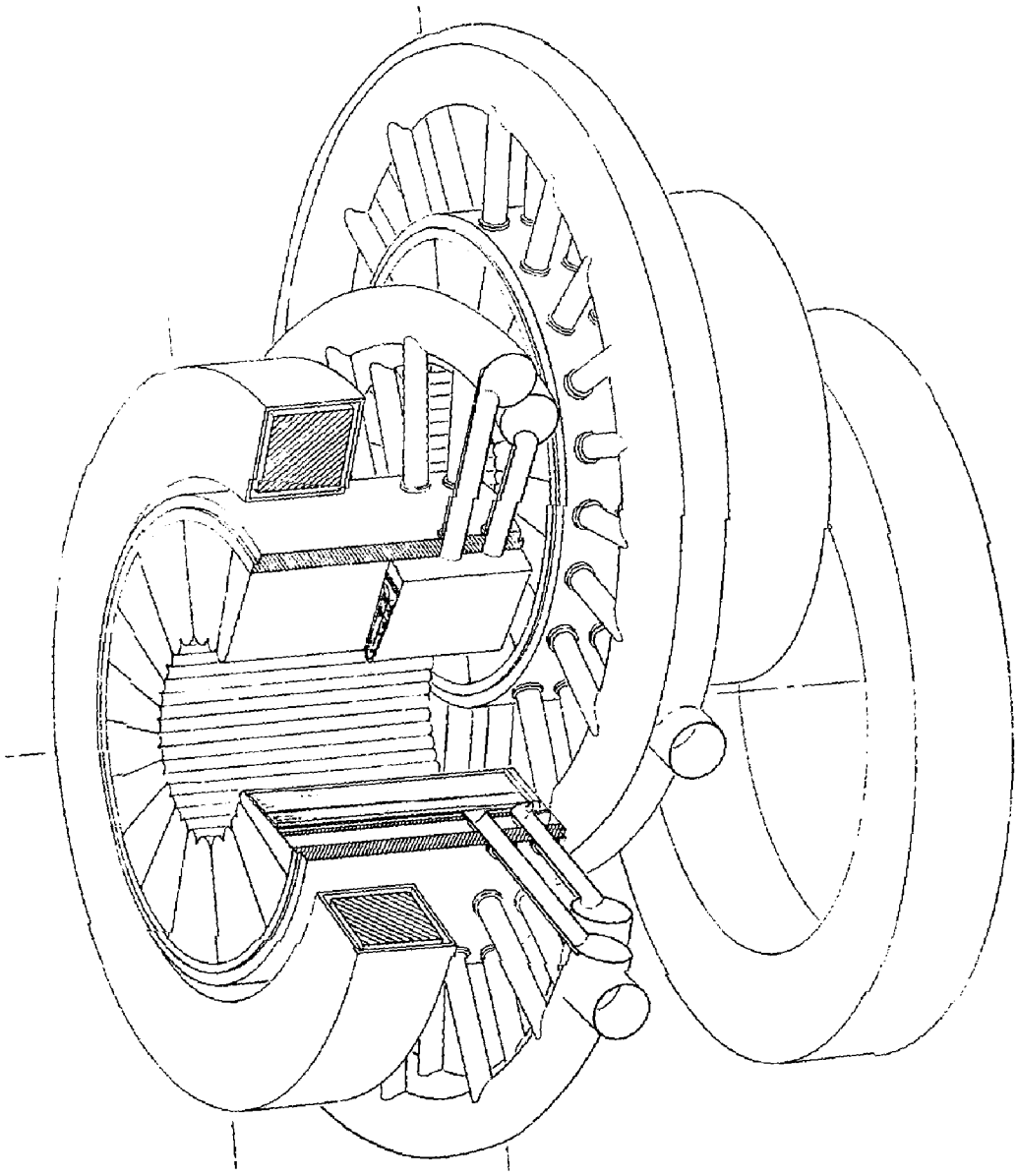

72-385-D12

Fig. 1.7 Ring module assembly

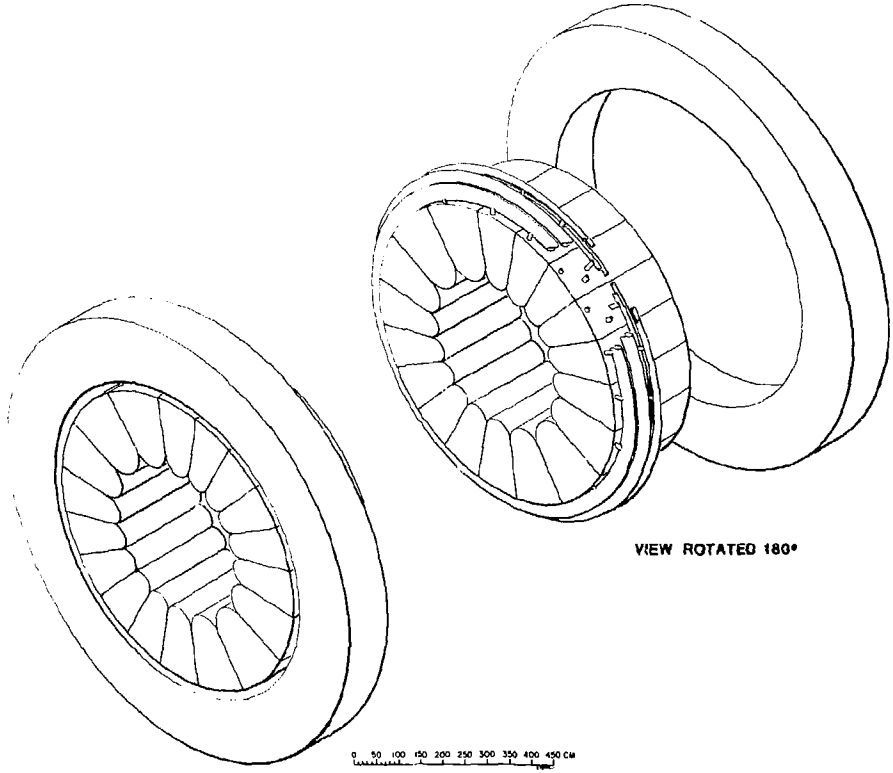

Fig. 1.8 The ring module installation is straightforward - solenoids stay in place

1.5.1 The Canister Structural Envelope: Data Summary and Conclusions

Table 1.2 lists the significant set of numerical values for the Canister envelope and first wall structure. The principal features of the design can be summarized as follows:

a) The Canister structural envelope, including the first wall, is purposely designed to run cooler than the moderating elements inside it; the maximum envelope temperature of only about 731 K is maintained by a separate helium coolant circuit. This is called the cool container concept.

b) The relatively cool structural temperature allows the Canister envelope to serve as a pressure vessel for the 5 MPa helium coolant flowing through the blanket moderating volume.

c) The combined hoop and thermal stress in the first wall is only about half the yield stress of the Tenelon alloy we have selected and less than 40% of the minimum stress for rupture in 3 years.

d) The fractional pressure drop in the first-wall helium coolant is only about 0.10%, resulting in a very small ratio of pumping power required to thermal power removed of only 0.17%.

e) The "cool container" concept allows great flexibility in the design of the Canister itself as well as the design of the tube-bank breeder blanket and hot shield inside it.

f) There appears to be sufficient strength of the Tenelon to allow moving the Canisters closer to the plasma up to a neutron wall loading of almost 5 MW/m^2. This has the possible advantage of decreasing the size and cost of the blanket and central cell magnet coils (at the expense of much shorter blanket lifetimes).

Table 1.2 *The Canister structural envelope and first wall data summary*

Neutronics of Plasma Heat Loads	
Design neutron wall loading, Γ_N	2 MW/m^2
Possible max. neutron wall loading	5 MW/m^2
Volumetric heat generation	18.34 MW/m^3 for Γ_N = 2.0
Incident charged particle flux to FW	2×10^4 W/m^2
Structural	
Plate thickness, first wall	0.006 m
Material	Tenelon
Maximum material temperature	731 K
Maximum combined stress	136 MPa
2/3 yield stress, Tenelon at 750 K	275 MPa
Thermal-Hydraulic of First Wall Flow	
Coolant medium	Helium
Pressure	5 MPa
Inlet temperature	525 K
Outlet temperature	625 K
Reynolds No.	5676
Nusselt No.	20.3
Flow velocity	10.18 m/s
Pressure drop	5158 Pa (< 1.0 psi)
Pumping power/half Canister	210 W
Power removed by first-wall coolant per half Canister	0.12 MW
% pumping power in cooling the first wall	0.17%

1.5.2 The Canister Moderating Volume and Hot Shield

Table 1.3 lists the Canister moderating volume and hot shield performance data. The principal features of the design can be summarized as follows:

a) The concept of the use of a solid Li_2O breeder material inside of tubes arranged as a two-pass, cross-flow heat exchanger appears to be very attractive.

b) This arrangement separates the tritium from the main helium flow which reduces the tritium recovery problems and makes the isolation of the tritium from the synfuel plant very effective.

c) The small purge helium flow inside the tubes for removing tritium from the Li_2O need only be at one or two atmospheres lower pressure than the main helium coolant flow to ensure that almost no tritium will get into the main flow in the event of a leak. This allows the hot tubes to be thin and still operate at very low stress levels, since they are almost pressure balanced.

d) The closely-spaced, cross-flow tube bank arrangement results in almost uniform tube wall temperatures around the circumference and high heat transfer coefficients; this helps to avoid hot spots on the tube walls.

e) The maximum tube wall temperature is only about 810 K at the worst point (near the exit of the second breeder section); it is only about 758 K where the combined stresses are a maximum of 5.6 MPa. These stresses are very low for Tenelon, about 3% of the 3-year rupture life.

f) The maximum and minimum Li_2O temperatures are 962 K and 666 K, respectively. This range of temperatures should result in good tritium release from the Li_2O and low tritium inventories.

Table 1.3 Summary of the canister performance data

Overall Central-Cell Blanket	
Number of ring modules	75
Number of half Canisters/ring module	36
Number of tubes and rods/half Canister	542
Neutronics	
Volumetric heat generation near the first wall for Γ_N = 2.0 MW/m^2:	
Li_2O cartridges	13.5 MW/m^3
Tenelon tubes	18.0 MW/m^3
Structural : Tubes	
Tube and rod material	Tenelon
Tube outer diameter	0.020 m
Tube wall thickness	0.0005 m
Tube nominal length	2.0 m
Maximum hoop stress	4.0 MPa
Maximum thermal stress	2.7 MPa
Maximum combined stress	6.7 MPa
Tube wall temperature (at exit of TA region where stress is maximum)	758 K
Creep rupture stress of Tenelon at 758 K (3 yr)	250 MPa
Structural: Tritium Breeder Material	
Solid breeder material	Li_2O
Percent theoretical density	90%
Assembled shape	Hollow cylinder

Table 1.3 con't.

Structural: Tritium Breeder Material con't	
Inner diameter	0.006 m
Outer diameter	0.017 m
Maximum thermal stress (estimated)	∿ 35 MPa
Tensile fracture stress (estimated)	∿ 69 MPa
Maximum temperature at inner surface (at exit of turnaround zone)	962 K
Minimum temperature at inner surface (at inlet to first breeder zone)	666 K
Thermal-Hydraulics of Tube Bank	
Coolant	Helium
Pressure	5 MPa
Inlet temperature	625 K
Outlet temperature	825 K
Minimum gap between tubes	0.002 m
Maximum Reynolds number	∿ 34,000
Maximum flow velocity	∿ 16 m/s
Average heat transfer coefficient	∿ 2000 W/m^2-K
Pressure drop inside Canister	0.016 MPa
Pumping power/half Canister	5.71 kW
Power removed by tube bank coolant/half Canister	1.12 MW
% pumping power in booling Canister tube bank	0.51%

g) The fractional pressure drop across the tube bank is only 0.32%, which results in a ratio of the pumping power required to the thermal power removed of only 0.51%.

h) A great deal of refinement and optimization of the tube bank design is possible, since some tailoring of the tube diameters and spacings can be used to compensate for the near-exponential decrease in the internal heat generation.

1.6 REACTOR BLANKET DESIGN, THE CANISTER/HIGH TEMPERATURE AXIALLY ZONED BLANKET WITH THE FLUIDIZED BED DECOMPOSER - OPTION 2

The Canister blanket discussed here is a high temperature design to be used in conjunction with the medium temperature design discussed in Section 1.5. This high temperature design does not breed tritium but instead relies upon the medium temperature design to provide the tritium breeding. The high temperature energy partition is accomplished by axially zoning the TMR into high and medium temperature zones as shown in Fig. 1.9. The required fraction of axial length for high temperature thermal energy involves a tradeoff between the fraction of high temperature energy supplied to the thermochemical process and the overall tritium breeding ratio.

Tritium breeding was excluded from the high temperature blanket to allow direct coupling with the SO_3 decomposer (1100 K) without concern for tritium contamination of the thermochemical process. An intermediate heat exchanger could be used to provide tritium isolation; however, this would increase maximum blanket temperature (from 1175 K to about 1375 K) to account for the necessary temperature differences in the heat exchanger. This was not considered to be an acceptable option at this stage of the study.

The primary advantage of providing high temperature thermal energy direct to the decomposer is the higher thermal energy utilization. The overall plant efficiency when using the direct-coupled fluidized bed decomposer is 43% as compared to 38% for the medium temperature blanket and

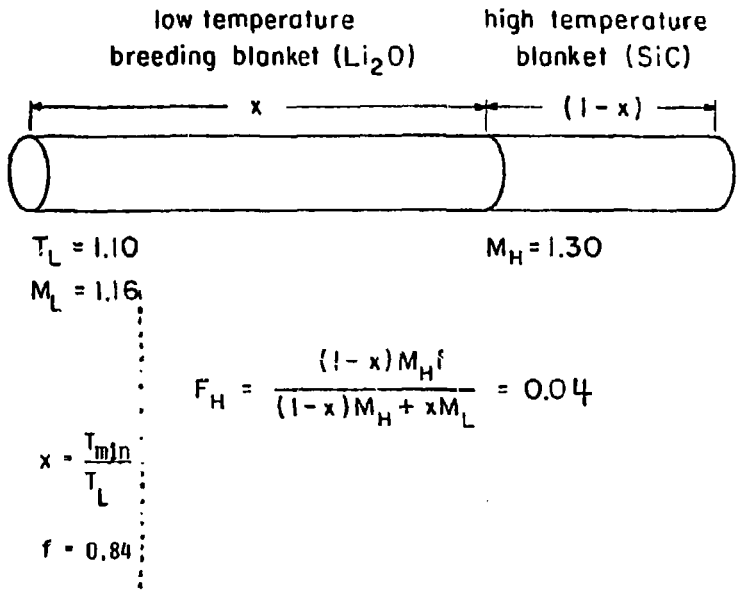

Fig. 1.9 Schematic of an axial-zoned TNR with low and high temperature modules

the Joule-Boosted decomposer. The primary disadvantage is the problem of finding materials with acceptable strength and chemical properties operating at $\sim$ 1100 K.

The design philosophy for the high temperature blanket is very similar to the medium temperature blanket. A gas-cooled Canister design was selected as shown in Fig. 1.10. It is intended to fit into the same modular structure shown in Figs. 1.6, 1.7 and 1.8.

1.6.1 The Canister Structural Envelope: Data Summary and Conclusions

Table 1.4 lists performance data for the Canister envelope and first wall structure. The principal features of the design can be summarized as follows:

a) The Canister wall is cooled by helium entering at 750 K and exiting at 800 K. The maximum wall temperature is 835 K and occurs at the "nose" of the Canister.

b) The relatively cool Canister wall allows the Canister to serve as the pressure vessel and contain the system pressure (50 atm).

c) The arrangement of Canisters is such that they are mutually self supporting. The stresses of concern are primarily thermal stresses and hoop stresses in the nose region. The hoop stress for a 6-mm-thick wall is a reasonable 110 MPa (13000 psi).

d) The pressure drop through the 3 mm coolant channel is 0.56 atm.

1.6.2 The Canister High Temperature Region

Table 1.5 lists performance data for the high temperature region. The principal features of the design are summarized as follows:

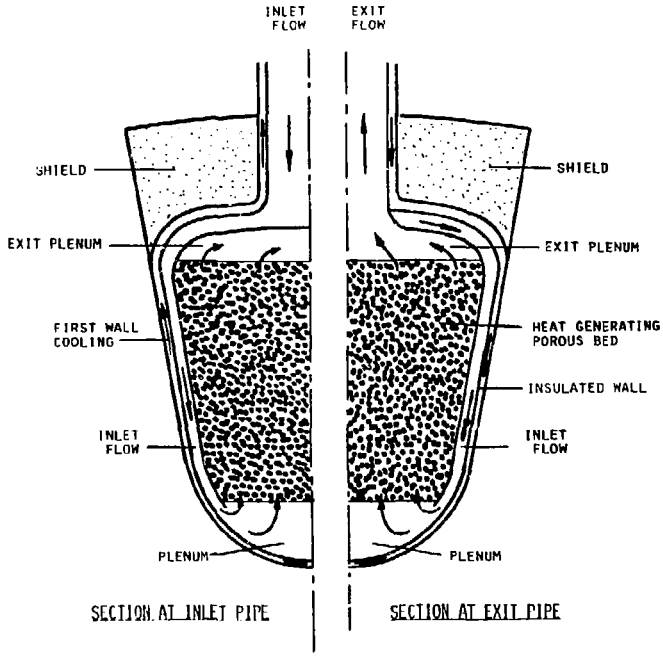

Fig. 1.10 Cross section illustration of the high temperature blanket canister

Table 1.4 The high temperature Canister structural envelope and first wall data summary

Neutronics of Plasma Heat Loads	
Design neutron wall loading	2 MW/m^2
Volumetric heat generation	18.34 MW/m^3
Structural	
First wall thickness	0.006 m
Maximum wall temperature	835 K
Maximum hoop stress	110 MPa
Thermal-Hydraulics of First Wall Flow	
Coolant	Helium
Pressure	50 atm
Inlet temperature	750 K
Outlet temperature	800 K
Channel thickness	0.003 m
Reynolds No.	28800
Nusselt No.	74.5
Flow velocity	59 m/s
Pressure drop	0.56 atm
Maximum wall temperature	835 K

Table 1.5 Summary of the high temperature Canister performance

Neutronics	
Volumetric heat generation:	
for Γ_N = 2.0 MW/m^2:	
Spheres (average)	17.5 MW/m^3
Spheres (maximum)	34.1 MW/m^3
Structural	
Sphere diameter	0.015 m
Core support wall thickness	0.003 m
Inlet channel thickness	0.025 m
Insulation thickness	0.01 m
Maximum sphere thermal stress	12.8 MPa
Thermal Hydraulics	
High temperature region overall:	
Coolant	Helium
Pressure	50 atm
Inlet temperature	1140 K
Outlet temperature	1160 K
Pressure drop	0.164 atm
Sphere bed:	
Reynolds No.	34000
Superficial flow velocity	16 m/sec
Heat transfer coefficient	1778 W/m^2-K
Pressure drop	0.021 atm
Maximum temperature	1175 K
Inlet Channel:	
Reynolds No.	91300
Flow velocity	31 m/sec
Heat transfer coefficient	1125 W/m^2-K
Pressure drop	0.011 atm

a) The non-breeding high temperature neutron moderating region is considered to be a porous bed of 15 mm diameter silicon carbide spheres. (While spheres were used for the current design, other forms could possibly be used to advantage.)

b) The high temperature region is separated from the Canister wall by the first wall cooling channel, an insulated wall, and the inlet flow channel. The insulated wall reduces the heat loss from the high temperature inlet stream to the first wall coolant.

c) The total energy available at high temperature is 84%. The remaining 16% is lost to the first wall coolant (12%) and to the shield (4%).

d) The high temperature region operates at 50 atm and is pressure balanced with the first wall coolant. The high temperature structure need only be self supporting.

e) The pressure drop of the primary helium flow through the entire Canister is 0.17 atm.

f) The maximum structural temperature is estimated to be 1175 K.

1.6.3 General Conclusions

Since the high temperature Canister blanket must operated in conjunction with the medium temperature blanket and synfuel plant, the following general conclusions are made:

a) Axial zoning is an attractive option for a fusion reactor designed to produce high temperature heat for a synfuel plant. The physical separation of the high temperature energy recovery and tritium breeding has the virtue of blanket module simplicity.

b) Since the high temperature blanket does not breed tritium, the medium temperature blanket must be a high breeder for the overall breeding ratio to be 1.1. This would require the use of a neutron multiplier to enhance the tritium breeding ratio to $\geq$ 1.4. Of the options considered thus far, the most promising appears to be a Li_2O design with a lead-zirconate multiplier.

c) Absolute helium pressure of about 50 atm is necessary to maintain acceptable pressure drop. The system pressure is contained by the specially cooled first wall (pressure boundary) and helium transport piping. The heat exchanger tubes of the fluidized bed decomposer must also contain system pressure and at high temperature.

d) The direct-coupled high temperature blanket concept presented here offers a high thermal efficiency for hydrogen production. The success of realizing this efficiency will require a high breeding medium temperature blanket and a successful heat exchanger design for the SO_3 decomposer.

1.7 "IN SITU" TRITIUM CONTROL - PRODUCING A TRITIUM-FREE HYDROGEN PLANT

We propose to fill the tubes shown in the Canister blanket module of Fig. 1.5 with half washers or split rings of Li_2O. The advantage of this shape is that the Li_2O cartrides are "pre-cracked" axially and radially so that thermal stress problems can be minimized. The sub-assembly is thus a long tube filled with half washers or split rings, as shown in Fig. 1.11. These filled tubes are assembled in the Canister normal to the helium coolant flow. The tubes are rigidly mounted in a tube sheet at one end of the blanket only, to allow for thermal expansion.

Purge flow helium is introduced into the annular gap around the outside of the Li_2O and returns through the tube center for tritium removal. The purge flow quantity may be less than 1% of the total flow. This circuit is

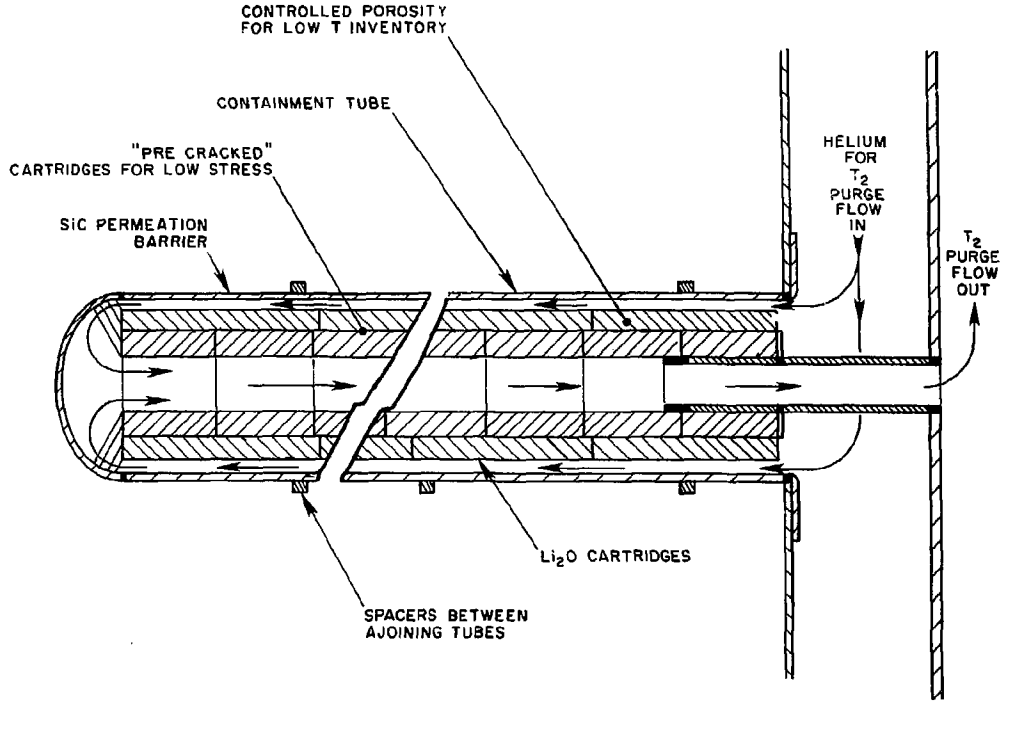

Fig. 1.11 Isolation of the Li_2O from mainstream coolant provides for "tritium-free" hydrogen product

completely separate from the main stream helium. The purge helium pressure is adjusted to be slightly less than the main flow helium pressure. The assembly of tubes are mutually supporting, separated by helically wound wires or by staggered rings.

The tubes must have low permeation for tritium since the main reason the tubes are used is to minimize the tritium release from the Li_2O to the main helium coolant stream. The other reason for placing the Li_2O in a tube container is to protect the Li_2O from possible disintegration due to the high velocity helium flow or chemical attack by trace impurities in the main helium flow.

The practical metals, such as our design choice of Tenelon, for use as Canister material or high temperature heat exchangers are too permeable to tritium to act as significant barriers. A thin coating (100 μm) of siliconized SiC on the inside or the outside of each tube would greatly reduce the permeation of tritium into the main helium coolant. At the operating temperature it can be postulated that the coating is self healing. It is calculated that only 900 std cc per day would permeate at 950 K into the main coolant. By slip stream processing 10^{-4} of the main helium coolant for tritium removal following the in situ control, the amount permeating into our *intermediate process steam cycle, for example, would be only* 1 *std cc/day.* This assumes another permeation barrier such as alumina is used on the tubes in the intermediate heat exchanger.

1.8 PROGRESS IN NEUTRONICS

In addition to the development of the neutronics data base necessary to support the present design of both the Joule-Boosted and the two-zone blankets, neutronics results have been obtained which have more general significance.

The combined use of a high density solid lead neutron multiplier together with a Li_2O breeding region makes a very versatile and synergistic

combination. Such a combination is very attractive in achieving acceptable tritium breeding rates with relatively thin blankets, very high tritium breeding rates (for auxiliary tritium supplies), or increasing energy deposition in a hot shield. Although lead zirconate (Zr_5Pb_3) has been used in the present work, some other solid lead compound might also be used if Zr_5Pb_3 is unacceptable for some reason.

The presence of a high Z material immediately behind the first wall has been shown to be an effective method for reducing the first wall power density for a given first wall loading. This result is produced by preferential absorption of gamma rays in the high Z material.

Tenelon has been shown to be a very attractive structural material. The combination of impressive neutronics performance together with high temperature materials properties is impressive and perhaps unique among structural materials that have been studied thus far.

1.9 THE JOULE-BOOSTED DECOMPOSER

The Joule-Boosted decomposer uses electrical energy to heat SiC heating elements to almost 1300 K. Such a decomposer design is depicted in Fig. 1.12. Large SiC heating elements, $\sim$ 5 cm in diameter and 3-m long, are arranged vertically with the process gases fed in crossflow, very similar to commercial crossflow shell and tube heat exchangers. The high effectiveness of this decomposer is evident from Fig. 1.13 where the conversion fraction is $\sim$ 84%, compared to 64% for the fluidized bed decomposer, our parallel design. The former can run 200 K hotter as a result of the Joule Boosting.

1.10 THE FLUIDIZED BED DECOMPOSER

Figure 1.14 illustrates a decomposer which provides the necessary production of SO_2 by efficiently using the high temperature heat from the two-zone blanket, our alternate blanket design. The decomposer is a catalytic fluidized bed reactor operating at 1100 K. The unit contains internal

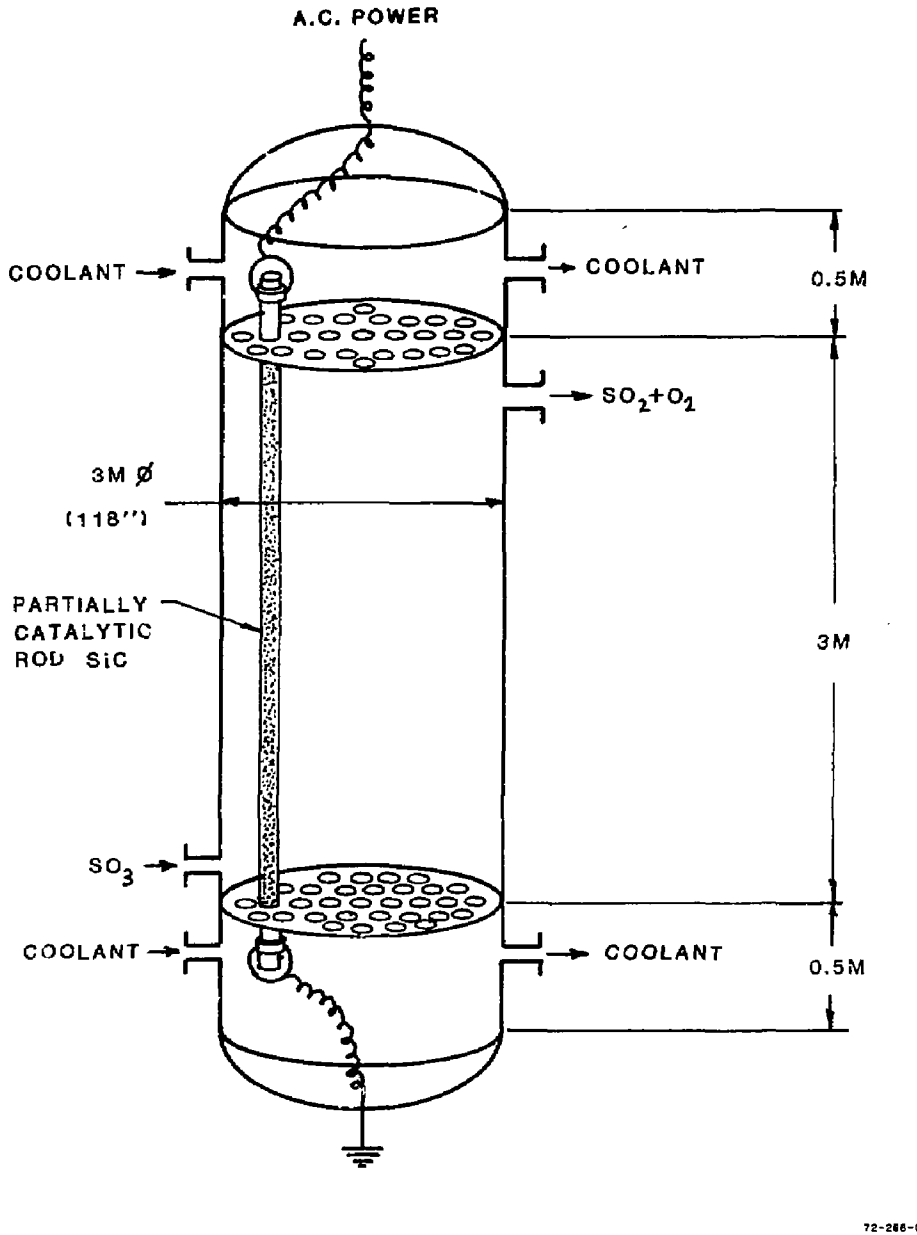

Fig. 1.12 Joule-Boosted decomposer

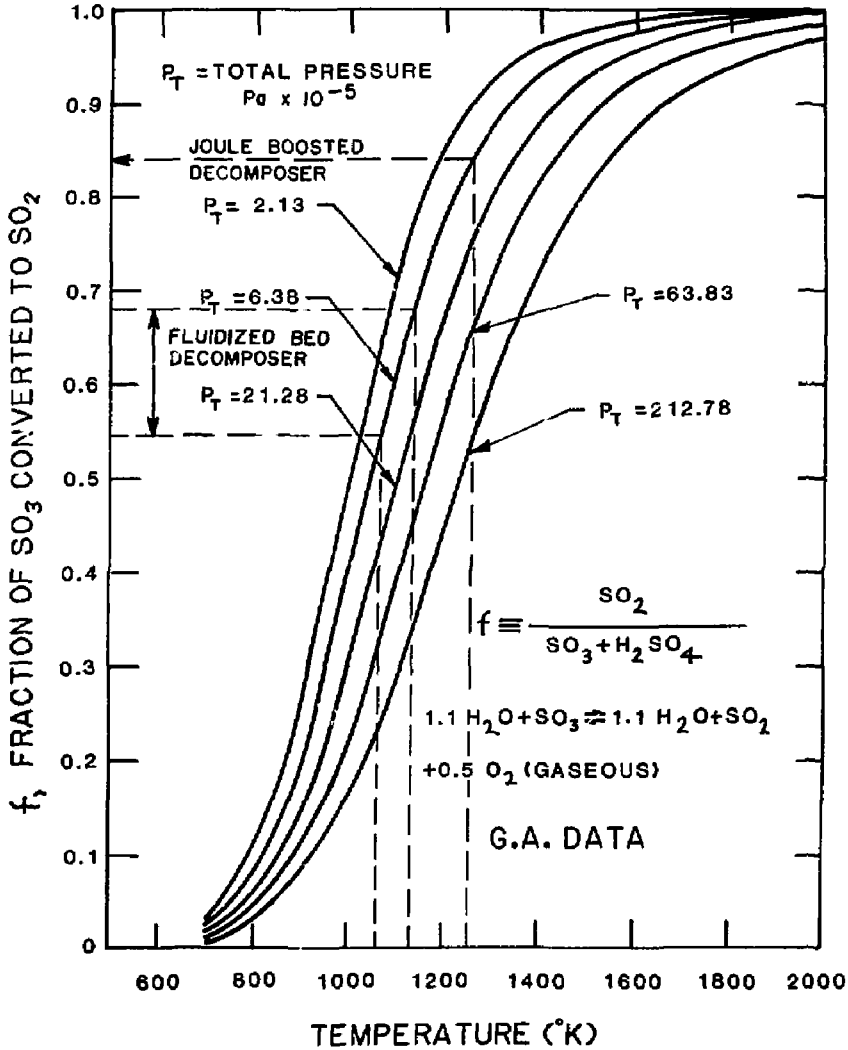

72-268-2

Fig. 1.13 Equilibrium decomposition curves for SO_3

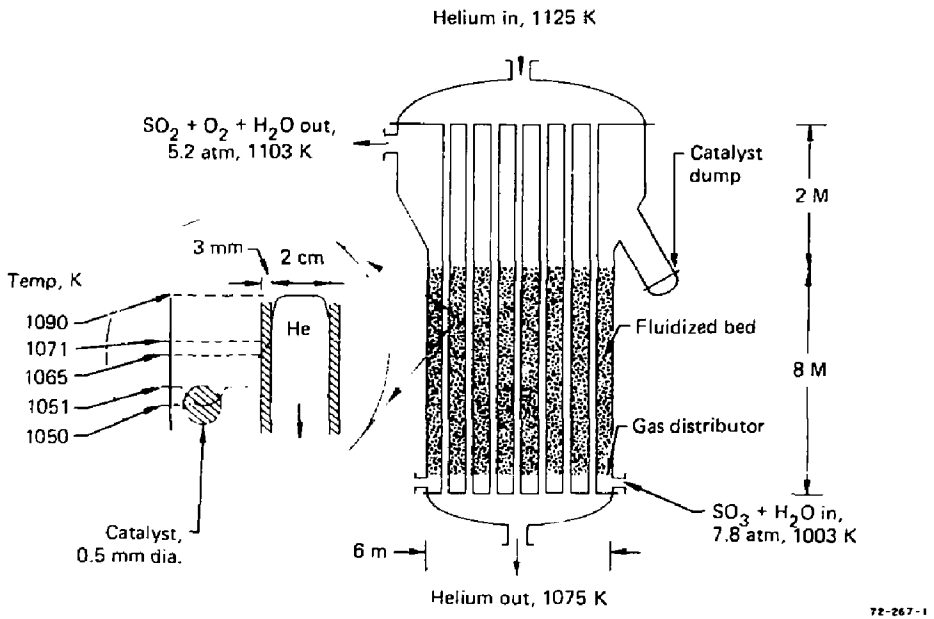

Fig. 1.14 Fluidized bed decomposer

heat exchanger tubes to provide the heat for the highly endothermic SO_3 decomposition. A 65% conversion can be obtained using a CuO catalyst, if sulfation of the substrate does not become a problem around 1050 K, or a more expensive platinum catalyst on a titania support can be used if sulfation is a serious problem.

1.11 MATERIALS

For the selection of materials in the corrosive atmosphere of the GA cycle four equations describe the four sections of the thermochemical plant:

Section I	$SO_2 + xI_2 + H_2O \rightleftarrows H_2SO_4(l) + 2HI(l)$
Section II	$H_2SO_4 \rightarrow H_2O + SO_2 + 1/2\ O_2$
Section III	$2HI_x \rightarrow 2HI + (x-1)I_2$
Section IV	$2HI \rightarrow H_2 + I_2$

An extensive materials testing program be carried out by GA during the process development effort. Since sulfuric acid is common to other thermochemical cycles and is industrially significant, other workers have extensively investigated materials for the H_2SO_4-H_2O system which we have taken advantage of in choosing materials.

A great deal of data exists on corrosion in iodine systems. Table 1.6 presents a summary of the test results. Early results indicated that niobium was an additional material impervious to attack by the HI-I_2-H_2O solutions typical of the main solution reactor, but the most recent work regarding the effect of the H_2SO_4 upon the system questions the use of niobium in this portion of the process. Tantalum can be substituted for the niobium, at higher cost, but this has not been done in the present equipment design.

Although glass-lined steel is an ideal material for use with the HI-I_2-H_2O system, it is unavailable in the equipment sizes required for the TMR-powered plant. Fluorocarbon-lined steel performs the same function and is available in the desired equipment sizes.

Table 1.6 Material candidates for handling process fluids containing HI_x and I_2

PRINCIPAL UNIT OPERATIONS	FLUIDS	TEMPERATURE RANGE		MATERIAL CANDIDATES FOR: HEAT EXCHANGERS, VESSELS, PUMPS AND HARDWARE
		°C	K	
MAIN SOLUTION REACTION	$SO_2 + I_2 + H_2O \longrightarrow$ $HI_x + H_2SO_4$ (55 wt % ACID)	125	398	GLASS-LINED STEEL; CERAMICS – SiC, Al_2O_3, CARBON FLUOROCARBON PLASTICS & ELASTOMERS; IMPERVIOUS GRAPHITE TANTALUM
I_2 AND H_2O SEPARATION	$HI_x + H_3PO_4$	120–158	393–431	GLASS–LINED STEEL; HASTELLOY B–2; TANTALUM–LINED STEEL; FLUOROCARBON PLASTICS
I_2 RECYCLE	I_2	120	393	HASTELLOYS B–2, G, C–276; GLASS
DECOMPOSITION OF LIQUID HI_x	HI_x (LOW H_2O); I_2; H_2	120	393	HASTELLOY B–2; GLASS–LINED STEEL; FLUOROCARBON PLASTICS;

72-487-0

Material selection for Sections III and IV is similar to that selected for Sections I and II. The information in Table 1.7 is applicable to the sulphuric acid section of the process.

1.12 A PLOT PLAN FOR THE HYDROGEN PLANT

An artist's conceptual drawing of the plot plan as given in last year's report is shown in Fig. 1.15. Changes in this year's design did not materially affect space requirements, so this plot plan still gives a rough idea of the approximate land area and relative sizes of the TMR nuclear island, turbine generator, steam generator and process heat exchanger building, as well as the rest of the chemical plant. We conclude from the plot plan that this plant is quite compact, and raises no new issues regarding heat transport distances, safety, etc.

1.13 PROGRESS IN MEETING THE HIGH TEMPERATURE REQUIREMENTS OF THE PROCESS

Roughly 22-25% of the energy demand of the thermochemical plant is at high temperature (> 1050 K) and is required to decompose SO_3 to SO_2, which is the final step in the H_2SO_4 decomposition. The remaining energy requirement is at much lower temperature.

Our introduction of the Joule-Boosted decomposer concept is an important system improvement in Fusion/Synfuels compatibility allowing very high SO_3 decomposition temperatures ($\sim$ 1250 K) to be provided electrically but significantly relaxing temperature demands on the reactor blanket to as low as 825 K exit gas temperature. This Joule Boosting works by using the unique high voltage direct current output from the TMR plus some additional electricity that is thermally derived from the blanket. The electric power produces high temperatures using electrical heating elements right in the decomposer itself rather than delivering high temperature process heat.

A fluidized bed decomposer, which we also introduced during the course of our study, requires the use of higher temperature $\sim$ 1200 K blankets.

Table 1.7 Candidate materials-of-construction for sulfuric acid

PRINCIPAL UNIT OPERATION	FLUIDS	APPROXIMATE FLUID TEMPERATURES		MATERIAL CANDIDATES FOR: HEAT EXCHANGERS, VESSELS, PUMPS AND OTHER HARDWARE
		°C	°K	
MAIN SOLUTION REACTION	$SO_2 + I_2 + H_2O \longrightarrow$ $HI_x + H_2SO_4$ (55 wt %)	125	398	GLASS-LINED STEEL; FLUOROCARBON PLASTICS & ELASTOMERS; CERAMICS–SiC, Al_2O_3, CARBON; IMPERVIOUS GRAPHITE TANTALUM
CONCENTRATION	H_2SO_4 55–65 wt %	95–150	368–423	HASTELLOYS B–2 OR C–276 IMPERVIOUS GRAPHITE; GLASS OR BRICK-LINED STEEL
CONCENTRATION	H_2SO_4 65–75 wt %	150–180	423–453	HASTELLOYS B–2 OR C–276 IMPERVIOUS GRAPHITE; GLASS OR BRICK-LINED STEEL
CONCENTRATION	H_2SO_4 75–98 wt %	180–420	453–693	BRICK-LINED STEEL; CAST Fe–14 wt % Si
VAPOR FORMATION AND DECOMPOSITION	$H_2SO_4 \longrightarrow H_2O + SO_3$	330–600	603–873	*BRICK-LINED STEEL; CAST Fe–14 wt % Si* SILICIDE COATINGS ON STEEL; HASTELLOY G
VAPOR DECOMPOSITION	$SO_3 + H_2O \longrightarrow$ $H_2O + SO_2 + 1/2\ O_2$	600–850	873–1123	INCOLOY 800H WITH ALUMINIDE COATING

72-438-D

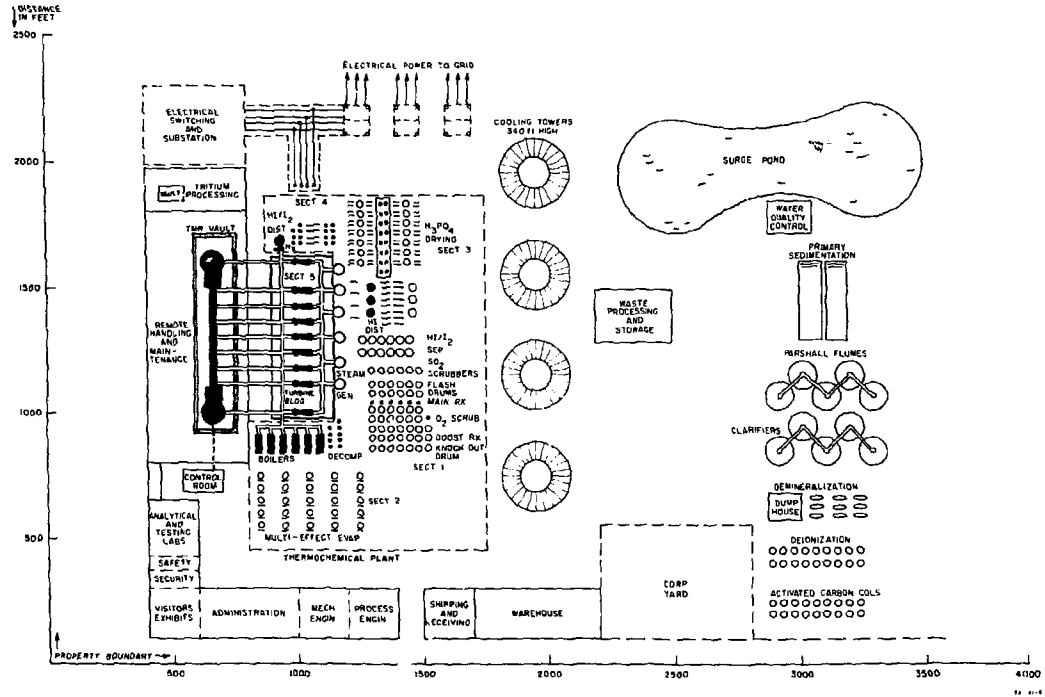

Fig. 1.15 Plot plan for the hydrogen plant

The fluidized bed is also a significant system improvement in reducing blanket temperatures compared to its pebble bed predecessor that started our study. Figure 1.16 illustrates very vividly how we have been able to reduce blanket temperatures using fluidized bed or Joule Boosting.

1.14 MATCHING POWER AND TEMPERATURE DEMANDS - PERFORMANCE AND EFFICIENCY EVALUATIONS FOR THE JOULE-BOOSTED DECOMPOSER

1.14.1 Option 1

In order to satisfy the interfacing requirements, the Tandem Mirror Reactor (TMR) interface must be designed to supply all the electrical and thermal power demands of the thermochemical plant (TCP) after satisfying all the TMR internal and auxiliary demands. In addition, the TCP thermal power demands must be supplied to each section of the synfuel plant at the correct temperatures. The heat exchangers, steam generators and power plants which comprise the actual interface are shown on Fig. 1.17 in greatly simplified form for the Joule-Boosted decomposer (JBD) concept.

A straightforward procedure has been presented for performing the interface power and temperature matching between the TMR and the thermochemical plant (TCP) for preliminary design purposes. For the Joule-Boosted decomposer (JBD) concept, an overall TCP efficiency of about 30% is predicted for the reference case (with a steam power plant efficiency of 35%). Improvements in the thermochemical plant which reduce the thermal demand by 100 kJ_t/mole H_2 and the electrical demand by 20 kJ_e/mole H_2 can raise the TCP efficiency to about 36% (using the improved estimate of the steam power plant efficiency of 38%).

This TCP efficiency appears to be achievable with remarkably low helium coolant temperatures compared to most other processes for synthetic H_2 production. The helium exiting the blanket and direct converters need only be at about 825 K, while the helium exiting the first wall need only be at about 625 K. This should lead to a very credible and cost-effective synfuel plant.

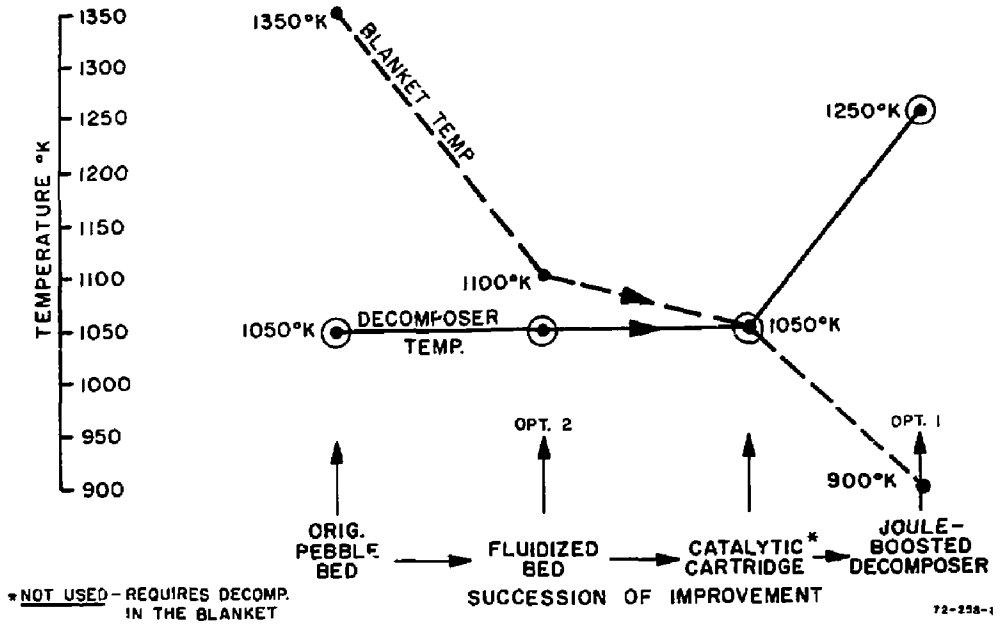

Fig. 1.16 Progress in lowering blanket temperature and raising decomposer temperature

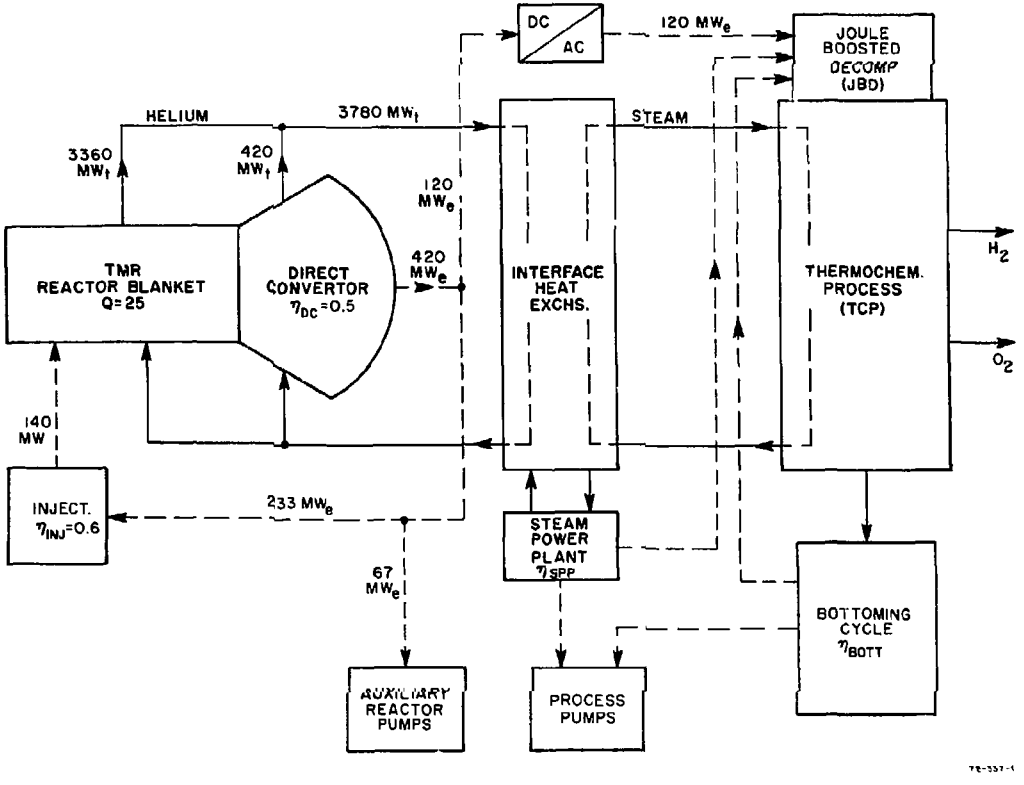

Fig. 1.17 Simplified energy balance - TMR/Synfuels for the Joule-Boosted decomposer concept

1.14.2 Option 2

Option 2 is concerned with the direct transfer of high temperature thermal energy from the TMR to the thermochemical process. This is done by replacing the Joule-Boosted decomposer with a fluidized bed decomposer (FBD) which is driven by a helium transport loop from the high temperature blanket as shown in Fig. 1.18

By using the same data and by following the same methodology as for Option 1, the FBD achieves an overall efficiency of 43%. This requires that 34% of the blanket thermal energy be delivered at 1160 K with a return stream temperature of 1040 K. The remaining lower temperature thermal energy is supplied at a maximum of 825 K with a return stream at a minimum of 525 K.

The successful use of the FBD concept will require resolution of two important issues. The first issue is the simultaneous satisfaction of the required high temperature energy fraction and tritium breeding. Since the high temperature blanket does not breed tritium, all tritium production must be done in the low temperature blanket. The second issue is a satisfactory design of the SO_3 decomposer heat exchanger. The current FBD operating at 7 atm and 1100 K must have a heat exchanger tube design to contain the primary helium at 50 atm and 1160 K. With resolution of these issues the FBD concept can offer a greater degree of thermal utilization for the TMR.

1.15 COST OF PRODUCING THE HYDROGEN

The production of hydrogen using the TMR energy source and the GA thermochemical cycle has good economic promise. Our preliminary cost estimate indicates a price of $12/GJ for the FBD and $15/GJ for the JBD (1980 dollars). In comparison, a barrel of oil priced at $50 at the wellhead and valued at $75/bbl after refining has a cost of $12.30/GJ.

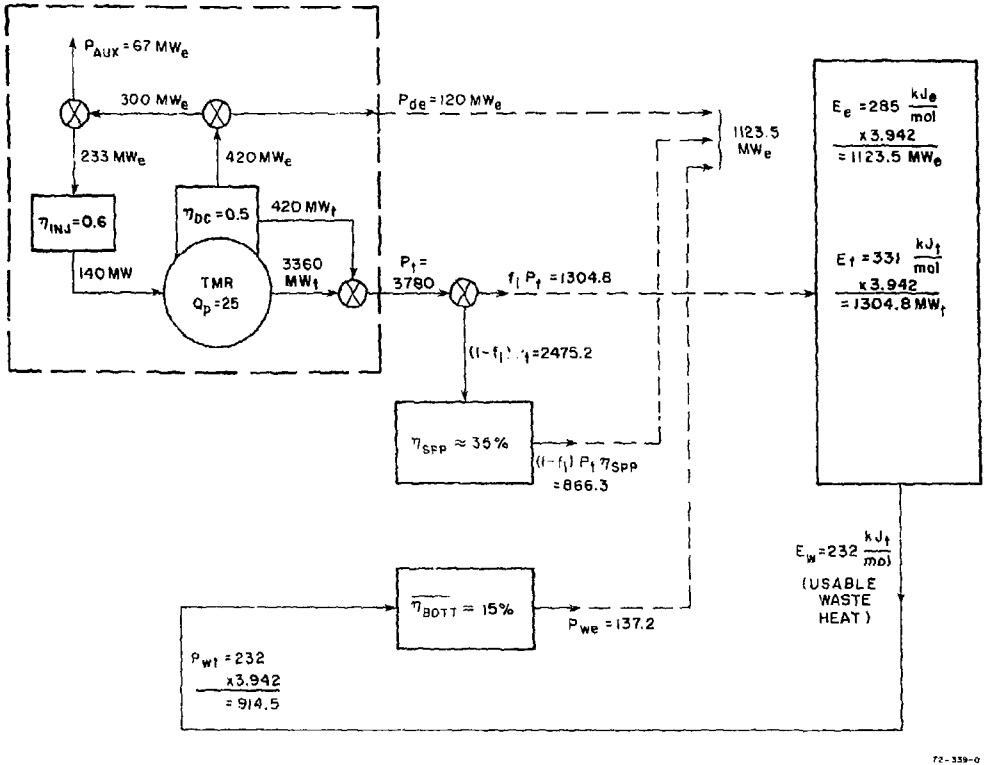

Fig. 1.18 Power balance diagram for the Joule-Boosted decomposer concept (with vapor recompression in Section III and some pressure staging in Section II)

1.16 CHEMICAL PLANT OPERATIONAL DEPENDABILITY

With an appropriate degree of process unit redundancy that we have included, we can predict a high, combined TMR/chemical plant availability of ∿ 74%, and this figure is included in our cost figures for the hydrogen produced.

1.17 PROBLEM AREAS

Blanket design remains an area of principal concern but is progressing well. Even with Joule Boosting or fluidized bed decomposers relaxing the temperature demands of the blanket, the design is difficult because of the myriad demands the blanket must satisfy. Much more attention is needed here. This concern is true for all blankets--for synfuels, for electricity, for co-generation, for hybrids. We feel that we have converged on a highly effective design approach using the non-flowing lithium-oxide blanket module with helium as a coolant. The module shows strong promise of being functional over a range of temperatures useful for synfuel production for electrical power production, or both.

In the chemical plant we wish to make substantial improvements in the HI separation and purification. This process requires a large amount of power and has high capital costs (∿ 1/3 of the chemical plant).

The fluidized bed decomposer also needs additional design development for its high temperature and pressure service in a hostile chemical environment.

1.18 RECOMMENDATIONS FOR FURTHER STUDY

Our analytical studies have been very fruitful and produced innovative ideas and technical contributions that help to lend good credibility to the Fusion/Synfuel tie. We recommend that the conceptual design for the reactor and chemical plant components continue to be refined and that an experi-

mental program to complement or verify the conceptual design efforts be initiated. There are numerous process elements in the chemical plant that we have identified for technical or economic improvement and these should be studied. We should increase our understanding of the overall process and the system integration.

Specifically we would recommend the following for the near term.

- Continue the purely analytical studies in greater depth and couple them to experiments that the analytical studies suggest. We particularly cite the following:
  - Refine the helium-cooled Li_2O blanket designs.
    - Medium temperature (breeding)
    - High temperature (non-breeding)
  - Fabricate and test laboratory-scale components of a Li_2O blanket module.
  - Obtain experimental property data on Li_2O.
  - Obtain property data on low activity structural materials for the blanket.

  It should be noted that these areas would be of value to the entire fusion technology community.

- Continue design development of a high temperature thermally driven SO_3 decomposer.

- Optimize system interfacing to enhance thermal energy use and reduce cost.

SECTION 2

MOTIVATION FOR THE STUDY

Contributor:

R. W. Werner

TABLE OF CONTENTS

LIST OF FIGURES

2.0 MOTIVATION FOR THE STUDY

It seems evident that the U.S. must have domestic sources of energy, both to fuel our electrical plants and to respond to our other areas of energy flow in portable fuels for the transportation, industrial, residential and commercial sectors. Energy self-sufficiency is vital to this country's well-being and we must work to that end as a national goal. In the long term we expect that this energy will be provided by the fusion reactor as an energy driver for Fusion/Electric plants and the complementary Fusion/Synfuel plants. The output of the Fusion/Synfuel plants will be hydrogen.

The hydrogen produced is to be used as a portable fuel or as a feedstock for other portable fuels of more complex molecular structure; methane, methanol, gasoline, for instance. A reminder of the extreme importance to the U.S. economy of synthesizing these portable fuels is suggested by Fig. 2.1, the familiar spaghetti chart showing our U.S. energy flow for 1979 and how it is distributed in the consumption process; roughly 73% used as fuels and chemicals, and 27% used for electricity generation. As these non-renewable energy supplies of oil, coal and gas predictably diminish in the early decades of the 21st century and are replaced by the renewables--fusion being one of these--it seems clear that not only must the renewable energy sources produce electricity but they also must produce fuels and chemical feedstock in even greater quantity.

Beyond postulating a method for producing fuel there is a logical case for studying synthetic fuel production in conjunction with the fusion reactor. At least three objectives important to fusion are served by these fusion/synfuel studies:

1. The base for fusion's applicability to our future national overall energy needs is broadened.

2. Fusion reactor studies for the production of electricity gain measurably by the reactor designs carried out for synfuels. Different

(NET PRIMARY RESOURCE CONSUMPTION 77.8 QUADS)

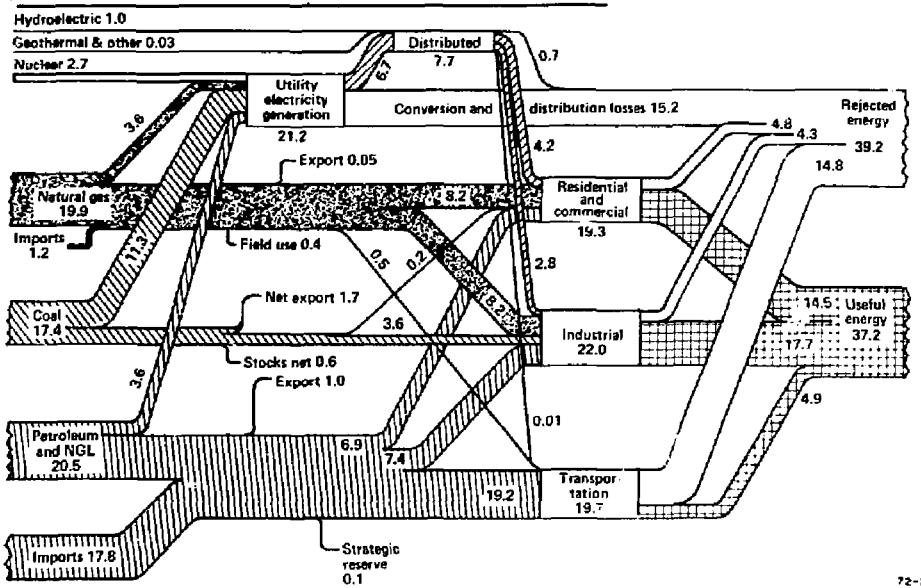

72-256-0

scientific disciplines become involved. Different industrial partners become aware of fusion.

3. The timing of fusion's availability and the need for synfuels coincide. About the time when fusion energy sources are on the threshold of commercial reality, synthetic fuels will be needed to bolster the waning supplies of the exhaustibles. Figure 2.2 illustrates the rise and fall of our various exhaustible energy sources starting with wood from 1850 up through the 2000's. Somewhere around 2010 or perhaps a decade thereafter there is a high probability of an energy shortfall and it is then that fusion must begin to be commercialized using the inexhaustibles.

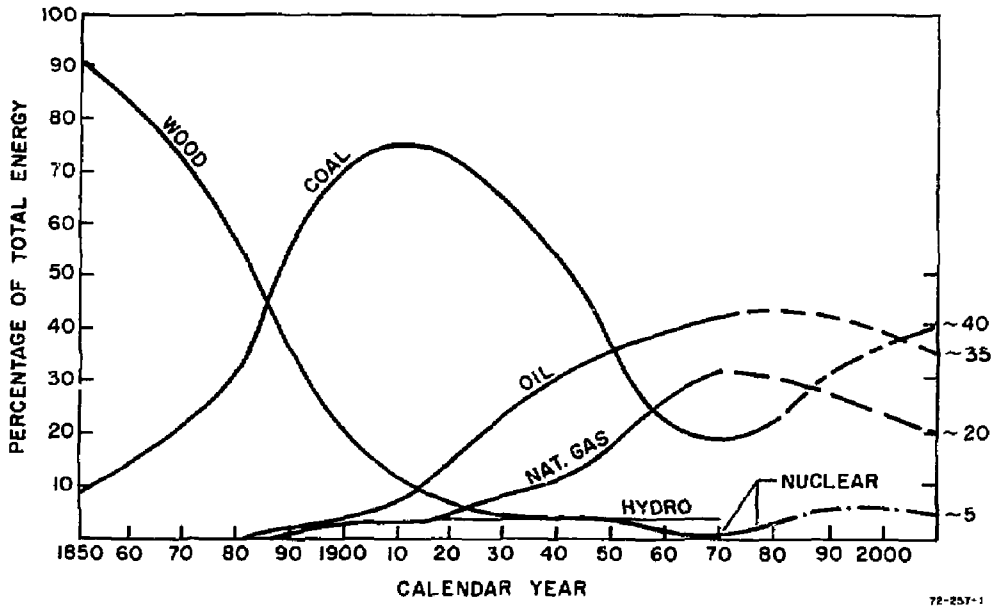

Fig. 2.2 Contribution of various energy sources

SECTION 3

THE TANDEM MIRROR REACTOR AND ITS PHYSICS

Contributors:

T. H. Zerguini and F. L. Ribe

TABLE OF CONTENTS

LIST OF TABLES

LIST OF FIGURES

3.1 GENERAL DESCRIPTION OF THE REACTOR AND ITS PHYSICS

The Tandem Mirror Reactor in this year's report has a MARS[1,2] (Mirror Advanced Reactor Study) axial design (Fig. 3.1). MARS is a linear magnetic mirror fusion device which uses electrostatic plugs to confine a steady-state fusion plasma in a long solenoid, called the central cell. The central cell plasma is self-sustained by alpha particle heating (ignition), while continuous injection of neutral beams and ECRH (Electron Cyclotron Resonance Heating) are required to maintain the plug electrostatic confining potential and to pump out (by charge exchange) the ions which get trapped into the negative potential of the thermal barrier. Maintaining the thermal barrier moderates significantly the plug injection power.

The primary motivation for the modification of the previous MFTF-B A-cell Geometry[3,4] (FY 1981) to the present axial configuration is its improved engineering promise as a fusion reactor. A comparative evaluation[5] of several end plug configurations for tandem mirror fusion reactors with thermal barriers led to the selection of the axicell configuration for its higher Q-value, lower plug magnet capital cost, and reduced radial transport. In addition, the axicell operating mode is also required to prevent trapped particle instability as it is presently understood theoretically. In comparing the axicell configuration to the previous A-cell geometry, one sees a number of differences which significantly affect the reactor physics performance, the most obvious being the different magnet sets at the end of each reactor (Fig. 2). In the A-cell TMR, ECRH in the A-cell establishes the peak potential barrier to confine the center-cell ions, and the yin-yang plug retains the function of providing MHD stability to the whole configuration. The functions of electrostatic confinement and MHD stability were separated to allow the A-cells and the yin-yang cells to be better optimized to achieve their respective functions.

In the axicell configuration, the axicell is formed by two circular, high-magnetic-field coils at each end of the central cell. The highest magnetic field generated helps to obtain a sufficiently high

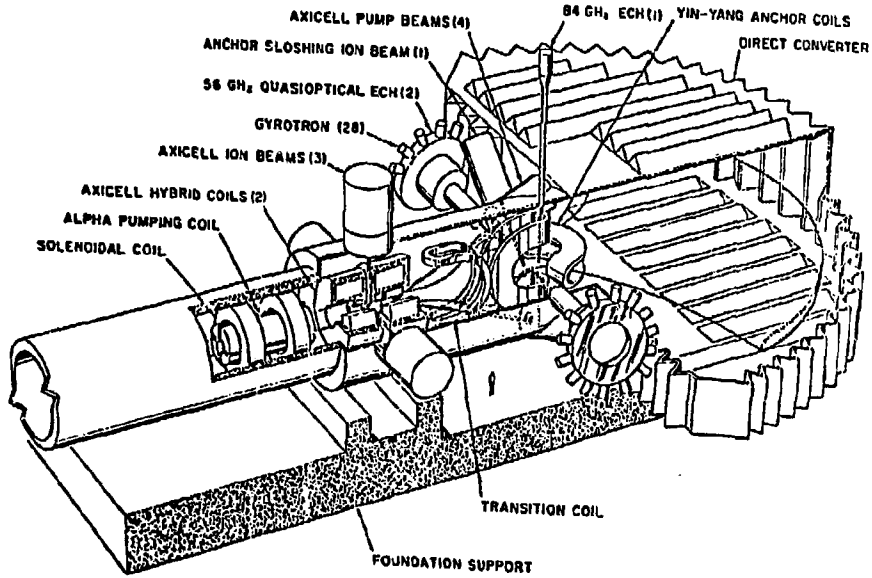

Fig. 3.1 Tandem Mirror Reactor (MARS)

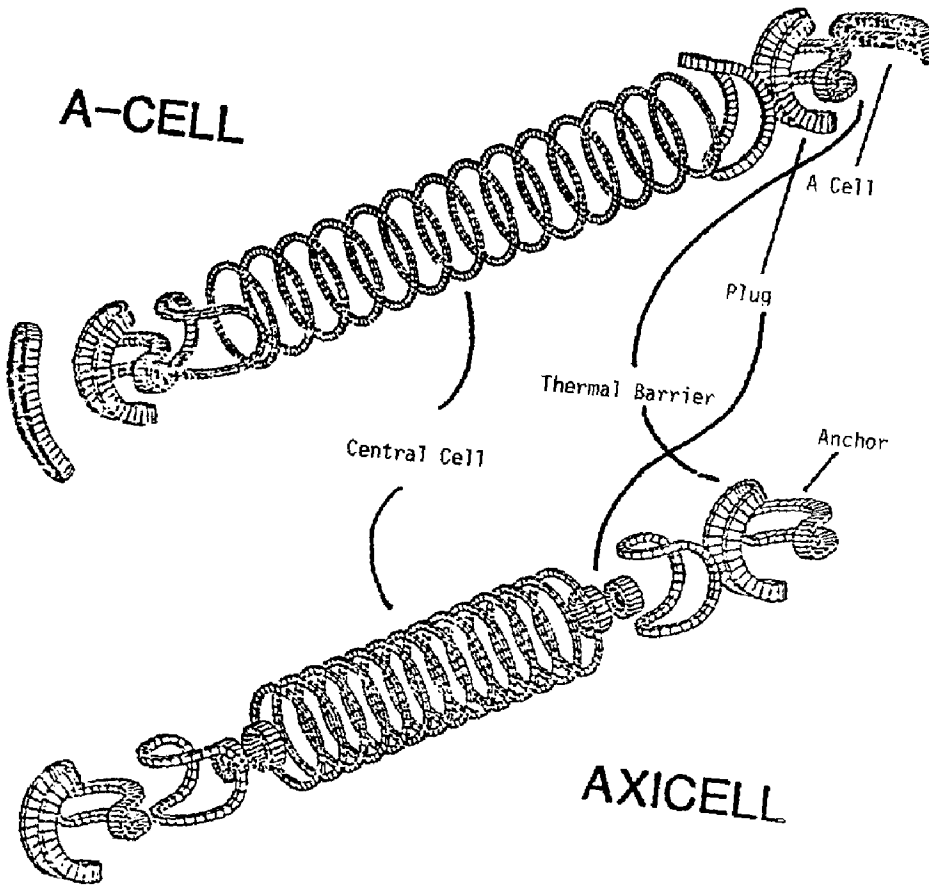

Fig. 3.2 Comparison of A-cell and axicell magnet set configurations.

central cell density relative to plug density and results in a sufficiently high Q value. The combination of magnetic constriction and reflection from a potential peak formed by mirror trapped ions in the axicell throttles the flow of ions to the end cells. Those ions confined in the central cell by the axicell see only axisymmetric magnetic and electrostatic fields. There is a minimum fraction of central cell ions that must be confined by the end cells to stabilize the trapped particle mode[5] which is a curvature driven electrostatic instability sensitive to the fraction of particles passing between regions of good and bad magnetic curvature, becoming severe in configurations having a small fraction of such particles. Regulating this minimum flow of ions from the axicell led to redesigning the ion confining potential in the yin-yang cells so that more ions reach the end regions. Fig. 3.3a illustrates the magnetic field variation along the axis generated by the axicell magnet configuration of Fig. 3.2. The anchors at the ends of the reactor have the function of providing MHD stability to the whole configuration. Figs. 3.3.b and c show the ambipolar potential and the density profiles at one end of the reactor. These are tailored by the magnetic field, ECRH heating, and neutral beam injection:

- Neutral beams in the axicell generate the first ion confining potential and fuel the central cell (since the lowest axicell mirror magnetic field is toward the central cell).
- Neutral beams in the transition region are used to pump out particles (by charge exchange and also to fuel the central cell). The ions formed have enough energy to pass over the axicell potential hill into the central cell but not over the potential peak (ϕ_c) at the ends of the reactor.
- Neutral beam injection off-midplane in the anchor (point a') forms sloshing ions which bounce back and forth in the yin-yang cell, creating density maxima near their turning points. These ions help form the final ion confining potential (ϕ_c) and the potential barrier which separates central-cell and yin-yang electrons. The injection of beams on the inside of the yin-yang is preferred to avoid the cooling effect on the ECRH

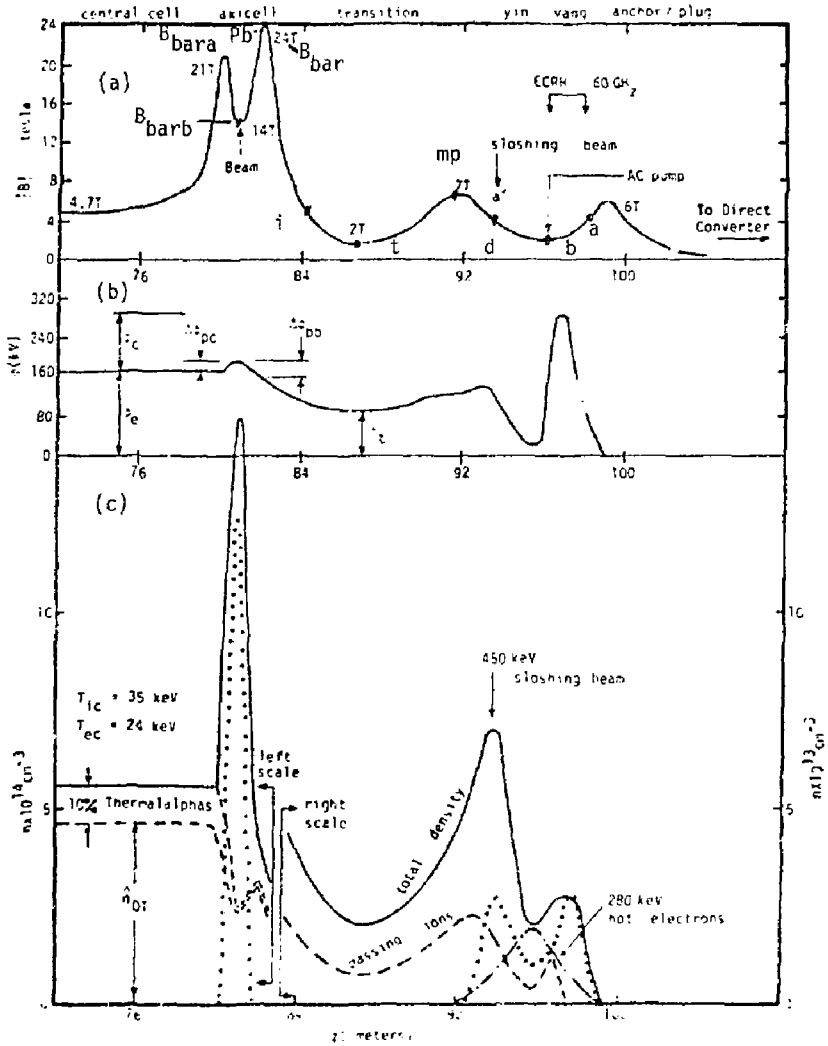

Fig. 3.3 Axicell (MARS) magnetic field, ambipolar potential and density along axis.

heated electrons in the potential peak Φ_c by the newly formed electrons from the injection.

- ECRH at the thermal barrier minimum (point b) serves to reduce the fraction of cold central cell electrons passing into the anchor and confine them magnetically. A reduction of the cold-electron density required for quasineutrality further deepens the thermal barrier potential minimum.
- ECRH heats electrons trapped within the outer peak in ion density in the anchor. This heating increases dramatically the height of the corresponding potential peak forming the final ion confining potential.

In combination with the magnetic and potential shapes along the axis, high energy neutral beams and electron cyclotron resonance heating give ion and different electron temperatures and average energies at different locations in the reactor. Fig. 3.4 shows the resulting density profiles in the end cells. The passing-ion and electron density at different points can be scaled from their respective central cell densities by integrating an assumed distribution function of the particle species over the passing region, for each kind of considered particle, at the chosen point. Hot ions and electrons are magnetically trapped in their respective wells (μ-trapped). The trapped cold ions are one of the principal reasons for the use of sloshing-ions in the end cells of TMR's because they help stabilize loss cone modes.

We see in Fig. 3.4 that a concentration of thermalized alpha particles has been included in the plasma model. This reduces the Q value by approximately a third. On the positive side, the now ignited central cell can provide some power to sustain a plasma halo outside the central cell plasma dense enough to shield the plasma from impurities, and provide a means of reducing the central cell radial electric field and associated $\underline{E}\times\underline{B}$ rotation.

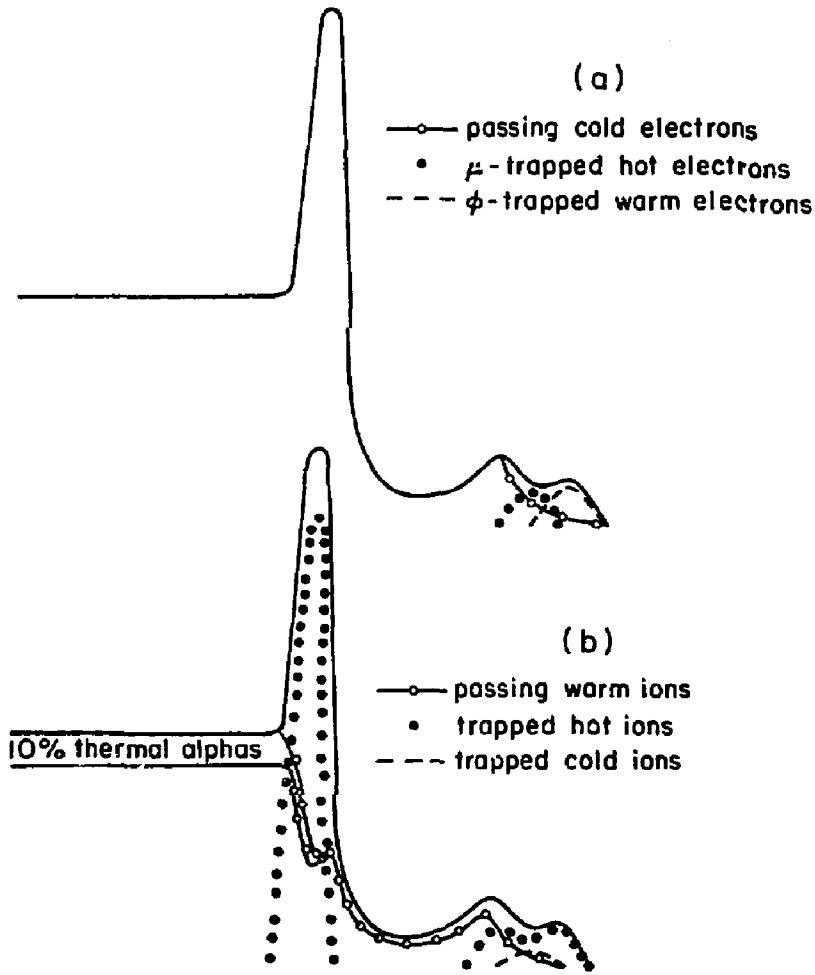

Fig. 3.4 Profiles of electron (a) and ion (b) densities within the end cell regions of an axicell operated TMR.

3.2 THE PLASMA MODELING CODE

3.2.1 General Description of the Plasma Model

The plasma is assumed to have radial density profiles of the form

$$n_c = n_{oc}\left(1 - \frac{r}{r_c}\right)^{X_p}$$

where the profile parameter X_p is an input value. Different density values along axis are calculated by a scaling from the central cell density, (integral over velocity of assumed distribution functions over the passing regions of the particles). In all other respects, the model is zero-dimensional. The equations used are steady state so that the model cannot deal with reactor startup and particle build up.

3.2.2 Input and Output Variables

The code used in this study was developed at the Lawrence Livermore National Laboratory and at the time of writing includes the most up to date information on TMR's. The input parameters for the TMRBAR Code are:

P_{Fus} = Central cell fusion power
L_c = Central cell length
$B_{oc,vac}$ = Central cell vacuum magnetic field
$B_{ob,vac}$ = Yin-yang midplane vacuum magnetic cell
$B_{ma,vac}$ = Yin-yang mirror magnetic field
B_{bara} = Inner axicell mirror magnetic field
B_{barb} = Midplane axicell vacuum magnetic field
B_{bar} = Outer axicell mirror magnetic field
$B_{ot,vac}$ = Vacuum magnetic field on the transition region
R_{slosh} = Magnetic field ratio at the point a
R_p = Magnetic field ratio at the injection point in the transition region
β_c = Central cell beta

β_p = Axicell beta

β_b = Yin-yang beta

C_α = Alpha particle fraction confined in the central cell

X_p = Plasma density profile exponent

$L_{A\text{-}cell}$ = Yin-yang cell length

L_{Tran} = Transition region length

G = Ratio of total ion density to passing ion density at the point b

F_{Ioniz} = Charge exchange ionization parameter in the transition region (the neutral product after a charge exchange reaction can be ionized, and has to be pumped out again).

P_{cx} = Charge exchange coefficient in the transition region

The output parameters consist of

- All the particle energy exchange rates
- The particle loss rates from the different regions of the reactor
- The temperature/average energy of the different particle kinds
- The different densities and potentials in the central cell, the axicell (pb and pc), the pump beam injection point (i), the transition region (t), the sloshing ion injection point (a'), the thermal barrier potential minimum (b), the inner mirror of the anchor (mp), and at the potential maximum in the anchor (a).
- Injection powers and ECRH powers required
- The plasma radius, the first wall neutron loading and the reactor Q value.

3.2.3 General Description of the TMRBAR Code

A complete listing of all the equations used in the TMRBAR code is given in Appendix 1. The program contains eleven iterative loops (see Fig. 3.5). Starting from the inner ones, we have

- Three nested loops to calculate all the axicell parameters. The equations used form the Logan-Rensink plug model[8].
- Six simple loops to calculate the density of the different particle kinds and the ambipolar potential (using quasineutrality) at the points pb, i, b, t, mp, and a', respectively.
- One loop to compute the electron temperature in the central cell (T_{ec}) and the electron potential to temperature ratio (η_e). This loop uses the quasineutrality equation and the electron energy balance. A Newton's method[9] (with two unknowns) helps to solve for T_{ec} and η_e.
- Finally, the outermost loop uses the ion energy balance to compute $\eta_c = \phi_c/T_c$.

After reading the input parameter, the program calculates (the equations listed below are in the Appendix):

- The plasma magnetic field in the axicell (Eq. 1)
- The vacuum magnetic field at the injection point (Eq. 2)
- The fusion reaction parameter (Eq. 3)
- The alpha particle confining parameter (Eq. 4)

After entering the ion energy loop and the central cell quasineutrality and electron energy loop, the program calculates

- The slowing down alpha particle energy fraction on electrons (Eq. 5)
- The central cell density (Eq. 7)
- The central cell plasma radius (Eq. 9)
- The first-wall loading (Eq. 10)
- The central cell plasma volume (Eq. 11)
- The profile averaged betas in the central cell, axicell, and anchor, respectively (Eq. 12, 13, 14)
- The plasma magnetic field in the axicell (Eq. 15)
- The potentials $\phi_{a'}$, ϕ_b, ϕ_c, ϕ_e, ϕ_t (Eq. 16)

- The effective anchor injection energy (Eq. 17)
- The plasma magnetic fields at the points b, a, and a', respectively (Eqs. 18, 19, 20)
- The mirror ratio at the sloshing ion injection point (Eq. 21)
- The effective mirror ratio of the sloshing ions (Eq. 22)
- The barrier and the transition region volumes (Eqs. 23, 24)
- The axicell inner mirror ratio (Eq. 25)
- All the axicell parameters (Eq. 36-40). These equations are a self consistent set which form the Logan-Rensink plug model. A maxwellian formula is used to calculate the potential difference ϕ_{pc} (Eq. 40).
- The axicell neutral beam current (Eq. 41)
- The plasma axicell outer mirror ratio (Eq. 42)

The next step in the program is to guess the values of the potential ϕ_{pb}, and the passing ion density at the point pb. These guesses will be used to calculate the passing ion density, the passing alpha-particle density, the potential-to-electron-temperature ratio η_{pb}, the alpha particle fraction and the potential ϕ_{pb} (Eq. 43, 44, 45). A few iterations are needed for the code to converge toward the solution of the potential ϕ_{pb}.

The program uses a quasineutrality condition at the point pb. The different densities which are used to help calculate the potential ϕ_{pb} are found through a mapping from the central cell where magnetic field, ambipolar potential and density are known.[10]

The code then calculates the plasma magnetic field at the pumping injection point (Eq. 46) and follows the same procedure, which is used to calculate the potential ϕ_{pb}, to compute the potential ϕ_{pi} (Eq. 48, 49). The mirror-ratio calculations of R_{bold} and R_{told} are intermediate steps to evaluate the different densities at the point i.

After exiting the ϕ_{pi} loop, the code computes:

- The beta value at the injection point (Eq. 50)
- The mirror ratios R_{p1mir} and R_{p2mir} (Eq. 51)
- The pumping energy at the point i (Eq. 54).

The same procedure followed to calculate the potentials ϕ_{pb} and ϕ_i is carried out to evaluate the barrier and the transition region potentials (ϕ_b, ϕ_t) (Eq. 56. and Eq. 58).

The program then calculate

- The alpha particle fraction and the beta in the transition region (Eq. 60)
- The electron cutoff energy E_b' (Eq. 61)
- The parallel pressure in the barrier region (Eq. 62)
- The rest of the pressure in the barrier region (Eq. 63)
- The hot electron average energy in the barrier (Eq. 64)
- The passing cold electron fraction (Eq. 65)
- The hot electron density in the barrier (Eq. 66)
- The cold electron density in the barrier (Eq. 67)
- The hot electron density at the point a (Eq. 68)
- The sloshing ion density at point a (Eq. 69)
- The warm electron density at a (Eq. 70)
- The profile-averaged beta at a (Eq. 71)

Quasineutrality conditions are again used to find the potential at the sloshing ion injection point a' and at the inner maximum field of the anchor (point mp). Other parameters calculated in the a' loop are the sloshing ion density and the hot electron density at the point a' (Eqs. 73, 74).

The effective beta value and the vacuum magnetic field at the point a' are computed, followed by

- The barrier pumping power (Eq. 77)
- The transition pumping power (Eq. 78)
- The total pumping power (Eq. 79)
- The neutral beam power at the point a' (Eq. 80)
- The ECRH power at a (Eq. 81)
- The Syncrotron power (Eq. 82)
- The ECRH power at b (Eq. 83)

As mentioned above, the quasineutrality condition and the electron energy equation in the central cell close the first big loop. The quasineutrality condition includes (Eq. 101), respectively

- The loss of ions by burn through fusion reactions (Eq. 99)
- The loss of ions and electrons through the ends (Eq. 100)
- The addition of electrons from sloshing ion beams (Eq. 85)

The electron energy balance includes:

- Cooling from the axicell injection beam electrons (Eq. 101)
- ECRH heating at a and at b (Eqs. 103, 104)
- Drag from ions in the central cell (Eq. 105)
- Cooling from the sloshing ion-beam electrons (Eq. 106)
- Pastukhov loss of electrons (Eq. 107)
- Addition of energy from alpha particle (Eq. 108)
- Loss of electrons through charge exchange pumping (Eq. 109)

The ion energy balance written in a newton's form (newton's method) concludes the calculations in the most outer loop. The ion energy balance includes:

- Pastukhov energy losses (Eqs. 111, 112)
- Addition of energy from alpha particles (Eq. 113)
- Addition of ions from the axicell beams (Eq. 114)
- Addition of ions from the pumping beams (Eqs. 115, 116).

Before ending, the program calculates

- The total ion fueling rate/loss rate from the whole reactor (Eq. 119)
- The reactor Q value (Eq. 120)
- The beam trapping fractions for the sloshing ions and for the axicell (Eqs. 124, 126).

The Code ends by checking the adiabaticity condition (Eq. 127) and by reading the output values.

3.3 COMPUTED TANDEM MIRROR PARAMETERS

Table 3.1 shows the reactor parameters for coupling to a synfuel plant which uses a fusion power of 3500 Mwf, a first wall loading of 5 MW/m^2 and a first wall radius of 0.6 m. These numbers represent state of the art TMR fusion parameters in considering reactor Q value, magnet cost, radial transport, and trapped particle instability; but are not appropriate for coupling to the blanket used in other sections of this report, where P_F = 2600 Mwf, Γ_W = 2 MR/m^2 and r_W = 1.5 m are taken. These later numbers will be sealed in future work to match the MARS TMR parameters. Figure 3.6 shows the power balance of a MARS electricity producing plant[11] which uses the TMR parameters of Table 3.1. The overall efficiency of the system is 0.34 or 0.39, depending on the blanket multiplication factor (1.37 or 1.16).

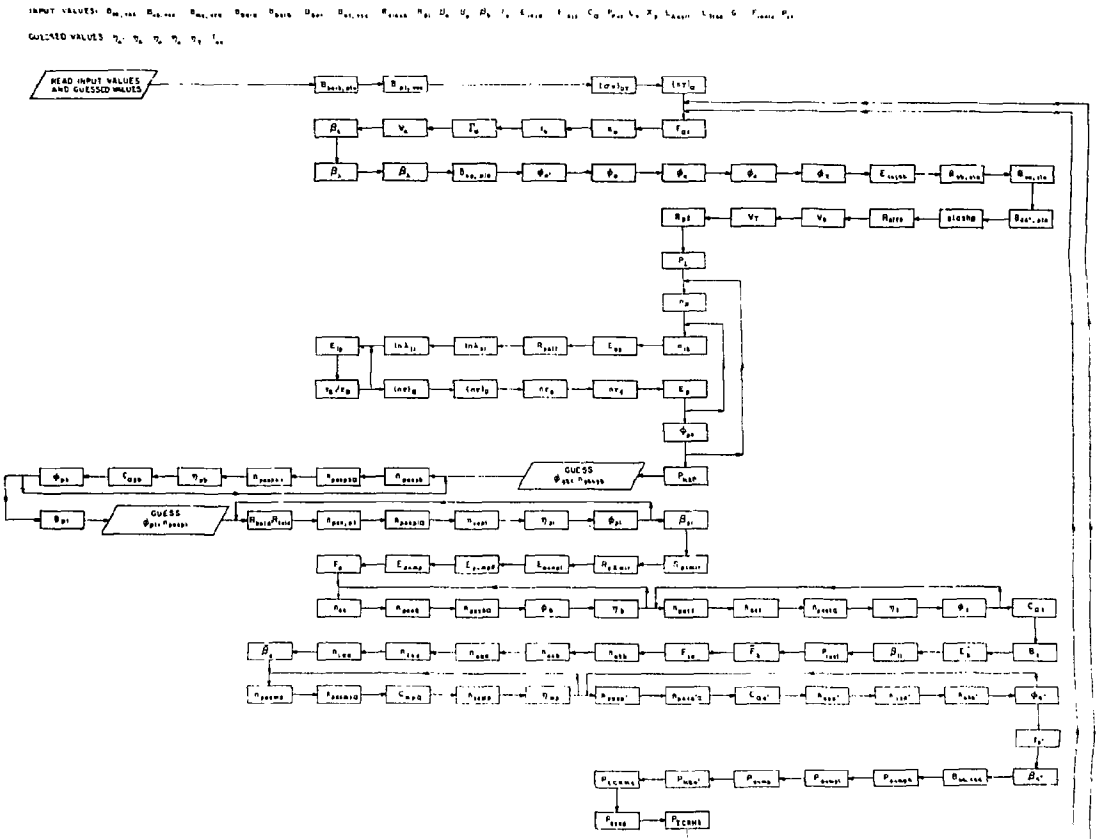
INPUT VALUES:
GUESSED VALUES
READ INPUT VALUES AND GUESSED VALUES
GUESS
GUESS

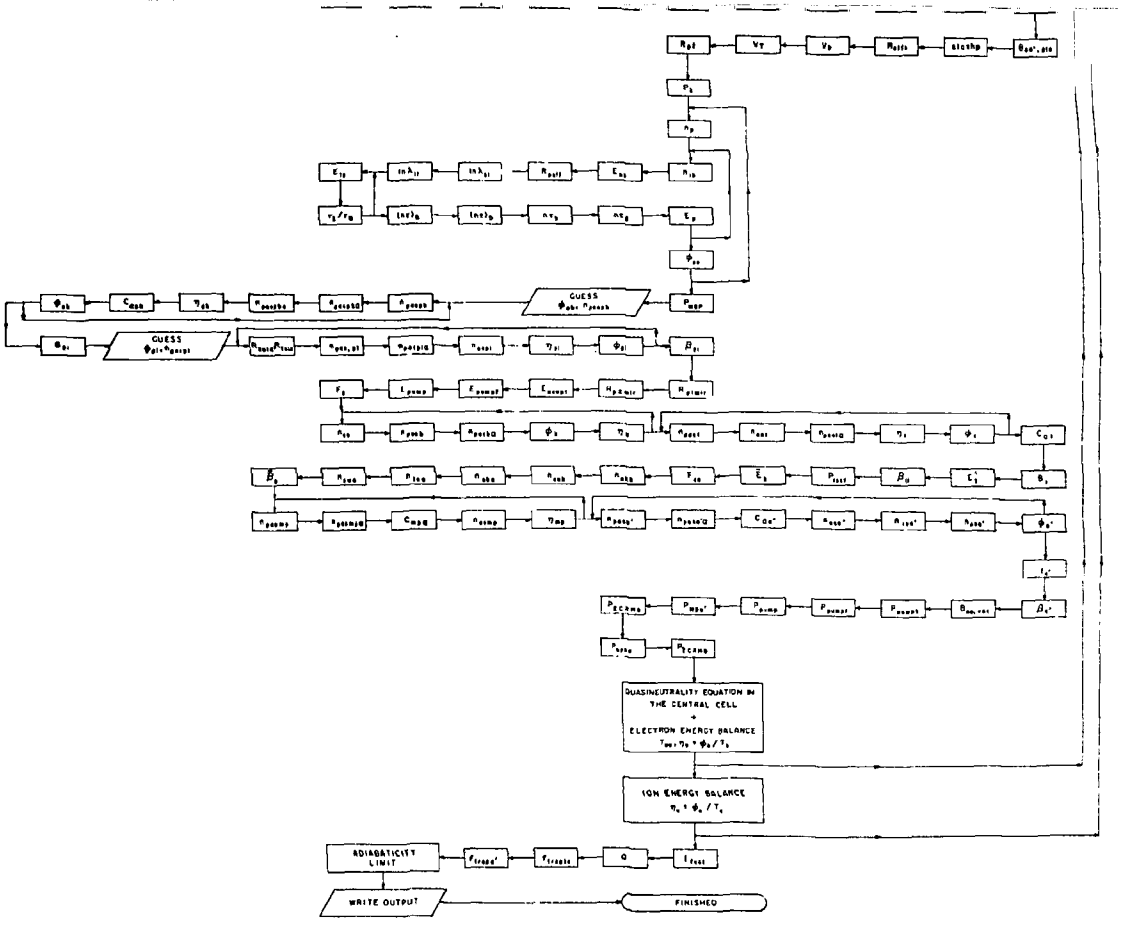

Fig. 3.5 TMRBAR Program Flow Chart

Table 3.1 TMR Parameters for Coupling to a Plant
Using P_{Fus} = 3500 Mwf and Γ_W = 5 MW/m^2

Central Cell Output:

Density cm-3 = 4.1 e + 14
Ion temp., Kev = 35
Electron temp., Kev = 29.1
Radius, m = 0.42 Length, m = 150 Wall radius, m = 0.6
Vacuum field, t = 4.7 beta = 0.7
Phie, Kev = 205.5
Density profile exponent = 3

Axicell Output:

Total density, cm -3 = 1.0 e + 15
Hot ion density, cm -3 = 8 e + 14
Av. ion energy, Kev = 200
Radius, m = 0.23 Length, m = 2 Beam trapping fraction = .998
Vac mid field, t = 14
Vac. mirror rat. (inner) = 1.5 vac mirror rat. (outer) = 1.7 beta = .4
Phipc, Kev = 22.85 phipb, Kev = 35.3 Passing density at pb (cm-3) = 2.42 e + 14

Transition Region Output:

Transition length, (m) = 10 beta = 0.16
Vacuum filed, (t) = 1.6 phit, (Kev) = 122.5
Pump beam trapping = 0.992 passing density (cm-3) = 5.7 e + 12

Pump Beam Location Output:

Passing density = 4.0 e + 13
Potential at injection pt. = 61.4 injection angle = 25°
Beta at injection pt. = 5.3 e -2

Plug/Barrier/Anchor Output:

Barrier vacuum field, t = 2.17
At pt. a', 5.1

Table 3.1 Cont'd

Plug/Barrier/Anchor Output Cont'd

Total barrier beta = 1.24 perp. beta = .65
Passing ion density at b, cm -3 = 4.1 e + 12
Passing ion density at mp, cm -3 = 3.5 e + 13
eb', Kev = 19.65 eeh, Kev = 391.8
tew, Kev = 35.5 fec = 1.98 e -02
Barrier length, m = 8
a-cell mirror field, t = 6
Beta at pt. a = .47
Beta at pt. a' = .4
ϕ_b, Kev = 198.4 ϕ_c, Kev = 142.1
$\phi_{a'}$, Kev = 73.3 ϕ_{mp} = 64

Power Balance:

n.b. power at: b, mw = 34.7	a', mw = 8.7
ecrh power at: a, mw = 3.4	b, mw = 69
Pumping pwr. (total), mw = 133	energy = 81.7
Transition power, mw = 103	barrier power, mw = 29.5
Sync radiation power, mw = 11.3	
Fusion power, mw = 3500	*Wall loading, mw/m^2 = 5*
Q value = 14.2	

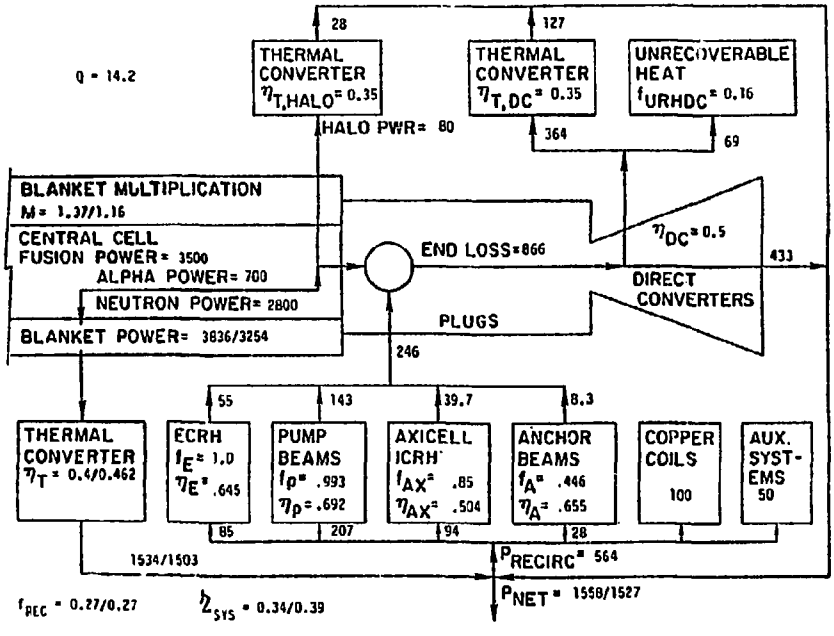

Fig. 3.6 Power Balance of an Electricity Producing Tandem Mirror Reactor Plant

Appendix 3.1

The TMRBAR Code Equations

$$B_{barb,p\ell} = B_{barb}\,(1-\beta_p)^{1/2} \tag{1}$$

$$B_{pi,vac} = B_{bar}/R_{pi} \tag{2}$$

$$\langle\sigma v\rangle_{DT} = \frac{3.05 \times 10^{-13}\ \exp\ (-17.7/T_c^{.348})}{1 + 0.154\ T_c^{1/3} - .1418\ T_c^{2/3} - .05\ T_c^{1} + .0364\ T_c^{4/3}} \tag{3}$$

$$(n\tau)_\alpha = \frac{4C_\alpha}{.7\ \langle\sigma v\rangle_{DT}} \tag{4}$$

$$F_{\alpha e} = .88155\ \exp\ (-T_{ec}/67.4036) \tag{5}$$

$$T_{sum} = T_c + T_{ec} + 8.310^{10}\ \langle\sigma v\rangle_{DT}\ T_{ec}^{3/2} \times 3520\ F_{\alpha e} + (T_c + 2T_{ec})\ C_\alpha \tag{6}$$

$$n_c = \frac{\beta_c\ B_{oc,vac}^2}{2\mu_o\ T_{sum}} \tag{7}$$

$$B_{oc,pla} = B_{oc,vac}(1-\beta_c)^{1/2} \tag{8}$$

$$r_c = \left(\frac{P_F}{0.25\ n_c^2\ \langle\sigma v\rangle_{DT}\pi L_c}\right)^{1/2} \frac{\sqrt{(X_p+1)(X_p+2)}}{X_p} \tag{9}$$

$$r_W = \frac{.8\ P_F}{2\pi\ \left[r_c + 3 \times \left(\frac{27.11}{B_{oc,vac}}\right)\right] L_c} \tag{10}$$

$$V_c = \pi r_c^2\ L_c \tag{11}$$

$$\bar{\beta}_c = \beta_c\ \frac{X_p}{X_p+2} \tag{12}$$

$$\bar{\beta}_p = \beta_p\ \frac{X_p}{X_p+2} \tag{13}$$

$$\bar{\beta}_b = \beta_b \frac{\chi_p}{\chi_p + 2} \tag{14}$$

$$B_{op,pla} = B_{op,vac}\,(1-\beta_p)^{1/2} \tag{15}$$

$$\phi_{a'} = \eta_{a'} T_{ec},\ \phi_b = \eta_b T_{ec},\ \phi_c = \eta_c T_c,\ \phi_e = \eta_e T_{ec},\ \phi_T = \eta_T T_{ec} \tag{16}$$

$$E_{injab} = E_{inja'} + \phi_b - \phi_{a'} \tag{17}$$

$$B_{ob,pla} = B_{ob,vac}(1-\beta_b)^{1/2} \tag{18}$$

$$B_{oa,pla} = \text{slosh} \times B_{ob,vac}(1-\beta_a)^{1/2} \tag{19}$$

$$B_{oa',pla} = \frac{B_{oa,pla}}{1 + (\phi_{pc} - \phi_{a'} - \phi_c)E_{inja'}} \tag{20}$$

$$\text{slosh}_p = B_{oa',pla}/B_{ob,pla} \tag{21}$$

$$R_{effs} = \frac{B_{ma,vac}}{\text{slosh}\ B_{ob,vac}(1-\beta_b)^{1/2}\,[1 + (\phi_c+\phi_e)/E_{inja}]} \tag{22}$$

$$V_b = 2\pi\, r_c^2\, L_{Acell} \frac{B_{oc,vac}}{B_{ob,vac}} \left(\frac{1-\bar{\beta}_c}{1-\bar{\beta}_b}\right)^{1/2} \tag{23}$$

$$V_T = 2\pi\, r_c^2\, L_{Tran} \frac{B_{oc,vac}}{B_{cT,vac}} \left(\frac{1-\bar{\beta}_c}{1-\bar{\beta}_T}\right)^{1/2} \tag{24}$$

$$R_{p2} = \frac{B_{bara}}{B_{barb}(1-\beta_p)^{1/2}} \tag{25}$$

$$P_\perp = \beta_b\, B_{barb}^2/2\mu_o \tag{26}$$

$$n_p = \frac{P_\perp + n_c(.9E_p - T_c)\exp(1-\frac{\phi_{pc}}{T_c}) + (.9E_p - T_c - T_{ec})n_c C_\alpha \exp(-\frac{2\phi_{pc}}{T_c})}{.9E_p + T_{ec}} \tag{27}$$

$$n_{ih} = n_p - n_c \exp\left(-\frac{\phi_{pc}}{T_c}\right) - C_\alpha n_c \exp\left(-\frac{2\phi_{pc}}{T_c}\right) \tag{28}$$

$$E_{cp} = \phi_p/(R_{p2}-1) \tag{29}$$

$$R_{peff} = R_{p2}/(1 + \phi_p/E_{injp}) \tag{30}$$

$$\ell n\ (\lambda_{ei}) = \ell n\ (5.7 \times 10^{13}\ T_{ec}/n_p^{1/2}) \tag{31}$$

$$\ell n\ (\lambda_{ii}) = \ell n \left(1.4 \times 10^{15} \sqrt{\frac{T_c \bar{=} p}{n_p}}\right) \tag{32}$$

$$E_{Lp} = \left(E_{injp} + E_{cp}\frac{\tau_s}{\tau_D}\right) / \left(1 + \frac{\tau_s}{\tau_D}\right) \tag{33}$$

$$\frac{\tau_s}{\tau_\Delta} = .11\ \frac{\left(\frac{E_{injp}}{T_{ec}}\right)^{3/2} \ell n\ R_{peff}\ \ell n\ \lambda_{ei}}{\ell n\ \frac{E_{injp}}{E_{Lp}}} \tag{34}$$

$$(n\tau)_s = 3.9 \times 10^{12}\ E_{injp}^{3/2}\ \ell n_{10}\ R_{peff}\ \ell n\ \lambda_{ii} \tag{35}$$

$$(n\tau)_D = \frac{2 \times 10^{13}\ T_{ec}^{3/2}}{\ell n\ \lambda_{ei}}\ \ell n \left(\frac{E_{injp}}{E_{Lp}}\right) \tag{36}$$

$$(n\tau)_p = (n\tau)_s (n\tau)_D / [(n\tau)_s + (n\tau)_D] \tag{37}$$

$$(n\tau)_{drag} = \frac{2\ 10^{13}\ T_c^{3/2}}{\ell n\ \lambda_{ei}} \tag{38}$$

$$E_p = (E_{injp} - E_{Lp})\ \frac{(n\tau)_{drag}}{(n\tau)_p} + 1.5\ T_{ec} \tag{39}$$

$$\phi_{pc} = T_{ec}\ \ell n\ \frac{n_p}{n_c(1 + 2C_\alpha)} \tag{40}$$

$$P_{NBp} = e\,\eta_p\,\eta_{ih}\,E_{injp}\,\frac{V_p}{(\eta\tau)_p} \tag{41}$$

$$R_o = \frac{B_{bar}}{B_{barb}(1-\beta_b)^{1/2}} \tag{42}$$

$$n_{paspbe} = n_c\ exp\ [-\frac{(\phi_{pb}-\phi_{pc})}{T_{ec}}\ ] \tag{43}$$

$$\eta_{pb} = \eta_{pc} - \ell n\ \left[\frac{X_{lilgpb}\,n_{paspb} + 2\,n_{paspb\alpha}}{n_{paspbe}\ exp\ (\frac{\phi_{pb}-\phi_{pc}}{T_{ec}})}\right] \tag{44}$$

$$C_{\alpha pb} = \frac{n_{paspb}}{n_{paspb}}\ ,\ \phi_{pb} = \eta_{pb}\,T_{ec} \tag{45}$$

$$B_{pla,pi} = B_{vac,pi}\,\sqrt{1-\beta_{pi}} \tag{46}$$

$$R_{bold} = \frac{B_{bar}}{B_{ob,vac}(1-\beta_{bp})^{1/2}}\ ,\ R_{told} = \frac{B_{bar}}{B_{ot,vac}(1-\beta_t)^{1/2}} \tag{47}$$

$$\eta_{pi} = \eta_{pc} - \ell n\ \left[\frac{1.16\ X_{\ell i\ell g}\ n_{paspi} + 2\,n_{aspi\alpha}}{n_{ecpi}\ exp\ (\frac{\phi_{pi}-\phi_{pc}}{T_{ec}})}\right] \tag{48}$$

$$\phi_{pi} = \eta_{pi}\,T_{ec} \tag{49}$$

$$\beta_{pi} = \frac{2\mu_o \times 1.16\ X_{\ell i\ell g}\ n_{paspi}(T_c+T_{ec}) + (2T_{ec}+T_c)n_{paspi\alpha}}{B^2_{pi,vac}} \tag{50}$$

$$R_{plmir} = \frac{B_{bar}}{B_{pi}} \qquad R_{p2mir} = \frac{B_{barb}}{B_{pi}} \tag{51}$$

$$E_{pump1} = \frac{\phi_{pi}}{1-R_{plmir}\,\sin^2\Theta_{injpi}} \tag{52}$$

$$E_{pump2} = \frac{\phi_{pi}-\phi_{pb}}{1-R_{plmir}\,\sin^2\Theta_{injpi}} \tag{53}$$

$$E_{pump} = \text{Max}\ (E_{pump1},\ E_{pump2}) \tag{54}$$

$$F_p = \frac{\phi_{pi} - \phi_{pc}}{\phi_e} \tag{55}$$

$$\phi_b = \phi_{pc} - T_{ec} \ell n \left[(1 - \exp \frac{-\phi_e}{T_{ec}}) \left(\frac{GF_{ec}\ n_{pasb} + 2n_{pasb\alpha}}{n_{ec}} \right) + \exp \left(\frac{\phi_e}{T_{ec}} \right) \right] \tag{56}$$

$$\eta_t = \eta_{pc} + \ell n \left[\frac{\exp \left(\frac{\phi_t - \phi_{pc}}{T_{ec}} \right) n_{ect}}{\overline{X}_{\ell i \ell g}\ n_{past} + 2n_{past\alpha}} \right] \tag{57}$$

$$\phi_t = \eta_t\ T_{ec} \tag{58}$$

$$C_{\alpha t} = \frac{n_{past\alpha}}{n_{past}} \tag{59}$$

$$\beta_t = \frac{2\mu_o\ X_{\ell i \ell g}\ n_{past}\ (T_c + T_{ec}) + (2T_{ec} + T_c) n_{past\alpha}}{B^2_{ot,vac}} \tag{60}$$

$$E'_b = \frac{\phi_b}{R_b - T} \tag{61}$$

$$\beta_{//} = 2\mu_o\ n_{pasb} \left\{ \frac{.5T_c + \phi_b - \phi_{pc} + (1 - F_{ec}) G \times .2\overline{E}_b}{B^2_{ob,vac}} + \frac{(G - X_{\ell i \ell g}) \left[\left(1 - \frac{1}{sloshp} \right) E_{inja'} + \phi_b - \phi_{a'} \right] + \phi_b}{B^2_{ob,vac}} \right\} \tag{62}$$

$$P_{rest} = 2\mu_o\ n_{pasb}\ \ X_{\ell i \ell g} T_c + GF_{ec} T_{ec} + E_{inja'} \left(\frac{G - X_{\ell i \ell g}}{sloshp} \right) \tag{63}$$

$$\overline{E}_h = \frac{B^2_{ob,vac}\ \beta_{bp} - P_{rest}}{.8G \times 2\mu_o\ n_{pasb} (1 - F_{ec})} \tag{64}$$

$$F_{ec} = \frac{1}{1 + \left(\frac{\overline{E}_h}{T_{ec}} \right)^{3/2}} \tag{65}$$

$$n_{ehb} = (1 - F_{ec})Gn_{pasb} \tag{66}$$

$$n_{ecb} = GF_{ec}n_{pasb} \tag{67}$$

$$n_{eha} = \frac{n_{ehb}(B_{ma,vac} - B_{oa,p\ell a})}{\left(\frac{1+\Delta\phi_a}{.2\bar{E}_h}\right)^{1.2}(B_{ma,vac} - B_{ob,p\ell a})} \tag{68}$$

$$n_{isa} = (G \times X_{\ell i \ell g})n_{pasb}\left(1 + \frac{\Delta\phi_a}{E_{inja}}\right)\left(\frac{B_{oa,p\ell a}}{B_{ob,p\ell a}}\right)^{1/2} \tag{69}$$

$$n_{ewa} = n_{isa} - n_{eha} \tag{70}$$

$$\bar{\beta}_a = \frac{\left(n_{ewa}T_{ew} + .8\bar{E}_h n_{eha}\frac{B_{oa,p\ell a}}{B_{ob,p\ell a}} + E_{inja}n_{isa}\right)2\mu_o}{(B_{ob,vac} \times slosh)^2} \tag{71}$$

$$n_{mp} = n_{pc} + \ell n\left\{\exp\left(\frac{\Delta\phi_{mp}}{\bar{T}_{ec}}\right)\frac{n_{ecmp}}{(X_{\ell i \ell g}n_{pasmp} + 2n_{pasmp\alpha})}\right\} \tag{72}$$

$$n_{isa'} = (G\text{-}X_{\ell i \ell g})n_{pasb}\left[1 + \left(\frac{\phi_b - \phi_{ap}}{\bar{E}_{inja'}}\right)\right]^{1/2}\left(\frac{B_{oa',p\ell a}}{B_{ob,p\ell a}}\right)^{1.24} \tag{73}$$

$$n_{eha'} = \frac{n_{ehb}(B_{ma,vac} - B_{oa',p\ell a})}{\left[1 + \frac{(\phi_b - \phi_{a'})}{.2\bar{E}_h}\right]^{1/2}(B_{ma,vac} - B_{op,p\ell a})} \tag{74}$$

$$f_{a'} = \frac{2\mu_o n_{pasa'}T_c n_{isa'}E_{inja'}n_{esa'}T_{ec} + .8\bar{E}_{eh}\left(\frac{B_{oa',p\ell a}}{B_{ob,p\ell a}}\right)n_{eha'}}{B^2_{oa',p\ell a}} \tag{75}$$

$$\beta_{a'} = \frac{1}{1 + \frac{1}{f_{a'}}} \qquad B_{oa',vac} = \frac{B_{oa',p\ell a}}{1 - \beta_{a'}} \tag{76}$$

$$P_{pumpb} = 4.49 \times 10^{-33}\, n_{psab}^2\, V_b \times \frac{5}{8}(1+.0441R_{bold})^{3.33}(1+4C_{\alpha b}+16C_{\alpha b}^2)E_{pump} \left(\frac{1.16X_{\ell i\ell g}}{1.16X_{\ell i\ell g}-1}\right) \frac{F_{ioniz} X_{\ell i\ell g}}{(X_{\ell i\ell g}-1)^{2.33}\, p_{cx} T_c^{1.5}} \tag{77}$$

$$P_{pumpt} = 4.49 \times 10^{33} V_t n_{past}^2 (1+0.0441R_{told})(1+4C_{\alpha t}+16C_{\alpha t}^2) X E_{pump} \left(\frac{1.16X_{\ell i\ell g}}{1.16X_{\ell i\ell g}-1}\right) F_{ioniz} \frac{X_{\ell i\ell g}^{3.33}}{(X_{\ell i\ell g}-1)^{2.33}\, p_{cx} T_c^{1.5}} \tag{78}$$

$$P_{NBa'} = \frac{1.41 \times 10^{21}\, n_{pasb}^2 E_{inja'} V_b \times 1.83 \frac{(G-X_{\ell i\ell g})^2}{4}}{\ell n_{10}\, R_{effs}\, (1.58 \times 10^{10}\, E_{inja}^{3/2}) \frac{\beta_{oa,p\ell a}}{\beta_{ob,p\ell a}}} \tag{80}$$

$$P_{ECRHa} = \frac{10.66 \times 10^{-23} n_{ewa} V_b\, (T_{ew}-T_{ec})}{1.82 \times 10^{8}\, T_{ew}^{3/2} \left[\exp\left(\frac{\Delta\phi_a}{T_{ew}}\right)-1\right]\left[1+\frac{\beta_{ob,p\ell a}}{\beta_{oa,p\ell a}}\right]} \tag{81}$$

$$P_{sync} = X_{ksync}\, B_{ob,vac}^2\, n_{pasb}\, V_b \left(\bar{E}_h+\bar{E}_h^2 \times \frac{11}{3}\right) \tag{82}$$

$$P_{ECRHb} = \left[X_{kmub}\, 1\text{-}F_{ec}\, n_{pasb}^2 \bar{E}_h \times \frac{11}{3} V_b \left(\frac{.68}{2.3 \times 10^{8} \bar{E}_h^{1.5}\, \ell n_{10} R_{beff}}\right) + P_{sync} \left(\frac{G}{4}\right)^2\right] \tag{83}$$

$$I_{pump/v} = \frac{P_{pump}}{E_{pump}} \tag{84}$$

$$I_{a'} = \frac{P_{NBa}}{E_{inja'}} \tag{85}$$

$$I_x = \frac{P_{Nbp}}{E_{injp}} \tag{86}$$

$$\ln \lambda_{ii} = \ln \left(2 \times 10^{15} \sqrt{T_{ec} T_c / n_c}\right) \tag{87}$$

$$\ln \lambda_{ee} = \ln \left(4.66 \times \cdots \frac{T_{ec}}{n_{ec}^{1/2}}\right) \tag{88}$$

$$\ln \lambda_{ei} = \ln \left(9.34 \times 10^{13} \frac{T_{ec}}{n_o^{1/2}}\right) \tag{89}$$

$$\sigma(R) = \left(1+\frac{1}{R}\right)^{1/2} \ln \left[\frac{\left(1+\frac{1}{R}\right)^{1/2}+1}{\left(1+\frac{1}{R}\right)^{1/2}-1}\right] \tag{90}$$

$$\sigma\left(\frac{R}{2}\right) = \left(1+\frac{2}{R}\right)^{1/2} \ln \left[\frac{\left(1+\frac{2}{R}\right)^{1/2}+1}{\left(1+\frac{2}{R}\right)^{1/2}-1}\right] \tag{91}$$

$$(n\tau)_{c\alpha} = \frac{3.1 \times 10^{11} \, \sigma\left(\frac{R}{2}\right)}{\left[\ln \lambda_{ii} \, (1+4C_\alpha) T_c^{1/2}\right] \phi_c \exp \frac{\phi_c}{T_c}} \tag{92}$$

$$(n\tau)_{\alpha \text{created}} = \frac{4C}{.7 \langle \sigma v \rangle DT} \tag{93}$$

$$(n\tau)_{ci} = \left(\frac{1}{(n\tau)_{c\alpha}} + \frac{1}{(n\tau)_{\text{created}}}\right)^{-1} \tag{94}$$

$$(n\tau)_{e\alpha} = \frac{3.6 \times 10^{9} \, \sigma(R)}{\left(\ln \lambda_{ee} \, T_{ec}^{1/2}\right) \phi_e \exp \frac{\phi_e}{T_c}} \tag{95}$$

$$(n\tau)_{er} = \frac{(1+2C_\alpha) \, 4C_\alpha}{.7 \langle \sigma v \rangle DT} \tag{96}$$

$$(n\tau)_{ce} = \frac{1}{\frac{1}{(n\tau)_{ea}} + \frac{1}{(n\tau)_{er}}} \tag{97}$$

$$(n\tau)_{ei} = 10^{13} \frac{T_{ec}^{1.5}}{\ell n \lambda_{ei}} \tag{98}$$

$$T_{pburn} = \frac{1}{2} en_c^2 \langle \sigma v \rangle_{DT} V_c \frac{X_p^2}{(X_p+1)(X_p+2)} \tag{99}$$

$$T_{ptran} = en_o^2 V_c \left[\frac{1}{(n\tau)_{ci}} - \frac{(1+2C_\alpha)^2}{(n\tau)_{ce}} \right] \frac{X_p^2}{(X_p+1)(X_p+2)} \tag{100}$$

$$F_{pB} = T_{pburn} + T_{ptran} + I_{a'} \tag{101}$$

$$T_{ex} = (E_{injp} - E_{loss} - \phi_{pc}) I_x \tag{102}$$

$$T_{ECRHa} = P_{ECRHa} \tag{103}$$

$$T_{ECRHb} = P_{ECRHb} \tag{104}$$

$$T_{Eei} = \frac{1.5 en_c^2 (T_c - T_{ec}) V_c}{(n\tau)_{ei}} \frac{X_p^2 (1+2.5C_\alpha)(1+2C_\alpha)}{(X_p+1)(X_p+2)} \tag{105}$$

$$T_{Eslosh} = (\phi_{a'} - \phi_{pc}) I_{a'} \tag{106}$$

$$T_{Eetran} = \frac{en_o^2 (\phi_e + T_c)}{(n\tau)_{ce}} V_c \frac{X_p (1+2C_\alpha)^2}{(X_p+1)(X_p+2)} \tag{107}$$

$$T_{Efus} = en_c^2 \langle \sigma v \rangle_{DT} E_\alpha F_{\alpha e} V_c \frac{X_p^2}{(X_p+1)(X_p+2)} \tag{108}$$

$$T_{Epump} = I_{pump} (1 - P_{cx}) (\phi_{pi} - \phi_{pc}) \tag{109}$$

$$F_{EB} = T_{ex} + T_{ECRHa} + T_{ECRHb} + T_{Eei} + T_{Eslosh} + T_{Eetran} + T_{Efus} + T_{Epump} \quad (110)$$

$$T_a = \frac{3.1 \times 10^{11} \left(\frac{R}{2}\right) T_c^{1/2} X_p^2}{\ell n \lambda_{ii} (1+4C_\alpha) e n_c^2 V_c [1+\frac{\pi}{4\eta_c}]^{1/2} \exp(\eta_c) erf(\eta_c^{1/2}) (1+\eta_c)(X_p+1)(X_p+2)} \quad (111)$$

$$T_{al} = \frac{1.5 e n_c^2 X_p^2 V_c T_c}{(X_p+1)(X_p+2)(n\tau)_{cr}} \quad (112)$$

$$T_b = F_\alpha e n_c^2 \langle \sigma v \rangle_{DT} V_c (E_\alpha F_{\alpha i} - 90 - 3T_c) \frac{X_p^2}{(X_p+1)(X_p+2)} \quad (113)$$

$$T_d = (E_{LP} + \phi_{pe}) I_x \quad (114)$$

$$T_e = I_{pump/v} (1-P_{cx})(E_{pump} - F_p \phi_e) \quad (115)$$

$$T_f = I_{pump/v} P_{cx} (E_{pump} - F_p \phi_e - 1.5T_c) \quad (116)$$

$$F_{iEB} = T_a [T_b - T_{ei} - T_{ai} - 1.5 \frac{\sigma_i}{\sigma_{cx}} T_c (T_{pbum} - T_{pump/v})(1-P_{cx}) - T_{a'} - I_x + T_d + T_e + T_f + P_{ICRH}] \quad (117)$$

$$\eta_c = \frac{\phi_c}{T_c} \quad (118)$$

$$I_{fuel} = T_{pburn} + \frac{X_p}{(X_p+1)(X_p+2)} \frac{e n_c^2 V_c}{(n\tau)_{ci}} - I_x - I_{a'} - I_{pump/v}(1-P_{cx}) \quad (119)$$

$$Q = \frac{P_{fus}}{P_p + P_{pump} + P_{a'} + P_{ECRHa} + P_{ECRHb}} \quad (120)$$

$$R_{bs} = \left[\frac{\eta_{e\ell i} B_{oc,vac}(1-\beta_c)}{B_{oa',pla}}\right]^{1/2} r_c \quad (121)$$

$$n_{a'} = n_{isa'} + n_{pasa'} \, X_{\ell i \ell g} \tag{122}$$

$$\Gamma_{bs} = 1.85 \times 10^{-14} \, n_{a'} \, \frac{X_p}{(X_p+2)} \, R_{bs} \left(\frac{A_{mass}}{E_{inja'}} \right)^{.91} \tag{123}$$

$$F_{trapbs} = 1 - \exp\,(-\Gamma_{bs}) \tag{124}$$

$$\Gamma_{a'} = 1.85 \times 10^{-14} \, n_p \, \frac{X_p}{(X_p+1)} \, r_p \left(\frac{P_{mass}}{E_{injp}} \right)^{.91} \tag{125}$$

$$F_{trap} = 1 - \exp(-\Gamma_{a'}) \tag{126}$$

$$E_{alimit} = 3.1 \times 10^{-3} \, B^2_{ob,vac} (1-\beta_{op})^{1.5} \, L^{\frac{2}{3}}_{A\text{-cell}} \left(\frac{B_{ob,vac}}{B_{mp,vac}} \right) - (\phi_b - \phi_{a'}) \tag{127}$$

$E_{inja} > E_{alimit}$ (for adiabaticity)

References for Section 3.0

1. D. E. Baldwin and B. G. Logan, "Physics Basis for an Axicell Design for the End Plugs of MFTF-B", LLL Report UCID-19359 (1982).

2. J. Kesner, R. S. Post, B. D. McVey and D. K. Smith, "A Tandem Mirror with Axisymmetric Central Cell Confinement", MIT Report PFC/JA81-11 (1981), to be published in Nucl. Fusion.

3. R. W. Werner et al., "Synfuels from Fusion - Using the Tandem Mirror Reactor and a Thermochemical Cycle to Produce Hydrogen", LLL Report UCID 19311 (February 1982).

4. D. E. Baldwin, B. G. Logan and T. C. Somonen, "Physics Basis for MFTF-B", LLL Report UCID-18496, Vol. 1 (1980).

5. G. A. Carlson et al., "Designs of Tandem Mirror Fusion Reactors", LLL Report UCRL-86576 (1981).

6. M. N. Resenbluth, H. L. Berk, H. V. Wong, D. E. Baldwin and T. Antonsen, "Fast-Growing Trapped Particle Modes in Tandem Mirrors", 1982 Sherwood Meeting, Santa Fe, NM.

7. L. D. Pearlstein, D. E. Baldwin, R. H. Cohen, T. K. Fowler and B. G. Logan, "Stabilization of Tandem Mirror Trapped Particle Modes by Incomplete Cancellation of Trapped Particle Drifts", 1982 Sherwood Meeting, Santa Fe, NM.

8. B. G. Logan, M. Rensink, LLL Memorandum MFE/CP/78-181 (1978).

9. R. W. Werner et al., ibid, p. 3-21.

10. B. M. Boghosian et al., "A Potential Solver for Sloshing Ion Thermal Barriers", LLL Report UCID 19215 (1981).

11. B. G. Logan, *Private Communication* (1982).

SECTION 4

ENERGY BALANCE - THE TANDEM MIRROR REACTOR AS AN ENERGY SOURCE

Contributors:

F. L. Ribe, R. W. Werner, T. H. Zerguini

TABLE OF CONTENTS

LIST OF TABLES

LIST OF FIGURES

4.1 TANDEM MIRROR PARAMETERS

Table 4.1 shows the physics parameters for a reactor producing 3500 Mw of fusion power at a Q value of 14.2 as computed with the TMRBAR code described in Section 3. These values are not appropriate for coupling the reactor plasma physics to the engineered blanket found in other sections of this report and to the synfuel plant itself.

Late in the synfuel study year the parallel MARS study, whose physics parameters we follow for synfuel use, indicated this lesser value of Q than the value of 25 we have cited in other portions of this study. At the writing of this report the MARS Q was 14.2. The impact of this smaller Q is felt both in the reactor performance and its energy balance but it also impacts the synfuel plant and its requirement for energy in both electrical and thermal form.

4.2 THE INFLUENCE OF Q ON THE REACTOR ENERGY BALANCE AND ON THE SYNFUEL PLANT

Figure 4.1 illustrates the energy balance for a Q of 25 and a reactor injection/heating system used for the synfuel work.

Figure 4.2 illustrates the energy balance for the more recent Q value of 14.2 plus the use of a more sophisticated injection/plasma heating system and a more detailed energy recovery system for the direct convertor.

Comparing these two figures in terms of energy delivered to the synfuel plant by a 3500 Mwf reactor it can be seen that both the thermal differences and the electrical differences are significant. The reason is mainly due to the fact that at the 14.2 Q value the reactor is very nearly at breakeven as far as utilization of the direct convertor output is concerned. Both the high voltage dc electrical energy and the direct convertor thermal energy, after its conversion to electricity, have to be fed back to the reactor to drive it. When Q is as high as 25, not only can the thermal energy from the

Table 4.1 Physics parameters for a TMR producing 3500 Mwe at a Q = 25

Central cell output:

Density cm^{-3} = 4.1 e + 14

Ion temp., Kev = 35

Electron temp., Kev = 29.1

Radius, m = 0.42; length, m = 150

Vacuum field, t = 4.7, beta = 0.7

Phie, Kev = 205.5

Density profile exponent = 3

Axicell output:

Total density, cm^{-3} = 1.0 e + 15

Hot ion density, cm^{-3} = 8 e + 14

Av. ion energy, Kev = 200

Radius, m = 0.23; length, m = 2; beam trapping fraction = .998

Vac. mid field, t = 14

Vac. mirror rat. (inner) = 1.5; vac. mirror rat. (outer) = 1.7; beta = .4

Phipc, Kev = 22.85 phipb, Kev = 35.3; passing density at pb (cm^{-3}) = 2.42 e + 14

Transition region output:

Transition length, (m) = 10; beta = 0.16

Vacuum field, (t) = 1.6; phit, (Kev) = 122.5

Pump beam trapping = 0.992; passing density (cm^{-3}) = 5.7 e + 12

Pump beam location output:

Passing density = 4.0 e + 13

Potential at injection pt. = 61.4; injection angle = 25^0

Beta at injection pt. = 5.3 e -2

Plug/barrier/anchor output:

Barrier vacuum field, t = 2.17

At pt. a', 5.1

Table 4.1 con't.

Plug/barrier/anchor output con't

Total barrier beta = 1.24; perp. beta = .65

Passing ion density at b, cm^{-3} = 4.1 e + 12

Passing ion density at mp, cm^{-3} = 3.5 e + 13

eb', Kev = 19.65; eeh, Kev = 391.8

tew, Kev = 35.5; fec = 1.98 e -02

Barrier length, m = 8

a-cell mirror field, t = 6

Beta at pt. a = .47

Beta at pt. a' = .4

ϕ_b, Kev = 198.4; ϕ_c, Kev = 142.1

ϕ_a', Kev = 73.8; ϕ_{mp} = 64

Power balance:

n.b. power at: p, mw = 34.7; a', mw = 8.7

ecrh power at: a, mw = 3.4; b, mw = 69

Pumping power (total), mw = 133; energy = 81.7

Transition power, mw = 103; barrier power, mw = 29.5

Sync radiation power, mw = 11.3

Fusion power, mw = 3500

Q value = 14.2

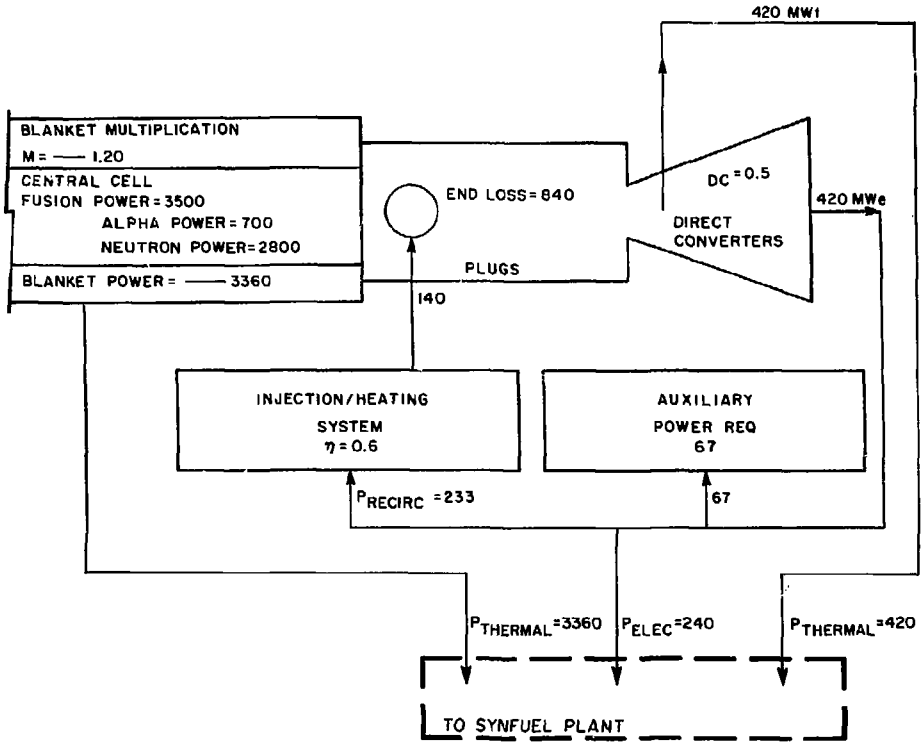

Fig. 4.1 Power balance of a TMR used for producing Synfuels, Q = 25 and M = 1.37 or 1.2 (Synfuel model)

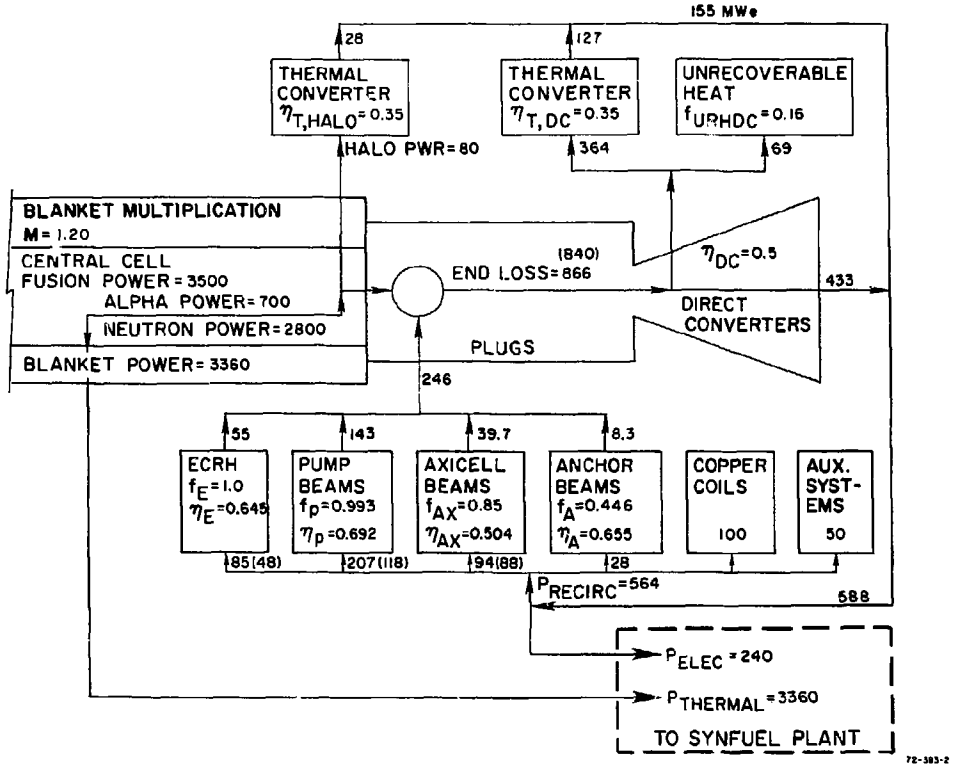

Fig. 4.2 Power balance of a Tandem Mirror Reactor used for producing synfuels, Q = 14.2 and M = 1.20

direct convertor go directly to the thermochemical plant but there is also an excess of high voltage dc that can also be utilized. Since the synfuel plant has significant internal electric demands this extra convertor electrical is quite significant. This is true in either our Joule-Boosted or our Fluidized Bed design case. Clearly high Q values are desirable. This applies also to the case where the reactor is used for the production of electricity as well as synfuels.

SECTION 5

THE LITHIUM OXIDE CANISTER BLANKET SYSTEM

Contributors:
R. W. Werner, E. N. C. Dalder, D. W. Dorn, R. G. Hickman,
M. A. Hoffman, G. L. Johnson, O. H. Krikorian, R. C. Maninger

TABLE OF CONTENTS

TABLE OF CONTENTS

TABLE OF CONTENTS

LIST OF TABLES

LIST OF TABLES

LIST OF FIGURES

LIST OF FIGURES

LIST OF FIGURES

LIST OF FIGURES

5.0 THE LITHIUM OXIDE CANISTER BLANKET SYSTEM

5.1 GENERAL DESCRIPTION

The Lithium Oxide Canister Blanket is central to the fusion reactor engineering system used for translating fusion neutron kinetic energy to a more useful form, i.e., thermal energy, which may then be used in the production of portable fuels as is the case of this Synfuel report or for the production of electricity, or both.

In addition to the neutron moderation and energy conversion the blanket must also produce tritium for the reactor fuel cycle via neutron reactions with lithium. Implicit in this tritium production are two requirements: 1) means must be provided for recovering the tritium and delivering it where it is needed; and 2) the tritium inventory in the blanket and in the tritium loop must be kept at as low a level as possible for reasons of safety. A typical target for the tritium inventory level in the blanket is of the order of 1 kilogram for a reactor producing 3000-4000 MW of fusion power. In this design we are well below the 1-kilogram target.

In this particular Canister blanket we have elected to use a combination of lithium oxide as the moderator and helium as the coolant in the belief that gas-cooled "dry" blankets offer distinct advantages of simplicity, safety and ease of startup and shutdown over those blankets using some combination of water, liquid metals and/or molten salts. We also use "in situ" tritium control rather than slip stream processing to assure that our hydrogen product is tritium free. In situ tritium control isolates the tritium from the main helium flow. Recovery of the tritium is by an independent purge circuit.

The four candidate structural materials we examined were 316 SS, 2-1/4 Cr - 1 Mo, Inconel and Tenelon. The structural material selected for the blanket is Teneion (a steel using manganese instead of nickel), chosen for its low residual radioactivity. The waste disposal rating (WDR) of

Tenelon is 0.40, which means that surface disposal of spent blankets is acceptable and deep burial is not required. Tenelon also has very attractive neutronic performance and structural properties.

This Canister blanket is one of two complementary blanket designs we have studied for Synfuel applications. The Canister blanket as used here can be characterized as a medium temperature blanket when used with the Joule-Boosted decomposer (JBD). By joule-boosting we refer to the utilization of electrically heated, commercial SiC furnace elements in place of using a heat exchanger to transfer process heat to the highest temperature step of the thermochemical process. The General Atomic Sulfur-Iodine Thermochemical Cycle has, as its highest temperature step (1100-1200 K), the thermal decomposition of SO_3 to SO_2 and O_2.

High Q tandem mirror reactors (TMR) have a distinct advantage in coupling with the Joule-Boosted Decomposer design because surplus electricity from the Direct Converter can be used to provide a significant fraction of the electrical requirement for the Decomposer.

The most important advantage of this Joule-Boosted approach from the TMR Blanket standpoint is that the temperature requirements of the blanket can be reduced dramatically. The exit temperature of the coolant from the Canister blanket is 825 K as compared with $\sim$ 1200 K exit temperature for our alternate design. The alternate design, the Two-Zone blanket discussed in Section 6, may be characterized as a high temperature blanket used with the fluidized bed decomposer (FBD).

The "system" for the fusion energy recovery and ultimate delivery to the thermochemical plant includes a number of principal elements which are interactive. They will be described briefly so that the Canister blanket module may be better understood in the context of its surroundings.

5.1.1 *The Central Cell of the Fusion Reactor*

The physics base for the energy-producing central cell of the TMR is described fully in Section 2.0 of this report. For purposes of the blanket design, the central cell is characterized by the parameters listed in Table 5.1 and illustrated in Fig. 5.1.

Table 5.1 Parameters for the central cell needed for blanket design

Central cell nominal length, L	150 m
Number of solenoidal coils	38
Spacing between successive solenoidal coils, l	4 m
Coil I.D., including all structure, coolant circuit, shielding, etc.	6.3 m
Coil O.D.	9.1 m
Coil width, w	2.0 m
Coil height, h	2.4 m
Clear space between coils axially	2.0 m
Plasma radius, r	0.6 m
First wall radius, rw	1.49 m
Fusion power, P_f	3500 MW
Average neutron wall loading, Γ	2.0 MW/m^2

The blanket assembly must be physically located outside of the plasma region and within the bore of the solenoidal coils. The distance from the plasma is a function of permissible wall loading and at the closest approach the wall must be some number of Larmor radii (typically 3) from the plasma edge. The distance from the coils is determined by clearances for assembly. It is also an established convention to divide the total blanket into a series of axial modules and circumferential submodules. The axial length of a blanket module may be the half distance between successive solenoidal coils or some other submultiple if a design constraint is one of being able to

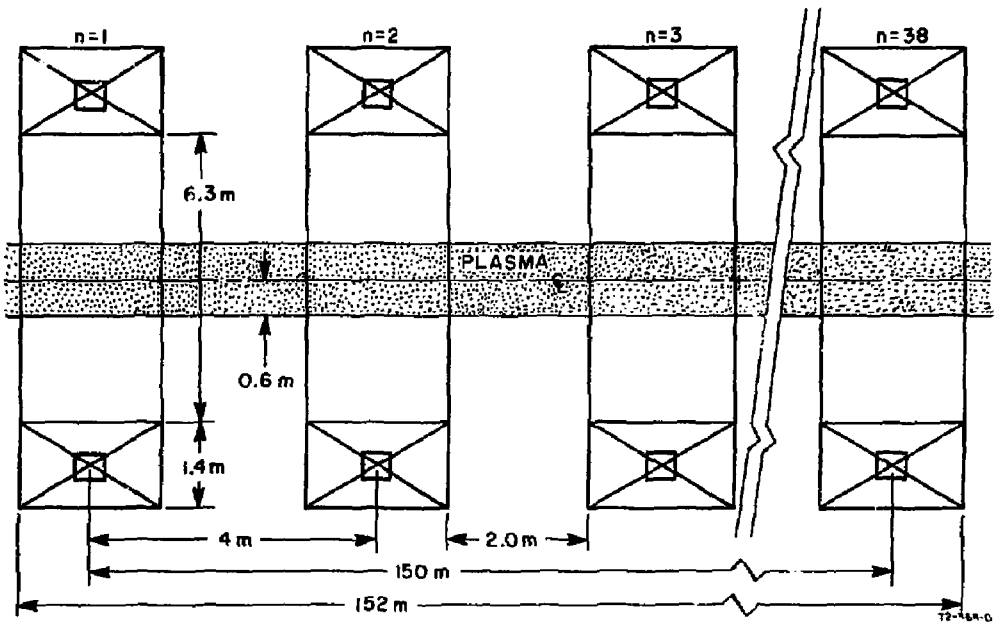

Fig. 5.1 Cross section through the fusion reactor central cell showing principal dimensions

leave the coils in place when blanket installation or removal is required. This is a highly practical consideration and one adopted here since the superconducting solenoidal coils and all their associated circuitry are generally designed for the life of the plant (~ 30 years), whereas blanket module life expectancy is limited to approximately 3 to 5 years.

Figure 5.2 illustrates, in a highly schematic way, the principle of module placement or removal for the blanket design to be discussed in this section. Module A, shown in place, is installed by a vertical motion to the reactor $\mathbb{Q}$, followed by an axial translation placing it partially under the solenoid. Module B, a mirror image of A, is shown partially installed and need only be lowered to the reactor $\mathbb{Q}$ to be in place. Structural supports between the fixed solenoidal coils are spaced so that vertical placement or removal of the blanket can be accommodated. Ring manifold piping is separately installed after the ring module is in place.

5.1.2 The Axial Blanket Module - The "Ring" Modules Within the Central Cell

The central cell is filled with a number (75) of ring modules arranged in series axially along the 150-m central cell. The ring module is illustrated in Fig. 5.3. One ring module occupies the half space between the solenoidal coils. Module A, as Fig. 5.2 indicated, is partially under the solenoid, while module B lies in the free space between coils. The modules are exactly identical, one being turned 180 degrees with respect to the other. The ring manifolding transfers the coolant (helium) to the supply and return headers located outboard of the solenoidal coils. The set of four header circuits run longitudinally along the length of the central cell and terminate in a set of intermediate steam-generator heat exchangers (IHX) that are located as closely as possible to the fusion reactor but is isolated by protective concrete wall barriers.

Radially inward from the ring headers the cold shield forms the support structure for both the ring headers and the moderating blanket/hot shield.

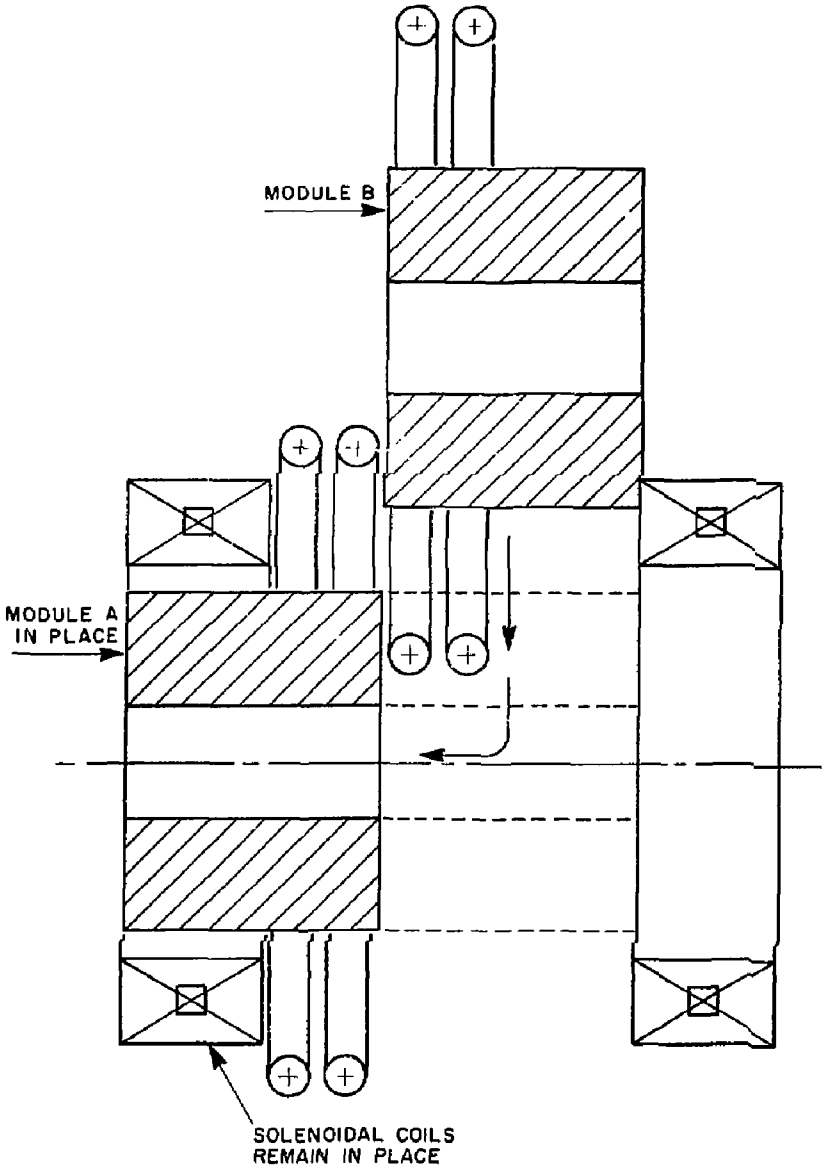

72-384-C

Fig. 5.2 Method of Canister removal from the central cell of the TMR

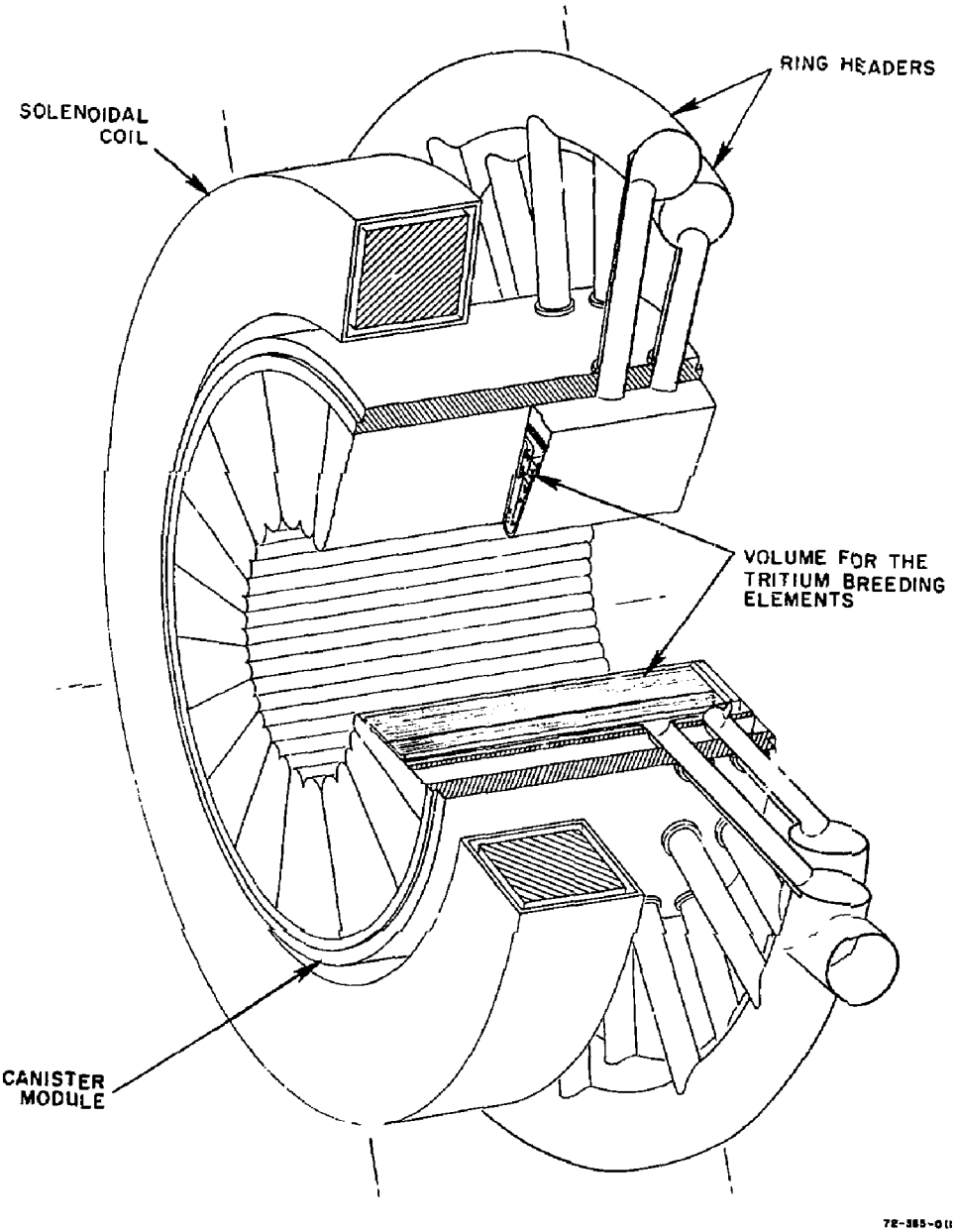

Fig. 5.3 A ring module shown in position under one of the solenoidal coils

The individual submodules of the blanket/shield are designated as Canisters. The bulk of the blanket design focuses on these Canisters. The number of Canisters within the ring module is not an arbitrary choice but is dictated by considerations of thermal and hoop stress since the Canister is a pressure vessel. We have chosen to use 18 Canisters within the ring module. These Canisters are further divided into mirror-image halves to reduce stresses.

5.1.3 Fitting the Canisters in the Ring Module

The 18 Canister modules nested within the ring module are assumed to be individually fabricated and may be proof tested and pressure tested before assembly. This will provide good quality control of a unit that is physically of reasonable size. The Canister as a unit consists of:

1. A relatively cool pressure vessel or container.
2. The assembly of lithium-oxide-filled tubes in the container.
3. A hot shield of solid metallic rods.
4. A plenum section in which flow manifolding is accommodated.
5. A cold shield that acts as the outer ring section of the Canister pressure vessel.
6. Piping couplings penetrating the cold shield and leading to the ring manifolds.

A cross section through a Canister is shown in Fig. 5.4.

When all the Canisters have been assembled in the ring module, the ring module may then be proof tested as a unit before installation in the reactor central cell.

It is anticipated that a Canister module, after some time in operation in the reactor, can no longer be individually replaced but that all 18 Canisters must be replaced simultaneously. This will be due in part to the fact that when all modules are pressurized and operating at a temperature o:

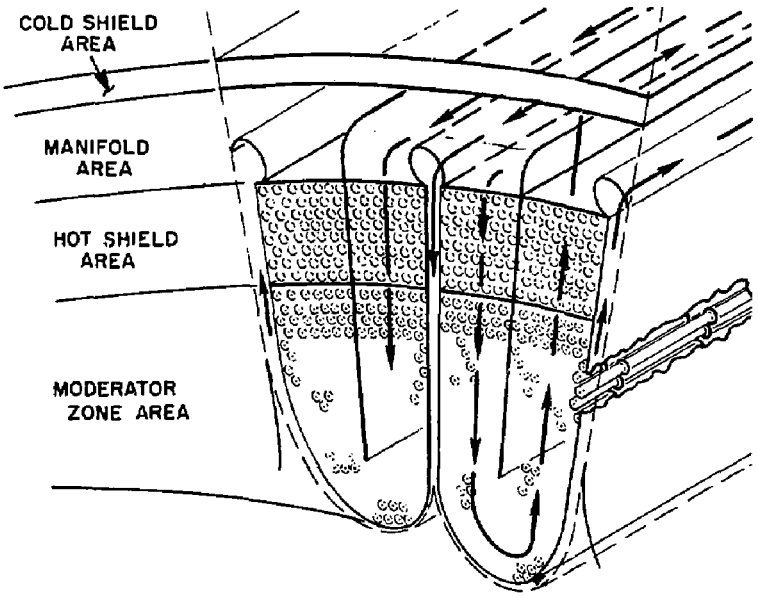

Fig. 5.4 Cross section through a Canister blanket module

approximately 700 K - 750 K in a vacuum environment, local yielding and conforming of surfaces will take place. The materials, having ultra clean surfaces for plasma purity reasons, may also vacuum weld together. It would be necessary to use bond breakers of one kind or another--oxide coatings, for instance--to eliminate the vacuum welding. However, the initially planar surfaces of the module side walls will not remain planar after some hours of operation and some number of thermal cycles. Consequently, disassembly to the individual Canister level is felt to be impractical.

5.1.4 Lithium Oxide Cartridges - The Moderator for the Canisters

Figure 5.4 shows the moderator and hot shield of the Canister within its container envelope. The moderator zone is comprised of an assembly of tubes that are closely spaced on a triangular pitch across which the helium coolant is caused to flow. The assembly of tubes constitutes a multiple pass, cross-flow heat exchanger. In this moderating section the tubes are filled with lithium oxide "cartridges" designed in the form of half washers, split rings or short cylinders as depicted in Fig. 5.5. The advantage of using one of these general shapes is that the cartridges are "pre-cracked" both axially and radially and thermal stress problems can be minimized. They can be readily loaded into a long tube and fabrication with good dimensional tolerance should not be difficult. The density of the lithium oxide can also be precisely controlled.

A sub-assembly of the Canister is thus a long tube ($\sim$ 2 m) within which the lithium oxide resides. The tube protects the oxide from the mainstream coolant so that it does not tend to disintegrate due to the high velocity flow or trace contaminant action. Most importantly the sub-assembly also provides in situ first-line tritium control, as illustrated in Fig. 5.6. Tritium control is discussed in detail in Section 5.4. Briefly, however, the matrix of lithium-oxide-filled tubes are mounted in a tube sheet. The tube sheet is at one end only of the Canister and is oriented normal to the main-stream helium coolant flow. Purge helium, totally separated from the main helium flow but at substantially the same pressure, flows first in the

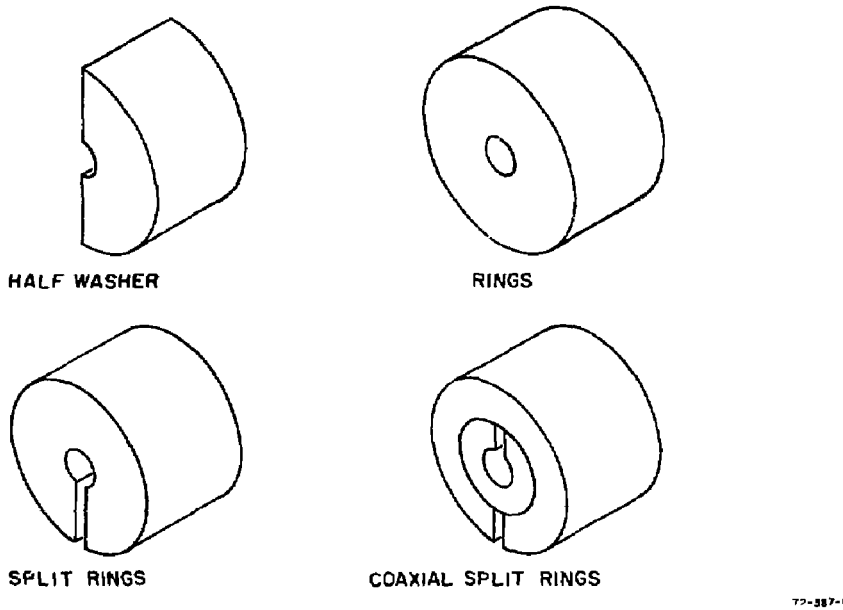

Fig. 5.5 Possible configurations for the Li_2O cartridges

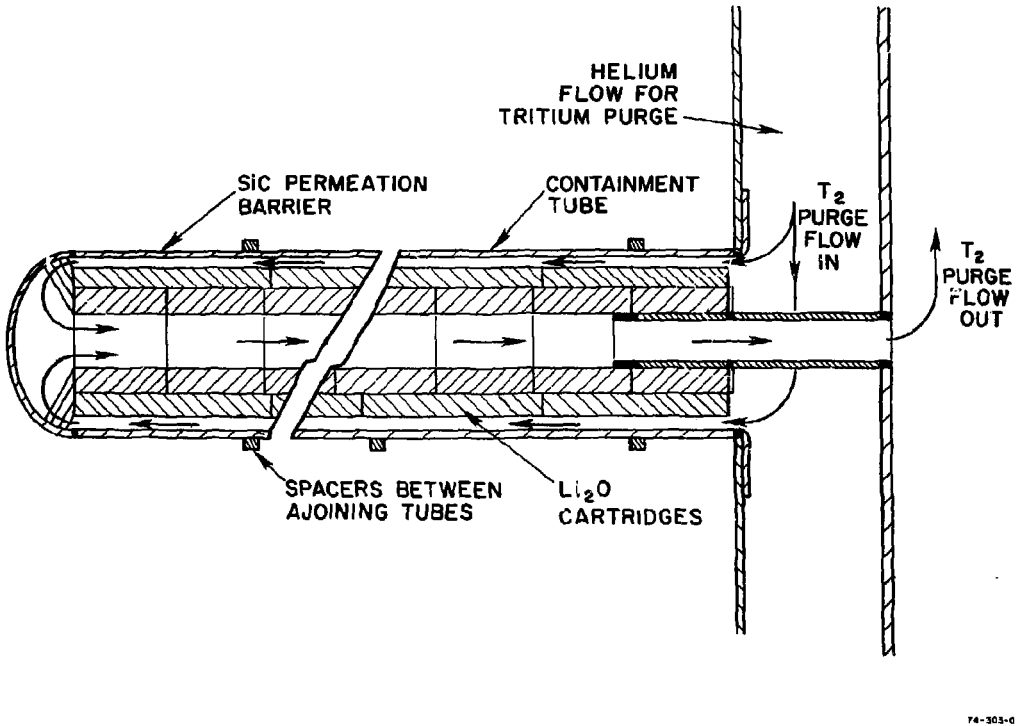

Fig. 5.6 In situ tritium control

annular space between the tube wall and the Li_2O cartridge and then returns through the central hole in the cartridge. The mass flow of this helium used to purge the tritium is very low and inconsequential compared to the main-stream coolant flow.

In the hot shield zone of the Canister the tubes are replaced by solid rods. In the cases that were studied for the Canister thermal-hydraulic performance, all tubes and rods were assumed to be the same diameter. This need not be the case nor is it necessary to have all moderating tubes the same diameter. In fact, tubes could progressively increase in diameter as a function of increasing blanket radius to partially compensate for the exponentially decreasing energy deposition. For this particular study we concentrated mainly on sizing the tubes to match overall neutronics/thermal-hydraulic needs and have not as yet used the second order refinement of having graded sizes.

5.2 THE CANISTER FIRST WALL AND STRUCTURAL ENVELOPE--THE "COOL" CONTAINER

The Canister structural container is an independently cooled, double-walled envelope surrounding the lithium-oxide-moderating medium and the hot shield. The coolant circuit for the first wall is shown in Fig. 5.7. High pressure helium enters the Canister at its centerline at a temperature of 525 K, flows radially inward to the first wall where the flow divides equally, flowing outward in an enveloping flow around the Canister module to collecting plenums. The helium exit temperature is 625 K. The pressure of the first wall helium coolant circuit is in the range of 40 to 60 atmospheres, dictated by the pressure of the mainstream coolant flow, to which it is set equal, and further dictated by the need to have highly efficient heat transfer in the first wall. From 5 to 15% of the total blanket energy can be deposited in the first wall. The helium temperature and flow rate is selected so as to limit the maximum material temperature in the first wall structural envelope to approximately 750 K. This maximum material temperature is chosen to limit radiation damage (discussed in Section 5.6 on materials) and to stay below the threshold of creep behavior so as to design for stresses based on yield strength. The principal stress in the first wall is a membrane stress arising because the Canister is a pressure vessel with a first wall curved surface subjected to hoop stress. Thermal stresses also occur due to heat removal from one side only of the first wall. The thermal stresses are additive to the hoop stresses at the inner surface of the first wall.

5.2.1 Stresses in the First Wall of the Canister Blanket Module

For our reference design we have assumed that there are 18 Canisters or blanket submodules in a ring module. We have further assumed that the individual modules bear one against the other circumferentially until a point is reached where they separate. The first wall of any one Canister is defined as the curved surface that exists between successive separation points. The first wall and its separation points are depicted in Fig. 5.8A and B.

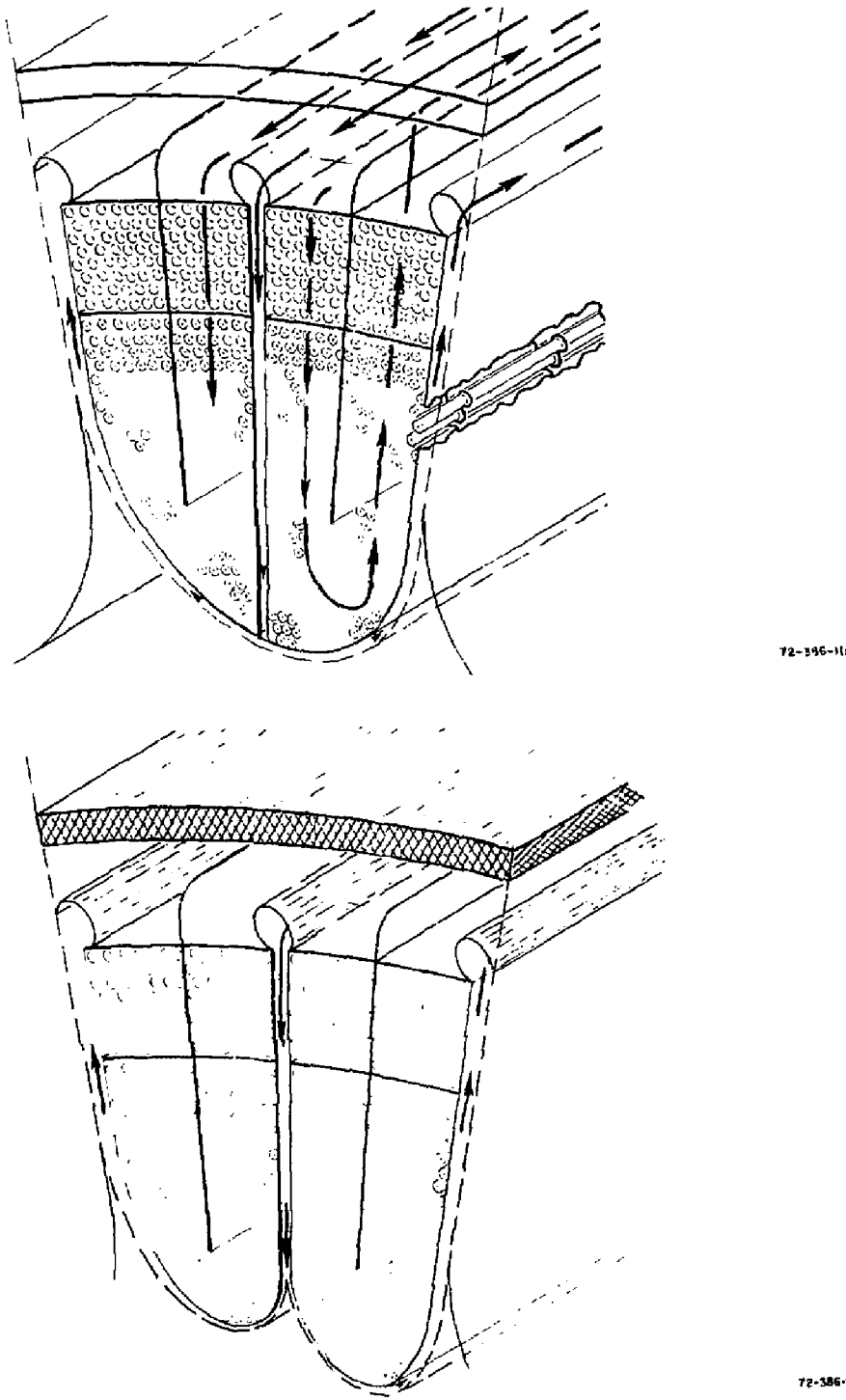

Fig. 5.7 Cooling circuit for the first wall

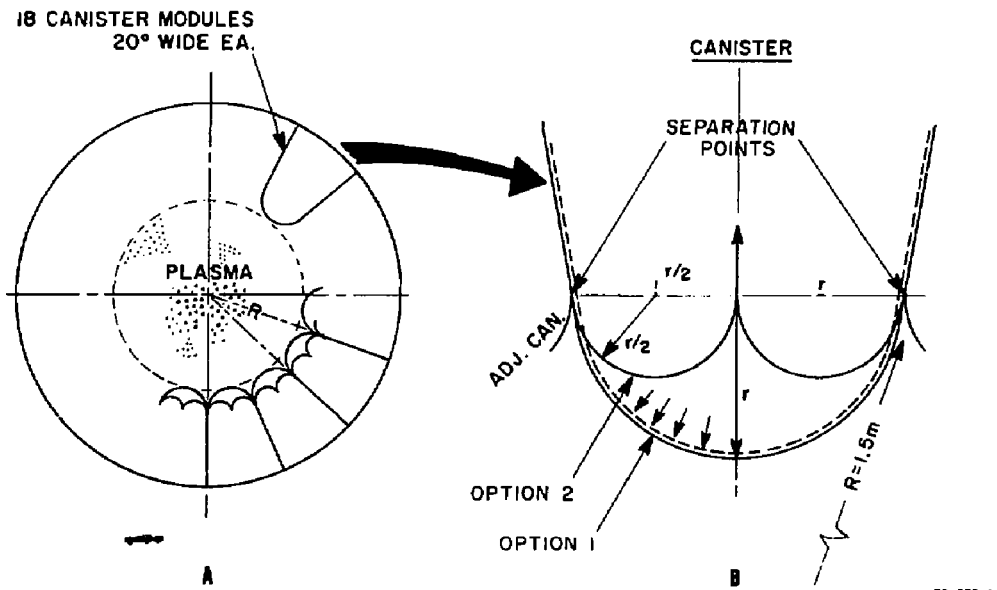

Fig. 5.8 The first wall of the Canister; defined as the circular arc(s) between successive separation points

5.2.2 Hoop Stresses Due to Pressure Loading

At the point of separation of the curved first wall from the side walls, each module has a circular arc first wall of some radius, r. The value of r will determine the hoop stress in the first wall. The stresses arise because the blanket module is a pressure vessel operating at a pressure, P. The reference design pressure is 50 atm.

We take 1.5 meters as the distance from the plasma centerline to the separation point of the first wall. The least value of r for a circular arc first wall for the entire Canister (option 1 in Fig. 5.7) is when the arc is a half circle. For the half circle:

$$r = \frac{2 \times 1.5}{18 \times 2} = 0.26 \text{ m}$$

This least value r yields the lowest stress from the simple hoop stress equation:

$$\sigma = \frac{P \times r}{t}$$

The least value of r also minimizes any bending stresses that occur at the separation point between first wall and side wall.

There is no discernable advantage in increasing the radius of curvature of the first wall in order to move the point of closest approach of the first wall away from the plasma. The small decrease in wall loading that results cannot compensate for the increased level of stresses due both to hoop stress and to the bending stress introduced near the separation point. If the stresses were quite low then the situation might be different. Such is not the case and therefore we not only used the least value of r but also looked to other means of lowering the hoop stress since, when it was combined with the thermal stress, we found the allowable design stress to be exceeded. Referring back to Figs. 5.7 and 5.8, it may be noted that two options for the first wall radius are shown. Option 1, where r = 0.26 m, has just been discussed. As a straightforward means of decreasing stress, option 2

involves subdividing the Canister into two independent halves, as shown in Fig. 5.7. Option 2 halves the hoop stresses of option 1 by halving the value of r. With option 2 the thermal hydraulics and the basic coolant flow circuit remains substantially unchanged from option 1. Our design uses option 2.

5.2.3 Thermal Stress Due to Power Density at the First Wall

From representative neutronics data shown in Table 5.2, the power density due to neutron and gamma heating in the material of the first wall, w, at the point of separation is 16.80 MW/m^3 when the wall loading is 2 MW/m^2 and the design material is Tenelon. For option 2 where r = 0.13 m, the power density in the first wall, w, at the point of closest approach to the plasma (i.e., 1.5 m - 0.13 m from plasma ℄) is thus ∿ 18.34 MW/m^3. In terms of energy that must be removed by the helium coolant from one side only of the first wall material, this power density can be significant if the wall has to be relatively thick to accommodate hoop stress. Very large film drops could arise. Furthermore, thermal stresses are induced due to the heat disposition in the wall and increase with increasing wall thickness. These stresses must be added to the hoop stress.

Table 5.2 Selected neutronic data used for comparative stress calculations

Material	Energy Deposition at First Wall Separation Point	Max. Energy Deposition	Tritium Breeding	Energy Mult
Tenelon	16.8	18.3	1.13	1.24
316 SS	18.4	20.0	1.12	1.21
2-1/4 Cr 1 Mo	15.2	16.5	1.30	1.18
Incone1*	27.0	29.3	1.11	1.16

65 cm thick moderator, 40% Li_2O; 8% structure

* Must be 60% Li_2O to breed adequately.

In addition to the internal heat generation, there is an incident flux on the first wall surface facing the plasma due to bremsstrahlung, charged-particle bombardment and synchrotron radiation. This is small ($\sim 2 \times 10^4$ W/m^2) and is ignored here in determining stresses.

For the thicknesses of the first wall, t, that will be both structurally adequate while at the same time having minimal effect on the overall neutronic performance of the blanket (it is likely that t must be < 0.01 m), we can ignore the exponential change in power density across t and assume that w, the local energy density, is an average in the first wall. The heat removal is from one side only and the resulting inner surface heat flux, q, is:

$$q = wt \qquad (W/m^2)$$

From the conduction equation, assuming that the uniform power density is equivalent to a concentrated flux located at $\Delta x_{equiv} = t/2$:

$$q = \frac{k\Delta T}{\Delta x_{equiv}} = \frac{k\Delta T}{\left(\frac{t}{2}\right)}$$

The equation for the thermal stress is:

$$\sigma_{th} = \frac{E\alpha\Delta T}{2(1-\nu)}$$

So we have finally:

$$\sigma_{th} = \frac{E\alpha w t^2}{4(1-\nu)k}$$

where

E	=	modulus of elasticity
α	=	coeff. of thermal expansion
ν	=	Poissons ratio ≈ 0.3
k	=	thermal conductivity coefficient
t	=	thickness of first wall
w	=	average power density in first wall material

Example:

For t = 0.01 m using a familiar structural material such as 316 stainless steel

$$\sigma_{TH} = \frac{1.65 \times 10^{11} \times 20 \times 10^{-6} \times 20.0 \times 10^{6}(.01)^2}{4(1 - 0.3)\ 17}$$

$$= 138 \text{ MPa}$$

$$\simeq 20000 \text{ psi}$$

For structural materials with much higher strength than 316 SS, such as Inconel 800H, the thermal conductivity is higher (24 vs 17), the coefficient of expansion is lower (17 vs 20), but the local internal heat generation is much higher (29.3 w/cm^3 vs 20.0) due to the high nickel content of the alloy. The resulting thermal stresses are slightly lower for the Inconel than for the 316 SS, $\sim$ 127 MPa for the example cited.

For Tenelon, our choice for the first wall material, optimum for its low residual radioactivity and minimal waste disposal problems, the thermal stress level is the lowest of the materials considered--78 MPa for the same example. This low stress is due to both lower internal heat generation and a thermal conductivity that is reasonably high. The 2-1/4 Cr Mo provides an attractive alternate but has a higher waste disposal rating (WDR) (15 vs 0.4 for the Tenelon). The WDR is the dilution factor that must be used in disposing of the spent material. For instance, a WDR of 15 means that 15 m^3 of inert diluent would have to be added to 1 m^3 of spent material and the total then homogenized and sealed in containers for acceptable disposal.

Complete property data for all four materials can be found in the appropriate subsection. Table 5.3 provides the data required here for the thermal stress calculations. The data are at 750 K.

Table 5.3 Selected material property data for comparative stress calculations, ref. temp. = 750 K

Material	ν	E (10^{11} Pa)	σ_y (MPA)	2/3 σ_y	α (10^{-6} $^oC^{-1}$)	k (W-K)
Tenelon	0.3	1.65	275	175	18	25
316 SS	0.3	1.65	125	83	20	17
2-1/4 Cr 1 Mo	0.3	1.80	205	137	15	32
Inconel 800H	0.3	1.72	900	597	17	24

The combined tangential stresses at the inner surface of the first wall as a function of wall thickness for option 2, where the radius of curvature is 0.13 m, are compiled in Table 5.4 and plotted in Fig. 5.9 for the four materials.

From Fig. 5.9 it can be seen that the low-activity Tenelon is an excellent choice for the first wall material based on using 2/3 of the yield stress as a working stress. The stress curve has a rather shallow minimum, and wall thicknesses ranging from 5 to 10 mm would be acceptable. Since neutronically one wishes the first wall to be as thin as possible, there would be some tendency to choose 5 mm as the design point. However, we use 6 mm as our reference, which lessens the stress $\sim$ 8% at the price of increasing the local energy deposition $\sim$ 17% but also provides an important allowance of $\sim$ 1 mm for surface sputtering.

From the neutronic data for Tenelon, the maximum heat flux to be removed by the helium from the first wall surface (max) would be $\sim$ 18.34 MW/m^3 x 0.006 = 0.11 MW/m^2 or 11 w/cm^2. This is quite a reasonable value since flux levels as high as 40-50 w/cm^2 are plausable with gas coolants. This suggests that, other things being equal, higher wall loads than our design level 2 MW/m^2 are possible. Total stress as a function of wall load is

Table 5.4 Total stress in the first wall as a function of wall thickness, t, for a first wall radius of curvature of 0.13 m and a coolant pressure of 5 MPa (~ 50 atm.)

Wall Thickness m t	Hoop Stress, σ_H (MPa) (All Materials)	Thermal Stress, σ_{TH} (MPa)				Total Stress (MPa)			
		316	Inconel	Tenelon	2-1/4 Cr - 1 Mo	316	Inconel	Tenelon	2-1/4 Cr - 1 Mo
0.010	65	138	127	78	50	203	195	143	115
0.009	72	112	103	63	41	184	175	135	113
0.008	81	88	81	50	35	169	164	131	116
0.007	93	68	62	38	25	161	157	131	118
0.006	108	50	46	28	18	158	155	136	126
0.005	130	35	32	20	13	165	163	150	143
.004	162	22	20	12	8	184	183	174	170
.003	217	12	11	7	5	229	229	224	222

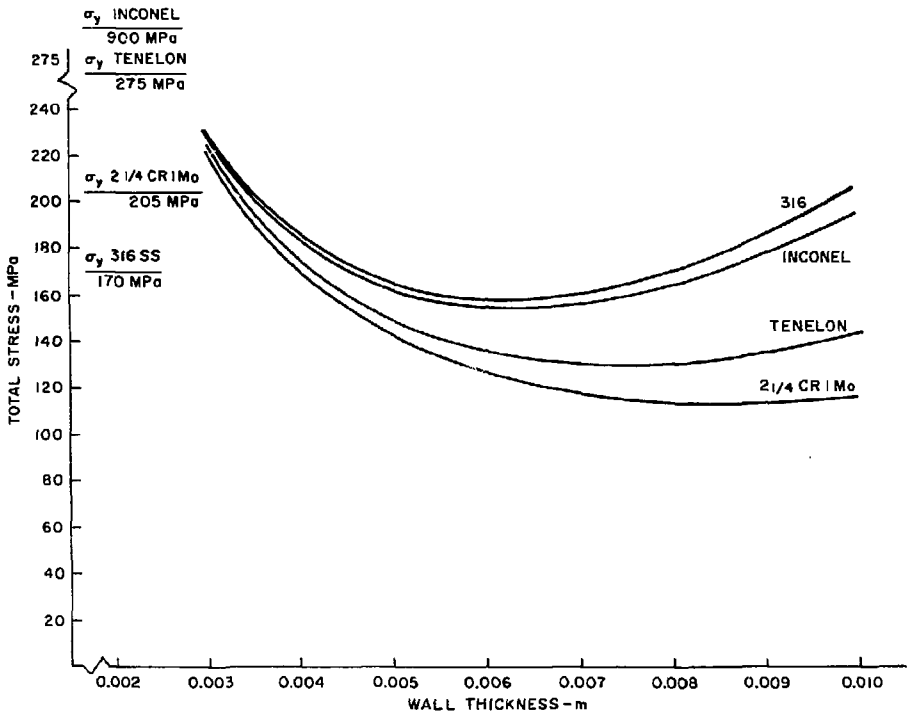

Fig. 5.9 Total stress in the first wall as a function of first wall thickness for a first wall radius of curvature of 0.13 m and a coolant pressure of 50 atm at a temperature of 750 K

plotted in Fig. 5.10. The acceptable design stress, 2/3 the yield stress, is not reached until the wall loading is 5.0 MW/m^2. This is a very favorable situation. The effect of wall loading on the heat transfer in the Canister moderating volume is discussed in Section 5.3. Here it will be seen also that wall loadings substantially higher than our 2 MW/m^2 are feasible.

5.2.4 Material Temperature at the First Wall

To optimize the interfacing of the overall reactor blanket modules with the thermochemical plant (see Section 10 for details), the following specific design parameters were chosen for the wall coolant circuit:

- Coolant - helium
- Inlet temperature, T_{BIN} = 525 K
- Outlet temperature, T_{BOUT} = 625 K
- Coolant pressure, P = 50 atm
- First wall is independently and integrally cooled
- A quasi-adiabatic surface is assumed to exist between the first wall coolant circuit and the main body of the moderating blanket
- Wall thickness = 0.006 m

With these data and one further simplifying assumption, it is possible to closely estimate the maximum material temperature in the first wall. The approximation is that all energy deposition occurs in the curved surface of the first wall of length, $\ell = 0.13 \times \pi = 0.41$ m, and that essentially no energy deposition takes place in the lead-in and lead-out lengths. The annular spacing, δ, between the first wall and the adiabatic surface forms the cooling channel. This channel is kept intentionally small to enhance heat transfer. Flow spacers can be provided as illustrated in Fig. 5.11. The hydraulic diameter of this channel is 2 δ.

The quantities to be determined in arriving at the material temperature are:

a) The energy to be removed

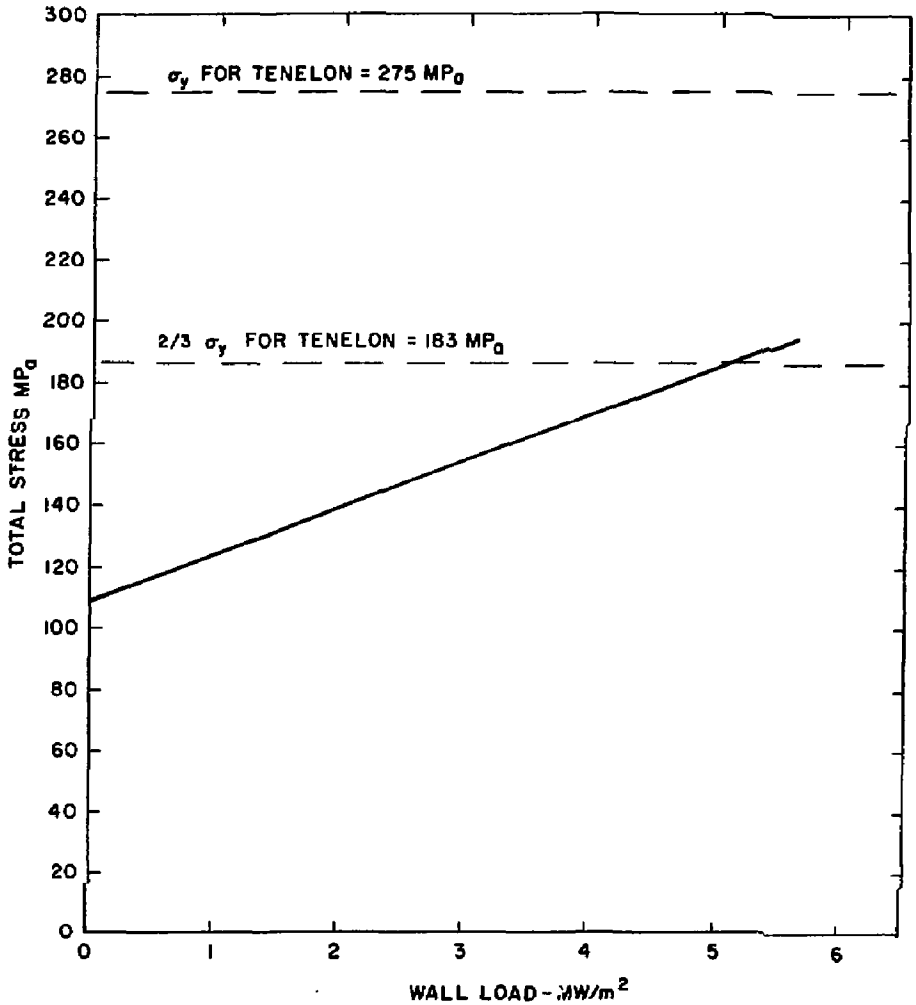

78-380-0

Fig. 5.10 The effect of wall loading on total stress in the first wall for Tenelon 6 mm thick

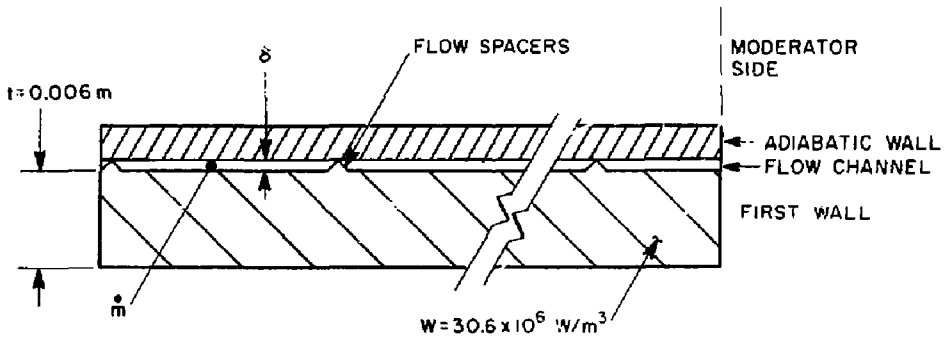

Fig. 5.11 Cross section through the first wall showing a simple flow channel with flow spacers

$$Q_{\substack{UNIT \\ WIDTH}} = wt\ell = 18.34 \times 10^6 \times 0.006 \times .41 = 45,116\ W/m$$

b) The mass flow rate

$$\dot{m} = \frac{Q}{C_p \Delta T_B} = \frac{45,116}{5.2 \times 10^3 \times 100} = 0.085\ kg/s\ (per\ mete.\ of\ width)$$

c) The average flow velocity assuming flow gap $\delta = 0.002$ m

$$\bar{u} = \frac{\dot{m}}{\delta(\bar{\rho})} = \frac{0.085}{0.002(4.18)} = 10.18\ m/s$$

where $\bar{\rho} = \frac{P}{R\bar{T}} = \frac{50 \times 10^5}{2079 \times 575} = 4.18\ kg/m^3$

d) The average Reynolds number, based on the hydraulic diameter, is

$$\overline{Re} = \frac{2\delta\bar{u}(\bar{\rho})}{\mu} = \frac{.004 \times 10.18(4.18)}{300 \times 10^{-7}} = 5676$$

To determine the average film coefficient, $\bar{h}$, we may use the correlating equation:

$$Nu = \frac{\bar{h}D_H}{k} = 0.023(Re)^{0.8}(Pr)^{0.33}$$

$$= .023\ (5676)^{0.8}(.67)^{0.33} = 20.3$$

$$\bar{h} = \frac{20.3 \times 0.233}{0.004} = 1183\ w/m^2K$$

Finally, with a heat flux, q, equal to $18.34 \times 10^6 \times .006 = 1.10 \times 10^5$ W/m^2 we obtain

$$\Delta T_{FILM} = \frac{1.10 \times 10^5}{1183} = 93\ K$$

The temperature drop across the wall is

$$\Delta T_W = \frac{qt}{2k} = \frac{1.1 \times 10^5 \times .006}{2 \times 25} = 13.2 \text{ K}$$

The maximum material temperature is thus:

$$T_{MAX} = T_{BOUT} + \Delta T_{FILM} + \Delta T_{WALL}$$

$$= 625 + 93 + 13$$

$$\approx 731 \text{ K}$$

The film temperature drop of 93 K is somewhat high but acceptable since the material temperature of 731 K is well below a design limit of 823 K imposed by radiation damage considerations and low enough to be below the creep stress regime. However, it is desirable to reduce the film temperature drop as much as is reasonably possible and one method for doing this is to resort to a grooved first wall design. The grooved first wall increases the area available for heat transfer and decreases the average inner surface flux, q. The complication, beyond that of having introduced a first wall that is more costly and difficult to fabricate, has to do with enhancing the heat transfer by making the first wall into a finned surface as shown in Fig. 5.12 results in the hydraulic diameter of the finned surface being intrinsically less than the hydraulic diameter for a simple gap. When the same flow velocity is retained, the Reynolds number thus decreases and tends to offset somewhat the surface area gain made by introducing the fin. Figure 5.12 illustrates a rough optimum for the fin proportions where the fin height (equal to its width) is equal to two-thirds of t.

5.2.5 Conclusions on the Stresses in the First Wall

It is important to note that the stresses in this curved first wall sheet are purely tensile membrane stresses and local thermal stresses. There are no bending stresses that can be caused by the pressure-vessel-type loading (except at the ends where a transition is made from the first wall to the end walls or from the first wall to the side walls). Therefore there is no

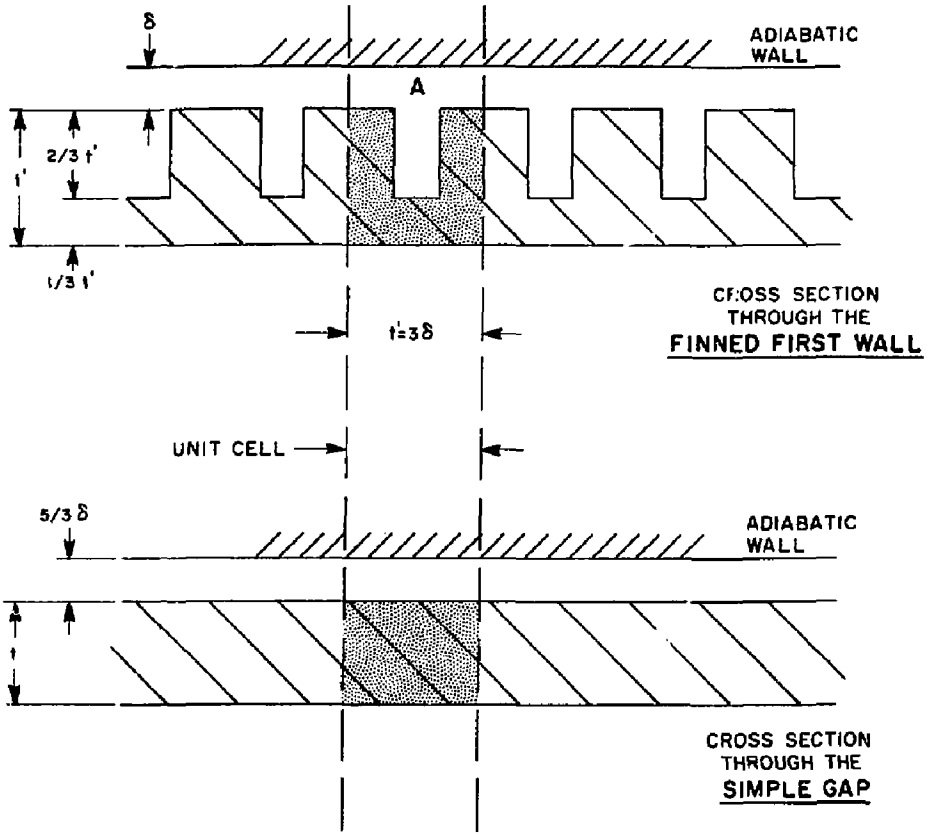

PARAMETER	FINNED	SIMPLE GAP
AREA, FLOW	A	A
HYDRAULIC DIA.	2δ	(10/3)δ
HEATED SURFACE AREA	7δ	3δ

78-392-0

Fig. 5.12 Cross section through the first wall using finned surfaces for improved heat transfer

additional strength benefit to be derived by adding fins for stiffening since there is no moment of inertia term in the hoop stress equation or in the thermal stress equation. The fins do help the heat transfer as was just indicated. However, our choice for the first wall design is the flat plate with the uniform flow gap, based mainly on its simplicity, its structural adequacy and the fact that it is tolerant of wall loads as high as 5 MW/m^2.

5.2.6 Comparison with an Alternate Canister Design

The first wall presents a significant but manageable stress problem as it is presently configured. If it should prove desirable to depart from the pressurized, curved sheet approach presently used (actually the Canister is two coaxial curved sheets separated by a cooling space) then the way the module is pressure loaded must be changed. A possibility may appear to exist of making the curved sheets into a tube array where the tube radius would be a characteristic dimension for hoop stress caused by first wall coolant (Fig. 5.13). However, the pressure loading from the mainstream coolant flow would still create a hoop stress on the tubes which is still determined by the radius of curvature of the first wall. Thus, in order to unload this pressure from the Canister first wall so as to decrease the stress, it would be necessary to flow the mainstream coolant within tubes that pass through the solid Li_2O moderator rather than having the Li_2O on the inside of the tubes and the flow on the outside.

Figure 5.13 illustrates the main differences in principle between the pressurized Canister design concept and the pressurized tube design concept. The pressurized tubes making up the first wall must be welded continuously, one to the next, presenting additional problems of structural integrity and first wall life.

It is our contention that the pressurized Canister design is a much better choice than the pressurized tube design. The only proviso is that the structural envelope (the cool container) comprising the pressurized Canister must be independently cooled and held at modest temperatures as we have done.

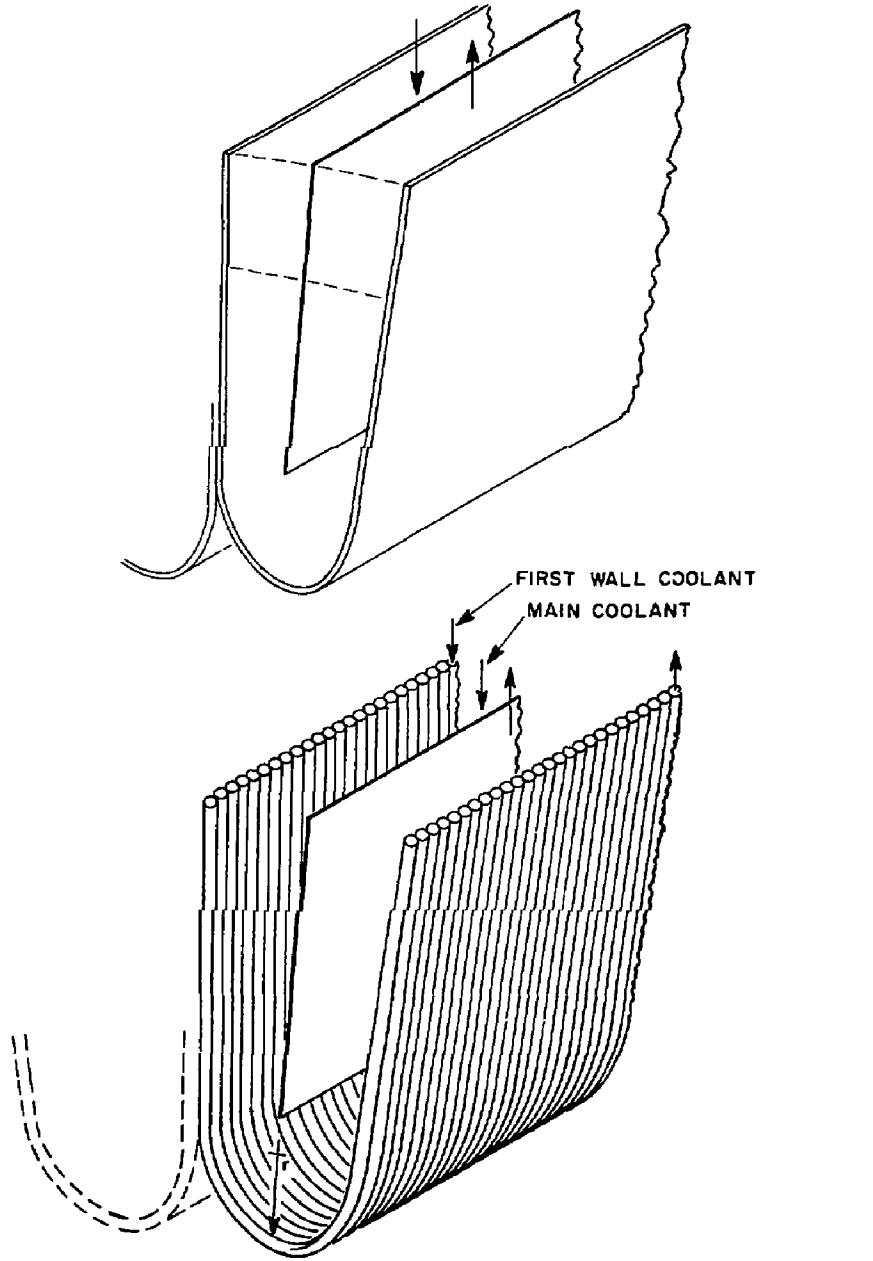

Fig. 5.13 The difference in principle between the pressurized Canister design and the pressurized tube design concept

With the pressurized Canister design concept, the helium pressure across the tubes containing the Li_2O in the moderator zone can be balanced. Even though the tube temperatures are high, the stresses are very low because of the pressure balancing. With the non-pressurized Canister the pressurized tubes in the moderator zone have relatively high hoop stresses which cannot be accommodated at high temperatures without resorting to materials that are much less desirable than Teneion for low residual radioactivity.

5.2.7 Coolant Pressure Drop and Pumping Power in the First Wall

The frictional pressure drop in the first wall is given by the equation:

$$\Delta P_f = f \times \frac{\rho u^2}{2} \frac{L}{D_h}$$

The Darcy-Weisbach friction factor, f, for flow between parallel plates may be obtained from (Ref. Rohsenow & Hartnett, Handbook of Heat Transfer - McGraw Hill):

$$f = 0.316\ (Re)^{-0.25}$$

$$(6000 < Re < 300{,}000)$$

The turning loss where the flow divides at the first wall is:

$$\Delta P_t = \frac{\rho u^2}{2} \times K_L$$

where K_L = loss coefficient ≈ 1.0.

For the reference case we have:

$$f = 0.316(5676)^{-0.25} = 0.0365$$

$L_F \approx 2.5$ m = flow length

$D_H = 0.004$

W = Canister axial length = 2 m

$$\Delta P_{TOT} = \Delta P_f + \Delta P_t = 0.0365 \left(\frac{4.18 \times 10.18^2}{2}\right)\frac{2.5}{0.004}$$

$$+ \left(\frac{4.18 \times 10.18^2}{2}\right) \times 1.0$$

$$= 4941 + 217 = 5158 \text{ Pa } (< 1. \text{ psi})$$

where we have neglected the small acceleration pressure drop, and where entrance and exit losses are accounted for elsewhere.

The pumping power per Canister half module, the pressure drop times the volumetric flow rate, is:

$$PP = \Delta P_{TOT}(Au)$$

$$= 5158(2 \times 0.002 \times 10.18)$$

$$= 210 \text{ W per half Canister}$$

The thermal power to the first-wall coolant flow per half Canister is $\approx$ 0.12 MW:

$$P_{th(PW)} = \frac{3500 \times 1.2 \times .8 \times .1}{75 \times 18 \times 2} \quad 0.124 \text{ MW}_t$$

for 10% of the neutron power to the first wall. Clearly the pressure drop and the pumping power are of little consequence for the first wall coolant.

5.2.8 Pressure Balancing the Side Walls of the Canister Module - The Effect of Leaks

As mentioned in Section 5.2.1, the individual Canisters assembled in the ring module bear against one another circumferentially until the point of separation between adjacent Canisters is reached and the first wall begins. Moving radially outward from the point of separation and away from the region of the first wall, the pressures between adjacent Canisters are balanced during normal operation and the assembly is mutually supporting. The common manifolding that ties the coolant flow of these Canisters together serves as a means of keeping pressures in balance. In the event of a pressure leak in

any one Canister or in the ring module, it is reasonable evident that the common manifolding of both the inlet and outlet ring headers will tend to freeze pressures to remain in balance from one side wall to the next and also from ring module to ring module. This should preclude any "domino" effect where the Canisters would progressively fail circumferentially around the ring module or failure would progress from ring module to ring module. In principle the assembly of Canisters and ring modules should be fail-safe in this conceptual design. However, the dynamics and time constants of this system must be studied to verify this assumption. The following calculation gives some insight into the dynamics. The size of a leak naturally is significant. We do know the total mass flow of helium in the blanket assembly. We know also that the velocity of the helium venting across a hole or fault is the acoustic velocity because of the high pressure ratio, i.e., $\sim$ 50 atmospheres on one side and vacuum on the other.

The mass flow rate through the hole or fault is

$$\dot{m}_F = \overline{\rho u} A \approx 4.18 \times 1587 \times A = 6634 \times A \text{ kg/s}$$
$$\approx 6600 \times A \text{ kg/s}$$

where the acoustic velocity $\bar{a} = \sqrt{\gamma RT} = \sqrt{1.67 \times 2079 \times 725} = 1587$ m/s.

The total mass flow of the system coolant is

$$\dot{m}_{TOT} = \frac{Q}{C_p \Delta T} = \frac{(3360 - 285) \times 10^6}{5.2 \times 10^3 \times 200} = 2957 \text{ kg/s}$$

Leaks typically are pin-hole size. However, if we assume a very large fault diameter of 1 cm or a long crack of equivalent area, then the loss rate is

$$\dot{m}_F = 6600 \times \frac{\pi(.01)^2}{4} = 0.5 \text{ kg/s}$$

Compared to the total mass flow the venting flow is only 0.017%. Long before the flow or the pressure balancing is perturbed the plasma would be quenched or the system vacuum pumps would be overloaded, or both.

This area--the effect of leaks on the plasma--must be studied further. It seems reasonably evident that the effect on the plasma will normally be of more consequence than the effect of small leaks on the structural integrity of the assembly of Canisters.

5.2.9 *The Canister Structural Envelope: Data Summary and Conclusions*

Table 5.5 lists the significant set of numerical values for the Canister envelope and first wall structure. The principal features of the design can be summarized as follows:

a) The Canister structural envelope is purposely designed to run cooler than the blanket elements inside it; the maximum envelope temperature of only about 731 K is maintained this low by a separate helium coolant circuit.

b) The relatively cool structural temperature allows the Canister envelope to serve as a pressure vessel for the 5 MPa helium coolant flowing through the blanket tube bank.

c) The combined hoop and thermal stress in the first wall is only about half the yield stress of the Tenelon alloy selected for a neutron wall loading of 2.0 MW/m^2.

d) The fractional pressure drop in the first-wall helium coolant is only about 0.10%, resulting in a very small ratio of pumping power required to thermal power removed of only 0.17%.

e) The "cool container" concept allows great flexibility in the design of the Canister itself as well as the design of the tube-bank breeder blanket and hot shield inside it.

f) There appears to be sufficient strength of the Tenelon to allow moving the Canisters closer to the plasma up to a neutron wall

Table 5.5 The canister structural envelope and first wall data summary

Neutronics of Plasma Heat Loads	
Design neutron wall loading, Γ_N	2 MW/m^2
Possible max. neutron wall loading	5 MW/m^2
Volumetric heat generation	18.34 MW/m^3 for Γ_N = 2.0
Incident charged particle flux to FW	2×10^4 W/m^2
Structural	
Plate thickness, first wall	0.006 m
Material	Tenelon
Maximum material temperature	731 K
Maximum combined stress	136 MPa
2/3 yield stress, Tenelon at 750 K	275 MPa
Thermal-Hydraulic of First Wall Flow	
Coolant medium	Helium
Pressure	5 MPa
Inlet temperature	525 K
Outlet temperature	625 K
Reynolds No.	5676
Nusselt No.	20.3
Flow velocity	10.18 m/s
Pressure drop	5158 Pa (< 1.0 psi)
Pumping power/half Canister	210 W
Power removed by first-wall coolant per half Canister	0.12 MW
% pumping power in cooling the first wall	0.17%

loading of almost 5 MW/m^2. This has the possible advantage of decreasing the size and cost of the blanket and central cell magnet coils (at the expense of much shorter blanket lifetimes).

5.3 HEAT TRANSFER IN THE CANISTER VOLUME

Early calculations in our first model of the Canister blanket indicated that it would be difficult to obtain a relatively large rise in the bulk coolant temperature (say 300 or 400 K) as the coolant flows across the lithium-oxide-filled tubes. The reason for the difficulty was the short travel distance, h, of the coolant since in this model of the Canister it was initially designed as a single pass heat exchanger as illustrated in Fig. 5.14. As a single pass system the thermal hydraulics were characterized by very low flow velocities, poor film coefficients of heat transfer, larger centerline temperatures in the lithium oxide than would be manageable, and higher tube temperatures than could be tolerated. Furthermore, in this model the first wall was not independently cooled.

Since the heat load and temperature range requirements are significantly different for the first wall than for the moderator volume, it was considered a better choice to provide separate cooling circuits. To cope with these anticipated design considerations of improving the thermal hydraulics and providing separate circuitry, a multiple pass heat exchanger was adopted as shown in Fig. 5.15. The illustration shows a two-pass heat exchanger. However, it is possible to use multiples of two passes with the same calculational procedure. Because of the independent cooling circuit adopted for the first wall and the way this circuit is routed to deliver coolant down the center of the Canister and then up the sides, a half Canister serves as the calculational model for the thermal hydraulics and neutronics of the moderator/shield volume.

The calculational model for the blanket heat transfer may be described as a staggered tube, triangular pitch, crossflow heat exchanger. The dimensional parameters for the tubes and rods in this heat exchanger are shown in Fig. 5.16. All nomenclature used in the calculations and illustrations are listed in the appendices to this section.

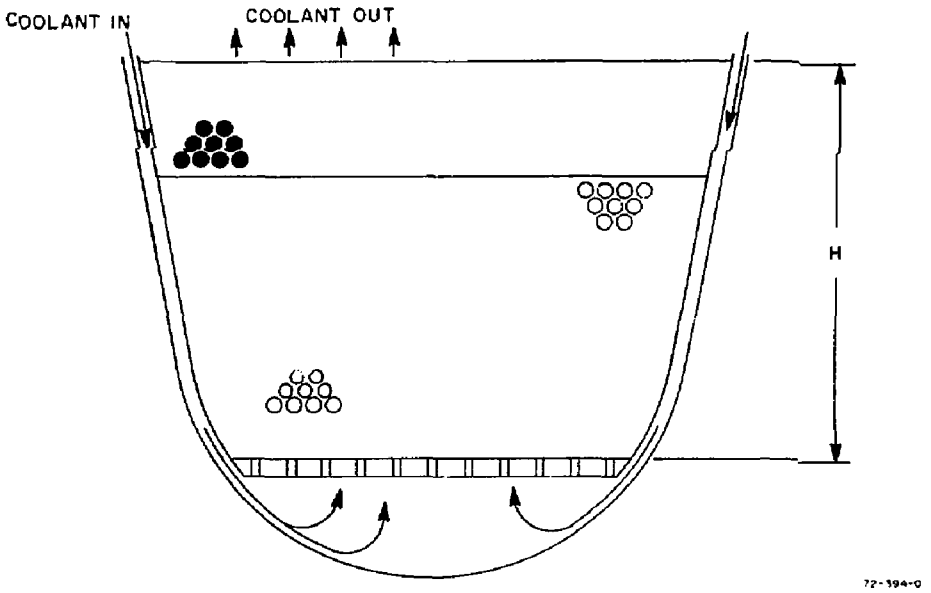

Fig. 5.14 The Canister blanket module as a single pass heat exchanger

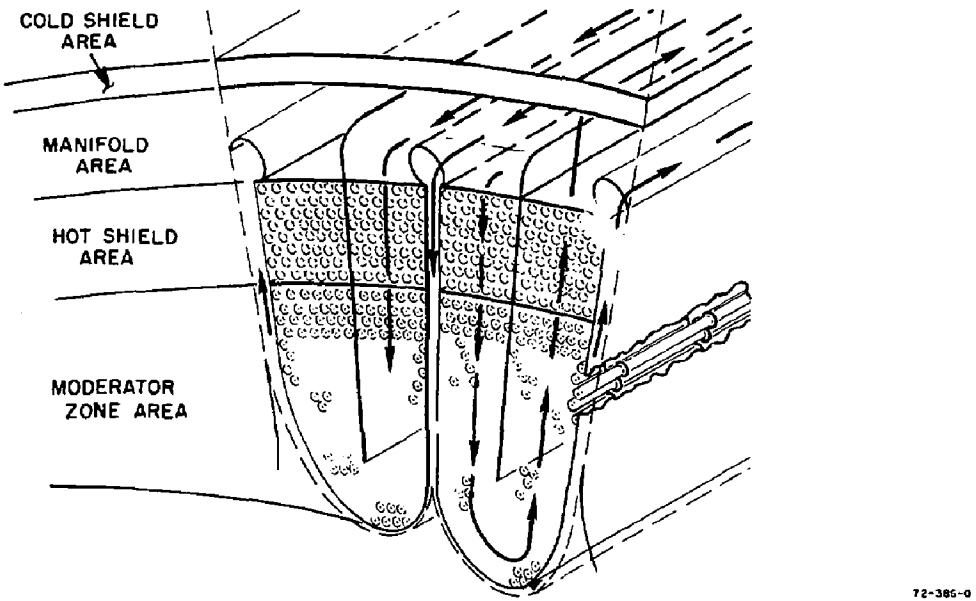

Fig. 5.15 The multiple-pass heat exchanger Canister model

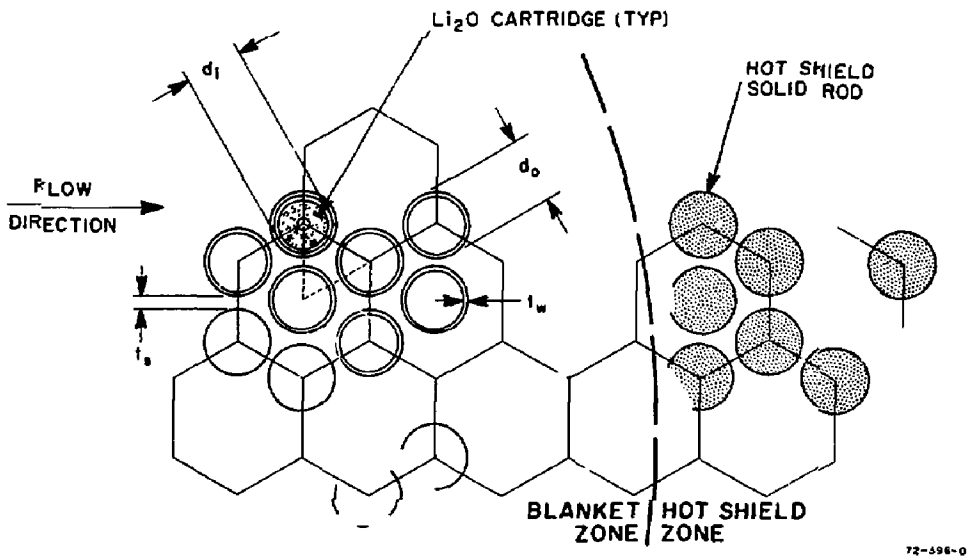

Fig. 5.16 Staggered tube flow arrangement within the Canister

5.3.1 Li_2O Fractions in the Canister Blanket for Neutronics and Heat Transfer

A very important parameter influencing the thermal hydraulics of the blanket is the fraction of Li_2O that can be contained within the volume. Neutronically this fraction has to have a certain minimum value to assure adequate tritium breeding for a given radial depth of the moderator. Since the Li_2O is within the heat exchanger tubes, the tube diameters and the spacing between tubes are very important.

The following equation allows this fraction to be calculated. The basic unit of the tube assembly and the key dimensions are shown in Fig. 5.17.

$$f_L = \frac{\pi f_{TD}}{2}\left[\frac{\left(d_i - 2t_g\right)^2 - d_h^2}{\left(d_i + 2t_w + t_s\right)^2 \tan 60^0}\right] = \frac{\pi f_{TD}}{2}\left[\frac{d_i^2 - d_h^2}{s_t^2 \tan 60^0}\right]$$

We can illustrate a final fraction that is Li_2O using the following tube diameter and spacings.

$d_i = 0.040$ $\qquad$ $t_g = 0.001$

$t_w = 0.001$ $\qquad$ $t_s = 0.001$

$f_{TD} = .90$ $\qquad$ $d_h = 0.001$

$$f_L = \frac{\pi}{2} \cdot 0.9\left[\frac{(.04 - .002)^2 - .001^2}{(.04 + .002 + .002)^2 \tan 60^0}\right] = 0.608$$

The fraction that is structure is determined by the following equation:

$$f_s = \frac{\pi}{2}\left[\frac{d_o^2 - d_i^2}{s_t^2 \tan 60^0}\right] = 0.077$$

Since it is desirable to keep the Li_2O fraction high and also useful to keep tube diameters as small as possible, an interesting and practical alternative to the use of round tubes is to use tubes that are hexagonal.

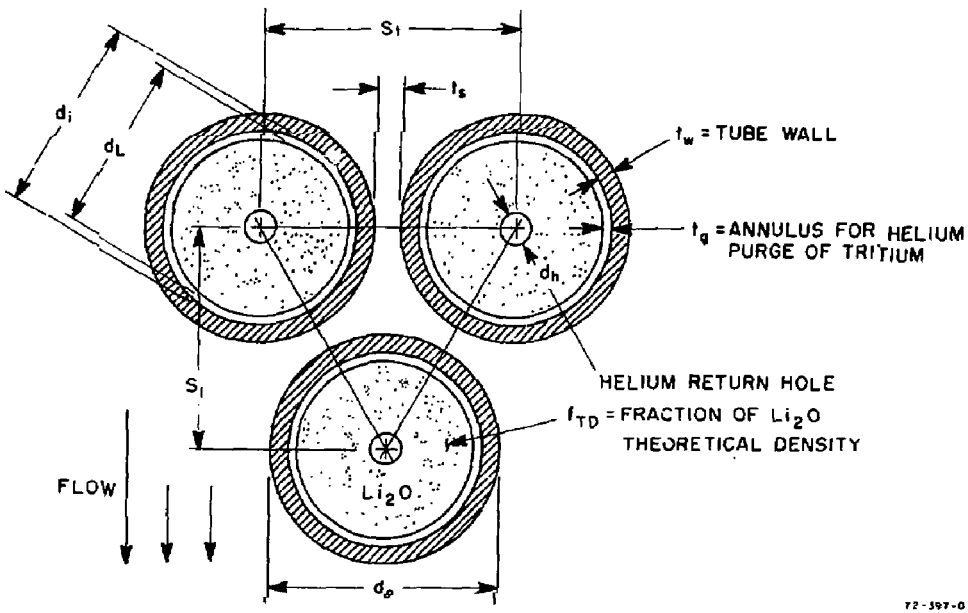

Fig. 5.17 Unit cell for the tube bank employing round tubes

The gain, due to improved packing, is about 10%. That is, for the previous example, $f_{L(HEX)} = 0.608 \times 1.1 \approx 0.67$. The equations for the Li_2O fraction and the structural fraction using hex tubes are as follows:

$$f_{L(HEX)} = \frac{4r_t^2 - 4t_w(2r_t - t_w) - 6t_g(2r_t - 2t_w - t_g)}{(2r_t + 2t_s)^2} = 0.69$$

For the structural fraction with hex tubes we have:

$$f_{s(HEX)} = \frac{A_{cell,struct}}{A_{cell}} = \frac{4t_w(2r_t - 1t_w)}{(2r_t + 2t_s)^2} = \frac{4t_w(2r_t - t_w)}{(2r_t + 2t_s)^2} = 0.088$$

The basic unit of this attractive hex cell arrangement is shown in Fig. 5.18. However, for this present study, we decided to use the somewhat simpler round tube arrangement shown in Fig. 5.17, even though the hexagonal tubes are more effective and the blanket is pressure balanced across the tube wall so stress problems are minimal.

Fig. 5.19 shows how the breeding ratio varies as a function of Li_2O fraction using a nominal $f_s = 0.08$ for three different lithium oxide fractions and for three different structural materials; 316 SS, Inconel, and our material choice Tenelon. It is evident from the figure that more than adequate tritium breeding is achievable with Tenelon even at relatively low Li_2O fractions and/or relatively shallow radial depths of the blanket. This implies that tubes whose diameters are 2 cm or slightly less would satisfy the neutronics criteria. (Hexagonal tubes could be somewhat smaller.) The small-diameter tubes are strongly preferred for packing in the Canister volume. If, due to other criteria, larger tube diameters prove more desirable, then the breeding would either increase or blanket thicknesses could decrease. We have found that a range of tube diameters from $\sim$ 2 to 4 cm is highly practical.

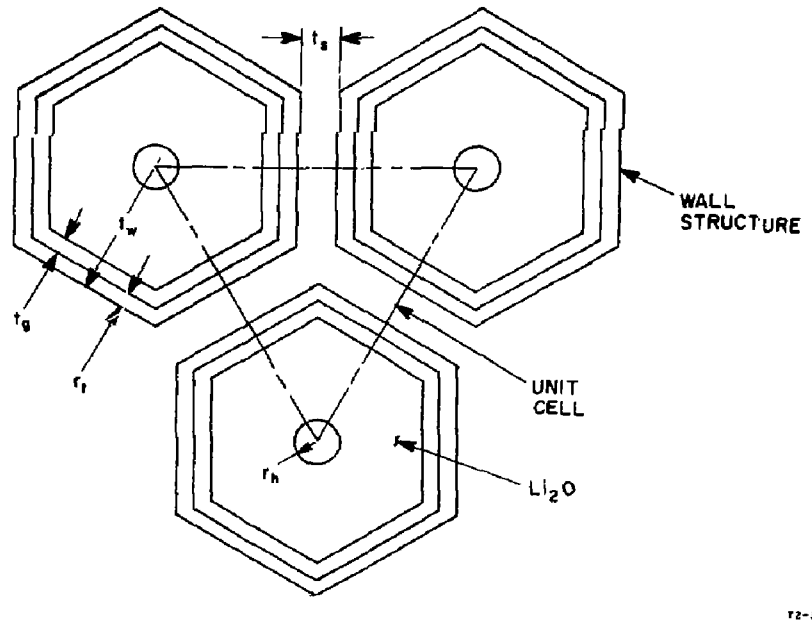

Fig. 5.18 Unit cell for the tube bank employing hexagonal tubes

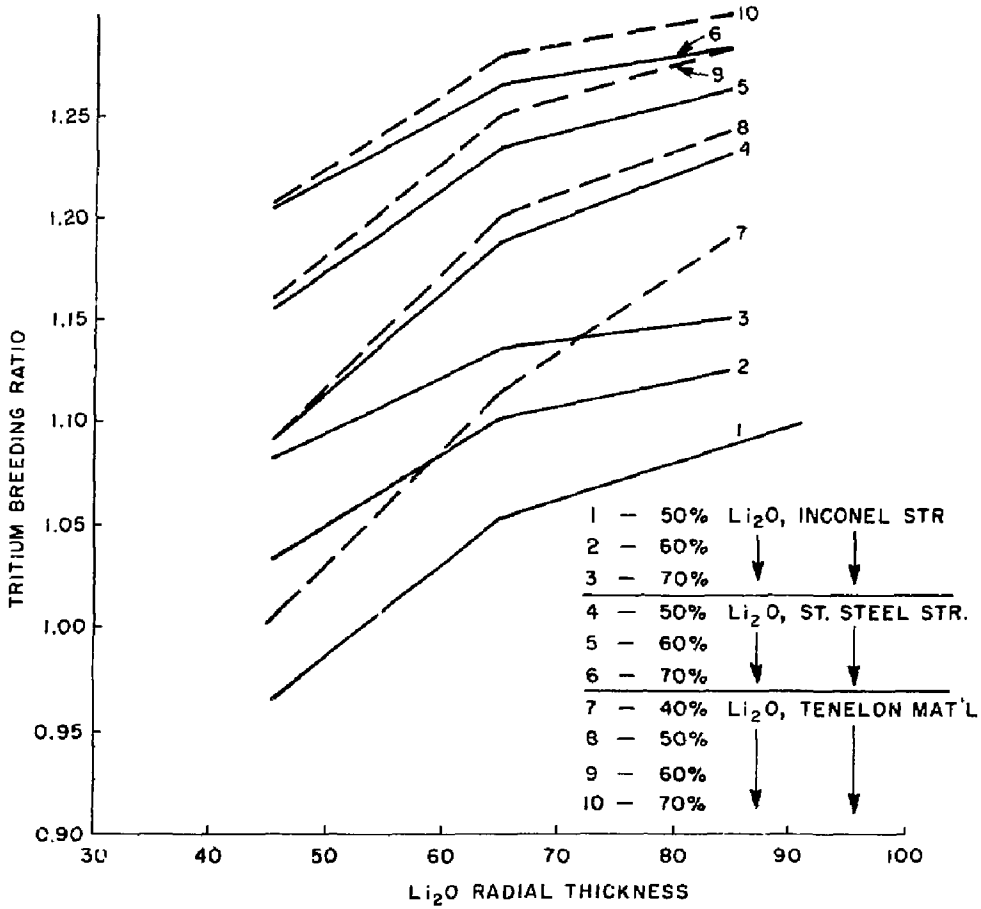

Fig. 5.19 Variation in tritium breeding ratio as a function of Li_2O fraction for different radial thicknesses of moderator blanket and different structural materials (structural fraction = .08)

5.3.2 Tube Bundles in Crossflow

The heat transfer in flow over tubes in crossflow depends to a large extent on:

- o flow pattern
- o degree of turbulence
- o velocity of the coolant
- o size and arrangement of tubes
- o entrance effects
- o first row effects
- o numbers of rows and columns
- o side wall geometry

Furthermore, these influences are interrelated and consequently the flow pattern is too complicated to be treated purely analytically. Fortunately, there are experimental data available and empirical correlation equations have been developed that may be used to accomplish the heat transfer calculations with good accuracy. It is interesting that these experiments indicate the transition from laminar to turbulent flow for staggered tubes in crossflow is more gradual than in flow through a pipe, whereas for in-line tube bundles in crossflow the transition phenomena resemble those in pipe flow. This seems contrary to intuition since one would guess that the continuous velocity deflection in staggered tubes would more quickly induce turbulence. For our analysis this is informative but not directly relevant because the staggered tube arrangement is, in fact, a necessary selection over the in-line arrangement for minimizing neutron streaming. In either staggered or parallel tubes, the transition Reynold's number, important for our heat transfer calculations, begins at about 200, based on the velocity at the minimum flow area specified by t_s of Fig. 5.17. The flow is fully turbulent at a Reynold's number $\approx$ 6000.

For our engineering calculations, where the local internal heat generation, w, in the Li_2O and in the tube material falls off exponentially with

increasing radial distance from the first wall facing the plasma, we must be interested in both the local heat transfer coefficient, h_ℓ, and the average heat transfer coefficient $\bar{h}$ for the entire tube bundle. The local h_ℓ and its accurate determination can be critical, particularly at the first row or so of tubes if this is where the energy deposition is the highest because the flow phenomena is singularly different than in the homogenized flow further into the array. For our particular model the energy deposition per unit volume falls off by about a factor of 20 from the first wall region to the back of the blanket (see the section on blanket neutronics). A built-in advantage of the flow model of our blanket heat exchanger is that flow enters at the hot shield at the back of the blanket where power density is least. Thereafter the flow across the continuously packed tubes is beyond the entrance effects. Local heat transfer coefficients are therefore not critical at the entrance region because heat fluxes are low and film temperature drops small. Recalling our first model single-pass heat exchanger, flow would flow across the tubes at the first wall where the power density is highest producing a much more severe condition of local heat transfer. This is another reason for preferring the multiple-pass system.

5.3.3 Heat Removal and Pressure Drop - Empirical Correlation Equations

The experimental data for flow across tube banks can be correlated by an equation of the form

$$(\bar{N}u)_D = \text{const}(Re)^m\ (Pr)^n$$

which can be recognized as being similar in form to correlations for flow in a tube or flow across a single tube. We have investigated the correlation equations of Kreith,[1] of Kays and London,[2] of Grimison[3], and of Eckert and Drake.[4] They differ in detail, as for instance, how the velocity is determined or what reference length should be used in calculating the Reynold's number. However, the results of the four methods are comparable within $\sim$ 10%, which is quite good. Table 5.6 illustrates how well the methods compare.

Table 5.6 Heat transfer in flow across tubes. Comparison of sample results using different correlation equations

Source	Re	$\overline{Nu}$	$\bar{h}\left(\frac{W}{m^2 - K}\right)$	ΔT_{film} at FW
Kreith 3rd Ed. p. 478-9	$\frac{G_{MAX} D_t}{\mu_f} \approx 11{,}550$	$\frac{\bar{h} D_t}{k_f} = 78.7$	1074	$\frac{q_o''' f_L D_t}{4\bar{h}(1-\varepsilon)} \approx 48$
Kays & London p. 7,127	$\frac{G_{MAX} D_h}{\mu} \approx 1402$	$\frac{\bar{h} D_t}{k} = 95.2$	1300	$\frac{q_o''' f_L D_t}{4\bar{h}(1-\varepsilon)} \approx 44$
Grimesen Fig. 12 (1959)	$\frac{G_{MAX} D_t}{\mu} \approx 11{,}550$	$\frac{\bar{h} D_t}{k} = 80$	1092	$\frac{q_o''' f_L D_t}{4\bar{h}(1-\varepsilon)} \approx 52$
Eckert & Drake Fig. 9-12	$\frac{G_{MAX} D_t}{\mu} \approx 11{,}550$	$\frac{\bar{h} D_t}{k} = 85$	1159	$\frac{q_o''' f_L D_t}{4\bar{h}(1-\varepsilon)} \approx 54$

In the data that follow the equations of Kreith have been used. In the correlation equation for the average $\bar{h}$ found in Kreith, the velocity from which the Reynold's number is calculated is based on the minimum free area available for flow (t_s). Since our tube arrangement is an equilateral triangle, the value of t_s (the space between tubes shown in Fig. 5.17) is the same whether it is measured between tubes normal to the flow or on the diagonal.

The correlation for the Fanning friction factor, f', of Bergelin given in Fig. 5.20 was used for the tube bank pressure drop calculations (Kreith).

5.3.4 The Analytical Model Equations

Figure 5.21a shows the trace of the helium flow through the Canister as a two-pass heat exchanger. Figure 5.21b illustrates the local power density in the Canister for the numbered flow locations. It can be seen that the local power density repeats every two passes so that the general form of analysis presented here could be used for 2-n-pass systems. It was found early in our calculations that the two-pass heat exchanger was most appropriate for this particular blanket design because of required tube diameters (2-4 cm) and the need to have a sufficient number of tube rows and columns so that the correlation equations for large tube banks would be valid. However, we also check film coefficients for the first tube row and check for edge effects for a tube that is in a first or last column.

The analysis deals first with the assembly of tubes followed by single tube analysis at appropriate locations.

The assumptions used in the analysis are as follows:

1) The power density has the form $w = w_0 e^{-r/r^*}$ for each pass, where r is measured from the first wall region.
2) Negligible effect of turnarounds on temperature profiles.
3) Constant tube diameter of the staggered array.

MODEL	ROWS	D_o IN.	PITCH/D_o
1	10	3/8	1.25
2	10	3/8	1.25
3	14	3/8	1.25
4	10	3/8	1.50
5	10	3/8	1.50

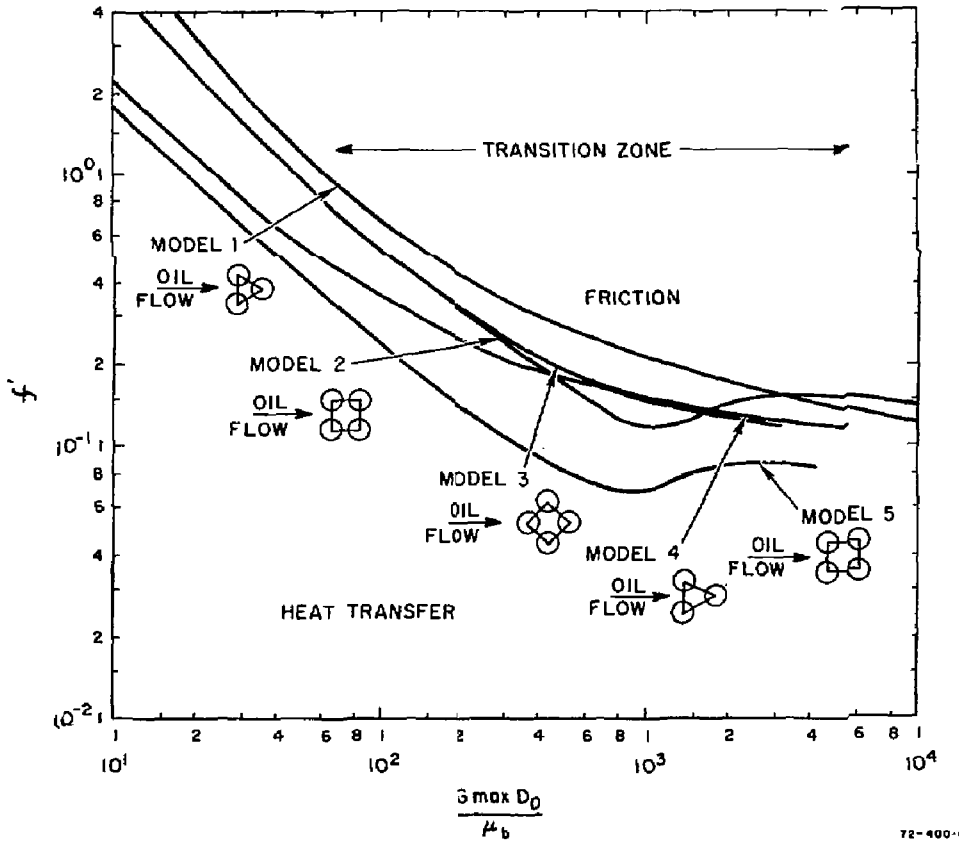

Fig. 5.20 Correlation for the Fanning fraction factor, f', of Bergelin used for the tube bank pressure drop calculations (Kreith)

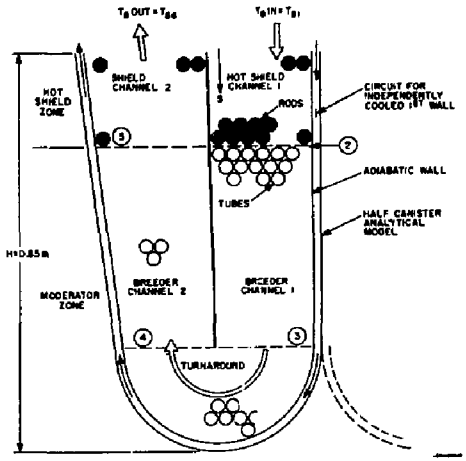

Fig. 5.21a Half Canister analytical model - cross section through the two-pass heat exchanger illustrating the numbering system for the thermal-hydraulic analysis

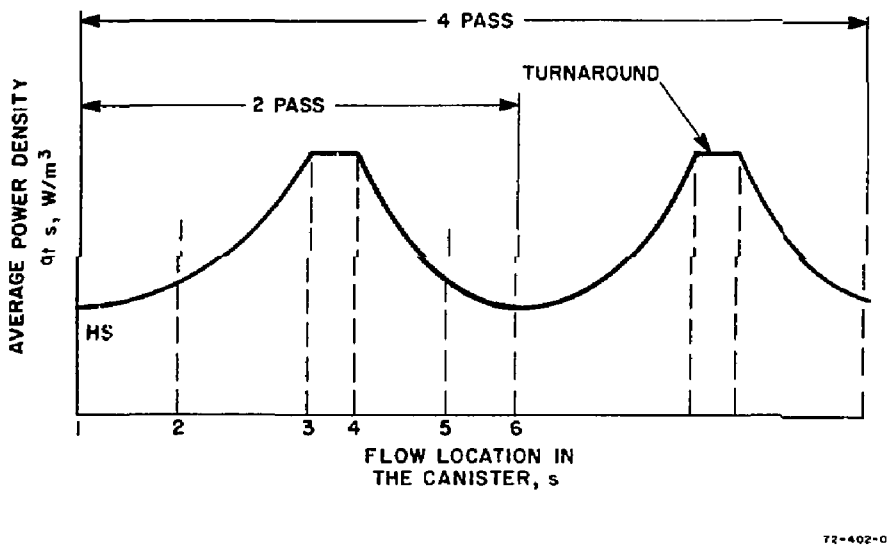

Fig. 5.21b Profile of the local power density in the Canister depending on flow location

4) Thermal isolation of the hot shield and moderator region from the internal manifolds and first wall regions.

5) f_s is that fraction of structure within the first wall envelope but not including the first wall itself.

6) The total "void" fraction for a unit cell (Fig. 5.17) is:

$f_r = 1 - f_s - f_L$.

The analytical model of the two-pass cross flow heat exchanger evaluates the thermal and hydraulic response of the moderator and hot shield zones of the Canister blanket module for a range of geometric parameters such as tube diameter and spacing, diameter of the lithium oxide cartridge within the tube, and the size of the purge channel used for tritium recovery in the tube. Another important set of parameters relate to temperature of the coolant; T_{BIN}, T_{BOUT} and $(T_{BOUT} - T_{BIN})$ and to the wall loading, Γ_N.

The following general equations are used. The computer code uses these equations in integral form in a zone-by-zone progression starting with the hot shield then through the moderator, turnaround, etc.

The bulk coolant (helium) temperature rise is given by

$$dT_B(s) = \frac{dQ(r)}{\dot{m}\, c_p} \tag{5.1}$$

where

$\dot{m}$ = mass flow rate of the helium coolant

c_p = the specific heat capacity. The length s is in the direction of the flow while r is radially outward.

The total heat deposited, dQ(r), over increment ds is

$$\begin{aligned} dQ(r) &= w_L(r)dV_L(r) + w_s(r)dV_s(r) \\ &= (w_L f_L + w_s f_s)dV_c(r) \\ &= (w_L f_L + w_s f_s)A_c(r)ds \end{aligned} \tag{5.2}$$

where dV_L, dV_S, and dV_C are the differential volumes of Li_2O, structure, and total blanket, respectively. The variables, f_L, f_S are the volume fractions of Li_2O and structure in a unit cell. The variable A_C is the total channel cross-sectional area.

For the internal heat generation in the lithium and the structure, respectively,

$$w_L = w_{o,L} \exp\left(-\frac{r}{r_L^*}\right) \tag{5.3}$$

$$w_S = w_{o,S} \exp\left(-\frac{r}{r_S^*}\right) \tag{5.4}$$

and, therefore, for all regions except the turnaround zone:

$$\frac{dT_B}{ds} = \frac{\left[(w_{o,L} f_L \exp(-r/r_L^*) + w_{o,S} f_S \exp(-r/r_S^*)\right] A_C(r)}{m\, c_p} \tag{5.5}$$

For the turnaround zone:

$$\Delta T_{B(TA)} = \frac{\left\{w_{o,L} f_L \left[1 - \exp\left(\frac{-\bar{r}_{TA}}{r_L^*}\right)\right] + w_{o,S} f_S \left[1 - \exp\left(\frac{-\bar{r}_{TA}}{r_S^*}\right)\right]\right\} A_{TA} \Delta S_{TA}}{m\, c_p} \tag{5.6}$$

The annular gap, t_g, between the tube wall and the Li_2O cartridge is provided for helium purge flow to scavenge tritium from the Li_2O. Its width vs the radial location r is specified by the linear relation

$$t_g(r) = B_1 + B_2 r \tag{5.7}$$

where B_1 and B_2 are coefficients defined for each blanket region.

The diameter of the hole in the Li_2O, d_h, is chosen to give one half the flow area of the annulus,

$$d_h \cong \sqrt{2t_g(d_o - 2t_w - t_g)} \tag{5.8}$$

The hole diameter and the Li_2O thickness are based on the average gap in each region, $\bar{t}_g$, in order to guarantee a linear variation in the Li_2O volume fraction.

The Li_2O volume fraction vs the radial location r is specified by:

$$f_L(r) = B_3 + B_4 r \tag{5.9}$$

where

$$B_3 = 4\epsilon_t \left(\frac{t_L}{d_o}\right)\left(1 - \frac{2t_w}{d_o} - \frac{t_L}{d_o} - \frac{2B_1}{d_o}\right) \tag{5.10}$$

$$B_4 = 4\epsilon_t \left(\frac{t_L}{d_o}\right)\left(-\frac{2B_2}{d_o}\right) \tag{5.11}$$

$$\epsilon_t = \frac{\pi}{2\sqrt{3}\left(1 + \frac{t_s}{d_o}\right)^2} \tag{5.12}$$

Since the structural volume fraction, f_s, is constant, the helium (void) volume fraction, f_v, also varies linearly.

To allow simple channel area changes, the channel cross section area vs the radial distance r is defined by the linear relation

$$A_c(r) = B_5 + B_6 r \tag{5.13}$$

where the coefficients B_5 and B_6 are defined for each blanket region.

Integrating Eq. (5.1) with the linear relations for channel area (5.13) and Li_2O volume fraction (5.9) over the length of each successive region (except for the turnaround zone) gives the bulk He temperature rise for these blanket regions.

$$\Delta T_B = C6 \left\{ \left\{ \exp\left[\left(-\frac{r_1}{r_L^*}\right) C1 + C2\left(\frac{r_1}{r_L^*} + 1\right) + C3\left(\frac{r_1^2}{r_L^{*2}} + 2\frac{r_1}{r_L^*} + 2\right)\right] \right.\right. \quad (5.14)$$

$$- \exp\left(-\frac{r_2}{r_L^*}\right)\left[C1 + C2\left(\frac{r_2}{r_L^*} + 1\right) + C3\left(\frac{r_2^2}{r_L^{*2}} + 2\frac{r_2}{r_L^*} + 2\right)\right]$$

$$+ C7 \exp\left(-\frac{r_1}{r_s^*}\right)\left[C4 + C5\left(\frac{r_1}{r_s^*} + 1\right)\right]$$

$$\left.\left. - C7 \exp\left(-\frac{r_1}{r_s^*}\right)\left[C4 + C5\left(\frac{r_2}{r_s^*} + 1\right)\right]\right\}\right\}$$

where

r_1 = distance from the first wall to the region inlet

r_2 = distance from the first wall to the region exit

$C1 = B_3 B_5$

$C2 = (B_4 B_5 + B_3 B_6) r_L^*$

$C3 = B_4 B_6 r_L^*$

$C4 = B_5 f_s$

$C5 = B_6 r_s^* f_s$

$C6 = w_{o,L} r_L^* / (m C_p)$

$C7 = (w_{o,s}/w_{o,L})(r_s^*/r_L^*)$

The average ΔT_{film} between the local bulk temperature and the tube wall is inversely proportional to the average heat transfer coefficient, $\bar{h}$. The average heat transfer coefficient for turbulent flow in a cross flow multi-tube heat exchanger of 10 tube rows or more is given by the correlation *(Kreith ref.)*:

$$\frac{\bar{h}d_o}{k} = 0.33C_H(Re)^{0.6}(Pr)^{1/3} \qquad (5.15)$$

$(Re > 6000,\ 0.7 < Pr < 300)$

where

$\bar{h}$ = average h over all tubes in the section (no. rows > 10)

$\bar{k}$ = average thermal conductivity of the He bulk flow

$Re = \bar{\rho}U_{max}d_o/\mu = G_{MAX}d_o/\mu \qquad (5.16)$

$\bar{\rho}$ = average density of the He bulk flow

U_{max} = maximum velocity of the He flow (occurs @ narrowest point between tubes)

$\bar{\mu}$ = average viscosity of the He bulk flow

$Pr = (\mu Cp/k) \qquad (5.17)$

In our actual Canister model the number of tube rows is always greater than 10, satisfying the correlation equation, but the number of tubes in each row varies between 3 and 6. The correlation equation for $\bar{h}$ (5. 15) was developed assuming quasi-infinite row lengths so the effects of any end walls on the value of h would be negligible. In our design study because of the small number of tube columns, the walls at the end of the tube rows could significantly effect the $\bar{h}$. Obviously any actual design would have to be supported with experimental measurements under similar geometries. We would also note that flow in the turnaround section of the Canister with the main flow turning 180^o may not provide the flow conditions which give an $\bar{h}$ defined by (5. 15).

The film temperature drop in the helium from the bulk flow to the tube wall O.D. relative to the average heat transfer coefficient is

$$\Delta T_{film}(r) = \frac{q}{\bar{h}} \qquad (5.18)$$

where the surface heat flux, q, is determined from

$$q = \frac{w_L V_L + w_s V_s}{A_{tube}}$$

$$q = \frac{w_L f_L + w_s f_s}{4\epsilon_t / d_o} \qquad (5.19)$$

The temperature rise across the tube wall is determined by combining the contribution due to the local power generation in the tube wall with the contribution due to the heat flux from the Li_2O traversing the tube wall. The final equation is

$$\Delta T_{wall} = \frac{w_s \left(\frac{d_o}{2}\right)^2 \left[1 - \left(\frac{d_i}{d_o}\right)^2 + 2\left(\frac{d_i}{d_o}\right)^2 \ln\left(\frac{d_i}{d_o}\right)\right]}{4k_w} + \frac{w_L f_L \sqrt{3}(d_o + t_s)^2 \ln\left(\frac{d_i}{d_o}\right)}{4\pi k_w} \qquad (5.20)$$

For the solid rods used in the hot shield zone, the ΔT to the rod centerline

$$\Delta T_{rod} = \frac{w_s d_o^2}{16 k_w} \qquad (5.21)$$

The temperature drop across the internal helium gap (the annulus provided for tritium purge) can be determined assuming pure conduction in the helium and essentially zero velocity flow using the equation

$$\Delta T_g = \frac{w_L f_L \left[\ln\left(\frac{d_o - 2t_w}{d_o - 2t_w - 2t_g}\right)\right] \sqrt{3}\left(d_o + t_s\right)^2}{4\pi k} \qquad (5.22)$$

Alternately, if laminar flow of the purge gas in the annular space is important and the heat fluxes at the annulus inner and outer boundaries, S_i and S_o, are defined, then the ΔT_g across the gap is given by

$$\Delta T_g = \frac{d_h}{k}\left[S_i\left(\frac{1}{Nu_{ii}} + \frac{\theta_i}{Nu_{oo}}\right) - S_o\left(\frac{1}{Nu_{oo}} + \frac{\theta_o}{Nu_{ii}}\right)\right] \qquad (5.23)$$

where d_h is the hydraulic diameter and θ and Nu are function coefficients of the tube geometry and internal gap.

The mass flow of the purge gas is a small fraction of the mainstream flow, i.e., 0.1%. The largest mainstream flow for ΔT_β = 100 K would be $\sim$ 6500 kg/sec. For the base case with 75 modules of 18 Canisters each and about 600 tubes per Canister, the flow in the annulus of one tube is about 8 mg/sec. This flow is so slow as to preclude significant heat removal by the purge flow, i.e., $\Delta Q \approx 0$, where ΔQ = heat transferred to the purge gas.

To check the possibility of enhanced heat transfer rate caused by circumferential natural convection loops set up around the annulus, the Grashof number, $Gr = \rho\, g\, \beta\, \Delta T_g t_g^3/\mu^2$ was calculated. For a typical case the Grashof number was equal to 0.30 ΔT_g which for the largest ΔT_g (pure conduction) was less than that needed to establish the natural convection.

On the basis of these calculations, the maximum value of ΔT_g across the annulus can be calculated using the pure conduction solution. This will be mitigated somewhat by radiation heat transfer in locations where the energy deposition is the highest.

If it is assumed that there is no heat transfer across the hole in the Li_2O cartridge and that heat flow is radially outward, then the ΔT_L across the heat generating Li_2O is given by

$$\Delta T_L = \frac{w_L d_L^2\left[1 - (d')^2 + 2(d')^2 \ell n(d')\right]}{16L} \qquad (5.24)$$

where

$d' = d_h/d_L$

d_L = outer diameter of the Li_2O cylinder

d_h = inner diameter of the Li_2O cylinder

5.3.5 Illustration of a Design Case

Tables 5.7a through 5.7g contain sample output for a reference case where T_{BIN} = 625 K and T_{BOUT} = 825 K.

5.3.6 The Influence of Structural Material Composition on Canister Design

The influence of structural materials and their composition on the neutronic performance of the Canister blanket was found to be a highly important, if not the most important, consideration in design. As can be inferred from Fig. 5.19, the use of materials such as Inconel drives the system to high lithium oxide fractions in order to get the tritium breeding greater than 1.0. Structurally, because the lithium oxide is contained within the tubes, the tube diameters must increase. With Inconel, tube diameters must be approximately 4 cm to achieve proper tritium breeding. With large tube diameters the inner temperature of the lithium oxide at the purge hole surface increases and this sets a constraint on the design. Inconel also has high internal heat generation due to high neutron/gamma capture, the net result of which is to lower the blanket energy multiplication, M. Topologically, larger tube diameters also make it more difficult to load a given Canister uniformally with tubes. The number of tube columns and the number of tube rows simply cannot be an integer multiple of a dimension as large as 4 cm.

The non-nickel alloys, such as Tenelon or 2.25 Cr-1 Mo or 316 SS, allow substantially lower lithium oxide fractions and hence smaller tube diameters (if temperature permits). Tube diameters of 2 cm, producing 0.4 lithium oxide fraction, intrinsically yield breeding ratios greater than 1.10 for our Tenelon design case where the moderator radial thickness is 0.65 m. Furthermore, for Tenelon, the blanket multiplication factor is 1.24 as compared with the Inconel case where M was 1.16, a gain of almost 7% or, in terms of power, an additional 224 MW. If the 0.4 lithium oxide fraction is retained and the blanket radial thickness decreased to 0.45 m, the blanket multiplication increases to 1.26, yielding approximately 280 MW more than would be obtain-

Table 5.7a Li_2O solid breeder blanket thermal-hydraulic analysis Case no. 7: final design case with 2 cm diameter tube of Tenelon - blanket module Canisters

```
INPUT DATA FOR BLANKET MODULE CANISTERS

        FUSION POWER= 3500  MW
        POWER FRACTION TO BLANKET= .8
        FRACTION OF POWER DEP. IN FIRST WALL= .1
        WALL LOADING= 2  MW/M2
        BLANKET MULTIPLICATION FACTOR-M= 1.2

        HELIUM EXIT TEMPERATURE= 825  K
        HELIUM TEMPERATURE RISE= 200  K

        REACTOR CENTRAL CELL LENGTH= 150  M
        FIRST WALL RADIUS= 1.485  M
        MODULE AXIAL LENGTH= 2  M
        NO. HALF CANISTERS/RING MODULE= 36

        HOT SHIELD THK./CHANNEL 1= .2  M
        BREEDER+TURNAROUND THK./CHANNEL 1= .65  M
        BREEDER THK./CHANNEL 2= .52  M
        HOT SHIELD THK./CHANNEL 2= .2  M

        CHANNEL DIVIDER THK.= .01  M
        FIRST WALL THK.= 6E-03  M
        FIRST WALL FLOW ANNULUS GAP= .02  M

        MODULE END WALL THK.= .01  M
        PURGE HEADER WIDTH= .025  M
        TURE SPACER FLOW BLOCKAGE= .05


OUTPUT FOR BLANKET MODULE CANISTERS

        POWER GENERATED IN THE BLANKET= 3360  MW
        NO. OF RING MODULES= 75
        NO. OF HALF CANISTERS= 2700
        POWER PER HALF CANISTER GEN. IN FIRST WALL= .124444  MW
        POWER PER HALF CANISTER GEN. IN THE MODERATOR/SHIELD SECTION= 1.12 MW
        REQ. HELIUM PER HALF CANISTER MODERATOR/SHIELD SECTIONS= 1.07938  KG/SEC
        FIRST WALL NOSE RADIUS= .129591  M
```

Table 5.7b Case no. 7: final design case with 2 cm diameter tube of Tenelon - hot shield section, channel 1

```
INPUT DATA FOR HOT SHIELD SECTION-CHANNEL 1

 RADIUS OF SECTION INLET= .856  M **     RADIUS OF SECTION EXIT= .656  M **
 ROD DIAMETER= .02  M                    SPACING BETWEEN RODS= 2E-03  M
 HT/GEN(QR=0)-ST= 4.63969E+07  W/M3      RSTAR-ST= .230636  M
 T-BULK OF SECTION INLET= 625  K
 P-BULK OF SECTION INLET= 5E+06  PA
 HEAT TRANSFER COEF. FLAG= 1  INDICATING THE KREITH CORRELATI
 PRESSURE LOSS FLAG= 1  INDICATING THE BERGELIN CORRELATION
 UNOBSTRUCTED CHANNEL CROSS SECTION AREA 1 INLET= .205343 AND NO. OF COLUMNS= 5
 UNOBSTRUCTED CHANNEL CROSS SECTION AREA 2 EXIT= .205343 AND NO. OF COLUMNS= 5
 VALUES FOR CA,CB= .205343 ,  0 , RESPECTIVELY


OUTPUT FOR HOT SHIELD OF CHANNEL 1

 ROD SPACING= .022  M                    ROW SPACING= .0190526  M
 AVG. NO. OF COLUMNS= 5                  AVG. NO. OF ROWS= 10
 SECTION DELTA T-BULK= 9.92051  K        SECTION DELTA P-BULK= 2365.81  PA
 SECTION EXIT TEMPERATURE= 634.921  K    SECTION EXIT PRESSURE= 4.99763E+06  PA

PARAMETER          INLET          EXIT           MID SECTION
 MIN. FLOW AREA    .0186675       .0186675       .0186675  M2
 LIQD VOL. FRACT   0              0              0
 STRUCT VOL. FRAC  .749503        .749503        .749503
 HE VOL. FRACT     .250497        .250497        .250497
 BULK HE TEMP      625            634.921        629.96  K
 BULK HE PRESS     5E+06          4.99763E+06    4.99882E+06  PA
 REY NO.,MAX       34853.2        34472.2        34661.4
 HE VEL, MAX       15.0159        15.2543        15.1351  M/SEC
 HT/XFER COEFF     1977.88        1986.6         1982.25  W/M2 K
 DELTA T FILM      3.8248         9.06371        6.44426  K
 ROD O.D. TEMP.    628.825        643.984        636.405  K
 ROD DELTA TEMP.   .977586        2.32681        1.6522  K
 ROD MAX. TEMP.    629.802        646.311        638.057  K

** RADII MEASURED FROM THE MODERATOR-SIDE SURFACE OF THE FIRST WALL
```

Table 5.7c Case no 7: final design case with 2 cm diameter tube of Tenelon - breeder section, channel 1

```
INPUT DATA FOR BREEDER SECTION-CHANNEL 1

 RADIUS OF SECTION EXIT= .112229  M        TUBE DIAMETER= .02  M
 SPACING BETWEEN TUBES= 2E-03  M           TUBE WALL THK= 5E-04  M
 LI2O WALL THK= 5.5E-03  M
 HT/GEN(@R=0)-LI= 1.34701E+07  W/M3        RSTAR-LI= .319342  M
 HT/GEN(@R=0)-ST= 1.79601E+07  W/M3        RSTAR-ST= .3016  M
 TUBE INTERNAL GAP COEF-F= 1E-03  M        COEF-G= 0  M/M
 LI2O FRACTION T.D.= .9
 HEAT/TRANSFER COEF FLAG= 1  INDICATING THE KREITH CORRELATION
 PRESSURE LOSS FLAG= 1  INDICATING THE BERGELIN CORRELATION
 UNOBSTRUCTED CHANNEL CROSS SECTION AREA @ INLET= .205343 AND NO. OF COLUMNS= 5
 UNOBSTRUCTED CHANNEL CROSS SECTION AREA @ EXIT= .205343 AND NO. OF COLUMNS= 5
 VALUES FOR CA,CB= .205343 ,  0 , RESPECTIVELY


OUTPUT FOR BREEDER SECTION OF CHANNEL 1

 TUBE SPACING= .022  M                     ROW SPACING= .0190526  M
 AVG. NO. OF COLUMNS 5                     AVG. NO. OF ROWS= 28
 SECTION DELTA T-BULK= 51.387  K           SECTION DELTA P-BULK= 6908.59  PA
 SECTION EXIT TEMPERATURE= 686.308  K      SECTION EXIT PRESSURE= 4.99073E+06  PA

PARAMETER          INLET          EXIT           MID SECTION
 MIN. FLOW AREA    .0186675       .0186675       .0186675  M2
 TUBE ID GAP       1E-03          1E-03          1E-03  M
 LI2O VOL. FRACT   .474061        .474061        .474061
 STRUCT VOL. FRAC  .0730764       .0730764       .0730764
 HE VOL. FRACT     .452863        .452863        .452863
 BULK HE TEMP      634.921        686.308        660.614  K
 REY NO.,MAX       34472.2        32649.8        33530.9
 HE VEL, MAX       15.2615        16.4967        15.8791  M/SEC
 BULK HE PRESS     4.99763E+06    4.99073E+06    4.99418E+06  PA
 HT/XFER COEFF     1986.6         2030.23        2008.72  W/M2 K
 DELTA T FILM      3.24955        17.7374        10.4934  K
 TUBE O.D. TWALL   638.17         704.045        671.108  K
 TUBE DELTA TWALL  .108234        .582653        .343943  K
 TUBE MAX. TWALL   638.275        704.628        671.451  K
 TUBE ID GAP DT    24.5159        125.598        75.0571  K
 LI2O O.D. TWALL   662.791        830.226        746.509  K
 LI2O DELTA TWALL  3.30834        22.0082        12.6568  K
 LI2O MAX. TWALL   666.097        852.234        759.165  K
```

Table 5.7d Case no. 7: final design case with 2 cm diameter tube of Tenelon - turnaround section between channel 1 and channel 2

```
INPUT DATA FOR TURNAROUND SECTION BETWEEN CHANNEL 1 & CHANNEL 2

 RADIUS OF SECTION EXIT= .112229  M        TUBE DIAMETER= .02  M
 SPACING BETWEEN TUBES= 2E-03  M           TUBE WALL THK= 5E-04  M
 LI2O WALL THK= 5.5E-03  M
 HT/GEN(@R=0)-LI= 1.34701E+07  W/M3        RSTAR-LI= .319342  M
 HT/GEN(@R=0)-ST= 1.79601E+07  W/M3        RSTAR-ST= .3016  M
 TUBE INTERNAL GAP COEF-F= 1E-03  M
 LI2O FRACTION T.D.= .9                    SECTION LENGTH= .18335  M
 HEAT/TRANSFER COEF FLAG= 1  INDICATING THE KREITH CORRELATION
 PRESSURE LOSS FLAG= 1  INDICATING THE BERGELIN CORRELATION
 UNOBSTRUCTED CHANNEL CROSS SECTION AREA @ INLET= .205343 AND NO. OF COLUMNS= 5
 UNOBSTRUCTED CHANNEL CROSS SECTION AREA @ EXIT= .205343 AND NO. OF COLUMNS= 5
 VALUES FOR CA,CB= .205343 ,  0 , RESPECTIVELY

OUTPUT FOR TURNAROUND SECTION BETW. CHANNEL 1 & CHANNEL 2

 TUBE SPACING= .022  M                     ROW SPACING= .0190526  M
 MEAN NO. OF COLUMNS= 5                    MEAN NO. OF ROWS= 9
 SECTION DELTA T-BULK= 46.2746  K          SECTION DELTA P-BULK= 2234.2  PA
 SECTION EXIT TEMPERATURE= 733.582  K      SECTION EXIT PRESSURE= 4.98849E+06  PA

PARAMETER          INLET          EXIT @ 1ST WALL    MID SECTION
 MIN. FLOW AREA    .0186675       .0186675           .0186675  M2
 TUBE ID GAP       1E-03          1E-03              1E-03  M
 LI2O VOL. FRACT   .474061        .474061            .474061
 STRUCT VOL. FRAC  .0730764       .0730764           .0730764
 HE VOL. FRACT     .452863        .452863            .452863
 BULK HE TEMP      686.308        732.582            660.614  K
 BULK HE PRESS     4.99073E+06    4.98849E+06        4.98961E+06  PA
 REY NO.,MAX       32649.8        31196.4            33530.9
 HE VEL, MAX       16.3195        17.4734            15.9011  M/SEC
 HT/XFER COEFF     2030.23        2067.55            2008.72  W/M2 K
 DELTA T FILM      17.7374        24.8384            20.8287  K
 TUBE O.D. TWALL   704.045        757.42             681.443  K
 TUBE DELTA TWALL  .582653        .829571            .676489  K
 TUBE MAX. TWALL   704.628        758.25             682.119  K
 TUBE ID GAP DT    125.598        169.583            149.05  K
 LI2O O.D. TWALL   830.226        927.833            831.169  K
 LI2O DELTA TWALL  22.0082        34.4776            25.5970  K
 LI2O MAX. TWALL   834.334        962.31             856.727  K
```

Table 5.7e Case no. 7: final design case with 2 cm diameter tube of Tenelon - breeder section, channel 2

```
INPUT DATA FOR BREEDER SECTION-CHANNEL 2

 RADIUS OF SECTION EXIT= .632229  M        TUBE DIAMETER= .02  M
 SPACING BETWEEN TUBES= 2E-03  M           TUBE WALL THK= 2E-03  M
 LI2O WALL THK= 5.5E-03  M
 HT/GEN(QR=0)-LI= 1.34701E+07  W/M3        RSTAR-LI= .319342  M
 HT/GEN(QR=0)-ST= 1.79801E+07  W/M3        RSTAR-ST= .3016  M
 TUBE INTERNAL GAP COEF-F= 1E-03  M        COEF-G= 0  M/M
 LI2O FRACTION Y.O.= .9
 HEAT/TRANSFER COEF FLAG= 1  INDICATING THE KREITH CORRELATION
 PRESSURE LOSS FLAG= 1  INDICATING THE BERGELIN CORRELATION
 UNOBSTRUCTED CHANNEL CROSS SECTION AREA @ INLET= .205343 AND NO. OF COLUMNS= 5
 UNOBSTRUCTED CHANNEL CROSS SECTION AREA @ EXIT= .410685 AND NO. OF COLUMNS= 10
 VALUES FOR CA,CB= .161025 ,  .394889 , RESPECTIVELY

OUTPUT FOR BREEDER SECTION OF CHANNEL 2

 TUBE SPACING= .022  M                     ROW SPACING= .0190526  M
 AVG. NO. OF COLUMNS= 7.5                  AVG. NO. OF ROWS= 27
 SECTION DELTA T-BULK= 69.4199  K          SECTION DELTA P-BULK= 3449.48  PA
 SECTION EXIT TEMPERATURE= 902.002  K      SECTION EXIT PRESS= 4.98504E+06  PA

PARAMETER          INLET          EXIT           MID SECTION
 MIN. FLOW AREA    .0108675       .037335        .0280013  M2
 TUBE ID GAP       1E-03          1E-03          1E-03  M
 LI2O VOL. FRACT   .474061        .474061        .474061
 STRUCT VOL. FRAC  .0730764       .0730764       .0730764
 HE VOL. FRACT     .452863        .452863        .452863
 BULK HE TEMP      732.582        902.002        787.292  K
 BULK HE PRESS     4.98849E+06    4.98504E+06    4.98677E+06  PA
 REY NO.,MAX       31196.4        14643.1        20136.4
 HE VEL, MAX       17.6412        9.45647        12.318  M/SEC
 HT/XFER COEFF     3967.55        1398.99        1842.15  W/M2 K
 DELTA T FILM      17.4172        4.97436        11.1958  K
 TUBE O.D. TWALL   749.999        806.976        778.488  K
 TUBE DELTA TWALL  .582653        .113469        .34803  K
 TUBE MAX. TWALL   750.582        807.09         778.836  K
 TUBE ID GAP DT    120.181        22.4208        71.3007  K
 LI2O O.D. TWALL   870.763        829.511        850.137  K
 LI2O DELTA TWALL  22.9438        4.31594        13.6299  K
 LI2O MAX. TWALL   893.706        833.827        863.766  K
```

Table 5.7f Case no. 7: final design case with 2 cm diameter tube of Tenelon - hot shield section, channel 2

```
INPUT DATA FOR HOT SHIELD SECTION-CHANNEL 2

 RADIUS OF SECTION EXIT= .632229  M        TUBE DIAMETER= .02  M
 SPACING BETWEEN RODS= 2E-03  M
 HT/GEN(QR=0)-ST= 4.63969E+07  W/M3        RSTAR-ST= .230636  M
 HEAT/TRANSFER COEF FLAG= 1  INDICATING THE KREITH CORRELATION
 PRESSURE LOSS FLAG= 1  INDICATING THE BERGELIN CORRELATION
 UNOBSTRUCTED CHANNEL CROSS SECTION AREA @ INLET= .410685 AND NO. OF COLUMNS= 10

 UNOBSTRUCTED CHANNEL CROSS SECTION AREA @ EXIT= .451754 AND NO. OF COLUMNS= 11
 VALUES FOR CA,CB= .280862 ,  .205343 , RESPECTIVELY

OUTPUT FOR HOT SHIELD OF CHANNEL 2

 ROD SPACING= .022  M                      ROW SPACING= .0190526  M
 MEAN NO. OF COLUMNS= 10.5                 MEAN NO. OF ROWS= 10
 SECTION DELTA T-BULK= 22.9379  K          SECTION DELTA P-BULK= 894.954  PA
 SECTION EXIT TEMPERATURE= 824.94  K       SECTION EXIT PRESSURE= 4.98435E+06  PA

PARAMETER          INLET          EXIT           MID SECTION
 MIN. FLOW AREA    .037335        .0410685       .0392018  M2
 LI2O VOL. FRACT   0              0              0
 STRUCT VOL. FRAC  .749503        .749503        .749503
 HE VOL. FRACT     .250497        .250497        .250497
 BULK HE TEMP      802.002        824.94         813.471  K
 BULK HE PRESS     4.98504E+06    4.98435E+06    4.98469E+06  PA
 REY NO.,MAX       14643.1        13052.5        13806.3
 HE VEL, MAX       9.66313        9.03593        9.3346  M/SEC
 HT/XFER COEFF     1398.99        1331.67        1364.02  W/M2 K
 DELTA T FILM      14.268         6.29958        10.2828  K
 ROD O.D. TEMP.    816.27         831.237        823.754  K
 ROD DELTA TEMP.   2.57943        1.08372        1.83158  K
 ROD MAX. TEMP.    818.849        832.321        828.585  K
```

Table 5.7g Case no. 7: final design case with 2 cm diameter tube of Tenelon - blanket synopsis

```
TOTAL ROD COUNT PER CANISTER= 158          TOTAL TUBE COUNT PER CANISTER= 337
EXIT TEMPERATURE= 824.94  K               EXIT PRESSURE= 4.98435E+06  PA
BLANKET DELTA T= 199.94  K                BLANKET DELTA P= 15652  PA
BLANKET HEAT TOTAL= 1.11966  MW           PUMPING POWER= .511578  %
```

able with the Inconel. The provision in this case would be that the tube diameters would have to be 3 cm. As can be seen from the above examples, there are many combinations of tube diameters, lithium oxide fraction, breeder radial thickness, etc., that will produce a good blanket assembly. What follows are some of the preliminary
results of the parametric studies.

5.3.7 Parameter Study Preliminary Results - Minimum and Maximum Lithium Oxide Temperatures

Figure 5.22 illustrates the minimum lithium oxide temperature as a function of tube diameter for four different helium coolant flow rates producing four different levels of helium bulk temperature rise from inlet to outlet of the blanket. In this figure it can be seen that there is essentially zero sensitivity of the oxide minimum temperature due to tube diameter, which is as one would expect since the minimum temperatures occur at the flow entry into the blanket where the energy deposition is the least. The strong influence is the bulk temperature rise which determines the flow velocities and hence film temperature coefficients of heat transfer. At the reference case where the bulk temperature rise is 200 K, the lithium oxide minimum temperature is estimated to be approximately 770 K, well above the minimum temperature required to maintain a tritium inventory less than 1 kilogram (see Section 5.6).

Figure 5.23 shows the more important maximum lithium oxide temperature as a function of tube diameter and bulk helium temperature rise. In this case the maximum temperature occurs at the inner surface of the lithium oxide for the cartridge located at the point of maximum energy deposition, i.e., near the exit of the turnaround in the blanket near the first wall. Here the bulk temperature rise has little effect but the dominant influence is the tube diameter. This dominance of the diameter is because the energy deposition is increasing in proportion to the diameter squared and at the same time the path length for energy removal is increasing with the diameter so the effect is roughly a cubic. Of concern here is to stay well below the temper-

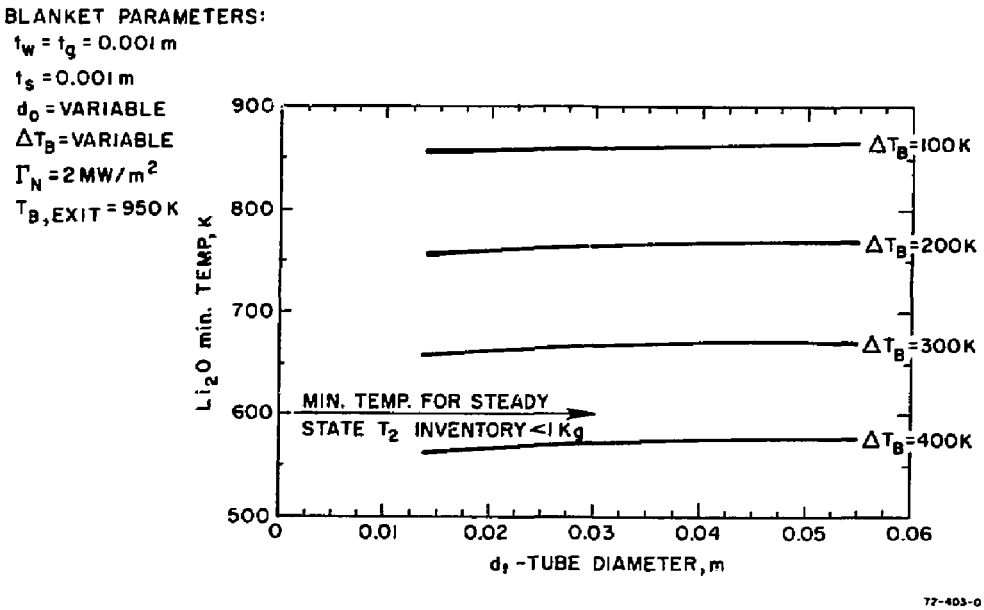

Fig. 5.22 The minimum Li_2O temperature vs tube diameter and bulk helium temperature at a spacing between tubes = .001 m

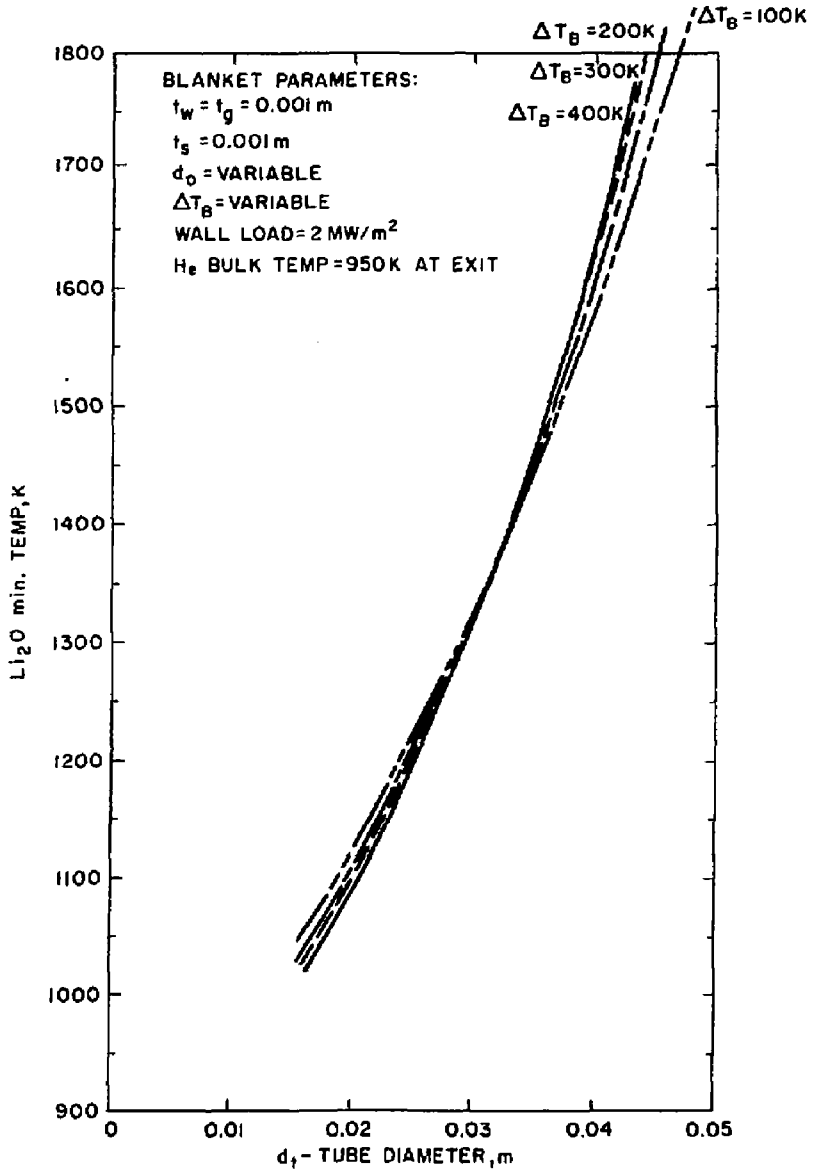

72-404-D

Fig. 5.23 The maximum Li_2O temperature vs tube diameter and bulk helium temperature rise at a spacing between tubes = .001 m

ature at which the lithium oxide melts (1970 K). Initially, it was felt that there was a critical sintering temperature but a new method of fabricating the lithium oxide may eliminate that problem. This sintering and the method for Li_2O fabrication are discussed in Section 5.4 on tritium recovery. Nevertheless, it is advantageous to use the smaller diameter tubes. The actual temperature rise across the lithium oxide as a function of tube diameter is shown in Fig. 5.24.

Figure 5.25 illustrates lithium oxide maximum temperature as a function of neutron wall loading for a family of tube diameters. Clearly the smaller tube diameters are superior and if the higher wall loadings are to be achieved, then tube diameters of about 2 cm or 2.5 cm are to be strongly preferred. We do not know definitively how near to the melting point it is possible to operate the Li_2O but a safe value may be approximately 0.80 or about 1575 K. This may be unduly optimistic, forcing the design to smaller diameter tubes.

5.3.8 Parametric Study - Maximum Tube Temperatures

Figure 5.26 shows maximum tube temperatures as a function of wall loading for selected tube diameters. For this parametric study, the wall loading was increased by moving the Canisters closer to the central-cell plasma while keeping the total fusion power constant. In addition, the radius of the first wall of the Canisters was kept constant, and the number of Canisters per ring module was reduced appropriately as the Canisters were moved closer to the plasma. The helium inlet and exit bulk temperatures were also held fixed at 625 K and 825 K, respectively.

The maximum tube-wall temperatures were found to occur close to the exit of the second breeder zone (point 5 on Fig. 5.21). As can be seen from the results in Fig. 5.26, this temperature, T_{w5}, does not vary appreciably for a factor of 2.5 change in the wall loading or a factor of 2 change in the tube diameter. This result can be explained as follows. The total helium flow rate to each ring module did not change for all of the above calculations,

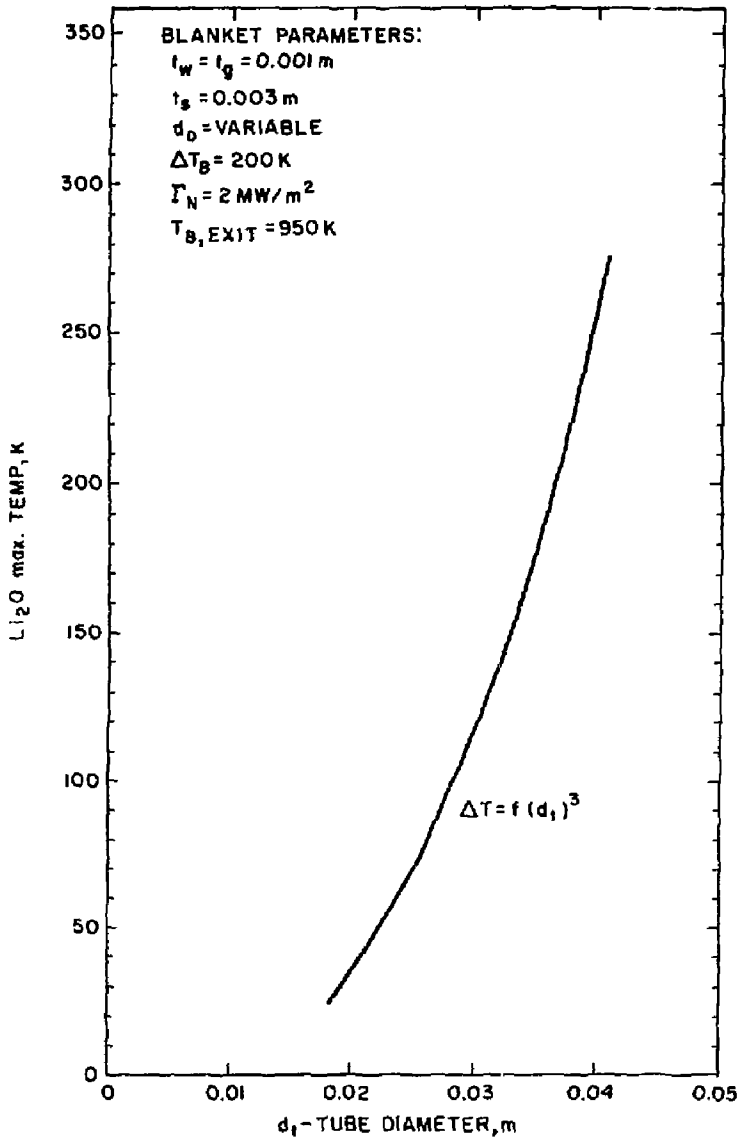

Fig. 5.24 Maximum temperature rise across the Li_2O vs tube diameter for ΔT_B = 200 K and Γ_N = 2 MW/m^2

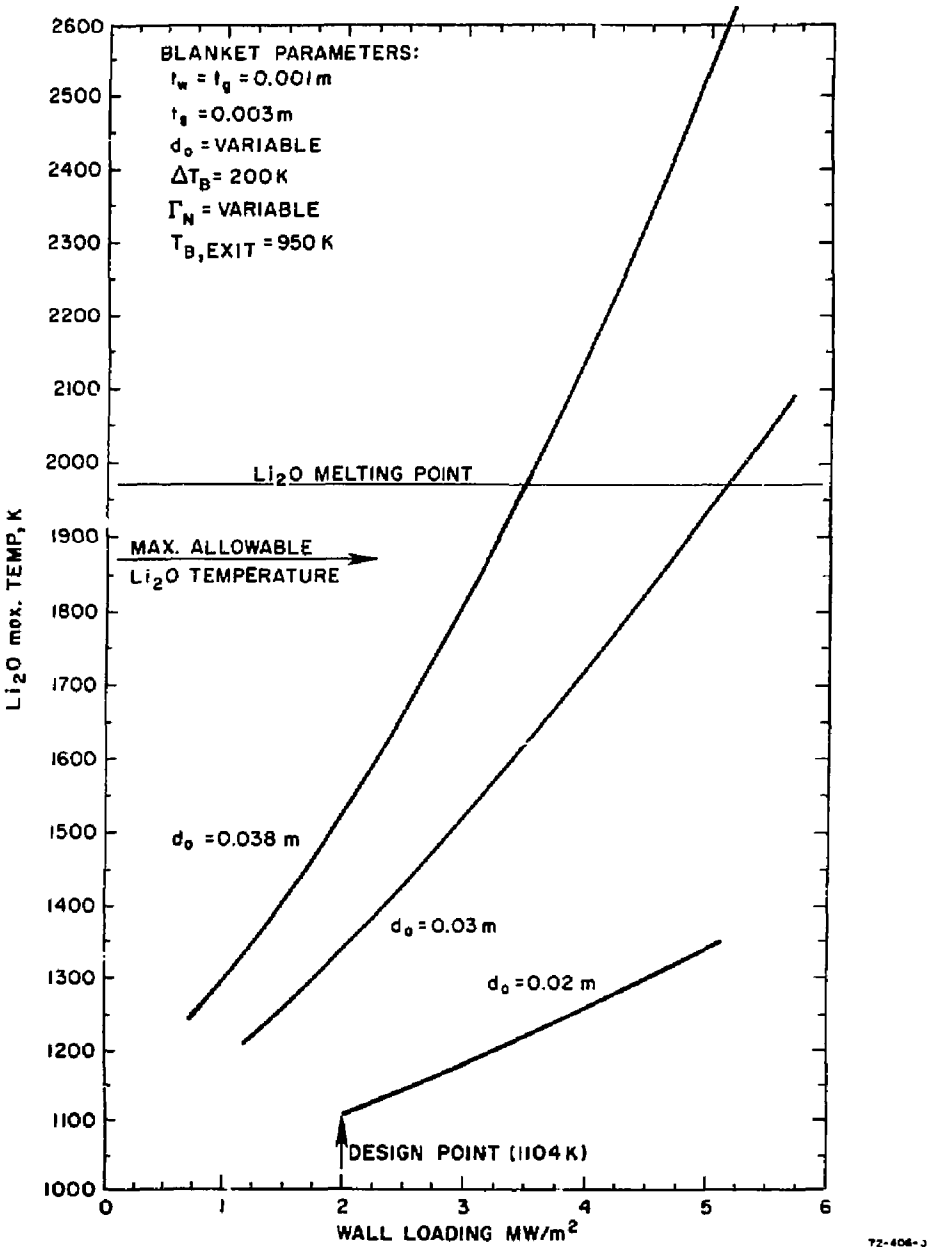

Fig. 5.25 Maximum Li_2O temperature as a function of wall loading for selected tube diameters at ΔT_B = 200 K and T_B = 950 K

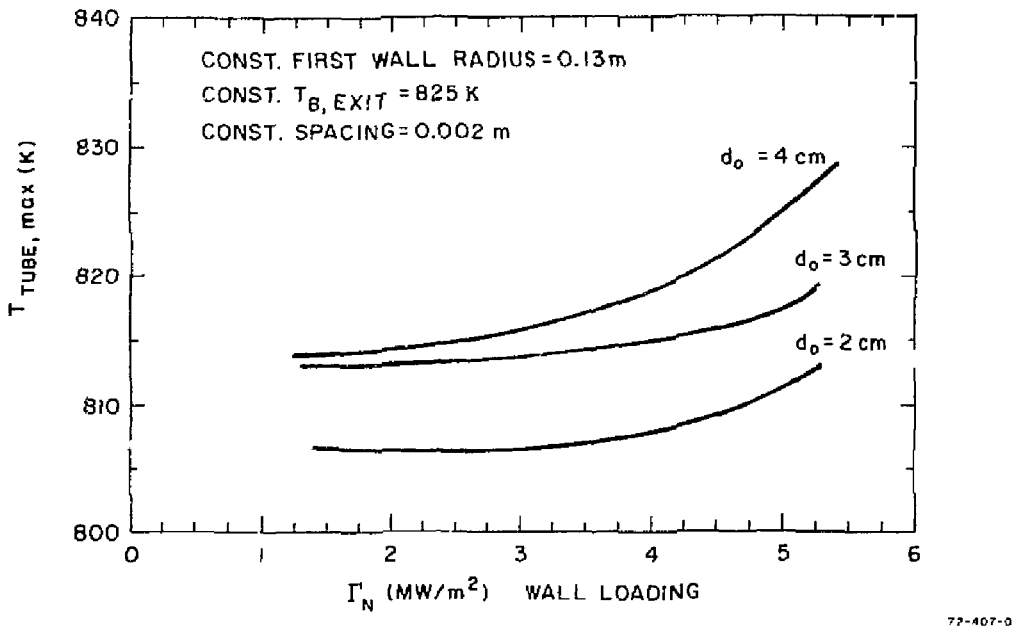

Fig. 5.26 Maximum tube temperature as a function of wall loading for selected tube diameters

since the same power must be removed from each ring module. When the wall loading is doubled (by moving the Canisters in to half the original distance from the centerline of the plasma), the number of Canisters is reduced to half and the internal heat generation in each Li_2O-filled tube doubles. However, the number of these tubes at each radius is almost exactly half the original number for a given tube diameter (except for some minor geometrical adjustments). With half the number of Canisters, the helium flow rate in each Canister is doubled. This almost doubles the heat transfer coefficient, which just about compensates for the doubling of the internal heat generation in the Li_2O and tube walls. The net result is that the film drop stays almost the same at each location in the Canister. Consequently, the temperature distribution in the Li_2O cartridges and tube walls, as well as in the helium, does not change appreciably for all the above cases.

It can be seen from Fig. 5.26 that these maximum tube wall temperatures of 807 to 825 K fall within a reasonable range for Tenelon. It should be recalled that the Tenelon tubes only have 1 to 2 atm differential pressure across them, so the stresses are low.

5.3.9 Stresses in the Thin-Walled Tubes

The stresses in the thin-walled tubes containing the lithium oxide result from two causes: (a) the pressure difference between the purge helium flow on the inside of the tube and the higher pressure mainstream helium flow on the outside of the tube (this difference can range from 1 to 2 atmospheres and is provided as part of the tritium control system); (b) the radial temperature gradient across the tube wall due to removal of the heat generated in the lithium oxide and in the tube itself to the mainstream coolant. It has been determined that the film coefficient around the tube in this crossflow heat exchanger environment is sufficiently uniform so that significant circumferential temperature gradients do not exist.

The hoop stress is determined by

$$\sigma_H = \Delta P \times d_o/2t_w$$

where

d_o = tube outer diameter

t_w = tube wall thickness

Tube diameters range from 2 to 4 cm and wall thicknesses from 0.05 to 0.1 cm. The range of hoop stresses is therefore:

$$2.0 \text{ MPa} \leq \sigma_H \leq 8.0 \text{ MPa}$$

$$(290 \text{ psi} \leq \sigma_H \leq 1160 \text{ psi})$$

The thermal stresses are calculated from:

$$\sigma_{TH} = E\alpha\Delta T_w/2(1 - \nu)$$

The modulus of elasticity, E, for Tenelon is approximately 1.52×10^{11} Pa at a temperature of 1000 K to 1100 K. The coefficient of thermal expansion, α, is $18 * 10^{-6}\ ^oC^{-1}$ at 1000 K.

The temperature gradient across the wall is a linear function of (a) the wall thickness, and (b) is roughly proportional to the square of the tube diameter due to the heat deposition in the lithium oxide. For the cases studied where the tube diameter was 3.8 cm, the maximum temperature difference was 10 K for a wall thickness of 0.1 cm. From this an approximate table of temperature differences versus tube diameter and wall thickness can be inferred:

d_o	t_w = 0.1 cm	t_w = 0.05 cm
2 cm	ΔT_w = 2.8 K	ΔT_w = 1.4 K
3 cm	ΔT_w = 6.3 K	ΔT_w = 3.15 K
4 cm	ΔT_w = 11 K	ΔT_w = 5.5 K

The thermal stresses range from a least value of 2.73 MPa (396 psi) to a maximum value of 21.4 MPa (3111 psi).

A conservative estimate of the combined stresses is plotted in Fig. 5.27. The advantage of the smaller tube diameters is clearly evident. At diameters of 2 cm, the combined stresses are low enough so that moderate strength materials such as Tenelon should prove adequate based on the creep rupture data available. Note also that at this diameter the tube thickness does not have a strong effect on the total stress. At tube diameters of about 4 cm, stresses begin to be quite significant and the tube wall thickness has a much stronger influence.

Tenelon should prove adequate based on the creep rupture data available. Note also that at this diameter the tube thickness does not have a strong effect on the total stress. At tube diameters of about 4 cm, stresses begin to be quite significant and the tube wall thickness has a much stronger influence.

5.3.10 Thermal Stresses in the Li_2O Cartridges

In order to make some preliminary, conservative estimates of the maximum permissible size of the lithium oxide pieces, the thermal stresses must be evaluated. A generalized expression for the thermal stress at the surface is:

$$\sigma_{th} = \frac{C_1 E \alpha \Delta T}{(1-C_2 \nu)} \tag{5.25}$$

where E is Young's modules of elasticity, α is the linear coefficient of thermal expansion, ΔT is the largest temperature difference across the piece, and ν is Poisson's ratio. The constant C_1 depends on the geometry of the piece and the nature of the thermal load applied, while C_2 is a "clamping factor" which depends on the shape and edge constraints. For thin-walled tubes or flat plate geometries, where the ΔT is produced by uniform internal heat generation with one of the surfaces adiabatic:

$$\Delta T = \frac{wt^2}{2k} \tag{5.26}$$

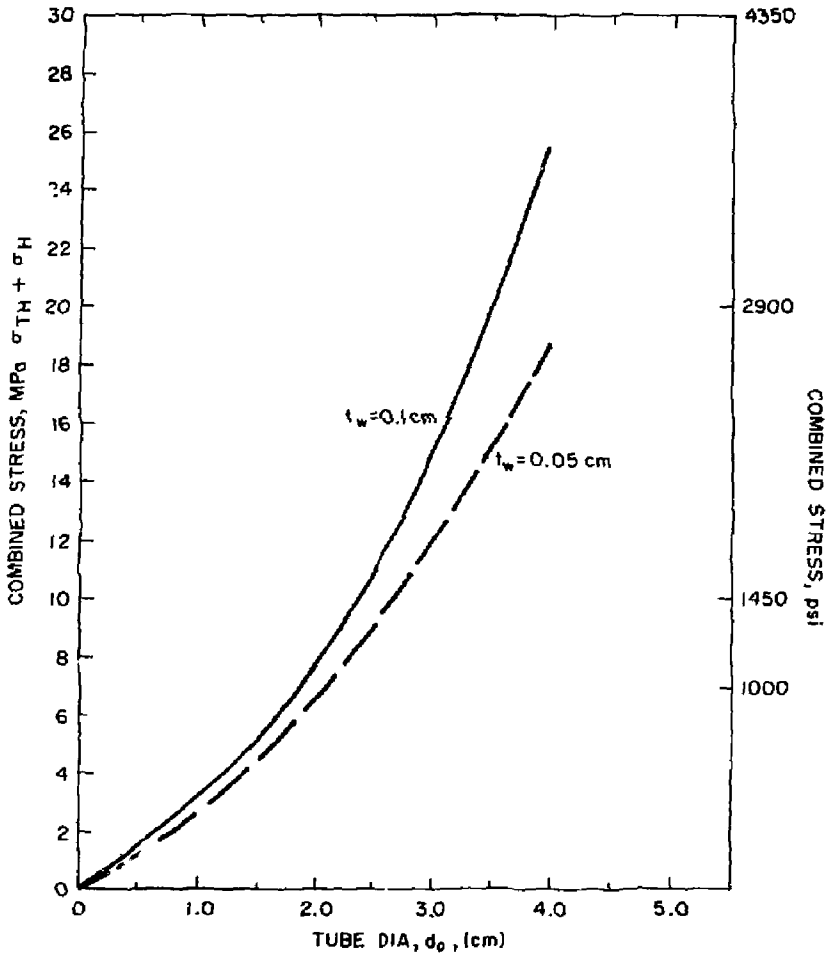

72-409-1

Fig. 5.27 Combined hoop and thermal stresses in the blanket moderator tubes as a function of tube diameter and tube wall thickness

where w is the internal heating in W/m^3, t is the characteristic thickness across which the maximum ΔT occurs, and k is the thermal conductivity.

For these two geometries, simple analytical relations for σ_{th} are available which permit us to evaluate C_1 and C_2 for the stress at the surface.

Long, thin-walled tube: $C_1 = 1/2$, $C_2 = 1$

Large, flat plate (unrestrained): $C_1 = 1/6$, $C_2 = 1$

Note that for complete restraint in the x,y and z directions $C_2 = 2$. However, for constraint in x and y only, $C_2 = 1$. We assume here that axial growth of the cartridge is unrestrained. Combining these relations, we obtain:

$$\sigma_{th} = \frac{C_1}{2k} \frac{E\alpha w t^2}{(1-\nu)} \tag{5.27}$$

We next must relate σ_{th} to the tensile stress for fracture of lithium oxide, σ_{TF}:

$$\sigma_{th} = \frac{\sigma_{TF}}{SF_{TF}} \tag{5.28}$$

where SF_{TF} is a tensile-stress safety factor. We have used $SF_{TF} = 2$ for these preliminary estimates.

We can now solve for the maximum allowable internal heat generation, w_{MAX}, as a function of the thickness of the pieces, t:

$$w_{MAX} = \frac{2\sigma_{TF}k(1-\nu)}{C_1 E\alpha t^2 SF_{TF}} = \left[\frac{M}{C_1 SF_{TF} t^2}\right]$$

where

$$M \equiv \left[\frac{\sigma_{TF}k(1-\nu)}{E\alpha}\right]$$

is referred to as the material thermal stress parameter. The larger M is for a given material, the higher are the thermal stresses which the material can withstand. For these two simple geometries with one adiabatic surface, we obtain the following relations:

Long, thin-walled tube: $w_{MAX} = 2M/t_t^2$

Large, flat plate (unrestrained): $w_{MAX} = 6M/t_p^2$

The following estimates of the property data were used for the Li_2O (assuming temperatures in the range of 600-900 K and for 90-100% theoretical density and a grain size of 1 to 5 μm):

$E = 1.2 \times 10^{11}$ Pa

$\alpha = 2.7 \times 10^{-5}$ $(K)^{-1}$

$k = 5.0$ W/m-K

$\nu = 0.25$

$\sigma_{TS} = 57$ MPa

This results in $M \approx 66$ for both geometries. There are large uncertainties in some of the available property data for lithium oxide (see Section 5.6). Consequently, the results should be used with caution. This is one of the reasons for choosing a reasonably large safety factor of 2 for tensile fracture.

For the present blanket design, a value of w_{MAX} of about 14 to 15 MW/m^3 corresponds to the internal heating in the lithium oxide cartridges closest to the first wall for a neutron wall loading of 2 MW/m^2. From Fig. 5.28 we see that this implies that long tubes could have a maximum thickness of about 3 mm, and large plates could have a maximum thickness of about 5 mm.

Based on these preliminary estimates, we decided to "pre-crack" the lithium oxide into a set of four coaxial half-cylindrical pieces, each of which is only a few centimeters long.

If the two cylinders are of equal thickness, the two outer half-

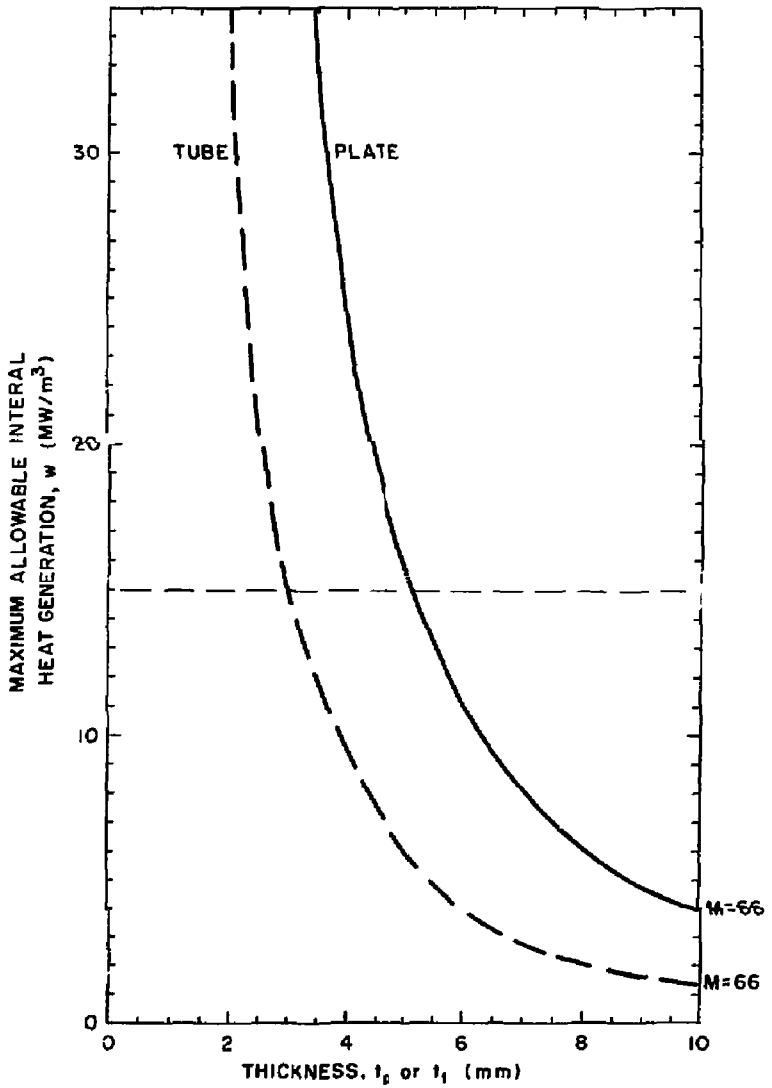

72-409-0

Fig. 5.28 Maximum allowable internal heat generation, w, as a function of the Li_2O cartridge thickness

cylinders will have higher thermal stresses than the inner two, since the heat flow is radially outward. This causes the outer pieces to have both the ΔT due to the internal heat generation and a ΔT due to the heat flow from the inner pieces. Consequently, the outer half-cylindrical pieces will probably have to be somewhat thinner than the inner pieces.

The thermal stresses for this pre-cracked design lie somewhere between those of the tube and those of the unrestrained flat plate shown on Fig. 5.28. If the half-cylinders are not tightly restrained, this design should be closer to the flat plate case than the tube case. Consequently, after some refinement, this geometry should insure that the thermal stresses will not cause premature failure. However, a more detailed 3-D computer stress analysis for the final geometry is certainly warranted as soon as more reliable Li_2O data are available.

5.3.11 Pressure Losses and Pumping Power

A series of schematics of the network of coolant pipes from the reactor blanket Canister to the primary side of the intermediate heat exchanger is shown in Figs. 5.29 through 5.33.

Calculations were run to estimate the total pressure drop and pumping power for the entire blanket coolant circuit including the primary side of the IHX. The equations used for these different losses follow.

The frictional pressure drop for flow in pipes is defined by:

$$\Delta p_{f\ell} = f\left(\frac{\ell}{d_i}\right)\frac{\rho v^2}{2} = f\left(\frac{\ell}{d_i}\right)\frac{G^2}{2\rho} = f\left(\frac{\ell}{d_i}\right)\frac{16\dot{m}^2}{\pi^2 d_i^4(2\rho)} \qquad (5.29)$$

where

ℓ = pipe length, m

d_i = pipe inside diameter, m

ρ = helium gas density, kg/m^3

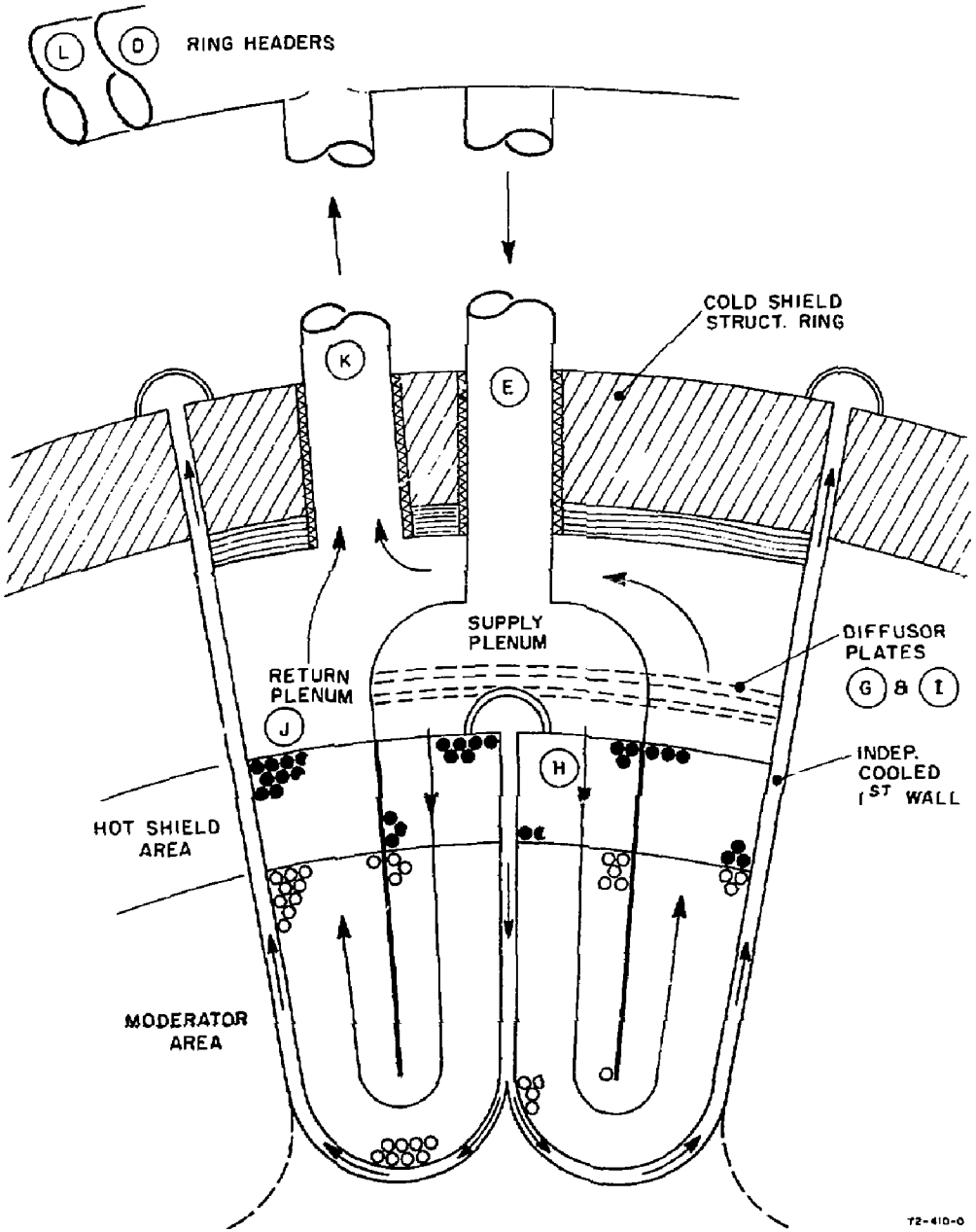

Fig. 5.29 Cross section through the Canister illustrating the lettering system for the pressure drop calculations

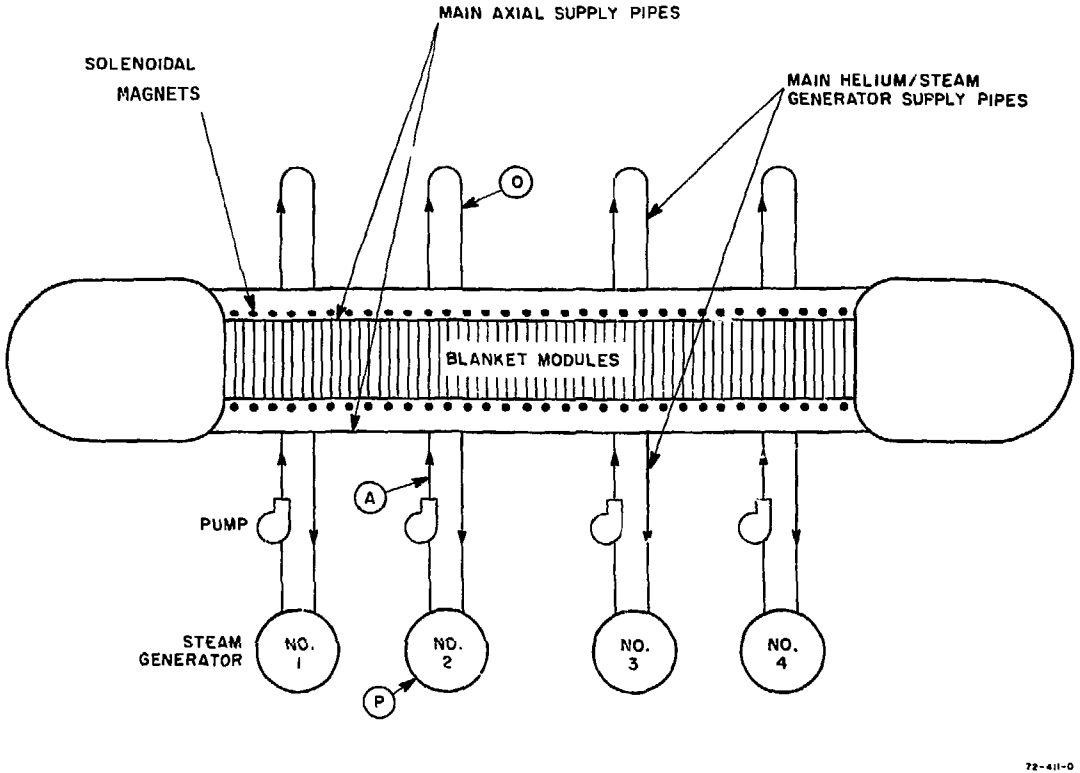

Fig. 5.30 Schematic of coolant loop for moderator portion of the blanket

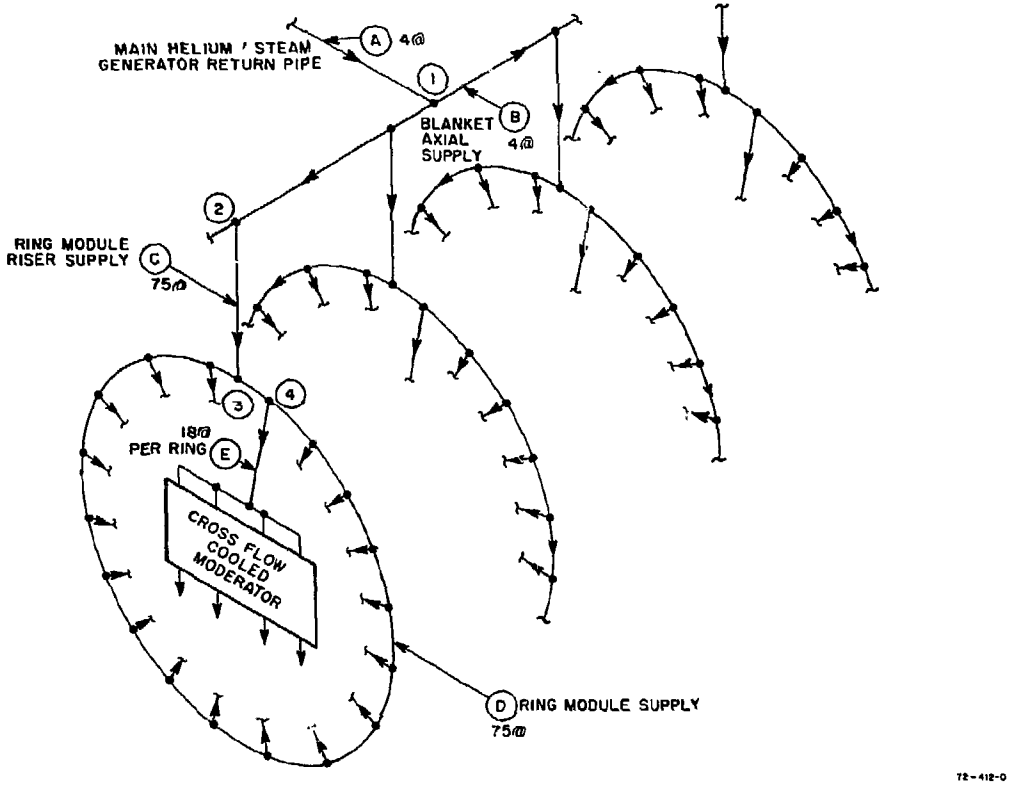

Fig. 5.31 Schematic of coolant supply lines to the crossflow-cooled cooled moderator of the blanket

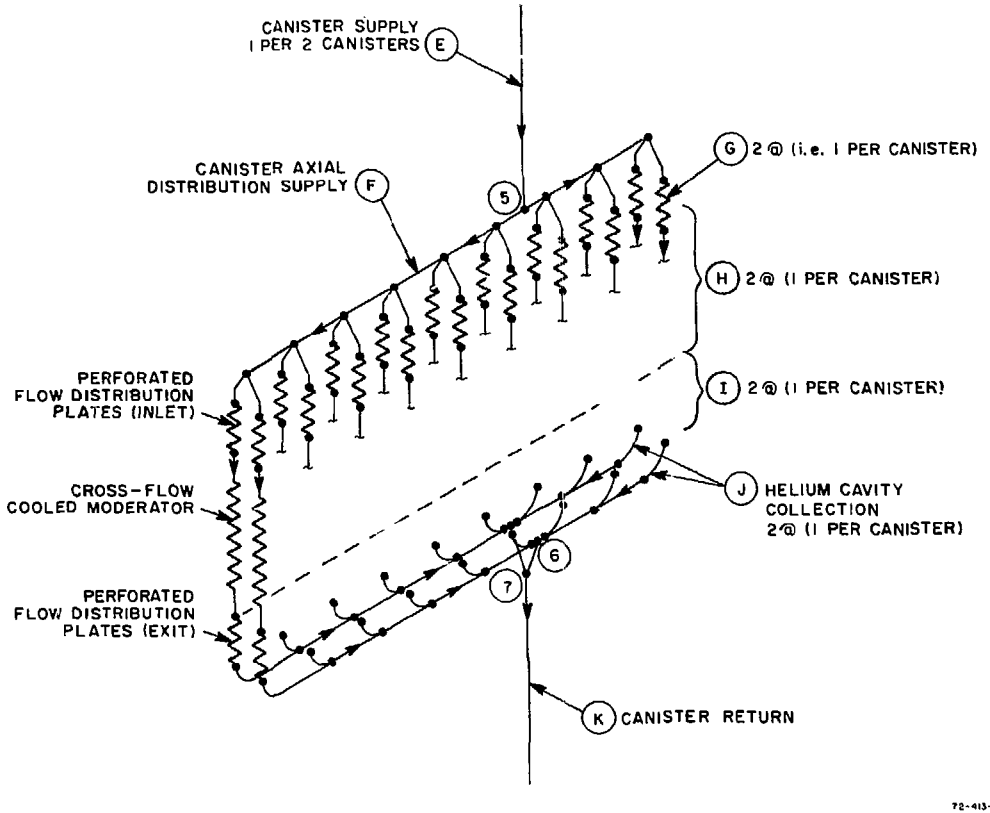

Fig. 5.32 Schematic of coolant supply/return lines to the crossflow-cooled moderator of the blanket

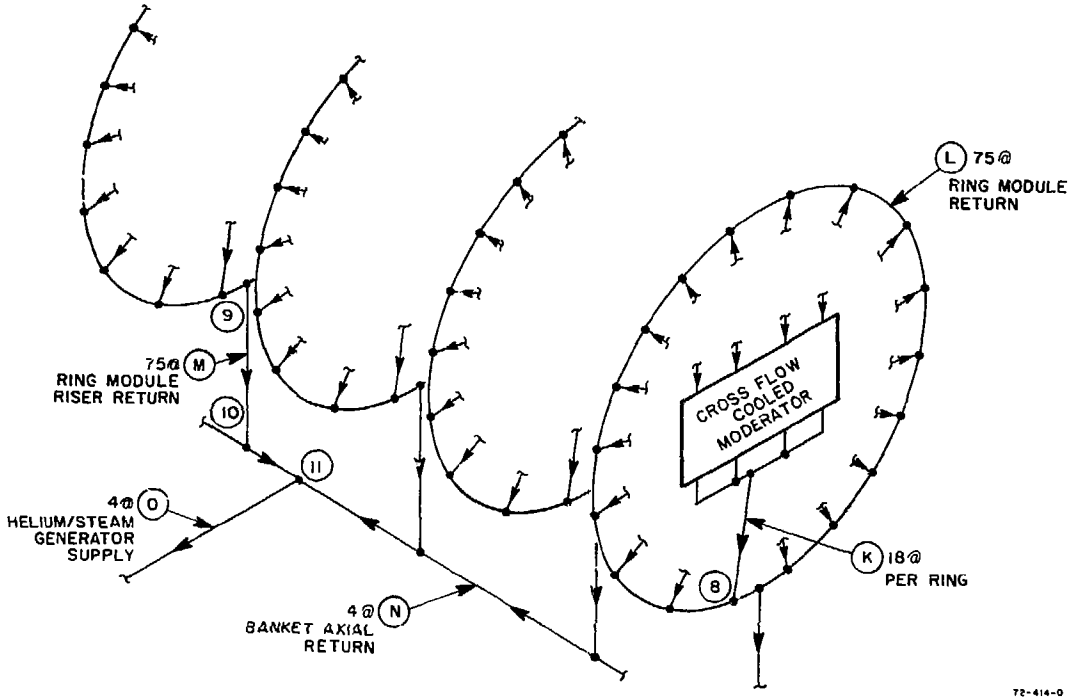

Fig. 5.33 Schematic of coolant return lines from the crossflow-cooled moderator of the blanket

v = gas flow velocity, m/s

G = gas mass flux, kg/m s

$\dot{m}$ = gas flow rate, kg/s

f = Darcy-Weisbach friction coefficient for flow in pipes

The friction coefficient is defined in terms of the Reynolds Number:

$$f = .316\ Re^{-0.25}$$
$$(6000 < Re < 300{,}000)$$

The losses due to turns and bends and the losses occurring due to dividing and the joining of flows are estimated in terms of the velocity head and an appropriate empirical loss coefficient K_L:

$$\Delta p_{t\ell} = K_L \frac{\rho V^2}{2} = K_L \frac{G^2}{2\rho} = K_L \frac{16\dot{m}^2}{\pi^2 d_i^4\, 2\rho} \tag{5.30}$$

The loss coefficient, K_L, for the various situations of flow are shown in Table 5.8 (Table of Loss Coefficients). The small acceleration pressure drops have not been included.

The pumping power is the product of the total pressure loss in the loop times the volumetric flow rate:

$$P_p = \frac{\dot{m} \cdot \Delta p}{\rho}$$

The pumping power ratio as a percentage of the blanket thermal power is:

$$PPR = \frac{P_p}{Q_b} \times 100$$

where Q_b = thermal output of the reactor blanket.

The pressure drops for the various locations in the flow circuit are

Table 5.8 Loss coefficients for turbulent flow

Type of Fitting or Valve	Additional Friction Loss, Equivalent No. of Velocity Heads, K
45-deg ell, standard [a,b,c,d,i]	0.35
45-deg. ell, long radius[b]	0.2
90-deg. ell, standard[a,b,c,d,i,m]	0.75
Long radius[a,b,c,d]	0.45
Square or miter[m]	1.3
180-deg. bend, close return[a,b,g]	1.5
Tee, standard, along run, branch blanked off[g]	0.4
Used as ell, entering run[g,k]	1.0
Used as ell, entering branch[b,g,k]	1.0
Branching flow[f,j]	1[n]
Coupling[b,g]	0.04
Union[f]	0.04
Gate valve,[a,g,j] open	0.17
⅞ open[g]	0.9
½ open[g]	4.5
¼ open[g]	24.0
Diaphragm valve,[a] open	2.3
¾ open[g]	2.6
½ open[g]	4.3
¼ open[g]	21.0
Globe valve,[a,j] bevel seat, open	6.0
½ open[g]	9.5
Composition seat, open	6.0
½ open[g]	8.5
Plug disk, open	9.0
¾ open[g]	13.0
½ open[g]	36.0
¼ open[g]	112.0
Angle valve,[a,g] open	2.0
Y or blowoff valve,[a,j] open	3.0
Plug cock[f] (Fig. 5-39) θ = 5°	0.05
10°	0.29
20°	1.56
40°	17.3
60°	206.0
Butterfly valve[f] (Fig. 5-40) θ = 5°	0.24
10°	0.52
20°	1.54
40°	10.8
60°	118.0
Check valve,[a,d,j] swing	2.0[o]
Disk	10.0[o]
Ball	70.0[o]
Foot valve[g]	15.0
Water meter,[m] disk	7.0[r]
Piston	15.0[r]
Rotary (star-shaped disk)	10.0[r]
Turbine-wheel	6.0[r]

[a] Flow of Fluids through Valves, Fittings, and Pipe, *Tech. Paper* 410, Crane Co., 1969.
[b] Freeman, "Experiments upon the Flow of Water in Pipes and Pipe Fittings," American Society of Mechanical Engineers, New York, 1941.
[c] Gibson, "Hydraulics and Its Applications," 5th ed., p. 250, Constable, London, 1952.
[d] Giesecke and Badgett, *Heating, Piping Air Conditioning*, 4(6), 443–447 (1932).
[e] Giesecke, *J. Am. Soc. Heat. Vent. Engrs.*, 32, 461 (1926).
[f] Gilman, *Heating, Piping Air Conditioning*, 27(4), 141–147 (1955).
[g] "Pipe Friction Manual," 3d ed., Hydraulic Institute, New York, 1961.
[h] Hoopes, Isakoff, Clarke, and Drew, *Chem. Eng. Progr.*, 44, 691–696 (1948).

shown in Table 5.9 for the frictional pressure drops and in Table 5.10 for the pressure drops due to bends and turns, etc. The location of these pressure drops may be found by referring to the appropriate figure. The circled letters in the figures refer to frictional pressure drops and the circled numbers refer to turns and bends.

The total pressure drop is about 57 kPa (~ 8.3 psi), a modest number that could possibly be reduced further by optimization. In terms of percentage of the blanket thermal power, about 1.3% is required to overcome these flow losses. It can be noted that the blanket/shield part of this flow circuit, i.e., the crossflow heat exchanger, accounts for less than 25% of the total pressure loss, whereas more than 50% is attributable to losses due to turns, bends, dividing flows and joining flows.

The relatively high velocity flow in pipes that terminates in a plenum section with an abrupt expansion of flow area is a cause for concern that needs further study. We have introduced diffusers in these regions that are used to smooth out the flow and distribute it uniformly to the blanket. They have not been designed in detail but it has been assumed that the perforations in the diffusor plates can be varied axially to balance the flow.

5.3.12 Heat Losses Through Insulation and Pipe Lagging

The coolant pipes in the immediate area of the reactor must, of necessity, be well insulated and thermally shielded to keep heat losses at a minimum. The energy transfer to components such as the superconducting coils must be guarded against since roughly 10 watts of refrigeration power are required to remove 1 watt of energy inadvertantly deposited in the liquid nitrogen coolant surrounding the helium-cooled coils. This is a serious design problem beyond the scope of this report but solutions must center on operating the reactor in a vacuum or near-vacuum environment so as to avoid the setting up of convective heat transfer loops and intolerable heat transfer.

Table 5.9 Functional pressure drops for various locations in the flow circuit

Pipe Line	Maximum Flow Rate (kg/s)	Average Flow Velocity (m/s)	Pressure Drop (kPa)	Pipe and Insulation I.D. (m)	Pipe and Insulation O.D. (m)	Inside Insulation Thickness (m)	Outside Insulation Thickness (m)	Pipe Wall Thickness (m)
(A) Main helium/steam generator return 4@	736	60	3.12	2.0	2.072	.015	--	.021
(B) Blanket axial supply 4@	368	19	.17	2.0	2.074	.016	--	.021
(C) Ring module riser supply 75@	39	52	2.05	0.5	0.544	.016	--	.006
(D) Ring module supply 75@	20	16	.44	0.5	0.662	.050	.025	.006
(E) Canister supply 1350@	2.2	18	.27	0.2	0.306	.030	.020	.0028
(F) Canister axial distribution supply	2.2	12	.05	0.25*	0.334	.026	.013	.0032
(G) Moderator inlet perforation plate	1.1	Var.	.02	N/A	N/A	N/A	N/A	.0032
(H) Cross-flow heat exchanger	1.1	Var.	13.65	N/A	N/A	N/A	N/A	N/A
(I) Moderator exit perforated plate	1.1	Var.	.02	N/A	N/A	N/A	N/A	.003
(J) Helium cavity collection region	1.1	Var.	~ 0	N/A	N/A	.025	.025	N/A
(K) Canister return	2.2	24	.36	0.2	0.384	.065	.024	.0032
(L) Ring module return	20	21	.59	0.5	0.756	.093	.028	.007
(M) Ring module riser return	39	68	2.73	0.5	0.564	.026	--	.006
(N) Blanket axial return	368	25	.22	2.0	2.094	.026	--	.021
(O) Main helium/steam generator supply	736	80	4.11	2.0	2.090	.024	--	.021
Total			27.8					

* Effective diameter

Table 5.10 Pressure drop due to bends and turns in the flow circuit

Location from Fig. 5.29	Type	K_L	kPa	
(A) → (B)	"T"	∿ 1.0	7.00	
(B) → (C) line loss	"T"	0.5	0.35	
(B) → (C) turning loss	"T"	1.0	0.70	
(C) → (D)	"T"	1.0	5.25	
(D) → (E) line loss	"T"	0.5	0.25	
(D) → (E) turning loss	"T"	1.0	0.50	
(E) → (F)	"T"	1.0	0.63	
(F) → (J)	"T"	0.5	0.14	Guess
(J) → (K)	Plenum	∿ 0	∿ 0	
(K) → (L)	"T"	1.0	0.85	
(L) → (M) turn loss	"T"	∿ 0.85	0.55	Joining flows
(L) → (M) line loss	"T"	0.5	0.23	
(M) → (N)	"T"	0.7	4.76	
(N) → (O)	"T"	∿ 0.85	8.01	Joining flow
Total			29.22	

Once beyond the immediate area of the reactor and its evacuated chamber, the problem reduces to one of relatively simple heat transfer that permits tolerable energy balances to be made. We assume in this region that the pipe wall is made up of both its structural components and the necessary insulation. Figure 5.34 illustrates a typical pipe in cross section. Following the method suggested by General Atomic, the theory is that the high temperature coolant is carried by an inner, essentially zero-stressed pipe filled with small-diameter pores through which the helium can permeate into an annular space between the inner pipe and an outer pipe that carries the structural load. The outer pipe is at a substantially lower temperature than the inner pipe due to the temperature gradient developed in the non-flowing helium in the annular space between pipes. Pressures are essentially balanced so that the inner pipe is stress free except for those stresses due to gravity forces. The outer pipe bears the brunt of the pressure-induced stresses. The annulus may be filled with a high-porosity matt insulator to prevent local convective mixing or the space may be filled only with the stagnant helium. The outer pipe is lagged further to decrease the heat loss from the system but not so much as to approach an adiabatic condition which would force the outer pipe temperature to approach the inner pipe temperature.

The outer diameter of the pipe can be defined in terms of the allowable heat loss, the maximum allowable temperature of the structural pipe wall, and the average bulk temperature of the helium flowing in the inner pipe. The average bulk temperature of the helium is determined from:

$$\bar{T}_b = \frac{-f_Q * Q_b}{2\dot{m} C_p} + T_{b,in}$$

where

f_Q = fraction of heat lost by the pipe

Q_b = total blanket heat generation

$\dot{m}$ = helium flow rate

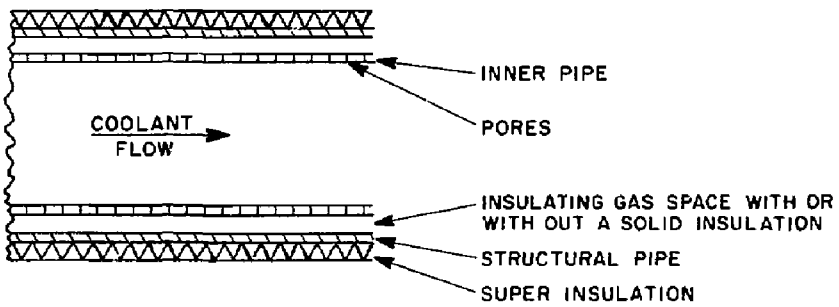

Fig. 5.34 Cross section through a typical helium transport pipe showing insulation

C_p = specific heat capacity of the helium

$T_{b,in}$ = bulk temperature of the helium at the inlet of the pipes

The hot side insulation thickness, $t_{i,h}$, in the stagnant gas-filled annular space is given by the equation

$$t_{i,h} \simeq \left[\frac{\bar{T}_b - T_{w,h}}{f_Q Q_b} - \frac{1}{h(\pi D_h \ell)}\right] k_{i,h} (\pi D_h \ell)$$

where the thermal resistance of the inner pipe wall has been neglected and where

h = heat transfer coefficient given by Eq. (5.15)

D_h = outer pipe hot-side diameter (i.e., inner diameter)

ℓ = pipe length

$T_{w,h}$ = maximum inner wall temperature of the outer pipe

$k_{i,h}$ = hot side insulation thermal conductivity

and the cold side insulation thickness, $t_{i,c}$, is given by

$$t_{i,c} = \left[\frac{T_{w,h} - T_{w,c}}{f_Q Q_b} - \frac{t_p}{k_p \pi (D_h + 2t_{i,h})\ell}\right] k_{i,c} \pi (D_h + 2t_{i,h} + 2t_p)\ell \qquad (5.31)$$

where

k_p = pipe thermal conductivity

$k_{i,c}$ = cold side insulation thermal conductivity

$T_{w,c}$ = maximum cold surface temperature of the outer pipe

The pipe wall thickness is determined by setting hoop stress for a 50-atmosphere delta pressure equal to the 1% creep stress (σ) at $T_{w,h}$ from the equation

$$t_{p,c} = \frac{\Delta p * (D_h + 2t_{i,h})/2}{\sigma_{creep}} \qquad (5.32)$$

5.3.13 Canister Blanket and Hot Shield: Performance Summary and Conclusions

The details of the thermal-hydraulic performance for the FY82 reference Canister blanket design are given in Tables 5.7a-g. A simplified summary of the key data are given in Table 5.11. We can draw the following conclusions about this blanket design:

a) The concept of the use of a solid Li_2O breeder material inside of tubes arranged as a two-pass, cross-flow heat exchanger appears to be very attractive.

b) This arrangement separates the tritium from the main helium flow which reduces the tritium recovery problems and makes the isolation of the tritium from the synfuel plant very effective.

c) The small purge helium flow inside the tubes for removing tritium from the Li_2O need only be at one or two atmospheres lower pressure than the main helium coolant flow to ensure that almost no tritium will get into the main flow in the event of a leak. This allows the hot tubes to be thin and still operate at very low stress levels, since they are almost pressure balanced.

d) The closely-spaced, cross-flow tube bank arrangement results in almost uniform tube wall temperatures around the circumference and high heat transfer coefficients; this helps to avoid hot spots on the tube walls.

e) The maximum tube wall temperature is only about 810 K at the worst point (near the exit of the second breeder section); it is only about 758 K where the combined stresses are a maximum of 5.6 MPa. These stresses are very low for Tenelon.

f) The maximum and minimum Li_2O temperatures are 962 K and 666 K,

Table 5.11 Summary of the canister performance data

Overall Central-Cell Blanket	
Number of ring modules	75
Number of half Canisters/ring module	36
Number of tubes and rods/half Canister	542
Neutronics	
Volumetric heat generation near the first wall for Γ_N = 2.0 MW/m^2:	
Li_2O cartridges	13.5 MW/m^3
Tenelon tubes	18.0 MW/m^3
Structural : Tubes	
Tube and rod material	Tenelon
Tube outer diameter	0.020 m
Tube wall thickness	0.0005 m
Tube nominal length	2.0 m
Maximum hoop stress	4.0 MPa
Maximum thermal stress	2.7 MPa
Maximum combined stress	6.7 MPa
Tube wall temperature (at exit of TA region where stress is maximum)	758 K
Creep rupture stress of Tenelon at 758 K	250 MPa
Structural: Tritium Breeder Material	
Solid breeder material	Li_2O
Percent theoretical density	90%
Assembled shape	Hollow cylinder

Table 5.11 con't.

Structural: Tritium Breeder Material con't	
Inner diameter	0.006 m
Outer diameter	0.017 m
Maximum thermal stress (estimated)	∿ 35 MPa
Tensile fracture stress (estimated)	∿ 69 MPa
Maximum temperature at inner surface (at exit of turnaround zone)	962 K
Minimum temperature at inner surface (at inlet to first breeder zone)	666 K
Thermal-Hydraulics of Tube Bank	
Coolant	Helium
Pressure	5 MPa
Inlet temperature	625 K
Outlet temperature	825 K
Minimum gap between tubes	0.002 m
Maximum Reynolds number	∿ 34,000
Maximum flow velocity	∿ 16 m/s
Average heat transfer coefficient	∿ 2000 W/m^2-K
Pressure drop inside Canister	0.016 MPa
Pumping power/half Canister	5.71 kW
Power removed by tube bank coolant/half Canister	1.12 MW
% pumping power in cooling Canister tube bank	0.51%

respectively. This range of temperatures should result in good tritium release from the Li_2O and low tritium inventories.

g) The fractional pressure drop across the tube bank is only 0.32%, which results in a ratio of the pumping power required to the thermal power removed of only 0.51%.

h) A great deal of refinement and optimization of the tube bank design is possible, since some tailoring of the tube diameters and spacings can be used to compensate for the near-exponential decrease in the internal heat generation.

5.4 TRITIUM CONTROL IN THE BLANKET

5.4.1 Tritium Processing and Control

There are significant advantages associated with having the breeder material, Li_2O, in tubes that isolate it from the main helium coolant flow. An obvious one is that imposition of an additional barrier protects the Li_2O from degradation by, and possible reaction with, contaminants that might intrude into the main helium coolant. The most likely contaminant is water. It could enter the main helium coolant due to a heat exchanger failure or a water-lubricated bearing failure on one of the helium circulators. The other obvious advantage is keeping the bulk of the tritium out of the main coolant. Reduced contamination of large parts of the system by tritium results. This makes maintenance easier. A high probability of reduced tritium losses is obtained. The volume of gas that must be processed in the tritium recovery system is greatly reduced, so equipment size can be minimized. With the reduced flow to the recovery system (that operates at room temperature), less waste heat is produced and plant efficiency is increased. Even if high temperature recovery processes are developed, all the other advantages are retained.

For adequate isolation of tritium in the high temperature regions, successful development of permeation barriers is required. Work in this area of tehcnology seems to have been stopped a few years ago. Prior to that, workers at ANL (Argonne National Laboratory) and NCSU (North Carolina State University) had both shown modest success along these lines. The most striking results were those of Tom Elleman and his co-workers at NCSU, but they were not all formally published. One of his papers gives the diffusion coefficient of tritium in a number of materials, most notably SiC.[1] This can be expressed as

$$D = 1.09 \times 10^{-2} \exp\left(\frac{-54.9 \frac{K\ cal}{mole}}{RT}\right)$$

Other ceramics had their diffusion coefficients measured and reported too, but without information on the corresponding solubility coefficients, little can be said about their permeability. In the case of SiC, the solubility coefficient was measured (but not published) and it followed the expression

$$S = 5.3 \times 10^{13} \exp\left(\frac{+38 \frac{K\ cal}{mole}}{RT}\right) \frac{atoms}{g \cdot atm^{1/2}}$$

From this, permeability can be calculated according to

$$P = DS = 5.78 \times 10^{11} \exp\left(\frac{-17 \frac{K\ cal}{mole}}{RT}\right) \frac{atoms \cdot cm^2}{g \cdot atm^{1/2}\ sec}$$

Normally, permeability is reported on a volumetric basis, so after multiplying by the density, 3.17 g/cm^3, and changing from atoms to std cc,

$$P = 3.42 \times 10^{-8} \exp\left(\frac{-17 \frac{K\ cal}{mole}}{RT}\right) \frac{std\ cc}{cm \cdot sec \cdot atm^{1/2}}$$

Another important result was their measurement of the permeability of high density polycrystalline alumina. It was found to obey the expression

$$P = 6.6 \exp\left(\frac{-53 \frac{K\ cal}{mole}}{RT}\right) \frac{std\ cc}{cm \cdot sec \cdot atm^{1/2}}$$

Both these materials are millions of times lower in permeability than metals. Inside the blanket, SiC should be preferred because of the radiation sensitivity of Al_2O_3. Silicides may be equally attractive and easier to work with and have the distinct advantage of being self healing. Development of the technology to create continuous thin films of these or other ceramics on metals is very desirable. The tritium control concept in this blanket design study depends on such a development.

The tritium control strategy relies on a pair of low permeability physical barriers. One minimizes dilution of the bred tritium as it escapes from the Li_2O and the other keeps the amount of tritium released from the plant to an acceptable minimum.

The amount of purge He that is passed through the Li_2O filled tubes is adjustable, not only in terms of total flow, but also as a function of position in the blanket. The breeding rate through the breeding zone as a function of distance from the plasma center follows the expression $G = 3.13 \times 10^{15} \exp(-4.35 \times 10^{-2} R)$ atoms/cm^3 • sec where $152 < R < 210$ cm. This is shown in tabular form below.

R	$G \frac{10^{12} \text{ atoms}}{\text{cm}^3 \text{ sec}}$
152	4.20
160	2.97
170	1.90
180	1.24
190	0.80
200	0.52
210	0.34

Because the breeding rate varies by more than a factor of ten, it is not necessary to have the same helium purge rate throughout the breeding zone. We could maintain a uniform concentration of tritium in the helium purge from each tube, or a uniform rate of tritium permeation to the main coolant, or a uniform rate of LiOT volatilization by reaction with T_2O. The latter two processes are temperature dependent. However, none of these factors has been shown to be critical design issue. We have chosen to use a much higher purge flow rate near the first wall where it is hottest and the tritium breeding is highest. This should reduce permeation into the main helium coolant.

In particular, in the 18 cm of the blanket nearest the plasma, the purge flow rate is chosen to be 100 times higher than in the outer 40 cm. This is done with a simple orifice at the outlet manifold tube sheet. Also, the total helium purge flow through the tubes is taken to be 10^{-3} of the main helium coolant flow. The main helium coolant flow is 3238 kg/sec, at 50 atm, so the purge flow is 3.24 kg/sec at 48 atm. The pressure differential is chosen to prevent leakage from the tritium breeding zone into the main helium coolant in case a leak develops. The parameters for the helium purge stream are chosen to illustrate the flexibility of this design, rather than to suggest that this represents a technological optimum of some kind.

The total number of tubes to be purged is 3.78×10^5 for tubes whose diameter is 0.038 m. Of these, 2.97×10^5 tubes will each receive the low purge flow rate of 3.85×10^{-4} g/sec and 8.1×10^4 tubes will each receive 3.85×10^{-2} g/sec. Converting these to volumetric flow rates is a little tricky because the helium temperature continuously rises as it passes first through the outer annulus between the Li_2O and the tube wall and then down the center hole of the Li_2O cartridge. The necessary data for each submodule are tabulated below.

	Inlet Channel	Turnaround Section	Outlet Channel
No. of tubes	130	60	90
Max. temp. (K)	709	839	819
Mean temp. (K)	671	706	812
Purge flow (g/s)	3.85×10^{-4}	3.85×10^{-2}	3.85×10^{-4}
Max. breeding atoms/ $cm^3 \cdot s$	2.2×10^{12}	4.2×10^{12}	1.9×10^{12}
Mean breeding atoms/ $cm^3 \cdot s$	1.0×10^{12}	3.0×10^{12}	0.8×10^{12}

These numbers are only approximate because we have a two-dimensional temperature distribution for the submodule and one-dimensional neutronics.

Now we examine the permeability phenomenon. Some authors convert the T_2 to T_2O by providing an excess of oxygen, and use this as a means to eliminate tritium permeation. It is well known that water does not permeate through metals. On the other hand, water can react with metals to form oxides and free the tritium right on the surface of the metal. If the oxide is dense and tightly adherent, a permeation barrier may form on the tube wall. Our approach is to not depend on this, but rather to ignore it and apply a separate permeation barrier.

Assume that tritium will be released uniformly into the purge helium on an area basis. Then, since the outer surface of the cartridge represents 0.78 of the area of the Li_2O exposed to the purge, the tritium will have reached 0.78 of its exit partial pressure at the closed end of the tube. The T_2O concentration profile along the annulus is expected to be linear. Thus, we can write

$$\phi = \frac{1}{\ell} \int_{x=0}^{x=\ell} \frac{PA\, p(x)^{1/2}}{t}\, dx$$

where P = permeability

ℓ = tube length = 2 m

ϕ = permeation

p = partial pressure of tritium

t = thickness of the barrier

x = distance along the tube

A = area of the tube wall

Remembering that $p(x) = 0.78\, p_{max}\, x/\ell$, we insert this into the previous equation and integrate between the limits.

$$\phi = \frac{2PA\ 0.88\ P_{max}^{1/2}}{3t}$$

We have assumed that the partial pressure in the main helium coolant is zero. The generation rate and purge rate will determine p_{max}, while only the temperature and choice of material will determine P. The choice of temperature is important, because of the strong dependence permeability has on it. We elect to use the mean tube wall temperature in each of the three breeding zones. This can be justified by remembering that previously we assumed that T_2O would permeate at the same rate as T_2. This would bias the result on the side of giving too much permeation. Selecting the mean temperature rather the one at which the mean permeability occurs gives a lower permeation and compensates for the earlier bias. For similar reasons as well as simplicity, we chose the mean generation rate in each zone in calculating the value of p_{max}.

The outer area of each tube is 2388 cm^2, and if we choose a SiC barrier thickness of 10^{-3} cm, then for each tube

$$\phi = (9.7 \times 10^5\ cm) P_{SiC} p_{max}^{1/2}$$

The results of the calculations for the zones are given in tabular form below.

	Inlet Channel	Turnaround Section	Outlet Channel
G_{mean} (g/sec·tube)	9.35×10^{-9}	28×10^{-9}	7.48×10^{-9}
p_{max} (atm)	21.2×10^{-5}	63.4×10^{-7}	16.9×10^{-5}
$p_{max}^{1/2}$ ($atm^{1/2}$)	14.6×10^{-3}	2.52×10^{-3}	13×10^{-3}
P std cc/cm·sec·$atm^{1/2}$	1.07×10^{-13}	2.01×10^{-13}	9.72×10^{-13}
ϕ (std cc/sec·tube)	1.51×10^{-9}	0.49×10^{-9}	12.25×10^{-9}
$\Sigma\phi$ (std cc/sec·zone)	1.96×10^{-7}	0.29×10^{-7}	11.02×10^{-7}

The sum of the figures in the last line give the total for half of a submodule. Multiplying this by 2 x 18 x 75 gives the total for the blanket which is 3.6×10^{-3} std cc/sec. It may be noted that a reduction in total permeation could probably have been achieved by using a higher purge rate in the outlet channel and a lower purge rate in the turnaround section.

The partial pressure in the main coolant was assumed to be zero for this permeation calculation. Using the calculated rate of 3.6×10^{-3} std cc/sec and the processing removal rate from the main coolant, this assumption can be verified. At steady state, the rate that tritium permeates into the main coolant must be equal to the rate at which it is removed. The removal rate consists of the processing removal rate plus the losses due to leakage and permeation into other parts of the plant. Again, we expect the losses to be minimal, so initially they are ignored. Then,

$$3.6 \times 10^{-3} \frac{\text{std cc}}{\text{sec}} = \eta C_T(fV) + \text{losses}$$

where fV is the volumetric flow rate going through the tritium removal processor. It is written as a fraction, f, of the total main helium flow, V. The concentration of tritium in the main helium flow as it enters the processor is C_T, and η is the fraction of this concentration that is removed in the processing section. Current technology allows η to be set at 0.99. The value of f is a design variable and is arbitrarily set at 10^{-4}. The mass flow rate is 3238 kg/sec, so at 50 atm, the volumetric flow rate is 3.63×10^{8} cm^3 sec. Substituting above, the concentration of tritium in the main helium is calculated to be 1.0×10^{-7} atm. This is a negligible "back pressure" for the permeation calculation, so the original approximation is justified and a second iteration is unnecessary.

Now we go to the next step and examine the amount of tritium that gets into the steam cycle that is the other side of the intermediate heat exchanger (IHX). Again, we will have the opportunity to check the validity of our assumption that losses can be ignored. The intermediate heat exchanger handles all of the thermal energy from the reactor, including the

direct converter. The methods for keeping tritium out of the direct converter have not been established. Tritium-free coolants for beam dumps appear feasible, so we assume here that the helium from the direct converter has the same tritium concentration as the blanket helium coolant.

The total thermal load on the He/steam IHX is 3780 MW. The first wall helium coolant is delivered at 625 K and falls to 525 K. The blanket and direct converter helium are delivered at 825 K and drop to 625 K. On the water (or steam) side, the temperatures range from 50 K to 200 K lower in temperature due to the film and tube wall drops that contribute to the overall heat transfer coefficient. Most of the temperature drop is on the helium side, so we will make the estimate that the IHX wall temperature is 30 K below the helium temperature. These figures will be used to estimate the heat exchanger area and subsequently the permeation of tritium into the steam cycle. Because the helium system runs at 50 atm or 750 psi and the steam system runs above 1200 psi, any leaks that occur in the IHX will not add tritium to the steam system. The loss question really is restricted to permeation.

In the section of this report on thermal interfacing, it is clear that no single temperature properly represents the IHX. Furthermore, the heat transfer mechanism is not uniform on the steam side. Sometimes water is present, sometimes it is superheated steam. Consequently, the area required to transfer a given heat load is also a variable.

This calculation will turn out not to be a critical one, so from Fig. 4, we will choose an overall U and ΔT to represent the IHX, and evaluate the permeation at the average outside wall temperature, which is 30 K below the average He temperature. The outside wall is where the permeation barrier is located. The assumed values are U_{AVE} = 1000 W/m^2 • K and ΔT_{AVE} = 50 K, so knowing that Q = 3780 MW, the area is calculated to be 75,600 m^2. Although the surface temperature ranges from 495 K to 795 K, only the surface area at relatively high temperature contributes to the permeation. Alumina is our choice of material barrier on the IHX and we select a barrier 10^{-3} cm

thick. Again, we assume that T_2O will show the same concentration (or partial pressure) dependence as T_2, because we are ignorant of the real case and we have a permeability expression for the case we postulate. This is a very conservative approach. Repeating,

$$\phi = \frac{PAp^{1/2}T_2O}{t}$$

The IHX shows a broad temperature range, and we have arbitrarily broken it into six zones of equal area and selected the temperatures to be evenly spaced 50^0 apart, which gives mean temperatures, permeabilities and permeations according to the following table.

T(K)	$P\left(\frac{\text{std cc}}{\text{cm} \cdot \text{sec} \cdot \text{atm}^{1/2}}\right)$	ϕ $\left(\frac{\text{std cc}}{\text{sec}}\right)$
770	7.46×10^{-15}	29.7×10^{-8}
720	0.684×10^{-15}	2.7×10^{-8}
670	0.044×10^{-15}	0.17×10^{-8}
620	0.001×10^{-15}	0.01×10^{-8}
570	--	--
520	--	--
Total	$3.258 \times 10^{-7} \frac{\text{std cc}}{\text{sec}} = 0.06 \frac{\text{Ci}}{\text{day}}$	

Permeation into the steam cycle is about 0.06 curies/day under the assumptions made. At steady state, that must be approximately the amount that will escape into the environment through steam leaks and blowdown.

Our 3780-MW IHX secondary side has a water inventory of $\sim$ 220,000 gallons based on comparable sized steam units for electrical production. For a 1000 MWe plant, the water inventory is $\sim$ 220,000 gallons and that is about

3500 MW_{th}. The makeup rate is as low as 77,000 gallons per day. Thus, the blowdown (and to a smaller extent leakage) removes a third of the water inventory per day. Consequently, the steady-state inventory of the steam plant is in the neighborhood of 0.18 curies. On a weight basis, this is about 6×10^{-14}. The amount of tritium that gets into the chemical plant will surely be a small fraction of that in the steam cycle, and it will be diluted by a very large flow of water into, and hydrogen out of, the thermochemical plant. If we assume a concentration drop of 10^{-3} or more, we are barely above the background level of tritium in the biosphere. It is detectable only with extraordinary procedures.

5.4.2 Tritium Inventory

Tritium inventory in the reactor blanket was investigated. The calculated value is under 1 kg, and if our assumptions are correct and our approximations are reasonably valid, it should be a good number for this design.

The inventory is strongly influenced by local temperature, both throughout the blanket in general as well as across the individual Li_2O cartridges inside each tube. In a real sense, it is a two-dimensional problem in two different regimes of size, and they are superimposed on one another. The strong dependence on temperature results from the exponential temperature dependence of tritium's diffusion coefficient in Li_2O. Another crucial parameter that must be known is the local tritium breeding rate. This, too, is a two-dimensional problem, particularly with our fluted first wall and cylindrical blanket configuration. So far these calculations are available only for one-dimensional geometries. Finally, the inventory depends on the amount and morphology of the Li_2O itself.

Let us first direct our attention to the lithium oxide. The Li_2O is shaped into hollow half cylinders. They are of radii such that they can be "nested" to form a fairly thick-walled hollow cylinder. When these pieces are formed, they are pressed from powder and then fired to create pieces that are very near 100% theoretical density. After conventional ceramic

fabrication, stacks of these pieces are made to be 10% porous in either of two rather unusual ways.

The first is to use a modification of the "pore former" technique. Very fine fibers would be chopped to short lengths of a millimeter or two. They would be in the micron range of diameters and have two chemical qualities. They wouldn't react with Li_2O, even at high temperature. They also could be burned or evaporated out, leaving a channel, if exposed to hot pure oxygen or some other suitable environment. That might just be high temperature in high vacuum, if the fiber is to evaporate. Any number of hydrocarbon fibers might work, or cadmium, and with study other alternatives would be discovered. The chopped fibers would be premixed with the Li_2O powder and hot-pressed to full density. Then a light cut would be taken off the inner and outer surfaces of the cartridge part to ensure the fibers actually were connected with the outside surface. Subsequent exposure to hot oxygen or vacuum would leave a 90%-dense, microporous ceramic body. The holes would be round, so the tendency to sinter would be minimal.

Alternatively, an array of holes are bored radially through the Li_2O tube wall to allow the tritium to escape after having diffused only a short distance in the solid. This array is a rectangular pattern on 14 μm centers. The hole diameter is 5 μm, and these holes needn't be perfectly straight or round. This array is produced very quickly by boring a very large number of holes simultaneously with laser beams. The array spacing and hole diameter were chosen to meet the requirements of Li_2O density, acceptable tritium inventory, and the ability of laser drilling technology to make the parts in a few years. Today there are commercial methods for creating porous surfaces on high speed aircraft using laser drilling. The holes are about 2 mm deep but are 50 μm in diameter. People working in this field believe 5 μm holes could be developed in a year or two of development time. Given the rapid progress in fiber optics, high powered lasers, and laser- based fabrication technologies, this seems like a reasonable extrapolation.

One element of an array like this is shown in Fig. 5-35. The heavy

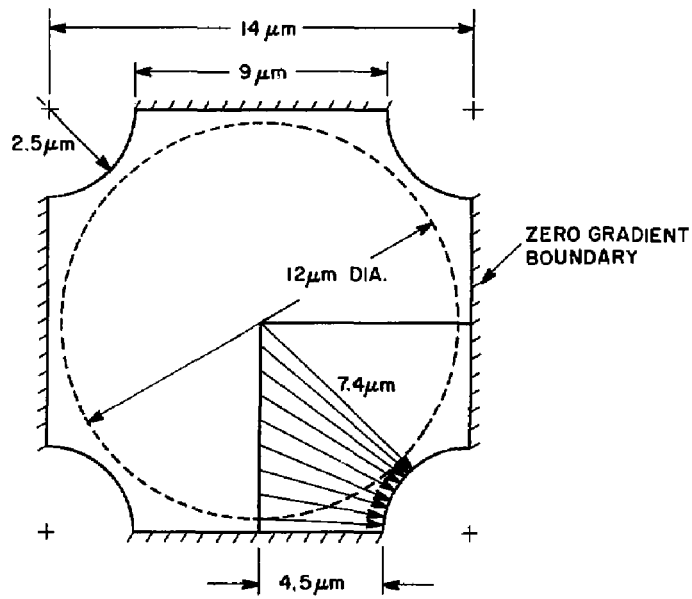

Fig. 5.35 End view representation of a Li_2O element on 14 μm centers by a 12 μm diameter right circular cylinder

lines indicate planes across which tritium does not diffuse. This element is slightly tapered because it runs radially through the Li_2O piece, but this taper is ignored. The end planes of the element are curved because of the boundary planes on the Li_2O piece, and this is ignored. Now we approximate this element as a solid right circular cylinder of infinite length. The distance a tritium atom must diffuse ranges from 4.5 μm to 7.4 μm, depending on where the atom is formed. For the purpose of estimating the tritium inventory, we set this element's distance for diffusion purposes to be 6 μm, which will be the radius of the cylinder that approximates the element. To account for the fact that much of the element's boundary does not allow tritium to escape, we increase the concentration of tritium in proportion to the fraction of inactive boundary, while using mathematics appropriate to a fully active boundary. Some of these approximations are more appealing than others. A full two- or three-dimensional numerical model with good data is needed to exactly calculate the behavior that will be observed. Under the circumstances the approach seems reasonable.

The calculation starts by writing the diffusion equation with a continuous uniform source term, G.

$$Gr = -D \frac{d}{dr}\left(r \frac{dC}{dr}\right)$$

After integrating once and using the fact that dc/dr = 0 at r = 0, we have

$$\frac{dc}{dr} = \frac{Gr}{2D}$$

This is integrated again, and the homogeneous boundary condition is invoked at the outer boundary, i.e., C = 0 at r = x

$$C(r) = -\frac{G}{4D}(r^2 - x^2)$$

The inventory is obtained by integrating the concentration over the volume of the element and applying the fudge factor, f, for the partially blocked boundary:

$$I_e = f \int_{r=x}^{r=0} C(r) \ell 2\pi r dr = \frac{G\pi\ell x^4 f}{8D}$$

where ℓ is the length of the element. This is taken to be the difference between the inner and outer radii of the Li_2O cartridge. The inventory in the tubes in all 75 of the blanket modules at this position is I_e times the number of elements in the full length of tubes, which is 150 m. The number of elements is calculated by taking the log mean circumference of the cartridge divided by the element dimension, 14 μm, times 150 m/14 μm (which is the same operation for the length).

$$Ne = \frac{\frac{2\pi(1.8 - 0.5)cm}{\ln \frac{1.8}{0.5}}}{14\ \mu m} \times \frac{150\ m}{14\ \mu m} = 4.88 \times 10^{10} \frac{\text{elements}}{\text{tube position}}$$

There are 18 identical submodules and within each submodule, particularly in the outlet and inlet sections, tubes are arranged in duplicate banks of 5. There are 180 tube positions in the blanket at the same operating temperature. Thus, the inventory as a function of position in the blanket is obtained by appropriately summing 180 NeIe. This can be written

$$I_i = 180(4.88 \times 10^{10}) \frac{G_i}{D_i} \frac{\pi\ (1.8 - 0.5)\ (14 \times 10^{-4})^{\ 4}\ 3.3(0.9)}{8}$$

where the fudge factor is the ratio of total boundary to active boundary, or 3.3, and a factor of 0.9 has been added to reflect the fact that the Li_2O is only 90% theoretical density. Finally,

$$I_i = \frac{G_i}{D_i} 51.2\ cm^5$$

The value for G_i is obtained from the breeding rate expression $G_i = 3.13 \times 10^{15} \exp(-4.35 \times 10^{-2} R)$ T atom/cm^3 sec where 152 cm < R < 210 cm.

Calculation of the diffusion coefficient requires that the lithium oxide temperatures be known (Fig. 5-36) and that we have an equation for the

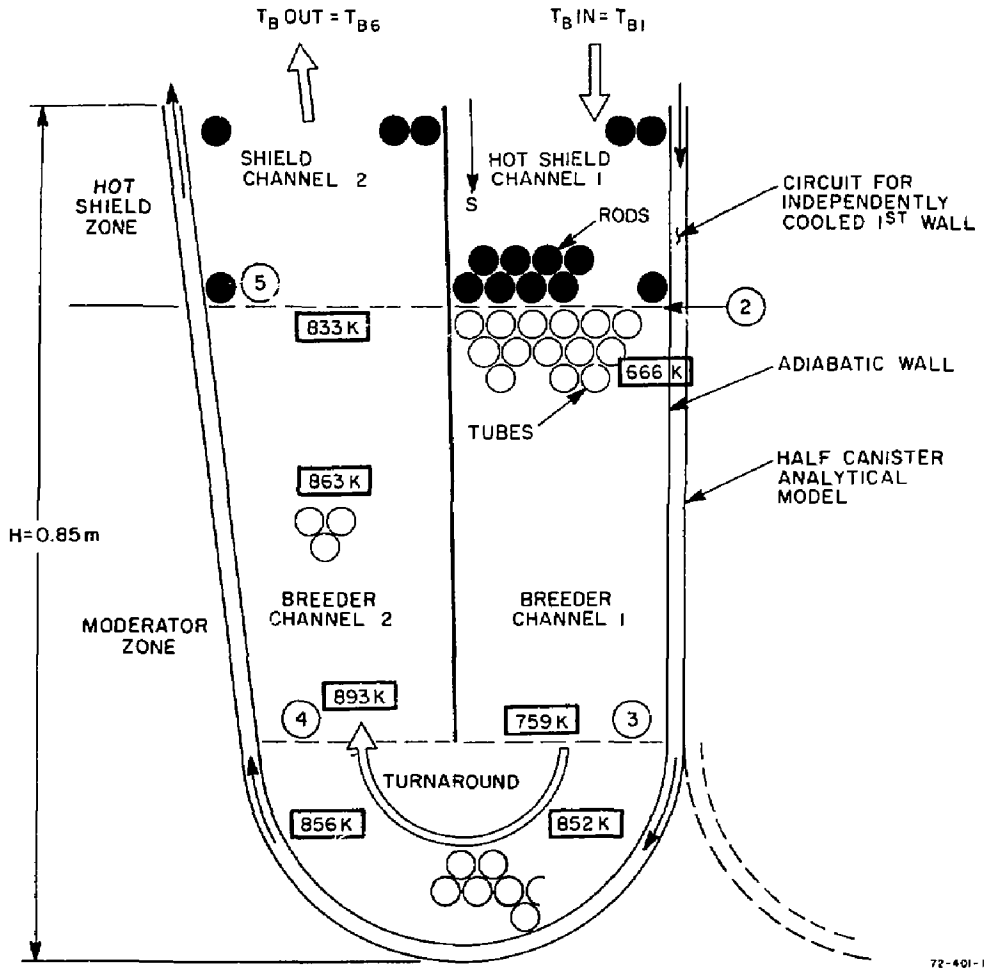

Fig. 5.36 Li_2O temperatures as a function of position in the blanket

temperature dependence of the diffusion coefficient. This latter equation doesn't exist, so one was invented. A composite of the available data suggests that at 1000 K, the diffusion coefficient is 6×10^{-11} cm^2/sec.[2] Activation energies for diffusion of hydrogen in oxides cover a fairly broad range.[3] An intermediate value was chosen, to not bias the results in either direction. Thus, we have chosen $D_i = 7.1 \times 10^{-8} \exp(-7074/T)$ cm^2/sec.

As is normally the case, we find that most of the tritium holdup is in the coolest regions of the blanket. Below, we sum the inventories by tube bank through the inlet channel and outlet channel for the entire blanket. The turnaround section near the first wall is treated in less detail because it makes a rather small contribution. The inlet and outlet are given in Table 5-12.

The turnaround section is estimated to have an average value of R = 165.2 cm and T = 1160 K. Then $G = 2.37 \times 10^{12}$ $atoms/cm^3 \cdot sec$ and $D = 159 \times 10^{-12}$ cm^2/sec, so $G/D = 0.015 \times 10^{24}$ $atoms/cm^5$ for the 30 tubes in this section. Summing this for a five-tube-per-bank basis to put it on the same basis as the rest and permit one more calculation gives $G/D = 0.09 \times 10^{24}$ $atoms/cm^5$. Finally,

$$I_{TOTAL} = \sum_i \frac{G_i}{D_i} 51.2 = (1.928 + 0.218 + 0.09)51.2 \times 10^{24}$$

$$= 114.4 \times 10^{24} \text{ atoms} = 572 \text{ g}$$

This amount of tritium is judged to be acceptable.

After the tritium escapes the solid, presumably as T_2O, it may have to diffuse back and forth between the nested parts of the cartridge to reach the helium purge stream. This gas phase diffusion does not seriously invalidate the previous assumption of a homogeneous boundary condition. If the laser-drilled holes go all the way through the pieces it permeates through the Li_2O. The longest distance it might reasonably have to diffuse is 3 cm but 1 cm is more probable. The gas phase diffusion coefficient also is tempera-

Table 5-12 Calculation of tritium inventory by blanket position

T(K)	R(cm)	$D_i\left(10^{-12}\ \frac{cm^2}{s}\right)$	$G_i\left(\frac{10^{12}\text{atoms T}}{cm^3 sec}\right)$	$\frac{G_i}{D_i}\left(\frac{10^{24}\text{ atoms T}}{cm^5}\right)$
		Inlet Channel		
654	208.3	1.42	0.36	0.253
669	204.6	1.81	0.43	0.237
684	200.9	2.29	0.50	0.218
700	197.2	2.90	0.59	0.203
725	193.5	4.11	0.69	0.168
750	189.8	5.69	0.81	0.142
775	186.1	7.71	0.96	0.124
800	182.4	10.25	1.12	0.109
823	178.7	13.13	1.30	0.099
846	174.2	16.6	1.62	0.097
869	169.7	20.7	1.92	0.092
890	165.2	25.1	2.37	0.094
		last bank (est.)		0.092
				1.928
		Outlet Channel		
852	208.3	17.6	0.36	0.020
864	204.6	19.7	0.43	0.022
876	200.9	22.1	0.50	0.023
888	197.2	24.6	0.59	0.024
903	193.5	28.2	0.69	0.024
918	189.8	32.0	0.81	0.025
934	186.1	36.5	0.96	0.026
950	182.4	41.4	1.12	0.027
968	178.7	47.6	1.30	0.027
				0.218

ture dependent and varies through the blanket. Let us assume on the average, the gas temperature in the nested pieces is 900 K. Then the diffusion coefficient in the gas, D_G, is given by[4]

$$D_G = \frac{BT^{3/2}\sqrt{\frac{1}{M_1} + \frac{1}{M_2}}}{P\, r_{12}^2\, I_D(T)} \quad \frac{cm^2}{sec}$$

where

$$B = \left(10.82 - 2.50\sqrt{\frac{1}{M_i} + \frac{1}{M_2}}\right) \times 10^{-4}$$

M_1 and M_2 are the molecular weights

T is in Kelvin

P is in atm.

r_{12} is the mean collison diameter

$I_D(T)$ is the temperature-dependent collision integral for diffusion

$$D_G = \frac{\left(10.85 - 2.5\sqrt{\frac{1}{4} + \frac{1}{22}}\right) \times 10^{-4}\ (900)^{3/2}\sqrt{\frac{1}{4} + \frac{1}{22}}}{48(2.68)^2 0.33} = 0.11\ \frac{cm^2}{sec}$$

Further details on collision integrals can be found in other references.[5,6] Now the impedence for diffusion is the distance divided by the area and diffusion coefficient, and we don't know how tightly the cartridge pieces will be nested. It can be determined by design, however. For the gas phase, ℓ/D = 1 cm/0.11 cm^2/sec = 9.1 sec/cm. For the solid phase, $\ell/D = 6 \times 10^{-4}$ cm/28 x 10^{-12} cm^2/sec = 2.1 x 10^7 sec/cm. Simple calculations show the ratio of solid area for diffusion to gas phase area for diffusion to be 2 x 10^5 if 1 mm space is left between the nested parts of the Li_2O cartridge. Thus, 90% of the impedence is in the solid phase. The diffusion in the solid appears likely to dominate the tritium inventory relative to diffusion in the gas phase. The possible errors in the existing data make it too close to judge with confidence.

Another factor needs to be considered, however. As the purge flow passes through the tube, the T_2O content increases along both the external and internal traverse of the cartridge assembly. Consequently, there is a varying partial pressure throughout the tube, and it varies between tubes according to the generation rate and purge rate. The amount of LiOT dissolved in the Li_2O depends on all these factors as well as the temperature of the Li_2O, which varies within a given tube and also throughout the blanket depth.

Some work at ANL on determining the solubility experimentally was reported, but so far there are no results at our mean Li_2O temperature of 900 K. This could be one of the more significant effects influencing the total tritium inventory and deserves more study.

Using their lowest temperature data (1123 K), a rough calculation suggests an additional tritium inventory of 2.3 kg. Their data are not easy to extrapolate to lower temperatures, but the trend suggests the inventory would be lower at lower temperatures. Furthermore, by increasing the purge rate to 10^{-2} of the bulk helium flow from the present value of 10^{-3}, the estimate above would drop to 230 g. This assumes that Henry's law is obeyed. That would keep the total blanket inventory below 1 kg even without taking advantage of the lower solubility expected at our temperatures.

5.4.3 Volatilization of LiOT

A question that has been raised in the past is that of volatilization of LiOT when it is in the presence of water vapor. This concern is quite valid, for we anticipate most of the tritium produced will be in the form of T_2O. The extent of volatilization and Li_2O loss can be seen to depend on both the temperature as well as the partial pressure of water vapor from the following equation[7]:

$$\log P_{LiOH} = -\frac{9210}{T} + \log P_{H_2O} + 5.04 \qquad (1)$$

where pressure is atm and temperature is Kelvin. The partial pressure of water vapor depends on the local breeding rate as well as the sweep rate of the helium purge gas through the tubes.

Referring to Section 5.4.7 on tritium processing and control, it may be seen that the flow is not uniform. The purge mass flow rate through the hottest, highest breeding rate zone is selected to be 100 times larger than through other parts of the breeding blanket. In the hottest part, the flow through each tube was therefore set at 3.85×10^{-2} g/sec. The volumetric flow rate is harder to work with for it increases constantly as the purge helium heats up as it passes through the tube. The breeding rate equals the evolution rate at steady state, so from the breeding rate equation, at the first wall where R = 152,

$$G = 3.13 \times 10^{15} \exp(-4.35 \times 10^{-2} R) \frac{\text{atoms}}{\text{cm}^3 \cdot \text{sec}}$$

and from the volume of lithium oxide in the tube

$$V = \pi(1.8^2 - 0.5^2)200 \text{ cm}^3$$

the evolution rate is found to be 7.89×10^{15} atoms/sec. Multiplying the flow rates by the appropriate factors, we can convert this information to that needed to calculate partial pressure.

$$\frac{7.89 \times 10^{15} \frac{\text{atoms}}{\text{sec}}}{3.85 \times 10^{-2} \frac{\text{gHe}}{\text{sec}}} \times \frac{4 \frac{\text{gHe}}{\text{mole He}}}{\frac{2 \text{ atoms}}{\text{molecule}} \times \frac{6.02 \times 10^{23} \text{ molecules}}{\text{mole}}}$$

$$= 6.8 \times 10^{-7} \frac{\text{mole } T_2O}{\text{mole He}}$$

If this were a 1-atm system, the pressure would be very nearly 6.8×10^{-7} atm, but since it is a 48-atm system, the T_2O pressure is 3.27×10^{-5} atm. Inserting into Eq. (1),

$$\log P_{LiOT} = -\frac{9210}{1244} + \log(3.27 \times 10^{-5}) + 5.04$$

where I have chosen the mean of the maximum Li_2O temperatures (on the inner diameter of the Li_2O) within this high breeding rate zone of the submodule. The calculated pressure is $P_{LiOT} = 1.4 \times 10^{-7}$ atm. The mass ratio of LiOT(g) to T_2O(g) is the molar (or partial pressure) ratio times appropriate molecular weight factors

$$\frac{1.4 \times 10^{-7}}{3.29 \times 10^{-5}} \times \frac{25}{22} = 0.005 \frac{g\ LiOT}{g\ T_2O}$$

The mass flow rate of T_2O is

$$7.89 \times 10^{15} \frac{atoms}{sec} \times \frac{molecule\ T_2O}{2\ atoms\ T} \times \frac{mole\ T_2O}{6.02 \times 10^{23} molecules}$$

$$\times \frac{22g\ T_2O}{mole\ T_2O} = 1.44 \times 10^{-7} \frac{g\ T_2O}{sec}$$

So, the rate of LiOT loss is

$$0.005 \times 1.44 \times 10^{-7} = 7.2 \times 10^{-10}\ g/sec$$

This turns out to be about 7 mg from this tube during a lifetime of three operating years. Deeper in the blanket, the breeding rates and temperatures are lower, which will reduce the volatility. Offsetting this partially is the purge flow rate that is reduced by a factor of 100. Nevertheless, it does not seem to pose a serious problem in this design.

5.5 NEUTRONICS

All of the neutronics calculations were performed with the one-dimensional code, ONEDANT. This is the most recent version of the discrete ordinates neutron transport code ONETRAN[8] and includes the synthetic diffusion approximation developed by Alcouffe.[9] The calculations were performed with S_4 quadrature and used 30 neutron groups coupled with 12 gamma groups to facilitate neutron transport and gamma ray production and transport. The group constants are of order P_3 and were obtained from the MATXS library by the TRANSX code.[10] A similar translation produced the neutron and gamma kerma factors utilized in the heating edits. All of the cross section data are from the ENDF V files.

The initial blanket design was a helium cooled, lithium oxide design with Inconel structure. The initial design had excess breeding capacity, and neutronics work focused on lowering the breeding ratio and improving the overall blanket performance by placing additional structure in the breeding zone (see Table 5.13). The additional structure reduced the breeding ratio and increased the blanket energy multiplication, and also provided additional shielding for the superconductor coil. These results suggest that, in general, when excess tritium breeding is available, neutronics performance can be improved by adding structure beyond the amounts required for physical integrity.

Tritium recovery later became a primary concern, and led to the development of the blanket design described in Section 5.5.1. Neutronically, this design is similar to the previous designs, but contains a smaller Li_2O volume fraction, and correspondingly greater void and structural fractions. The work at this point focused on finding the best combination of breeding region thickness, Li_2O volume fraction, and structure fraction that would satisfy all the requirements. Figures 5.37 and 5.38 show the results of some of this work. Details of this design are given in Table 5.14 and the results are presented in Table 5.15.

Table 5.13 Li_2O Initial Blanket Design

	R	
Plasma	150 cm	Void
First Wall	151	Inconel 100%
Breeder Zone 1	164.5	83% Li_2O* 6.5% HT9
Breeder Zone 2	196	80% Li_2O* 13% HT9
Reflector	226	Inconel 95%
Manifold	251	St. St. 10%
Shield	287	Pb, S. St. B_4C
Dewar, Ins. Coil	337.2	

Case	Description	T	M	Dose**	Energy in Sc***
1	36 cm shield	1.157	1.185	7.1×10^{7}	1.8×10^{-6}
2	48 cm shield	1.157	1.184	1.38×10^{7}	3.59×10^{-7}
3	36 cm shield 5% added str zone 1 (78% Li_2O, 11.5% HT9)	1.134	1.194	6.65×10^{7}	1.65×10^{-6}
4	36 cm shield 5% added str. zone 2 (75% Li_2O, 18% HT9)	1.142	1.189	6.47×10^{7}	1.63×10^{-6}
5	36 cm shield 10% added str. zone 1 (73% Li_2O, 16.5% HT9)	1.113	1.203	6.35×10^{7}	1.56×10^{-6}
6	36 cm shield 10% added str. zone 1 (70% Li_2O, 23% HT9)	1.128	1.194	6.04×10^{7}	1.51×10^{-6}

*Li_2O 80% theoretical density

**Dose in grays after 30 years at 2 MW/m^2

***Fraction of total energy deposited in s.c. coil in one-D model

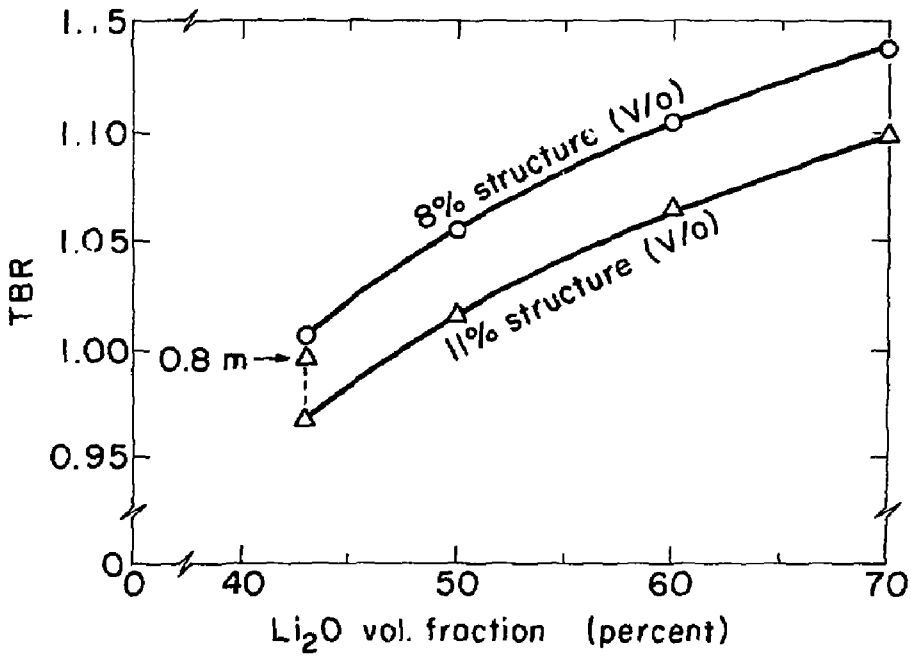

Fig. 5.37 Tritium breeding ratio (TBR) vs Li_2O volume fraction

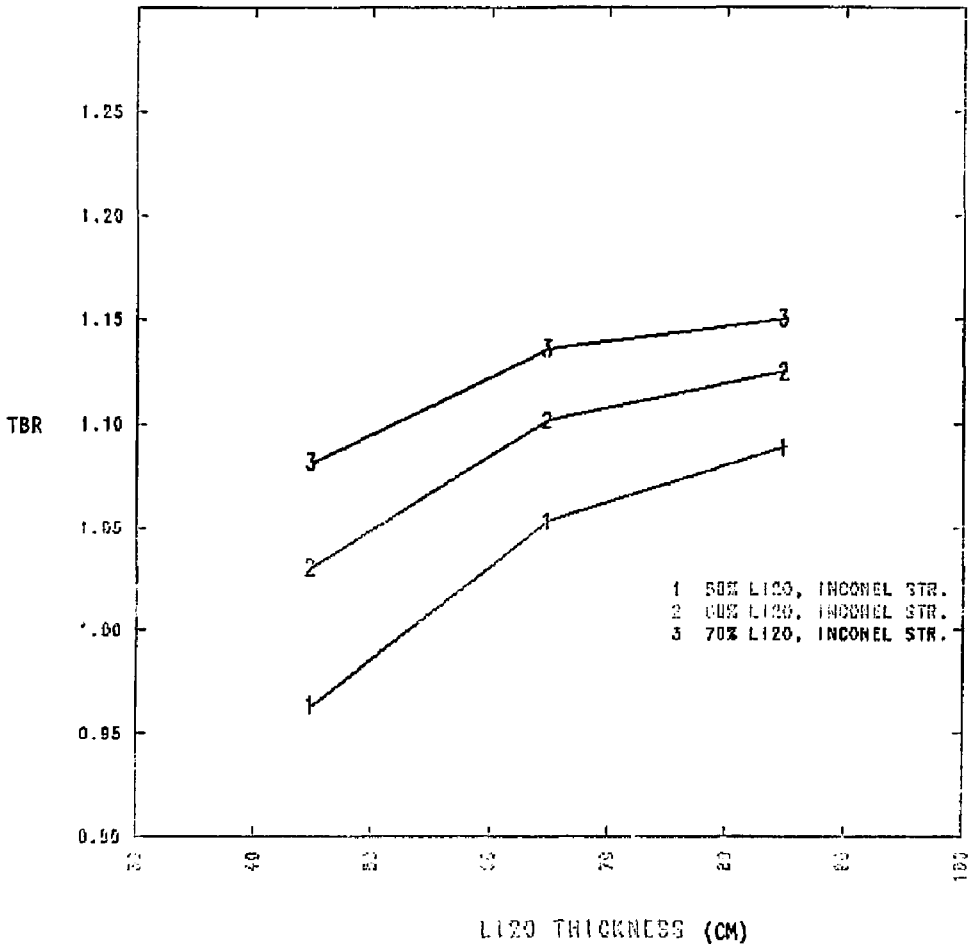

Fig. 5.38 Tritium breeding ratio (TBR) vs Li_2O thickness

Table 5.14 Li_2O Blanket Configuration

Ro(m)	Description	Composition
1.50	Vacuum	
1.51	First Wall	Inconel (Ni 77%, Cu 15%, C .08%, Mn .25%, Si .25%, Cr 15%, Fe 7%)
2.16	Breeder Zone	Li_2O 60% (theoretical density = 0.9) Inconel 8%, Void 32%
2.36	Reflector	Inconel 75%, Void 25%
2.61	Manifold	Stainless Steel 15% (St. St. - Fe 67.5%, Cr 15%, Mn 1.5%, Ni 14%, Mn 2%) Void 85%
2.67	Shield Zone A	Pb 90%, H_2O 5%, St. St. 5%
2.73	Shield Zone B	B_4C 87%
2.79	Shield Zone C	St. St. 95%, H_2O 5%
2.85	Shield Zone D	Pb 90%, H_2O 5%, St. ST. 5%
2.91	Shield Zone E	B_4C 87%
3.00	Shield Zone F	St. St. 95%, H_2O 5%
3.038	Dewar	St. St. 100%
3.04	Insulation	G-10CR, C 40%, H 52%, O 8%
3.44	Coil	Cu 65%, St. St. 10%, Insulation 10%

Table 5.15 Neutronics Results for Li_2O Blanket

TRITIUM BREEDING

T_6 = 0.777

T_7 = 0.326

T = 1.103

ENERGY DEPOSITION

	MeV/S.n)	(%)
First Wall	1.836	11.2
Breeding Zone	14.101	86.2
Reflector	0.367	2.2
Manifold	0.019	0.1
Shield	0.038	0.2
	16.361	

M = 1.16

RADIATION DAMAGE

	DPA/YR	He(APPM/YR)	H(APPM/YR)
First Wall	24.8	689.4	2.01×10^3

S.C. Coil

Insulation Dose (30 yr @ W = 2 MW/m^2) = 8.7×10^7 Gy

Fraction of Energy Deposition = 7.6×10^{-6}

MAX. Cu DPA/YR = 8.2×10^{-5}

Required Annealing Frequency $\approx$ 6 Mos.

Later in the project year it became apparent that the use of Inconel as a structural material imposed significant penalties in neutronic performance. A systematic comparison of neutronic results was then performed for four structural materials:

(1) Inconel

(2) Stainless steel

(3) Tenelon

(4) 2.25 Cr - 1 Mo

These results are discussed in Section 5.5.4. Much of the work described here is for the Initial Reference Blanket Design which includes Inconel structure. The final Reference Blanket Design, which is described in Section 5.5.4, is based on the use of Tenelon as the structural material. As shown below, the latter is a superior choice which offers the combination of better neutronic performance together with the needed materials characteristics.

Work has also begun on a low temperature, high breeding blanket. The axial-zoned high temperature blanket design described in Section 6.1 requires a low temperature blanket design with a breeding ratio of at least 1.4. The reference blanket design described in Section 5.5.1 does not provide adequate breeding for a two-axial-zone blanket concept as presently structured. However, some very promising results have been obtained with a modification to this blanket design using a lead zirconate (Zr_5Pb_3) neutron multiplier. This design should be capable of producing high tritium breeding ratios (1.4 or greater) with enriched lithium oxide, or a tritium breeding ratio of 1.1 with approximately 25% of the blanket high temperature energy being deposited in a hot shield as in a radially zoned blanket design. In the second option, the coolant system would be split immediately after passing through the breeding region, with the majority of the coolant bypassing the hot shield. The remaining coolant would pass through the hot shield and emerge at a substantially higher temperature.

The improved neutronic performance of the final reference blanket design may be sufficient to permit its use as the low temperature, high breeding blanket in an axial-zoned reactor without the presence of a neutron multiplier.

As described below in Section 5.5.4 the breeding ratio of this design can be fairly high for high volume fractions of Li_2O. Depending on the details of the system integration, larger volume fractions might be acceptable in an axial-zoned reactor. In any event the improved neutronic results associated with the use of Tenelon provides substantially greater design flexibility for both axial- and radial-zoned system, both with and without the use of a neutron multiplier.

5.5.1 Lithium Oxide Initial Reference Blanket Design

The one dimensional representation of the reference Li_2O blanket is presented in Table 5.14. The breeding ratio has been homogenized, but this should not significantly affect the results.

The radial power density is shown in Figure 5.39. The power density is based on blanket volume rather than material volume. This particular design has a very high power density in the first wall, which is probably due to a combination of the large amount of nickel in the Inconel structure, and the predominantly low Z material nearby.

Figure 5.40 shows the spatial distribution of the tritium breeding from both Lithium-6 and Lithium-7. The small upturn at 210 cm is due to peaking off of the reflector. The Li-7 tritium production is exponential.

5.5.2 Radiation Damage

Radiation damage is an important consideration in any blanket design. Adequate shielding is necessary to prevent damage to the superconducting coils, and to reduce the heat lead on the coil coolant system. Radiation damage to the first wall and blanket structure will cause a reduction in structural integrity. The most common means of measuring radiation damage are atomic displacements and gas production. Atomic displacements occur as a result of reactions with high energy neutrons. Atoms in a solid structure are displaced from their equilibrium lattice position, leaving a vacancy. Gas production occurs through both (n,p) and (n,alpha) reactions. Displacements are typically

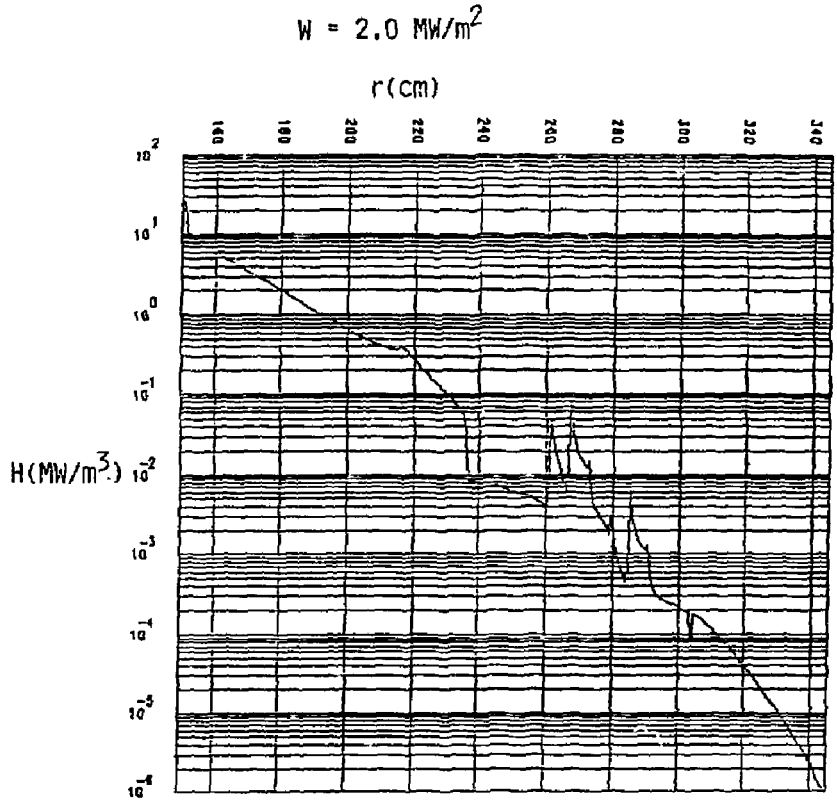

Fig. 5.39 Spatial distribution of power density in Li_2O blanket

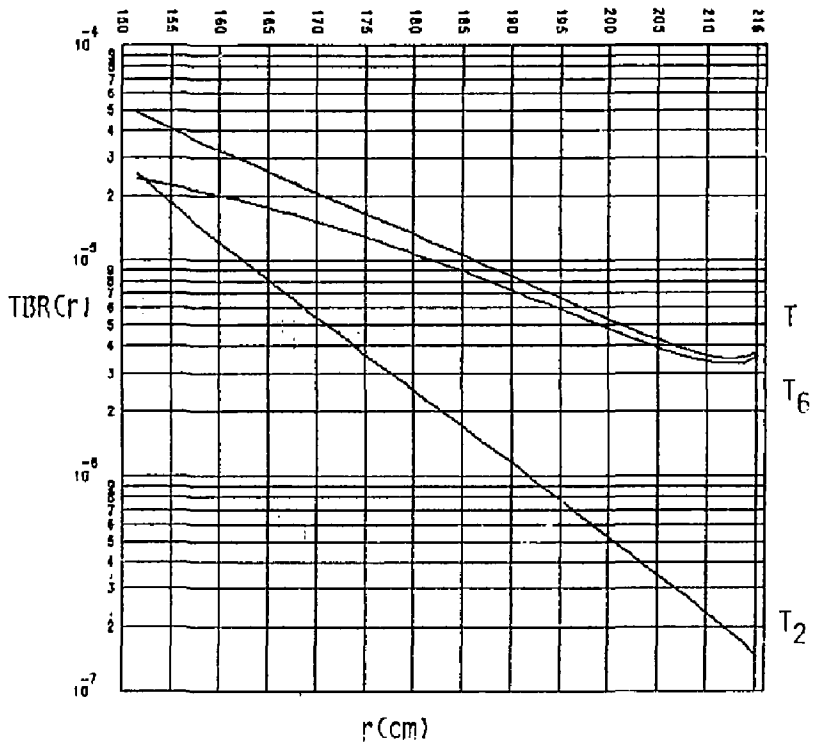

Fig. 5.40 Spatial distribution of tritium breeding in Li_2O blanket

reported in displacements per atom per year, and gas production in atom parts per million per year. All of these values are dependent upon the wall loading. Shielding requirements are generally determined by the radiation dose to the superconductor electrical insulation and by the displacements in the copper stabilizer. An additional consideration is the amount of energy deposited in the coil and dewar. Probably the most critical of these requirements is the superconductor insulation radiation dose. Current insulating materials are fairly radiation sensitive, and breakdown of the insulation would cause a failure of the coil. A widely used limit for the dose to the superconductor insulation is 5×10^7 grays over the life time of the coil. Displacements in the copper stabilizer may not be as serious a problem if they can be annealed out with an acceptable cycle frequency.

In general, for every joule deposited in the superconducting coil and dewar, 1000 joules are required to remove it. Because of this problem, an additional shielding requirement has been defined, namely, that the fraction of the total blanket energy deposited in the superconducting coils and dewar be less than 10^{-6}. The amount of shielding required to meet this limit is usually sufficient to provide adequate protection of the superconducting coil insulation. The shield design used here is similar to the shield used in the WITAMIR report, consisting of alternating layers of lead, boron carbide, and steel.

Displacements and gas production rates have been computed by ONEDANT by taking constitutent edits and using displacement and gas production cross sections. The results of these calculations are shown in Figure 5.41, 5.42, and 5.43. A summary of this information is presented in Table 5.15.

5.5.3 Zr_5Pb_3 Blanket

The use of a Zr_5Pb_3 as a neutron multiplier was first suggested in the STARFIRE study.[11] The properties of Zr_5Pb_3 (Lead Zirconate) are mostly unknown, and its characteristics can only be implied from information on other intermetalic compounds. The properties are generally considered to be

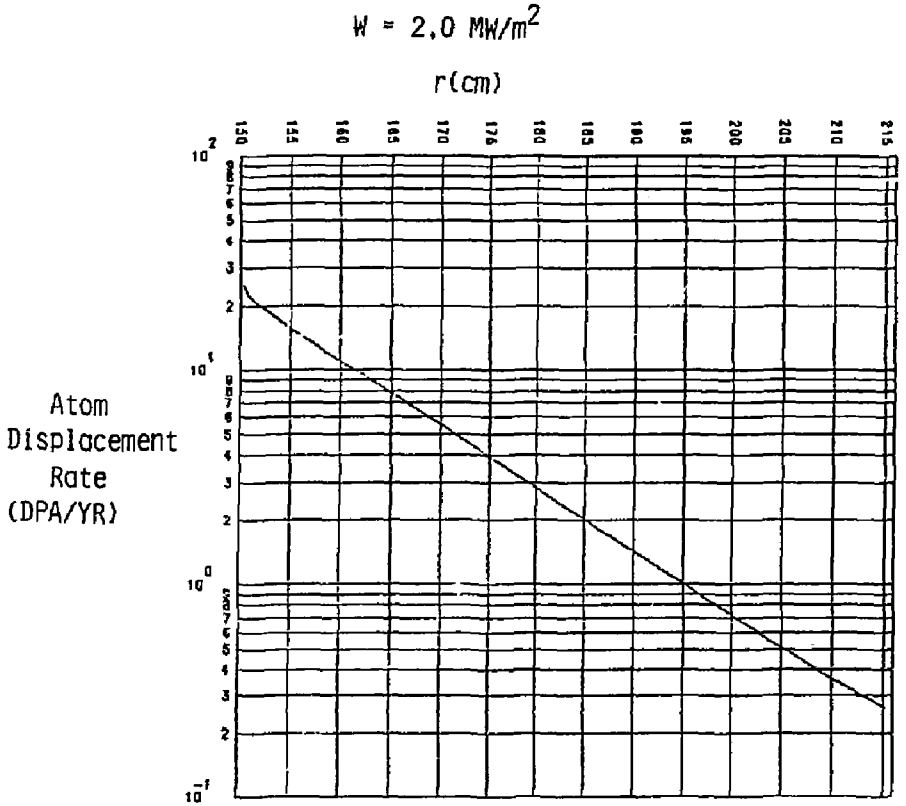

Fig. 5.41 Spatial distribution of atom displacement rate in Li_2O blanket

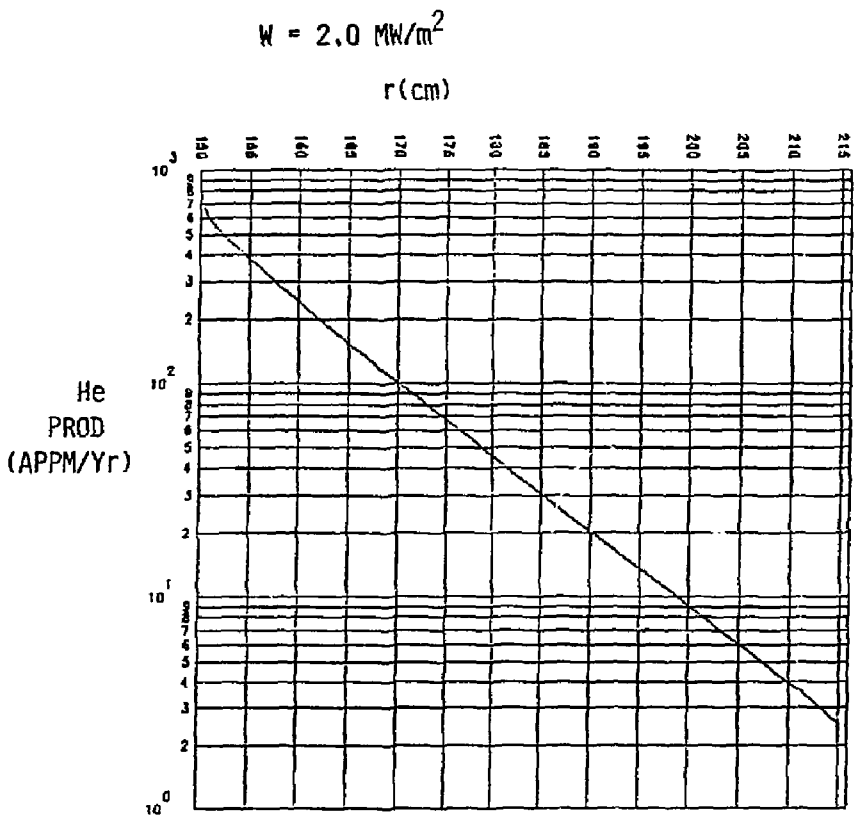

Fig. 5.42 Spatial distribution of He production rate in Li_2O blanket

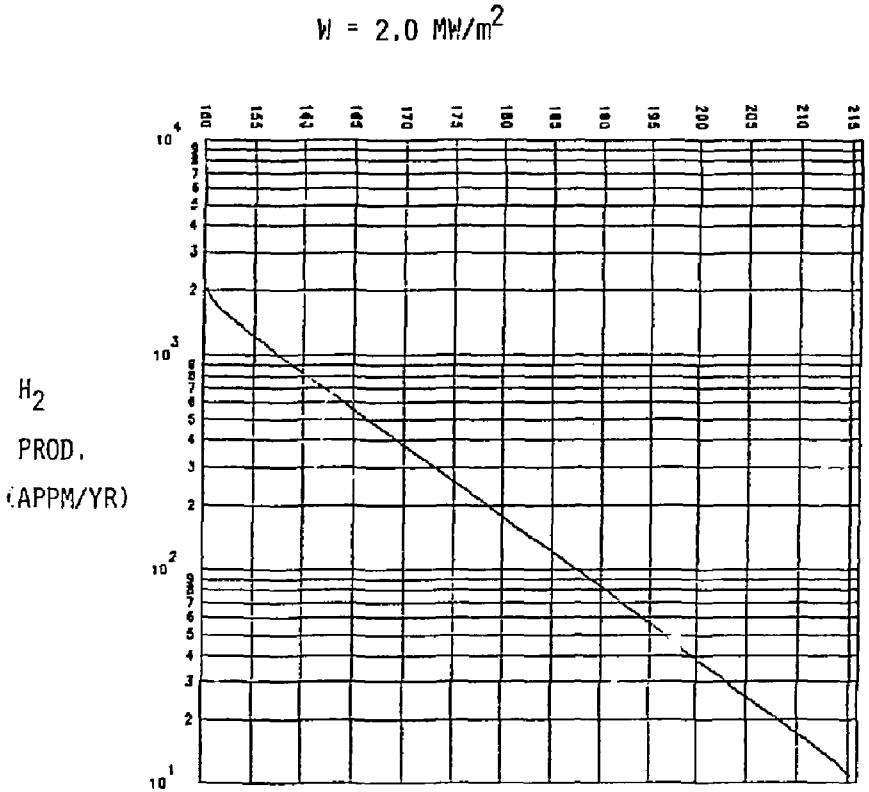

Fig. 5.43 Spatial distribution of hydrogen production in Li_2O blanket

attractive, particularly the high melting point (1400 C).

An initial design using a 19.5 cm Zr_5Pb_3 multiplier directly behind the first wall is shown schematically in Figure 5.44 This type of design has several advantages. The blanket energy miltiplication is much higher than a non-multiplier design. Also, the breeding region can be relatively thick with fairly uniform lithium burnup (Figure 5.45). The multiplier also provides an additional benefit. The high Z multiplier material near the first wall acts as a shield to gammas generated internally in the blanket. This results in a significant reduction in the energy deposition in the first wall.

Additional work on this design indicates that a breeding ratio of 1.1 can be obtained with a 10 cm multiplier region and a 10 cm breeding zone with 60% Li-6 enrichment. There are any number of combinations of multiplier thickness and breeding zone thickness that will provide a tritium breeding ratio of 1.1, with the general trend of increasing M value with increasing multiplier thickness (Figure 5.46). In all cases, at a T value of 1.1 the amount of energy deposited in the hot shield is approximately 25%.

This particular blanket design can also achieve very high breeding ratios by increasing the Li_2O thickness. A breeding ratio greater than 1.4 is quite possible. This one blanket design has the flexibility, therefore, to be adapted to either a radially zoned design, or an axially zoned design.

5.5.4 Blanket Structure

The initial reference low temperature blanket design achieves a breeding ratio that is only barely adequate despite the fact that it contains a large amount of Li_2O. The reason for this poor neutronic performance was previously thought to be due to the high structure fraction in the breeding zone. But a comparison with a similar design using different structural materials indicated that the problem was due more to the type of structure rather than the amount of structural material used.

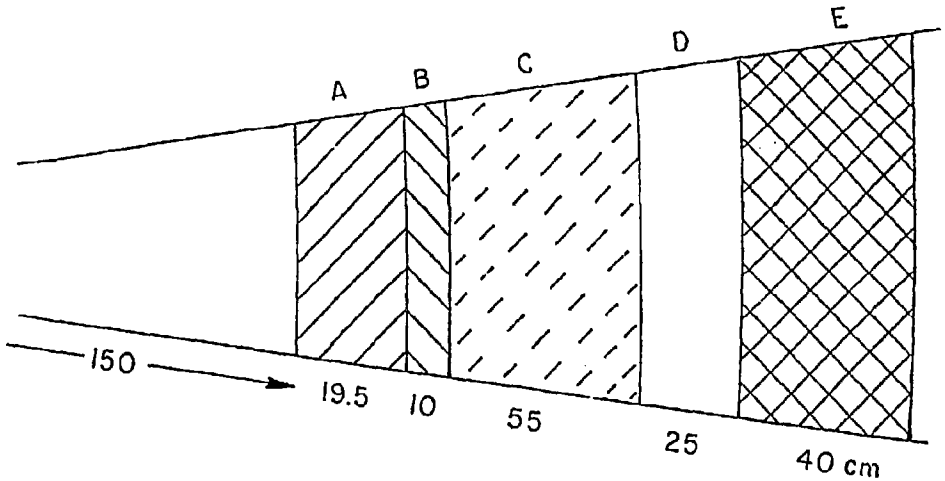

A	Zr_5Pb_3	75%
B	Li_2O	60% Enrich.
		60% Li_2O
		8% Inconel
C	S.S.	75%
D	Manifold	15% Structure
E	Shield	

T = 1.18

M = 1.32

F_H = 19%

Ins. Dose = 1.19×10^8 Gray

Heat Fraction in S.C. = 4.5×10^{-6}

Fig. 5.44 A Lead Zirconate/Li_2O Blanket Design

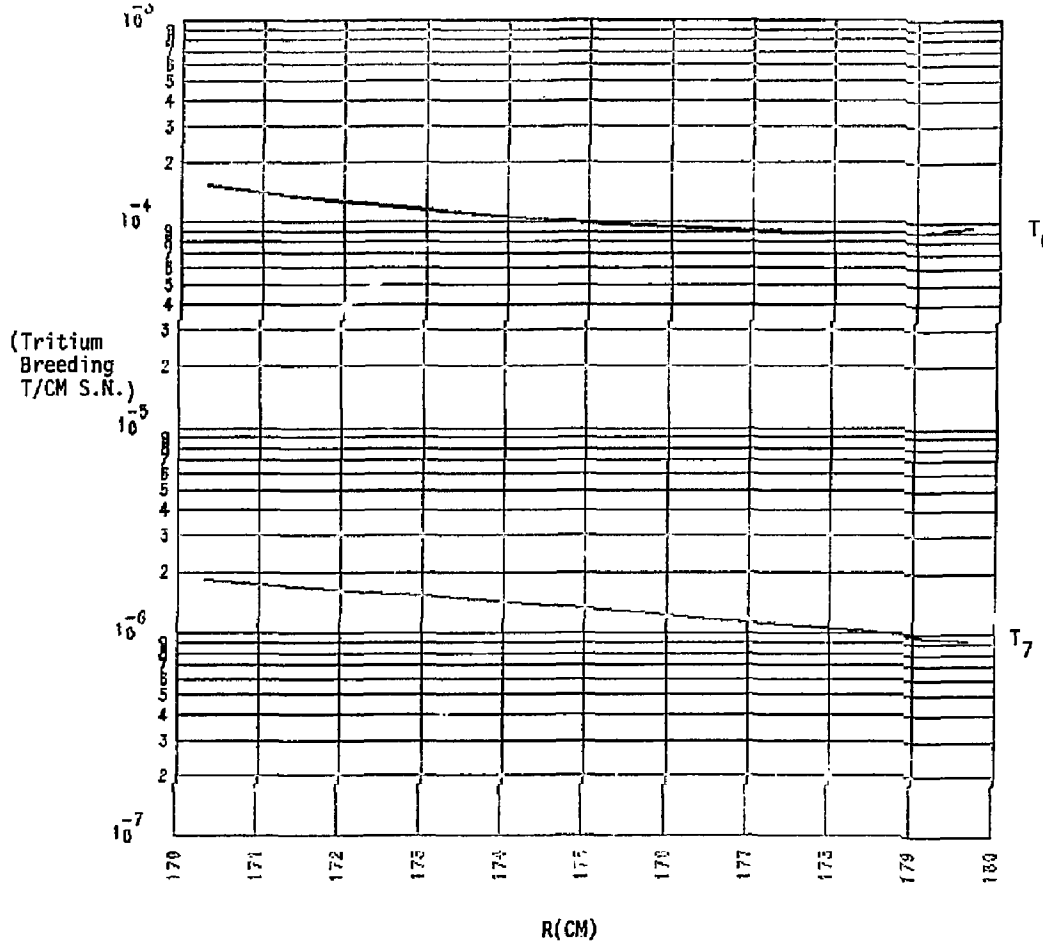

Fig. 5.45 Spatial distribution of tritium breeding in an Li_2O blanket with Zr_5Pb_3 multiplier

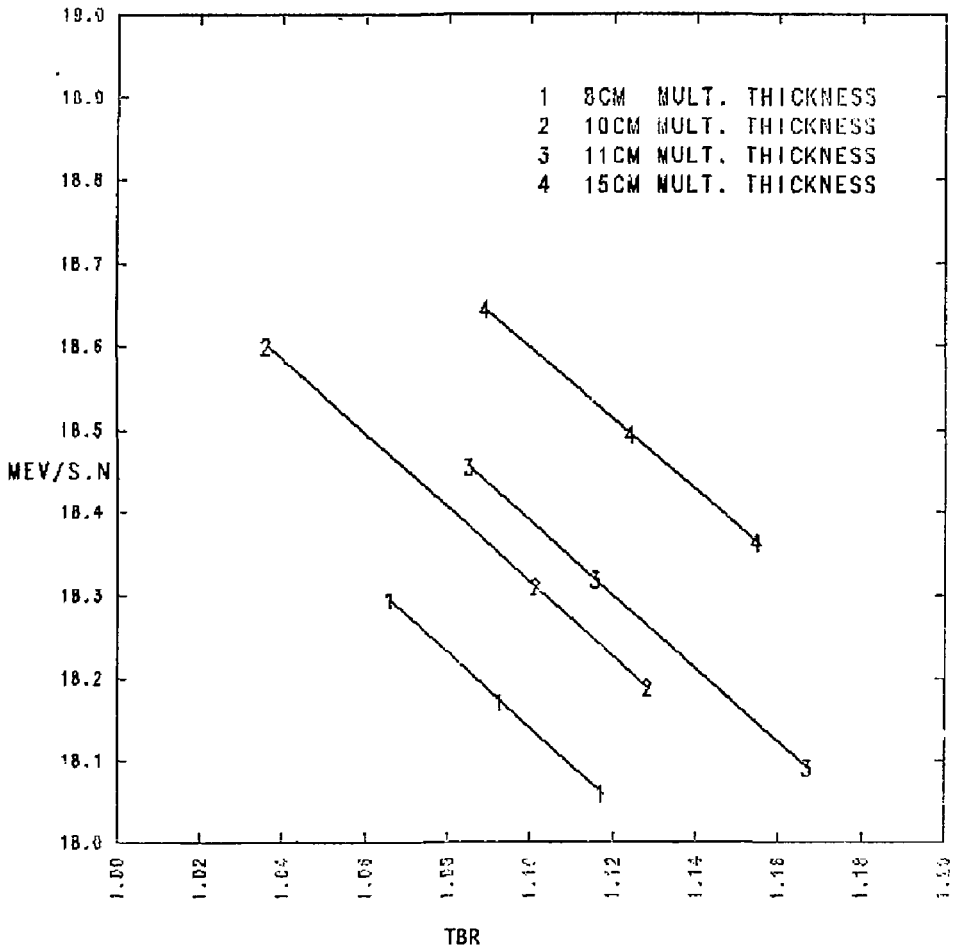

Fig. 5.46 Blanket energy/tritium breeding ratio trade-offs for varying Li_2O and multiplier thicknesses

Four different structural materials were used with the compositions given below.

Material	Composition (%)									
	Fe	C	Si	Mn	P	S	Cr	Ni	Mo	Cu
Inconel	7	0.08	0.25	0.25			15	77		0.2
Stainless Steel (316)	67.5			1.5			15	1.5	2	
Tenelon	68	0.08	0.3	14.5	0.045	0.03	17			
2.25 Cr-1 Mo.	94.6	0.15	0.5	0.45	0.035		2.25	0.5		1.0

In Figure 5.47, the tritium breeding ratio is shown for several lithium oxide fractions using the reference design and different structure in the first wall, breeding zone, hot shield/reflector, and manifold. The use of any one of the iron base alloys, stainless steel, tenelon, or 2.25 Cr-1 Mo. in place of the nickel base Inconel structure results in a significant improvement in the tritium breeding ratio.

An additional advantage of the iron base alloys is a lower first wall power density. Using the reference Li_2O blanket design with the four different structural materials, the first wall power density was:

Inconel	26.964 watts/cc
Stainless Steel	17.909 watts/cc
Tenelon	16.233 Watts/cc
2.25 Cr 1 Mo	14.663 watts/cc

The gamma energy deposition in the first wall for all four materials is approximately the same. The difference is a result of a much lower neutron kerma value for iron at the high end of the neutron energy spectrum. Nickel, on the other hand, has a much higher neutron kerma value which produces the high power density figure for Inconel.

There is also a significant difference in the blanket energy multiplication depending upon the type of structure used. This difference is illustrated in

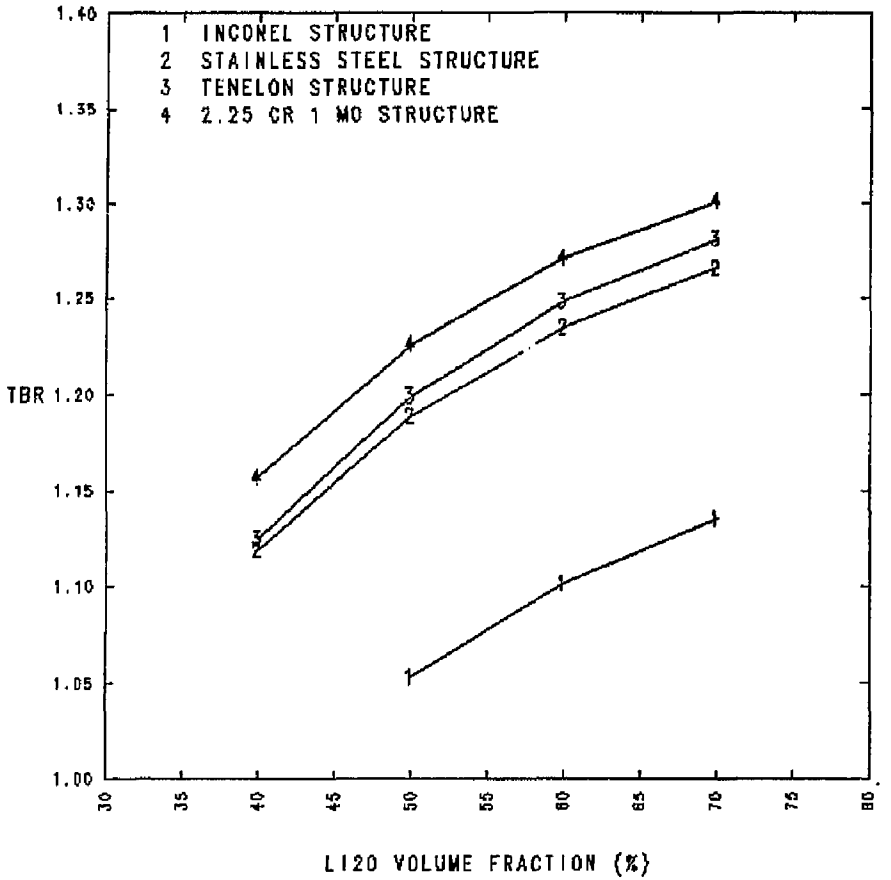

's Li_2O

Fig. 5.47 Tritium breeding rati· (?) vs Li_2O volume fraction

Figure 5.48, which shows the tradeoff between the blanket energy multiplication and the tritium breeding ratio for various Li_2O volume fractions. At a tritium breeding ratio of 1.1, a blanket design with tenelon structure would produce approximately 2% more energy than a blanket design using 2.25 Cr 1 Mo or stainless steel structure, and 7% more energy than a blanket with Inconel structure.

5.5.5 Reduced First Wall Radius

A blanket design with a reduced first wall radius was analysed neutronically in order to determine the effects on shielding. The fusion power was assumed to remain the same, so the reduction in the first wall radius from 1.5 meters to 0.6 meters results in an increase in the wall loading from 2 MW/m^3 to 5 MW/m^3. The results of this analysis indicate that, although the shielding would have to be thicker in order to adequately shield the superconductor coils, the total volume of the shield is reduced approximately 10%. The superconductor coils are also reduced in size by about 25%. There are, however, significant problems related to first wall radiation damage and thermal hydraulics analyses with such high first wall loadings and accompanying power densities.

5.5.6 Neutronics Conclusions

Several important conclusions related to neutronics have emerged from the study of the Li_2O blanket.

(1) The use of a Tenelon as a structural material appears to be very attractive. The elimination of Ni as a constituent reduces radiation damage and increases tritium breeding, while retaining the necessary structural features necessary for designs of the type considered here.

(2) The use of a Zr_5Pb_3 neutron multiplier together with an Li_2O breeding region is a very effective combination. Although there are remaining unknowns related to Zr_5Pb_3, it is a very attractive material. The neutron multiplication through (n,2n) reactions in pb produces low energy neutrons which can be very rapidly absorbed in ^6Li. A number of attractive combinations are possible: a very small required combined multiplier/breeder thickness; a high tritium breeding ratio; a greatly reduced spatial gradient of the power

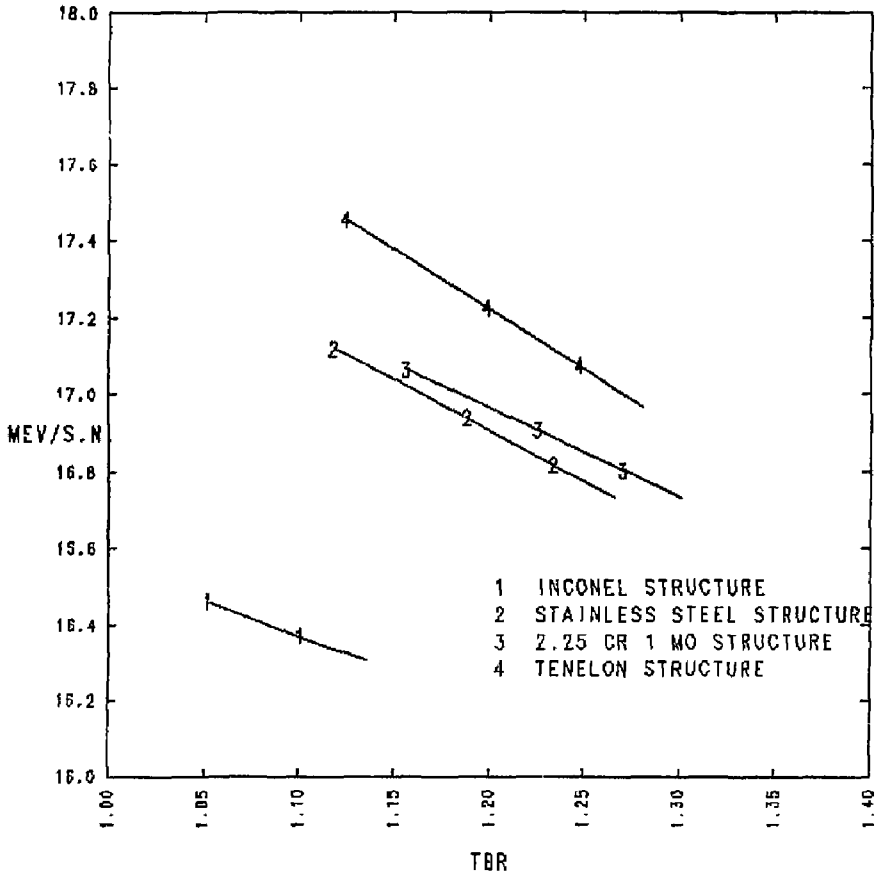

Fig. 5.48 Total blanket energy disposition vs tritium breeding ratio (TBR) for different structural materials

density; a relatively high percentage of energy deposited in the hot shield (with a constr ⁻ of $T \geq 1.1$).

(3) The power density in the first wall of a typical blanket design is significantly impacted by the type of material used in the adjacent region. The use of a high Z material, such as Zr_5Pb_3 or LiPb for example, causes gamma ray absorption to be concentrated there rather than in the first wall. This reduces the first wall power density and makes its design less difficult.

5.6 ESTIMATION OF THE PHYSICAL AND MECHANICAL PROPERTIES OF Li_2O

5.6.1 Li_2O Microstructure

Very little is available in the literature on the microstructural characteristics of fabricated Li_2O specimens. Hence, the limited information reported by Takahashi and Kikuchi[12] on specimens that they had fabricated for thermal diffusivity measurements is of considerable interest to us. They used the following fabrication procedure. Granules of the starting Li_2O material (designated as CERAC/PURE) were first heated in a platinum crucible under vacuum for four hours at 973 K to decompose LiOH and Li_2CO_3 impurities. The resultant material was then ground with an agate mortar and pestle in an argon atmosphere, pressed into pellets (10 mm diameter by 13 mm high) without a binder at 100-500 MPa, and sintered at temperatures of 1373 and 1473 K in covered platinum crucibles under vacuum for four hours. Specimens prepared in this way were sliced into discs 10 mm in diameter and 1.3 mm thick for the thermal diffusivity measurements.

Characterization of the above specimens indicated the following. Total cation impurities were found to be 0.05 wt%, with Ca being the highest at 0.02 wt%. The x-ray lattice parameter was determined as 0.46117 ± 0.00005 nm which compares well with an NBS reference value of 0.46114 nm.[12]

Bulk densities for the specimens ranged from 70.8 to 93.4% of theoretical density (TD) with the average grain size ranging from 20 μm for 70.8% TD to 60 μm at 93.4% TD. Open porosity was found to be dominant at the lower densities, but as density increased the pores began to close off rapidly above about 86% TD. At 88% TD closed pores and open pores were found to be about equal, while above 90% TD closed pores dominated over open pores by about 5:1 (see Fig. 5.49).

An understanding of the pore structure variation with density is of value not only for interpreting physical and mechanical property behavior for Li_2O, but also for the insight it can give us on the mechansisms of tritium and helium release. We should especially note that although Li_2O that has been sintered to temperatures as high as 1473 K and to a density of 93.4% TD, some 20% of the porosity still consists of open pores that should

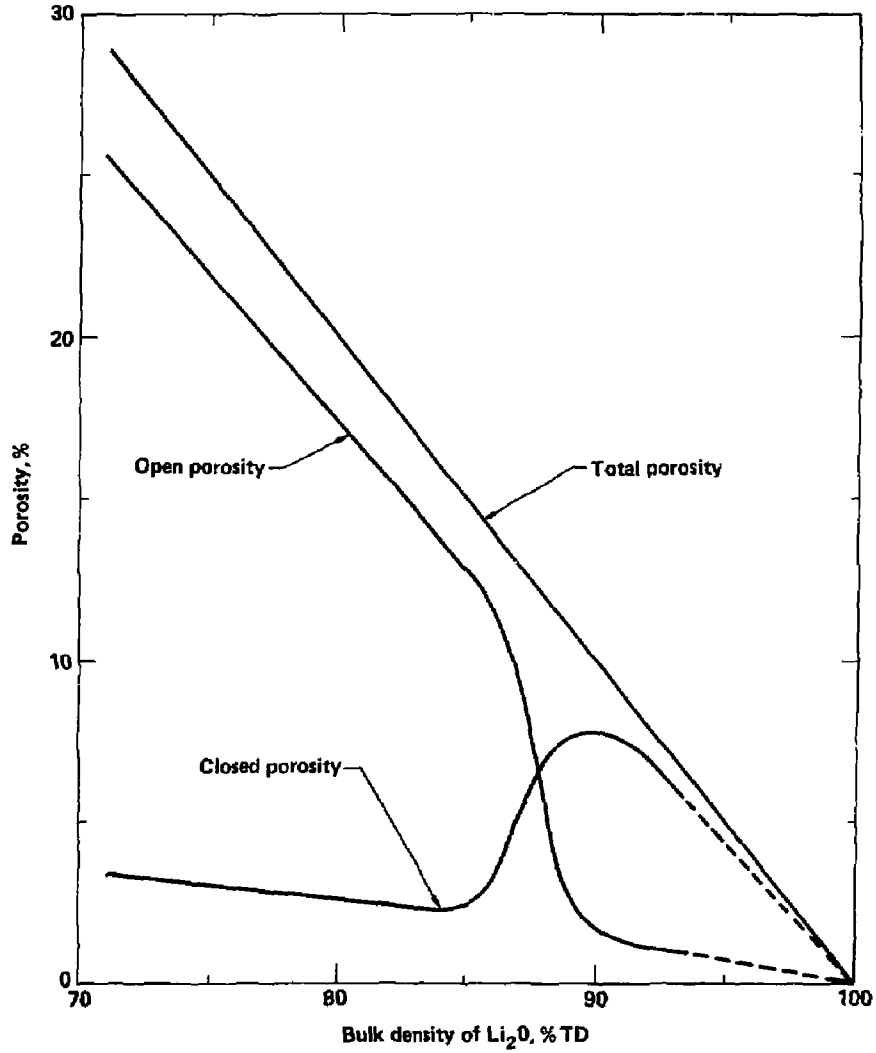

Fig. 5.49 The dependence of open and closed porosity in Li_2O as a function of overall specimen density is illustrated for Li_2O specimens fabricated by sintering.

provide a network of passages throughout the structure for release of tritium and helium.

5.6.2 Thermal Conductivity

Using the methods of specimen preparation described above, Takahashi and Kikuchi[12] measured thermal diffusivities of Li_2O in the range of 70.8 to 93.4% TD and temperatures of 473 to 1173 K. Thermal conductivities were then calculated from the thermal diffusivity values using literature information on specific heat and density to make the calculation. The data thus derived are summarized in Fig. 5.50, which also shows an extrapolation to 100% TD using the Maxwell-Eucken equation to make the extrapolation. The analytical expression used by Takahashi and Kikuchi to fit their data is slightly modified here to express it in terms of volume fraction porosity (instead of fraction of theoretical density) as follows:

$$k = (1 - p)^{1.94} (0.0220 + 1.784 \times 10^{-4} T)^{-1} \quad (5.33)$$

5.6.3 Thermal Expansivity

Kurasawa[13] has recently measured the percent thermal expansion up to ~1200 K for both single crystal and sintered specimens of Li_2O using a dilatometer to make the measurements. Two single crystal specimens, prepared from molten Li_2O by a floating zone technique, were used. Each specimen was 8 mm in diameter by 88 mm long. Five sintered specimens were prepared for the measurements using the method described by Takahashi and Kikuchi[12] (see above). The sintered specimens were in the form of bars 4 x 4 x 10 mm, and had densities of 75.5, 80.0, 86.7, and 92.5% TD.

Kurasawa's measurements on the single crystals showed a fair degree of variability between runs, especially at the higher temperatures. For example, the percent linear expansion from room temperature to 1173 K ranged from 2.47 to 2.82% for five different runs, which gives a spread of ± 6.6% about the mean. For each individual run, however, the standard deviation about a fitted curve for that run was quite good, being about 1-2%. Individual data points are not given for the sintered samples, but standard

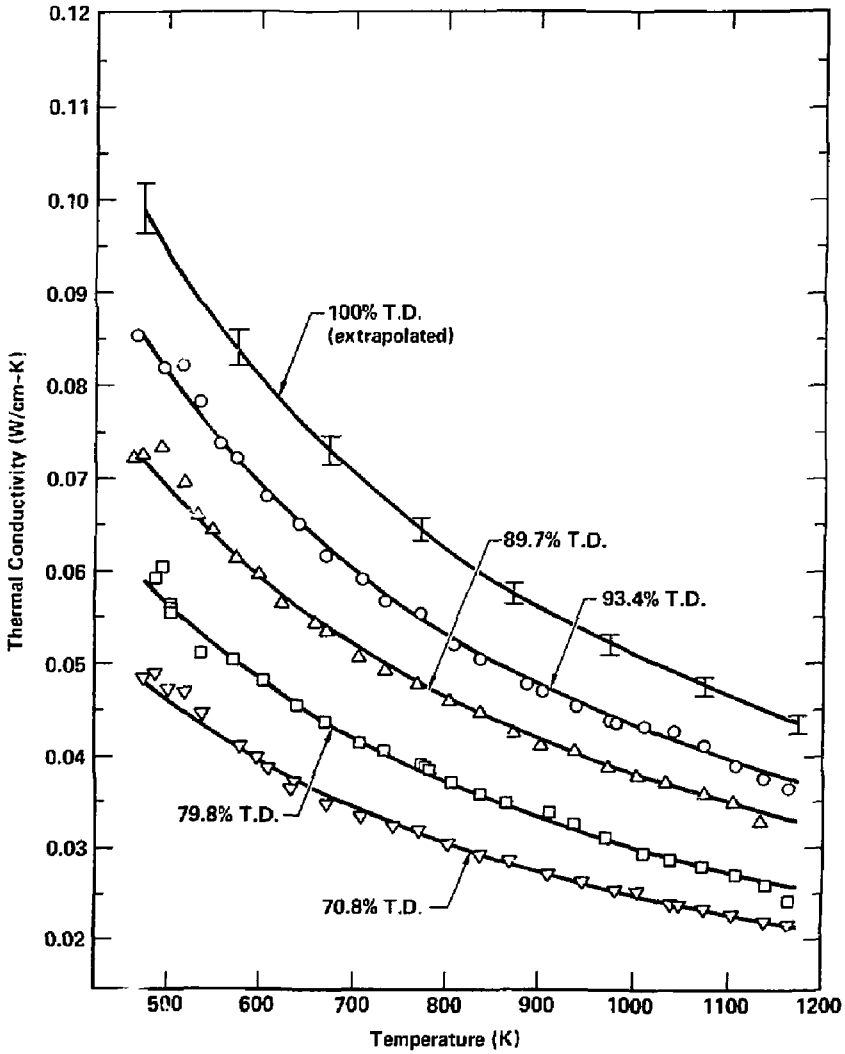

Fig. 5.50 Thermal conductivities of Li_2O are shown as a function of percentage of theoretical density and temperature according to the data of Takahashi and Kikuchi.[12]

deviations are indicated to be of the order of 1% about the fitted curves. Agreement appears to be good for percent thermal expansion from room temperature up to about 1100 K for the averaged single crystal data and the sintered samples. Above 1100 K, the percent expansion curve shows a drop-off in slope with increasing temperature for samples with 80.0, 86.7, and 91.1% TD, but a normal continuation of the curves for 75.5, 92.5, and 100.0% TD.

In order to obtain thermal expansivity values from Kurasawa's data, we need to differentiate the fractional expansion curves. We have a problem in doing this because of the variations in the data, especially at high temperatures. Therefore, our approach is to fit an average curve to the data up to 1100 K, and then allow the curve to rise in a normal manner above that temperature. The functional form of the curve is taken to be one that has previously been shown to be applicable to a large number of substances, including metals, oxides, borides, carbides, and nitrides.[14] Thus, the averaged expression for fractional linear expansion, $\Delta L/L_0$, and the derived linear thermal expansivity, α, are found to be as follows:

$$\Delta L/L_0 = -4.275 \times 10^{-3} + 1.4692 \times 10^{-6} T^{1.4} \qquad (5.34)$$

$$\alpha = d(\Delta L/L_0)/dT = 2.0569 \times 10^{-6} T^{0.4}, \ K^{-1} \qquad (5.35)$$

Fractional linear expansions calculated using equation (5.34) are compared in Table 5.16 with the averaged single crystal data and the 92.5% TD sintered data given by Kurasawa.[13] The linear thermal expansivity obtained from equation (5.35) is also summarized in Table 5.16.

5.6.4 Mechanical Properties

Experimental information on the mechanical properties of Li_2O is totally lacking at the present time. We must therefore rely on correlations based on other oxides to obtain some rough values with which to proceed with design calculations. Some theoretical guidance is also available in regard to variation of mechanical properties with grain size and specimen porosity. The main design need for mechanical properties for Li_2O is to

Table 5.16 The fractional linear expansions for single crystal Li_2O and 92.5% TD sintered Li_2O reported by Kurasawa,[13] are compared here with a best-fit equation to all of the Li_2O data. The linear thermal expansivity derived from the best-fit equation is also given.

T(K)	$\Delta L/L_0$, single crystal	$\Delta L/L_0$, 92.5% TD	$\Delta L/L_0$, best-fit equation	$\alpha(K^{-1})$, best-fit equation
298	-0.00004	0.00006	0.00000	2.01×10^{-5}
400	0.00210	0.00196	0.00218	2.26×10^{-5}
500	0.00447	0.00408	0.00455	2.47×10^{-5}
600	0.00712	0.00642	0.00711	2.66×10^{-5}
700	0.01003	0.00901	0.00986	2.83×10^{-5}
800	0.01321	0.01184	0.01276	2.98×10^{-5}
900	0.01667	0.01491	0.01582	3.12×10^{-5}
1000	0.02040	0.01822	0.01901	3.26×10^{-5}
1100	0.02440	0.02176	0.02233	3.39×10^{-5}
1200	0.02867	0.02554	0.02578	3.51×10^{-5}
1300	0.03321	0.02957	0.02934	3.62×10^{-5}

evaluate the thermal stress parameter, M, defined as follows:

$$M = \frac{\sigma_t (1 - \nu)k}{E\alpha}, \ W/m, \tag{5.36}$$

where σ_t is the short term tensile strength, ν is Poisson's ratio, k is thermal conductivity, E is Young's modulus, and α is the linear thermal expansivity. Both k and α are available for Li_2O and the values were summarized earlier in this section. The problem remains to estimate values for the tensile strength, Young's modulus, and Poisson's ratio.

We consider first the estimation of tensile strength of Li_2O. The only property measurement that we are aware of that may be an indication of tensile strength is the microhardness of Li_2O which has recently been measured by Nasu et al.[15] These workers prepared sintered discs of

Li_2O, 10 mm in diameter and 3 mm thick, using isostatic hot pressing at 1323 K under 100 MPa pressure. The as-prepared specimens (grain size ~50 μm) gave a Vickers microhardness of 180 ± 8 using a 300 g load for 30s on a diamond indentor. The microhardness was found to increase upon irradiation, saturating to a value of 230 ± 7 with neutron doses exceeding 5×10^{17} neutrons/cm^2. The microhardness returned to its original value after annealing at temperatures above 623 K. It is not unusual to experience an increase in microhardness (and strength) of ceramics upon exposure to radiation as these workers found for Li_2O.

In order to develop a correlation between microhardness and tensile strength, we need data on oxides that have been adequately characterized for grain size and porosity. Such data are very limited because not only have relatively few oxides been well-characterized, but because of the brittleness of ceramics, tensile strength is a difficult property to measure. Recognizing these difficulties, we have nonetheless used data on microhardness and tensile strength given in standard references[16,17] to obtain a rough correlation (see Fig. 5.51). Knoop rather than Vickers microhardness is used since that is what is generally available. The two types of microhardness are usually about equal where comparisons can be made. Grain sizes for the oxides are about 30 μm, porosities about 3%, and tensile strengths refer to ultimate short-term tensile strengths for the examples shown in Fig. 5.51. These oxide materials are generally believed to be of high purity except for ZrO_2 which is CaO-stabilized. From Fig. 5.51, we predict a tensile strength of about 20.5 MPa for Li_2O having a 30 μm grain size and 3% porosity.

The variation of strengths of ceramics with grain size and porosity is expressed in a generalized form by the following empirical expression given by Knudsen:[18,19]

$$\sigma = \sigma_0 \, d^{-n} \exp(-bp), \tag{5.37}$$

where σ is the strength, d is grain diameter, p is the volume porosity, and σ_0, n, and b are empirical constants. The general form of this

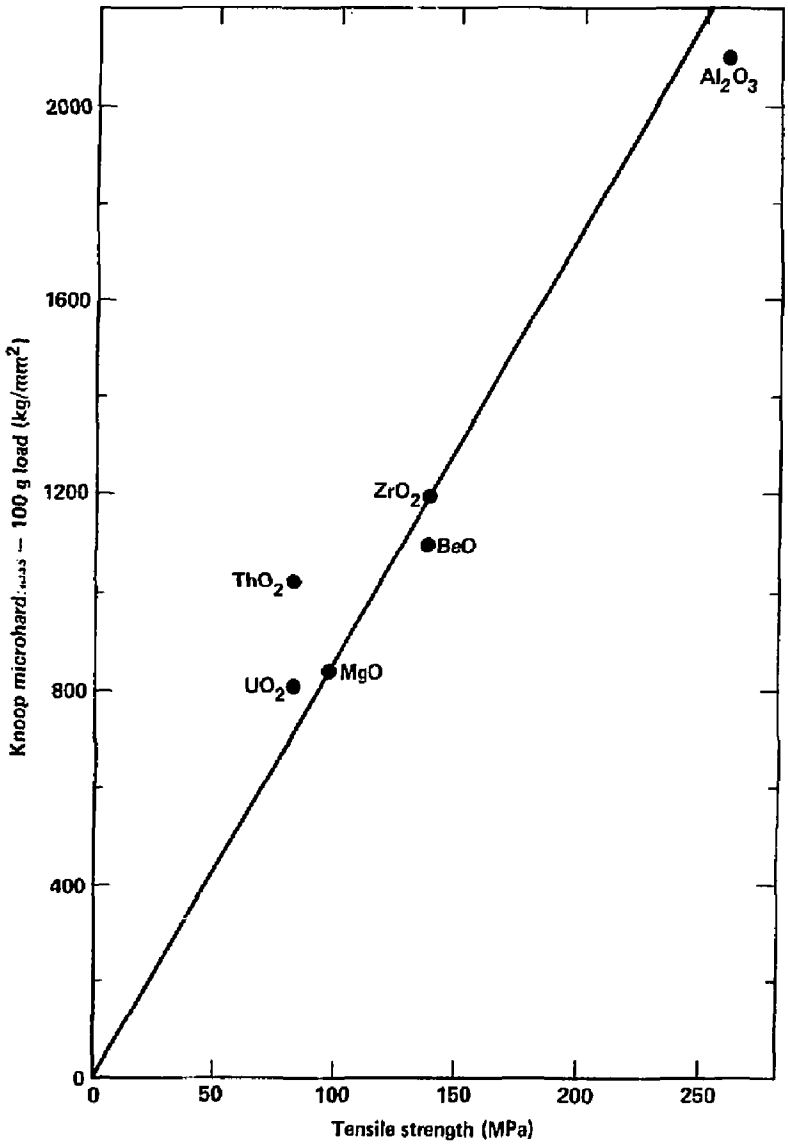

Fig. 5.51 A correlation of Knoop microhardness with tensile strength is illustrated for several oxide ceramics having an approximate grain size of 30 μm and a porosity of about 3%. For Li_2O with a reported Vickers microhardness of 180 kg/mm^2, this correlation predicts a tensile strength of 20.5 MPa.

equation differs slightly from that obtained from theoretical approaches, but the empirical expression seems to correlate well with oxide ceramics that have been studied. The value of n is usually somewhat less than 0.5, and b is about 10.[18,19] Thus, using the value of 20.5 MPa for tne tensile strength of Li_2O at a grain size of 30 μm and a porosity of 3%, we obtain:

$$\sigma_t(Li_2O) = 108\ d^{-0.4}\ \exp(-10p), \tag{5.38}$$

where d is expressed in μm and p as volume fraction porosity. Based on this equation, the variation of $\sigma_t(Li_2O)$ with grain size and porosity is illustrated in Table 5.17. Thus we see that grain size should be maintained below ~10 μm and porosity below ~10% in order to optimize the strength of the ceramic body.

This initial estimate of the tensile strength of Li_2O is probably good to within a factor of 2-3 of the true value, and most likely on the low side for the following qualitative reasons. Li_2O has a relatively high melting point for a material with such a low microhardness. The high melting point is indicative of high bond strengths in the crystal and consequently of a high tensile strength. Furthermore, trace impurities or intentional additives in the Li_2O will also likely increase its strength above that expected from the correlation curve.

We expect that the strength of Li_2O will not vary significantly with temperature up to about 55% of its melting temperature at which point the strength will begin to decrease. Because of the large uncertainty that exists in the melting point of Li_2O, which has reported values of 1696 K[13] 1843 K,[20], and 1973 K,[21] we would predict that this decrease in strength begins somewhere in the region of 900-1200 K. This behavior can be expressed approximately by the relationship

$$\sigma_t = \sigma_0\ (1 - 44\ \exp(-7000/T)) \tag{5.39}$$

We discuss next the estimation of Young's modulus for Li_2O. Wachtman[19] and Conrad [18] have reviewed the theory and general

Table 5.17 Predicted variation of the estimated tensile strength (MPa) of Li_2O with grain diameter and fractional porosity in a fabricated body.

Grain Diameter, μm	Fractional Porosity				
	0	0.05	0.10	0.20	0.30
1	108.0	65.5	39.7	14.6	5.4
5	56.7	34.4	20.9	7.7	2.8
10	43.0	26.1	15.8	5.8	2.1
50	22.6	13.7	8.3	3.1	1.1

behavior of elastic moduli for ceramics. From their observations and data presented by Shaffer[17] and Samsonov,[16] we conclude the following. We can make a rough estimate of Young's modulus for Li_2O by correlating values of Young's modulus with the melting point of oxides. Grain size has no significant effect on Young's modulus at temperatures below the onset of grain-boundary sliding (i.e., below ~0.55 of the absolute melting point). However, porosity has a major effect on the modulus, leading to a decrease in modulus with increasing porosity. The effect of temperature is to give a slow rate of decrease of Young's modulus with increasing temperature until grain-boundary sliding sets in, at which point the modulus decreases rapidly until the melting point is reached. Elastic constants are very dependent on structure, so that the various generalized conclusions discussed above only apply if phase transitions do not occur over the temperature interval of interest. Li_2O meets this criterion.

In order to obtain the best possible estimate of Young's modulus, we apply the correlation of Young's modulus versus melting point to only the cubic oxides (Li_2O has a cubic inverse fluorite structure), and use the available data from Shaffer[17] and Samsonov,[16] after extrapolating to zero porosity. Data on non-cubic oxides such as Al_2O_3 and BeO deviate

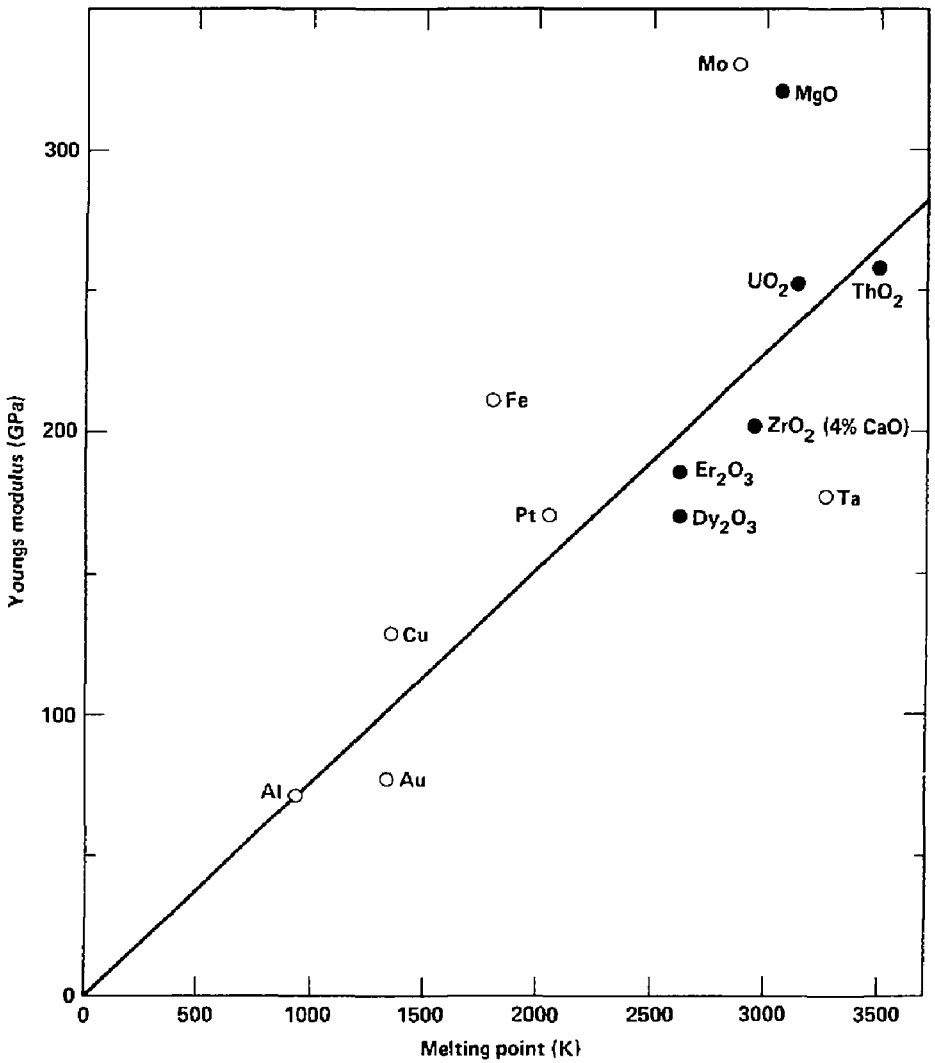

Fig. 5.52 The correlation of Young's modulus of elasticity with melting point is illustrated here for cubic oxides and metals. On the basis of this correlation, Young's modulus for Li_2O is predicted to be about 140 GPa.

significantly from the correlation, thus emphasizing structural effects. The cubic oxide correlation is illustrated in Fig. 5.52, where several representative cubic metals[22] are also included to show that a generalized correlation between Young's modulus and melting point is expected to be approximately linear. For Li_2O with a melting point somewhere in the 1696-1973 K region, we predict from Fig. 5.52 a Young's modulus of about 140 GPa at room temperature and zero porosity.

To predict the variation of Young's modulus with porosity of Li_2O, we use the empirical Spriggs expression:[18,19]

$$E = E_o \exp(-bp), \tag{5.40}$$

where E_o is the value of Young's modulus at zero porosity (i.e., 140 GPa), b is an empirical constant, and p is the fractional porosity. We find b values of 4.0 for Al_2O_3, 4.7 for MgO, and 3.4 for BeO from the literature.[16-19] We therefore take b = 4.0 for Li_2O as our best guess, and the Spriggs expression for Li_2O becomes:

$$E(Li_2O) = 140 \exp(-4.0\ p),\ GPa \tag{5.41}$$

The temperature dependence of Young's modulus for many ceramics can be described by an empirical expression of the type:[19]

$$E = E_o - AT \exp(-B/T), \tag{5.42}$$

where E_o is Young's modulus at absolute zero, and A and B are empirical constants for each material.

We find that we can put equation (5.42) into a more generalized form by assuming (1) that E goes to zero at the melting point for those ceramic materials that do not undergo phase transitions prior to melting, and (2) that the constant B is equal to the melting temperature. The expression thus becomes

$$E = E_o - (T/T_m)\ E_o \exp(1 - T_m/T), \tag{5.43}$$

where T_m is the melting point. Examining the available data for Al_2O_3, MgO, ThO_2, UO_2, MgO stabilized and CaO stabilized ZrO_2,[16,17] we find that there

is good agreement with this expression up to at least 1200 K, and in some cases up to 1800 K. BeO, which undergoes a phase transition near its melting point, shows agreement up to ~ 1300 K, but the experimental data indicate rapid drop-off of E above this temperature. In Table 5.18, the experimental and calculated temperature dependences of Young's modulus are compared for several representative oxides. We find that the agreement is quite good, expecially considering the substantial systematic errors that are usually present in experimental data of this type. Predicted values for Li_2O with zero porosity are summarized in the last column of Table 5.18.

Table 5.18 The observed variation of Young's modulus (in GPa) with increasing temperature is compared for several oxide ceramics with the behavior calculated using equation (5.43) and assuming the calculated values of Young's modulus to be identical to the observed values at room temperature. Equation (5.43) is used to predict the values for Li_2O in the last column. Sample porosities are given for the experimental data, and the melting points used in the calculations are also indicated.

	Al_2O_3 (p = 2%, T_m = 2320 K)		MgO (p = 2%, T_m = 2850 K)		ZrO_2 - 4% CaO (p = 4%, T_m = 3000 K)		ThO_2 (p = 3%, T_m = 3490 K)		Li_2O (p = 0%, T_m = 1850 K)
T,K	obs.	calc.	obs.	calc.	obs.	calc.	obs.	calc.	calc.
298	376	376	295	295	167	167	235	235	140
600	366	370	278	294	164	166	231	235	134
800	356	357	267	289	161	164	224	233	124
1000	344	333	257	279	155	159	216	229	108
1200	324	300	246	264	149	152	209	223	87
1400	294	258	234	244	122	142	200	214	63

Finally, we need to estimate Poisson's ratio for Li_2O. When a specimen is loaded in tension, there occurs a decrease in thickness along with the increase in length. The ratio of this decrease in thickness to increase in length is called Poisson's ratio and is given by

$$\nu = - \frac{\Delta d/d}{\Delta \ell/\ell} \tag{5.44}$$

Poisson's ratio is also related to Young's modulus and the shear modulus by the following equation:

$$\nu = \frac{E}{2\mu} - 1 \tag{5.45}$$

Poisson's ratio for most materials, including ceramics, generally is between 0.15 and 0.4.

To a first approximation, Poisson's ratio should be independent of specimen porosity and temperature since both Young's modulus and the shear modulus show nearly the same porosity and temperature dependence. There are minor differences, however, and we especially might expect an increase in ν at high temperatures when grain boundary sliding becomes important (e.g., see Fig. 5.53). Small amounts of chemical additives may also influence Poisson's ratio. For example ThO_2 that contains 0.5% CaO exhibits a Poisson's ratio of twice that of pure ThO_2 (see Fig. 5.53).

It is difficult to make an accurate estimate of Poisson's ratio for Li_2O. Wide variations are seen in the reported data for even conventional ceramic materials such as Al_2O_3 and MgO[16,17,23] (see Fig. 5.53). We therefore choose to take roughly a mean value, based on all materials, of $\nu = 0.25$ for Li_2O, and further assume that ν is independent of porosity, temperature, and chemical purity. The uncertainty in this value could be as much a factor of two.

5.6.5 Thermal Stress Parameter

We are now in a position to calculate values of the thermal stress parameter M for Li_2O as defined in equation (5.36). Analytical

expressions are summarized in Table 5.19 for each of the input parameters, together with estimates of the uncertainties. It is evident from Table 5.19 that the uncertainties in the mechanical properties (σ_t, E, and ν) are quite large and translate into an overall uncertainty of about an order of magnitude in the thermal stress parameter M. Clearly, experimental data on the mechanical properties of Li_2O are essential if we are to calculate accurate values for the thermal stress parameter.

Even though the absolute value of the thermal stress parameter is not very accurate, it is still useful for us to know the dependence of M on grain size, porosity, and temperature in attempting to optimize use conditions for Li_2O in the blanket. The porosity and temperature dependence of M for Li_2O with a grain diameter of 10 μm is illustrated in Fig. 5.54 It is apparent from this figure that a relatively large gain can be made in thermal stress parameter by using low porosity materials, especially with porosities less than about 5%. Figure 5.54 also shows that M drops off fairly rapidly with temperature initially, but levels off at temperatures above ~800 K.

As can be seen from Table 5.19, grain size (d) affects only the tensile strength, and this effect is translated directly to M as a $d^{-0.4}$ dependence. Using a 10 μm grain diameter as a unit reference value, we calculate the following factors for the dependence of M on grain size:

grain dia (μm)	2	5	10	20	50	100
factor for M	1.90	1.32	1.00	0.76	0.53	0.40

We see that maintaining a small grain size can greatly increase both tensile strength and the thermal stress parameter, e. g., an increase of a factor of 4 in σ_t and M is to be expected if the grain size is maintained at 5 μm instead of 50 μm. In a sense, this is an indirect temperature dependent effect, since higher operating temperatures lead to the development of larger grains. It is possible, however, in many ceramic materials to limit grain

Table 5.19 Analytical expressions for the estimated physical and mechanical properties of Li_2O are summarized here together with an assessment of the expected uncertainties.

Tensile strength (in MPa):

$$\sigma_t = 108\ d^{-0.4} \exp(-10p)\ (1 - 44 \exp(-7000/T)),$$

where d = grain diameter in μm

and p = volume fraction porosity.

Estimated uncertainty in σ_t is a factor of 2 to 3.

Young's modulus (in GPa):

$$E = 140 \exp(-4p) - 140(T/T_m) \exp(-4p) \exp(1 - T_m/T),$$

where T_m is the melting point of Li_2O (~1850 K).

Estimated uncertainty in E is a factor of 2 to 3.

Poisson's ratio:

$$\nu = 0.25$$

Estimated uncertainty in ν is a factor of 2.

Thermal conductivity (in W/m-K):

$$k = (1 - p)^{1.94}\ (0.0220 + 1.784 \times 10^{-4}\ T)^{-1}$$

Estimated uncertainty in k is about ± 5%.

Linear thermal expansivity (in K^{-1}):

$$\alpha = 2.0569 \times 10^{-6}\ T^{0.4}$$

Estimated uncertainty in α is about ± 7%.

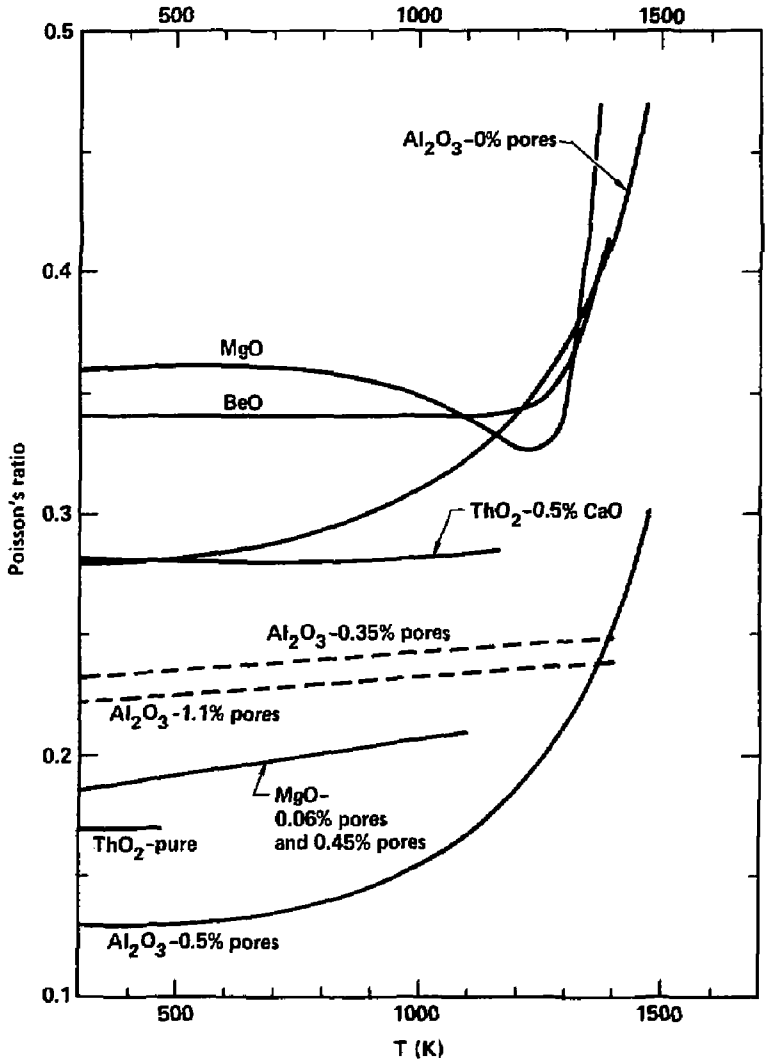

Fig. 5.53 Poisson's ratio is shown as a function of temperature for several oxides. The solid curves are from Samsonov,[16] and the dashed curves from Soga and Anderson.[23] The latter data are believed to be the more accurate and indicate that Poisson's ratio increases gradually with temperature and is relatively insensitive to porosity. Chemical additives, such as 0.5% CaO added to ThO_2, can have an effect on Poisson's ratio.

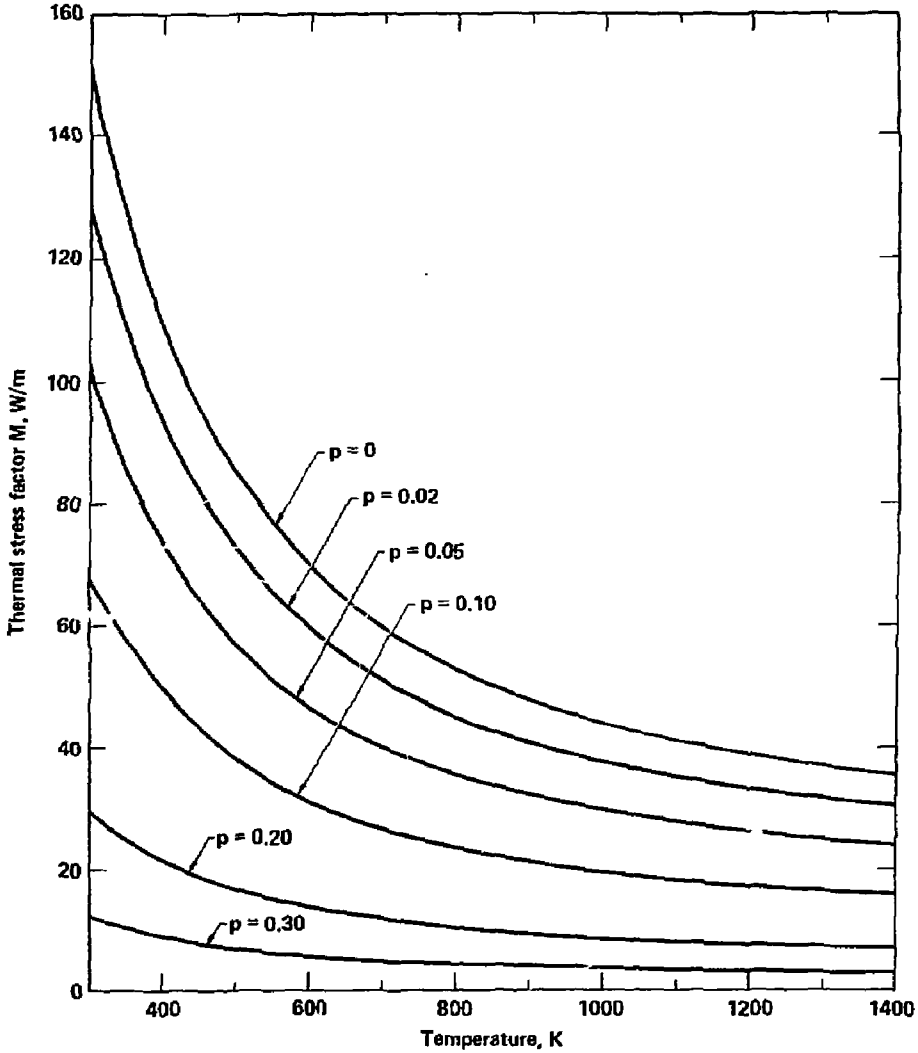

Fig. 5.54 Illustrated here is the variation of the thermal stress factor M for Li_2O as a function of temperature and porosity at a fixed grain diameter size of 10 μm.

growth by the use of suitable chemical additives. This then points out an important area for future research on fabrication studies of Li_2O to obtain materials with controlled grain sizes.

5.7 MATERIALS PROPERTIES AND INFORMATION TO SATISFY FIRST WALL ENVIRONMENTS

To permit a meaningful assessment of candidate first-wall structural materials to be conducted, an extensive data base covering the four classes of property information discussed below, i.e., physical properties, unirradiated mechanical properties, irradiation performance properties, and compatibility with expected special environments, such as breeding materials, and heat transport fluids, must be available for these materials. While the ideal situation is to select a material based on review of extensive data bases for numerous candidates, the usual situation is to select a material for which either (1) the available data base is complete enough to indicate that no obvious shortcomings (i.e., melting, vaporization, or total loss of ductility for prototypic irradiation conditions) exist; or (2) the available data base is lacking information in one (or more) important categories, but the remaining data base indicates strong advantages that outweigh the lack of data.

The five classes of structural materials are: (1) light metals, i.e., Mg, Al, Ti, and their alloys, (2) ferritic (ferromagnetic) steels; (3) austenitic (paramagnetic) Fe-Cr-Ni and Fe-Mn-X (X may be one or more of the following: Cr, Ni, Mo, Cu, Nb, Al) steels; (4) austenitic (paramagnetic) nickel-based "superalloys", and (5) refractory metal alloys based on either V or Nb. After a cursory examination of the factors limiting the utility of the light-metal alloys, it was recognized that the relatively low-maximum use temperatures set forth below:

Mg alloys:	$\sim$ 340 K
Al alloys:	$\sim$ 366 K
Ti alloys:	$\sim$ 727 K

would seriously compromise the thermodynamic efficiency of any fusion-based power conversion system to an unacceptable degree. Hence, these alloys were eliminated from further consideration, and emphasis placed on development and evaluation of data bases for the remaining alloy classes.

Considering what physical properties are of prime importance, a significant fraction of stresses generated in both the first wall and blanket are thermally induced stresses, i.e., stress brought about by sudden temperature changes in the first wall due to plasma disruptions and the passage of slugs of either very cold or very hot working fluids in the blanket, causing local expansion or contraction of the structure with respect to its unperturbed attached adjoining members or regions. Hence, the perturbed portion of the structure is unable to undergo an unrestrained dimensional change, leading to the creation of "thermal-induced stress" in the restrained area or members.[24] In general, the resulting thermal stress, S_t may be expressed by Eq. (5-46):

$$f\left[\frac{E\alpha\Delta T}{(1-\nu)}\right] = S_t \tag{5.46}$$

where ΔT is the temperature difference over the member. The exact functional relationship depends on the nature of the constraint, geometric configuration of the restrained element, and the configuration of the temperature field with respect to the surfaces of the restrained element. Examination of Eq. (5.46) shows that the value of the elastic modulus, E, the instantaneous coefficient of thermal expansion, α, and Poisson's ratio, ν, are three physical properties that must be known for any candidate structural material. Since $\nu \sim 0.25$ to 0.3 for most materials (Ref. 25, for instance), and since calculation of thermal gradients across a structure requires a knowledge of the material's thermal conductivity, K, a physical property data base comprising E, α, K, and their variations with temperature was developed.

Figure 5.55 summarizes the variation with temperature of the elastic modulus, E, of class 2-5 candidate high temperature structural alloys, whose nominal compositions are given in Table 5.20. The data on the one ferritic steel, 2-1/4 Cr-1 Mo, the three austenitic Fe-Cr-Ni alloys (Types 304 and 316 stainless steels and the alloy 800H), and one of the nickel-based superalloys (alloy 718) came from Ref. 26. The data on "Tenelon," a Fe-Mn-Cr austentic steel came from Ref. 27. The data for V came from Ref. 28, while the data for various Nb alloys came from the following sources: Nb-1-Zr

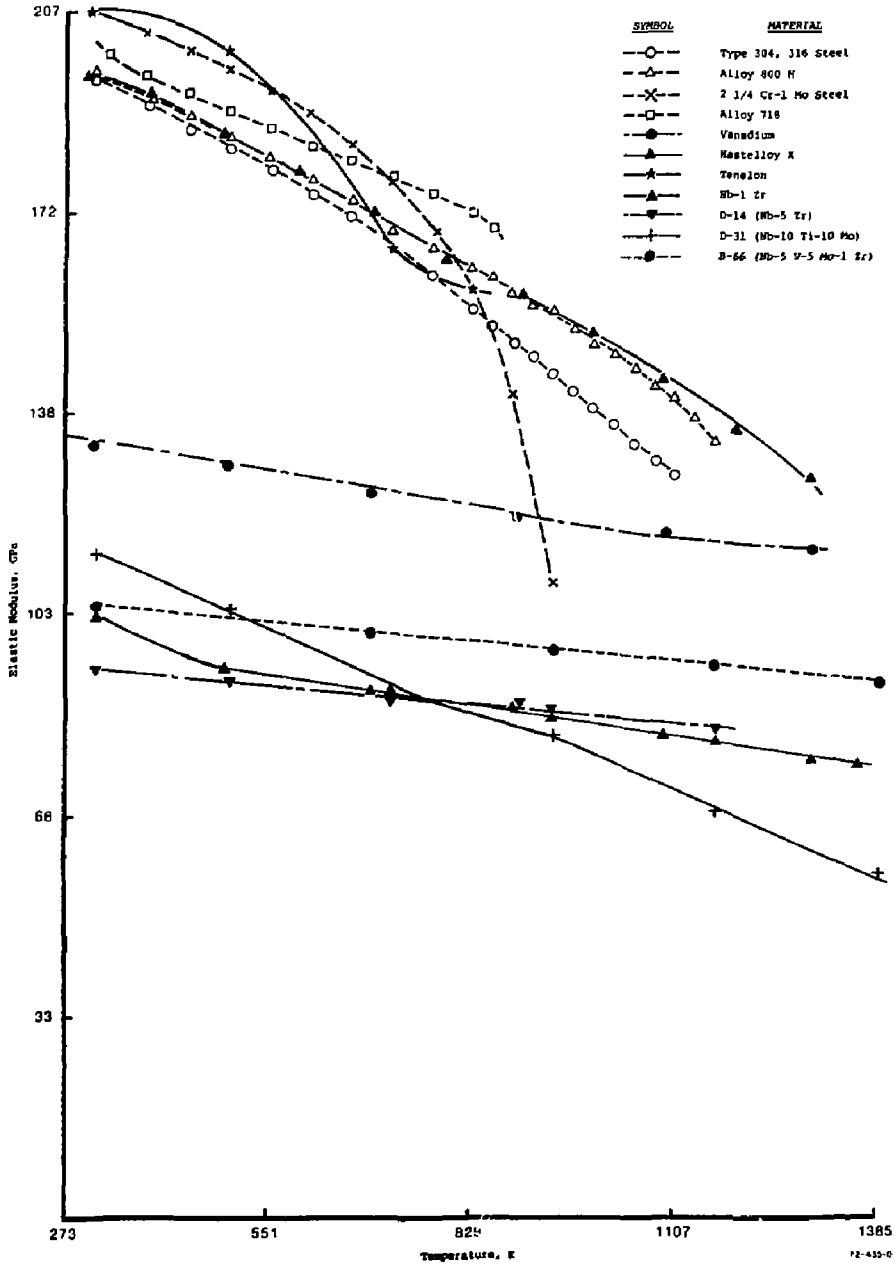

Fig. 5.55 Elastic modulus versus temperature for various high temperature materials

Table 5.20 Chemical compositions of some high temperature structural alloys

Alloy Designation	Fe	Cr	Ni	Mo	Mn	Si	W	Co	C	N_2	Nb	V	Ti	Zr	Al
Type 304 steel	Bal.	$\frac{20}{18}$	$\frac{10.5}{8.0}$	--	2.0	1.0	--	--	.08	.10	--	--	--	--	--
Type 316 steel	Bal.	$\frac{18}{16}$	$\frac{14}{10}$	$\frac{3}{2}$	2.0	1.0	--	--	.08	.10	--	--	--	--	--
2-1/4 Cr - 1 Mo steel**	Bal.	$\frac{2.75}{2.00}$	.50	$\frac{1.20}{.90}$	$\frac{.6}{.3}$	.50	.10	--	.15	--	--	.03	--	--	--
Alloy 800H	Bal.	$\frac{23}{19}$	$\frac{35}{30}$	--	1.5	1.0	--	--	.10	--	--	--	$\frac{.60}{.15}$	--	$\frac{.60}{.15}$
Alloy 718	Bal.	$\frac{21}{17}$	$\frac{55}{50}$	$\frac{3.3}{2.8}$	.35	.35	--	1.0	.08	--	$\frac{5.50}{4.75}$	--	$\frac{1.15}{.65}$	--	$\frac{.8}{.2}$
Hastelloy alloy X	$\frac{20}{17}$	$\frac{23.0}{20.5}$	Bal.	$\frac{10.0}{8.0}$	1.0	1.0	$\frac{1.0}{.20}$	$\frac{2.50}{.50}$	$\frac{.15}{.05}$	--	--	--	--	--	--
Tenelon	Bal.	$\frac{19.0}{17.0}$	.10	--	$\frac{16.5}{14.5}$	1.0	--	--	--	$\frac{.50}{.30}$	--	--	--	--	--
V-20 Ti	--	--	--	--	--	--	--	--	--	--	--	Bal.	$\frac{20.5}{19.5}$	--	--
V-15 Cr-5 Ti	--	$\frac{15.5}{14.5}$	--	--	--	--	--	--	--	--	--	Bal.	$\frac{5.5}{4.5}$	--	--
Vanstar 7	$\frac{3.5}{3.0}$	$\frac{9.5}{9.0}$	--	--	--	--	--	--	.10	.01	--	Bal.	--	$\frac{1.2}{0.8}$	--
Nb-1 Zr	--	--	--	--	--	--	--	--	.01	--	Bal.	--	--	$\frac{1.25}{.75}$	--
Nb-5 Zr	--	--	--	--	--	--	--	--	.01	--	Bal.	--	--	$\frac{5.6}{4.4}$	--
D-31	--	--	--	$\frac{11.0}{9.0}$	--	--	--	--	$\frac{.12}{.08}$	--	Bal.	--	$\frac{11.0}{9.0}$	--	--
B-66	--	--	--	$\frac{5.5}{4.5}$	--	--	--	--	.02	--	Bal.	$\frac{5.5}{4.5}$	--	$\frac{1.3}{.85}$	--

Footnotes: * All compositions in wt. percent. ** Less restrictive specs. exist.

(Refs. 29-31), Nb-5-Zr (Ref. 32), Nb-10 Ti-10 Mo (Refs. 32-33), and Nb-5V-5 Mo-1 Zr (Ref. 34). Note that the iron- and nickel-based alloys have higher elastic modulus values ($\sim$ 127.6 GPa) at 1366 K than the refractory metal alloys ($\sim$ 60.7-110.3 GPa).

Figure 5.56 summarizes the variation with temperature of the instantaneous coefficient of thermal expansion, α, of class 2-5 candidate high temperature structural alloys. The data on the 2-1/4 Cr-1 Mo ferritic steel, the three austenitic Fe-Cr-Ni alloys (Types 304 and 316 stainless steels and alloy 800H) and one of the nickel-based alloys (alloy 718) came from Ref. 26. The data for nickel-based Hastelloy X came from Ref. 35. The data on the Fe-Mn-Cr austenitic alloy (Tenelon) came from Ref. 28. The data on the various Nb-based alloys came from the following references: Nb-1 Zr (Refs. 29, 36), Nb-10 Ti-10 Mo (Ref. 37), and Nb-5 V-5 Mo-1 Zr (Ref. 34). Note that the ferritic and austenitic alloys have α values at 811 K of about 14.8 to 21.3 x 10^{-6} K, while the Nb alloys have α values of about 7.6 x 10^{-6} K at the same temperature.

Figure 5.57 summarizes the temperature variation of thermal conductivity of various class 2-5 candidate high temperature structural alloys. The data on the 2-1/4 Cr-1 Mo ferritic steel, the three austenitic Fe-Cr-Ni alloys (Types 304 and 316 stainless steel and alloy 800H) and one of the nickel-based alloys (alloy 718) came from Ref. 25. The data on the one Nb alloy (Nb-1 Zr) came from Ref. 38. Note that the α:T behavior for the austenitic (face-centered cubic) alloys are all similar, starting at about .086-.138 watts/cm K at room temperature and increasing monotonically to a value range of .241-.267 watts/cm K at about 1089 K. The α:T behavior for the two body centered cubic alloys, Nb-1 Zr Nb alloy and 2-1/4 Cr-1 Mo ferritic steel are much different from that exhibited by the austenitic alloys, starting at room temperature at values of about .448 and .362 watts/cm K, respectively, and increasing with increasing temperature in the former case versus decreasing with increasing temperature in the latter case.

Given the values of E and α at 1089 K, and assuming a value of ν of 0.3,

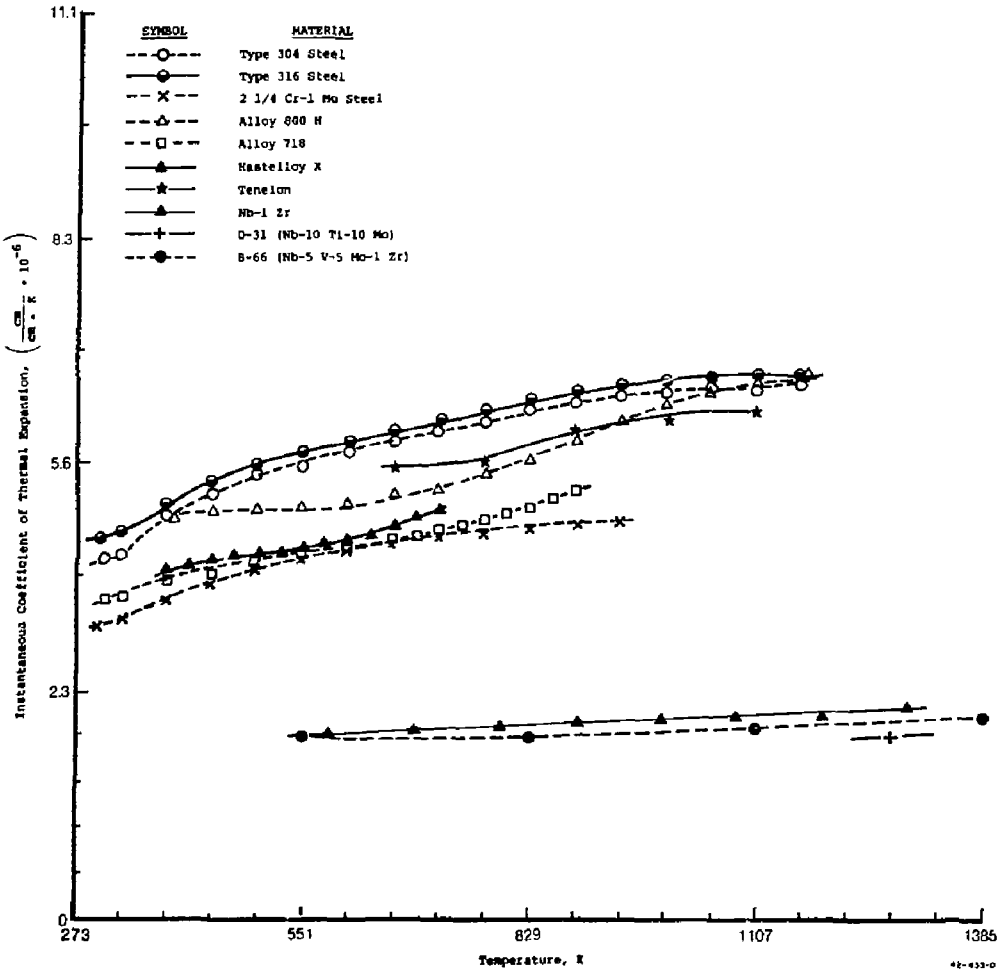

Fig. 5.56 Coefficient of thermal expansion versus temperature in some high temperature materials

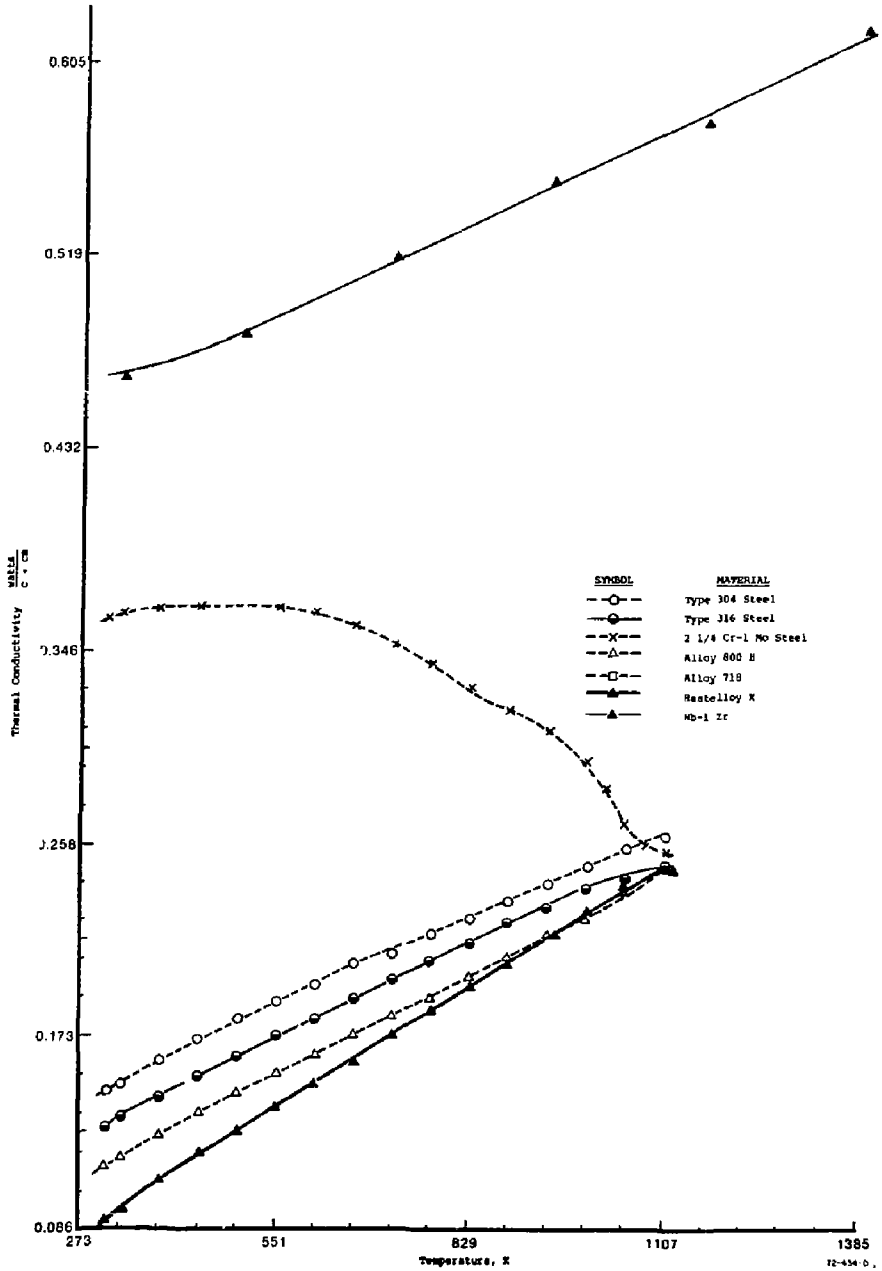

Fig. 5.57 Thermal conductivity versus temperature for some high temperature materials

one can develop a relative thermal shock rating for these candidate materials by calculation of the quantity $E\alpha\Delta T/(1-\nu)$ at a typical first-wall temperature of 811 K.

Material	Thermal Shock Parameter
316	2382 MPa
304	2340
Tenelon	2242
Hastelloy X, alloy 800H	2165
Alloy 718	2109
2-1/4 Cr-1 Mo steel	1830
Nb-5 V-5 Mo-1 Zr	531
Nb-1 Zr	506
Nb-5 Zr	489
Nb-10 Ti-10 Mo	441

The larger the value of "thermal shock parameter", the more susceptible to failure due to sudden temperature changes will be components made from the particular alloy. Note that all the austenitic Fe-Cr-Ni, Fe-Mn-Cr, and Ni-based superalloys have roughly comparable values. The value for the ferritic steel, 2-1/4 Cr-1 Mo, is about 23% less than the average value for the austenitic alloys, while the average value for the Nb alloys is about 78% less than the corresponding average value for austenitic alloy. Hence, to maximize the resistance to thermal shock, select a material from among the Group VA refractory metals (i.e., V-based or Nb-based alloys).

Consider now what might comprise a "minimum set" of unirradiated mechanical properties to comprise a data base for comparative purposes. Static yield strength as a function of temperature provides the needed information for preliminary sizing of components on the basis of avoiding

permanent deformation (yielding) during short-time operation. Since the design life has been set at 3 years (or 26298 hours) of full-power operation, the stress to rupture and stress to produce 1% total deformation in a time of 3 years as functions of temperature enable the effects of time-dependent deformation to be evaluated. Lastly, since the plant will be subject to some small number of perturbations from steady-state operation during the 3-year life of the blanket, a knowledge of the low-cycle strain-controlled fatigue performance of candidate structural material is desirable.

Information on the minimum expected yield strength (S_y):temperature (T) behavior of several candidate structural materials from classes 2-5 is presented in Fig. 5.58. The method of obtaining "minimum expected S_y:T" trends is the same as that used in derivation of ASME Boiler and Pressure Vessel Code design allowables (Ref. 39). Data for the three Fe-Cr-Ni austenitic alloys (Types 304 and 316 stainless steels and alloy 800H) was taken from Ref. 26, while data on the Fe-Cr-Mn austenitic alloy (Tenelon) was taken from Ref. 27. Data for the two nickel-based superalloys came from Ref. 27 (alloy 718) and Ref. 35 (Hastelloy X). Data on the V-20 Ti alloy came from Refs. 40-44, while data for the Vanstar-7 alloy came from Refs. 41-42 and 45-48. Data on the Nb-1 Zr alloy cane from Refs. 40-41 and 49-54, while data on the Nb-10 Ti-10 Mo alloy came from Refs. 32-33, 37, and 54-55. Data on the Nb-5 Mo-5 V-1 Zr alloy came from Refs. 34 and 56-61.

Examination of the S_y:T information presented on Fig. 5.58 indicates that, referred to Type 304 austenitic stainless steel at 811 K, the S_y values of the other high temperature structural materials rank as follows:

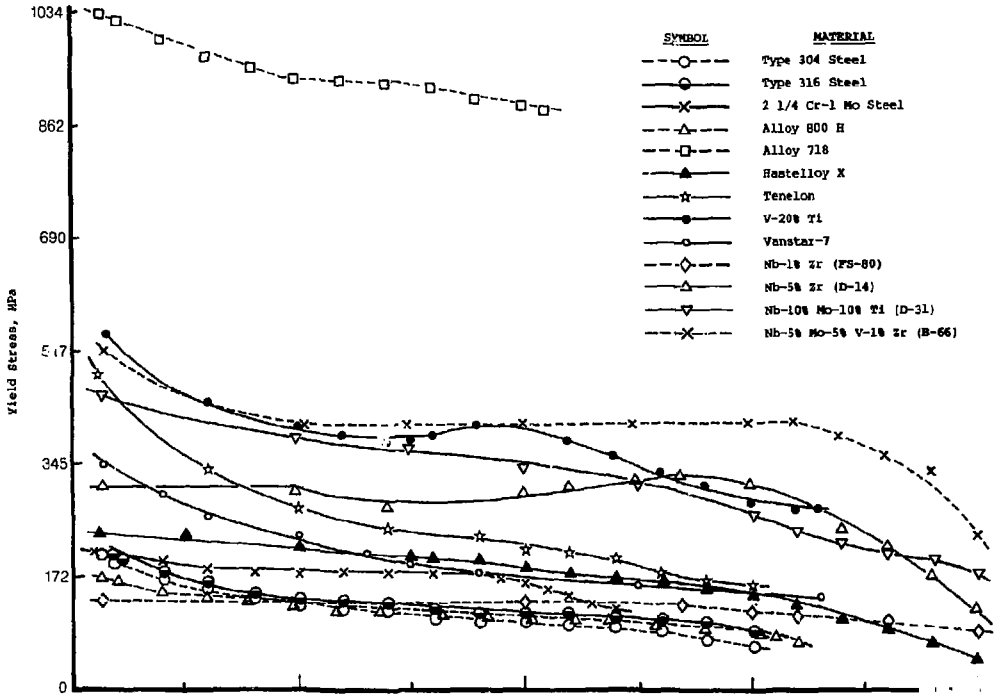
1034
862
690
517
345
172
0
Yield Stress, MPa
SYMBOL
MATERIAL
Type 304 Steel
Type 316 Steel
2 1/4 Cr-1 Mo Steel
Alloy 800 H
Alloy 718
Hastelloy X
Tenelon
V-20% Ti
Vanstar-7
Nb-1% Zr (FS-80)
Nb-5% Zr (D-14)
Nb-10% Mo-10% Ti (D-31)
Nb-5% Mo-5% V-1% Zr (B-66)

Alloy	S_y ÷ S_y of Type 304 Stainless Steel at 811 K
304	1.0
Alloy 800H	1.067
316	1.133
Nb-1 Zr	1.267
2-1/4 Cr - 1 Mo ferritic steel	1.567
Vanstar 7	1.667
Hastelloy X	1.867
Tenelon	2.267
Nb-5 Zr	2.867
Nb-10 Mo-10 Ti	3.533
V-20 Ti	4.20
Nb-5 Mo-5 V-1 Zr	3.933
Alloy 718	8.667

Note that at 811 K, use of a ferritic steel can result in a decrease in component thickness by about 63.8% (1 ÷ 1.567). Note also that the highest S_y conventional alloy without Ni (Ni is a known He producer in a neutron environment and is to be avoided) is Tenelon, with a 811 K S_y ratio of 2.267, relative to Type 304 stainless steel. For a material stronger than Tenelon, one is forced to either experimental (and expensive) refractory metal alloys (such as the V-rich or Nb-rich alloys) or Ni-rich precipitation-hardenable superalloys, which are expensive, difficult to fabricate, and prone to embrittlement by He formation on neutron irradiation (Ref. 62, for example).

Information on the minimum expected stress (S_R) to rupture in 3 years (the life of the first wall and blanket) as a function of temperature is

shown in Fig. 5.59 for Fe-Cr-Ni and Fe-Cr-Mn austenitic steels, a ferritic steel, and a nickel-based precipitation-hardening superalloy. The data sources are as follows: Ref. 26 for Types 304 and 316 stainless steel, alloy 800H, and 2-1/4 Cr-1 Mo ferritic steel; Refs. 26 and 62 for alloy 718, Refs. 35, 63-66 for Hastelloy alloy X, and Ref. 27 for Tenelon. The method of derivation of the S_R values was based on use of the Larson-Miller parameter (Ref. 67), P_{LM}, to condense the referenced data for these alloys, which is usually presented as tables of average stress for failure (rupture) as a function of temperature (T) and time (t_R). The procedure is used as follows:

1. *Calculate P_{LM} for each datum point, i.e., for each S_R, T, t_r combination.*

2. Plot the resulting information on semi-logarithmic paper in the form of S_R (the dependent variable) against P_{LM} (the independent variable),
   where P_{LM} is given by (Ref. 67):

   $$P_{LM} = T\,[C + \log_{10}(t_r)] \times 10^{-3} \qquad (5.47)$$

   and C is assumed to equal 20, per Ref. 67.

3. *Calculate P_{LM} for various (T, 3 years) combinations over the range of temperatures of interest i.e., 644 K to about 1144 K.*

4. *Construct the "expected minimum curve" to the S_R:P_{LM} data array.* For our purposes, the "expected minimum curve" was drawn parallel to the "average smooth curve" through the data array and was reduced to pass through the lowest data point in the array.

5. *Using the information in (3) and (4), pick off S_R values,* corresponding to t_r values of 3 years, as a function of temperature.

Considering the information thus generated and summarized in Fig. 5.59 in a manner similar to the S_y:T information presented in Fig. 5.58, one obtains the following:

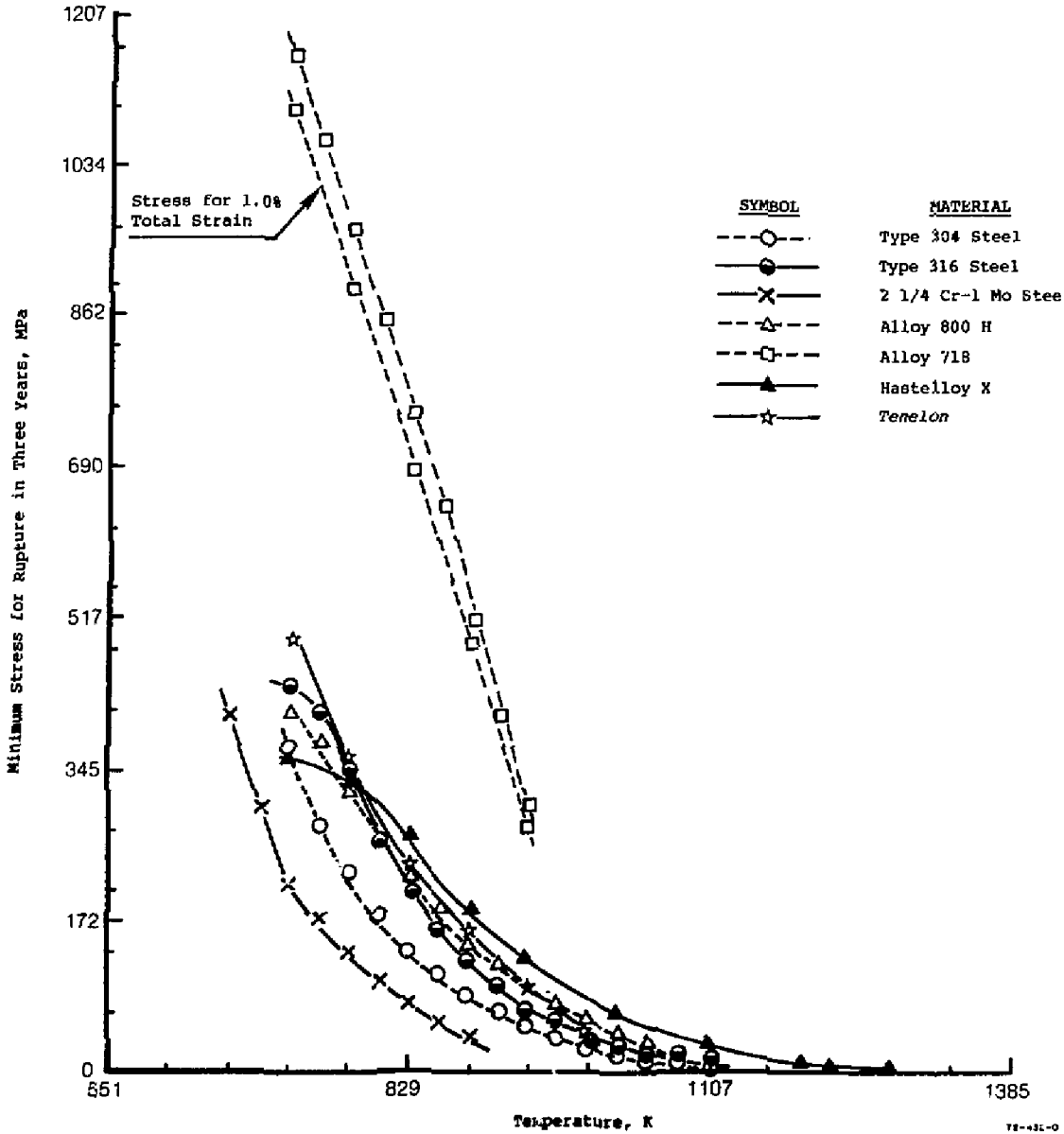

Fig. 5.59 Minimum rupture life in three years versus temperature for some high temperature materials

Alloy	$\frac{S_R}{(S_R)_{304\ steel}}$ at 811 K	$\frac{S_R}{(S_R)_{304\ steel}}$ at 1089 K
2-1/4 Cr- 1 Mo	0.60	....
304	1.00	1.00
316	1.50	1.33
Alloy 800H	1.65	....
Tenelon	1.75	....
Hastelloy alloy X	2.00	3.33
Alloy 718	5.45	....

At 811 K, the ferritic steel, 2-1/4 Cr - 1 Mo, is weaker in time-dependent deformation than Type 304 stainless steel. Both Fe-Cr-Ni and Fe-Cr-Mn austenitic alloys, such as alloy 800H in the former case and Tenelon in the latter case, are superior to Type 304 stainless steel. Again, the nickel-based superalloys, such as Hastelloy alloy X (a solid solution strengthened alloy) and alloy 718 (a precipitation-strengthened alloy) are much superior to any of the Fe-based austenitic alloys. At 1089 K, the same rank ordering of alloy classes occurs, i.e., Fe-based austenitic alloys lower and a Ni-based solid-solution-strengthened austenitic Hastelloy alloy X, higher. The alloy 718, which was the strongest alloy at 811 K, no longer appears at 1089 K, due to instability of the precipitating phases making the alloy unsuitable for use above about 894 K for long times.

In Fig. 5.60 is presented a summary of 3 year minimum expected stress-to-rupture (S_R) data versus temperature for various V-based and Nb-based alloys. The method of determination of S_R is the same as was previously described for iron- and nickel-based alloys. Data for the V-15 Ti-5 Cr and V-20 Ti alloys came from Refs. 41-43 and 45-46; and for the Vanstar 7 alloy from Refs. 45-46. Data for the Nb-1 Zr alloy came from Refs. 54 and 68-74 while data for the Nb-5 Zr alloy came from Refs. 32 and 71. Data for the

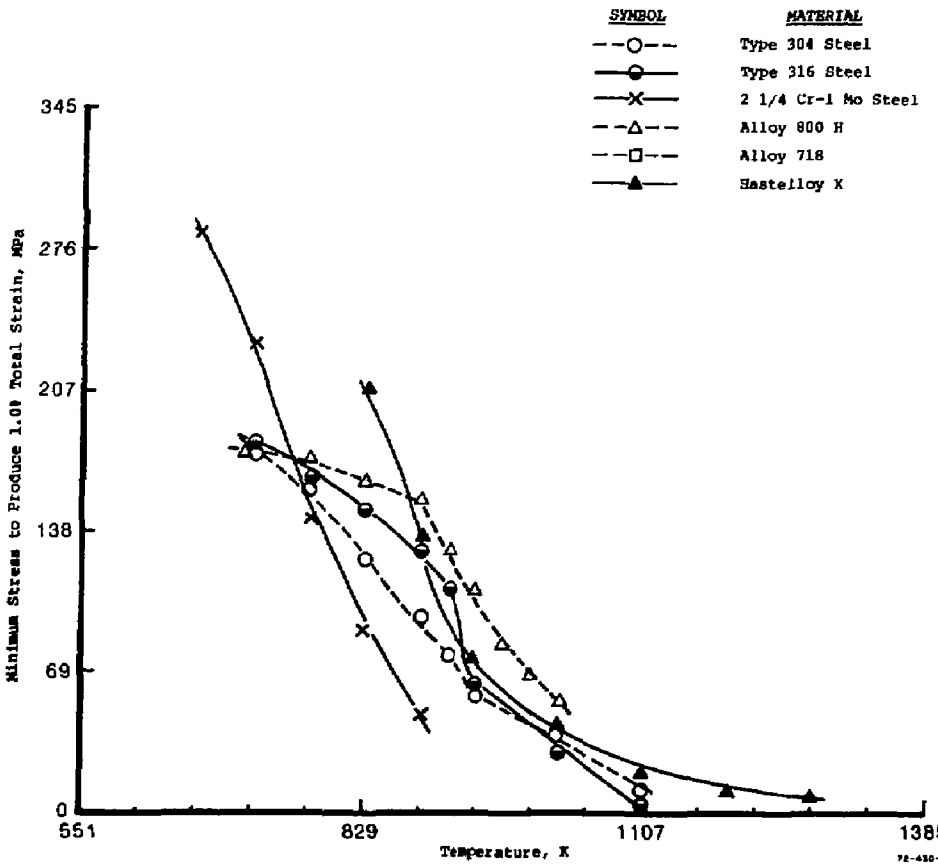

Fig. 5.60 Stress to produce 1.0% total strain in three years versus temperature for some high temperature materials

Nb-10 Ti-10 Mo alloy came from Refs. 32-33, 68, and 75; while date for the Nb-5 Mo-5 V-1 Zr alloy came from Refs. 34, 54, 56, 68, and 76.

Comparing S_R values at 1089 K and 1366 K in the same manner as done previously for iron- and nickel-based alloys, one finds that:

Alloy	$\frac{S_R}{(S_R)_{Nb\text{-}1\ Zr}}$ at 1089 K	$\frac{S_R}{(S_R)_{Nb\text{-}1\ Zr}}$ at 1366 K
V-20 Ti	0.148	....
Nb-10 Ti-10 Mo	0.852	2.000
Vanstar 7	0.904	....
Nb-1 Zr	1.000	1.000
V-15 Ti-5 Cr	1.138	....
Nb-5 Zr	2.034	....
Nb-5 Mo-5 V-1 Zr	2.759	1.667

Note that at 1089 K, the V-15 Ti-5 Cr alloy is about 13.8% stronger than the "reference alloy", Nb-1 Zr, and that the Nb-10 Ti-10 Mo alloy is about 15% weaker than Nb-1 Zr. At 1366 K, however, the Nb-10 Ti-10 Mo alloy is twice as strong as Nb-1 Zr, and no V alloy data could be found.

In Fig. 5.61 is summarized the minimum estimated stress to 1.0% total strain in 3 years for various iron-based and nickel-based structural materials as a function of temperature. The method of determination of $S_{1\%}$ is the same as that used to develop the S_R:T information presented in Figs. 5.59 and 5.60. Data on the three iron-based Fe-Cr-Ni alloys (Types 304 and 316 stainless steels and alloy 800H), the ferritic steel (2-1/4 Cr - 1 Mo), and the precipitation-strengthened Ni-Cr-Fe (alloy 718) came from Ref. 26, while data on the solution-strengthened Ni-Cr-Fe alloy (Hastelloy alloy X) came from Refs. 35, 63-64, and 66. Comparing $S_{1\%}$ values at 811 K and

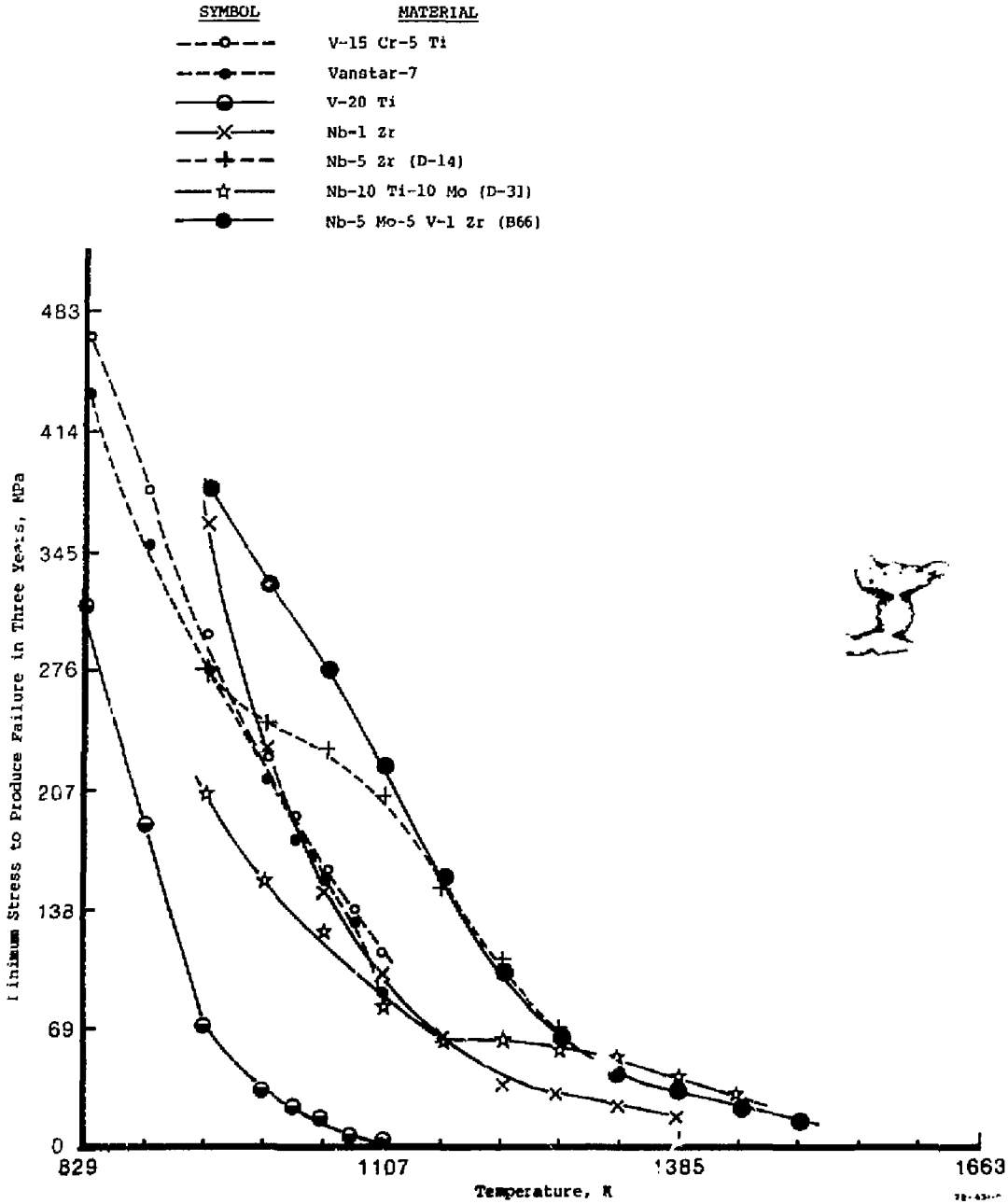

Fig. 5.61 Stress for a three-year life versus temperature for various vanadium and base alloys

1089 K in the same manner as done previously for the S_R and S_y behaviors of these materials, one finds that:

Alloy	$\frac{S_{1\%}}{(S_{1\%})_{304\ steel}}$ at 811 K	$\frac{S_{1\%}}{(S_{1\%})_{304\ steel}}$ at 1089 K
2-1/4 Cr - 1 Mo	0.722	....
304	1.000	1.000
316	1.194	0.389
Alloy 800H	1.306	....
Hastelloy alloy X	1.667	1.778
Alloy 718	5.556	....

At 811 K, the ferrite steel is weaker, the three solid-solution-strengthened Fe-Cr-Ni austenitic alloys are next and stronger than Type 304 stainless steel, and the precipitation-hardened nickel-based alloy (alloy 718) is again the strongest. The relative order is the same, weakest to strongest, as was the case at 811 K. At 1089 K, the weakest alloy is Type 316 stainless steel, followed by Type 304, and Hastelloy alloy X is the strongest.

Irradiation effects information on Fe-Cr-Mn or Fe-Cr-Mn-Ni alloys is sparse. In Fig. 5.62 is plotted the swelling behavior, $\Delta v/v_o$, of 20% cold-worked Type 316 stainless steel after irradiation in EBR-II (Ref. 77). At 773 K, superimposed in Fig. 5.62, is preliminary swelling information at 773 K for ferritic steels such as 2-1/4 Cr-1 Mo, 9 Cr-1 Mo, and HT-9 (Ref. 77). Also shown are some preliminary results for two Fe-Cr-Mn-Ni alloys; ICL 16 (Fe-17.3 Cr-7.18 Ni-8.3 Mn-1.39 Mo-.022 C, Ref. 78) and AMCR (Fe-10 Cr-17.5 Mn-0.67 Ni-0.2 C, Ref. 79). The former alloy was irradiated with 46.5 MeV Ni^{+6} ions at 898 K, and the latter alloy was irradiated with energetic electrons at temperatures from 673 K to 923 K. Given the inherent differences in behavior due to irradiation temperatures other than 773 K for

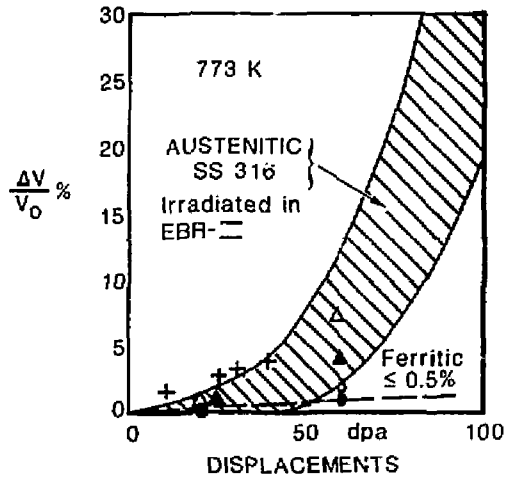

ALLOY	IRRAD. TEMP.	SPECIMEN CONDITION	SYMBOL	TYPE OF IRRADIATION
ICL 16	898 K	ST	○	Ni^{+6} ions, 46 dpa
		STA	●	Ni^{+6} ions, 46 dpa
		ST + 10 appm He	△	Ni^{+6} ions, 46 dpa
		STA + 10 appm He	▲	Ni^{+6} ions, 46 dpa
AMCR	773 K	ST	+	Electrons

F2-429-0

Fig. 5.62 Swelling behavior of austenitic Fe-Cr-Ni, Fe-Cr-Mn-Ni, and ferritic steels irradiated in various sources

the JCL 16 and the known differences in response of the substrates due to different damage rates produced by neutrons, ions and electrons at various evergy levels, it appears that the swelling behavior of the two Fe-Cr-Mn-Ni alloys is comparable to that of 20% cold-worked Type 316 stainless steel at 773 K.

At 811 K, a comparison of tensile ducticity parameters for Tenelon (irradiated to a total fluence of about 4.5×10^{25} n/m^2 (1.5×10^{25} n/m^2 E > 1 MeV) Ref. 80) with results of recent work on 20% cold-worked Type 316 stainless steel (irradiated in HFIR to a fast fluence of about 1×10^{26} n/m^2 (E > 0.1 MeV) (Ref. 81) yielded the following results:

Alloy	form Elongation	Total Elongation
Tenelon	7.5%	8.0%
20% C.W. SS 316	5.0	8.3

Given the differences in spectra and end-of-life fluences, Tenelon, a Ni-free austenitic Fe-Cr-Mn alloy, appears to exhibit comparable ducticity to 20% cold-worked Type 316 stainless steel at 811 K.

5.8 THE INFLUENCE OF WASTE DISPOSAL ON MATERIAL SELECTION

One of the important considerations in the design of fusion reactors is the impact of materials selection upon the generation and disposal of radioactive wastes from neutron activation of structural materials. Recent developments in regulations for the disposal of radioactive wastes (NRC-proposed regulation 10CFR61, "Licensing Requirements for Land Disposal of Radioactive Wastes") furnish a basis for classifying wastes with respect to composition, form, and method of disposal. The key factor from 10CFR61 for reactor designers is the limit on specific activity for a given disposal method and for each combination of radioactive isotopes in waste. This limit can be combined with predicted activities for elemental components in structural alloys to give an index of waste disposal ratings (WDR). This is:

$$WDR = \sum_i \frac{A(i)}{L(i)} \qquad A(i) \text{ and } L(i) \text{ in units of curies/m}^3$$

where A(i) is the activity of the i^{th} isotope in an alloy and L(i) is the limit from 10CFR61 for the i^{th} isotope. If WDR $\leq$ 1, then according to 10CFR61, the waste could be disposed of by near-surface burial as low-level waste. If WDR $\geq$ 1, the disposal could not be near-surface but would have to be by some accepted method for "high" level waste such as deep geologic disposal.

The WDR for several steels that might be used in fusion reactors have been calculated.[82,83] The list of these steels and their nominal elemental compositions are given in Table 5.21. The predicted specific activities for the critical elements for long-term disposal are shown in Table 5.22 for the first wall of one of the conceptual reactor designs done on MARS. The corresponding WDR's for this design are shown in Table 5.23. From the column for Total Alloy in Table 5.23, it can be seen that first-wall alloys 5, 7, 10 and 11 are the only ones that could be directly disposed of by near-surface burial. All the others would have to be processed to make WDR $\leq$ 1. The processing might be simple dilution in a concrete matrix. The amount of dilution would be in direct properties to the original WDR. Thus the alloy

Table 5.21 Composition of various steels by weight percent of the element in the alloy

Steel	Element														
	Fe	C	Si	Mn	P	S	Ni	Cr	Nb	Al	N	V	Mo	W	Cu
1. SS316	64.44	.06	.46	1.43	.03	.01	14	16.7	--	--	--	--	2.8	--	--
2. PCA	64.68	.05	.5	1.8	.01	.005	16	14	.03	.03	.01	--	2.0	--	--
3. HT-9	85.1	.2	.4	.55	.02	.02	.5	11.5	--	--	--	.3	1.0	.5	--
4. 2.25-1	94.58	.15	.5	.45	.035	--	.5	2.25	--	--	--	--	1.0	.1	.5
5. TENELON	68.0	.08	.3	14.5	.045	.03	--	17.0	--	--	--	--	--	--	--
6. NOMAGNE	79.35	.65	.5	15.	.03	.02	2.2	2.2	--	--	--	--	--	--	--
7. NM-1	76.92	.5	.5	20.	.05	.03	--	2.0	--	--	--	--	--	--	--
8. 25-5-1	66.22	.17	.6	26.	.03	.01	1.2	5.5	.07	--	--	--	--	--	--
9. 32-7	60.24	.14	.6	31.6	.022	.006	.23	7.04	--	.12	.13	--	--	--	--
10. JUS289-N	72.45	.6	.65	20.	.08	.025	--	6.0	--	--	.2	--	--	--	--
11. JUS289-V	72.15	.6	.65	20.	.08	.025	--	6.0	--	--	.2	.3	--	--	--

NOMAGNE is made by Kobe Steel, NM-1 by Nippon Korean, 25-5-1 by Nippon Steel Ltd., and 32-7, JUS289-N and JUS289-V by Japan Steel Works. Tenelon is a steel developed by the U.S. Steel Corp. We have no information on these steels regarding radiation damage in high flux neutron fields. The other steels are discussed in R. E. Gold, et al., "Materials Technology for Fusion: Current Startup and Future Requirements," Nuclear Technology/Fusion, 1, April 1981, pp. 165-237.

Table 5.22 Activities of major long-lived isotopes (Ci/m^3)
First wall: MARS (TRW) @ 4.8 MW/m^2 and 3 years
(Parent elements in parentheses)

Alloy	Isotope					
	Ni-59	Ni-63	Nb-94	Mo-93	Tc-99	Mn53
1. SS316	500(Ni)	50000(Ni)	3E-2(Mo)	560(Mo)	11(Mo)	7.73(Fe)
2. PCA	580(Ni)	58000(Ni)	27(Nb)	400(Mo)	8(Mo)	7.78(Fe)
3. HT-9	18(Ni)	1800(Ni)	1E-2(Mo)	200(Mo)	4(Mo)	10.2(Fe)
4. 2.25-1	--	--	1E-2(Mo)	200(Mo)	4(Mo)	11.2(Fe)
5. Tenelon	--	--	--	--	--	8.81(Fe/Mn)
6. Nomagne	80(Ni)	7900(Ni)	--	--	--	10.1(Fe/Mn)
7. NM-1	--	--	--	--	--	10.0(Fe/Mn)
8. 25-5-1	43(Ni)	4300(Ni)	63(Nb)	2E-3(Nb)	--	9.04(Fe/Mn)
9. 32-7	8(Ni)	825(Ni)	--	--	--	8.59(Fe/Mn)
10. JUS289-N	--	--	--	--	--	9.49(Fe/Mn)
11. JUS289-V	--	--	--	--	--	9.46(Fe/Mn)
10CFR61 Limit	22	700	2E-2	22	3	22

Table 5.23 Waste disposal ratings (WDR)
First wall: MARS (TRW) @ 4.8 MW/m^2 and 3 years
(Parent elements in parentheses)

Alloy	WDR						
	Ni-59	Ni-63	Nb-94	Mo-93	Tc-99	Mn53	Total Alloy
1. SS316	22.7(Ni)	71.4(Ni)	1.5(Mo)	25.5(Mo)	3.67(Mo)	0.351(Fe)	125
2. PCA	26.4(Ni)	82.9(Ni)	1350(Nb)	18.2(Mo)	2.67(Mo)	0.354(Fe)	1480
3. HT-9	0.818(Ni)	2.57(Ni)	0.5(Mo)	9.09(Mo)	1.33(Mo)	0.464(Fe)	15
4. 2.25-1	--	--	0.5(Mo)	9.09(Mo)	1.33(Mo)	0.509(Fe)	11
5. Tenelon	--	--	--	--	--	0.4(Fe/Mn)	0.40
6. Nomagne	3.64(Ni)	11.3(Ni)	--	--	--	0.459(Fe/Mn)	15
7. NM-1	--	--	--	--	--	0.46(Fe/Mn)	0.46
8. 25-5-1	1.95(Ni)	6.14(Ni)	3150(Nb)	9.09×10^{-5}(Nb)	--	0.411(Fe/Mn)	3159
9. 32-7	0.364(Ni)	1.18(Ni)	--	--	--	0.39(Fe/Mn)	1.93
10. JUS289-N	--	--	--	--	--	0.431(Fe/Mn)	0.43
11. JUS289-V	--	--	--	--	--	0.430(Fe/Mn)	0.43

$$WDR = \sum_i A(i)/L(i)$$

A(i) = activity of i^{th} isotope in Ci/m^3

L(i) = maximum permissable activity of i^{th} isotope (Ci/m^3) from 10CFR61.

If WDR < 1, material can be disposed of by near-surface burial without processing.

25-5-1 would require by far the most dilution because of its niobium content. The alloy PCA requires the next largest dilution, again primarily because of niobium. Stainless steel 316 requires the third largest dilution because of its high nickel and molybdenum content. The tables indicate that nickel and molybdenum are undesirable for long-term waste disposal in all the alloys. The high manganese alloys without nickel and/or molybdenum would be highly desirable from a waste management viewpoint since they would require no waste processing except for transportation packaging.

5.9 SUMMARY

The solid Li_2O Canister blanket concept appears to offer many advantages over previous designs. The main advantages are summarized below:

(a) The relatively cool structural envelope of each Canister can use a steel alloy such as Tenelon which has much lower radioactivation than ferritic or stainless steels.

(b) The Canister acts as the primary blanket pressure vessel with good structural safety factors.

(c) The solid Li_2O tritium breeder material is separated from the main helium coolant flow by putting it in tubes inside the Canister. This greatly facilitates tritium separation and isolation of the tritium from the thermochemical plant.

(d) These tubes can run at very high temperatures and still be made of Tenelon, because they are almost pressure-balanced and hence experience very low stresses.

(e) The design of the blanket as a bank of staggered tubes allows us to take advantage of the very good heat transfer and low pumping power requirements of a cross-flow-type heat exchanger.

(f) The tube bank can be designed as a multi-pass heat exchanger so that the main helium inlets and exits can be conveniently located at the back of the blanket Canisters.

(g) The hot shield is designed as a set of staggered rods which are a direct extension of the tube bank. This provides a low pressure drop flow path for the helium while at the same time eliminating most neutron streaming.

(h) The blanket can be proof-tested initially at the Canister level; this is a very convenient small-size unit. The next level of test can be at the ring module level which consists of a compact assembly of 18 Canisters.

(i) Two ring modules fit in the region between each two central cell magnet coils in such a way that assembly and disassembly is possible with simple motions without moving the magnets.

(j) The Canisters of each ring module are mutually supporting along the sides of the Canisters, resulting in reduced structural requirements. The use of common headers minimizes the possibility of total depressurization of one Canister and a domino-type failure of the remaining Canisters.

Many detailed design questions remain to be answered. However, this blanket concept has survived a critical review and remains one of the most attractive concepts we have seen in the past 15 years.

Section 5 Nomenclature

a	=	speed of sound in helium
A	=	area
A_c	=	flow channel total cross-sectional area
C_p	=	specific heat of helium
d_h	=	diameter of the He purge hole in the Li_2O
d_i	=	inner diameter of the tube
d_L	=	diameter of the Li_2O cartridge
d_o	=	outer diameter of the tube
D	=	diameter
D_H	=	hydraulic diameter
f_L	=	fraction of Li_2O in the tube bank
f_s	=	fraction of structure in the tube bank
f_{TD}	=	fraction of 100% theoretical density of the Li_2O
f_v	=	total "void" fraction in the tube bank
f	=	Darcy-Weisbach friction factor
f'	=	Fanning friction factor = f/4
G	=	mass flux, ρv
$\bar{h}$	=	average convective heat transfer coefficient
k	=	thermal conductivity of helium
k_i	=	thermal conductivity of insulation
k_L	=	thermal conductivity of Li_2O
k_p	=	thermal conductivity of the large pipe walls
k_w	=	thermal conductivity of the tube wall
$\dot{m}$	=	mass flow rate

Nu	=	Nusselt number
P	=	pressure
Pr	=	Prandtl number
Q	=	heat flow or input
q	=	heat flux
r	=	radius measured from the first wall at the Canister separation point
r_L^*	=	decay length for internal heat generation in Li_2O
r_S^*	=	decay length for internal heat generation in the tube material
Re	=	Reynolds number, GD_H/μ
s	=	path length along the flow in the canister
s_t	=	transverse stagger of the tube bank
s_l	=	longitudinal stagger of the tube bank
t	=	thickness of the first wall
t_g	=	annular gap for helium purge flow
t_L	=	thickness of the Li_2O annular cartridge
t_s	=	width of the minimum spacing between tubes
t_w	=	thickness of the tube wall
T	=	temperature
T_B	=	bulk mean temperature of the helium
T_w	=	wall temperature
v	=	velocity
V	=	volume
w	=	internal heat generation
$w_{o,L}$	=	internal heat generation in the Li_2O at r = 0
$w_{o,s}$	=	internal heat generation in the structure at r = 0

γ = ratio of specific heats, C_p/C_v

Γ_N = neutron wall loading

δ = height of the first wall coolant passage

ε_t = fraction of the tube bank unit cell occupied by the tube

μ = helium dynamic viscosity

ρ = helium density

References for Section 5

1. T. Elleman, University of North Carolina, personal communication via E. Dalder, Lawrence Livermore National Laboratory (February 1982).

2. K. Okula and D. K. Sze, "Tritium Recovery from Solid Breeders," University of Wisconsin (Madison), Rept. UWFDM-351 (April 1980).

3. R. Hickman, "Some Problems with Tritium in Fusion Reactors," Technology of Controlled Thermonuclear Fusion Experiments, U.S. AEC Rept. CONF-721111 (April 1974).

4. Chemical Engineers' Handbook, R. Perry and C. Chilton, Eds., (McGraw-Hill, New York, 1973) 5th ed., pp. 3-230.

5. R. Reid, J. Praushitz and F. Sherwood, The Properties of Gases and Liquids (McGraw-Hill, New York, 1971).

6. J. Hirschfelder, C. Curtis and R. Bird, Molecular Theory of Gases and Liquids (J. Wiley, New York, 1954).

7. Chemical Engineering Division Annual Technical Report, Argonne National Laboratory, ANL-82-23, p. 135 (1981).

8. T. R. Hill, "ONETRAN, A Discrete Ordinates Finite Element Code for the Solution of the One-Dimensional Multigroup Transport Equation," LA-5900-MS, Los Alamos National Laboratory (June 1975). (The pre-release availability of ONEDANT to the study is a result of the courtesy of Donald J. Dudziak of Group T-1, Los Alamos National Laboratory.)

9. R. E. Alcouffe, "Diffusion Synthetic Acceleration Methods for the Diamond-Difference Discrete Ordinates Equation," Nucl. Sci. Eng. 64, 344 (1977).

10. R. E. MacFarlane and R. J. Bennett, LANL Internal Memo T-2-L, Los Alamos National Laboratory (August 24, 1978).

11. C. Baker, et al., "STARFIRE - A Commercial Tokamak Fusion Power Plant Study," ANL-FPP-80-1, Argonne National Laboratory (1980).

12. T. Takahashi and T. Kikuchi, "Porosity Dependence on Thermal Diffusivity and Thermal Conductivity of Lithium Oxide Li_2O from 200 to 900°C," J. Nucl. Mater., 91, 93(1980).

13. T. Kurasawa, "Thermal Expansion of Lithium Oxide," private communication from T. Kurasawa, Japan Atomic Energy Research Institute, Tokai-mura, Japan, November 24, 1981, submitted for publication to J. Nucl. Mater.

14. *O. H. Krikorian, "Estimation of Heat Capacities and other Thermodynamic* Properties of Refractory Borides," Lawrence Livermore National Laboratory, Lievermore, CA, UCRL-51043, (April 27, 1971).

15. S. Nasu, K. Fukai, and T. Tanifuji, "Microhardness and Microstructures of Neutron Irradiated Li_2O Pellets," J. Nucl. Mater., 78, 254(1978).

16. "The Oxide Handbook," edited by G. V.Samsonov, translated to English from Russian by C. N. Turton and T. T. Turton, IFI/Plenum Data Corporation, New York, 1973.

17. P. T. B. Shaffer, "Plenum Press Handbooks for High - Temperature Materials - No. 1. Materials Index," Plenum Press, New York, 1964.

18. H. Conrad, "Mechanical Behavior of Ceramic Materials - III. Deformation and Fracture Related to Design and Use," in Chemical and Mechanical Behavior of Inorganic Materials, edited by A. W. Searcy, D. V. Ragone, and U. Colombo, Wiley - Interscience, New York, 1970, pp 391-411.

19. J. B. Wachtman, Jr., "Mechanical Properties of Ceramics: An Introductory *Survey," Ceramic Bulletin 46, 756(1967).*

20. D. R. Stull and H. Prophet, "JANAF Thermodynamic Tables," second edition, U. S. National Bureau of Standards, Washington, D. C. (1971), with supplements through December 31, 1979 from M. B. Chase, Project Director, The Dow Chemical Company, Midland, MI.

21. O. Kubaschewski and C. B. Alcock, "Metallurgical Thermochemistry," fifth edition, Pergamon Press, Oxford, 1979.

22. "Handbook of the Physicochemical Properties of the Elements," edited by G. V. Samsonov, revised and updated American edition, IFI/Plenum Data Corporation, New York, 1968.

23. N. Soga and O. L. Anderson, "High-Temperature Elastic Properties of Polycrystalline MgO and Al_2O_3," J. Amer. Ceram. Soc., 49, 355(1966).

24. R. J. Roark and W. C. Young", Formulas for Stress and Strain", Fifth Edition, McGraw-Hill Book Company, New York, 1975, pp 582-586.

25. *G. W. C. Kaye and T. H. Laby, "Tables of Physical and Chemical* Constants," 14th Edition, Longman Group (London), 1973, p. 31.

26. Anon., "Class 1 Components in Elevated Temperature Service", Section III, Division 1, American Society of Mechanical Engineers Boiler and Pressure Vessel Code, Code Case N47-17, 8/30/79.

27. Anon., "USS Tenelon Stainless Steel", U.S. Steel Corporation, ADUSS-03-03496-03, December 1972.

28. P. E. Armstrong and H. L. Brown, Transactions of the Metallurgical Society of A.I.M.E., 230, pg 962, Aug. 1964.

29. T. E. Tietz and J. W. Wilson, "Mechanical Oxidation, and Thermal Property Data for Seven Refractory Metals and Their Alloys", Lockheed Missiles and Space Company, Contract No-as-60-6119-c, September 1961.

30. T. J. Heal, "The Mechanical and Physical Properties of Mg and Nb Canning Materials", in "Second International Conference on Peaceful Uses of Atomic Energy", IAEA, Geneva, 1958.

31. D. P. Laverty and E. B. Evans, "Columbium Metallurgy", D. L. Douglass and F. W. Kunz, Eds., Interscience, New York, 1961, pp 299-307.

32. Anon., "DuPont Metal Products ...Columbium Product Data', E. I. duPont de Nemours and Co., Sheet No. 3, 1967.

33. R. O. Carlson, "The Development of Optimum Manufacturing Methods for Columbium Alloy Forgings", Crucible Steel Company, Contract No. AF 33(600)-39944, ASD Interim Report 7-782(V), August 1961.

34. Anon., "B-66 Columbium (Niobium) Base Alloy Refractory Metal", Westinghouse Electric Corporation, Special Technical Data 52-364, June 1962.

35. Anon., "Hastelloy Alloy X", Stellite Division, Cabot Corporation, 10/74.

36. C. R. Tottle, "The Physical and Mechanical Properties of Niobium", Journal of the Institute of Metals, 85, April 1957, p 377.

37. Anon., "Technical Bulletin, DuPont Columbium Alloy D-31;", E.I. duPont de Nemours and Co./Thompson Ramo Wooldridge (Tapco Group) April 1960.

38. I. B. Fieldhouse, J. C. Hedge, and J. I. Lang, "Measurements of Thermal Properties", WADC TR 58-274, November 1958.

39. G. V. Smith, "An Evaluation of the Yield, Tensile, Creep, and Stress-Rupture Strengths of Wrought 304, 316, 321, and 347 Stainless Steels at Elevated Temperatures", ASTM Data Series DS552, American Society for Testing and Materials, February 1969.

40. F. W. Wiffen, "Defects and Defect Clusters in B.C.C. Metals and Their Alloys", Nuclear Metallurgy, 18, 1973, pp 176-197.

41. R. E. Gold and D. L. Harrod, Journal of Nuclear Materials, 85-86, 1979, pp 805-815.

42. D. L. Harrod and R. E. Gold, International Metallurgical Reviews, 23 (4), (No. 255), 1980, pp 163-221.

43. K. F. Smith and R. J. Van Thyne, in "Reactive Metals", W. R. Clough, Ed., Interscience, N.Y., 1959, pp 403-427.

44. M. P. Tanaka, E. E. Bloom, and J. A. Horak, "Alloy Development for Irradiation Performance", DOE/ER-0045/4, Quarterly Progress Report for Period Ending September 30, 1980, pp 82-99.

45. W. Pollack, R. W. Buckman, R. T. Begley, K. C. Thomas, and E. C. Bishop, "Development of High Strength Vanadium Alloys - Final Report", WCAP-3487-16, Westinghouse Electric Corporation, June 1967.

46. G. A. Whitlow, R. A. Nadler, and R. C. Svedberg, "Vanadium Alloy Cladding Development - Final Report", WARD-3791-47, Westinghouse Electric Coirporation, November 1970.

47. G. E. Korth and R. E. Schmunk, "Effects of Radiation on Structural Materials", J. Sprague and D. Knamer, Eds., American Society for Testing and Materials, ASTM STP 683, 1979, pp 466-476.

48. G. A. Whitlow, R. J. Horvak, S. L. Schrock, and E. C. Bishop, Journal of Less Common Metals, 18, 1969, pp 357-371.

49. Anon., "Proposed ASTM Specifications for Columbium and Columbium Alloy Mill Product Forms", Sixth Draft, American Society for Testing and Materials, March 13, 1962.

50. Anon., "Product Specification - Columbium Base Alloys", E.I. duPont de Nemours and Co., Metal Products - Pigments Department, 1962.

51. Anon., "Columbium and Tantalum Base Alloys for Structural and Nuclear Applications", Teledyne Wah Chang-Albany, 1 (2), 1962.

52. Anon., "SCb-990 Electron Beam Columbium Alloy:, Data Sheet, Stauffer Metals Division, 1961.

53. Anon.,; "Haynes Alloy Cb-751", New Product Data, Cabot Stellite Corp., 1962.

54. F. F. Schmidt and H. R. Ogden, "The Engineering Properties of Columbium and Columbium Alloys", Defense Metals Information Center, DMIC Report 188, Sept. 6, 1963.

55. A. W. Dana et al, "Columbium and Columbium Alloy Extrusion Program" E.I. du Pont de Nemours & Co., Contract No. AF-33(600)-40700, Interim Report No. 1, 6/30/60.

56. Anon., "B66 Columbium (Niobium) Base Alloy Refractory Metal", Correction Sheet, Westinghouse Electric Corporation, Special Technical Data 52-364, November 1, 1962.

57. Letter from J. R. Lane, National Academy of Sciences National Research Council, to members of the Alloy Requirements and Selection Subpanel Refractory Metals Sheet Rolling Panel (October 12, 1962).

58. Begley, R. T., "Development of Niobium-Base Alloys", Westinghouse Electric Corp., WADC TR57-344, Part V (January, 1961.

59. Clark, J. S., "Columbium Alloy Extrusion Program", E.I. duPont deNemours and Co., Inc., Contract No. AF33(600)-40700, Phase V: Tubing Program Interim Report VII (February, 1963).

60. Personal communication with G. P. Trost, Metals and Controls Inc., regarding "Development of Optimum Processing Parameters for Refractory Metal Foil", Contract No. AF 33(657)-9384 (June, 1963).

61. Savage, C. H., and Root, D. C., "Determination of Mechanical and Thermophysical Properties of Coated Refractory and Superalloy Thin Sheet", North American Aviation, Inc., Contract No. AF33(657)-9416, Third Progress Report, SID 62-1219-3 (April 15, 1963).

62. Anon., "Supplement to Alloy 718 Bolting Material Code Case", Atomics International, Unpublished Manuscript, 11-25-74.

63. J. W. Tackett, "The Creep-Rupture Properties of Hastelloy Alloy X Sheet", Tech. Dept. Rpt. No. 8745, Stellite Division of Cabot Corp., 1975.

64. Anon., "Component and Systems Development Program", Quarterly Progress Report, General Atomic Company, Report No. GA-A13778, 12/31/75.

65. C. R. Brinkman et al, "Application of Hastelloy X in Gas-Cooled Reactor Systems", ORNL TM-5405, October 1976.

66. D. I. Roberts, S. N. Rosenwasser, and J. F. Watson, "Alloys for the Eighties", R. Q. Barr, Ed., AMAX Corp., 1981, pp 119-130.

67. J. B. Conway, "Stress-Rupture Parameters: Origin, Calculation, and Use," Gordon and Breach Science Publishers, Inc., New York, 1969.

68. E. S. Bartlett and J. A. Van Echo, "Creep of Columbium Alloys", Battelle Memorial Institute, DMIC Memorandum 170, June 24, 1963.

69. R. T. Begley, "Development of Niobium-Base Alloys", WADL TR 57-344, Part I; Westinghouse Electric Corporation, November 1957.

70. H. E. McCoy, "Creep-Properties of the Nb-1% Zr Alloy", Journal of the Less Common Metals, 8, 1965, p 20.

71. R. W. Hall and R. H. Titran, "Refractory Metals and Alloys III: Applied Aspects, Part 2", R. I. Jaffee, Ed., Gordon and Breach, 1966, p 885.

72. J. R. Stewart, W. Lieberman, and G. H. Rowe, "Columbium Metallurgy", Interscience Publishers, New York, 1961, pp 407-432.

73. D. P. Gregory and G. H. Rowe, "Columbium Metallurgy", Interscience Publishers, New York, 1961, pp 309-339.

74. W. H. Chang, "A Study of the Influence of Heat Treatment on Microstructure and Properties of Refractory Alloys", General Electric Company, ASD-TDR-62-24, April 1962.

75. R. L. Churchill, "Compilation of Unpublished Materials Information", Phase II, Report FPR-003, General Dynamics Corporation (Forth Worth, TX), November 1962.

76. R. L. Stephenson, "Comparative Creep-Rupture Properties of D-43 and B-66 Alloys", ORNL TM-944, November 1964.

77. Anon., Compilation of Data from US DOE-DAFS and US DOE-ADIP Quarterly Progress Reports.

78. D. J. Mazey, J. A. Hudson, and J. M. Titchmarsh, Journal of Nuclear Materials, 107, August 1982, pp. 2-19.

79. M. Snykers and E. Ruedl, "Fusion Technology 1980," Proceedings of the Eleventh Symposium, IAEA, Pergammon Press, Vol. 2, 1981, pp. 1269-1273.

80. M. Kangalaski, S. Peterson, J. Perrin and R. Wulla___, Nuclear Applications and Technology, 9, October 1970, pp. 550-560.

81. F. W. Wiffen and P. J. Maziasz, Journal of Nuclear Materials, 104 (1-3), 1981, pp. 821-826.

82. R. C. Maninger and D. W. Dorn, "Gases in Radioactive Waste Management for Fusion Power," Lawrence Livermore National Laboratory, to be published.

83. R. C. Maninger, "Environment and Safety - Major Goals for MARS," Lawrence Livermore National Laboratory, to be published.

SECTION 6

HIGH-TEMPERATURE BLANKET

Contributors:

D. Rowe, G. Woodruff, M. Lloid

TABLE OF CONTENTS

TABLE OF CONTENTS

LIST OF TABLES

LIST OF FIGURES

6.0 HIGH-TEMPERATURE BLANKET

The General Atomic Sulfur-Iodine Thermochemical Cycle discussed in Section 10 has thermal energy requirements that can be split into two temperature ranges. The process requires approximately 22% of the energy at high temperature (~1125 K) and approximately 78% of the energy at a lower temperature (~870 K). Section 5 presented a concept under evaluation at LLNL where all of the thermal energy is supplied at 875 K using a helium-cooled, tritium breeding, blanket. A fraction of this thermal energy is directed to the process and the remainder would be used to produce electricity. A portion of the electricity is combined with that from the Direct Converter and used to provide the high temperature energy portion by Joule-heating the SO_3 Decomposer. This section considers an alternate approach being evaluated at the University of Washington where part of the energy is generated in a high temperature blanket and is used to provide the high temperature energy fraction for SO_3 decomposition. The resulting reactor concept, therefore, has two temperature-zones and each temperature zone supplies its required fraction to the process.

During the previous study for FY 1981[1], the two temperature-zones were contained in the same blanket and the blanket was divided into radial zones. For the current FY 1982 study, the low and high temperature blankets are separate, and the TMR is divided axially into low and high temperature-zones.

6.1 PROCESS AND DESIGN REQUIREMENTS

The high temperature blanket design must satisfy the requirements of the thermochemical process and geometric constraints of the Tandem Mirror Fusion Driver; plus, temperature limitations and a variety of factors that comprise a set of design criteria. This section considers the process requirements in summary detail as it affects the blanket design.

6.1.1 System Process Requirements

Section 10 discusses the system energy flow and temperature requirements as they would apply to a two-temperature blanket. There are two parallel streams from the reactor to the process. One is at high temperature and supplies energy to the SO_3 decomposer. The other is at low temperature and supplies energy to other parts of the thermochemical process and to electrical energy production. The thermochemical process requires thermal energy in the range from 1050 to 1150 K. The amount required at this temperature depends upon the specifics of the plant integration but is generally on the order of 22%.

Helium is used as a working fluid because of its technology base in high-temperature process-heat applications. Liquid metals could also be used but were not selected because of potential safety problems.

6.1.2 Design Criteria

In addition to the system process requirements there are a number of other factors affecting design.

The blanket design must accommodate the geometric constraints imposed by the fusion driver with its 4 m incremental location of field coils. The blanket is assumed to be modular and fit within the field coils. The wall loading is taken to be 2.0 MW/m^2 and the first wall radius is 1.5 m.

The lower temperature blanket is used for tritium breeding and the overall tritium breeding ratio is to be at least 1.1. The requirements for tritium breeding and the fraction of energy generated in the high-temperature-zone must both be satisfied since these related requirements are critical to the success of the concept. Since the high-temperature blanket does not breed tritium, breeding in the low temperature blanket must be quite good.

The flow rates in the process components are fixed by the process requirements. The blanket design however must maintain temperatures of the flow and structure to acceptable levels consistent with the performance capability of the materials involved. The flow channel and piping design must also have sufficiently low pressure drop. A pressure drop of 0.04 of the absolute helium pressure is a typical limit for high temperature helium loops.

6.2 SUMMARY DESIGN DESCRIPTION

The TMR is divided into axial segments as defined by the field coil spacing of 4 m. Each blanked segment (ring module) is 2 m long and can be either a low or a high temperature blanket. The fraction of the TMR central cell length covered by high temperature blanket segments is determined from considerations of tritium breeding and the fraction of high temperature required for the thermochemical process.

6.2.1 Ring Module

The high temperature blanket ring module has the same general design as the low temperature blanket ring module described in Section 5. Each module consists of 18 canisters that surround the plasma and the associated connecting piping (ring headers) as shown in Figure 6.2-1.

6.2.2 Canister Module

Figure 6.2-2 shows the design philosophy for the high temperature canister. The design is "staged" thermally such that the pressure boundary can operate at a much lower temperature than the high temperature central region. This is accomplished with dual coolant paths--one for the first wall and the other for the primary coolant. The first wall coolant removes energy generated within the first wall and heat lost from the primary coolant entrant flow. The primary coolant flows radially inward toward the TMR centerline. The direction reverses at the plenum and flows radially outward through the high temperature generating region. A structural wall is used to separate the two streams; and any heat loss is recovered by raising the plenum temperature. The heat generating region is currently taken to be a spherical packed bed. Concentric pipes are used for inlet and outlet flows to maintain the pressure boundary at the minimum helium temperature and to reduce heat loss from the high temperature stream. Figure 6.2-3 shows the dimensions used for the canister.

6.2.3 Transport Piping

The transport of high temperature process fluids requires special considerations to reduce heat loss and to maintain structural integrity of the pressure boundary. The general philosophy of the transport piping design from the canister module to the process is shown in Figure 6.2-4 . The design uses concentric insulated pipes where the hot helium is carried in the center and a

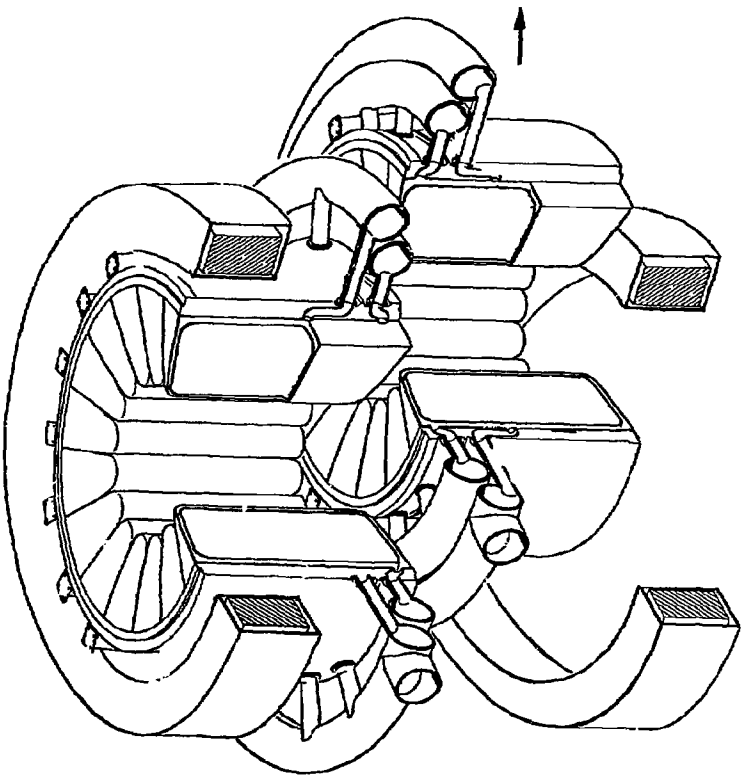

Figure 6.2-1. Ring Module Assembly.

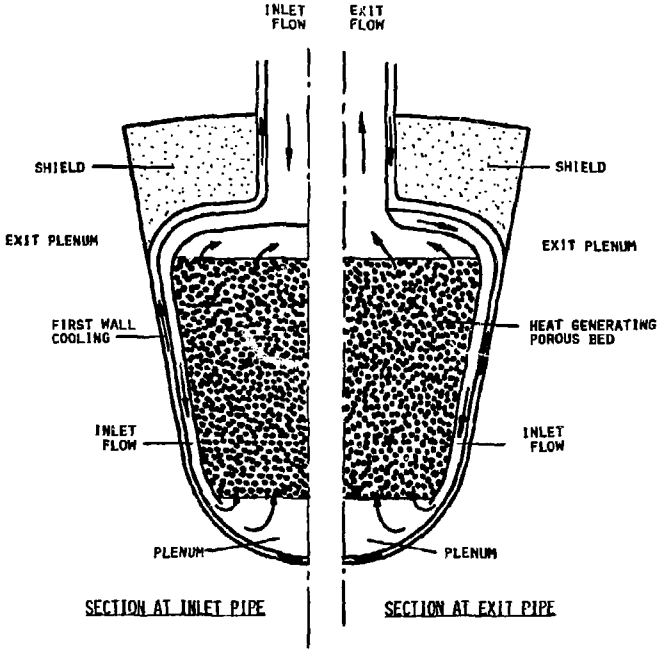

Figure 6.2-2 High temperature blanket module.

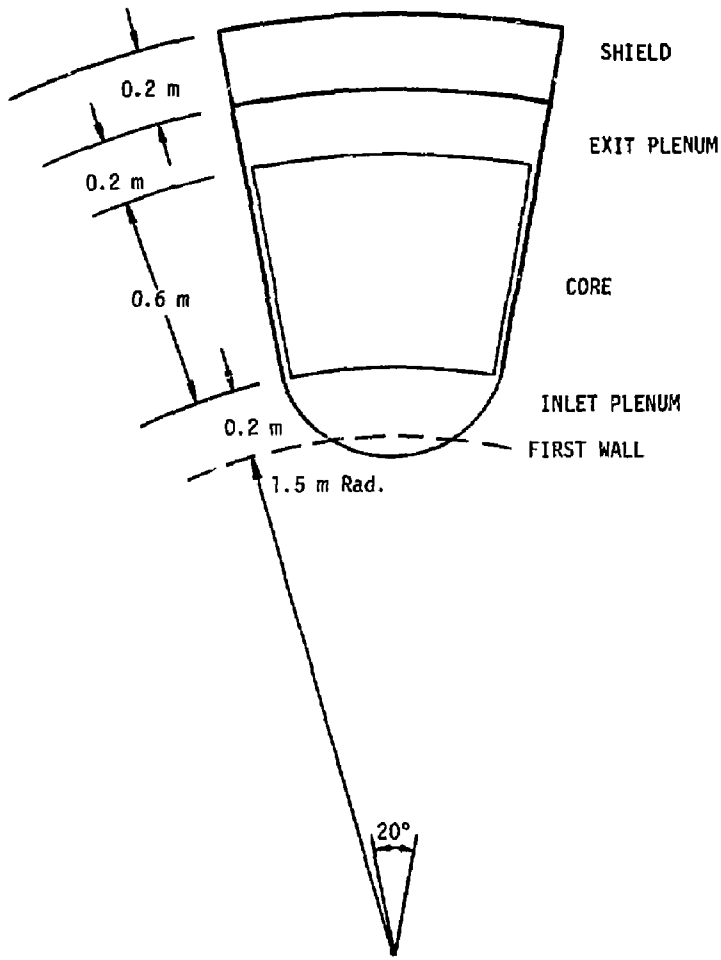

Figure 6.2-3 Principal dimensions of the high temperature blanket canister.

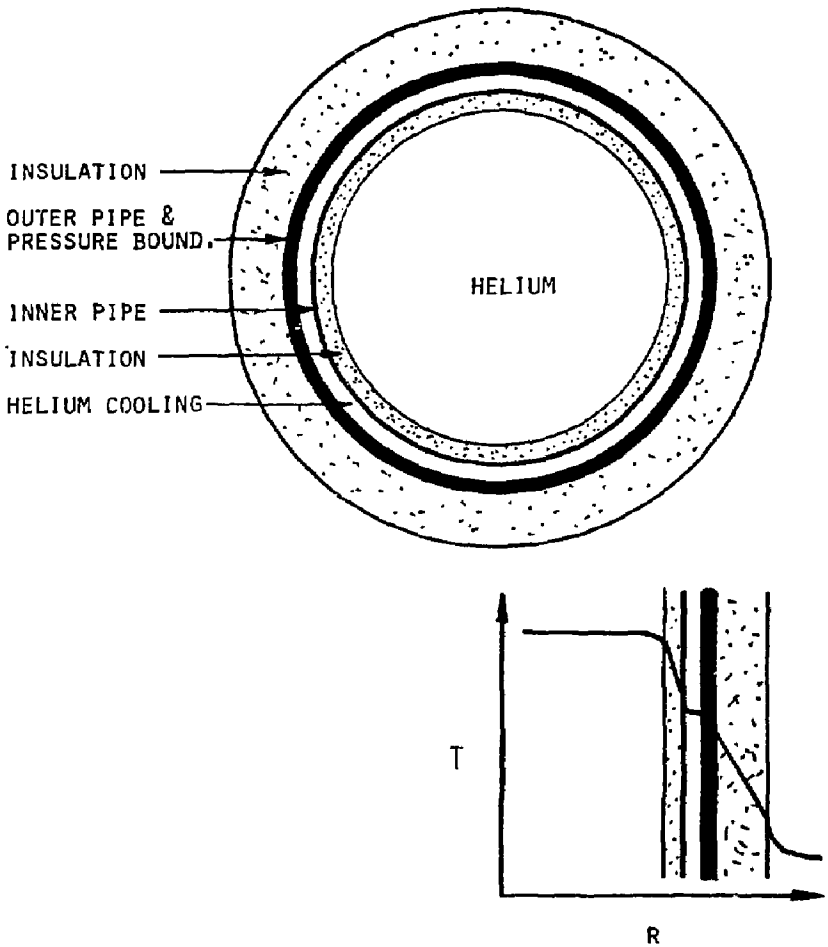

Figure 6.2-4 High temperature helium transport pipe.

coolant is carried in the outer annulus. The helium coolant maintains the outer pressure boundary at a moderate temperature to assure strength. Heat loss from the transported helium is kept small by the internal insulation. Pressure balancing between the two helium streams relieves the stress load on the inner pipe and insulation.

6.3 NEUTRONICS ANALYSIS

An alternative to the joule boosted concept where the high temperature heat for the decomposer is produced electrically is a two zone blanket design where the high temperature heat is produced directly in the blanket. This can be accomplished by either radial or axial zoning. An axial-zoned system divides the blanket axially into a high temperature blanket, which usually does not produce tritium (in order to avoid difficulties with tritium production and control at high temperatures), and a low temperature blanket. The low temperature blanket is required to breed tritium at a rate that is adequate to fuel the entire reactor (see Figure 6.3-1). A radially zoned blanket consists of only one type of blanket, and divides the tritium breeding and high temperature functions radially, with the tritium breeding region usually being located near the first wall, and the high temperature region in the outer portion of the blanket.

A primary concern associated with any two zone blanket design, whether axial or radial, is the tradeoff between tritium breeding and the fraction of energy deposited in the high temperature zone. In the previous year's work the feasibility of a radially zoned blanket was examined.[1] This design has been replaced by the axially zoned concept depicted in Figure 6.3-1. This type of design faces many of the same problems as the radially zoned blanket but could result in a less complicated design. In this section are described the neutronics analyses of the high temperature modules for the axially zoned blanket design.

The neutronics calculations for these analyses have been performed with the Oct. 1980 version of the one dimensional discrete ordinates transport code ONEDANT.[2] This code is described in more detail in Section 5.5.

6.3.1 Energy Split and Tritium Breeding

In an axially zoned blanket design, the fraction of heat produced in a high temperature, F_H, is dependent upon several variables: TBR, the tritium breeding ratio; M_H and M_L, the high and low temperature zone blanket energy

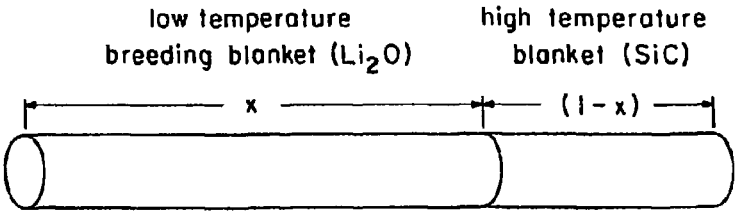

$T_L = 1.10$

$M_L = 1.16$

$M_H = 1.30$

$$F_H = \frac{(1-x)M_H f}{(1-x)M_H + xM_L} = 0.04$$

$$x = \frac{T_{min}}{T_L}$$

$f = 0.84$ (Rowe)

Fig. 6.3-1. Schematic of an Axial-Zoned TMR With Low-Temperature and High-Temperature Modules

multiplication factors; f, the fraction of heat deposited in the high temperature zone and recovered at high temperature. Figure 6.3-2 illustrates the relationship between these factors. The overall breeding, TBR, is equal to the breeding ratio in the breeding region, denoted by T_L, times the fraction of the overall length devoted to the breeding region, denoted by x. Since the dominant constraint is a value of 1.1 for TBR, once T_L is determined the value of x becomes fixed as shown in the single curve for the right ordinate in Figure 6.3-2. Obviously, higher values of T_L permit the use of shorter fractional lengths of the breeding region. Similarly, F_H is then also determined using the equation shown in Figure 6.3-1. The family of curves in Figure 6.3-2 show that F_H increases with both increasing values of T_L (because a greater fraction of the length can be devoted to high temperature operation) and M_H (because more energy is being deposited in the high temperature blanket).

The reference high temperature blanket design is the silicon carbide module design described in Section 6.1. Two other high temperature blankets were also analyzed neutronically, a helium cooled aluminum oxide blanket similar to the silicon carbide blanket, and a sodium cooled blanket with TZM structure. The results of all three designs are presented in Table 6.3-1.

The silicon carbide and aluminum oxide designs have similar results with the latter producing a higher energy multiplication factor. Neutronically, the TZM/Na design is superior to both, with a higher energy multiplication factor and much higher f value. The higher f value is a consequence of the assumption that a separate first wall cooling system would not be required for this system. These neutronics advantages must, of course, be weighted against the disadvantages of a Na-cooled design, including safety and MHD pressure drop. There are also advantages to a SiC design in terms of materials properties.

Several axial zoning blanket combinations are listed in Table 6.3-2. The current value required for F_H is approximately 25 to 30%, which implies that the tritium breeding ratio in the low temperature blanket must be in the 1.4 to 1.5 range. The initial reference low temperature blanket design had a breeding ratio of only 1.1. The results given in Table 6.3-2 show that while such a design can breed adequately for a one zone joule boosted concept,

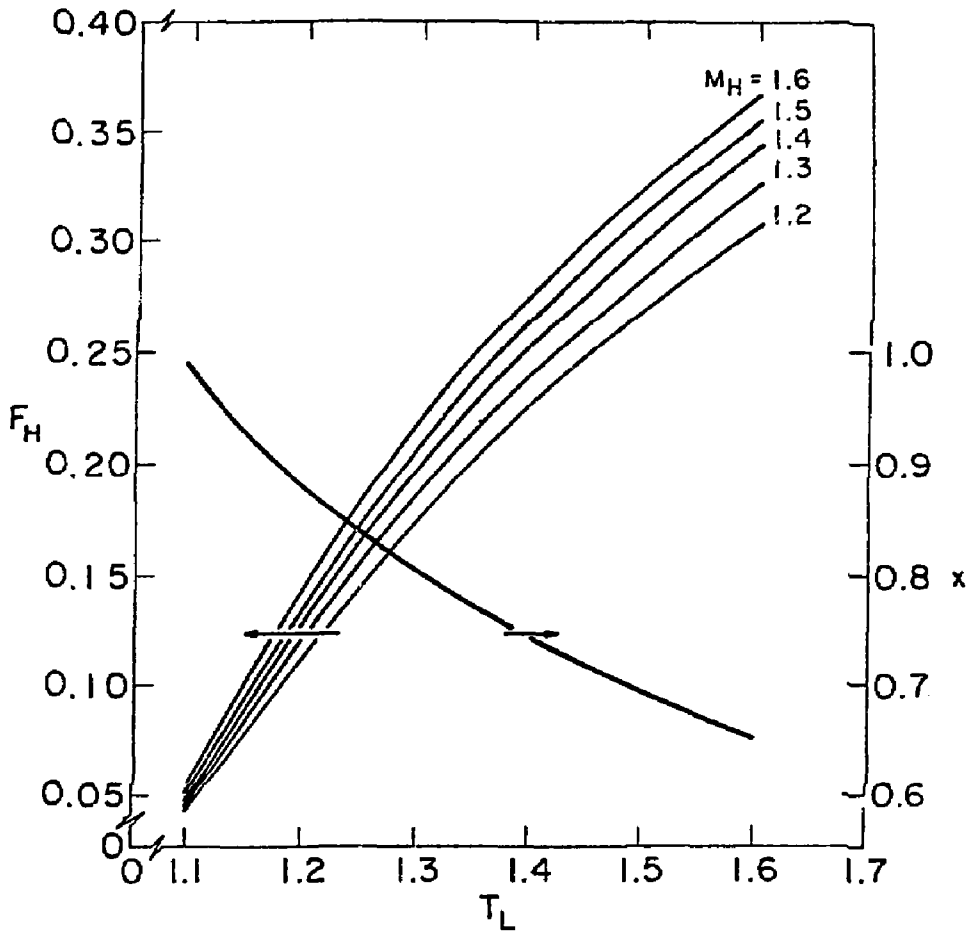

Fig. 6.3-2. High Temperature Fraction and Breeding Length Fraction vs Breeding Ratio

Table 6.3-1 High Temperature Blanket Neutronics Results

Fractional Energy Deposition	SiC	Al_2O_3	Na/TZM
First Wall	.11	.063	.034
Insulation	.01	-	-
High Temperature Zone 1	.468	.633	.206
High Temperature Zone 2	.217	.189	.225
High Temperature Zone 3	.103	.074	.253
High Temperature Zone 4	.052	.028	.261
Shield	.04	.008	.021
Blanket Energy Multiplication	1.30	1.40	1.47
Max. First Wall Heat Deposition (Watt/cc - at 2 MW/m^2)	25.27	29.16	25.49
Superconductor Insulation			
Radiation Dose in Grays (30 yrs at 2 MW/m^2)	3.66×10^8	2.88×10^7	3.47×10^7
Fraction of Energy Deposited in the Superconductor	7.96×10^{-6}	6.3×10^{-7}	7.1×10^{-7}

Table 6.3-2 Neutronics Results for Axial Zoning Combinations

LOW TEMPERATURE BLANKET

	T_L	M_L
A. Li_2O	1.10	1.16
B. Goal	1.40	1.10

HIGH TEMPERATURE BLANKET

	M_H	f
1. SiC	1.30	0.84
2. Al_2O_3	1.40	0.84
3. TZM/Na	1.47	0.96

COMBINATIONS

	X	F_H(%)
A - 1	0.95	4.3
A - 2	0.95	4.6
A - 3	0.95	4.8
B - 1	0.75	23.8
B - 2	0.75	25.0
B - 3	0.75	29.4

higher values are needed for the breeding region of an axial-zoned reactor. The results described in more detail in Section 5.5.3 indicate that the axially zoned breeding requirement can be met with a design using a neutron multiplier and enriched lithium oxide. It is also possible that a version of the final reference design incorporating tenelon structure and a high volume fraction of Li_2O could be successful.

6.3.2 Radial Power Distribution

The radial power distribution is computed with the ONEDANT code by first determining the spatial flux dependence of each neutron and gamma group. The energy deposition in eV/cm^3 per source neutron is then calculated using the appropriate neutron and gamma kerma factors. Conversion of MW/m^3 is dependent upon the wall loading, which, in this case is 2 MW/m^3. The radial power distribution of the silicon carbide blanket is shown in Figure 6.3-3. In order to calculate the energy deposition in the module side walls, the main silicon carbide region was divided into 4 radial 20 cm zones. Each zone was then homogenized to include the appropriate contribution from the graphite felt insulation and the module side walls. These values are listed in Table 6.3-3.

The results of these calculations indicate that 78% of the energy is deposited in the silicon carbide region, 11% in the first wall, 6% in the walls (included in zones 1-4 in Table 6.3-1), 1% in the graphite felt thermal insulation, and 4% in the outer shield.

The power density in the first wall is relatively high. This is because the material adjacent to the first wall is silicon carbide which is a fairly low-Z material. This result is to be expected consistent with the discussion in Section 5.5.3. The spatial gradient of the power density is also fairly high with a decrease of approximately a factor of 30 over the 0.8 meters of the SiC region.

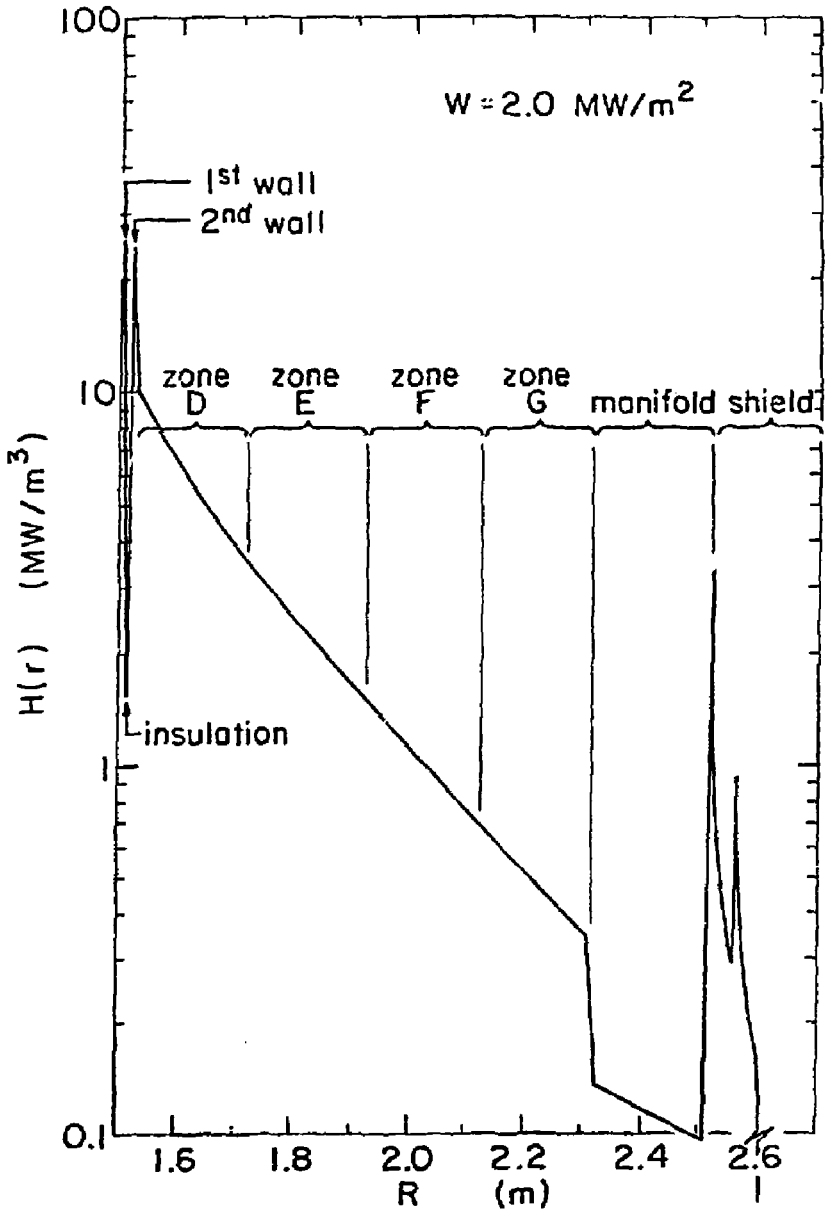

Fig. 6.3-3. Power Density vs Radius, High Temperature Module

Table 6.3-3 SiC High Temperature Blanket Configuration

Ro(m)	Description	Composition			
1.500	Vacuum				
1.505	First Wall	St. St.			
1.515	Insulation	C 14%, void 86%			
1.518	Second Wall	St. St.			
		SiC	St.St.	Graphite	Void
1.718	Zone D	55.14	3.19	3.19	38.48
1.918	Zone E	55.68	7.83	2.83	38.66
2.118	Zone F	56.10	2.56	2 56	38.78
2.318	Zone G	56.46	2.33	2.33	38.88
2.518	Manifold	St. St. 10%			
2.558	Shield Zone A	Same as Li_2O Reference Configuration (Table 5.5-2)			
2.648	Shield Zone B				
2.758	Shield Zone C				
2.808	Shield Zone D				
2.898	Shield Zone E				
2.998	Shield Zone F				
3.098	Dewar				
3.100	S.C. Coil				

6.3.3 Radiation Damage

Table 6.3-1 listed the values of the superconducting insulation radiation dose and the fraction of heat deposited in the coil and dewar system. The values for the silicon carbide blanket are quite high, mainly due to the fact that silicon carbide is not a very good shielding material. Based on a limit of 5×10^7 grays, the insulation would only have a 4 year lifetime. An additional 20 cm of shielding will probably be required in order to reduce the refrigeration power requirements and increase the insulation lifetime of acceptable values.

A general discussion of the parameters relevant to radiation damage and the limitations considered acceptable is included in Section 5.5.2.

6.3.4 Neutronics Conclusions

Axial zoning is an attractive option for a fusion reactor designed to produce high temperature heat for a synfuel plant. The physical separation of the high temperature energy recovery, and the tritium breeding has the virtues of blanket module simplicity (and, therefore, probably reliability), and more efficient use of space (and, therefore, smaller field coils and lower cost) by requiring only one cooling system per module. Any radial-zoned system is likely to suffer by comparison in these respects.

The high temperature module analysed in this work appears to be a credible approach in terms of neutronics performance. It must, however, be coupled with a low temperature module which can produce a tritium breeding ratio ≥ 1.4. Of the options considered thus far, the most promising appears to be a Li_2O design with a lead-zirconate multiplier as described in Section 5.5.3.

6.4 BLANKET THERMAL-HYDRAULIC ANALYSIS

The thermal-hydraulic analysis is concerned with the calculation of: 1) coolant and structural temperature; 2) heat loss from the high temperature stream; and 3) pressure drop through various flow paths. The analysis was performed by using an analytical model that considers the basic heat transfer and flow processes within the canister.

The heat transfer processes considered are shown in Figure 6.4-1. Thermal energy generated within the first wall structure is transferred to the first wall coolant stream. There is also heat transferred to the first wall coolant from the energy generated within the insulating wall and from heat lost through that wall from the primary coolant inlet stream. The energy transferred to the first wall coolant is lost from the high temperature zone but can be used for lower temperature energy loads. Energy generated within the core is transferred to the primary coolant which is heated to its maximum temperature at its exit from the core. There is some heat loss from the core region to the inlet flow because of the temperature difference. There is also transfer of energy generated in the core wall to inlet flow. Those heat transfers are not lost but only increase the inlet temperature enroute to the inlet plenum. The analytical model uses simplified thermal energy balances and heat transfers based on key temperatures.

Pressure drop through various components of the coolant paths are computed based upon the results of the thermal analysis. In general the analysis starts with a set of given temperatures (in and out) and the module power from which the flow rate is calculated. The flow rate is used to define coolant velocity, heat transfers and friction coefficients.

The following discussion presents additional details of the analysis for the first wall and high temperature region.

6.4.1 First Wall Analysis

The first wall is assummed to be adiabatic (no heat transfer) at its outer surface so all generated energy flows through the inner surface to the first wall coolant. The resulting temperature of the first wall therefore exceeds

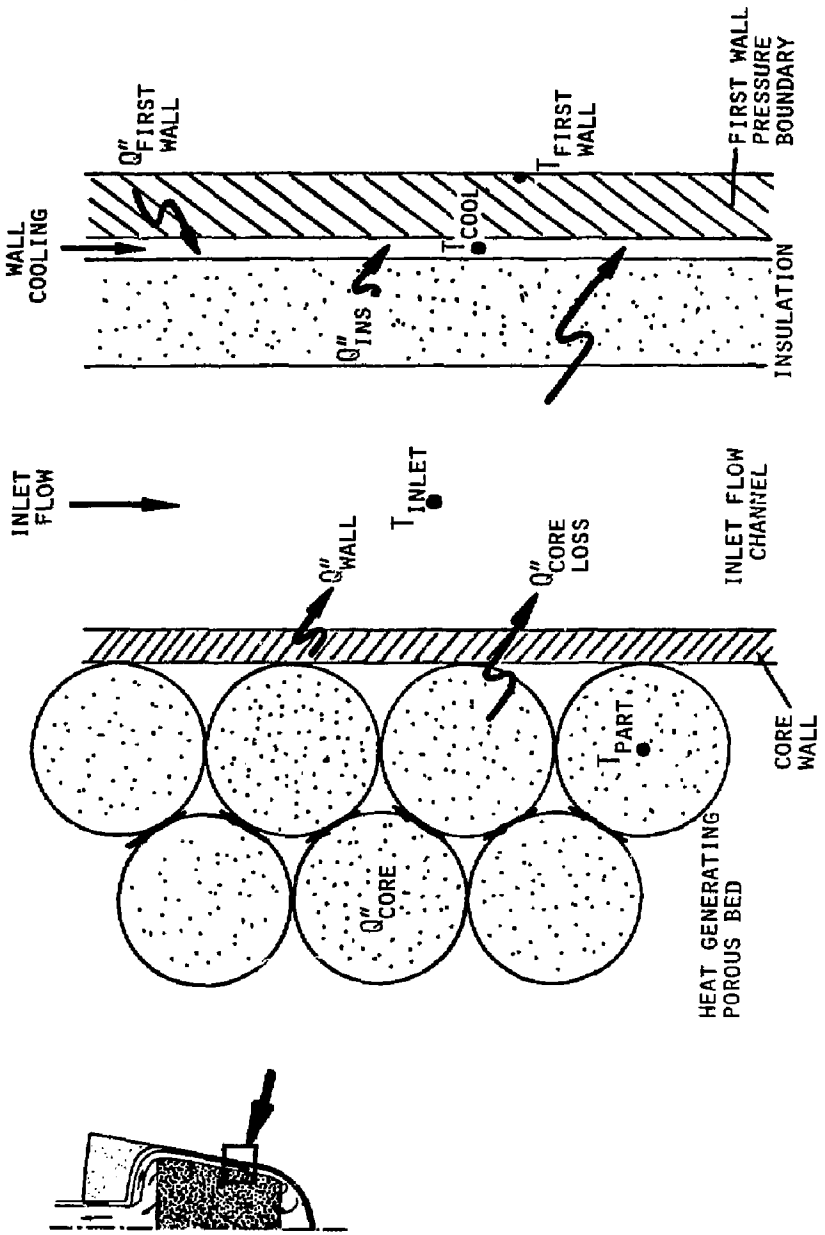

Figure 6.4-1 Illustration of heat transfer processes.

the coolant temperature by the sum of the temperature rise at the inner surface plus the rise in the metal. The most limiting location is at the "nose" of the canister and the maximum first wall temperature is estimated from

$$T_{fw} = T_{cool} + \frac{q'''_{max_{fw}} t_{fw}}{h_{fw}} + \frac{q'''_{max_{fw}} t_{fw}^2}{2k_{fw}} \qquad (6.4\text{-}1)$$

where T_{cool} is the average first wall coolant temperature, q''' is the maximum first wall power density, t is the first wall thickness and k is the first thermal conductivity. The flowing helium heat transfer coefficient h is defined by the Dittus-Boelter relationship[3]

$$\frac{hD}{k} = 0.023\ Re^{0.8} Pr^{0.4} \qquad (6.4\text{-}2)$$

where the Reynolds (Re) and Prandtl (Pr) numbers are defined in the standard way.

The first wall cooling flow rate is set to satisfy the desired inlet and exit temperatures and the total heat load defined as

$$q_{\substack{fw \\ channel}} = q_{fw} + \left(q''_{ins} + q''_{loss}\right) A_{ins} \qquad (6.4\text{-}3)$$

where all energy generated from the first wall and inslulation is assumed transferred to the coolant. The heat loss through the insulation is given by

$$q''_{loss} = u_{loss} A_{ins} (T_{inlet} - T_{cool}) \qquad (6.4\text{-}4)$$

where

$$u_{loss} = \frac{1}{1/h_{channel} + (t/k)_{ins} + 1/h_{fw}} \qquad (6.4\text{-}5)$$

and the heat transfer coefficients are defined by using Equation (6.4-2). The pressure drop is calculated from

$$\Delta P = \frac{fL}{D} \frac{1}{2} \rho v^2 \qquad (6.4\text{-}6)$$

where the friction factor is defined as

$$f = 0.186\ Re^{-0.2} \qquad (6.4\text{-}7)$$

to represent friction factor in smooth channels[4]. The flow channel thickness is selected to maintain an acceptably low pressure drop.

The various parameters used for the first wall calculations are summarized in Table 6.4-1 and the results are in Table 6.4-2 . The important results are as follows:

1) A first wall temperature of 835 K located at the "nose" of the canister. This is 67 K above the average coolant temperature of 775 K.

2) A channel width of 3 mm gives a pressure drop of 0.56 atm. With an absolute pressure of 50 atm, this gives $\Delta P/P = 0.011$ which is acceptable.

3) The fraction of high temperature module energy lost to the first wall coolant is 0.12 plus 0.04 loss to the shield giving a total high temperature zone energy loss fraction of 0.16.

6.4.2 High Temperature Region

The primary inlet flow is heated enroute to the plenum. The plenum temperature is given by

$$T_{plen} = T_{inlet} + \left(q''_{\substack{core \\ wall}} + q''_{\substack{core \\ loss}}\right) A_{wall} + q''_{loss} A_{ins} \qquad (6.4\text{-}8)$$

All energy generated in the core wall is assumed to be transferred to the inlet flow. The heat transfer through the wall is defined analogously to Equation 6.4-4 but with an assumed high heat transfer at the inner core wall.

All energy generated within the core is transferred to the primary coolant. This heats the coolant from the inlet plenum temperature to the exit temperature which is calculated from

$$T_{exit} = T_{plen} + q''_{core} A_{core} - q''_{\substack{core \\ loss}} A_{wall} \qquad (6.4\text{-}9)$$

Adding Equations (6.4-8) and (6.4-9) gives

$$T_{exit} = T_{inlet} + q''_{core} A_{core} - q''_{loss} A_{ins} \qquad (6.4\text{-}10)$$

which indicates that the heat loss through the insulation is the net loss from the high temperature region. The primary flow rate is adjusted iteratively to match the desired inlet and outlet temperature and heat loss.

The core is assumed to consist of a bed of spherical particles. The temperature rise to the center of a particle can be calculated from

$$\Delta T_{part} = \frac{q'''}{(1-\epsilon)} \frac{D_p}{6h_{surf}} + \frac{q'''}{(1-\epsilon)} \frac{D_p^2}{24k_p} \qquad (6.4\text{-}11)$$

The spheres are assumed to have a porosity (ϵ) of 0.4 and a thermal conductivity of 25 W/m-k which is typical of Silicon Carbide. The heat transfer coefficient for a bed of spheres is estimated from the Denton[5] relationship given by

$$\frac{hD_p}{k} = 0.8\, Re_p^{0.7} Pr^{0.333} \qquad (6.4\text{-}12)$$

where particle diameter D_p is used for the characteristic dimension. At the maximum power density near the core inlet, Equation (6.4-11) gives a particle temperature rise of 29 K. At the average power density of the particle the temperature rise is 15K. The maximum core temperature is estimated at 1175 K.

The pressure drop along the primary core coolant path has several major components: inlet and outlet nozzles, inlet channel and spherical particle bed. The flow areas of those components were sized such that $\Delta P/P \leq 0.01$.

The pressure drop through the nozzles was calculated using pressure loss coefficients of 2.0 each. The pressure drop through the inlet channel was calculated using the friction factor defined by Equation (6.4-7) plus a plenum pressure loss coefficient of 1.0.

The pressure drop through the packed bed of the spheres was calculated by using

$$\Delta P_{core} = \frac{1}{2} K_{core} \rho v^2 \qquad (6.4\text{-}13)$$

where v is the velocity based on the core flow area without spheres. K_{core} was calculated from the Ergun[5] relationship

$$K_{core} = 2 \frac{L}{D_p} \frac{(1-\varepsilon)}{\varepsilon^3} \left[1.75 + 150 \frac{(1-\varepsilon)}{Re_p} \right] \quad (6.4.14)$$

where ε is the porosity (0.40).

A summary of selected parameters used for high temperature region calculations is summarized in Table 6.4-1 and the results are presented in Table 6.4-2 . The important results are as follows:

1) The maximum spherical particle temperature is estimated to be 1175 K based on core average power density and exit plenum temperature. (The particle diameter is 15 mm based on thermal stress considerations).

2) The core wall thickness of 3 mm is sufficiently thin to keep its temperature midway between the inlet and exit temperature.

3) The fraction of the core energy lost through the insulation to the first wall coolant is 0.04.

4) The most limiting pressure drop components are the inlet and outlet nozzles. The pressure drop there is responsible for the primary coolant pressure of 50 atm.

Table 6.4-1 Key parameters used for the thermal-hydraulics analysis.

First Wall Loading	2 MW/m^2
Neutron Multiplication	1.3
Canister Power	2.72 MW
Power Fractions:	
Core	.78
Core Wall	.06
Insultaion	.01
First Wall	.11
Shield	.04
Power Densities:	
First Wall (max)	18 MW/m^3
Spheres (average)	17.5 MW/m^3
Spheres (max)	34.1 MW/m^3
Primary Helium Coolant	
Pressure	50 atm
Inlet Temperature	1040 K
Exit Temperature	1160 K
First Wall Helium Coolant	
Pressure	50 atm
Inlet Temperature	750 K
Exit Temperature	800 K

Table 6.4-1 Continued.

Packed Sphere Bed:	
Sphere Diameter	0.15 m
Porosity	0.40
Thermal Conductivity	25 W/m-k
Length	0.6 m
Width	0.7 m
Core Wall:	
Thickness	0.003 m
Thermal Conductivity	35 W/m-k
Length	0.90 m
Inlet Flow Channel:	
Thickness	0.025 m
Hydraulic Diameter	0.050 m
Length	0.90 m
First Wall:	
Thickness	0.006 m
Thermal Conductivity	40 W/m-k
FW Coolant Channel:	Helium
Channel Thickness	0.003 m
Hydraulic Diameter	0.006 m
Length	2.5 m
Insulation:	
Thickness	0.01 m
Thermal Conductivity	0.08 W/m-k

Table 6.4-2 Thermal-hydraulic analysis results for high-temperature canister.

Structure Temperatures		
First Wall (max)		835 K
Core Spheres (max)		1175 K
Core Wall (max)		1160 K
Insulation (max)		1067 K
Helium Flow Rates		
Primary Coolant		3.65 kg/sec
First Wall Coolant		0.58 kg/sec
Velocity and Pressure Drop		
Inlet Pipe	55 m/sec	0.069 atm
Inlet Flow Channel	31 m/sec	0.011 atm
Core	1.2 m/sec	0.021 atm
Outlet Pipe	55 m/sec	0.063 atm
First Wall	59 m/sec	0.556 atm
Heat Transfer Coefficients		
First Wall Channel		3725 W/m^2-k
Inlet Channel		1125 W/m^2-k
Core		1778 W/m^2-k
Heat Transfers		
From Core Spheres		2.124 MW
Core Helium to Inlet Channel		.347 MW
Core Wall to Inlet Channel		.163 MW
FW to Coolant		.299 MW
Insulation to FW Coolant		.027 MW
Inlet Channel to FW Coolant		.008 MW
Shield Cooling		.109 MW

6.5 STRESS ANALYSIS

Stress analysis was performed to assure reasonable sizing of the first wall thickness for pressure containment and to size the core spheres based on thermally induced stresses. Additional discussion of canister module stresses is included in Section 5.0.

6.5.1 First Wall

First wall hoop stress was calculated to help determine the required thickness of the first wall. It is desired to have a thin first wall to reduce temperatures but a thick wall for strength. The circumferential hoop stress at the "nose" of the canister is most limiting and can be calculated by[6]

$$\sigma_t = \frac{R}{t} (P_i - P_o)$$

where $(P_i - P_o)$ is the pressure difference (50 atm), R is the radius of curvature (0.13 m) and t is the thickness (0.006 m). The resulting stress of 110 MPa (13000 psi) is reasonable.

6.5.2 Core Spheres

Each sphere in the core will have thermal stresses because of the radial temperature gradients existing in each sphere. The inside of the sphere is hotter than the outside so, the differential expansion causes compressive stress at the inside and tensile stress at the outside. The maximum tensile stress at the surface of the sphere at the maximum power density is limiting and can be calculated from[7]

$$\sigma_{t\ max} = \frac{\alpha E}{1 - \nu} \frac{2q'''R^2}{30k}$$

The property values used are $\alpha = 26 \times 10^{-6}$, $\nu = 0.3$, $k = 25$ W/m-k, $R = 0.0075$ m, $E = 1.38 \times 10^5$ MPa, $q''' = 16.6$ MW/m^3 and result in a stress of 12.8 MPa (1854 psi).

6.5.3 Other Considerations

There are additional stress considerations important to the canister design. These are primarily concerned with the stresses in the pressure boundary of the canister. Each canister is considered to be self supportive of its neighbor.

This works well for the flat surfaces of canisters in a ring because depressurization in one would lead to simultaneous depressurization in the others. There could be a problem with the ends, however, depending upon the degree of axial isolation of each ring module. Stresses in these end regions have not been considered for the high temperature canister.

While the pressure boundary (first wall) is cooled, there are temperature gradients that would lead to thermal stresses. This is of most concern for the rather large flat panels making up each canister and at the corner joints. These thermal stresses have not been considered in the present analysis. These have been considered in Section 5.2.

6.6 HIGH TEMPERATURE BLANKET CONCLUSIONS

The following conclusions can be made regarding the high temperature blanket:

- The high temperature blanket provides a direct replacement (geometrically) for the low temperature tritium-breeding, blanket presented in Section 5.
- Since the high temperature blanket does not breed tritium, the low temperature blanket must be a high breeder for the overall breeding ratio to be ≤ 1.1.
- Absolute helium pressure of about 50 atm is necessary to maintain acceptable pressure drop.
- The system pressure is contained within the specially cooled first wall (pressure boundary) and helium transport piping. (The heat exchanger tubes of the fluidized bed decomposer must also contain system pressure and at high temperature).
- First wall (pressure boundary) cooling can maintain the structural temperatures at levels consistent with the low temperature blanket. The high temperature internal structure and components only need to be self supporting.
- Heat transfer within the blanket is quite good and can maintain component temperatures at less than 1175 K. The coolant exit temperature is 1160 K.
- Structural and mechanical design issues need further development and study--especially mechanical and thermal stress analysis. Many of these issues are common to both the low and high temperature blanket canister modules.

References for Section 6.0

1. R. W. Werner, et. al., Synefuels from Fusion - Using the Tandem Mirror Reactor and a Thermochemical Cycle to Produce Hydrogen, UCID-19311, Lawrence Livermore Laboratory (February 9, 1982).

2. T. R. Hill, "ONETRAN" A Discrete Ordinates Finite Element Code for the Solution of the One-Dimensional Multigroup Transport Equation," LA-5900-MS, Los Alamos Scientific Laboratory (June 1975). (The pre-release availability of ONEDANT to the study is a result of the courtesy of Donald J. Dudziak of Group T-1, Los Alamos Scientific Laboratory.)

3. J. P. Holman, Heat Transfer, (McGraw-Hill, N.Y., 1976).

4. H. Rouse, Elementary Mechanics of Fluids, John Wiley & Sons, (1946).

5. E. R. G. Eckert and R. M. Drake, Jr., Heat and Mass Transfer, Second Edition. McGraw Hill (1959).

6. E. P. Popov, Mechanics of Materials, Prentice-Hall (1952).

7. S. P. Timoshenko and J. N. Goodier, Theory of Elasticity, Third Edition, McGraw Hill (1970).

SECTION 7

ENERGY TRANSPORT SYSTEM - REACTOR TO PROCESS

Contributor:

R. W. Werner

TABLE OF CONTENTS

7.0 ENERGY TRANSPORT SYSTEM - REACTOR TO PROCESS

The two reactor blanket designs discussed in Sections 5 and 6 provide energy for the General Atomic Sulfur-Iodine Thermochemical Cycle in two different ways and in two different temperature ranges. The first, the Canister blanket discussed in Section 5, produces 825 K process heat for the bulk (78%) of the thermochemical plant needs, while the SO_3 decomposer, which is the high temperature demand part of the cycle, is driven electrically using the Joule-Boosted SO_3 Decomposer. The second, the Axial Two-Zone blanket described in Section 6, provides both high temperature thermal energy (1160 K) for the top end of the plant and 825 K process heat for the remainder of the plant.

This section discussed the options and alternatives available for transporting this energy to the chemical plant. System evaluations addressing both the problems of matching heat source to heat sink and designing for safe energy transport have been studied. The transport system selected for both blanket designs uses helium as the heat transport fluid.

7.1 OBJECTIVES AND SAFETY CONSTRAINTS

Both blanket concepts, the Canister blanket and the Axial Two-Zone blanket, must deliver heat at the appropriate amounts and temperatures to the chemical plant in order to achieve an overall efficient and economic process. The majority of the chemical engineering effort in this project has been devoted to developing techniques of matching the heat source to the heat demands of the process and then developing process unit designs that can effectively and economically make use of this heat profile.

Safety considerations have been an integral part of the chemical engineering. Attention to potential problems in liquid metal safety, helium coolant over-pressuring of process vessels, tritium permeation and contamination, and migration of neutron-activated corrosion products are some of these safety considerations.

7.2 ENGINEERING OPTIONS

A very large number of engineering approaches for matching the heat source to the heat demands of the chemical process were examined in order to identify those which met the following desired characteristics:

- The majority of piping for long-distance heat transport within the chemical plant shall use high quality steam.
- Liquid metal coolants shall not be used within the chemical plant.
- Piping distances of high pressure helium piping shall be minimized to reduce pumping power.
- Multiple barrier isolation shall be provided between the neutron-activated blanket materials and the hydrogen product.
- Highly redundant modularity shall be used whenever possible to increase plant availability and reduce the quantity of neutron-activated materials that could be accidently released.

7.3 CASE STUDIES

Space does not permit us to outline in detail the large number of case studies that were made in order to select and design a blanket process interface and then evaluate its performance. Some of these cases have been covered in earlier papers[1-3] and prior year's reports.[4,5] Both He and Na were considered for heat transport in the process in FY80, and were coupled with steam-Rankine cycles for electrical power generation. Only He was used in FY81 and this year for heat transport out of the blanket. Various cycles were evaluated for electrical power generation, i.e., steam-Rankine, steam-Freon, steam-ammonia, and Brayton-steam in FY81. In FY82 we used the steam-Rankine exclusively in our study.

The TMR Q was parametrically varied from 10 to 35. In the resultant cases, there were blanket temperatures or process conditions that needed to be varied. The following approaches were investigated:

o	Heat pipe blanket (He)	800 - 1150 K
o	Heat pipe blanket (Na)	800 - 1150 K
o	Two-zone blanket:	
	Low temperature (He)	800 - 950 K
	High temperature (He)	900 - 1150 K
o	First wall (Na or He)	700 - 850 K
o	Direct convertor Hx (He)	850 - 1050 K

System evaluations were made for these approaches by attempting to match the heat source to the process heat demand as follows: by developing a heat exchanger network train, by developing electric power generating systems on both topping and bottoming cycles, and by roughly optimizing the network and then evaluating the thermal efficiency. For cases involving helium-Brayton turbine cycles, each of these helium loops had to be optimized with a small computer program by varying temperatures, He flow rates and turbine wheel compression ratios. The loops were linked and the network system optimized factorily. This tedious process was required to produce the best set of temperatures, helium flows, and heat exchanger match-ups consistent with the highest efficiency. Thermal efficiency ranged from 32 to 58% for the thermochemical process depending mainly upon the particular selection of topping and bottoming cycles. As expected, an increase in Q from 10 to 35 also gave an increase in process efficiency (up to an incremental gain of $\sim$ 4%) because of the increased availability of electricity at a high conversion efficiency from the direct convertor. In our FY82 studies, the helium-Brayton turbine cycles were abandoned in favor of a steam cycle with an intermediate heat exchanger containing the helium coolant in the primary loop.

7.4 CYCLE EFFICIENCY AND PLANT AVAILABILITY

We have explored the variation of cycle efficiency with changes in the energy transport system and coupling of the blanket to the process. Generally, we found high cycle efficiency was obtained when liquid sodium was used to generate steam and drive process units. But we felt that liquid metal coolants also provided a serious fire and safety risk which would result in a reduction in total plant availability. The damage consequences from accidents could be severe.

High pressure helium was found to have the disadvantages of poor heat transfer (and thus large temperature gradients within the heat transfer equipment), significant pumping power, and the hazards associated with high pressure. Helium coupling generally produced higher plant availability than with liquid metal heat transport. We conclude that the safety and availability advantages of helium make it the preferred heat transport fluid.

7.5 HELIUM PIPING OPTIMIZATION STUDIES

In carrying out the case studies, it became clear that although helium had clear safety and operational advantages, there were also clear economic debits in terms of pumping power and high pressure equipment capital costs. Therefore, a tradeoff study was done between capital costs and operational pumping power costs. The details of this rough optimization study were reported earlier.[4] For heavy wall Inc loy-800H piping, using a perforated liner to help keep the outer wall cooler, the minimum total operating and amortized capital cost was found for a 2-m-diameter, 100-m-long, 1.0 MPa pressure, 7-pipe transfer system feeding a helium-heated decomposer or boiler using blanket heat. The minimum cost was around $35M--somewhat high.

After this earlier study, we developed a design using Kao-Wool insulation[6] in place of the stagnant helium gap between the perforated liner and the heavy outer wall. This more effective insulation allowed us to drop the outer wall temperature so that mild steel would be acceptable (i.e., 1%

creep in ∿ 20 years) and allow the helium pressures to be increased to 3.0 MPa. This improvement dropped the total operating and amortized capital cost to about $10M--a substantial improvement.

7.6 CONCLUSIONS ON ENERGY TRANSPORT

In this section we have outlined the range of transport system alternatives that were examined in developing a design concept that employs a helium-steam-Rankine cycle approach. This satisfies our desire to achieve good isolation of the chemical plant from radioactivity by using helium coolants, and to substitute for liquid sodium the more conventional process steam approach to driving the chemical plant.

References for Section 7

1. T. R. Galloway, "Interfacing the Tandem Mirror Reactor to the Sulfur-Iodine Process for Hydrogen Production," presented at the 15th Intersociety Energy Conversion Engineering Conference, Seattle, WA, August 18-22, 1980, Lawrence Livermore National Laboratory Rept. UCRL-84212 (1980).

2. T. R. Galloway, "Some Process Aspects of Hydrogen Production Using the Tandem Mirror Reactor," presented at the 4th ANS Topical Meeting, King of Prussia, PA, October 14-17, 1980, Lawrence Livermore National Laboratory Rept. UCRL-84785 (1980).

3. T. R. Galloway and R. W. Werner, "Some Chemical Engineering Challenges in Driving Thermochemical Hydrogen Processes with the Tandem Mirror Reactor," presented at the 73rd Annual Meeting of American Institute of Chemical Engineers, Chicago, IL, November 10-20, 1980, Lawrence Livermore National Laboratory Rept. UCRL-84632 (1980).

4. R. W. Werner, et al., "Synfuels from Fusion - Producing Hydrogen with the Tandem Mirror Reactor and Thermochemical Cycles," Vols. I and II, Lawrence Livermore National Laboratory Rept. UCID-18909 (1981).

5. Babcock and Wilcox Company, La Mirada, CA, private communication (1981).

6. "Synfuels from Fusion - Using the Tandem Mirror Reactor and a Thermochemical Cycle to Produce Hydrogen," O. H. Krikorian, ed., Lawrence Livermore National Laboratory Rept. UCID-19311 (1982).

SECTION 8

THERMOCHEMICAL HYDROGEN PROCESSES

Contributor:

O. Krikorian

TABLE OF CONTENTS

LIST OF TABLES

LIST OF FIGURES

8.0 THERMOCHEMICAL HYDROGEN PROCESSES

In this section we describe the basic principals of thermochemical cycles for water splitting to produce hydrogen, including the criteria that determine cycle efficiencies and influence process design. We also describe in a very introductory way the GA Sulfur-Iodine Cycle for hydrogen production that we are coupling to the TRM in our current design studies.

8.1 BASIC PRINCIPLES OF THERMOCHEMICAL CYCLES

8.1.1 Introduction

A thermochemical cycle for hydrogen production is a process in which water is used as a feedstock along with a non-fossil high temperature heat source to produce H_2 and O_2 as product gases. (Fossil fuels can be converted directly to hydrogen by chemical processing in a more energy efficient and cost effective manner than by using them as a heat source for thermochemical cycles.) The water splitting process is accomplished through a closed loop sequence of chemical reaction steps in which the chemical reagents are continuously recycled and reused in the process with essentially no loss of material. Practical thermochemical cycles, as currently envisioned, require input temperatures of $\sim$1200 K, for the highest temperature chemical step, and operate at a thermal efficiency of $\sim$50%. Here, the thermal efficiency is defined as the higher heating value of the H_2 produced, 286 kJ/ mol H_2 (combustion enthalpy of the H_2 to give liquid water at 298.15 K), divided by the thermal heat per mole of H_2 delivered by the dedicated heat source.

Currently, there are some 30 thermochemical cycles world-wide that are under various stages of investigation and development. Energy sources that are being considered for these cycles are: (1) high-temperature, gas-cooled reactors providing a maximum temperature of $\sim$1200 K, (2) solar central receivers providing a maximum temperature somewhere in the 1200-2000 K range, and (3) magnetic fusion reactors anticipated to provide a maximum

temperature in the 1200-2000 K range. Selection of an actual maximum operating temperature depends upon the process needs of the thermochemical cycle as well as on overall system design. Cycle efficiency, system economics, and materials needs are all important considerations. Electrical energy for process equipment is required in addition to high temperature heat for operation of thermochemical hydrogen plants.

Of the cycles under study, only three have thus far been developed to the stage where closed-loop, table-top or bench-scale models have been built and tested in the laboratory; these are the cycles that we are considering for magnetic fusion applications. They are illustrated in terms of their principal chemical steps and reaction temperatures in Fig. 8.1. Note that in each case the sum of the chemical reaction steps is $H_2O = H_2 + 1/2\ O_2$. The main efforts on the development of the Sulfur-Iodine Cycle are underway at the General Atomic Company,[1-3] on the Sulfur Cycle at the Westinghouse Electric Corporation,[4,5] and on the Sulfur-Bromine

Cycle at the Joint Research Centre-Ispra Establishment.[6-8]

8.1.2 Basic Principles

The energetics of water decomposition are as follows:

$$H_2O(\ell) = H_2(g) + 1/2\ O_2(g) \qquad (1)$$

$$\Delta H^\circ_{298} = 285.8 \text{ kJ/mol}$$

$$\Delta G^\circ_{298} = 237.2 \text{ kJ/mol}$$

Thus, the energy requirement for decomposing water to the elements is quite high; it can be further shown that if water were to be decomposed in a single step, temperatures of about 2500-3000 K would be required to obtain significant yields. Furthermore, there are a number of major problems associated with decomposing water in a single step, even if such high temperatures could be attained, i.e., back reaction of H_2 and O_2 during

SULFUR-IODINE CYCLE

$$2\,H_2O + SO_2 + x\,I_2 \xrightarrow{\text{AQUEOUS}} H_2SO_4 + 2\,HI_x$$

$$2\,HI_x \xrightarrow{\sim 400\ K} x\,I_2 + H_2$$

$$H_2SO_4 \xrightarrow{\sim 1100\ K} H_2O + SO_2 + 1/2\,O_2$$

SULFUR CYCLE (PART ELECTROCHEMICAL)

$$2\,H_2O + SO_2 \xrightarrow[\text{ELECTROLYSIS}]{\text{AQUEOUS}} H_2 + H_2SO_4$$

$$H_2SO_4 \xrightarrow{\sim 1100K} H_2O + SO_2 + 1/2\,O_2$$

SULFUR-BROMINE CYCLE (PART ELECTROCHEMICAL)

$$2\,H_2O + SO_2 + Br_2 \xrightarrow{\text{AQUEOUS}} H_2SO_4 + 2\,HBr$$

$$2\,HBr \xrightarrow[\text{ELECTROLYSIS}]{\text{AQUEOUS}} Br_2 + H_2$$

$$H_2SO_4 \xrightarrow{\sim 1100\ K} H_2O + SO_2 + 1/2\,O_2$$

Fig. 8.1 Thermochemical cycles whose chemistry and closed loop operation have been verified in the laboratory.

cooldown, serious materials problems, and the need for considerable recycle because of low decomposition yields.

If the decomposition of water is carried out in two or more chemical reaction steps, a number of advantages result. For example, the production of H_2 and O_2 can be separated into different reaction steps, thus avoiding the back reaction problem. Also, by picking a proper combination of reactions, the maximum reaction temperature can be lowered with resultant benefits in reaction yields and availability of suitable materials. In actual practice, it is found that two-step cycles have shown only minimal lowering of the temperature compared to the single-step decomposition of water, unless one of the steps involves an electrochemical assist (e.g., see the Sulfur Cycle in Fig. 8.1). A cycle that includes an electrochemical step is called a "hybrid" cycle. With three or more steps, cycles based only on thermal input for the chemical reactions become possible at reasonable temperatures (e.g., see the Sulfur-Iodine Cycle in Fig. 8.1), and many will work efficiently at maximum temperatures of about 1200 K.

In order to illustrate some of the important considerations in developing and evaluating thermochemical cycles, we can use a generalized two-step cycle represented as follows:

$$R + H_2O(\ell) \xrightarrow{T_1} RO + H_2(g), \quad \Delta G^\circ \leq 0, \ \Delta H^\circ = \Delta H_1 \qquad (2)$$

$$RO \xrightarrow{T_D} R + 1/2\ O_2(g), \ \Delta G^\circ \leq 0, \quad \Delta H^\circ = \Delta H_D \qquad (3)$$

In reaction (1), a reducing agent R is used to reduce water to produce H_2 at temperature T_1, forming the oxide RO in the process. Reactions such as this are usually carried out near room temperature or at slightly elevated temperatures. In order to achieve a near zero or negative ΔG° to make the reaction go, the enthalpy change is usually governing and ΔH_1 is negative (an exothermic reaction). Heat produced by reaction (1) is usually of limited value for reuse in the cycle because of the low temperatures involved. Reaction (2) is carried out at a high temperature, and is the decomposition step that regenerates the reducing agent R and O_2. Reaction

(2) is highly endothermic (ΔH_D is positive) and requires a large change in entropy ($\Delta S°$) to produce a near zero or negative $\Delta G°$. This can be readily seen from the well-known second law expression $\Delta G° = \Delta H° - T\Delta S°$ where the $T\Delta S°$ term becomes increasingly important as the temperature is raised. Hence, one of the requirements in selecting RO is that it have as large a $\Delta S°$ of decomposition as possible, to minimize the maximum temperature required in the thermochemical cycle. As an example, the gaseous molecule SO_3 ($R = SO_2$) meets the requirement for reaction (2), but SO_2 falls short of the requirement for reducing water to produce H_2 in reaction (1). The fix for this problem is to use an assist for reaction (1) by either (a) forming a hydrogen compound of intermediate stability, such as HI or HBr, which can be subsequently decomposed to obtain the desired H_2 product, or (b) using an electrolysis assist at a voltage substantially less than for direct water electrolysis (e.g., the Sulfur Cycle in Fig. 8.1). In the case of HBr decomposition, an electrolysis assist is also required (see Sulfur-Bromine Cycle in Fig. 8.1), since the yield is low for thermal decomposition of HBr.

Two types of cycle efficiencies are used in evaluating thermochemical cycles. The work efficiency, i.e., the efficiency of converting heat into work, E(w), is given by

$$E(w) = \frac{237.2}{\Sigma\Delta H_D} \leq \frac{T_D - 298}{T_D} . \qquad (4)$$

The thermal efficiency, or the efficiency of heat utilization, E(H), is given by

$$E(H) = \frac{285.8}{\Sigma\Delta H_D} \leq 1.21 \frac{T_D - 298}{T_D} . \qquad (5)$$

In expression (4), the number 237.2 (in kJ/mol) represents the maximum work ($\Delta G°$) available from the hydrogen produced, (see expression (1), while $\Sigma\Delta H_D$ represents the total external heat requirements for the cycle, i.e., the heat provided by the non-fossil fuel heat source. For electricity required in the cycle, the $\Sigma\Delta H_D$ term includes the equivalent heat required to produce the electricity; or as in the case of the Tandem Mirror Reactor

as an energy source, some of the energy is available as electrical energy from the Direct Converter, and we add this directly to the $\Sigma\Delta H_D$ term assuming it to be equivalent to thermal energy at 100% conversion. We see that E(w) is limited by a Carnot expression for the maximum efficiency. The thermal efficiency, E(H), compares the combustion energy of the hydrogen produced to form liquid water at room temperature as the final product, with $\Sigma\Delta H_D$. The thermal efficiency could conceivably exceed the Carnot efficiency up to a maximum value given by the ratio of 285.8/237.2 = 1.21.

8.1.3 Some Important Criteria

A listing of the major reaction steps (such as in Fig. 8.1) gives only an indication of the complexity of a thermochemical cycle system. Choosing the best cycle and optimizing it in terms of efficiency and economics are challenging research goals. The criteria that must be considered include:

- Favorable thermodynamics.
- Fast reactions.
- High reaction yields.
- Simple separations.
- Process design factors (such as efficient use of heat, avoidance of scarce or hazardous reagents, and simplicity of construction).

Favorable thermodynamics implies both a negative and a very small free energy change ($\Delta G°$) for each reaction step. If the free energy change were positive, the equilibrium constant of the reaction would be unfavorable, and much energy would be wasted in separating or concentrating the reaction products. If the free energy change were too negative, on the other hand, one or more of the reaction products would be too stable and hard to

regenerate into the original reactants.

Fast reactions are desirable, especially for reactions involving gaseous reactants, because they enable us to use smaller and less expensive reaction vessels. The requirement that the free energy change be nearly zero makes it difficult to achieve fast reactions, however, because it allows very little driving force for the reactions. Reactions need to be selected in which the energy barriers are low enough to permit a very small free energy change to drive them rapidly. In many instances, the reaction rates can be enhanced by the use of catalysts.

High reaction yields are important to minimize recycling of unreacted reagents or diversion of material into undesirable by-products.

By using simple separations, we can avoid another area in which hidden costs can be substantial. Operations such as boiling, compression, and filtering can involve expensive process equipment and energy losses, and they need to be minimized.

Finally, careful process design can do much to provide the optimim tradeoff between the efficient use of heat energy and the economies of construction and operation. Process design contributions include new and innovative process equipment, plant layout, and siting.

8.2 GENERAL ATOMIC CYCLE

8.2.1 Selecting a Cycle

We have selected the GA Sulfur-Iodine Cycle for our current TMR/Thermochemical Cycle coupling studies because it is the closest of the most advanced cycles to a pure thermal cycle. This permits the economies of scale to apply for chemical process units in a large chemical plant of the type considered here. Scale-up does not permit a similar reduction in costs for electrolysis units which are modular in construction. The Sulfur-Iodine Cycle also involves the handling of only liquids and gases, which is advantageous from a chemical engineering standpoint.

8.2.2 Chemical Description of GA Cycle

The current Sulfur-Iodine Cycle can be described chemically as follows:

$$2\ H_2O + SO_2 + x\ I_2 \rightarrow H_2SO_4 + 2\ HI_x \qquad (390\ K) \qquad (1)$$

$$2\ HI_x \rightarrow H_2 + x\ I_2 \qquad (420\ K) \qquad (2)$$

$$H_2SO_4 \rightarrow H_2O + SO_2 + 1/2\ O_2 \qquad (\sim 1050\ K\text{-}1250\ K) \qquad (3)$$

All reactions in this system have been verified in the laboratory and total recycle has been illustrated in a small closed-loop cycle experiment.[1] Major parts of the process are associated with separation and purification of the reaction products. A critical aspect for the successful operation of the process is the separation of the aqueous reaction products in reaction (1) above. Workers at the General Atomic Company have solved this problem by using an excess of I_2 in reaction (1), which leads to separation of the products into a lower density phase, containing H_2SO_4 and H_2O, and a higher density phase, containing HI, I_2 and H_2O. Reaction (2) shows the catalytic decomposition of HI, which is carried out under pressure ($\sim$80 atm) with HI and I_2 in liquid forms, in order to enhance the decomposition yield. Laboratory decompositions are around 30% per pass and,

therefore, use a recycle step. Unreacted HI is condensed out of the H_2 product and distilled away from the I_2 product. Pure H_2 is obtained by scrubbing out the remaining I_2 with H_2O.

The equilibrium for reaction (3) lies to the right at temperatures above 1000 K, but up to temperatures of ~1150 K, catalysts are needed to attain sufficiently rapid decomposition rates. Catalysts are available for this process, but careful consideration needs to be given to cost versus effectiveness. The SO_3 Decomposition Reactor is a challenging unit to design, owing to the high temperatures and corrosive products involved. All of the H_2SO_4 based cycles currently under study need such an SO_3 decomposer. Each of the three laboratories involved has approached this problem from a different standpoint. The Joule-Boosted Decomposer introduced by LLNL in this year's study provides a breakthrough in this difficult area by overcoming the materials and catalyst problems, and giving increased decomposition yields.

Figure 8.2 is a simplified schematic flow diagram of the GA Sulfur-Iodine Cycle conceptually showing product flows and recycle streams.

A complete description of the GA Cycle is given later in Section 9 of this report. For purposes of flowsheeting and process design, the GA Cycle has been divided into the following process sections.

- Section I, H_2SO_4-HI Production and Separation.
- Section II, H_2SO_4 Concentration and SO_3 Decomposition.
- Section III, HI Separation and Purification.
- Section IV, HI Decomposition and H_2 Purification.
- Section V, Energy Distribution and the TMR-Chemical Plant Interface.

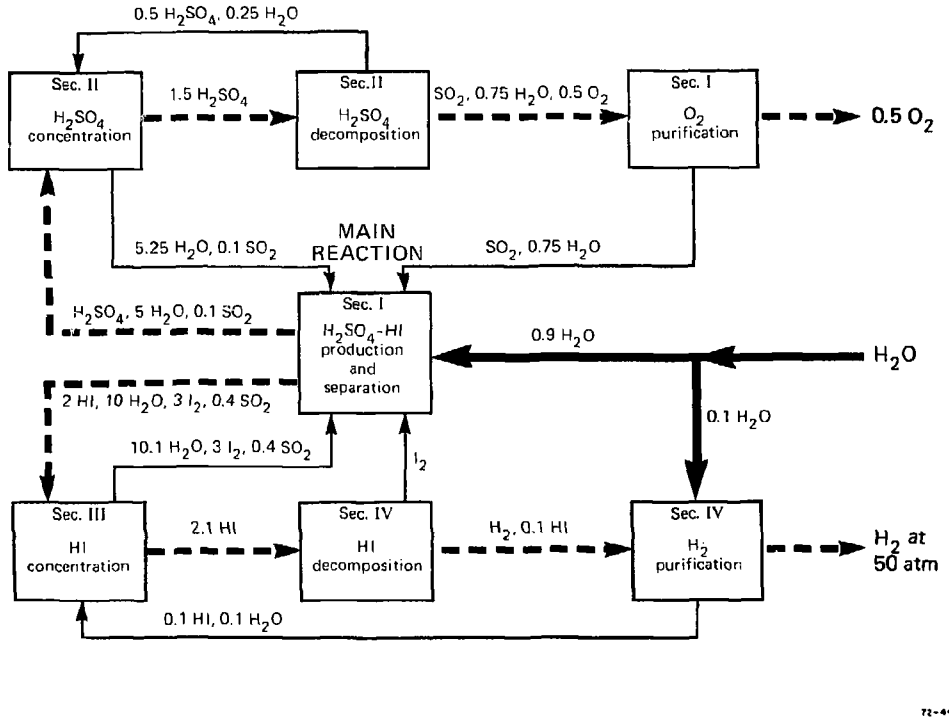

Fig. 8.2 Block diagram for General Atomic sulfur-iodine cycle

8.3 THERMODYNAMIC DATA BASE FOR SECTION II

The thermal efficiency for conversion of water to hydrogen is very sensitive to heat-matching in the thermochemical process plant. This conversion efficiency directly impacts the capital cost of the total plant, including the TMR energy source. For example, for a given hydrogen production rate, an increase of 10% in cycle efficiency would lead to an approximate 10% reduction in size and cost for both the TMR and the chemical plant.

A large proportion of the energy supplied by the TMR is required for operation of Section II. Primary reactor heat put into Section II is generally recovered and reused several times before discharge as waste heat. Because of the large magnitude of heat handled in this Section, proper heat-matching and reuse of heat are very critical to achieving a high efficiency process. Furthermore, the accuracy of the thermodynamic data base used here is important if we are to achieve a realistic optimum or near optimum in efficiency of heat utilization in Section II.

Only a portion of the thermodynamic data that are needed to do heat-matching and mass and energy balances for Section II is currently available in the literature. However, we are able to fill in some portions of the missing data by deriving approximate thermodynamic data based on recent unpublished measurements by Lennartz,[10] who gives pressure-composition-temperature (P,x,T) data for the H_2O-H_2SO_4 system. In addition, for our current purposes, we have made some additional rough estimates as needed in order to obtain a complete thermodynamic data base for use in Section II. This data base will be described and summarized in the following sub-sections.

8.3.1 Sequence of Process Steps

Before developing the thermodynamic data, we briefly describe below and in Fig. 8.3 an illustration of the process steps for which the thermodynamic data will be used. The illustration given here is for the Joule-boosted decomposer approach.

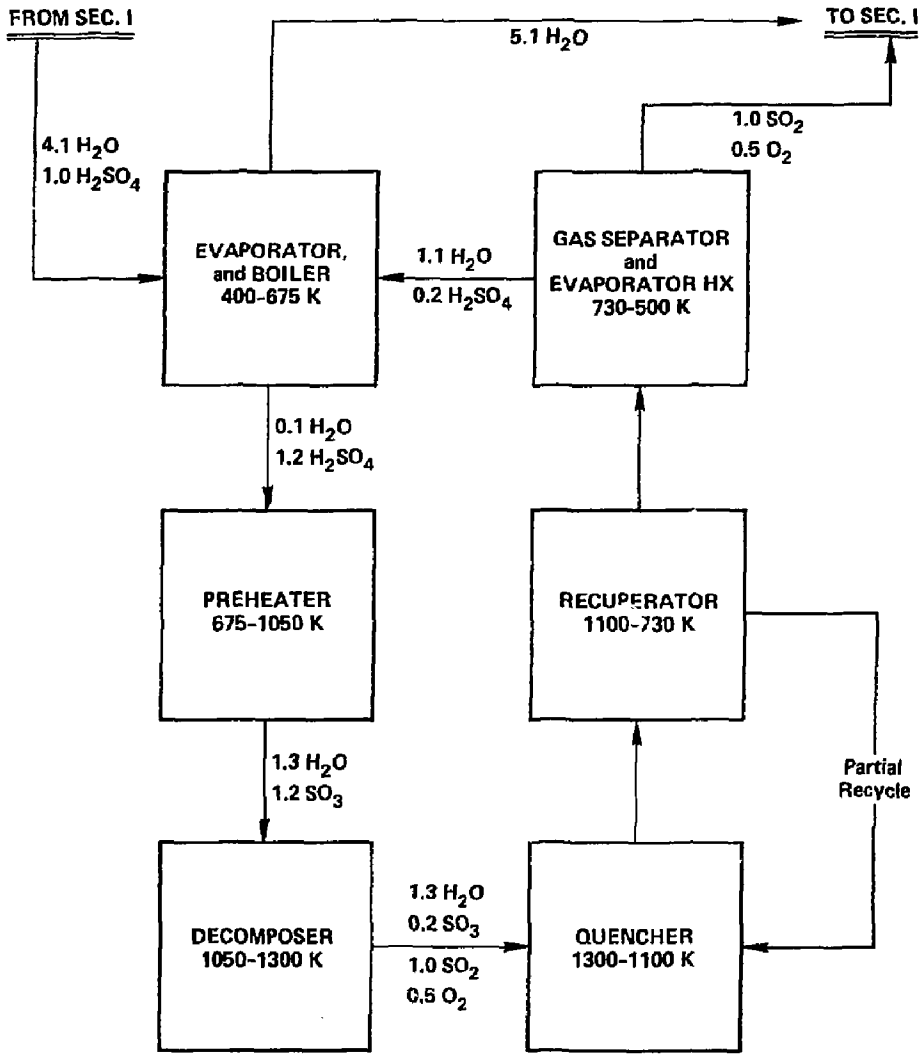

Fig. 8.3. This simplified flow diagram for the Joule-boosted decomposer approach for Section II illustrates the process steps, temperatures and approximate mass flows for which thermodynamic data need to be developed.

Concentration of H_2SO_4. The feed material for this process step consists of two streams: (1) the 57 wt% (20 mole %) sulfuric acid product from Section I at ~400 K which supplies about 80% of the feed, and (2) a 50 wt% (15 mole %) sulfuric acid from the decomposer product stream at about 500-600 K which makes up the balance of the feed. These acid streams are concentrated in sulfuric acid by selectively vaporizing off water in a staged evaporator to produce the 98 wt% (90 mole %) H_2SO_4 azeotrope at ~675 K. Pure water recovered from the evaporation is returned to Section I.

Boiling of Azeotrope. The 98 wt% H_2SO_4 azeotrope is boiled isothermally at about 5 atm and 670 K to obtain the gaseous feed for the decomposer. Gaseous species produced by the boiler are H_2SO_4, SO_3 and H_2O.

Preheating of Gas. The gas from the boiler is preheated from ~670 K to about 1000-1100 K to prepare it as feed to the decomposer. Molecular H_2SO_4 decomposes endothermically to $SO_3 + H_2O$ during this preheat.

Decomposition of SO_3. The gaseous feed from the preheater now contains about 50 mole % each of SO_3 and H_2O. About 90% of the SO_3 is decomposed at 5 atm and 1300 K to form SO_2 and O_2 as products.

Cooldown of Decomposition Products. The gaseous products from the decomposer are quenched to ~1100 K to prevent back reaction of $SO_2 + O_2$. Quenching is accomplished by recycling some of the cooled decomposition product gases into the decomposer product stream. The product stream is then passed through a tube and shell recuperator to preheat the gas feed entering the decomposer. A portion of the cooled recuperator output gas (at ~700 K) is used as quench gas (see above) and the balance is used to supply heat to the evaporator through a heat exchanger. Undecomposed SO_3 remaining in the product gas combines with H_2O and condenses out as aqueous H_2SO_4 at about 500-600 K. This aqueous H_2SO_4 is added to the evaporator stream for recycle, and gaseous SO_2 and O_2 are separated and sent to Section I.

8.3.2 Thermodynamic Data Requirements

The thermodynamic data requirements for each of the process steps described above will now be discussed in a general way. Details of the data derivation and methods for use of the thermodynamic data are covered in a later subsection.

Thermodynamic Data for Concentration of H_2SO_4

As the sulfuric acid solutions are concentrated in a staged evaporator, we need to have information on several thermodynamic parameters for each stage, i.e., (1) we need to know the uptake of sensible heat as the solution is heated, (2) the vapor pressures of gaseous products and the resultant change in liquid phase composition, (3) the vaporization enthalpies to the gas phase, (4) the sensilbe heat, the condensation temperature and the condensation enthalpy of the gas phase product, and (5) the sensible heat available in the condensate as it cools.

The chemical processes occurring in a single evaporation stage and the approximate enthalpy changes associated with the processes are illustrated in the following simplified example.

$$\underset{400K,\ aq}{(H_2SO_4 + 4\ H_2O)} \rightarrow \underset{600K,\ aq}{(H_2SO_4 + 4\ H_2O)};\ \Delta H_{1a} = 35.7\ kJ/mol \qquad (11a)$$

$$\underset{600K,\ aq}{(H_2SO_4 + 4\ H_2O)} \rightarrow \underset{600K,\ aq}{(H_2SO_4 + 3\ H_2O)} + \underset{600K,\ 1\ atm}{H_2O(\ell)};\ \Delta H_{1b} = 8.1\ kJ/mol \qquad (11b)$$

$$\underset{600K,\ 1\ atm}{H_2O(\ell)} \rightarrow \underset{600K,\ 40\ atm}{H_2O(g)};\ \Delta H_{1c} = -27.1\ kJ/mol \qquad (11c)$$

$$\underset{600K,\ 40\ atm}{H_2O(g)} \rightarrow \underset{525K,\ 40\ atm}{H_2O(g)};\ \Delta H_2 = -4.2\ kJ/mol \qquad (12)$$

$$\underset{525K,\ 40\ atm}{H_2O(g)} \rightarrow \underset{525K,\ 40\ atm}{H_2O(\ell)};\ \Delta H_3 = -29.5\ kJ/mol \qquad (13)$$

$$H_2O(\ell) \rightarrow H_2O(\ell) \quad ; \Delta H_4 = -8.9 \text{ kJ/mol} \qquad (14)$$
525K, 40 atm 430K, 5.6 atm

The first reaction above, corresponding to the uptake of enthalpy and boiling off of part of the water, is broken down into three parts for the convenience of thermodynamic calculations. Thus, (11a) represents the increase in sensible heat of the initial (H_2SO_4 + 4 H_2O) solution, (11b) represents the exsolution of water into a hypothetical 1 atm reference state, and (11c) the boiling of the 1 atm reference state of water to the equilibrium partial pressure of steam above the final (H_2SO_4 + 3 H_2O) solution. The equilibrium steam pressure is estimated by extrapolating the data of Lennartz[10] to higher pressures.

Reactions (12), (13), and (14) represent the enthalpy available for reuse in the evaporated steam. This enthalpy is available as sensible heat in the steam, the condensation energy of the steam, and sensible heat in the condensed water down to 430 K. Thus, with a total enthalpy input of 70.9 kJ/mol (35.7 + 8.1 + 27.1), 42.6 kJ/mol (4.2 + 29.5 + 8.9) or 60% is available for reuse above 430 K, with most of it actually available above ~600 K. The balance of the enthalpy remains primarily as sensible heat in the concentrated sulfuric acid.

In subsequent evaporation stages as the H_2SO_4 is heated hotter and gets more concentrated, the thermodynamics get complicated, as first $H_2SO_4(g)$ and then $SO_3(g)$ contribute in increasing amounts to the gas-phase composition. Upon reaching the azeotrope composition, the gas phase will consist of roughly 40% $H_2SO_4(g)$ and 30% each of $SO_3(g)$ and $H_2O(g)$. Also, the enthalpy for exsolution of $H_2O(\ell)$, reaction (11b) above, will increase by nearly an order of magnitude. Thus, for the more concentrated H_2SO_4 solutions the condensate from the gas phase will contain a substantial amount of H_2SO_4, and several additional evaporation stages are needed to obtain a separation of relatively pure water. Consequently, both the complexity of the H_2SO_4 concentration process and the energy requirements increase as the azeotrope is approached; and it becomes especially important in this region to have accurate thermodynamic data and to do careful heat-matching.

Thermodynamic Data for Boiling of the Azeotrope

The azeotrope represents the invariant boiling composition at which the gas-phase and liquid-phase compositions are identical at a given temperature. For the H_2O-H_2SO_4 system, the azeotrope occurs at ~90 mole% H_2SO_4, and is an experimentally determined parameter. At a given temperature, we can write down the following relationships for the gas phase above the boiling azeotrope.[11]

$$K_{eq} = (p_{SO_3})(p_{H_2O})/(p_{H_2SO_4}) \quad (15)$$

$$x_{H_2SO_4} = (p_{H_2SO_4} + p_{SO_3})/(p_{H_2SO_4} + p_{H_2O}) \quad (16)$$

$$P_{tot} = p_{H_2SO_4} + p_{SO_3} + p_{H_2O} \quad (17)$$

Reaction (15) represents the equilibrium degree of decomposition of $H_2SO_4(g)$, reaction (16) gives the experimentally determined azeotropic composition expressed as mole fraction H_2SO_4, and reaction (17) gives the experimentally determined total gas pressure for the particular azeotropic temperature. Using these relations, and assuming that decomposition of $SO_3(g)$ into $SO_2(g)$ and $O_2(g)$ is kinetically hindered under these conditions, we can calculate the partial pressures of $H_2SO_4(g)$, $SO_3(g)$ and $H_2O(g)$ for each azeotopic boiling point.

Having obtained the gas-phase compositions, we can now proceed to calculate the enthalpy of boiling, as illustrated by the following example for the 5 atm azeotrope which boils at 671.5 K at a composition of $x_{H_2SO_4} = 0.907$.[10]

$$H_2SO_4 \text{ (azeo. liq.)} + 0.102\ H_2O \text{ (azeo. liq.)} \rightarrow H_2SO_4(\ell) + 0.102\ H_2O(\ell);\ \Delta H_{18a} = 8.4 \text{ kJ/mol} \quad (18a)$$

$$H_2SO_4(\ell) \rightarrow H_2SO_4(g);\ \Delta H_{18b} = 56.5 \text{ kJ/mol} \quad (18b)$$

$$0.102\ H_2O(\ell) \rightarrow 0.102\ H_2O(g);\ \Delta H_{18c} = 2.2 \text{ kJ/mol} \quad (18c)$$

$$H_2SO_4(g) \rightarrow 0.620\ H_2SO_4(g) + 0.380\ SO_3(g) + 0.380\ H_2O(g);\ \Delta H_{18d} = 35.9\ kJ/mol \quad (18d)$$

Here again the reactions are broken down into intermediate steps for thermodynamic convenience, with $H_2SO_4(\ell)$ and $H_2O(\ell)$ representing 1 atm hypothetical reference states. The sum of the enthalpies for (18a) through (18d) gives 103.0 kJ/mole, which represents the boiling enthalpy per mole of H_2SO_4 for the 5 atm azeotrope.

Thermodynamic Data for Preheating the Gas

Molecular $H_2SO_4(g)$ gradually decomposes into $SO_3(g)$ and $H_2O(g)$ as the azeotropic gas mixture is preheated from the boiling point up to the point where it is introduced into the decomposer. It is assumed that the $H_2SO_4(g)$ decomposition equilibrium is rapid, and that the decomposition of $SO_3(g)$ into $SO_2(g)$ and $O_2(g)$ does not occur because it is kinetically hindered. Thermodynamic data that are required are the equilibrium constant for $H_2SO_4(g)$ decomposition; enthalpies for the sensible heats of gaseous H_2SO_4, SO_3, and H_2O; and the decomposition enthalpy of gaseous H_2SO_4. An illustration of the calculations involved is given in an earlier report.[11]

Thermodynamic Data for Decomposition of SO_3

Decomposition of $SO_3(g)$ is assumed to reach equilibrium at the exit temperature and pressure of the decomposer. Thermodynamic data required are the equilibrium constant and enthalpy for decomposition, and enthalpies for the sensible heat changes in the gaseous species between inlet and outlet of the decomposer.

Thermodynamic Data for Decomposition Products

The thermodynamic data required for cooldown of the decomposition products involves enthalpies for sensible heats, recombination enthalpies, condensation enthalpies, and various equilibrium constants. Data for these processes are similar to that during heatup.

8.3.3 Summary of Thermodynamic Data

A summary is given here of the current status of the thermodynamic data base. Major progress has been made during the past year in bringing this data base up to date and putting it into a form where it can be used to obtain reasonably accurate energy balances for Section II. Some work still remains to complete the data evaluations and summaries. The next step would be to convert the data base into a form suitable for computer use in doing process optimization.

Table 8.1 provides a concise summary of the thermodynamic data requirements, the current data sources, and a listing of the tables and figures in this section that summarize the current data. In the discussions that follow, we describe the bases for the data.

Equilibrium Constant Data

Of the items designated in Table 8.1 under equilibrium constant data, the partial pressures of gaseous species above aqueous H_2SO_4 and the azeotrope parameters are the most difficult data to obtain. The balance of the items are readily obtained from standard tabulations.[12,13]

Some years ago, Gmitro and Vermeulen[14] did an excellent theoretical job of calculating the equilibrium vapor compositions above H_2O-H_2SO_4 mixtures up to 673 K. The difficulty with their work was that they were limited to the room temperature experimental data of Giauque and coworkers[15] for input data. As a consequence, their high temperature data do not agree with the recent experimental total pressure values and azeotrope compositions of Lennartz.[10]

Lennartz's total pressure data is summarized in tabular form in Table 8.2, and in graphical form in Fig. 8.4. Pressures and temperatures in Fig. 8.4 have been extrapolated beyond the experimental range for convenience in doing pressure-staging calculations for the evaporator process step. An example of Gmitro and Vermeulen's data is given in Fig. 8.5. Note that the propor-

Table 8.1 Summarized here are the thermodynamic data requirements for Section II. Included are references to the thermodynamic data sources currently in use, and a listing of the tables and figures where the data have been summarized.

Thermodynamic Data Required	Data Source	Summarized In
Equilibrium Constants for:		
• Partial pressures of $H_2O(g)$, $H_2SO_4(g)$, and $SO_3(g)$ above aqueous H_2SO_4 as f(x,T)	Gmitro and Vermeulen,[14] Lennartz[10]	Table 8.2, Figs. 8.4 and 8.5
• Azeotrope x and T for aqueous H_2SO_4 as f(P)	Derived from Lennartz[10]	Table 8.3
• $H_2SO_4(g) = H_2O(g) + SO_3(g)$	JANAF[12]	
• $SO_3(g) = SO_2(g) + 1/2\ O_2(g)$	JANAF[12]	
• $H_2O(\ell) = H_2O(g)$, at saturation	Steam Tables[13]	
Reaction Enthalpies for:		
• Exsolution of aqueous H_2SO_4 into pure $H_2O(\ell)$ and $H_2SO_4(\ell)$ in their 1 atm reference states	Derived from Giauque,[15] Lennartz,[10] and estimates	Figs. 8.6 and 8.7
• $H_2O(\ell, 1\ atm) = H_2O(g)$	JANAF,[12] plus extrapolations	Fig. 8.8
• $H_2SO_4(\ell, 1\ atm) = H_2SO_4(g)$	JANAF[12]	
• $H_2SO_4(g) = H_2O(g) + SO_3(g)$	JANAF[12]	
• $SO_3(g) = SO_2(g) + 1/2\ O_2(g)$	JANAF[12]	
• $H_2O(\ell) = H_2O(g)$, at saturation	Steam Tables[13]	Fig. 8.8
Sensible Heats (Enthalpies) for:		
• Aqueous H_2SO_4 as f(x)	JANAF,[12] and data derived from Lennartz[10]	Figs. 8.9 and 8.10
• $H_2O(\ell)$, 1 atm reference state	JANAF,[12] plus extrapolations	Fig. 8.11
• $H_2SO_4(\ell)$, $H_2SO_4(g)$, $SO_3(g)$, $SO_2(g)$, and $O_2(g)$	JANAF[12]	Fig. 8.11
• $H_2O(g)$ as f(P), and $H_2O(\ell)$ at saturation	Steam Tables[13]	Fig. 8.11

Table 8.2 Parameters are summarized for the expression ln P = A - B/T, which gives the total equilibrium pressure, P (in atm), above various H_2O - H_2SO_4 mixtures as a function of T (in K). The experimental data and A and B parameters are from Lennartz.[10]

Temperature Range, K	$x_{H_2SO_4}$	A	B
433-532	0.2144	12.2538	4968.27
443-538	0.2460	12.1593	5041.11
453-566	0.3173	12.5265	5507.69
463-576	0.3407	12.3389	5485.73
473-588	0.3832	12.5012	5718.92
464-598	0.3998	12.6682	5891.34
475-610	0.4187	12.4767	5875.56
479-622	0.4536	12.3088	5887.03
521-652	0.5512	12.6858	6471.72
534-682	0.6388	12.6410	6746.30
502-719	0.7181	13.0419	7287.66
589-718	0.7522	13.2453	7519.31
568-741	0.8189	13.4854	7840.62
503.744	0.8386	13.8296	8123.06
507-741	0.8840	14.5261	8659.33
621-693	0.8921	14.6010	8740.04
535-744	0.9050	14.6863	8792.67
583-603	0.9195	15.1161	9071.12
503-743	0.9296	15.1626	9101.92
503-744	0.9349	15.2487	9143.64
504-737	0.9806	15.3841	9076.25

Table 8.3 Temperature, pressure, and composition conditions for the H_2O - H_2SO_4 azeotrope based on the experimental data of Lennartz[10] and JANAF data[12] for the vapor species.

T,K	P,atm	x_{H_2O}[a]	$x_{H_2SO_4}$[a]	p_{H_2O},atm	$p_{H_2SO_4}$,atm	p_{SO_3},atm
522.6	0.1	0.0602	0.9398	0.02363	0.05763	0.01874
566.4	0.4	0.0682	0.9318	0.10576	0.21001	0.08423
600.3	1	0.0752	0.9248	0.28591	0.48625	0.22784
628.7	2	0.0818	0.9182	0.60345	0.91751	0.47904
646.9	3	0.0863	0.9137	0.93582	1.32331	0.74086
660.5	4	0.0899	0.9101	1.27763	1.71365	1.00872
671.5	5	0.0929	0.9071	1.62702	2.09141	1.28158
680.6	6	0.0954	0.9046	1.97991	2.46415	1.55595
688.8	7	0.0978	0.9022	2.34168	2.82162	1.83671
695.9	8	0.0998	0.9002	2.70528	3.17644	2.11828
702.3	9	0.1017	0.8983	3.07585	3.51899	2.40516
708.2	10	0.1035	0.8965	3.44943	3.85740	2.69317
749.7	20	0.1165	0.8835	7.29778	7.07937	5.62285

[a]Mole fraction in the liquid phase.

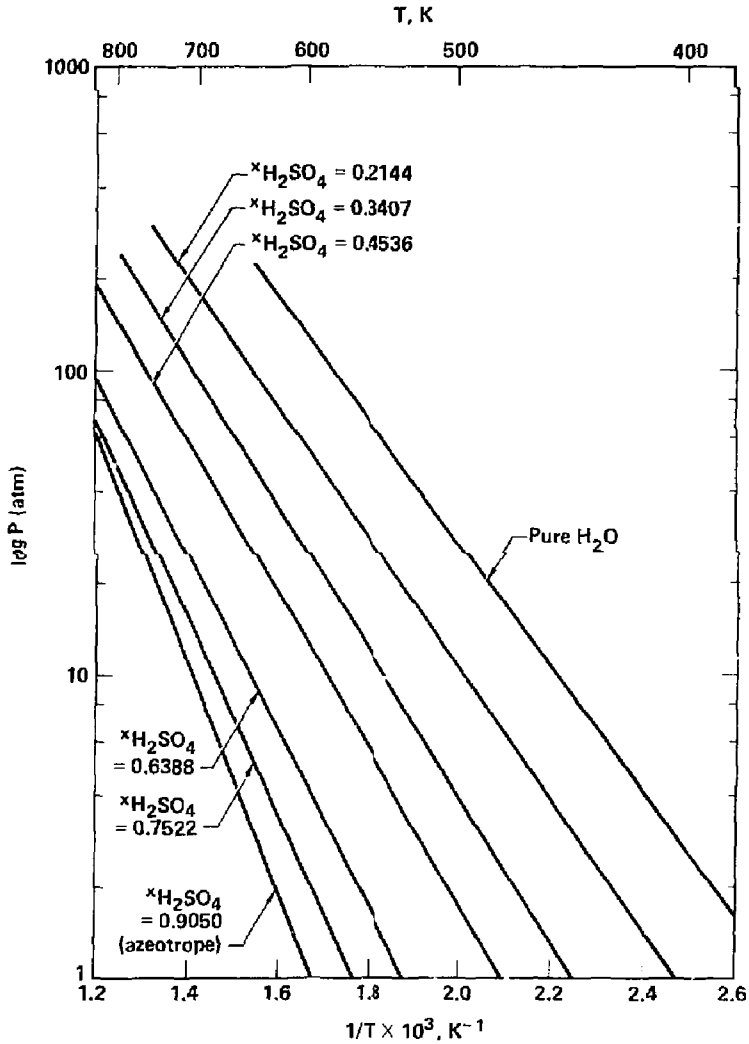

Fig. 8.4. The variation of total pressure above H_2O-H_2SO_4 mixtures as a function of composition and temperature is illustrated here. The curves include an extrapolation of Lemartz's data[10] to higher temperatures and pressures than the experimental determinations.

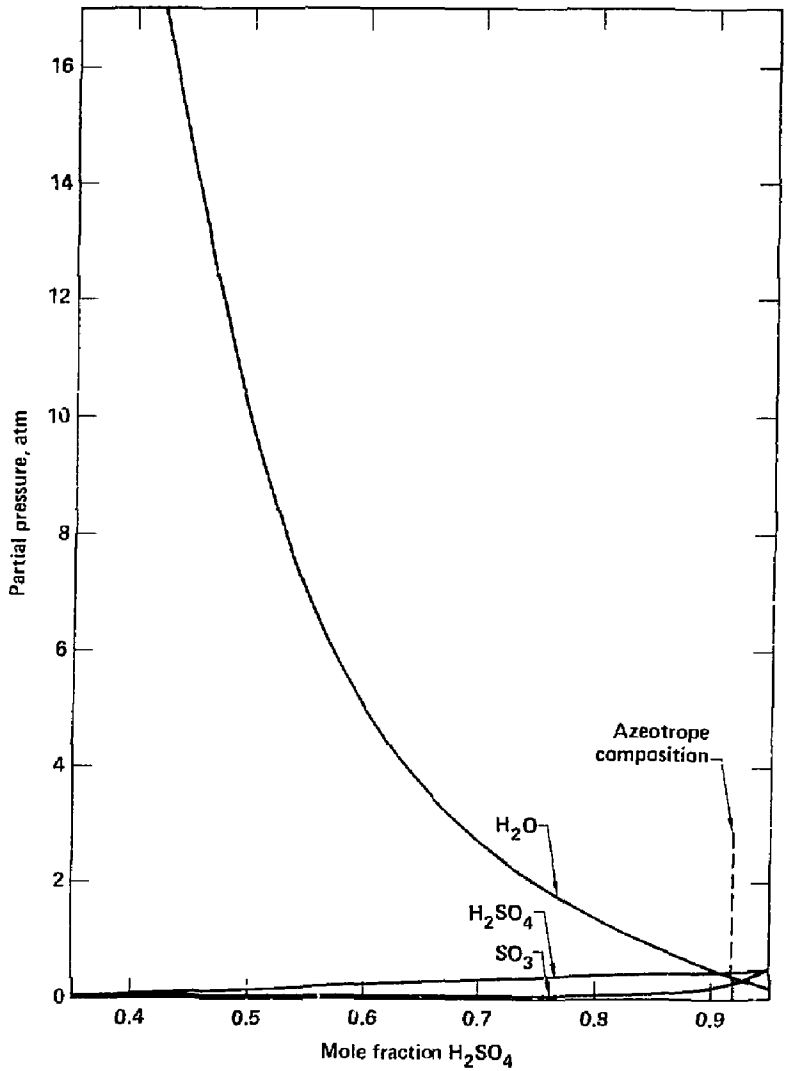

Fig. 8.5. Partial pressures are given of gaseous H_2O, H_2SO_4, and SO_3 above H_2O-H_2SO_4 mixtures at 600 K based on the calculated values of Gmitro and Vermeulen.[14]

tion of $H_2SO_4(g)$ in the vapor does not become important until ~85 wt% (50 mole%) H_2SO_4, and for $SO_3(g)$ until ~95 wt% (80 mole %) H_2SO_4 is reached.

Enthalpy of Reaction Data

Most of the enthalpy of reaction data that is required here can be readily obtained from standard compilations such as the JANAF Tables[12] and Steam Tables[13] (see Table 8.1). However, it is difficult to obtain data for the exsolution of aqueous H_2SO_4 into its pure components as indicated in reaction (18a), and an extrapolation needs to be made to higher temperatures to obtain data for vaporization of $H_2O(\ell)$ from its 1 atm reference state to $H_2O(g)$ (see reaction (18c)).

For exsolution of aqueous H_2SO_4 into its components at room temperature, we have available the excellent experimental data of Giauque et al.[15] These data are illustrated in terms of the solution reactions in Figs. 8.6 and 8.7 for the partial molal and integral enthalpies of solution at 298.15 K. (Enthalpies of exsolution are the negatives of these values.)

At higher temperatures, i.e., at ~600 K, we have derived approximate values for the enthalpies of solution from the P,x,T data of Lennartz.[10] Thus, examining Lennartz's data in Table 8.2, we find that the product of the gas constant R times the parameter B is the total enthalpy of vaporization for all gaseous species at ~600 K above the various aqueous H_2SO_4 solutions. Furthermore, based on the calculations of Gmitro and Vermeulen[14] (see Fig. 8.5), the vapor consists dominantly of $H_2O(g)$ up to about $x_{H_2SO_4} = 0.6$. Hence, by subtracting out the vaporization enthalpy of $H_2O(\ell)$ in its 1 atm reference state from Lennartz's enthalpy of vaporization values, we obtain the partial molal enthalpy of exsolution of $H_2O(\ell)$ at 600 K up to $x_{H_2SO_4} = 0.6$. We can also obtain an additional value for the partial molal enthalpy of exsolution of $H_2O(\ell)$ at the azeotrope composition by using the azeotropic relationships given by equations (15), (16), and (17) to obtain the partial pressure of $H_2O(g)$ as a function of temperature based on Lennartz's data. A $\ln(p_{H_2O})$ versus 1/T plot

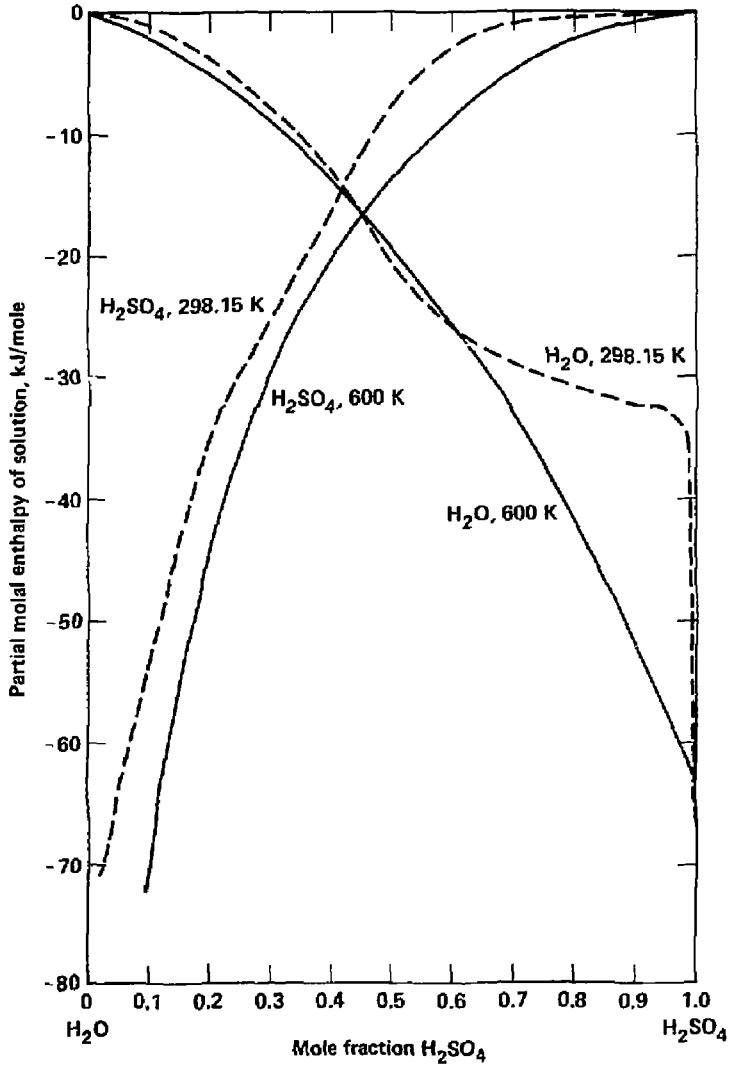

Fig. 8.6. The partial molal enthalpies of solution for H_2O and H_2SO_4 are shown for H_2O-H_2SO_4 mixtures at two temperatures. The curves at 298.15 K are from Giauque et al.,[15] and the curves at 600 K have been derived here based on the data of Lennartz.[10]

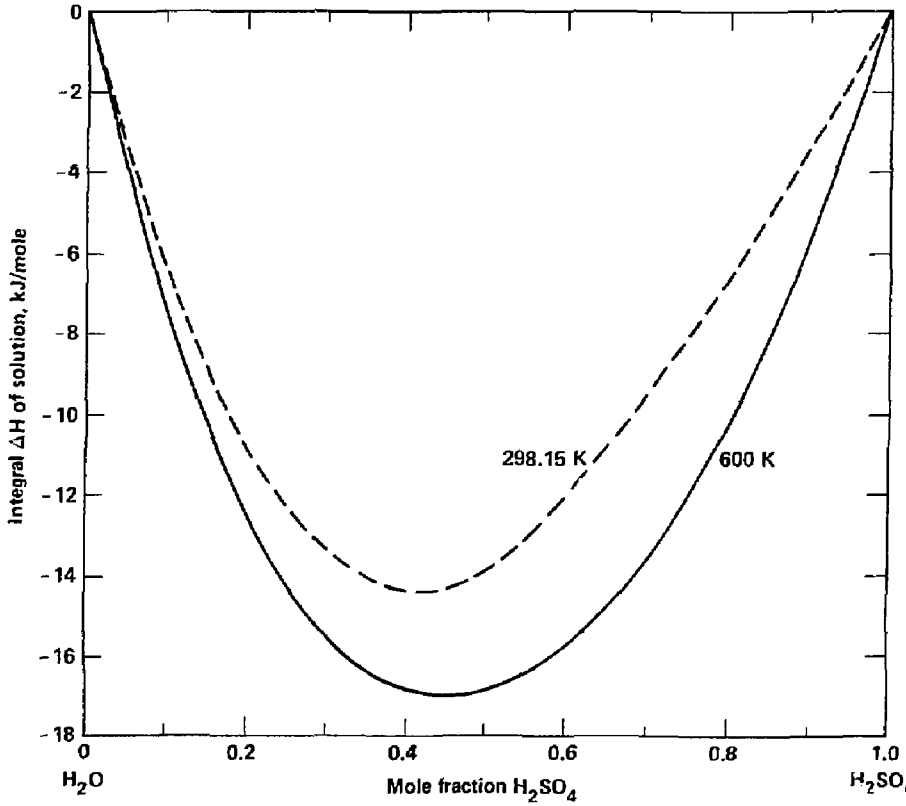

Fig. 8.7. The integral enthalpy of solution for H_2O-H_2SO_4 mixtures is shown for two temperatures. The curve at 298.15 K is from Giauque et al.,[15] and the one at 600 K has been derived here based on the data of Lennartz.[10] The data are presented for one total mole of solution.

then gives the enthalpy of vaporization of $H_2O(g)$ from the azeotropic composition, and subtracting out the enthalpy of vaporization of the reference state $H_2O(\ell)$ gives the enthalpy of exsolution, as before. These data, extending over the range of $x_{H_2SO_4}$ = 0.2 to 0.9, allow us to construct the partial molal enthalpy of solution curve for H_2O at ~600 K as shown in Fig. 8.6. The curve for H_2SO_4 at 600 K is then derived from the H_2O curve by using a Gibbs-Duhem integration procedure.

The integral enthalpies of solution (given in Fig. 8.7) are obtained by summing the partial molal enthalpies of solution as follows:

$$\Delta H_I = x_{H_2O}\,\overline{\Delta H}_{H_2O} + x_{H_2SO_4}\,\overline{\Delta H}_{H_2SO_4} \qquad (19)$$

Thus, the integral enthalpy of solution, ΔH_I, represents the solution enthalpy for one total mole of solution, and must be multiplied by the sum of the moles of $H_2O + H_2SO_4$ involved, when making calculations. It is more convenient for our purposes to use integral rather than the partial molal enthalpies of solution for calculations. Interpolations and extrapolations can be made as needed in Fig. 8.7 to obtain data at intermediate and higher temperatures.

Values for the enthalpy of vaporization of water from the hypothetical 1 atm reference state (see Fig. 8.8) were obtained as follows. Data up to 500 K were taken directly from the JANAF Tables,[12] while at higher temperatures an extrapolation was made down to 1 atm from higher pressure JANAF data. As is apparent in Fig. 8.8, there is a significant difference between the enthalpy of vaporization of water in its 1 atm reference state and at saturation.

Data on Sensible Heats (Enthalpies)

The area of greatest need for sensible heat (enthalpy increment) data is for aqueous H_2SO_4 as a function of composition (see Table 8.1). Data for the pure liquids and gases are either generally available in standard tabulations, or can be obtained by extrapolations.

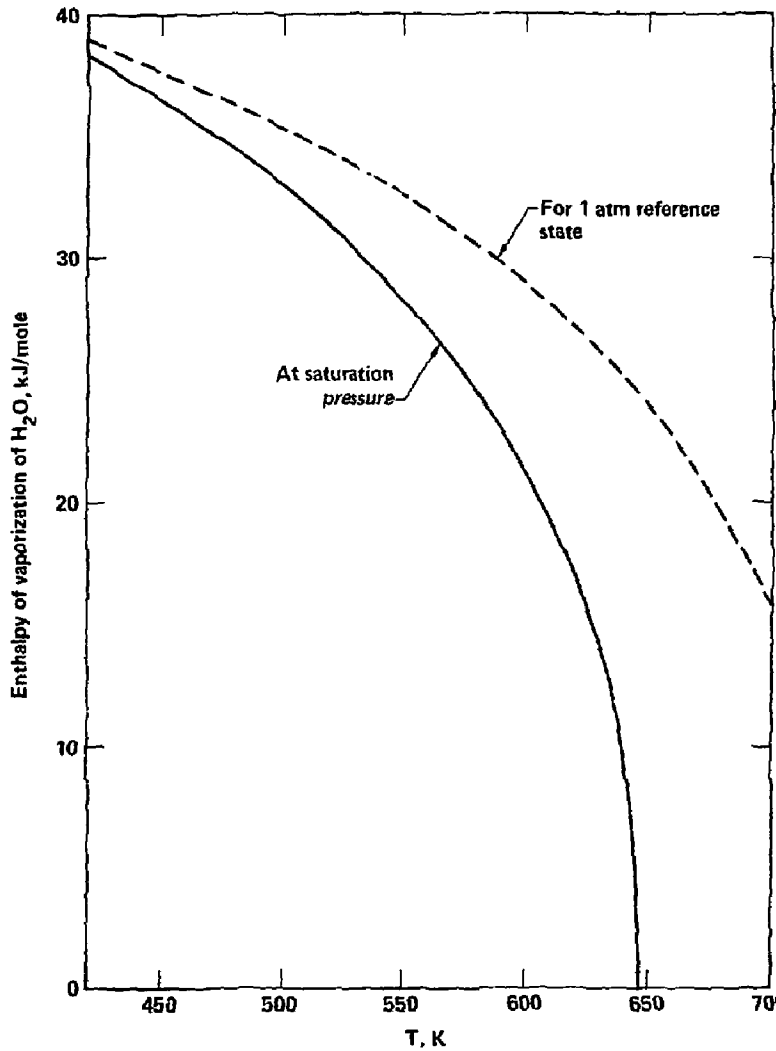

Fig. 8.8. The enthalpy of vaporization of water is shown for both the hypothetical 1 atm reference state and at the equilibrium saturation pressure.

There are two sources of data that we can draw on to estimate the enthalpy increments for aqueous H_2SO_4 : (1) values for $H_{600}-H_{298}$ derived from Lennartz's data,[10] and (2) the JANAF Tables[12] which summarize enthalpy increments for several compositions ranging from $H_2SO_4 \cdot H_2O$ to $H_2SO_4 \cdot 6.5\ H_2SO_4$.

To illustrate the derivation of $H_{600}-H_{298}$ values from Lennartz's data, consider the solution reaction:

$$0.5\ H_2O(\ell) + 0.5\ H_2SO_4(\ell) = 0.5\ H_2SO_4 \cdot H_2O(\ell) \qquad (20)$$

Here pure liquids H_2O and H_2SO_4 in their 1 atm reference states are combined to produce a 50:50 mole ratio solution. $\Delta H_{600}-\Delta H_{298}$ for the overall reaction is obtained from Fig. 8.7 and is found to be -16.87 - (-13.92) = -2.95 kJ/mol. This can be equated to the difference in individual $H_{600}-H_{298}$ values between the product 0.5 $H_2SO_4 \cdot H_2O(\ell)$ and the reactants. Thus X - 0.5(25.648) - 0.5(50.639) = -2.95, and X = 70.388 kJ/mol for the $H_{600}-H_{298}$ value of 0.5 $H_2SO_4 \cdot H_2O$. $H_{600}-H_{298}$ values thus derived as a function of composition across the H_2O - H_2SO_4 diagram are summarized in Fig. 8.9.

A comparison can now be made of the $H_{600}-H_{298}$ values derived from Lennartz with the JANAF data (see Fig. 8.10). We find that agreement is good for the two compositions $H_2SO_4 \cdot H_2O$ and $H_2SO_4 \cdot 2\ H_2O$, but that a major discrepency occurs in the more dilute H_2SO_4 concentrations. A comparision cannot be made at higher H_2SO_4 concentrations since JANAF data is not available. We believe that the values derived from Lennartz's data are the more reliable. Further work is needed to develop the data base over the full range of temperatures needed for the process studies.

Enthalpy increments for the other chemical substances involved in Section II are summarized in Fig. 8.11. Note the difference in enthalpy increments for saturated liquid H_2O and the 1 atm liquid H_2O reference state. Note also the differences in enthalpy increments for steam taken at different pressures.

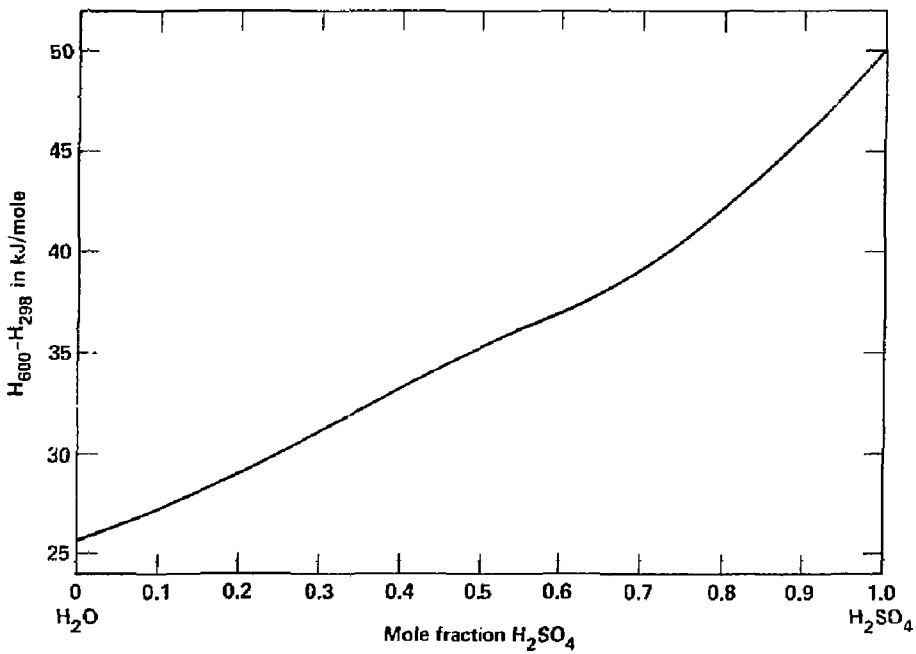

Fig. 8.9. The enthalpy increment $H_{600}-H_{298}$ is shown as a function of composition for one total mole of H_2O-H_2SO_4 solution. The curve is based on the $H_{600}-H_{298}$ values for pur H_2O and H_2SO_4 in their 1 atm reference states plus the integral $\Delta H°$s of solution given in Fig. 8.7.

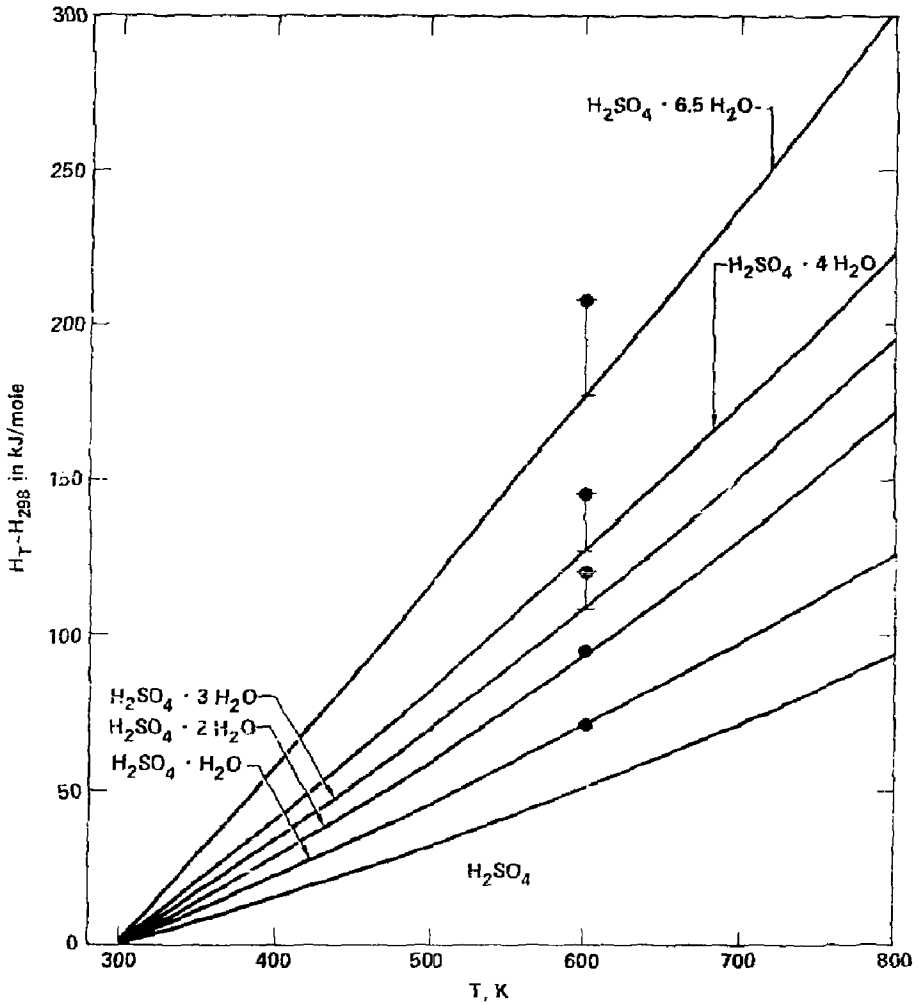

Fig. 8.10. Enthalpy increments, H_{600}-H_{298}, calculated from Lennartz's data[10] (circles) are compared with the JANAF data[12] (solid curves) for various H_2O-H_2SO_4 mixtures. It is apparent that large differences occur at the higher water contents. There is no JANAF data available for comparison in the region between 50 mole % H_2SO_4 and the 90 mole % azeotrope.

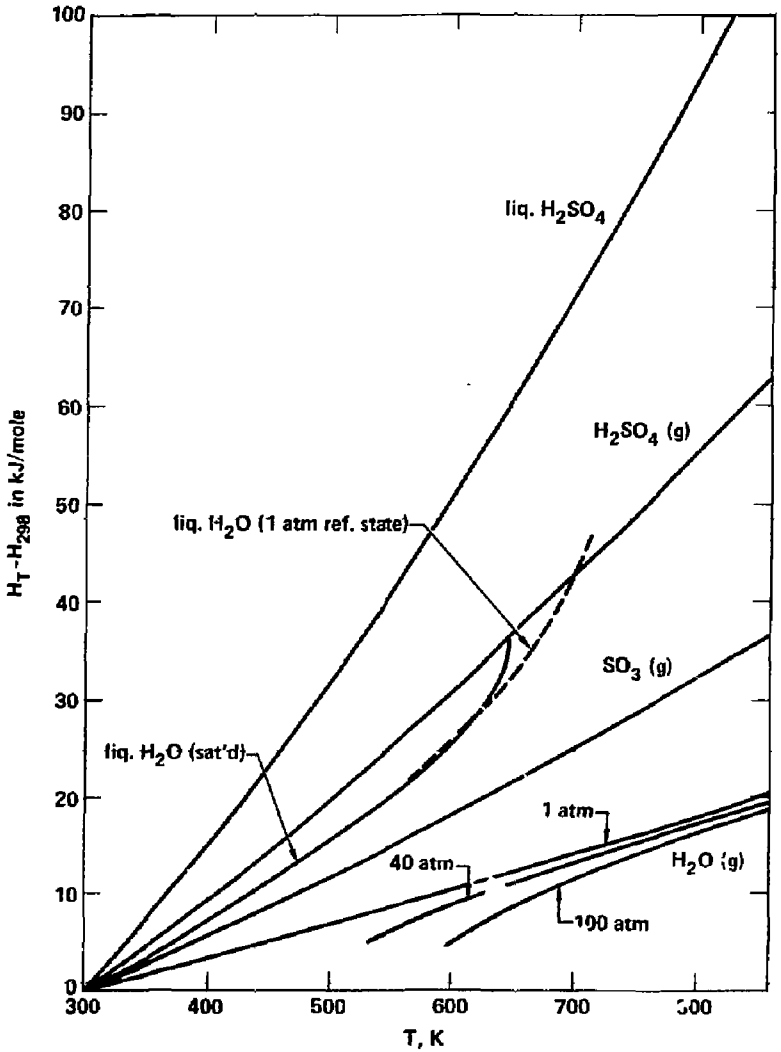

Fig. 8.11. Enthalpy increments above 298.15 K are summarized for various liquid and gaseous species.

References for Section 8

1. R. W. Werner, et al., "Synfuels From Fusion-Producing Hydrogen With the Tandem Mirror Reactor and Thermochemical Cycles," Lawrence Livermore National Laboratory, Report UCID-18909, Vol I. and II, , January 21, 1981.

2. G. E. Besenbruch, K. H. McCorkle, J. H. Norman, D. R. O'Keefe, J. R. Schuster, and M. Yoshimoto, "Hydrogen Production by the GA Sulfur-Iodine Process. A Progress Report," in Hydrogen Energy Progress, Proceedings of the 3rd World Hydrogen Energy Conference, Tokyo, Japan, 23-26 June 1980, Vol.1, edited by T. N. Veziroglu, K. Fueki, and T. Ohta, Pergamaon Press. Oxford, 1980, p. 243.

3. J. H. Norman, K. Mysels, R. Sharp, and G. G. Williamson, "Studies of the Sulfur-Iodine Thermochemical Water-Splitting Cycle," ibid., p. 257.

4. D. R. O'Keefe, and J. H. Norman, "The Liquid Hydrogen Iodide Decomposition Process Step for Water Splitting Applications," ibid., p. 277.

5. P. W. T. Lu and R. L. Ammon, "Development Status of Electrolysis Technology for the Sulfur Cycle Hydrogen Production Process," ibid., p. 439.

6. H. A. Irwin and R. L. Ammon, "Status of Materials Evaluation for Sulfuric Acid Vaporization and Decomposition Applications," in Hydrogen Energy Progress, Proceedings of the 3rd World Hydrogen Energy Conference, Tokyo, Japan, 23-26 June 1980, Vol.4, edited by T. N. Veziroglu, K. Fueki, and T. Ohta, Pergamaon Press, Oxford, 1981, p. 1977.

7. D. van Velzen and H. Langenkamp, "Status Report on the Operation of the Bench-Scale Plant for Hydrogen Production by the Mark-13 Process," loc. cit. reference 2, p. 423.

8. A. Broggi, K. Joels, G. Mertel, M. Morbello, and B. Spelta, "CHRISTINA - A Process for the Decomposition of Sulfuric Acid, loc. cit. reference 6, p. 1929.

9. P. J. Fiebelmann, and G. H. Schuetz, "Technological Aspects in HBr Electrolysis Development," loc. cit. reference 6, p. 1949.

10. H. Lennartz, "Experimental Investigation of the Vapor-Liquid Phase Equilibrium of the System H_2O-H_2SO_4," doctoral thesis submission at RWTH Aachen (University of Aachen), March 31, 1980. We acknowledge the advance availability of this data to us by Professors H. Hartmann and K. F. Knoche of the University of Aachen prior to publication.

11. O. H. Krikorian, "Hydrogen Production Based on Magnetic Fusion," Lawrence Livermore National Laboratory, Report UCRL-86600, August 17, 1981.

12. D. R. Stull and H. Prophet, "JANAF Thermodynamic Tables," second edition, U.S. National Bureau of Standards, Washington, D.C. (1971), with supplements through December 31, 1979, from M. B. Chase, Project Director, The Dow Chemical Company, Midland, MI.

13. "Steam and Air Tables in SI Units," edited by T. F. Irvine, Jr., and J. P. Hartnett, Hemisphere Publishing Corp., Washington, D.C., 1976.

14. J. I. Gmitro and T. Vermeulen, "Vapor-Liquid Equilibria for Aqueous Sulfuric Acid," Lawrence Berkeley National Laboratory, Report UCRL-10886, June 24, 1963.

15. W. F. Giauque, E. W. Hornung, J. E. Kunzler, and T. R. Rubin, J. Am. Chem. Soc. 82, 62 (1960).

SECTION 9.0

INTERFACING THE GA CYCLE

Contributors:
L. Brown and J. Norman

TABLE OF CONTENTS

TABLE OF CONTENTS (Continued)

SECTION 9.0

List of Figures

List of Tables

9.0 INTERFACING THE GA CYCLE

A viable fusion-powered thermochemical synfuels economy will only become reality through close matching of the thermal output of the fusion reactor to load demands of the thermochemical process. Likewise, thermal energy sources within the chemical process must be matched to heat demands within the chemical process, and to heat requirements of the power production systems or power bottoming cycles.

We have proceeded from the integrated TMR driven synfuels plant developed last year[1] and shown in Figure 9.0-1 to develop an even deeper understanding of the factors governing the economic match of the fusion reactor to the synfuels plant. Major modifications have been made to the sulfuric acid processing sections, and economies have been realized through applying energy conservation techniques to the HI purification section. Details of the preliminary design of each process unit in the chemical plant are discussed. The design description included consideration of heat and mass flow, equipment sizes, and safety, and is based on chemical processes that have been demonstrated by laboratory experimentation.

9.1 BASE CHEMICAL PROCESS

The GA water-splitting cycle[2,3] may be described by the four equations:

$$2\ H_2O + SO_2 + X\ I_2 \rightarrow H_2SO_4 + 2\ HI_X \qquad (9.1)$$

$$H_2SO_4 \rightarrow H_2O + SO_2 + 1/2\ O_2 \qquad (9.2)$$

$$2\ HI_X \rightarrow 2\ HI + (x-1)I_2 \qquad (9.3)$$

$$2\ HI \rightarrow H_2 + I_2 \qquad (9.4)$$

These equations represent three chemical reactions and one separations process. In these equations the species HI_X represents an aqueous complex of HI and I_2

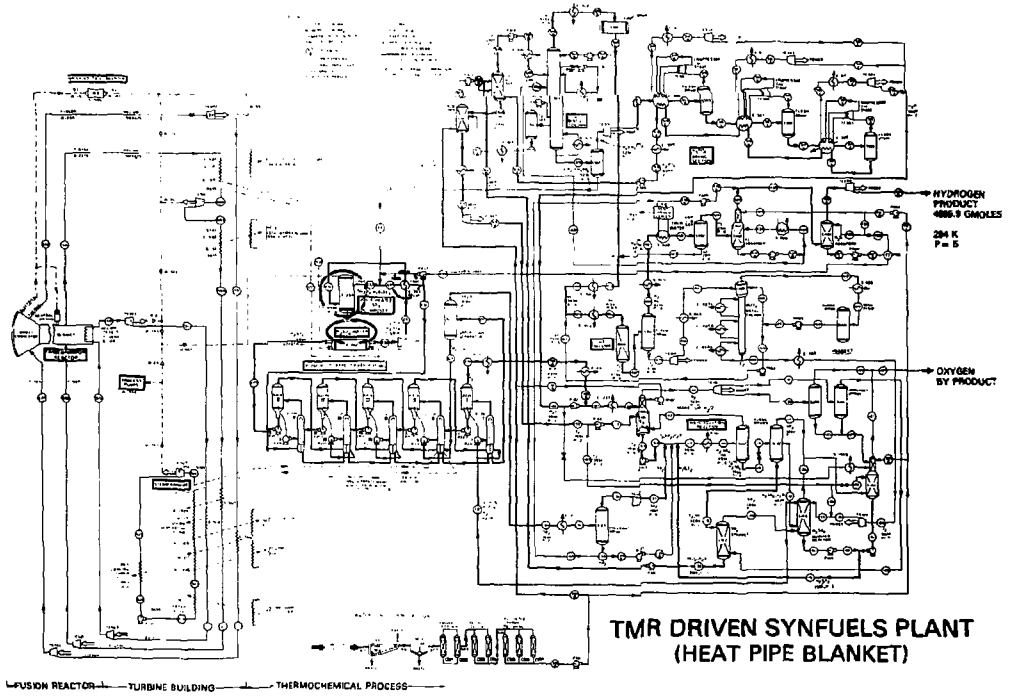

Figure 9.0-1 Overall Process Flow Diagram for the TMR/Synfuels Hydrogen Production Plant, 1981 Version

formed by reaction 1. The H_2SO_4 product of reaction 1 is obtained as a moderately concentrated aqueous solution which is immiscible with HI_x.

The overall process is divided into five sections for design purposes Sections I through IV roughly correspond to the four equations and section V represents the heat and energy transmission equipment required to match the fusion heat source to the chemical process. Descriptions of sections I through IV occupy the remainder of section 9 of this report. Section V is described in report section 10.

The developmental effort on the GA Sulfur-Iodine cycle has proceeded since 1974 along three parallel and mutually supportive lines:

- o Chemical investigations
- o Engineering flowsheet development
- o Process demonstration

Chemical investigations are the basis for the engineering flowsheet development and process demonstration. Synergistically, the flowsheet development and process demonstration efforts give impetus and direction to further chemical investigations. Likewise, each of these tasks raises new questions in its own area.

9.2 RECENT DEVELOPMENTS IN PROCESS CHEMISTRY

The GA water-splitting process is not a static entity but is constantly being upgraded. Information has recently been made available on three chemical innovations to the process[2,4]. In addition, other new techniques have not yet reached the publication stage.

We have investigated one of the three techniques, HBr based HI purification[2], but the initial energy balances are not favorable compared with the H_3PO_4 based HI purification process used in previous flowsheets. The other two techniques have been developed to the preliminary flowsheet stage under separate funding. HI decomposition via homogeneous catalysis[2] will

eventually be incorporated into the fusion synfuels design, but since HI decomposition is relatively inexpensive there is little urgency. The Sulfur-Sulfuric Acid Chemical Energy Storage system[4], developed for solar applications, has the potential for long-term energy storage. Long-term storage could benefit a fusion synfuel plant by permitting the synfuel plant to maintain operation during scheduled and nonscheduled outing of the TMR. In addition, this system could provide on-site power for cold start-up of the TMR.

None of these process improvements have been included in this year's final design.

Discussion of this year's design resumes with section 9.3

9.2.1 HBr Based HI Purifications[2]

In the sulfur-iodin cycle a solution of HI, I_2, and H_2O is produced. This solution is the latent source of H_2 from the cycle. The HI and the H_2O are present in this solution at partial molar free energies of -6.2 and -0.6 kcal/mole, respectively[5]. In order to separate these components, at least these energies must be supplied. The cycle, in its current embodiment, uses concentrated H_3PO_4 to act on the solution in such a way that most of the iodine separates into a second phase and, more importantly, the chemical potential of the H_2O is lowered by binding H_2O in the influence sphere of the H_3PO_4. This results in enhancement of the chemical potential of HI to the degree that it can be separated from the H_2O-H_3PO_4 solution by fractional distillation. Most of the energy associated with the HI-H_2O-I_2 solution separation is required during the separation of H_2O from H_3PO_4 to prepare the H_3PO_4 for recycle. In the present engineering design of this portion of the process, this energy is supplied as work in the form of vapor recompression by turbines which take H_2O vapor from the H_3PO_4 distillation and compress it, causing condensation and the concomitant release of the heat of vaporization at temperatures slightly higher than the heat used to evaporate the H_2O in the first place. This vapor-recompression scheme saves considerable heat energy but uses expensive work energy generated in expensive equipment.

Because of the costs of processing and not because of energy efficiency considerations, other techniques for HI recovery from HI-H_2O-I_2 solutions have been investigated. Finding other competitive methods to rectify this solution is not any easy task. The energies involved are those of chemical reactions not usually encountered in solution separations. A simple extraction agent for HI must react with HI with greater energies than HI has with H_2O-I_2 systems. While one may find appropriate agents, the problem then becomes how to get the HI out of the extraction agent. A number of organic reagents which may extract HI reasonably well fail at this later stage. Nevertheless, success has been achieved in the search for alternate methods of processing HI-I_2-H_2O solutions.

In an earlier publication[6], HI and H_2O mixtures were reported to form two liquid phases: (1) a nearly dry liquid HI, and (2) a strong superazeotropic solution of HI in H_2O. Mixtures of HCl-H_2O were also reported to phase separate[7]. This liquid-phase formation was concluded to have considerable value in separating HI from HI-I_2-H_2O product solutions from the H_2O-SO_2-I_2 reaction. However, to achieve separation conditions, the HI content of these product solutions needs to be considerably increased. Up to now, this seemed possible only by techniques already in use, such as H_3PO_4 treatment.

Still earlier, a high-pressure distillation to break the HI-H_2O-I_2 pseudoazeotrope was investigated[8] as an alternative to the H_3PO_4 treatment. This distillation process was found to be considerably less efficient than breaking the azeotrope of HCl-H_2O[9]. Thus, the pursuit of this technique was temporarily abandoned. However, some engineering evaluations of the small azeotrope shifting, found to occur in the HI-H_2O system (57% HI to $\sim$ 45%), indicated that this process is basically similar in efficiency to the H_3PO_4 treatment.

A process has been conceived which combines high-pressure azeotrope shifting, two-phase formation, solvent extraction using a hydrogen halide (HCl or HBr) for HI separation, and some other features to sharply reduce the amount of H_2O distilled in processing HI_x solutions. To establish the feasibility of this process, laboratory experiments were undertaken to study (1) the distribution of HI between a dry hydrogen halide phase and the wet phase,

(2) the behavior of I_2 in these phases, (3) the high-pressure distillation to separate H_2O and HBr, (4) the fate of the HBr and the degree of reaction of the reactants in the H_2O-SO_2-I_2 reaction, and (5) the recovery of HBr from these product solutions. The preliminary result of these studies was that an HBr based separation process had the potential for significant energy and capital savings over the HBr based process. The process flowsheets developed as part of this work did not demonstrate these potential savings. The flowsheet work is presented in section 9.6.

9.2.2 *HI Decomposition Via Homogeneous Catalysis*

The present version of the sulfur-iodine water-splitting process employs HI decomposition in the liquid phase. Theoretical calculations indicate that high conversion levels are possible using such a scheme, and indeed high conversions were verified experimentally[10]. In addition, the same article reports that the magnitude of extrapolated rate data to high process temperatures appears sufficient to result in a viable process for HI composition. The above rate data were obtained by extrapolating measured rate data from lower temperatures and pressures in batch studies performed on supported platinum and ruthenium catalysts.

Recently, some data for a supported platinum catalyst at closer to actual engineering temperatures and pressures were obtained in a new flowing liquid HI bench-scale system. The rate value obtained gave credence to the use of the extrapolated lower temperature data and thus is verification of the present flowsheet and equipment sizing calculations.

Further in-depth studies, however, revealed a problem associated with the use of heterogeneous catalysis to decompose liquid HI. This is associated with the finding that at least platinum, whether supported or not, does dissolve in the liquid HI to a non-negligible degree. This requires the use of some kind of catalyst recovery and remanufacture scheme. Catalyst recovery and remanufacture are commonplace in the chemical industry but add to the complexity and to the operational and capital costs of the overall process. It was due to the discovery of such an additional requirement of the process that

some consideration was given to the use of homogeneous catalysis to decompose HI and to potential separation schemes inherent in the practical application of homogeneous catalysis.

A homogeneous catalyst concept has been devised[2] in which there is an innate separation of the catalyst from the HI liquid, thereby allowing the catalyst to be totally recycled to the reactor. The concept is based on some unique findings surrounding the phase behavior of HI-I_2-H_2O mixtures. For certain compositions of these three chemicals, two liquid phases in equilibrium can exist. One phase is a very dry phase of HI and I_2; the other is an aqueous phase containing both I_2 and HI. It has been found that it is in this latter phase that certain homogeneous catalyst compounds tend to concentrate. This means that the aqueous phase acts essentially as the catalyst carrier and can be recycled to the HI decomposition reactor without having to recover the catalyst.

The potential advantages over a process employing heterogeneous catalysts with the need to recover and remanufacture 100% of the catalyst are clear. The proposed homogeneous process has been conceptually flowsheeted (but at too late a date for inclusion in this overall process design) and major areas requiring investigation have been identified. The needed information consists mainly in identifying the solubility and distribution of the catalyst in the fluids of the process train at engineering conditions, determining the best area of the HI-I_2-H_2O phase diagram in which to work, and determining the best schemes for catalyst recycle. The results of this work have supported this concept as a viable engineering process.

9.2.3 The Sulfur-Sulfuric Acid Chemical Energy Storage System

A sulfur-sulfuric acid energy storage system has been proposed for the GA sulfur-iodine water-splitting cycle for use in conjunction with a solar heat source[4]. This storage system has the potential for reducing the cost of fusion produced synfuels. During steady state operation of the TMR, a small amount of sulfuric acid could be converted to sulfur. During outages of the TMR, the sulfur could then be burned in air providing both the feed stock and

energy required to operate the hydrogen plant. Potentially, the system could provide sufficient energy for the cold start of the TMR after an outage.

Conversion of sulfuric acid to sulfur is a two step process. The first step is already included in the water-splitting process, Equation 9.2. Formation of sulfur from sulfur dioxide is then accomplished by the disproportionation reaction.

$$3SO_2 + 2H_2O \rightarrow S + 2H_2SO_4 \qquad (9.5)$$

Kinetics of this reaction have been studied[11] at temperatures between 100° and 140°C. The observed reaction rates are compatible with expected holding times for the S and dilute H_2SO_4 products.

Thermodynamically, data from the JANAF Tables[12] and Giauque[13] suggest that the H_2SO_4 product can be made at up to 57% H_2SO_4, which is the same concentration as the sulfur-iodine cycle sulfuric acid product. This reaction, then, provides a method of upgrading an SO_2 product into a much more valuable S product at the expense of cycling two-thirds of the SO_2 back as H_2SO_4 solution. The stored energy in the S is recovered by combustion (in air) to SO_2, and the produced SO_2 is used in the SO_2-H_2O-I_2 reaction to make recycle H_2SO_4 and HI, which is the source of the H_2 in the cycle. The thermodynamics of the storage cycle are presented in Table 9.2-1.

Table 9.2-1 Energetics of the S-H_2SO_4 chemical energy storage cycle (298°C)

	H_{298} (Kcal/mole)
$3H_2SO_4$ (57.6%) → $3H_2SO_4$ (conc)	38.7
$3H_2SO_4$ (conc) → $3H_2O(\ell) + 3\ SO_2 + 3/2O_2$	162.3
$2H_2O(\ell) + 3SO_2 \quad 2H_2SO_4$ (57.6%) + $S(\ell)$	-62.2
$S(\ell) + O_2 \rightarrow SO_2$	-71.8
$SO_2 + H_2O(\ell) + 1/2O_2 \rightarrow H_2SO_4$ (57.6%)[a]	-67.0

---

[a] Note this reaction is not part of the cycle but completes the material and energy balances of the cycle. The actual reaction that completes the sulfur cycle and produces HI, the precurser of hydrogen, is:

$SO_2 + 2H_2O + I_2 \rightarrow H_2SO_4$ (57.6%) + 2HI (sol).

The SO_2 disproportionation makes a low-grade heat which is utilized in the cycle (for instance, for dehydrating H_2SO_4), while the burning of the S makes the very high-grade heat which drives the hydrogen producing plant both electrically and thermally to produce H_2SO_4 and H_2 from SO_2. This storage cycle has inefficiencies as do all energy storage schemes; however, it stores energy densely, stores chemical products cheaply, and supplies a high-grade heat simply and in a very significant amount.

9.3 PLANT DESIGN STATUS

The present plant design is based on the most recent integrated flowsheet. The flowsheets for the main reaction (section I) and HI decomposition (section IV) are the same as for last year's report[1]. The HI purification flowsheet (section III) was revised with the goal of decreasing capital cost. This goal was realized along with small decreases in electrical and thermal energy usage.

The sulfuric acid processing section was revised for each blanket/decomposer combination. The primary emphasis was upon increasing thermal energy recovery of the sulfuric acid concentration step while maintaining a good thermal match to the blanket heat source. At this level of preliminary design the size of the process equipment is determined sufficient to development equipment costs. The design calculations make use of standard chemical engineering correlations for the sizing calculations. When the required physical and transport properties have been unavailable they have been approximated.

9.4 MAIN SOLUTION REACTION STEP (SECTION I)

9.4.1 Design Considerations

The main solution reaction step, Section I of the process, comprises all equipment associated with the chemical reaction:

$$2H_2O(\ell_1) + SO_2(g) + I_2(\ell_2) \quad H_2SO_4(\ell_1) + 2HI(\ell_2) \qquad (9.6)$$

where gaseous sulfur dioxide reacts with an excess of molten iodine and water to produce two immiscible liquid phases. The designation ℓ_1 indicates that water is the major component in the H_2SO_4 product phase, and ℓ_2 that iodine is the major component in the HI product phase. The H_2SO_4 phase which is the lighter (lower density) phase, also contains a trace of iodine. The heavy phase, referred to as HI_x, because it contains excess iodine in a complexed form, also contains water. The main solution reaction is exothermic and Section I requires no heat input from the fusion reactor but exports a significant quantity of low-grade heat to a power bottoming cycle. The Section I process is shown schematically in Figure 9.4-1.

Even though Section I requires no heat input from the fusion reactor, the design of the main solution reaction step has a major influence on the overall process efficiency and thus upon the reactor size and the hydrogen production cost. Although decisions on heat and power recovery within Section I have an effect on efficiency, the composition and temperature of the light phase flowing to process Section II (the H_2SO_4 processing step) and of the heavy phase flowing to Section III (the HI concentration step) strongly influence the overall efficiency of the process. In the interest of efficiency, both streams should leave Section I at as high a temperature as possible and at the highest acid concentration possible. Since the equilibrium of an exothermic reaction shifts towards the reactants as temperature is raised, a compromise must be made between high temperature and high acid concentrations in the product. In deciding the operating conditions for Section I some economic trade-off calculations were made but a full-scale process optimization was not in the scope of this work. The basis for the resulting decisions, as well as those for the rest of this study, may best be termed "engineering judgment." When trade-off calculations were not definitive, the decision was usually made on the side of "high efficiency" not "low capital cost."

Consideration of two factors dominates the design of Section I: (1) the large quantity of heat produced by the main solution reaction must be removed, and (2) the combination of hydrogen iodide and iodine in the heavy aqueous phase is extremely corrosive to materials normally employed for heat transfer surfaces. The only metals known to resist HI_x are refractory metals such as

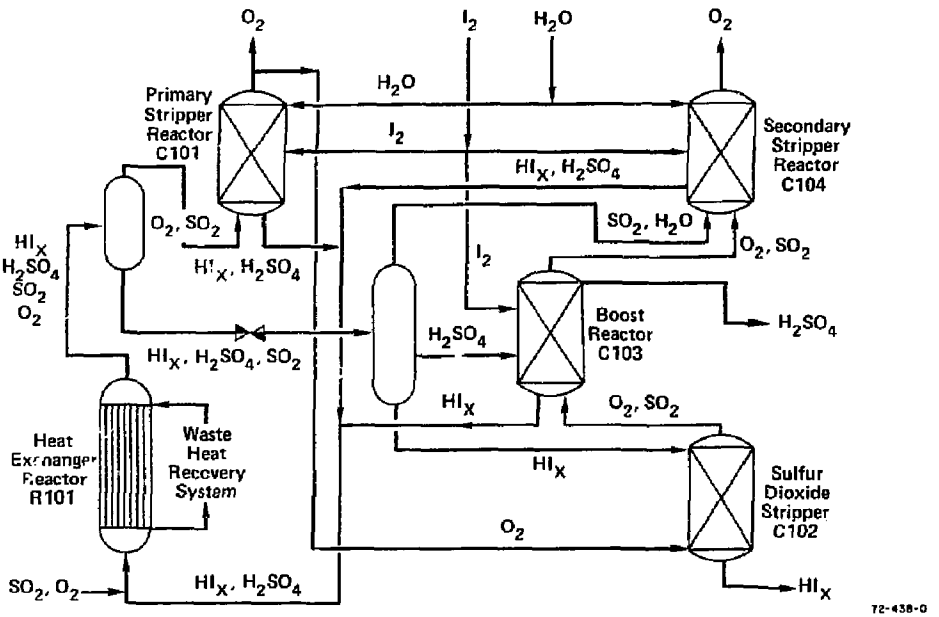

Figure 9.4-1 Schematic of Section I, Reaction of SO_2 with Iodine and Water to give H_2SO_4 and HI_x as Immiscible Liquid Products

niobium, tantalum, and molybdenum. The present design employs niobium for heat transfer surfaces contacting HI_x, which permits the reaction energy to be used in the power bottoming cycle.

Niobium is relatively expensive: therefore, to reduce the capital cost of Section I, a number of design techniques have been employed which improve heat transfer and decrease the amount of Nb required. Some of these are:

1. Cool feed streams to Section I. Prior to carrying out the main solution reaction, we transfer the heat from the Section I feed streams to the power bottoming cycle. This involves less expensive heat transfer materials than Nb and reduces the amount of heat transferred from the reaction products of the main solution reaction.

2. Operate adiabatically. Instead of cooling the reaction products from 393 to 368 K (to shift the equilibrium towards the products) and then reheating the separated products, we operate adiabatically, and maintain the desired production rate of the main solution reaction by increasing the iodine concentration to provide the needed shift in the equilibrium.

3. Use direct-contact heat exchange. Where possible, we employ direct contact heat exchange between immissible liquid phases or gas and liquid phases.

4. Apply enhanced heat transfer techniques. Utilizing two-phase gas-liquid flow through the heat exchanger gives higher than normal convective heat transfer coefficients. Spiral-fluted tubing provides enhanced heat transfer and, due to the wall stiffening effect, permits thinner tube walls.

9.4.2 Heat Exchanger Reactor

Almost 52% of the chemical reaction forming HI and H_2SO_4 takes place in the Heat Exchanger Reactor (R-101 in the flow diagram of Figure 9.4-1) and in

the piping immediately preceeding the reactor. The reactor selected is a shell and tube heat exchanger with fixed tube sheets. The vessel, tube sheets, and heads are fabricated from mild steel. The heads are lined with fluorocarbon and the spiral-fluted niobium tubes are welded to a niobium tube sheet liner. The process fluid is on the tube side of the heat exchanger and the shell side is part of the power bottoming cycle.

Upstream of the heat exchanger, the SO_2/O_2 from Section II (sulfuric acid processing) is mixed with the predominantly iodine stream from the Boost Reactor (C-103) and aqueous streams from the scrubbing reactors (C-101 and C-104). The combined streams react exothermically as they flow through a fluorocarbon-lined pipe and into the heat exchanging reactor. The pressure drop through the heat exchanger reduces the system pressure from an initial 0.50 MPa to 0.44 MPa at which point the temperature reaches 393 K. At the exit of the heat exchanger the O_2 is removed from the stream in the first of two separators (S-101). In the second separator (S-102), operating at 0.11 MPa, three phases separate: the heavy liquid phase (HI_x), the light liquid phase (H_2O/H_2SO_4), and a gas phase consisting of SO_2 and steam. The vaporization of water and SO_2 results in the temperature decreasing from 393 K to 385 K.

9.4.3 Lower Phase SO_2 Stripper

The lower phase solution (HI_x) is saturated with SO_2 which when allowed to remain forms sulfur and H_2S via tramp reactions. An oxygen recycle stream strips most of the SO_2 in a packed bed stripper (C-102) thus minimizing the tramp reactions. A minimum amount of oxygen is employed for this operation as the evaporation of water into the oxygen cools the HI_x requiring more heat input in Section III (HI purification). With a 10% O_2 recycle the HI_x is cooled from 385 K to 381 K.

The stripper, sized for operation at 70% of flooding, is a standard packed column design. The fluorocarbon-lined mild steel vessel is packed with 50 mm ceramic Raschig rings. Since the operating pressure is near atmospheric, a glass-lined steel vessel is a viable option but would require fluorocarbon packing to avoid liner damage.

9.4.4 Boost Reactor

In the boost reaction, the sulfuric acid concentration of the light phase is increased from 50% to 57% by contacting with molten iodine in the presence of sulfur dioxide. The increased H_2SO_4 concentration is realized through the action of the main solution reaction. Water is used up by reaction with SO_2 and I_2 to form H_2SO_4 and HI. Over 7% of the total chemical reaction of Section I occurs in the Boost Reactor. Since the contact is performed in a counter-current manner, the reactor also acts as a direct contact heat exchanger, raising the temperature of the sulfuric acid stream from 383 K to 393 K.

Although the mechanical design of the Boost Reactor is straightforward, i.e., a fluorocarbon-lined mild steel vessel packed with 50 mm ceramic Raschig rings, the sizing calculations are not. Common packed columns operate with either a gas rising through a decending liquid phase, or a light liquid phase rising through a decending heavy liquid phase. The Boost Reactor has both a gas phase (SO_2 in O_2) and a light liquid phase (H_2SO_4 and water) rising through the decending heavy liquid phase (I_2). The present design is based on adding the cross-sectional areas required if the gas and light liquid separately contacted the heavy liquid. This is a very conservative approach. We believe that a design based upon information gained in a pilot plant would result in a smaller Boost Reactor vessel.

9.4.5 Scrubbing Reactors

The oxygen is purified before discharge to the atmosphere in the Scrubbing Reactors. The packed column reactors operate in a titration mode in which sufficient iodine is added to the scrub water in the lower part of the column to react stoichiometrically with the sulfur dioxide present in the oxygen. In the upper part of the column the oxygen is washed with pure water. The primary Scrubbing Reactor (C-101) operates at 0.44 MPa purifying the gaseous product of the Heat Exchanger Reactor (R-101). Over 19% of the Section I reaction takes place in the primary Scrubbing Reactor. Almost 22% of the total reaction takes place in the secondary Scrubbing Reactor at 0.10 MPa. The secondary scrubber cleans up the oxygen stream exiting the Boost Reactor as well as the steam/SO_2

stream produced during depressurization of the liquid reaction product of the Heat Exchanger Reactor.

Both scrubbing reactors perform a second function as direct contact heat exchangers. Oxygen leaving the process is cooled to near ambient conditions while preheating the water entering the process. The scrubber vessels are of fluorocarbon-lined mild steel and the packing is 50 mm ceramic Raschig rings. Pilot plant tests may demonstrate reduced vessel costs. The upper portions of the scrubber contain only water and oxygen so no lining should be required in this area. Depending upon the temperatures reached in the lower portions of the scrubber, less expensive linings may be possible.

9.4.6 Heat and Power Recovery

The heat transferred to the steam power bottoming cycle from Section I totals 782 MW_t. The majority of this is transferred via the Heat Exchanger Reactor but significant quantities of heat are also transferred from the hot water products of Sections II and III and from the SO_2/O_2 product of Section II. Since the heat transfer materials used for water and SO_2 are much less expensive than the niobium used in the Heat Exchanger Reactor, there is the potential for further cost reduction by performing more of the cooling on water and SO_2 streams. Ultimately an economic optimization must determine the split in heat transfer duties on the basis of minimum hydrogen production cost.

A total of 5.4 MW is recovered in Section I using turbines for pressure reduction. Preliminary indications are that the turbines are economic but a final determination must await an analysis based on the hydrogen production cost resulting from this study.

9.5 H_2SO_4 PROCESSING STEP (SECTION II)

9.5.1 Design Considerations

The sulfuric acid processing step, Section II of the process, takes 57% H_2SO_4 from Section I, decomposes the H_2SO_4 and returns the resulting SO_2,

O_2, and H_2O back to Section I. Process flow diagrams are given in Figures 9.5-1 and 9.5-2 for the Joule Boosted and Fluid Bed versions of the process.

Major unit operations of Section II are sulfuric acid concentration, vaporization, and decomposition. Vaporization and decomposition equipment designs are based on last year's report, but the sulfuric acid concentration section has been completely re-flowsheeted.

In the interest of capital cost savings, last year's flowsheet left out the vapor recompression equipment which were part of the original GA design[14]. The process efficiency reported by GA (47%) cannot be achieved without recovering a large fraction of the heat of vaporization of the water accompanying the sulfuric acid. These new flowsheets accomplish this goal without resorting to vapor recompression techniques.

9.5.2 Acid Concentration

Several techniques were tried to accomplish the goal of heat recovery without vapor recompression. These included multi-effect evaporators, pressure staged flash evaporators (adiabatic and non-adiabatic) and column evaporators. It became evident that no single technique could achieve the desired goal. A combination of four different concentration techniques was used in the final flowsheet.

Staged isobaric boiling at 7.5 MPa was used to achieve the goal of water removable at useful steam temperatures. Atmospheric distillation was used for final concentration of the acid to the azeotropic composition. A single adiabatic flash stage at 1.1 MPa was used to match the isobaric staged boiling to the atmospheric distillation column. Finally, staged partial condensation was used to remove H_2SO_4 from the decomposed product along with a minimum of water.

The isobaric staged boiling is accomplished in what can be described as a horizontal distillation column. The design is patterned after the H_2SO_4 vaporizer described in last year's report and shown in Figure 9.5-3. The

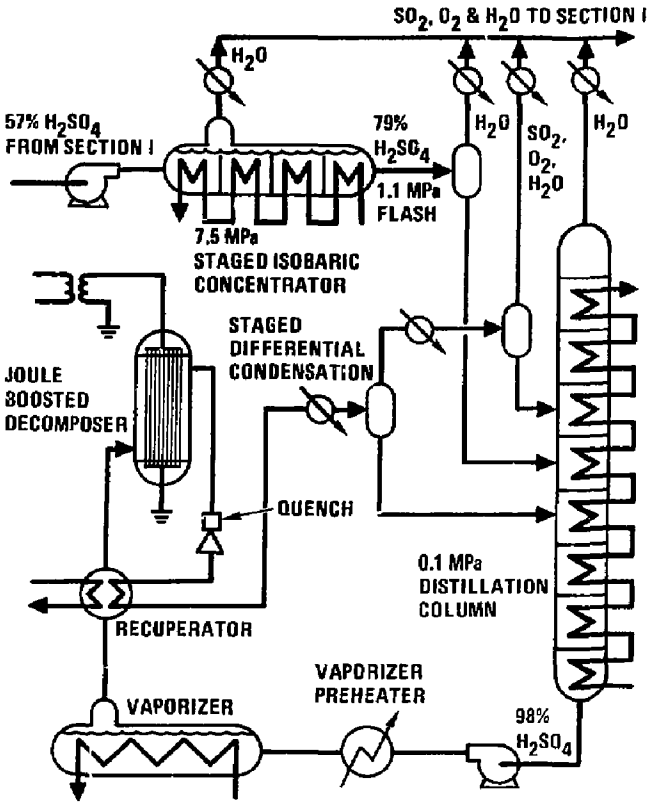

Fig. 9.5-1 Schematic of Section II, Joule-Boosted decomposer version. Concentration and decomposition of sulfuric acid.

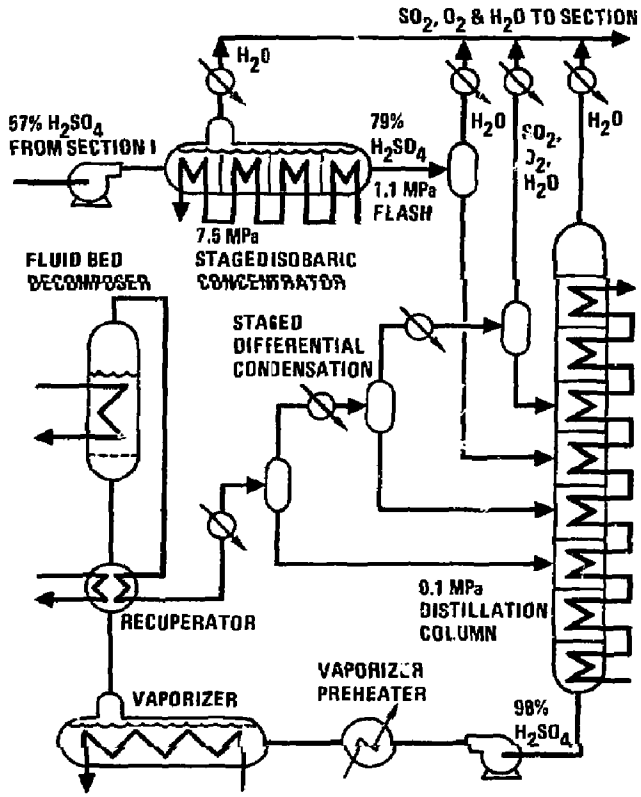

Fig. 9.5-2 Schematic of Section II, fluid bed decomposer version. Concentration and decomposition of sulfuric acid.

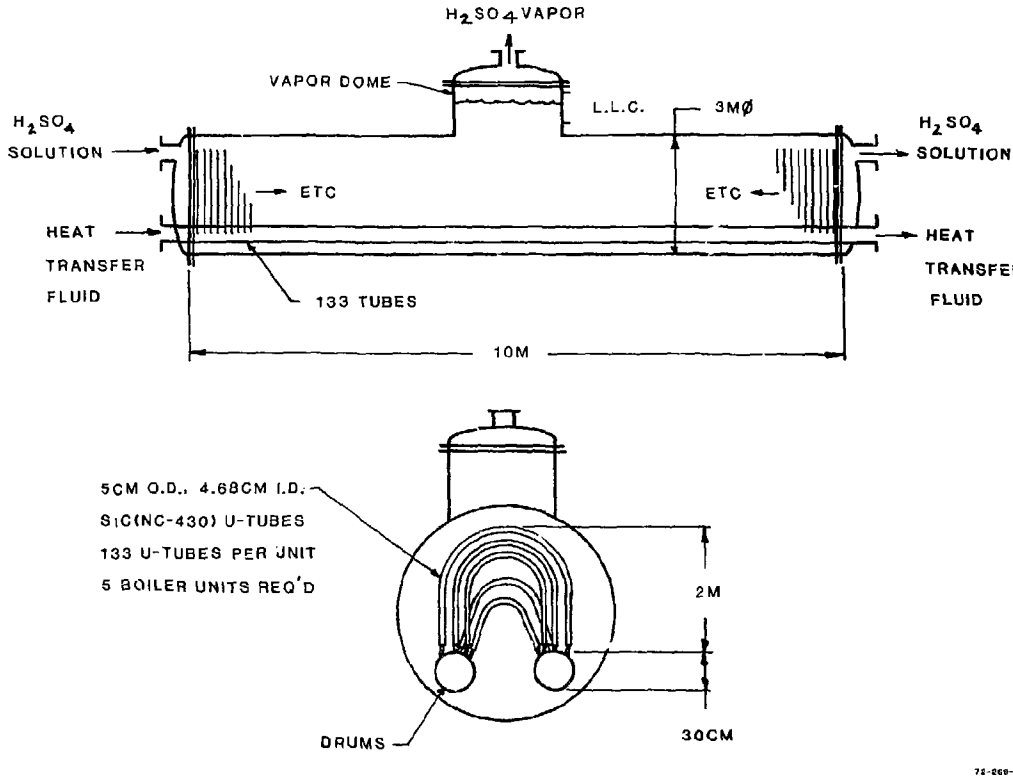

Figure 9.5-3 Design for the H_2SO_4 Azeotrope Boiler

horizontal vessel is fluorocarbon lined to protect the mild steel from the sulfuric acid and brick lined to protect the fluorocarbon lining from the heat. Siliconized silicon carbon tubes provide the treat of vaporization for the water. The vessel is partitioned into multiple stages by weirs made from acid brick. Above the weirs the vapor space is interconnected, with the vapor outlet at the low acid concentration end of the unit. Mixing of the vapors from many stages results in a vapor composition typical of the mass average temperature. Acid droplets are removed from the vapors in a ceramic demister pad. Concentration in this equipment is limited by the equilibrium acid concentration in the vapors to 79%.

The acid at 7.5 MPa is flashed first to 7.5 MPa and then to 0.1 MPa. After the first flash, the vapors are still low enough in H_2SO_4 to permit recycle to Section I. The combined liquid/vapor stream from the second flash is fed to the atmospheric distillation column.

A ten-stage distillation column completes the concentration of the acid up to 98%. Since the column must accommodate a large variation in liquid rates over its length, a tray type column is preferred over a packed column. Ceramic internals are used in the form of trough type trays. The bottom reboiler and the intermediate reboilers are again constructed with siliconized silicon carbide U-tubes. Each tray, except for the top, has its own intermediate reboiler.

The product gases from the decomposer are subjected to partial condensation so as to remove the undecomposed acid with a minimum of water. Two stages of partial condensation are required for the Joule Boosted Decomposer flowsheet and three for the Fluidized Bed Decomposer flowsheet. The liquid products from the partial condensation stages is returned to the atmospheric distillation column, the liquid from the final stage providing the column reflux.

9.5.3 H_2SO_4 Vaporizer

The H_2SO_4 Vaporizer is a particularly challenging design problem since either ceramic materials or high-silicon metallic alloys need to be employed to

simultaneously withstand the H_2SO_4 corrosion and the 3.0 MPa pressure from the helium heat transfer fluid.

Our best choice is to use siliconized silicon carbide U-tubes for the heat exchangers in the H_2SO_4 Boiler. This approach has been used on a developmental basis by the Norton Company[15] in conjunction with AiResearch, Inc. for high pressure (5 MPa) helium "heat exchanger applications." We developed a special geometric configuration that established a rough optimization between the heat transfer and pumping losses in the helium and the boiling instabilities that could occur in the liquid H_2SO_4. This configuration is shown in Figure 9.5-3. The heat transfer basis for this design can be briefly summarized as follows.

We selected nucleate boiling on the H_2SO_4 liquid side of the tubes and then used the Palen and Small correlation[16] to obtain an estimate of maximum obtainable heat flux:

$$\left(\frac{q}{A}\right)_{max} = 61.6 \frac{P}{D_o N^{1/2}} \rho_v \lambda \frac{\sigma_s (\rho_\ell - \rho_v)^{1/4}}{\rho_v^2} ,$$

where P = the pitch diameter for the tubes
D_o = outside tube diameter
N = number of tubes (twice the number of U-tubes)
λ = the heat of vaporization
σ_s = liquid-vapor interfacial surface tension
ρ_ℓ = density of the liquid
ρ_v = density of the vapor

A σ_s value of 43 dynes/cm at 680K and 1 atm was obtained from Gmelins [17]. Thus, a maximum heat flux limit of 2.42 MW/m^2 was calculated for a U-tube boiler unit with 133 tubes, each 5 cm O.D. with 3 mm walls. Since we wish to operate well below this critical heat flux level, say at 25%, we select q/A = 0.606 MW/m^2 as a shell-side value. We use the Eckert and Drake[18] correlation to obtain an estimate for the boiling side film drop of 0.3 to 1.5 K and conclude that the boiling side is well in hand. A parallel train of 5 boilers is required for the plant.

Next we needed to obtain the tube side heat transfer necessary to support this high flux (25% of the critical maximum heat flux). First we tried supercritical steam and found it unacceptable. Even at a Mach number of 0.5 or 336 m/s, the film drop with steam is ~110 K, which is too high. Following supercritical steam, we next considered helium, which also has greater safety advantages. A rough optimum was found for 2.5 MPa high pressure helium operating at a flow rate of 1074 kg/s or 30 m/s (0.05 Mach number), and Re = 137,000. Here the film drop was ~400 K. However, by using turbulence promoters, small finned tube fluting, and swirl vane inserts, this film drop was cut to ~50 K. For this operating condition, we calculated a 5.5 KPa (0.05 atm) pressure drop and a pumping power of 1.5 MW_e. A number of case studies were done varying parameters to establish the near-optimum design given above. further parametric studies may be able to reduce further this still large (150 K) film drop.

9.5.4 SO_3 Decomposer for the Lithium Oxide Blanket

The SO_3 Decomposer unit requires the highest temperature to be supplied from the TMR; therefore, the design of this unit and its relationship with the whole G.A. Cycle dictates the TMR interface concept. We have selected approximately 7 atm and 1250 K as the process conditions for the decomposer with the aim of obtaining a high decomposition yield, while eliminating the need for catalysts. The fraction of SO_3 converted to $SO_2 + O_2$ (quenched) under these conditions is expected to be around 84%. We have elected to supply the required 1250 K temperature by means of electrical heating; thus, this unit is called a Joule-Boosted Decomposer.

The Joule-Boosted Decomposer is shown in Figure 9.5-4 as we have developed the design. The heating elements are commercially available SiC electric (AC power) furnace elements. The vessel and headers are simple in design and can be silica brick-lined, Teflon-coated steel. From a materials standpoint SiC and silica brick should offer an acceptable life under the 1250 K, 7 atm SO_3, SO_2, O_2, H_2O environment. Eight units in parallel are needed to handle the required hydrogen production rate.

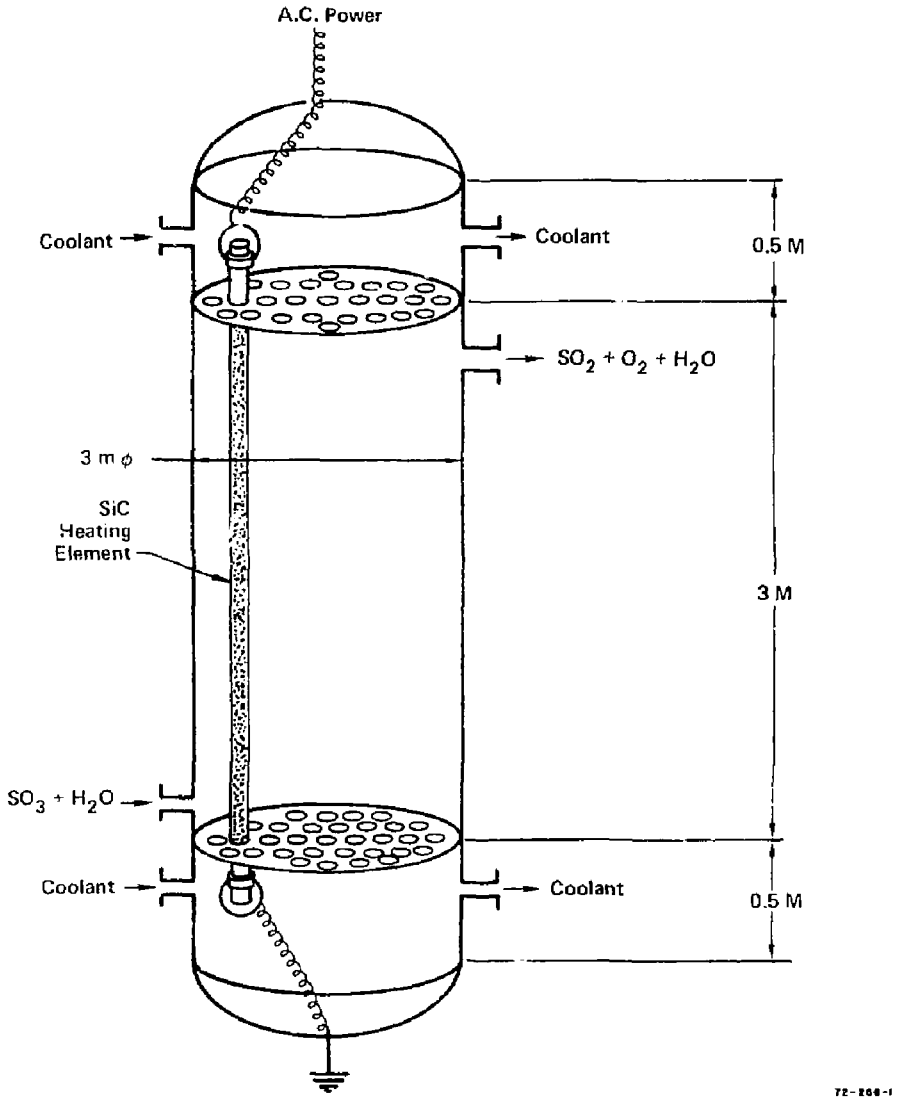

Figure 9.5-4 Design for the Joule-Boosted SO_3 Decomposer

The Joule-Boosted Decomposer offers the best possible safety isolation of the O_2-containing process gases from the hot, liquid metal-containing fusion blanket.

9.5.5 SO_3 Decomposer for the Two-Zone Blanket

For the Two-Zone blanket, the decomposer is a catalytic fluidized bed reactor operating at 1050-1100 K. The unit contains internal heat exchanger tubes to provide the heat for the highly endothermic SO_3 decomposition. It can achieve up to a 55% conversion using a CuO catalyst, if sulfation of the catalyst does not become a problem around 1050-1100 K. If sulfation presents a serious problem, our alternative is to use a more expensive platinum catalyst on a titania support. The details of this Fluidized Bed Decomposer were given in the 1980 Annual Report[19], so only a brief overview is provided here.

Figure 9.5-5 shows some of the details of the fluidized bed design, using 0.5 mm diameter catalyst spheres. The fluidized bed is on the shell side of the unit with the helium on the tube side. The Δ Ts across the helium film within the tube are about 20 K, and the Δ Ts on the outside of the tubes in the fluidized bed region are expected to be around 14 K. The helium Δ T presents a difficult design problem and the 20 K is a compromise between higher helium source temperatures and helium pressure.

The Fluidized Bed Decomposer requires seven units in parallel to handle the needed production rate. This approach of coupling the blanket to the process with helium offers good safety isolation for the process. More optimization work is needed to reduce the overall capital and operating costs further. This concept saves the costs of a large turbo-electric generator required in the Joule-Boosted Decomposer, at the expense of running a hotter fusion blanket and a more complex decomposer design.

9.5.6 Decomposer Recuperator

The Decomposer Recuperator is a heat exchanger unit that simultaneously preheats the feed to the decomposer using heat from the hot SO_2, O_2, H_2O, and

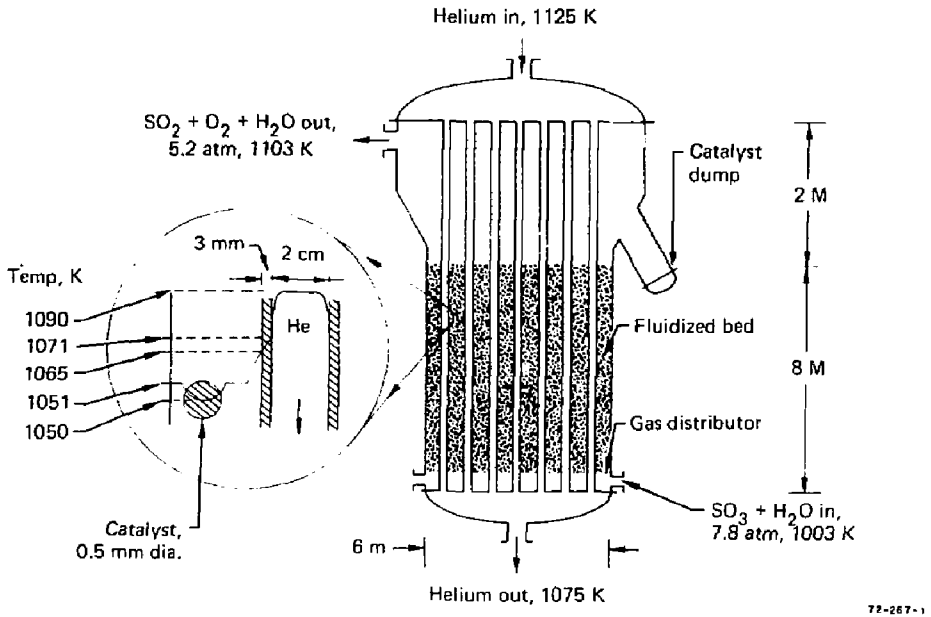

Figure 9.5-5 Design of the Catalytic Fluidized Bed SO_3 Decomposer for the Two-Zone Blanket

SO_3 that leave the decomposer. This unit is particularly important, since without it, a larger quantity of sensible heat in the temperature range of 680 K to 950 K would have to be supplied from the blanket. In the Joule-Boosted Decomposer design the feed is further heated from 950 K to 1250 K using electrical heat. In addition to the sensible heat requirement, there is, of course, additional heat required to supply the endothermic heat for decomposing SO_3 into SO_2 and O_2. Recuperation is insufficient to provide the total sensible heat required to treat the sulfuric acid vapors from the boiling point to the decomposer inlet temperature because the heat of decomposition of H_2SO_4 to H_2O and SO_3 must be provided over this temperature range. The Recuperator thus includes a "boost" loop of TMR-supplied heat. This Decomposer Recuperator is a difficult design to accomplish since it is a gas-to-gas heat exchanger, and these types of units characteristically have very low heat transfer coefficients. The result is a high pressure drop, high pumping power, large and expensive heat transfer areas, and high alloy temperatures. The design we evolved was again a techno-economic compromise. We used a standard shell and tube configuration as shown in Figure 9.5-6 and held the temperature low enough for Incoloy-800H.

The heat transfer analysis involved varying fluid temperature, wall temperature, heat exchanger surface areas, and pumping power, in order to produce a near optimum design. We found that the hot decomposed gases could be dropped from 1170 K to 730 K, while the feed could be preheated from 680 K to 950 K. The 950 K was selected to hold the average wall temperature to 1050 K so that the Incoloy-800H wall thickness could be kept at 3mm, with a maximum calculated creep rate of 1% in 20 years. The heat exchanger area was found to be 14,814 m^2 and the pumping power was 1.24 MW_e equally split between the shell and tube side.

The gas velocity within the tubes was 13.6 m/s with a Reynolds number of Re = 79,000 based on the tube diameter. A Nusselt number of 284 and heat transfer coefficient of 78.8 cal/m^2-s were used to obtain a gas to wall ΔT of 50 K.

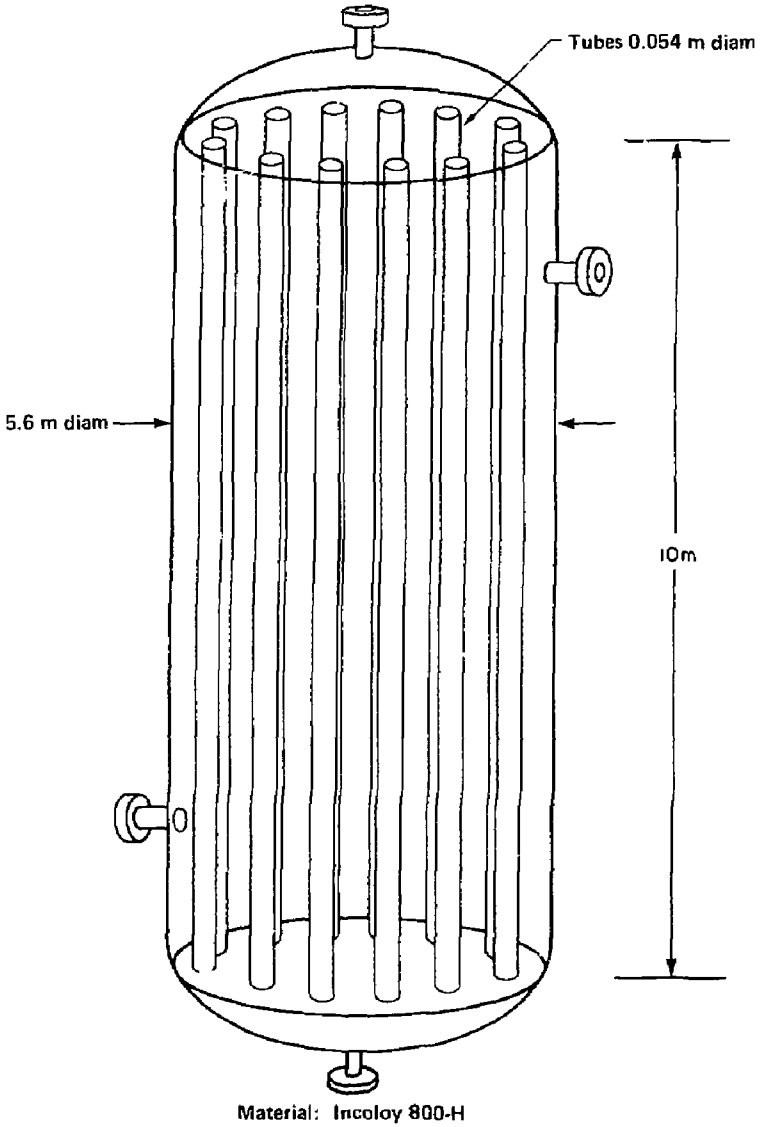

Figure 9.5-6 Design for the SO_3 Decomposer Recuperator

9.5.7 Decomposer Coolers

The Decomposer Cooler continues cooling the decomposer product after recuperation is no longer possible. Heat removed in the decomposer coolers is supplied to the atmospheric still and the multistage isobaric flash preheater. Sulfuric acid condenses out as the decomposer products are cooled. This sulfuric acid is removed in several stages, twice for the Joule-Boosted Decomposer case and three times in the case of the Fluid Bed Decomposer. The liquid phase from the final cooler is predominantly water; therefore, it is returned to Section I along with the gases.

Silicon carbide is required where sulfuric acid is condensing. At high temperatures, before the onset of condensation, Incoloy 800H would suffice except that silicon carbide is required for boiling sulfuric acid duty on the cold side of the tubes. After the majority of the sulfuric acid has been condensed and decanted, more conventional materials of construction are permitted. In the low temperature region the requirements of heating 57% sulfuric acid demonates the material selection.

9.6 HI CONCENTRATION VIA HBR EXTRACTION-CASE STUDY (SECTION III)

9.6.1 Design Considerations

A first cut flowsheet was made for HI concentration via liquid HBr extraction[2]. The design goal was to separate HI from the HI_x product of Section I in a cost effective manner. The flow diagram which resulted is shown in Figure 9.6-1. The design easily met the goal of low capital cost, but energy conservation in this new system has not progressed to the point where it can challenge the phosphoric acid based separation process.

9.6.2 HBr Extraction System

The HBr extraction (XC305) may be viewed as a traditional solvent extraction system employing partially miscible solvents. The two solvents HBr and H_2O counter currently contact each other in either a packed or plate type

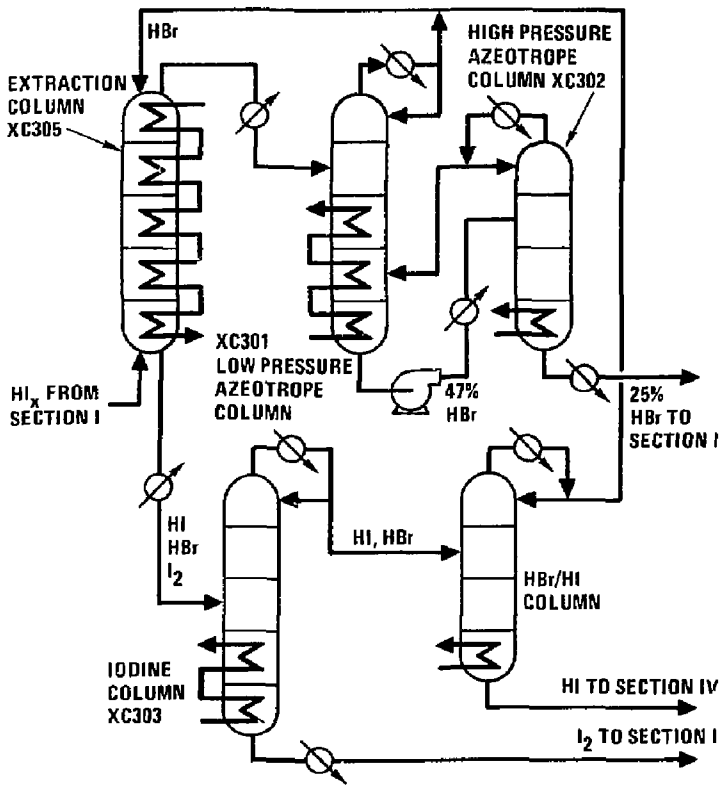

Fig. 9.6-1 Schematic of Section III, HBr version. Separation of HI_x into HI, I_2 and H_2O.

column or possibly in a multi-stage mixer-settler train. The HBr strips HI and I_2 from the H_2O. The solubility of H_2O in the HBr is very small, but HBr has a very significant solubility in H_2O. One factor which sets this system apart from most solvent extraction systems is the large heat liberation associated with the dissolution of HBr in H_2O. XE320 is provided to remove this exothermic heat. The temperature varies with position along the extraction system, but is allowed to build to 420 K at the HBr-HI-I_2 outlet. System pressure is 9.0 MPa.

9.6.3 Dry Phase Processing

The dry phase from the extraction system is subjected to two distillation steps to separate the HBr-HI-I_2 mixture. The first distillation column (XC303) removes the HBr and HI in the overhead and the I_2 in the bottoms. The column operates at 1.9 MPa which gives 633 K as the bottoms temperature and 330 K for the overhead temperature. The second distillation column (XC304) separates the HBr and HI at 4.2 MPa. The bottoms temperature is 380 K and the overhead 330 K.

Some energy savings would result if the I_2 distillation column were operated at the same pressure as the HBr/HI column. The column overhead would operate in a partial condensation mode sending a vapor feed to the HBr-HI column, thus reducing the its reboiler duty. A partially compensating effect would be the increase in reboiler temperature for the I_2 distillation column.

9.6.4 Wet Phase Processing

The H_2O-HBr phase cannot be easily separated by distillation. Initially, the H_2O-HBr stream is superazeotropic, thus pure HBr can be distilled away from azeotrope (XC301). The azeotrope cannot be completely broken even at the 22 MPa operating pressure of XC302, but it is shifted from 47% HBr to 25%. The dilute HBr is then recycled to Section I where the distillation column XC301 operates at 4.3 MPa. This pressure is set by the requirement that the overhead HBr be liquid at 330 K. Lowering the assumed cooling water temperature would permit the column pressure to be decreased. The bottoms temperature could also

be reduced from its present 546 K. Heat to the distillation column is provided by multiple reboilers. The overhead from XC302 is fed to XC301 which also delivers substantial heat to XC301.

The final distillation column, XC302, operates at 22 MPa and delivers a 25% HBr bottoms product to Section 1. The HBr, along with sufficient water to form azeotrope (48% HBr), acts as a diluent in Section 1 and the remaining water is free to participate in the prime reaction. Operating pressure of this column is set by the critical pressure of HBr.

9.6.5 Energetics of HBr Extraction Based HI Purification

Although the net enthalpy change was quite low, 132 kJ/mole H_2, the present version of the HBr based process, has excessively high heat flow to waste heat. This can most readily be seen in the large amount of low-grade heat produced in the extraction column XC305. 470 kJ, resulting from the heat of solution of HBr in water, is liberated over the temperature range of 420-330 K. There is little need for heat of this quality in the process; therefore, its only use would be in the power bottoming system where its efficiency of conversion to electrical energy would be very low. Additionally, 190 kJ is transferred to cooling water at 330 K in the condensers of XC301, 303, and 304 (mostly from XC301).

An analysis of the flowsheet shows some potential for reducing the condenser losses to cooling water, but a means of efficiently using the heat of solution of HBr in water must be found to make this process step viable.

9.7 HI CONCENTRATION STEP (SECTION III)

9.7.1 Design Considerations

The hydrogen iodide concentration step, Section III of the process, entails separation of a mixture of hydrogen iodide, iodine, and water (HI_x) into its component parts. A simplified flow diagram of Section III is presented in Figure 9.7-1. The iodine and water are separately returned to

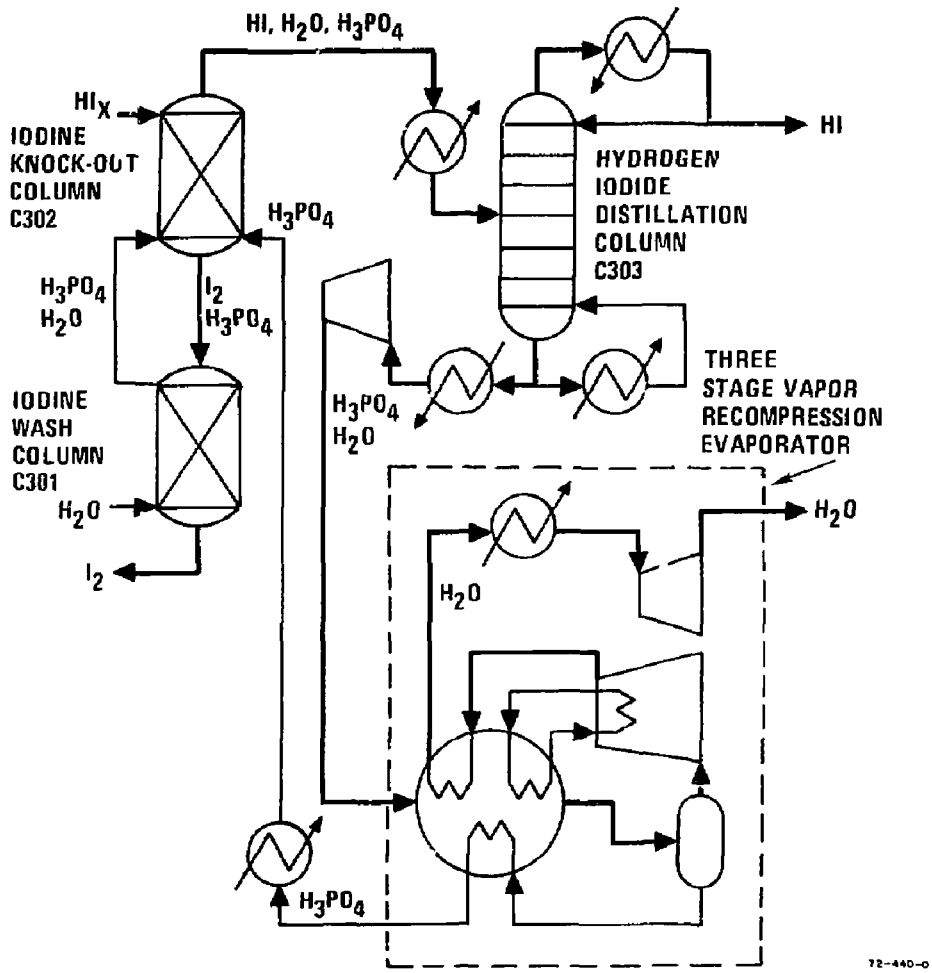

Figure 9.7-1 Schematic Flow Diagram of Section III, Separation of Aqueous HI_x into HI, I_2, and H_2O

Section I, the main solution reaction step, and the hydrogen iodide is decomposed in Section IV of the process. The use of phosphoric acid as an extractive distillation agent, first proposed in 1975[20], remains as the reference process for HI purification. The alternative of liquid HBr extraction, although attractive from a theoretical standpoint, is not yet able to compete with the H_3PO_4 process on an efficiency basis.

The system HI-H_2O forms a maximum boiling azeotrope at a composition of 57% HI which is approximately the composition of HI_x on an iodine free basis. Iodine is held in the HI-H_2O solution through the formation of polyiodides such as HI_3, HI_5, HI_7, etc., which are formed only in the presence of water. Addition of H_3PO_4 lowers the activity of water which performs two functions; first, it destabilizes the polyiodide complexes permitting iodine to form a separate liquid phase; secondly, it breaks the azeotrope which allows the HI to be distilled from the mixture. The HI distillation is performed under pressure so that liquid HI is available for decomposition in Section IV. Water is removed from the phosphoric acid by evaporation, and the phosphoric acid is recycled back into the process.

9.7.2 Iodine Separation

Liquid iodine is separated from the HI_x in two steps. Both operational steps are performed in fluorocarbon-lined mild steel vessels packed with 20-mm ceramic saddles. In the iodine knock-out column (C-302), the HI_x is contacted counter-currently with 96% H_3PO_4. The HI and H_2O are extracted into the H_3PO_4, leaving molten iodine saturated with H_3PO_4. H_3PO_4 is washed away from the iodine with water in the iodine wash column (C-301). The wash column is operated at 0.3 MPa ~~and 393°K~~ so as to maintain both iodine and water in the liquid state.

9.7.3 Hydrogen Iodide Distillation Column

HI is distilled from the H_3PO_4 solution in a plate column operating at 0.9 MPa. Operation at this pressure requires a higher temperature in the bottoms than would be required at low pressure, but an expensive HI liquefaction step

is eliminated. Efficient use of the thermal energy, required for operation of the HI Distillation Column, is made possible by producing the HI product as a liquid and thus eliminating the thermodynamic inefficiency associated with a liquefactions compressor and that associated with production of power to operate it. Additionally, an intermediate condenser allows part of the condensing heat to be withdrawn from the column at a useful temperature. Although a majority of the heat required to preheat the feed and to operate the column is obtained by heat recovery within Section III, 355 MW is required from Section V at 523 K.

Design of the HI Distillation Column entailed a trade-off between capital and operating costs. Use of an intermediate condenser and operation at a relatively low reflux ratio reduce thermal energy requirements, but require more trays in the column for adequate chemical separation. The final design included 50 Hastelloy-C trays in a Hastelloy-C clad mild steel tower. The trays selected were the trough type, being a reasonable compromise between the higher efficiency, higher cost of bubble cap trays and the lower efficiency, lower cost of sieve trays.

An additional small design complication arises because the feed to the HI Distillation Column is saturated with iodine. Liquid iodine must be removed continuously from the middle of the column to avoid buildup. A stream, containing two liquid phases consisting of phosphoric acid and liquid iodine, is withdrawn from the iodine buildup region. The phosphoric acid returns to the column from the top of a liquid-liquid separator and the bottom iodine phase passes to the iodine wash column for phosphoric acid removal before returning to Section I.

The small quantities of H_2SO_4 and SO_2, remaining in the lower phase product from Section I, react chemically with HI in the feed preheater for the HI Distillation Column. The product of the reactions are H_2O, I_2, H_2S, and S. The quantities involved are so small that the relative amounts of S and H_2S have not been determined. For flowsheeting and cost estimating purposes, it has been assumed that half the sulfur in H_2SO_4 and SO_2 ends up as H_2S and half as S. The H_2S will leave the column in the overhead product and the S is

assumed to exit the column with the H_3PO_4. The liquid S is separated from the H_3PO_4 and oxidized back to SO_2 in Section II.

9.7.4 Phosphoric Acid Concentration

Removal of water from the phosphoric acid is accomplished in three stages of vapor recompression-driven flash evaporation. The operating condition of each stage has been modified so as to reduce capital cost for heat exchange. Each stage now operates at a different pressure with the pressure decreasing as the acid concentration increases. The major cost saving came through elimination of the heat exchanger which conditioned the evaporator feed. Only the first and last stages require any heat input from the fusion reactor, but all three stages require significant quantities of power for vapor recompression. A total of 641 MW of shaft power is required to operate the compressors whereas only an additional 104 MW of thermal power at 484 K is required from Section V to heat the high temperature evaporator. Heat is recovered within each evaporation stage from interstage cooling of the six-stage compressor, from the condensation of the compressed steam and from the concentrated phosphoric acid product.

The phosphoric acid concentration step is simple in concept but capital costs of the turbine compressors and heat exchangers are significant in the overall hydrogen production cost. Even though a considerable reduction in the cost of H_3PO_4 concentration has been made, alternative chemical systems are under continuing investigation with the goal of eliminating H_3PO_4 from the process.

9.8 HI DECOMPOSITION STEP (SECTION IV)

9.8.1 Design Considerations

The HI decomposition step (Section IV of the process) requires the following operations:

- Decompose HI(l) to H_2(g) and I_2(l)

- o Separate HI from the I_2 and recycle to the decomposer
- o Separate HI from the H_2 and recycle to the decomposer
- o Scrub the H_2 product in preparation for distribution

A simplified schematic flow diagram of Section IV is presented in Figure 9.8-1.

Three process variables dominate the design of Section IV and have a direct impact on the fusion reactor interface. The temperature and pressure of the HI Decomposition Reactor govern the equipment size and amount of recycle through the reactor, whereas the HI-I_2 Distillation Column pressure determines the maximum process temperature required from the fusion reactor. Variables governing the cleanup of the hydrogen product have a smaller, but still significant, impact on the hydrogen production cost.

9.8.2 HI Decomposition

Hydrogen iodide decomposition is accomplished in the HI Decomposition Reactor (R-401). The extent of the decomposition reaction is limited by thermodynamic equilibrium. Therefore, to limit the amount of recycle of HI back through the reactor, process conditions must be chosen so as to give a high conversion per pass through the reactor. Previous studies at the General Atomic Company[10] have demonstrated that when decomposition is carried out under high pressures so that HI and I_2 are present as liquids, a much higher decomposition yield is obtained than with the analogous gas phase decomposition. Selection of the temperature and pressure involve a number of tradeoffs. The critical temperature of HI places an upper limit upon the initial reaction temperature of an adiabatic flow reactor, while the required hydrogen delivery pressure places a lower bound upon the system pressure.

For this system design we still rely upon an adiabatic flow reactor using an activated charcoal catalyst. The recently developed homogeneous catalysis concept[2] became available after this year's design base was fixed.

The reactor was sized for a 4-minute residence time. The mild steel vessel is lined with fluorocarbon to protect it from the HI and iodine. The

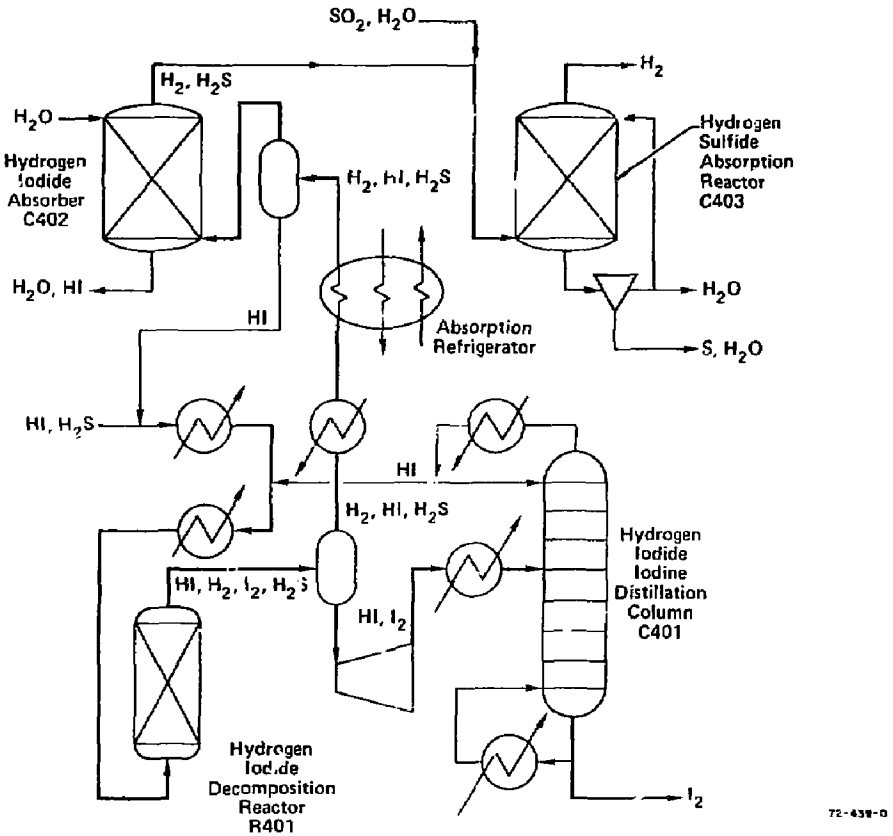

Figure 9.8-1 Schematic Flow Diagram of Section IV, The HI Decomposition Step

reactor operates at 8.3 MPa. the reaction temperature increases from 415 K at the inlet to 424 K at the outlet due to the slightly exothermic nature of the reaction under these conditions. The majority of the energy required to bring the HI to reaction temperature is supplied by heat reuse within Section IV. Only 6% of the energy (10.6 MW_t) must be supplied from the fusion reactor.

A design based upon a continuous stirred tank reactor deserves future consideration. It would require a considerably longer residence time than the adiabatic flow reactor, but the system pressure could be lowered to 5 MPa, which may lead to reduced capital costs.

9.8.3 $HI-I_2$ Distillation

The liquid product from the HI Decomposition Reactor passes through a pressure reducing turbine to the $HI-I_2$ distillation column (C-401). The pressure of the still (5.1 MPa) sets the temperature of the still bottoms at 713 K, which is the highest temperature required from the fusion reactor helium in the Joule-Boosted concept. The still pressure and temperature may be decreased further, thus decreasing the high temperature heat load on the fusion reactor but at the expense of increased low temperature heat requirements to reheat the still overhead product for recycle to the HI cracker. In addition, the heat now supplied from the overhead condenser to the evaporative refrigerator and from the bottoms product to the liquid HI heat exchangers, would instead have to be supplied from other sources.

In addition to the 41 MW required from the fusion reactor helium stream, an additional 36 MW is required at 522 K. This additional heat may be used at a lower temperature because the distillation column is designed with intermediate reboilers. The use of intermediate reboilers increases the capital cost due to the cost of both the boilers and additional trays in the column, but the overall thermal efficiency is improved significantly.

Each distillation column, constructed from Hastelloy-B clad mild steel, is 2.7 m in diameter for the bottom 12 m and expands to 4.7 m in diameter for the upper 3 m. There are 25 Hastelloy-B trough type trays in the bottom section

and 6 in the top. The expanded top section is required by both the higher flow rates and lower density encountered in this section of the column.

9.8.4 Hydrogen Cleanup

The hydrogen from the decomposer is cleaned in three operations. First, the bulk of the hydrogen iodide is removed by condensation. Second, remaining HI is removed with a water wash. Finally, the trace of H_2S is removed by a combination of chemical reaction and water wash.

The gaseous product of the HI Decomposition Reactor is cooled in three stages. A heat exchanger removes the high temperature portion of the heat to the power bottoming cycle and dumps the low temperature heat to cooling water. The stream is further cooled from 303 K to 291 K via an absorption refrigeration system. The LiBr based refrigeration[21] is driven by waste heat from the condenser of the HI-I_2 Distillation Column. After condensate separation, only a small quantity of HI and possibly H_2S remain in the hydrogen.

The remaining HI is easily removed via a water wash (C-402). A minimum amount of water is employed because any water added at this point must be removed by distillation in Section III. In the absence of iodine, HI is not corrosive to nonmetallics; therefore, hydrocarbon-lined mild steel is sufficient for this application. Since traces of iodine could enter the HI scrub column due to process upsets in the HI condensation system, the lower portions of the column are lined with fluorocarbon. The column is packed with 25-mm ceramic Raschig rings.

Due to the high acidity in the lower portions of the column, H_2S cannot be absorbed. H_2S builds up slightly in the upper section of the column until at steady state, H_2S passes on to the H_2S removal column (C-403) at the same rate it enters the HI scrub column. Since H_2S has a relatively low solubility in water, a simple water scrub would require that an excessive amount of water be processed through Section II to reconvert the H_2S to SO_2. The problem is solved by adding a small amount of SO_2 to the H_2S absorber. H_2S reacts with

SO_2 in the presence of water to produce a sulfur slurry. The slurry is concentrated via a filter with back-flush so only a small amount of water accompanies the S back to Section II where it is converted to SO_2 via reaction with SO_3. The mild steel column, packed with 25-mm ceramic Rashig rings, is hydrocarbon lined to prevent corrosion.

The H_2 pressure is dropped to the distribution pressure of 5.1 MPa via a power recovery turbine and thus exits the process.

9.9 MATERIALS SELECTION FOR THE THERMOCHEMICAL PLANT

The corrosive nature of the chemicals involved in the GA cycle has necessitated an extensive materials testing program be carried out during the process development effort. Since sulfuric acid is common to other thermochemical cycles and is industrially significant, other workers have extensively investigated materials for the H_2SO_4-H_2O system.

9.9.1 Materials Selection for Section I

The extensive material testing program for the GA cycle has produced a great deal of data on corrosion in iodine systems[22]. Table 9.9-1 presents a summary of the test results. Early results indicated that niobium was an additional material impervious to attach by the HI-I_2-H_2O solutions typical of the main solution reactor, but the most recent work regarding the effect of the H_2SO_4 upon the system questions the use of niobium in this portion of the process. Tantalum can be substituted for the niobium, at higher cost, but this has not been done in the present equipment design.

Although glass-lined steel is an ideal material for use with the HI-I_2-H_2O system, it is unavailable in the equipment sizes required for the TMR powered plant. Fluorocarbon-lined steel performs the same function and is available in the desired equipment sizes.

PRINCIPAL UNIT-OPERATIONS	FLUIDS	TEMPERATURE RANGE		MATERIAL CANDIDATES FOR: HEAT EXCHANGERS, VESSELS, PUMPS AND HARDWARE
		°C	K	
MAIN SOLUTION REACTION	$SO_2 + I_2 + H_2O \longrightarrow$ $HI_x + H_2SO_4$ (55 wt % ACID)	125	398	GLASS-LINED STEEL; FLUOROCARBON PLASTICS & ELASTOMERS; CERAMICS – SiC, Al_2O_3, CARBON IMPERVIOUS GRAPHITE TANTALUM
I_2 AND H_2O SEPARATION	$HI_x + H_3PO_4$	120–158	393–431	GLASS–LINED STEEL; HASTELLOY B–2; TANTALUM–LINED STEEL; FLUOROCARBON PLASTICS
I_2 RECYCLE	I_2	120	393	HASTELLOYS B–2, G, C–276; GLASS
DECOMPOSITION OF LIQUID HI_x	HI_x (LOW H_2O); I_2; H_2	120	393	HASTELLOY B–2; GLASS–LINED STEEL; FLUOROCARBON PLASTICS;

Table 9.9-1 Material candidates for handling process fluids containing HI_x and I_2

9.9.2 Materials Selections for Section II

Materials selections need to be made for the following process units for Section II:

- o Multi-Effect Evaporator
- o H_2SO_4 Boiler
- o Joule-Boosted Decomposer
- o Fluidized Bed Decomposer
- o Decomposer Recuperator
- o Decomposer Cooler

Table 9.9-2 presents a summary of the material investigations by GA[22] for the sulfuric acid sections of the process.

Multi-Effect Evaporator and H_2SO_4 Boiler

Materials problems are similar for the Multi-Effect Evaporator and the H_2SO_4 Boiler. The main problem is to provide a heat exchanger that is tolerant of hot concentrated sulfuric acid. All known metallic heat exchanger materials (except for expensive noble metals such as Au and Pt), are severely corroded by these H_2SO_4 solutions above temperatures of ~500 K. A number of ceramic and intermetallic materials have been tested in hot concentrated H_2SO_4 at 633-693 K in recent years at LLNL[23,24] and at Westinghouse[25]. The top candidate materials from both corrosion resistance and heat exchanger design standpoints are the following:

- o Siliconized SiC
- o "$CrSi_2$" coated Incoloy-800
- o Durichlor-51 (Fe-14% Si-4% Cr)

All of these materials depend upon the development of a corrosion resistant SiO_2 scale on the surface to provide protection against corrosion by H_2SO_4. Similarly, it is well known that pure silica glass (SiO_2), such as in the form of silica brick, is inert to corrosion by H_2SO_4.

PRINCIPAL UNIT OPERATION	FLUIDS	APPROXIMATE FLUID TEMPERATURES		MATERIAL CANDIDATES FOR: HEAT EXCHANGERS, VESSELS, PUMPS AND OTHER HARDWARE
		°C	°K	
MAIN SOLUTION REACTION	$SO_2 + I_2 + H_2O \longrightarrow HI_x + H_2SO_4$ (65 wt %)	125	398	GLASS-LINED STEEL; CERAMICS–SiC, Al_2O_3, CARBON; FLUOROCARBON PLASTICS & ELASTOMERS; IMPERVIOUS GRAPHITE TANTALUM
CONCENTRATION	H_2SO_4 55–65 wt %	95–150	368–423	HASTELLOYS B–2 OR C–276 GLASS OR BRICK-LINED STEEL IMPERVIOUS GRAPHITE
CONCENTRATION	H_2SO_4 65–75 wt %	150–180	423–453	HASTELLOYS B–2 OR C–276 GLASS OR BRICK-LINED STEEL IMPERVIOUS GRAPHITE
CONCENTRATION	H_2SO_4 75–98 wt %	180–420	453–693	BRICK-LINED STEEL; CAST Fe–14 wt % Si
VAPOR FORMATION AND DECOMPOSITION	$H_2SO_4 \longrightarrow H_2O + SO_3$	330–600	603–873	BRICK-LINED STEEL; CAST Fe–14 wt % Si SILICIDE COATINGS ON STEEL; HASTELLOY G
VAPOR DECOMPOSITION	$SO_3 + H_2O \longrightarrow H_2O + SO_2 + 1/2\ O_2$	600–850	873–1123	INCOLOY 800H WITH ALUMINIDE COATING

Table 9.9-2 Candidates construction materials for sulfuric acid

SiC currently presents the best prospect as a heat exchanger material. Siliconized SiC (a two-phase composition consisting of a mixture of SiC and Si) is produced at the Norton[26] and Carborundum[27] companies and is especially suited for this type of application. This type of material, which contains about a 10-15% excess of silicon metal, is impervious to gases, has a high thermal conductivity, high strength, good thermal shock resistance, and can be fabricated in complex shapes and bonded together to form heat exchanger assemblies[28]. Corrosion testing of SiC for 1121 h and Si for 592 h in 97% H_2SO_4 at 673 K at the Lawrence Livermore National Laboratory showed no evidence of corrosion[23], thus confirming the corrosion resistance of both SiC and Si for this application.

Specimens of Incoloy-800 coated with chromium silicide of nominal composition $CrSi_2$ were tested for corrosion for 240 h at 673 K in 97% H_2SO_4 at the Lawrence Livermore National Laboratory[24] and found to show a very low rate of corrosion (extrapolated weight loss rate of 15 mg/cm^2-y). The coatings were about 120 μm thick, uniform in thickness, well-bonded to the substrate, and without evidence of fractures. The coatings were prepared by Dr. Charles M. Packer of Lockheed Missiles and Space Company of Palo Alto, California, using a slurry coat and rapid melt technique. Although the above results are preliminary in nature, they are encouraging in that a conventional heat exchanger material such as Incoloy-800 can be protected against corrosion by a coating process.

Durichlor-51 is a commercial high silicon cast iron material that is yet another candidate as a heat exchanger or container material. It is basically an intermetallic compound with a composition of approximately Fe_3Si and, as such, presents the disadvantages common to most intermetallics of poor ductility, low tensile strength, and poor machining and fabrication characteristics. Also, being a cast material, the control of internal porosities and non-uniformities present production problems. Nonetheless, with proper quality control and with good engineering design and practices, these problems can be controlled. From a corrosion standpoint, tests of up to 524 h on Durichlor-51[23] have shown only a moderate amount of attack (5 μm surface penetration); but very importantly, corrosion appears to proceed very uniformly

over the surface of this material. It therefore seems reasonable to extrapolate to a lifetime of the order of 5 y for this application. In contrast to Durichlor-51, duriron is another high silicon cast iron alloy that shows a rather irregular corrosion behavior with grain pullouts, corrosion pits, and spallation in similar H_2SO_4 corrosion tests at 673 K[23].

In view of the developments thus far, our choice of material is siliconized SiC for the H_2SO_4 heat exchangers for both the Multi-Effect Evaporator and the H_2SO_4 Boiler. We select silica brick as a liner material for the vessels, both because of the inertness of silica to corrosive attack by sulfuric acid, and to provide thermal insulation so that more conventional materials (e.g., Teflon-lined steel) can be used for the vessel wall. We select Durichlor-51 for the bodies of the liquid H_2SO_4 circulation pumps.

Joule-Boosted Decomposer

For the Joule-Boosted Decomposer, we mainly need to select a material for the heating elements. We are in the fortunate position that Tiegs at Oak Ridge National Laboratory has recently exposed a number of materials to sulfuric acid vapors at 1 atm pressure for up to 1900 h at 1273 K and 3300 h at 1498 K[28]. Of the materials tested, SiC proved to be the best and to give an extremely low corrosion rate, e.g., $\sim$0.5 m depth of corrosion in 1000 h at 1273 K. Furthermore, corrosion appears to proceed according to a diffusion controlled mechanism through a protective silica (SiO_2) scale which, by extrapolating by the indicated $t^{1/2}$ law, we obtain $\sim$7 μm corrosion in 20 years - which is negligible.

Increase of pressure of gaseous sulfuric acid vapors from the 1 atm conditions used by Tiegs to the 7 atm required in the Joule-Boosted Decomposer will increase the corrosion somewhat due to volatility of SiO_2 in steam as gaseous $Si(OH)_4$, but the effect is not expected to be significant at 1250 K.

Two materials approaches are available for the vessel walls of the Joule-Boosted Decomposer. The wall can either be lined with silica brick

backed by 316 stainless steel maintained above the condensation temperature of sulfuric acid (680 K), or it can be constructed of Incoloy-800H which is limited to a maximum temperature of 050 K because of creep strength limitations (see further details on Incoloy-800H properties in the discussion of the Fluidized Bed Decomposer below). Selection of the materials approach to use will depend upon engineering considerations.

Fluidized Bed Decomposer

The main materials problem in the Fluidized Bed Decomposer is selection of a heat exchanger material to meet corrosion resistance and creep strength requirements.

Corrosion tests on a number of heat exchanger alloys for H_2SO_4 vapor decomposers have been carried out at JRC Ispra and at the General Atomic company at temperatures in the 773-1173 K range. Their results[29] indicate that as bare uncoated alloys, Incoloy-800H and Inconel-625 provide the best materials with anticipated lifetimes of a few years. A substantial gain in lifetime can be achieved by using an aluminide-coated Incoloy-800H on the surface exposed to the decomposing SO_3 gas. This gives an unusually stable coating-substrate combination that stabilizes in coating thickness and weight change after an exposure of 200-300 hours to the gaseous H_2SO_4 products[25]. Corrosion protection is apparently afforded by an Al_2O_3 film, and imperfections in the coating are self-healing. The useful life of aluminide-coated Incoloy-800H for this application is believed to be of the order of 20 years. On the high pressure helium side, corrosion is not a problem.

From a consideration of creep strength, cost, and fabrication issues, Inconel-617, Inconel-625, and Incoloy-800 (or Incoloy-800H) appear to provide the best alternatives. Stress rupture and creep properties for Inconel-625 and Incoloy-800 are comparable[30]. Although creep strength data are not available for Inconel-617, it shows 1000-hour stress rupture strengths that are three times higher[30] than for the other two alloys. Thus, extrapolations of the available data for Inconel-625 and Incoloy-800 suggest a tensile creep strength for 1% creep in 100,000 hours of 2000 $\pm$ 50% psi (1.4×10^7 Pa) at 1100 K and

1200 + 30% psi (8.2×10^6 Pa) at 1150 K. We estimate the corresponding values for Inconel-617 to be 6000 + 50% psi (4.1×10^7 Pa) at 1100 K and 3600 + 30% psi (2.4×10^7 Pa) at 1150 K based on the argument that the creep strengths scale as a fraction of the long-term creep rupture data similar to Inconel-625 and Incoloy-800. Although no creep data are available for Incoloy-800H, it is a material that has been designed for higher strength than Incoloy-800 and should give a better performance.

From a consideration of both corrosion and creep strength we select Incoloy-800H as the heat exchanger material for the Fluidized Bed Decomposer. A minimum wall thickness 3 mm is required to maintain material integrity after allowances for ~ 0.5 mm corrosion penetration. An aluminide protective coating is recommended on the SO_3 side of the heat exchanger to obtain a longer equipment life.

Selection of a vessel material for the Fluidized Bed Decomposer involves the same considerations as for the Joule-Boosted Decomposer. Either a silica brick-lined 316 stainless steel vessel or an Incoloy-800H vessel would be suitable.

Decomposer Recuperator

The main materials problem for the Decomposer Recuperator is for the Heat Exchanger, and as was the case for the Fluidized Bed Decomposer, corrosion and long-term creep strength are the main considerations. Temperatures are sufficiently lower here (~1050 K) that the problems are less severe. Therefore, an aluminide coating should not be needed. We select Incoloy-800H at a wall thickness of 3 mm as the preferred material with Inconel-617 as a backup for the Decomposer Recuperator heat exchanger. Selections for the vessel walls are either silica brick-lined 316 stainless steel or Incoloy-800H.

Decomposer Cooler

Transport piping from the Decomposer Recuperator to the Decomposer Cooler would be made from Incoloy 800H. The Decomposer Cooler heat exchanger is an

integral part of the Multi-Effect Evaporator and the heat exchanger tubes would be made from siliconized SiC.

Summary of Materials Selections for Section II

The selection of materials for Section II are summarized below in Table 9.9-3.

Table 9.9-3 Summary of Materials Selections for Heat Exchanger and Vessel Materials for Section II of the GA Thermochemical Cycle

PROCESS UNIT	Hx MATERIALS	VESSEL MATERIALS
Multi-Effect Evaporator	Siliconized SiC tubing, Durichlor-51 pumps	Silica brick liner on Teflon-lined mild steel
H_2SO_4 Boiler	Siliconized SiC tubing, Durichlor-51 pumps	Silica brick liner on Teflon-lined mild steel
Joule-Boosted Decomposer	SiC heating elements	Incloy-800H, or silica brick liner on 316 S.S.
Fluidized Bed Decomposer	Aluminide-coated Incoloy-800H	Incoloy-800H, or silica brick liner on 316 S.S.
Decomposer Recuperator	Incoloy-800H	Incoloy-800H, or silica brick liner on 316 S.S.
Decomposer Cooler	Siliconized SiC tubing	Vessel is integral part of Multi-Effect Evaporator

9.9.3 Material Selection for Sections III and IV

Material selection for Sections III and IV is similar to that selected for Sections I and II. The information in Table 9.9-1 is applicable to the iodine-HI regions of Sections III and IV. Phosphoric acid adds no new complexity except in the high temperature portions of the process, acid brick is necessary as a thermal protection for teflon liners. In addition, Hastelloy C has been recommended[31] for use with boiling concentrated phosphoric acid.

9.10 SAFETY CONSIDERATIONS

The main safety issues involve the control, handling, and containment of tritium, liquid lithium, and sulfuric acid. The safety issues regarding tritium and liquid lithium were reviewed and discussed in some detail in the 1980 report[19], and it was concluded that adequate controls were designed into the system to maintain proper safety. We have applied similar consideratoins in the current designs, including particular attention to both residual and accidental leakages of tritium into the environment or product, tritium inventories in the system, and potential problems of liquid lithium fires. We feel that the safety issues have been well met, and many of the details have been covered in this year's text. We refer the reader to last year's report for further details.

In regard to safety of sulfuric acid, it is important that conservative designs be maintained on the vessels and piping containing hot liquid and gaseous sulfuric acid and its decomposition products, since sulfuric acid introduced into the environment is a serious health hazard. We feel that we have taken adquate measures in our design studies, and recognize further that the sulfuric acid industry has been a large and well-established industry and one that we can draw on for future design information as needed for assuring a safe plant.

9.11 PLANT LAYOUT AND PLOT PLAN

9.11.1 Plant Layout

A complete plant process layout, assembling all of the sections, was prepared for last year's report[1] and is given earlier in the report in Figure 9.0-1, complete with important process parameters and labels on key process sections and on process units. The legend describes the symbolic representation used. Generally we have attempted to arrange the highest temperature processes at the top of the figure and the lower temperature processes at the bottom. At the immediate left is the Tandem Mirror Fusion driver and the associated helium coolant streams operating turbo-generators and process heat exchangers as a topping cycle and bottoming into a steam-Rankine cycle for additional electricity generation.

A larger version of this complete process flow diagram and flowsheet are available upon request. However, this reduced-size figure has been included to help one grasp the overall picture of the Fusion/Synfuels Process concept.

This year's version of the flowsheet has not been integrated into a similar one full layout but simplified flowsheets for each section have been presented in the text of this section. Last year's composite flowsheet still serves the purpose of presenting the scale of the total thermochemical process.

9.11.2 Plot Plan

An artist's conceptual drawing of the plot plan as given in last year's report[1] is shown in Figure 9.11-1. Changes in this year's design did not materially affect space requirements so this plot plan still gives a rough idea of the approximate land area and relative sizes of the TMR nuclear island, turbine-generator, steam generator and process heat exchanger building, as well as the rest of the chemical plant. We conclude from the plot plan that this plant is quite compact, and raises no new issues regarding heat transport distances, safety, etc.

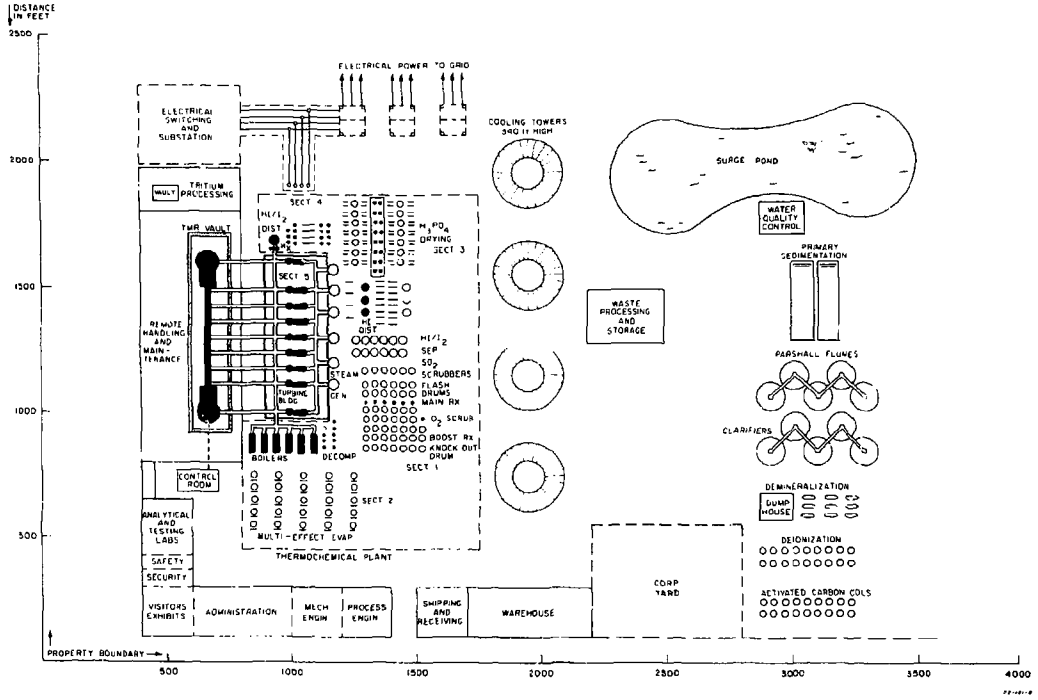

Figure 9.11-1 TMR-Synfuels Thermochemical Hydrogen Production Plant Plot Plan, 1981 Version

References for Section 9.0

1. R. W. Werner, et al., "Conceptual Design Study FY 1981, Synfuels from Fusion using the Tandem Mirror Reactor and a Thermochemical Cycle to Produce Hydrogen," Lawrence Livermore National Laboratory, Report UCID-19311, February 9, 1982.

2. J. H. Norman, G. E. Besenbruch, L. C. Brown, D. R. O'Keefe, and C. L. Allen, "Thermochemical Water-Splitting Cycle, Bench-Scale Investigations and Process Engineering, Final Report for the Period Ending February 1977 through December 31, 1981," DOE Report DOE/ET/26225-1, General Atomic Company Report GA-A16713, May 1982.

3. G. E. Besenbruch, K. H. McCorkle, J. H. Norman, D. R. O'Keefe, J. R. Schuster, and M. Yoshimoto, "Hydrogen Production by the GA Sulfur-Iodine Process, A Progress Report," Hydrogen Energy Progress, Proceedings of the 3rd World Hydrogen Energy Conference, Tokyo, Japan, 23-26 June 1980, Vol. 1 edited by T. N. Veziroglu, K. Fueki and T. Ohta, Pergamon Press, Oxford, 1980, p. 243.

4. J. H. Norman, G. E. Besenbruch, and L. C. Brown, "Solar Production of Hydrogen using the Sulfur-Iodine Thermochemical Water Splitting Cycle, Final Report," General Atomic Company Report GA-C-16493.

5. J. H. Norman, "Studies of the Sulfur-Iodine Thermochemical Water-Splitting Cycle," Hydrogen Energy Progress, Proceedings of the 3rd World Hydrogen Energy Conference, Tokyo, Japan, 23-26 June 1980, Vol. 1, edited by T. N. Veziroglu, K. Fueki, and T. Ohta, Pergamon Press, Oxford, 1980, p. 277.

6. D. R. O'Keefe and J. H. Norman, "The Liquid Hydrogen Iodide Decomposition Process Step for Water-Splitting Applications," Hydrogen Energy Progress, Proceedings of the 3rd World Hydrogen Energy Conference, Tokyo, Japan, 23-26 June 1980, Vol. 1, edited by T. N. Veziroglu, K. Fueki, and T. Ohta, Pergamon Press, Oxford, 1980, p. 277.

7. F. F. Rupert, "A Study of the System Hydrogen Chloride and Water," J. Am. Chem. Soc. 31, 851 (1909).

8. "Thermochemical Water-Splitting Cycle, Bench-Scale Investigations and Process Engineering, Annual Report for the Period February through December 31, 1977," General Atomic Company Report, GA-14950, April 1978.

9. L. N. Horsley, "Azeotropic Data III," Advances in Chemistry Series, Vol. 116, American Chemical Society, Washington, D.C., 1973.

10. D. R. O'Keefe and J. H. Norman, "The Liquid Hydrogen Iodide Decomposition Process Step for Water-Splitting Applications," Hydrogen Energy Progress, Proceedings of the 3rd World Hydrogen Energy Conference, Tokyo, Japan, 23-26 June 1980, Vol. 1, edited by T. N. Veziroglu, K. Fueki, and T. Ohta, Pergamon Press, Oxford, 1980, p. 277.

11. A. F. Ryabinina and V. A. Oshman, "Thermal Decomposition of Aqueous Sulfur Dioxide Solutions," Tr. Ural. Lesotekh, Inst. 1972, No. 28, 182 (Russ), Chem. Abstracts 79, 58115p, 1973.

12. "JANAF Thermochemical Tables," Dow Chemical Company, Midland, Michigan, September 30, 1977.

13. F. W. Giaugue, et al., "Thermodynamic Properties of Aqueous Sulfuric Acid Solutions and Hydrates from 15 to 300K," J. Am. Chem. Soc. 82, 62 (1960).

14. "Thermochemical Water-Splitting Cycle, Bench-Scale Investigations and Process Engineering Annual Report for the Period October 1, 1978 through September 30, 1979," DOE Report GA-A15788, General Atomic Company, March 1980.

15. M. Coombs, et al., "High-Temperature Ceramic Heat Exchanger, Final Report, July 1979," AiResearch Manufacturing Company of California, Torrance, CA, Report FP-1127, Research Project 545-1, report prepared for Electric Power Research Institute, Palo Alto, CA. R. H. Richman, EPRI Project Mgr., 1979.

16. R. H. Perry and C. W. Chilton, editors, "Chemical Engineers' Handbook," 5th edition, McGraw-Hill, New York, 1973, p. 10-21.

17. "Gemlins Handbuch der Anorganischen Chemie, Schwefel, System Number 9," Velag Chemie, GMbH, Weinheim/Bergstrasse, West Germany, 1960, p. 662.

18. E.R.G. Eckert and R. M. Drake, "Analysis of Heat and Mass Transfer," McGraw-Hill, New York, 1972, p. 562.

19. R. W. Werner, et al., "Synfuels From Fusion - Producing Hydrogen With The Tandem Mirror Reactor and Thermochemical Cycles," Lawrence Livermore National Laboratory, Report UCID-18909, Vol. I and II, January 21, 1981.

20. "HTGR Thermochemical Water-Splitting for Hydrogen Production, Annual Report for the Period January 1, 1975 through December 31, 1975," General Atomic Company Report GA-A13800, January 31, 1976.

21. F. J. Evans, Jr., "Equipment Design Handbook for Refinery and Chemical Plants," second edition, Vol. 1, Gulf Publishing Co., Houston, TX, 1979, pp. 184-191.

22. P. W. Trester and H. G. Staley, "Assessment and Investigation of Containment Materials for the Sulfur-Iodine Thermochemical Water-Splitting Process for Hydrogen Production, Final Report (July 1979-December 1980)," Gas Research Institute Report, GRI-80/0081, May 1981.

23. O. H. Krikorian, "Material Corrosion Studies for a Sulfuric Acid Vaporizer," Lawrence Livermore National Laboratory Report UCRL-81856, October 27, 1978.

24. O. H. Krikorian, "Corrosion Testing of Materials in Hot Concentrated Sulfuric Acid," Lawrence Livermore National Laboratory Report UCRL-83411, September 27, 1979.

25. R. L. Ammon, G. Yatsko, A. Irwin, and G. H. Furbman, "Materials Consideration for the Westinghouse Sulfur Cycle Hydrogen Production Process," unpublished paper presented at the Second World Hydrogen Energy Conference, Zurich, Switzerland, 21-24 August 1978.

26. M. L. Torti, J. W. Lucek, and G. Q. Weaver, "Densified Silicon Carbide - An Interesting Material for Diesel Applications," Technical paper Series 780071, Society of Automotive Engineers Congress and Exposition, Detroit, February 27 through March 3, 1978. See also brochures of the Norton Company, Worchester, Massachusetts on "Noralide Advanced Ceramics," and "Ceramics for Energy."

27. Edwin Craft, Carborundum Company, Niagara Falls, New York, private communication regarding bending of KT-Silicon carbide to form U-tubes, October 1979.

28. T. N. Tiegs, "Materials Testing for Solar Thermal Chemical Process Heat," Oak Ridge National Laboratory, Oak Ridge, TN, Report ORNL/TM-7833, October 1981.

29. O. H. Krikorian, "Materials Problems in Production, Transport and Storage of Hydrogen," Livermore National Laboratory Report, UCRL-83771, January 2, 1980.

30. Engineering Alloys Digest, Inc., Upper Montclair, New Jersey: Filing code Ni-179, Inconel alloy 617, September 1972; Filing code Ni-121, Inconel alloy 625, February 1967; and Filing code 55-136, Incoloy alloy 800, September 1972.

31. J. H. Perry, editor, "Chemical Engineers' Handbook," 3rd edition, McGraw Hill, New York, 1950, p. 1507.

SECTION 10

MATCHING POWER AND TEMPERATURE DEMANDS - PERFORMANCE AND EFFICIENCY EVALUATIONS

Contributors:

M. A. Hoffman, D. S. Rowe

TABLE OF CONTENTS

TABLE OF CONTENTS

LIST OF TABLES

LIST OF FIGURES

10.1 POWER AND TEMPERATURE MATCHING

10.1.1 Matching Philosophy and Procedure

In order to satisfy the interfacing requirements, the tandem mirror reactor (TMR) interface must be designed to supply all the electrical and thermal power demands of the thermochemical plant (TCP) after satisfying all the TMR internal and auxiliary demands. In addition, the TCP thermal power demands must be supplied to each section of the synfuel plant at the correct temperatures. The heat exchangers, steam generators and power plants which comprise the actual interface are shown on Fig. 10.1 in greatly simplified form for the Joule-Boosted decomposer (JBD) concept.

One possible procedure for accomplishing the matching of both the power and temperature demands of the TCP is as follows:

Step 1: Do the internal power balance for the TMR for selected plasma Q and component efficiencies.

Step 2: Evaluate the power demands of each section of the TCP and group them into an overall thermal demand and an overall electrical demand.

Step 3: Select tentative efficiencies for the steam power plant (SPP) and bottoming plant.

Step 4: Do a tentative interface power balance and determine the tentative values of the hydrogen production rate and the TCP efficiency.

Step 5: Construct a temperature-enthalpy (T-H) demand curve for the TCP.

Step 6: Select tentative inlet and outlet temperatures for the various TMR coolant flows which will meet the demands in Step 5 and construct a tentative T-H supply curve.

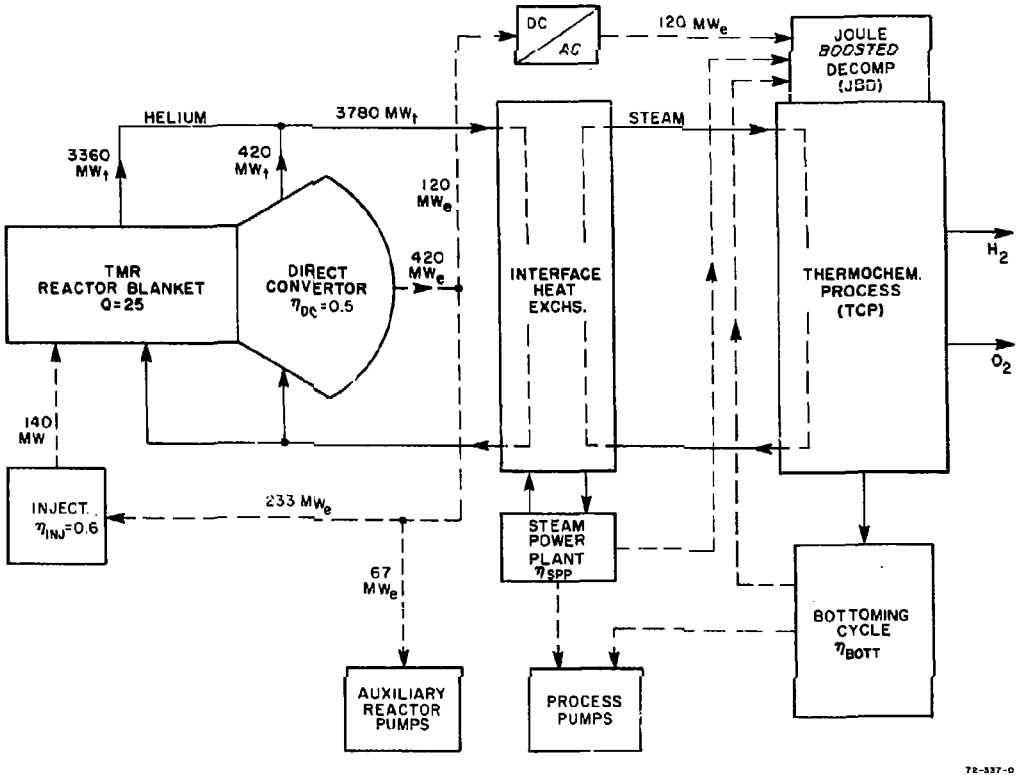

Fig. 10.1 Simplified energy balance - TMR/Synfuels for the Joule-Boosted decomposer concept

Step 7: Draw a tentative interface arrangement showing the various intermediate heat exchangers required (steam generators in this study).

Step 8: By trial and error, determine the optimum steam flows and temperatures in each part of the interface so that the steam T-H curve fits in between the supply and demand curves.

Step 9: Estimate the actual efficiencies of the steam power plant and the bottoming plant based on the actual temperatures at which heat is available to them.

Step 10: If these efficiencies are very different than those assumed in Step 3, or if some power or temperature demand cannot be satisfied, redo the procedure starting at Step 3.

When the final results are reasonably self-consistent, then one possible solution to the interface matching has been found. However, it may not be the "optimum" solution, so that it may be necessary to try other heat exchanger arrangements to see if a better matching can be obtained.

For this FY82 study, we set as our primary objective to try to minimize the first wall, blanket and direct converter material temperatures required for the JBD concept; obtaining a high overall TCP efficiency was made a secondary objective. It is felt that the low materials temperatures will lead to a highly credible and cost effective design even with relatively low TCP efficiency, as discussed in Section 1.

The above ten-step procedure has been used in this conceptual design study to give reasonably rapid, approximate results for a wide variety of cases. In the following sections, the procedure will be illustrated in detail for the reference case selected for this FY82 Final Report.

10.1.2 Power Balance for the TMR (Step 1)

The power balance for a TMR (Step 1 above) for a plasma Q = 25 and a fusion power of 3500 MW is already indicated on Fig. 10.1. It can be seen that the first wall (FW), the blanket (BL) and the direct converters (DC) supply a total of 3780 MW_t of thermal power to the TCP. In addition, the DC supplies a net electric power of 120 MW_e to the TCP.

This power balance is obtained as follows. The thermal power output from the TMR blanket and first wall is assumed to be equal to the neutron power times the blanket multiplication, M = 1.2:

$$P_{t(BL + FW)} = 0.8\ P_{fus} \times M = 3360\ MW_t$$

About 8.5% of this power (285 MW_t) is deposited in the first-wall helium coolant, while the remainder (3075 MW_t) is carried out by the blanket helium coolant.

The remaining 20% of the fusion power is assumed to eventually flow out the mirror exits to the direct converters as ion leakage (including the "halo" power) and be converted to electric power at an effective efficiency, η_{DC} = 50%:

$$P_{e(DC)} = 0.20 \times P_{fus} \times \eta_{DC} = 420\ MW_e$$

For a plasma Q = 25, the overall circulating power required to power the TMR (including neutral beam injection, RF heating, etc.) is:

$$P_{e(CIRC)} = \frac{P_{fus}}{Q\eta_{INJ}} = 233\ \ MW_t$$

where η_{INJ} is the overall average efficiency of all the injection devices, taken as 60%.

We assumed that roughly 67 MW_e would be required for auxiliaries such as vacuum pumps, helium refrigerators, etc. This leaves a net electric power

to the TCP of 120 MW_e as shown on Fig. 10.1.

The total thermal power to the TCP consists of the 3360 MW_t from the first wall and blanket plus 420 MW_t rejected at high temperature from the direct converters. This sum is the 3780 MW_t shown in Fig. 10.1.

In Section 10.2, the power and temperature matching for the TCP employing the Joule-Boosted decomposer concept is described. Then in Section 10.3 the matching for the TCP employing the fluidized bed decomposer concept is discussed.

10.2 JOULE-BOOSTED DECOMPOSER SYSTEM

10.2.1 Energy Demands of the Thermochemical Plant (Step 2)

The overall TCP is divided into Sections I, II, III, IV and V as described in Section 9 of this report. Section V of the TCP is the interface itself. Several different options for the TCP equipment and processes were investigated this year in an attempt to find the arrangement which appeared to be most cost effective, i.e., the lowest overall cost per mole of hydrogen produced.

The arrangement selected for the FY82 reference case for the Joule-Boosted decomposer (JBD) concept retained vapor recompression (VR) in Section III and added pressure staging (PS) in Section II. The final energy requirements for each section assumed in this FY82 study are summarized in Tables 10.1 and 10.2. (Some minor changes in these values were made by GA after this table was prepared. The effect of these small changes will be treated by a sensitivity analysis in Section 10.2.7.) The very important H_2SO_4 process stream requirements are shown on Fig. 10.2. It can be seen from Table 10.1 that the TCP requires a total of 285 kJ_e of electric energy and 331 kJ_t of thermal energy per mole of hydrogen produced.

The temperatures at which each thermal energy demand is required are

Table 10.1 Thermal and electrical demands of the TCP for the reference FY82 Joule-Boosted decomposer concept (with vapor recompressior (VR) in Section III and some pressure staging (PS) in Section II)

	Electric Demand (kJ_e/mole H_2)	Thermal Demand (kJ_t/mole H_2)	Temperature Range
Section II			
Decomposer	97	--	--
Preheater	57	--	--
Preheater	--	26	680 → 722 K
Boiler	--	108	680 K
Evaporator (with PS)	--	85.4	400 → 680 K
Section III			
HX E303	--	72.4	523 K
HX E308D	--	21.2	484 K
TC 301, 302, 303 (VR)	131	--	--
Section IV			
E404A		6.7	713 K
E404B2		1.7	616 K
E404C2		7.4	522 K
E402C		2.2	393 - 415 K
TOTALS	E_e = 285	E_t = 331	

Table 10.2 Usable waste heat flows from the TC processes (for use in the freon bottoming plant)

Source	Amount (kJ_t/mole H_2)	Temperature
Section I	111 21	393 K 425 K
Section II	44	430 K
Section III	56	368 → 417 K
TOTAL	E_w = 232	

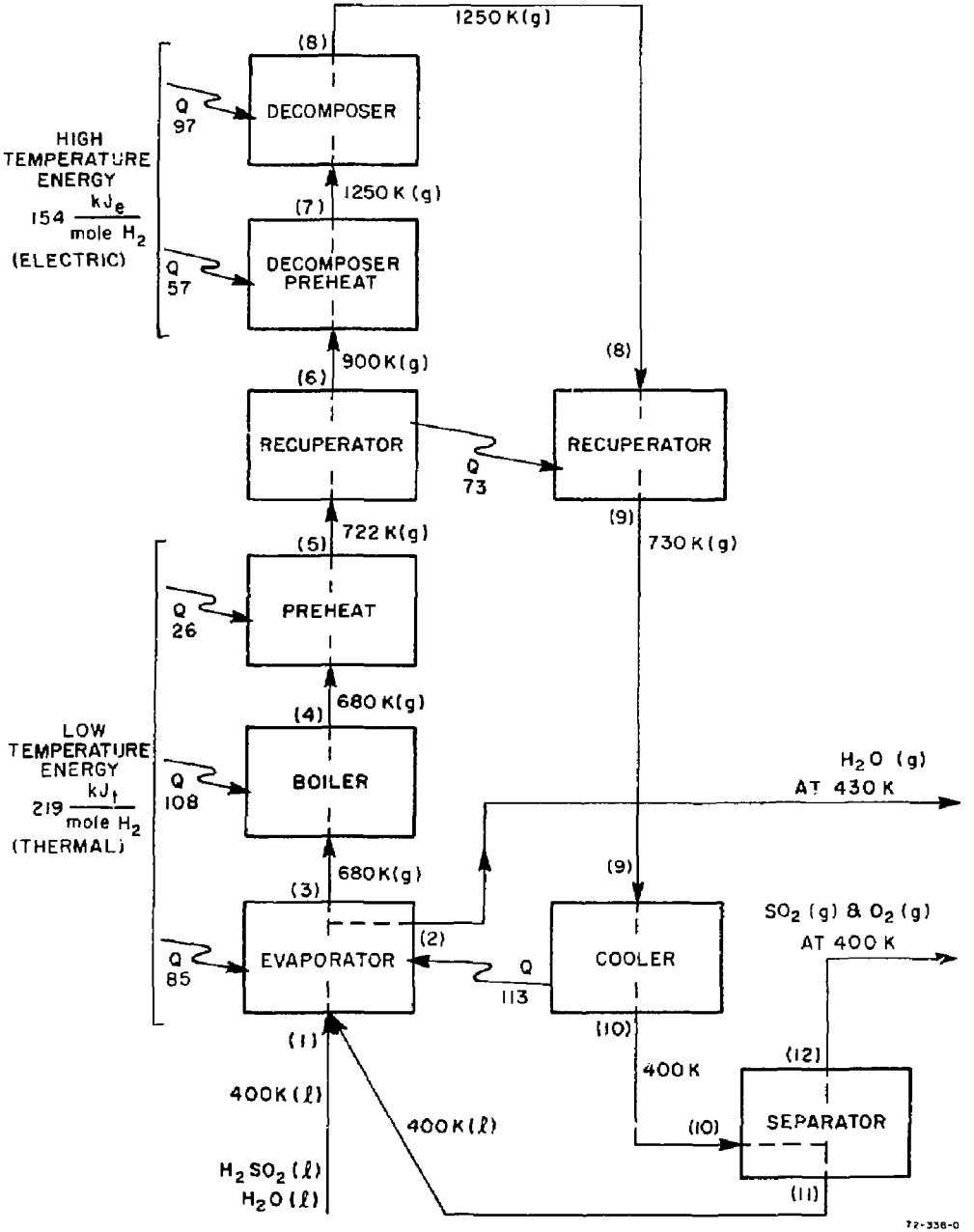

Fig. 10.2 H_2SO_4 process stream Joule-Boosted decomposer

also given in Table 10.1. These temperatures can be seen to range from 393 K to 722 K for the JBD concept. These temperature demands are not considered in detail until after a tentative interface power balance has been made (Step 4).

10.2.2 Simplified Power Balance Model (Steps 3 and 4)

The simplified interface power balance is illustrated in Fig. 10.3. The TCP total demands for the JBD concept (with vapor recompression in Section III) are:

$$E_e = 285 \text{ kJ}_e/\text{mole } H_2$$

$$E_t = 331 \text{ kJ}_t/\text{mole } H_2$$

It is necessary to know the number of moles of hydrogen produced per second, $\dot{N}$, before the power balance can be made, since the electric and thermal power demands of the TCP are $\dot{N}E_e$ and $\dot{N}E_t$, respectively.

In order to determine $\dot{N}$ in a self-consistent manner, it is first assumed that some fraction, f_1, of the TMR thermal power is required to satisfy the TCP thermal demand, and the remainder is available for electric power generation to help supply the TCP electric demand. The first relation which must be satisfied in thus the thermal power balance:

$$f_1 P_t = \dot{N} E_t \tag{10.1}$$

where P_t is the total thermal power available from the TMR (3780 MW_t), f_1 is the fraction of this power which goes directly to the TCP, E_t is the total thermal energy requirement of the TCP (331 kJ_t/mol H_2), and $\dot{N}$ is the number of moles of hydrogen produced per second.

The second relation which must be satisfied is the electrical power balance:

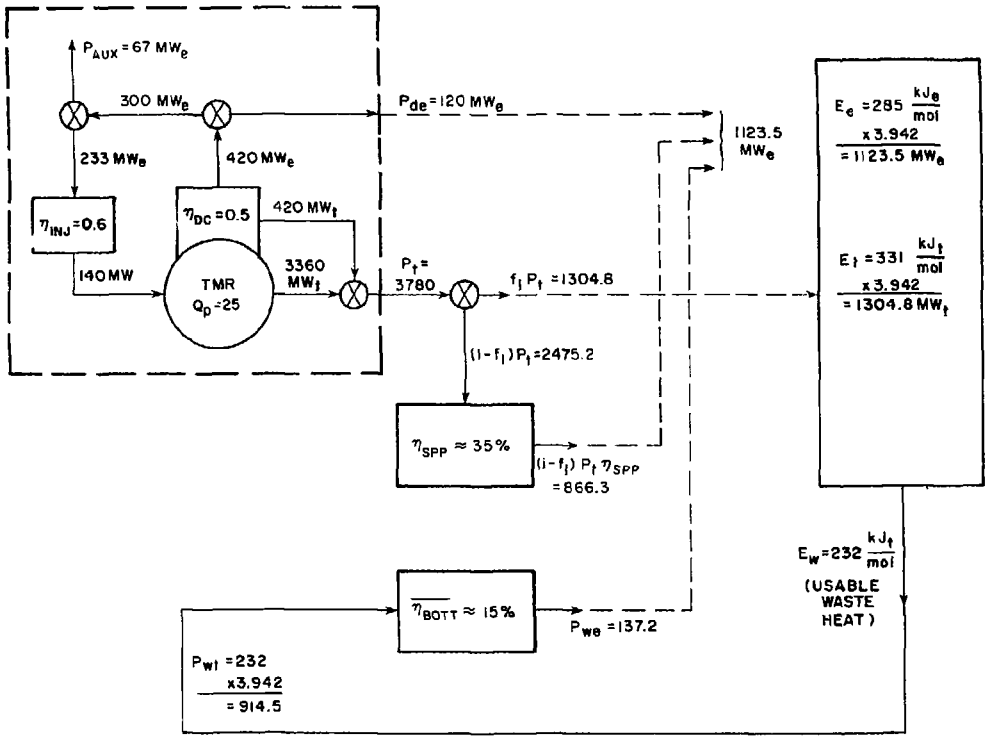

Fig. 10.3 Power balance diagram for the Joule-Boosted decomposer concept (with vapor recompression in Section III and some pressure staging in Section II)

$$P_{de} + (1 - f_1)P_t\eta_{SPP} + E_w\dot{N}\bar{\eta}_{BOTT} = \dot{N}E_e \qquad (10.2)$$

where P_{de} is the net electric power available to the TCP from the direct converters (120 MW_e), η_{SPP} is the thermal efficiency of the steam plant, E_w is the waste heat from the TCP which is at high enough temperature to be usable in a bottoming plant (such as a freon cycle), $\bar{\eta}_{BOTT}$ is the effective thermal efficiency of the bottoming plant (which depends on the temperature at which the various waste heats are available), and E_e is the total electrical energy demand of the TCP (285 kJ_e/mole H_2).

Solving these two simple algebraic equations for the two unknowns:

$$\dot{N} = \frac{P_{de} + P_t\eta_{SPP}}{E_e + E_t\eta_{SPP} - \bar{\eta}_{BOTT}E_w} \qquad (10.3)$$

$$f_1 = \frac{E_t}{P_t}\dot{N} \qquad (10.4)$$

For the reference case of Fig. 10.3, we find that $\dot{N}$ = 3.942 k moles H_2/sec and f_1 = 0.345. These values are for an estimated steam power plant efficiency, η_{SPP} = 35%, and an effective bottoming plant efficiency estimated to be 15%. The values of η_{SPP} and η_{BOTT} are our best guesses at this point (Step 3).

The overall efficiency of the thermochemical process (TCP) can now be calculated using the definition:

$$\eta_{TCP} \equiv \frac{\Delta H_{HHV}\dot{N}}{P_{de} + P_t} = 0.298 \qquad (10.5)$$

where ΔH_{HHV} is the higher heating value of the hydrogen produced plus a small amount of pressure energy (286 + 9 = 295 kJ/mole H_2). While this TCP efficiency is rather low, the maximum helium coolant temperatures required will be shown to be only 825 K for the blanket and 625 K for the

first wall. These temperatures are considered to be very low compared to other thermochemical process concepts. As a result, it is felt that these low TMR temperatures will result in a credible TMR reactor and a cost-effective synfuel plant.

10.2.3 TCP Temperature-Enthalpy Demand Curve (Step 5)

If the thermal energy demands of the thermochemical process are broken down in terms of the requirements in each temperature increment, we obtain the results shown in Table 10.3. When these results are plotted, we obtain the TCP demand curve as shown by the bottom curve of the temperature-enthalpy (T-H) plot on Fig. 10.4.

10.2.4 Interface Heat Exchanger Arrangement and Helium Coolant Temperatures (Steps 6 and 7)

As discussed above, one of the primary objectives of this design for the interface for the JBD concept was to try to obtain the minimum possible temperatures for the first-wall structure, the blanket structure and the direct converter collector plates. A second important objective was safety. This implies isolating the helium coolant streams from the TCP by use of intermediate heat exchangers. It was decided to use steam as both the heat transport fluid into the TCP and also as the working fluid in the main electric power plant. Thus, the intermediate heat exchangers are steam generators.

These objectives resulted in the interface diagram shown in Fig. 10.5. (It should be noted that this diagram has been simplified for the sake of clarity: for example, the TCP heat exchangers shown are strictly suggestive.) After considerable trial and error, it was found that the first-wall helium thermal power of 285 MW (about 8.5% of the total blanket power) matched the low temperature demands of the TCP very well. As a result, the first-wall helium coolant temperatures were chosen at 525 K into the TMR and 625 K out as shown on Fig. 10.5. The relatively low bulk temperature rise of 100 K

Table 10.3 Construction of the TCP demand (or load) curve (starting with H = 0 at 393 KO

Temperature	Approx. ΔH at Each Temp	$\Sigma\Delta H$
393 → 415 K	2.2 kJ_t	2.2
400 → 484 K	25.5	27.7
484	21.2	48.9
484 → 523 K	11.8	60.7
523	72.4 + 7.4 = 79.8	140.5
523 → 680 K	47.7	188.2
680 (+ 616)	108 + 1.7	297.9
680 → 713 K	20.4	318.3
713	6.7	325.0
713 → 722 K	5.6	330.6

331

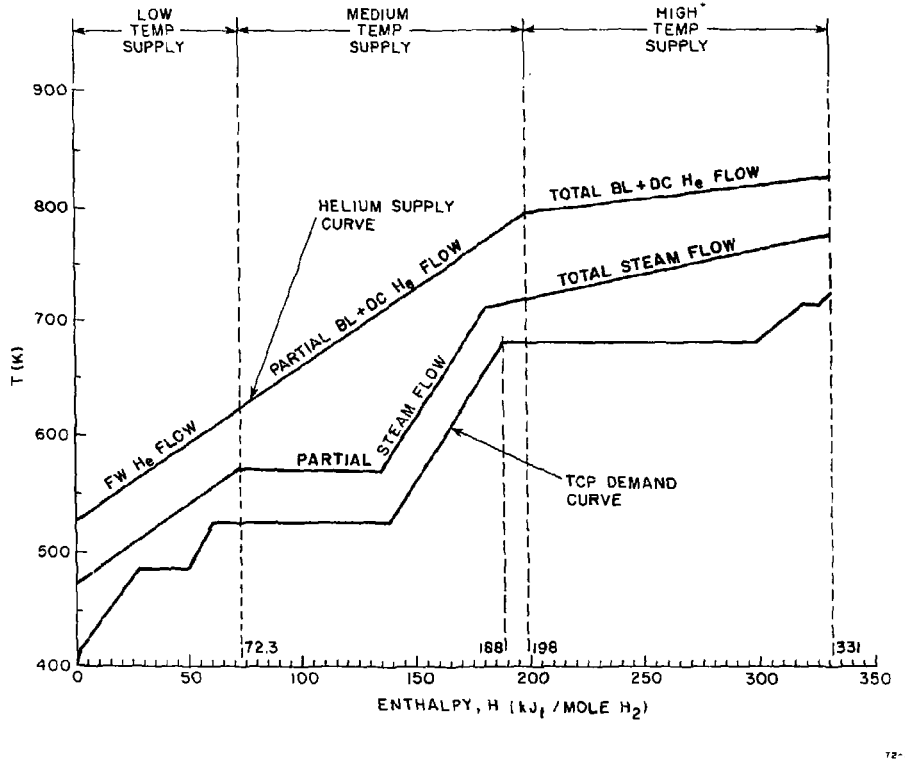

Fig. 10.4 Temperature-enthalpy curves for the TCP demand and the helium and steam supply curves

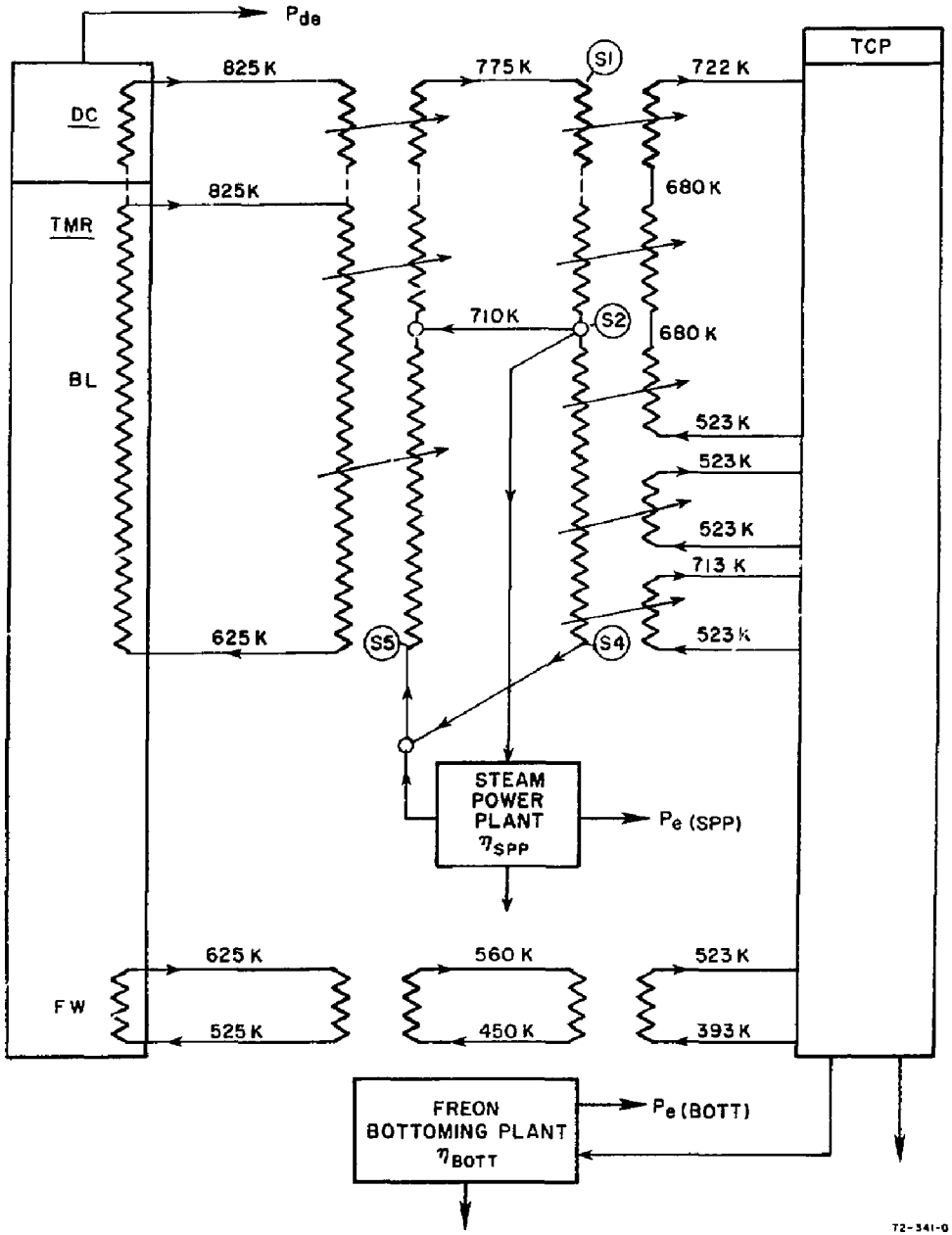

Fig. 10.5 Joule-Boosted decomposer interface steam generators and HXs

yields high heat transfer coefficients and relatively low temperatures for the first wall structure. This results in desirably high allowable creep strength (see Section 5 for details).

The first-wall thermal power can be converted to kJ/mole H_2 for plotting on Fig. 10.4 as follows:

$$E_{FW} = \frac{P_{t(FW)}}{\dot{N}} = \frac{285}{3.942} = 72.3 \text{ kJ}_t\text{/mole}$$

Using this value and the temperatures sited above, the low temperature portion of the helium supply curve can be drawn as shown at the left-hand side of Fig. 10.4 (defined as the "low temperature" region). The total first-wall helium flow rate required is thus calculated from:

$$\dot{M}_{FW} = \frac{P_{t(FW)}}{C_p \Delta T_{B(FW)}} = \frac{285 \times 10^6}{5200 \times 100} = 548 \text{ kg/s}$$

(See Section 5 for further details.)

In order to construct the medium and high temperature portions of the helium supply curve, we first must choose helium blanket and direct converter coolant temperatures. After several iterations we found that reasonable helium inlet and outlet temperatures for adequately high ΔT's between the steam and the helium were 625 K and 825 K, respectively, as indicated on Fig. 10.5. These temperatures not only match the blanket design well, but also provide a low enough bulk temperature rise in the blanket canisters for good heat transfer without excessive pressure drops. It should be noted that these "high" temperatures for the JBD concept are much lower than the corresponding high helium temperatures for the FDB concept.

For the high temperature portion of the supply curve on Fig. 10.4, it was determined that the entire thermal power from the blanket and direct converters would have to be used. This conclusion was reached when it was determined that the total helium flow rate from the blanket and direct

converters was just sufficient to give the desired slope of the high temperature helium supply curve shown on Fig. 10.4 between 331 kJ/mole (at 825 K) and 198 kJ/mole (at 795 K). This slope results in adequately high ΔT's between the supply and demand curves at all points. This, in turn, helps insure that the steam generator designs will be cost effective.

The total helium flow rates for the selected bulk temperature rise of 200 K for the blanket and direct converter flows are given by:

$$\dot{M}_{BL} = \frac{P_{t(BL)}}{C_p \Delta T_{B(BL)}} \simeq \frac{(3360 - 285) \times 10^6}{5200 \times 200} \simeq 2957 \text{ kg/s}$$

$$\dot{M}_{DC} = \frac{P_{t(DC)}}{C_p \Delta T_{B(DC)}} \simeq \frac{420 \times 10^6}{5200 \times 200} \simeq 404 \text{ kg/s}$$

The choice of the point at which to stop using all the thermal power in the helium flow (at 795 K and 198 kJ/mole on Fig. 10.4) is not unique. Other choices would lead to slightly different helium supply curves and steam conditions, but these changes would have a minor effect on the TCP efficiency for this reference design.

Finally, the medium temperature thermal demands can be met by the partial helium power curve shown connecting the high and low temperature portions of the supply curve on Fig. 10.4. It should be noted that this choice is also not optimum (because the ΔT's are larger than necessary around 140 kJ/mole), but it does lead to simple steam generator arrangements.

Table 10.4 summarizes the helium thermal powers available and required by the TCP in each temperature range. It can be seen that about 496 MW_t from the blanket and direct converter helium flows is required to satisfy the medium temperature demands of the TCP. This leaves about 2475 MW_t at helium temperatures from 795 K down to 625 K available to produce steam for the electric power demands of the TCP. The steam flow requirements and the steam supply curve which we arrived at will be discussed next.

Table 10.4 Thermal powers for the Joule-Boosted decomposer concept

Helium Supply	Helium Temp. Range	Source	Thermal Power Available from TMR	Thermal Power Required by TCP	Thermal Power Left for Elec. Power Generator
High temp.	825 → 795 K	Blanket + DC	524.3	524.3	0
Medium temp.	795 → 625 K	Blanket + DC	2970.7	495.5	2475.2
Low temp.	625 → 525 K	First Wall	285.0	285.0	0
TOTALS			3780 MW_t	1304.8 MW_t	2475.2 MW_t

10.2.5 Selection of the Steam Temperatures and Flows (Step 8)

The objective of this step is to select steam flow rates and temperatures so as to produce a steam curve which fits well in between the helium supply curve and the TCP demand curve of Fig. 10.4, i.e., a curve which gives adequate ΔT's for both heat transfer from the helium into the steam and for heat transfer from the steam to the process. In addition, it is felt to be desirable to keep the steam flow arrangements as simple as practical at this stage of the conceptual design study.

All the steam and water flows are at a nominal pressure selected as 8.0 MPa (where T_{SAT} = 568 K). This pressure has been purposely chosen to be higher than the helium coolant pressure of about 5.0 MPa to insure that minimal tritium would get into the steam generators in the event of a leak (see Section 5.4 for details). In addition, this steam pressure is felt to be acceptable in the TCP equipment.

The arrangement finally selected for the steam flows is shown in Fig. 10.5. The total steam flow is required to supply heat to the TCP in the high temperature region. Superheated steam can be generated up to a maximum temperature, T_{S1} = 775 K, as shown on Figs. 10.4 and 10.6. This steam flow is cooled to T_{S2} = 710 K and transfers:

$$\dot{Q}_{S(HIGH)} = \dot{N}\Delta H_{HIGH} = 3.942(331 - 180) = 595.2\ MW_t$$

to the thermochemical process as indicated by the high temperature portion of the steam supply curve on Fig. 10.4. The end point for this portion of the steam supply curve was chosen to give adequately large ΔT's between the helium and the steam flows on one side and between the steam and the TCP flows on the other side of the heat exchangers. However, it should be noted that this end point is not a unique choice nor even the optimum value. It is a reasonable compromise to give simple heat exchanger arrangements.

The total steam flow rate is calculated from the power balance:

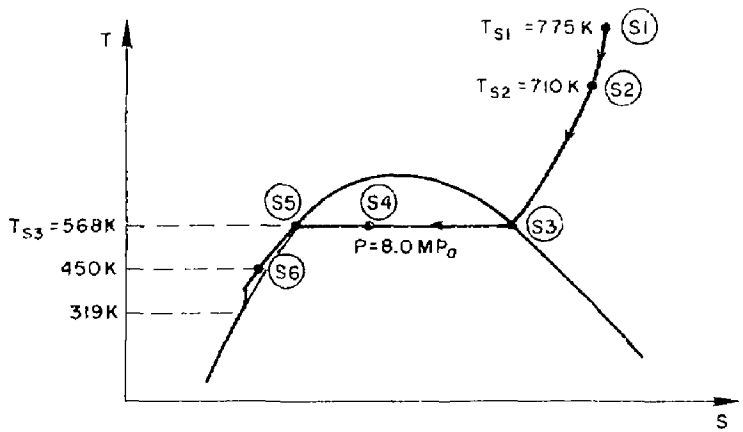

Fig. 10.6 Process steam states used in the calculation of the required steam flow rates

$$\dot{M}_{S(TOT)}(h_{S1} - h_{S2}) = \dot{Q}_{S(HIGH)} = 595.2 \text{ MW}_t$$

Thus

$$\dot{M}_{S(TOT)} = \frac{595.2 \times 10^3}{(3402 - 3236.7)} = 3601 \text{ kg/s}$$

where h_{S1} and h_{S2} are the superheated steam enthalpies (in kJ/kg) at states S1 and S2, respectively, on Fig. 10.6.

This flow then divides into three parts as indicated on Fig. 10.5. The first part of the steam flow, referred to as $\dot{M}_{S(MED)}$, has been chosen to be just sufficient to transfer the medium temperature heat down to the saturation temperature of 568 K and H = 72.3 kJ/mole, as shown on Fig. 10.4. The second part, referred to as $\dot{M}_{S(SPP)}$, is chosen to carry the 2475 MW of thermal power (shown on Fig. 10.3 and Table 10.4) to the steam power plant. The remaining third part, referred to as $\dot{M}_{S(RECIRC)}$, is recirculated directly back to the steam generator as shown on Fig. 10.5.

These three steam flows are determined quantitatively for the reference case as follows. From Fig. 10.4, we need a medium temperature steam flow rate to supply:

$$\dot{Q}_{S(MED)} = \dot{N} \times \Delta H_{MED} = 3.942\ (180 - 72.3) = 424.6 \text{ MW}_t$$

We choose the steam state S3 on Fig. 10.6 at 135 kJ and 568 K. This is the point on Fig. 10.4 where condensation of the steam at $T_{SAT} = 568$ K begins and appears to give the best match to the TCP demand curve in this region. This choice fixes the mass flow rate for the steam which supplies the medium temperature heat:

$$\dot{M}_{S(MED)} = \frac{\dot{N}\Delta H_{S2\text{-}S3}}{(h_{S2} - h_{S3})} = \frac{3.942(180 - 135) \times 10^3}{(3236.7 - 2757.5)}$$

$$= \frac{177.4 \times 10^3}{479.2} = 370 \text{ kg/s}$$

Only a part of the enthalpy of condensation is used in providing the remaining medium temperature energy from H = 135 kJ/mole down to H = 72.3 kJ/mole on Fig. 10.4. At the final steam state S4 of Fig. 10.6, the quality is still about 54%. Thus, this steam still has about 286 MW_t of power remaining as enthalpy of condensation.

One place to use this remaining heat of condensation is in the final stage of regeneration (i.e., feed water preheating) of the water flow out of the steam power plant condenser. This can raise the feed water to the saturated liquid state while reducing the $\dot{M}_{S(MED)}$ two-phase steam flow to the saturated state. This also avoids having to pump a two-phase mixture to make up for the pressure losses in the $\dot{M}_{S(MED)}$ flow.

The steam flow to the steam power plant is then determined from the following power balance:

$$\dot{M}_{S(SPP)}(h_{S2} - h_{S5}) = \dot{Q}_{SPP(TOT)} - \dot{Q}_{(S4-S5)}$$

where $\dot{Q}_{SPP(TOT)}$ is the total thermal power available to the SPP from the TMR (2475 MW_t as shown on the power balance diagram of Fig. 10.3). $\dot{Q}_{(S4-S5)}$ is that portion of the steam power plant heat input supplied by the remaining enthalpy of condensation of the $\dot{M}_{S(MED)}$ steam flow, i.e., 286 MW_t. Thus,

$$\dot{M}_{S(SPP)} = \frac{(2475 - 286) \times 10^3}{(3236.7 - 1317.0)} = 1140 \text{ kg/s}$$

The third part of the steam flow which is recirculated directly back to the steam generator at state S2 is thus given by:

$$\dot{M}_{S(RECIRC)} = \dot{M}_{S(TOT)} - \dot{M}_{S(MED)} - \dot{M}_{S(SPP)}$$

$$= 3601 - 370 - 1140$$

$$= 2091 \text{ kg/s}$$

This is about 58% of the total steam flow. It indicates that over half the superheated steam acts as a very effective gaseous heat transport fluid to

the TCP without ever condensing.

The low temperature heat is supplied by pressurized hot water heated by the first-wall heat exchanger (the bottom heat exchanger on Fig. 10.5). The heat required by the TCP is:

$$\dot{Q}_{S(LOW)} = (72.3 \text{ kJ/mole}) \times \dot{N} = 285.0 \text{ MW}_t$$

The water at 8.0 MPa is heated by the first-wall helium from state S5 at 450 K to state S5 at 568 K (shown on Fig. 10.6). For an average $\bar{C}_{pw}$ of the water of 4.86 kJ/kg-K, the required water mass flow is calculated from:

$$\dot{M}_{w(LOW)} = \frac{\dot{Q}_{LOW}}{\bar{C}_{pw}(T_{S4} - T_{S5})} = 598.3 \text{ kg/s}$$

The total thermal power supplied by the steam and hot water flows in thus:

$$\dot{Q}_{S(TOT)} = \dot{Q}_{S(HIGH)} + \dot{Q}_{S(MED)} + \dot{Q}_{S(LOW)}$$

$$= 595.2 + 424.6 + 285.0$$

$$= 1304.8 \text{ MW}_t$$

This exactly balances the thermal demand of the TCP, as it must:

$$\dot{Q}_{t(TCP)} = E_t \dot{N} = 331 \times 3.942 = 1304.8 \text{ MW}_t$$

This completes the preliminary design of a reasonable interface between the TMR and the TCP which meets both the power and temperature demands of the TCP. The final remaining questions regard the tentative choices for the steam power plant efficiency, η_{SPP}, and the bottoming plant efficiency, η_{BOTT}, made in Step 3. These will be checked next.

10.2.6 Estimation of the Power Plant Efficiencies (Step 9)

A simplified sketch of the steam power plant block diagram and cycle are given on Fig. 10.7. (Note that the steam cycle numbering on Fig. 10.7 is totally different from that for the process steam on Fig. 10.6.) The turbine receives the superheated steam flow $\dot{M}_{S(SPP)}$ at state 1 (710 K and 8.0 MPa) and expands it to state 2 in the high pressure part of the turbine. End state 2 is fixed by the maximum allowable moisture content of about 10%. Moisture is separated from the steam flow, which then flows to the medium pressure part of the turbine. The turbine from state 3 to state 6 is very much like those designed for light water reactors and hence is conventional nuclear steam turbine technology, and the overall turbine is estimated to have an efficiency of 90%.

In addition to moisture removal from the steam flow, some steam is extracted at various points to preheat the compressed water from state 8 to state 9 (referred to as regeneration), as indicated on the block diagram of Fig. 10.7. The final stage of the preheating from state 9 to state 10 is accomplished using the medium temperature steam flow as described in Section 10.2.5.

The steam exiting from the turbine at state 6 is assumed to be condensed at about 0.01 MPa and 319 K. This temperature is high enough to permit use of conventional cooling towers.

Preliminary estimates of the thermal efficiency of this steam power plant indicate that it may be as high as 37% to 38% (compared to the guess of 35% on Fig. 10.3). Rather than redo the entire interface using an improved η_{SPP} (as recommended in Step 10), we will first evaluate the effect of small changes in the steam power plant efficiency on the overall thermochemical plant efficiency using a sensitivity analysis in the next section. Then if the effect on η_{TCP} is large, a complete recalculation of the interface matching is probably justified. On the other hand, if the effect on η_{TCP} is small, use of the results of the sensitivity analysis to correct

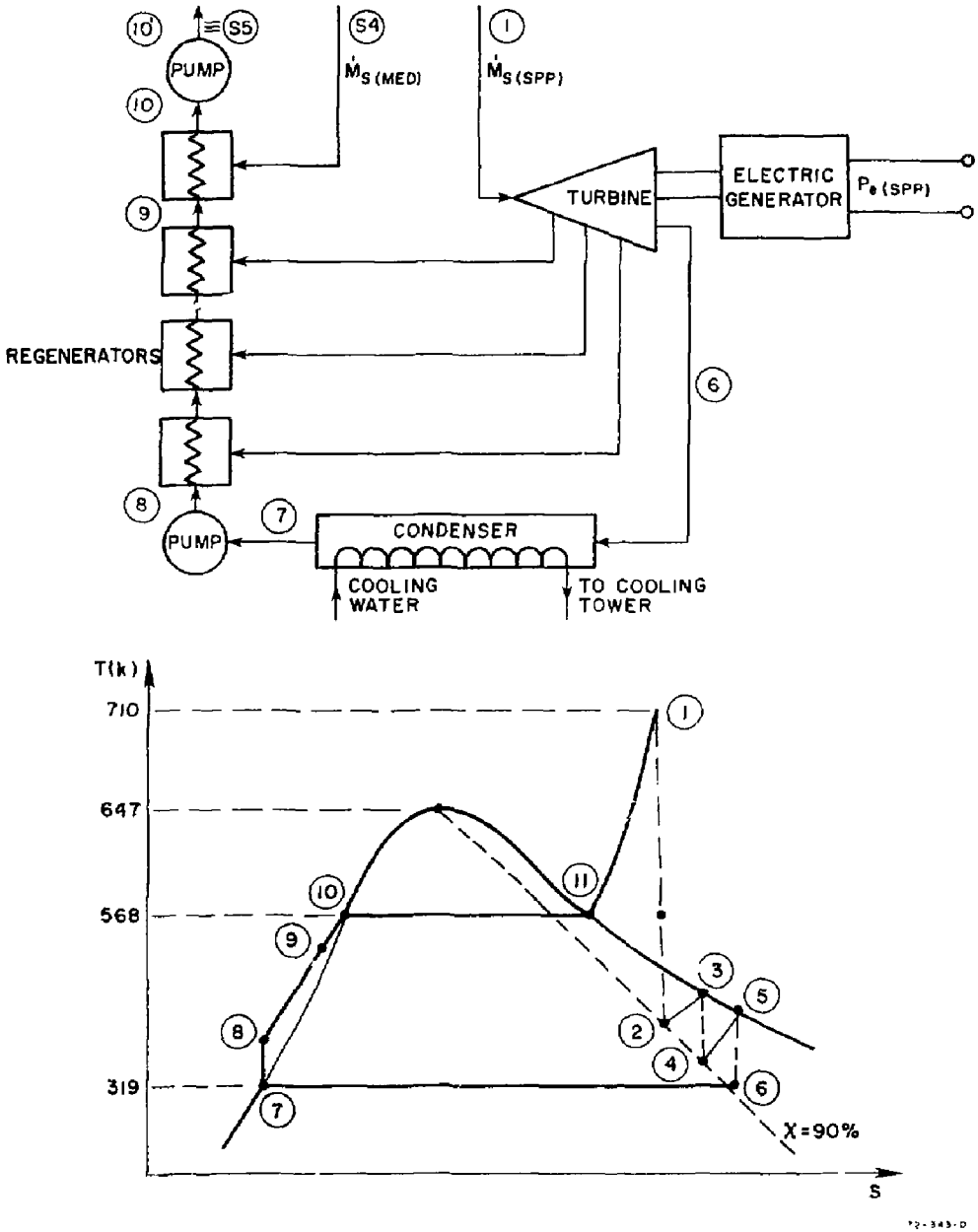

Fig. 10.7 Simplified sketch of steam power plant and cycle

η_{TCP} is probably sufficient for preliminary design purposes.

The bottoming plant receives usable waste heat flows from the TCP at a variety of temperatures, as indicated in Table 10.2. Evaluation of the average efficiency of a freon bottoming cycle using these waste heat flows indicates that $\bar{\eta}_{BOTT}$ may be as high as 15.6%. Consequently, the use of 15% in Fig. 10.3 is considered to be a reasonable, conservative estimate.

10.2.7 Sensitivity Analysis

Using the equations for $\dot{N}$ and η_{TCP} derived in Section 3, it is very straightforward to show that the sensitivity coefficient is:

$$\frac{\partial \eta_{TCP}}{\partial \eta_{SPP}} = \left[\frac{P_t - \dot{N}E_t}{P_{de} + P_t\eta_{SPP}}\right]\eta_{TCP} = 0.51$$

for our reference case. This implies that three percentage points improvement in η_{SPP} (from 35% to 38%) would result in about one-and-a-half percentage points improvement in η_{TCP} (from about 30% to about 31.5%). This small improvement in η_{TCP} does not justify redoing the entire interface matching at this point in time. We can simply assume that η_{TCP} is about 31.5% for the Joule-Boosted decomposer (JBD) concept, assuming that an η_{SPP} of 38% can be realized.

In order to further illustrate the usefulness of the sensitivity analysis, we will look next at some hypothetical improvements in the TCP energy demands. Suppose that the total thermal demand, E_t, can be reduced while all other parameters remain unchanged. The sensitivity coefficient is then given by:

$$\frac{\partial \eta_{TCP}}{\partial E_t} = -\frac{\eta_{TCP}\eta_{SPP}\dot{N}}{P_{de} + P_t\eta_{SPP}} = -2.85 \times 10^{-4}\left(\frac{kJ_t}{mol}\right)^{-1}$$

This implies that a 100 kJ_t/mole H_2 reduction in E_t can increase η_{TCP} by

2.85 percentage points. Such improvements appear possible for the JBD concept.

Finally, assume that it is possible to also reduce the electrical demand of the TCP, E_e, holding all other parameters fixed. This sensitivity coefficient becomes:

$$\frac{\partial \eta_{TCP}}{\partial E_e} = - \frac{\eta_{TCP} \dot{N}}{P_{de} + P_t \eta_{SPP}} = -8.14 \times 10^{-4} \left(\frac{kJ_e}{mol} \right)^{-1}$$

This implies that a 20 kJ_e/mole H_2 reduction in E_e can increase η_{TCP} by about 1.6 percentage points. Such an improvement also appears possible.

Thus, if both these improvements can be accomplished along with a steam power plant efficiency of 38%, the overall thermochemical process efficiency, η_{TCP}, can be raised to about 36% for the Joule-Boosted decomposer concept.

Recent refinements in the calculation for the usable waste heat from the evaporator of Section II of the TCP (see Fig. 10.2) indicates that as much as 103 kJ_t per mole of hydrogen may be available at 430 K in the water vapor stream. This is an increase of 59 kJ_t/mole over the value of 44 kJ_t/mole shown in Table 10.2. Using the sensitivity coefficient,

$$\frac{\partial \eta_{TCP}}{\partial E_w} = \frac{\eta_{TCP} \bar{\eta}_{BOTT} \dot{N}}{P_{de} + P_t \eta_{SPP}} = 1.22 \times 10^{-4} \left(\frac{kJ_t}{mol} \right)^{-1}$$

we see that 59 kJ_t/mole additional usable waste can raise η_{TCP} by about 0.7 percentage points.

10.2.8 Summary for the Joule-Boosted Decomposer System

A straightforward procedure has been presented for performing the interface power and temperature matching between the TMR and the thermochemical plant (TCP) for preliminary design purposes. For the Joule-Boosted

decomposer (JBD) concept, an overall TCP efficiency of about 30% is predicted for the reference case (with a steam power plant efficiency of 35%). Improvements in the thermochemical plant which reduce the thermal demand by 100 kJ_t/mole H_2 and the electrical demand by 20 kJ_e/mole H_2 can raise the TCP efficiency to about 36% (using the improved estimate of the steam power plant efficiency of 38%).

This TCP efficiency appears to be achievable with remarkably low helium coolant temperatures compared to most other processes for synthetic H_2 production. The helium exiting the blanket and direct converters need only be at about 825 K, while the helium exiting the first wall need only be at about 625 K. This should lead to a very credible and cost-effective synfuel plant.

10.3 FLUIDIZED BED DECOMPOSER SYSTEM

Section 10.1 has presented the basic procedure for matching the TMR to the TCP and Section 10.2 has presented the details of matching for the Joule-Boosted decomposer system. This section is concerned with the details of matching the fluidized-bed decomposer TCP to the TMR.

10.3.1 TMR Power Balance

Figure 10.8 shows the overall power balance arrangement for the TMR and fluidized bed TCP system. Following the discussion in Section 10.2, the TMR is assumed to have a Q of 25 and an injection energy of 140 MW giving 3500 MW fusion power. Twenty percent of this energy (alphas) plus the injection energy is assumed to be transferred to the direct converter (840 MWt). Eighty percent of the fusion energy is available as high energy neutrons to the blanket (2800 MW). Assuming an average M = 1.2, the thermal energy available in the blanket is 3360 MWt. This energy is split into two temperature ranges--one at high temperature for the fluidized bed decomposer and the other at low temperature for the TCP and electrical energy production. The low temperature streams are assumed to consist of thermal energies from

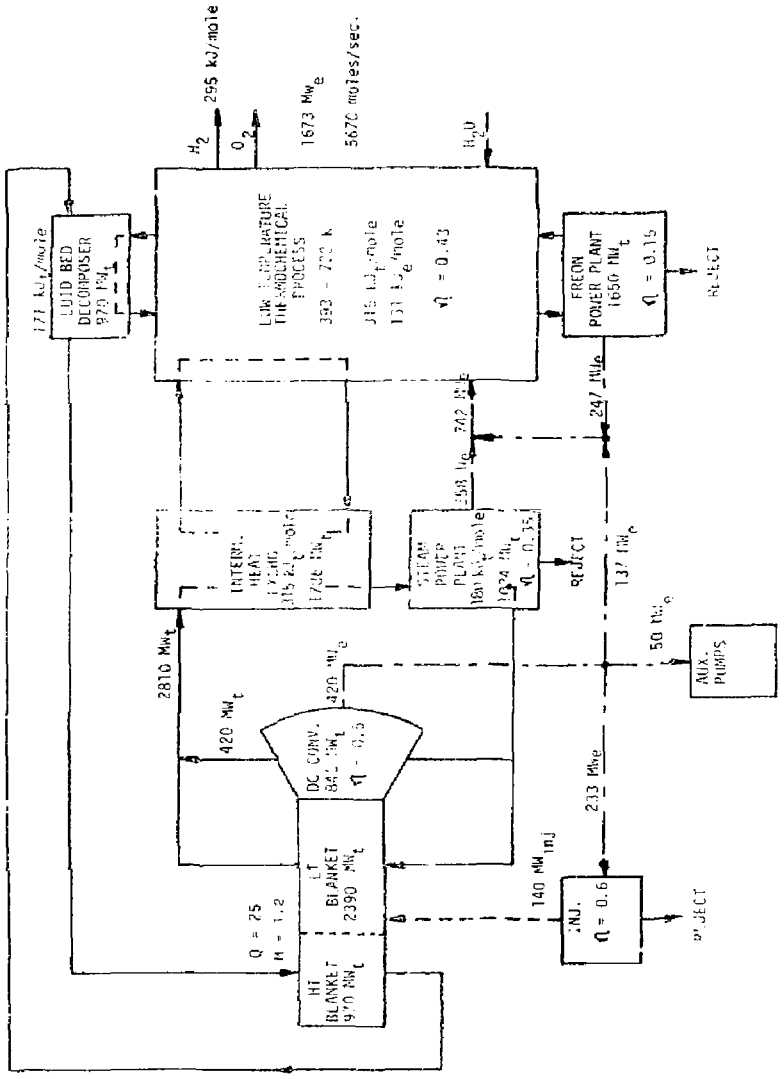

Figure 10.3 3500 MW TNR coupled to thermochemical process

the low temperature blanket, first wall cooling, and direct converter thermal discharge. The direct converter is assumed to have an efficiency of 0.5, giving 420 MWe and 420 MWt. The direct converter electrical output provides 232 MWe to the injectors, 50 MWe to TMR auxiliary pumps and 137 MWe to the TCP. The remaining TCP electrical demand is supplied by steam and freon bottom cycles. The combined direct converter and blanket thermal energy is 3780 MWt.

The relative split of low and high temperature thermal energy from the TMR depends upon the specific requirements of the TCP; however, it is possible to construct a set of algebraic relationships regarding the power balance as done in Section 10.2. The thermal energy balances for the low and high temperature portions of the process can be written as

$$f_1 P_t = \dot{N} E_{t_1} \tag{10.6}$$

and

$$f_2 P_t = \dot{N} E_{t_2} \tag{10.7}$$

where f_1 is the fraction of blanket thermal power used directly in the low temperature TCP, f_2 is the fraction used in the high temperature TCP. The quantity $(1-f_1-f_2)$ is the fraction of blanket thermal energy used to produce electricity. Other nomenclature is the same as that in Section 10.2.

The electrical energy balance can be written as

$$P_{d_e} + (1-f_1-f_2)P_t \, \eta_{SPP} + E_w \dot{N} \, \eta_{Bott} = \dot{N} E_e \tag{10.8}$$

All quantities except f_1, f_2 and $\dot{N}$ are known or can be assumed in the above equations so they can be solved simultaneously to give the hydrogen production rate

$$\dot{N} = \frac{P_{d_e} + P_t \, \eta_{SSP}}{E_e - (E_{t_1} + E_{t_2}) \, \eta_{SSP} - E_w \, \eta_{Bott}} \tag{10.9}$$

The fractions f_1 and f_2 can be calculated directly from Eqs. (10.6) and (10.7) once N is known. The plant efficiency can be calculated from

$$\eta_{TCP} = \frac{\Delta H_{HHV} \dot{N}}{P_{d_e} + P_t} \qquad (10.10)$$

10.3.2 Energy Requirements of the Thermochemical Plant

Table 10.5 presents a summary of the thermal and electrical energy requirements for the system using the fluidized bed decomposer system. They are the same as for the Joule-Boosted system except for Section II of the TCP where high temperature thermal energy is used for the decomposer and its preheater. The distribution of energy for the various components in Section II also change because the conversion ratio for SO_3 decomposition at 1100 K is 65% as compared to 84% at 1250 K.

Figure 10.9 shows the energy inputs calculated* for the various components of Section II. The important point to be noted here is that the energy for the decomposer and its preheater is supplied by thermal energy from the high temperature blanket rather than by Joule (electric) heating. The recuperator provides an important preheat and energy recovery function that separates the high and low temperature energy ranges.

The evaporator has two energy inputs as shown in Fig. 10.9. One is 29 kJ/mole from low temperature thermal energy and the other is 195 kJ/mole from recovery of energy from the decomposer cooler. The evaporator energy requirement is calculated by assuming that 55% of the water can be condensed by pressure staging. Condensation of the remaining vapor permits a further energy recovery of 103 kJ/mole at 430 K. The other recoverable energies are listed in Table 10.6

* Appendix A presents details of the thermochemical calculations used for Section II.

Table 10.5 *Thermal and electrical demands of the TCP for the reference FY82 fluidized-bed decomposer concept (with vapor recompression (VR) in Section III and some pressure staging (PS) in Section II)*

	Electric Demand (kJ_e/mole H_2)	Thermal Demand (kJ_t/mole H_2)	Temperature Range
Section II (High Temperature) (a)			
Decomposer	--	98 } E_{t_2}	1100 K
Preheater	--	73 }	825 → 1100 K
Section II (Low Temperature) (a)			
Preheater	--	34	680 → 722 K
Boiler	--	140	680 K
Evaporator* (net)	--	29	400 → 680 K
Section III (b)			
HX E303	--	72.4	523 K
HX E308D	--	21.2	484 K
TC 301, 302, 303 (VR)	131	--	--
Section IV (b)			
E404A		6.7	713 K
E404B2		1.7	616 K
E404C2		7.4	522 K
E402C		2.2	393 → 415 K
TOTALS	E_e = 131	E_t + E_t = 486	

(a) Calculated by using method described in Appendix 10A.

(b) Provided by General Atomic (see Section 9).

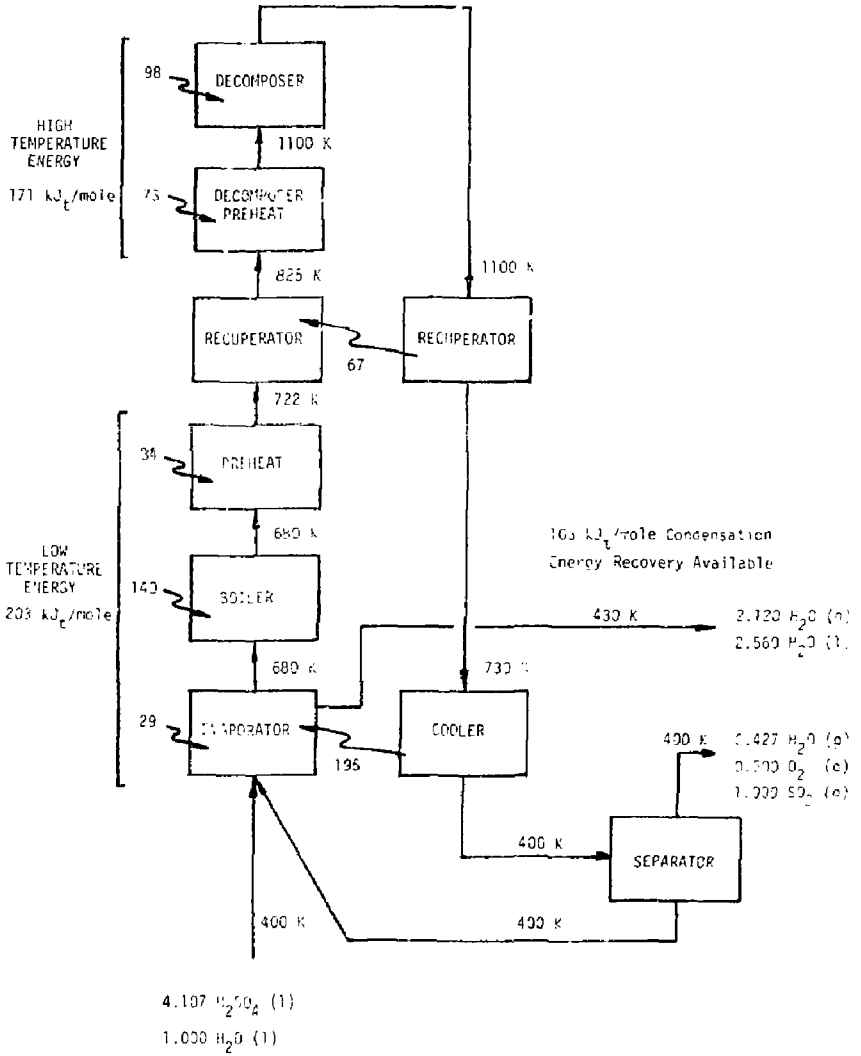

Figure 10.9 Thermal energy and temperature requirements for H_2SO_4 process steam (Section II).

Table 10.6 Usable waste heat flows from the TC processes

Source	Amount (kJ_t/mole H_2)	Temperature
Section I	111	393 K
	21	425 K
Section II	103	430 K
Section III	56	368 → 417 K
TOTAL	E_w = 291	

Sufficient information is now available to determine the hydrogen production rate for an assumed set of efficiencies for the stream and freon power systems. The results are summarized as follows:

η_{SSP}	=	0.35	assumption
η_{Bott}	=	0.15	assumption
P_t	=	3780 MWt	
P_{d_c}	=	137 MWe	
E_{t_1}	=	315 kJ/mole	
E_{t_2}	=	171 kJ/mole	
E_e	=	131 kJ/mole	
E_w	=	291 kJ/mole	
$\dot{N}$	=	5.67 k mole/sec	Eq. (10.9)
f_1	=	0.473	Eq. (10.6)
f_2	=	0.257	Eq. (10.7)
$1-f_1-f_2$	=	0.270	
η_{TCP}	=	0.43	Eq. (10.10)

10.3.3 TCP Temperature Enthalpy Demand Curve

The energy requirements of the TCP can be presented on a plot of temperature versus enthalpy. While several arrangements are possible, Fig. 10.10 shows a workable arrangement. The energy demands are shown by the arrows directed to the right. The numbers and temperature ranges for constructing the plot are given in Table 10.7. This is a reordering of the data presented in Table 10.5.

Figure 10.10 also shows the energy supply as indicated by the arrows moving to the left. The details of this supply and the intermediate stream

Table 10.7 Incremental and integral thermal energy demands for TCP

Component	Temperature	Energy Required (kJ_t/mole)	Integral Energy Required (kJ_t/mole)
E402C	393-415	2.2	2.2
E308D	484	21.2	23.4
E404C2	522	7.4	30.8
E303	523	72.4	103.2
E404B2	616	1.7	104.9
Steam Power	569-710	180	284.9
E404A	713	6.7	291.6
Evaporator	400-680	224	515.6
Boiler	680	140	655.6
Preheater	680-722	34	689.6
Recuperator (in)	722-825	67	756.6
Decomposer	825-1100	73	829.6
Decomposer	1100	98	927.6
Recuperator (out)	1100-730	-67	860.6
Decomp Cooler	730-430	-195	665.6

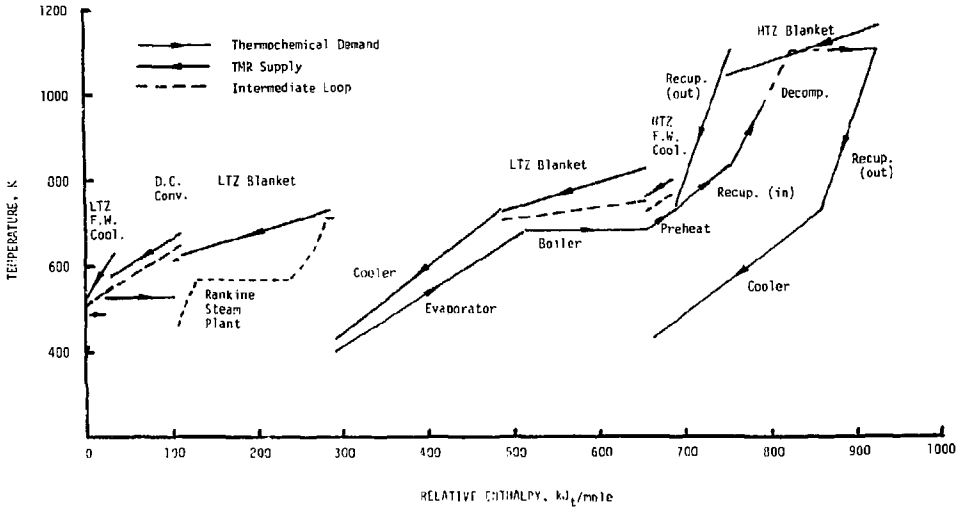

Figure 10.10 *Temperature versus enthalpy plot for TMR supply and TCP demand.*

or water loops (dashed lines) are covered in the following section.

10.3.4 System Matching

Now that the energy demand curve has been constructed, it is necessary to construct a match with the energies available from the TMR and the energy recoveries in the TCP.

Table 10.8 summarizes the sources of thermal energy available to satisfy the process. The low temperature energy contribution totals to 495 kJ_t/mole which can satisfy the 315 kJ_t/mole used directly as thermal energy by the TCP and 180 kJ_t/mole which is used to make part of the electricity required for shaft work. The four low temperature energy sources represent four separate heat transport streams. Since two of them can be contaminated with tritium and they all have different temperature ranges, each heat transport stream is kept separate. Each source has its own heat transport loop and intermediate helium-to-steam (or water) heat exchangers to isolate the TMR from the TCP.

The high temperature energy stream is presently assumed to be directly coupled to the SO_3 decomposer and its preheater. The use of an intermediate heat exchanger could be of value here to provide some pressure staging, but would increase the blanket temperature unacceptably.

The TCP demands and the available thermal energies can be matched reasonably well by selecting comparable energy matches. The arrangement shown in Fig. 10.10 is a workable one and has reasonable temperature differences for the intermediate steam or water heat transport loops (dashed lines). The steam-Rankine power cycle is the same as that discussed in Section 10.2. The pressure is 8 MPa, saturation temperature of 568 K, and superheat to 710 K, as shown in Fig. 10.7.

Figure 10.11 shows a schematic arrangement of the heat transport loops from the TMR, the intermediate steam (or water) isolation loops and the TCP

Table 10.8 Available thermal energies

Source	Amount kJ_t/mole	Temperature (k)
High Temperature Energy (a)		
HTZ Primary Coolant	171	1040-1160 K
	171	
Low Temperature Energy (b)		
HTZ First Wall Coolant (c)	33	750-800 K
LTZ Primary Coolant	355	610-825 K
LTZ First Wall Coolant (d)	33	525-625 K
Direct Converter Coolant	74	580-680 K
	495	
Total	666 (e)	

(a) 171 kJ_t/mole required

(b) 315 + 180 kJ_t/mole required

(c) 16% of HTZ deposited energy to first wall coolant

(d) 8.5% of LTZ deposited energy to first wall coolant

(e) Total blanket thermal energy is 592 kJ_t/mole (excludes direct converter)

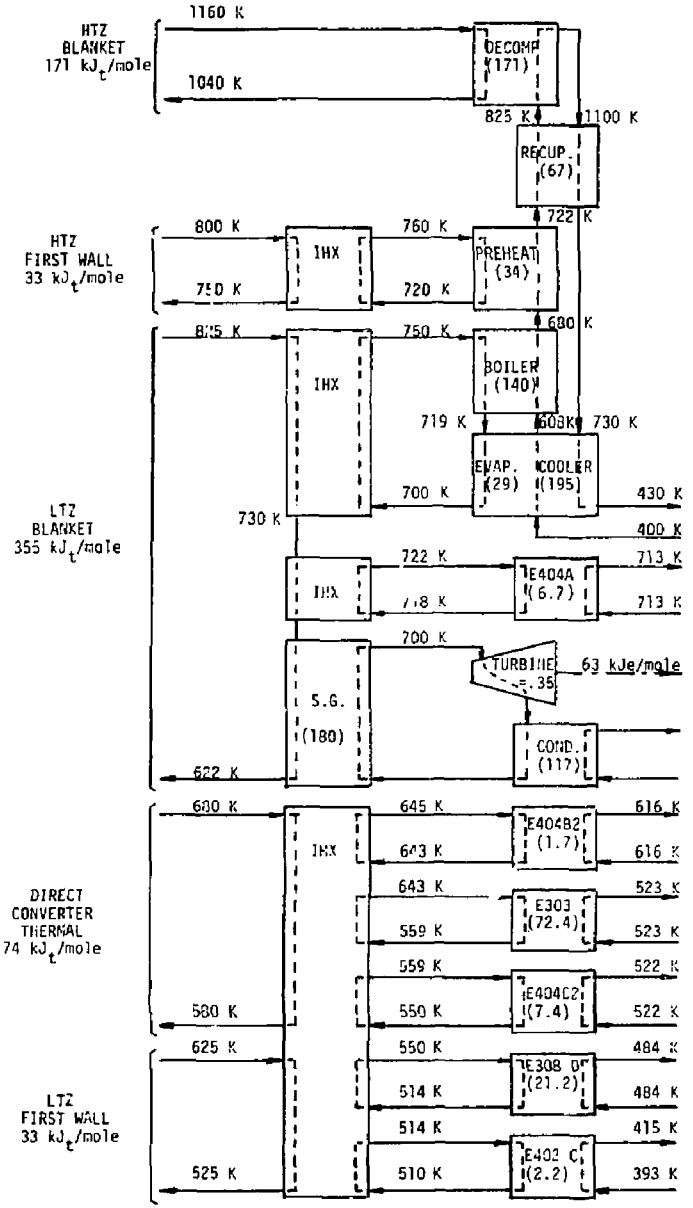

(*) ENERGY TRANSFERS ARE IN kJ_t/MOLE

Figure 10.11 Schematic diagram coupling the TMR to the TCP--Section IV.

process loops. The temperatures indicated provide reasonable temperature differences for the heat exchangers involved.

10.3.5 Summary for the Fluidized Bed System

Figure 10.11 presents an overall summary of how the TMR is coupled to the TCP. The arrangement shown is workable, but it is not necessarily optimum. Better matching of the supply and load curves to reduce some of the larger temperature differences could provide a more optimum system.

The energy that must be generated in the high temperature blanket is 171 kJ_t/mole plus 33 kJ_t/mole which is transferred to the first wall cooling. This is to be compared with the 592 kJ_t/mole totally supplied by the TMR blankets.* This requires high temperature blanket coverage of 0.34 which is not obtainable with an overall tritium breeding ratio of 1.1 and where all breeding is done in the low temperature blanket. A more realistic fraction would be about 0.25. The impact is that the system matching must find additional high temperature energy or must use a decomposer and recuperator design that has better thermal energy use. One possible source of additional high temperatur energy is the thermal discharge from the direct converter. Assuming it could be designed to supply 74 kJ_t/mole over the temperature range from 825 to 1100 K, the decomposer would need 97 kJ_t/mole from the high temperature blanket. This would require a total of 115 kJ_t/mole to be deposited in the high temperature blanket to cover the 15% transferred to the first wall coolant. The result would be a drop in the energy fraction from 0.34 to 0.19, which is feasible.

The following conclusions can be made regarding the fluidized bed decomposer system:

1. A reasonable match exists such that the TMR can supply the thermal

---

* Total blanket thermal energy excludes direct converter thermal; 666-74=592.

and electrical energy demands of the TCP. This conclusion requires that the high temperature blanket provides 0.34 m of the total blanket thermal energy.

2. If the tritium breeding is limited to the low temperature blanket, the high temperature blanket energy must be supplemented from another source or the high temperature thermal demand of the decomposer must be reduced to allow a feasible match. Use of the direct converter thermal energy could reduce the high temperature blanket energy fraction to 0.19.

3. With resolution of the high temperature energy fraction issue, the system could achieve an overall efficiency of 43%.

APPENDIX 10.A

THERMOCHEMICAL CALCULATIONS FOR H_2SO_4 PROCESS STREAM - SECTION II

By D. S. Rowe

As part of the University of Washington's support to LLNL, an independent calculation was done to define the energy requirements for the H_2SO_4 process stream. The discussion presented here grew out of work done by Mark Abhold as part of a student design project and computations performed by Oscar Kirkorian at LLNL.

The calculations considered the H_2SO_4 process stream as represented by Fig. 10.A-1. The objective of the calculation was to calculate the energy requirement for each component based upon the enthalpy of the inlet and outlet streams. Each numbered stream could have up to 7 chemical species and the molar flow rates were defined based upon the chemical processes taking place in each of the components.

The total mass flow rate for each stream (j) was calculated from

$$\dot{m}_j = \dot{N} \sum_i n_{i,j} M_i$$

where $\dot{m}_j$ = mass flow in stream j (g/sec);

$n_{i,j}$ = mole fraction of species i in stream j normalized to production of 1 mole of hydrogen ($mole_i/mole_{H2}$);

M_i = molecular weight of species i (g/mole);

$\dot{N}$ = molar production rate of hydrogen ($mole_{H2}/sec$).

The mass balance for each component was calculated from

$$\sum_j (m_j)_{out} - \sum_j (m_j)_{in} = 0 .$$

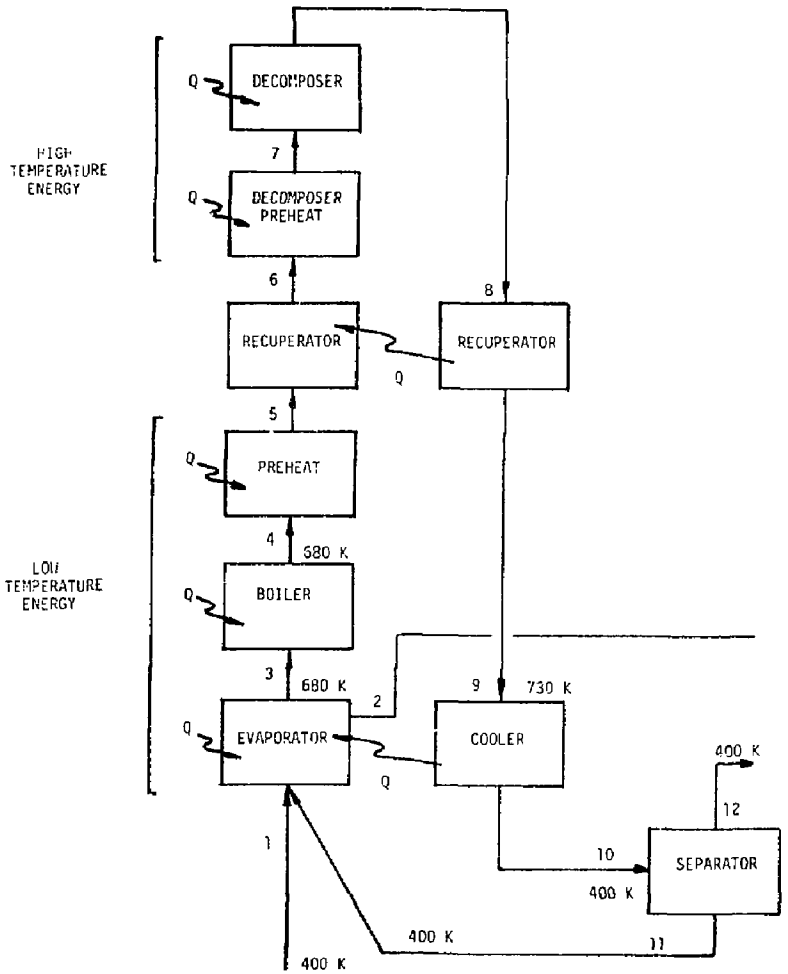

Figure 10.A-1 H_2SO_4 component and process stream identification.

The stream enthalpy was calculated from

$$h_j = \sum_i \left[n_{i,j} \left(h_i^o - h_{298}^o \right) + n_{i,j} \Delta h^o{}_f \right]$$

where h_j = mixture enthalpy of stream j ($kJ/mole_{H2}$);

$h_i^o - h_{298}^o$ = enthalpy of species i above 298 K ($kJ/mole_i$)

Δh_f^o = enthalpy of formation for species i ($kJ/mole_i$)

The thermal energy requirement for each component was calculated from

$$q = \dot{N} \sum_j (h_j)_{out} - \sum_j (h_j)_{in}$$

where q = net thermal power (kJ_t/sec).

The enthalpy data for each species was taken from the JANAF tables.[A1] The enthalpy of mixtures of liquid H_2O and H_2SO_4 was interpolated from the tables containing the various hydrates of H_2SO_4 and thus includes the enthalpy of mixing.

The molar flow rates for each species was taken from the compositions of Kirkorian[A2] and where the following assumptions were made for each stream:

Stream 1 - Input mixture of liquid H_2SO_4 and H_2O at 400 K.

Stream 2 - Partially condensed vapor (55%) as output from evaporator available for energy recovery at 430 K.

Stream 3 - Azeotrope mixture of liquid H_2O and H_2SO_4 at 680 K.

Stream 4 - Equilibrium molar composition of vapors (H_2O, SO_3 ...) based on calculations of Krikorian.[A2]

Stream 5 - Same as Stream 4.

Stream 6 - Same as Stream 4.

Stream 7 - Same as Stream 4.

Stream 8 - SO_3 decomposition has occurred at the conversion ratio:

0.65 Fluid bed 1100 K

0.84 Joule-Boosted 1250 K

Stream 9 - Sensible cooling of decomposer products to 730 K only--no recombination of SO_2 and O_2.

Stream 10 - Cooling of products to 400 K without recombination of SO_2 and O_2 but with recombination of SO_3 and H_2O to yield H_2SO_4.

Stream 11 - Liquid H_2O and H_2SO_4 recycle at 400 K.

Stream 12 - Product stream gases at 400 K.

The calculations were automated for a microcomputer and were performed iteratively to obtain stream temperatures that would allow energy matching of the recuperator. Stream temperatures, molar flow rates and enthalpy results for the fluidized bed and Joule-Boosted decomposers are presented in Tables 10.A-1 and 10.A-3. The energy requirement results are presented in Tables 10.A-2 and 10.A-4.

Table 10.A-1 H_2SO_4 process stream thermochemical calculations for fluidized bed decomposer.

H2SO4 PROCESS STREAM THERMOCHEMICAL CALCULATIONS
FLUIDIZED BED
CONVERSION RATIO 0.64
HYDROGEN PRODUCTION 5670 MOL/SEC

THERMOCHEMICAL CALCULATIONS BASED ON 1 MOL/SEC OF HYDROGEN

	MOLAR FLOW MOL/SEC	H-H298 KCAL/MOL	DELTAH KCAL/MOL	H KCAL/MOL	FLOWXH KCAL/SEC	MASS FLOW G/SEC
STREAM 1 400 K						
H2SO4(L)	1.000	9.877	-488.074	-478.197	-478.197	98.000
H2O(L)	4.107	0.000	0.000	0.000	0.000	73.926
STREAM 2 430 K						
H2O(G)	2.120	1.074	-57.798	-56.724	-120.256	38.160
H2O(L)	2.560	0.000	-68.315	-68.315	-174.886	46.080
STREAM 3 680 K						
H2SO4(L)	1.551	16.737	-202.957	-186.220	-288.827	151.998
H2O(L)	0.174	0.000	0.000	0.000	0.000	3.132
STREAM 4 680 K						
H2SO4(G)	1.032	9.633	-175.700	-166.067	-171.381	101.136
H2O(G)	0.693	3.214	-57.798	-54.584	-37.827	12.474
SO3(G)	0.519	5.646	-94.590	-88.944	-46.162	41.520
STREAM 5 722 K						
H2SO4(G)	0.755	10.851	-175.700	-164.849	-124.535	74.024
H2O(G)	0.970	3.590	-57.798	-54.208	-52.571	17.460
SO3(G)	0.796	6.352	-94.590	-88.238	-70.198	63.644
STREAM 6 825 K						
H2SO4(G)	0.240	13.921	-175.700	-161.779	-38.903	23.566
H2O(G)	1.480	4.535	-57.798	-53.263	-79.083	26.726
SO3(G)	1.311	8.127	-94.590	-86.463	-113.312	104.843
STREAM 7 1100 K						
H2SO4(G)	0.011	22.552	-175.700	-153.148	-1.622	1.038
H2O(G)	1.715	7.210	-57.798	-50.588	-86.742	30.864
SO3(G)	1.540	13.077	-94.590	-81.513	-125.563	123.233
STREAM 8 1100 K						
H2SO4(G)	0.002	22.552	-175.700	-153.148	-0.306	0.196
H2O(G)	1.723	7.210	-57.798	-50.588	-87.163	31.014
SO3(G)	0.549	13.077	-94.590	-81.513	-44.751	43.920
O2(G)	0.500	6.265	0.000	6.265	3.133	16.000
SO2(G)	1.000	9.540	-70.947	-61.407	-61.407	64.000
STREAM 9 730 K						
H2SO4(G)	0.002	11.087	-175.700	-164.613	-0.329	0.196
H2O(G)	1.723	3.663	-57.798	-54.135	-93.275	31.014
SO3(G)	0.549	6.489	-94.590	-88.101	-48.368	43.920
O2(G)	0.500	3.226	0.000	3.226	1.613	16.000
SO2(G)	1.000	4.804	-70.947	-66.143	-66.143	64.000
STREAM 10 400 K						
H2SO4(L)	0.551	5.880	-294.969	-289.089	-159.288	53.998
H2O(G)	0.427	0.825	-57.798	-56.973	-24.327	7.686
O2(G)	0.500	0.723	0.000	0.723	0.362	16.000
SO2(G)	1.000	1.016	-70.947	-69.931	-69.931	64.000
H2O(L)	0.747	0.000	0.000	0.000	0.000	13.446
STREAM 11 400 K						
H2SO4(L)	0.551	5.880	-294.969	-289.089	-159.288	53.998
H2O(L)	0.747	0.000	0.000	0.000	0.000	13.446
STREAM 12 400 K						
H2O(G)	0.427	0.825	-57.798	-56.973	-24.327	7.69.
O2(G)	0.500	0.723	0.000	0.723	0.362	16.00
SO2(G)	1.000	1.016	-70.947	-69.931	-69.931	64.000

Table 10.A-2 H_2SO_4 process stream thermochemical summary results--fluidized bed decomposer.

PROCESS STREAM SUMMARY

NO.	TEMPERATURE K	ENTHALPY KJ/MOL-H2	MASS FLOW KG/SEC	ENERGY FLOW MW
1	400.00	-2000.78	974.82	-11344.40
2	430.00	-1234.87	477.64	-7001.73
3	680.00	-1208.45	879.59	-6851.93
4	680.00	-1068.47	879.59	-6058.22
5	722.00	-1034.72	879.61	-5866.86
6	825.00	-967.75	879.61	-5487.15
7	1100.00	-895.07	879.61	-5075.06
8	1100.00	-797.03	879.59	-4519.16
9	730.00	-864.00	879.59	-4898.89
10	400.00	-1059.33	879.59	-6006.38
11	400.00	-666.46	382.41	-3778.83
12	400.00	-392.86	497.18	-2227.54

TOTAL MASS BALANCE ERROR 1.52588E-05

COMPONENT SUMMARY

	ENTHALPY CHG KJ/MOL-H2	NET POWER MW
EVAPORATOR	223.91	1269.57
BOILER	139.98	793.71
PREHEATER	33.75	191.36
RECUP(IN)	66.97	379.71
RECUP(OUT)	-66.97	-379.74
RECUP(NET)	-0.00	-0.03
DECOMP(PREHT)	72.68	412.09
DECOMP(REACT)	98.04	555.91
COOLER	-195.32	-1107.49
TOTAL	373.04	2115.12
SYSTEM TOTAL	373.04	2115.12

Table 10.A-3 H_2SO_4 process stream thermochemical calculations for Joule boosted decomposer.

H2SO4 PROCESS STREAM THERMOCHEMICAL CALCULATIONS
JOULE BOOSTED
CONVERSION RATIO 0.84
HYDROGEN PRODUCTION 3940 MOL/SEC

THERMOCHEMICAL CALCULATIONS BASED ON 1 MOL/SEC OF HYDROGEN

	MOLAR FLOW MOL/SEC	H-H298 KCAL/MOL	DELTAH KCAL/MOL	H KCAL/MOL	FLOW*H KCAL/SEC	MASS FLOW G/SEC
STREAM 1	400 K					
H2SO4(L)	1.000	9.877	-488.074	-478.197	-478.197	98.000
H2O(L)	4.107	0.000	0.000	0.000	0.000	73.926
STREAM 2	430 K					
H2O(G)	2.120	1.074	-57.798	-56.724	-120.256	38.160
H2O(L)	2.560	0.000	-68.315	-68.315	-174.886	46.080
STREAM 3	680 K					
H2SO4(L)	1.191	16.739	-202.982	-186.242	-221.815	116.718
H2O(L)	0.134	0.000	0.000	0.000	0.000	2.412
STREAM 4	680 K					
H2SO4(G)	0.793	9.633	-175.700	-166.067	-131.691	77.714
H2O(G)	0.532	3.214	-57.798	-54.584	-29.039	9.576
SO3(G)	0.398	5.646	-94.590	-88.944	-35.400	31.840
STREAM 5	722 K					
H2SO4(G)	0.580	10.851	-175.700	-164.849	-95.630	56.830
H2O(G)	0.745	3.590	-57.798	-54.208	-40.369	13.405
SO3(G)	0.611	6.352	-94.590	-88.238	-53.905	48.872
STREAM 6	900 K					
H2SO4(G)	0.067	16.213	-175.700	-159.487	-10.675	6.560
H2O(G)	1.258	5.240	-57.798	-52.558	-66.111	22.642
SO3(G)	1.124	9.448	-94.590	-85.142	-95.705	89.925
STREAM 7	1250 K					
H2SO4(G)	0.003	27.470	-175.700	-148.230	-0.385	0.254
H2O(G)	1.322	8.769	-57.798	-49.029	-64.826	23.800
SO3(G)	1.188	15.866	-94.590	-78.724	-93.556	95.072
STREAM 8	1250 K					
H2O(G)	1.325	8.769	-57.798	-49.029	-64.963	23.850
SO3(G)	0.191	15.866	-94.590	-78.724	-15.036	15.280
O2(G)	0.500	7.541	0.000	7.541	3.771	16.000
SO2(G)	1.000	11.536	-70.947	-59.411	-59.411	64.000
STREAM 9	0 K					
H2O(G)	1.325	3.663	-57.798	-54.135	-71.729	23.850
SO3(G)	0.191	6.489	-94.590	-88.101	-16.827	15.280
O2(G)	0.500	3.226	0.000	3.226	1.613	16.000
SO2(G)	1.000	4.804	-70.947	-66.143	-66.143	64.000
STREAM 10	400 K					
H2SO4(L)	0.191	9.217	-459.947	-450.729	-86.089	18.718
H2O(G)	0.427	0.825	-57.798	-56.973	-24.327	7.686
O2(G)	0.500	0.723	0.000	0.723	0.362	16.000
SO2(G)	1.000	1.016	-70.947	-69.931	-69.931	64.000
H2O(L)	0.707	0.000	0.000	0.000	0.000	12.726
STREAM 11	400 K					
H2SO4(L)	0.191	9.217	-459.947	-450.729	-86.089	18.718
H2O(L)	0.707	0.000	0.000	0.000	0.000	12.726
STREAM 12	400 K					
H2O(G)	0.427	0.825	-57.798	-56.973	-24.327	7.686
O2(G)	0.500	0.723	0.000	0.723	0.362	16.000
SO2(G)	1.000	1.016	-70.947	-69.931	-69.931	64.000

Table 10.A-4 H_2SO_4 process stream thermochemical summary results--Joule boosted decomposer.

PROCESS STREAM SUMMARY

NO.	TEMPERATURE K	ENTHALPY KJ/MOL-H2	MASS FLOW KG/SEC	ENERGY FLOW MW
1	400.00	-2000.78	677.39	-7883.06
2	430.00	-1234.87	331.91	-4865.40
3	680.00	-928.07	469.37	-3656.61
4	680.00	-820.61	469.37	-3233.19
5	722.00	-794.55	469.36	-3130.54
6	900.00	-721.70	469.36	-2843.51
7	1250.00	-664.28	469.36	-2617.27
8	1250.00	-567.52	469.37	-2236.02
9	730.00	-640.51	469.37	-2523.62
10	400.00	-753.06	469.37	-2967.07
11	400.00	-360.20	123.89	-1419.18
12	400.00	-392.86	345.48	-1547.89

TOTAL MASS BALANCE ERROR 1.33514E-05

COMPONENT SUMMARY

	ENTHALPY CHG KJ/MOL-H2	NET POWER MW
EVAPORATOR	198.03	780.23
BOILER	107.46	423.41
PREHEATER	26.05	102.66
RECUP(IN)	72.85	287.03
RECUP(OUT)	-72.99	-287.60
RECUP(NET)	-0.14	-0.57
DECOMP(PREHT)	57.42	226.24
DECOMP(REACT)	96.76	381.24
COOLER	-112.55	-443.45
TOTAL	373.04	1469.77
SYSTEM TOTAL	373.04	1469.77

References to Appendix 10.A

A1. JANAF Thermochemical Data, Dow Chemical, Midland, MI (data through 1979).

A2. O. H. Krikorian, "Hydrogen Production Based on Magnetic Fusion," Lawrence Livermore National Laboratory, UCRL-86600 (1981).

SECTION 11.0

PRELIMINARY COST ESTIMATES

Contributor:
L. Brown

TABLE OF CONTENTS

SECTION 11.0

List of Tables

11.0 PRELIMINARY COST ESTIMATES

Hydrogen production costs were estimated for two chemical plant -- fusion plant combinations. The plant based on a TMR with a two temperature zoned blanket and a Fludized Bed Decomposer (FBD) in the chemical plant gave a slightly lower hydrogen cost than the plant with a single temperature zone blanket and a Joule Boosted Decomposer (JBD). Assuming public utility financing (100% debt), the hydrogen cost for the FBD case was approximately $12/GJ (July 1980 dollars) and $15/GJ for the JBD case. Higher costs were indicated for the private utility (50% debt, 50% equity) and chemical industry (100% equity) financing methods. These costs are very favorable and indicate that fusion synfuels will be competitive in the time frame for the emergence of fusion in approximately 2030.

11.1 THE ECONOMIC BASIS

We assume that the plant would be operated at a time when fusion electric plants have been in operation for at least a decade (approximately 2030 to 2050). We present costs based on constant, July 1980 dollars, and use currently available chemical plant technology. Since the chemical portion of the plant will be manpower intensive and cannot be operated with as few people or as little supplies or maintenance as in an electric power plant, we have used chemical plant experience[1] in estimating all labor costs.

Ultimately, a Fusion-Synfuel Plant may produce a combination of pipeline quality synthetic natural gas (e.g. 10% H_2, 80% CH_4, and 10% C_2H_6 and higher hydrocarbons and other gases) together with liquid transportable fuel (e.g. CH_3OH) and chemical feed stocks for plastics, fertilizers, and solvents (e.g. C_2H_4, C_2H_3O, acetic anhydride, NH_3, etc.). If the production is mostly synthetic natual gas for pipelines, a utility is likely to finance, build, and operate the plant; whereas if the products are fuels and chemicals, a chemical company would be involved. Thus the method of financing could be by either

utility (public or private) or chemical industry. We will present costs for these three kinds of financing.

11.2 COSTING PROCEDURES

Both the fusion community and chemical industy have developed considerable expertise in estimating the capital cost as well as the projected operating costs of their respective plants. The basis of TMR capital costs were independently derived at LLNL[2] whereas the TMR operating costs as well as utility financing are calculated in the manner specified by Battelle[3] as the standard for fusion reactor conceptual designs.

The hydrogen production rate of the Joule Boosted Decomposer/Moderate Temperature Blanket based hydrogen plant is significantly lower than that of the Fluid Bed Decomposer/Two-Zone Blanket. Complete design of two different chemical plants was avoided by designing a standard size chemical plant and scaling the results to the two different cases. The standard plant, producing 4900 moles per second of hydrogen, is the same size as that reported last year [4]. A significant fraction of the plant is unchanged from last year (Sections I, IV and part of III) and thus was not recosted. Section II was costed separately for both the Joule Boosted and Fluid Bed Decomposer concepts. The size of the chemical plant is such that multiple parallel trains are used throughout most of the plant; therefore, a linear scaling law was used to produce cost estimates for the resized plants.

Costs for the Chemical Plant and the power systems interface are obtained by standard chemical engineering costing techniques. These costing techniques are based upon using actual construction experience from many chemical plants to predict capital and operating costs from FOB equipment costs. The new reference work by Peters and Timmerhaus[1] was used to augment the older Guthrie methods[5,6] both for estimating the FOB costs of equipment, as well as deriving from the FOB cost estimates of the installed direct capital cost,

the total plant investment and the operating cost. Where standard works could not provide capital costs, as in most of Section II and the power recovery systems, vendor estimates or other special sources of FOB cost data were used. The industry standard, Marshall and Swift (M&S)[7], equipment cost index was used to reduce all costs to the same basis, July 1980.

It is recognized that some of the best costing techniques are maintained as proprietary by A&E, chemical and oil companies. A proprietary costing method, available at GA was used to spot check costs for a representative number of items. No overall bias could be observed although variations between different types of equipment were noted.

We believe that our cost estimates are well within our goal of $\pm$ 30% accuracy.

11.3 PRELIMINARY CAPITAL COST

11.3.1 Main Solution Reaction Step (Section I)

The simplified schematic of Section I was presented in Figure 9.3-1. Table 11.3-1 presents a detailed list of the equipment required for performing the main solution reaction step, together with size and cost data. With the exception of the Heat Exchanger Reactor (R-101), all items have been costed by the Guthrie method.[5,6]

The structural material used throughout Section I is mild steel. If other than dry SO_2, oxygen and or water are present, the steel must be protected by an appropriate coating or lining. Although spray on hydrocarbon based coatings are adequate when moist SO_2 is present, liners of bulk fluorocarbon are specified when H_2SO_4, HI or I_2 are present. The installed cost of fluorocarbon linings is estimated to be \$1100/m^2.

Table II.3-1 Preliminary Capital Costs for Section I[a] - M$ July 1980

Item No.		Parallel Units	Diameter Meters	Length Meters	Equivalent Mild Steel FOB Cost	Actual FOB Cost Plus Adders	Installed Direct Capital Cost	Total Plant Investment Basis
C101	Primary scrubbing reactor	6	3.8	9.0	0.326	1.353[bc]	2.211	2.934
C102	Lower phase SO_2 scrubber	3	5.1	19.5	0.847	3.868[bc]	6.096	8.027
C103	Boost reactor	6	5.1	19.5	0.847	3.868[bc]	6.096	8.027
C104	Secondary scrubbing reactor	6	4.5	8.6	0.381	1.651[bc]	2.653	3.508
S101	High pressure flash drum	6	3.6	13.5	0.489	1.743[c]	2.929	3.956
S102	Low pressure flash drum	6	4.2	12.0	0.452	1.692[c]	2.875	3.849
S104	Primary water knockout drum	6	3.0	3.9	0.113	0.113	0.337	0.505
S105	Secondary water knockout drum	1	3.0	3.9	0.019	0.019	0.056	0.084
R101	Heat exchanger reactor	6	1.8	7.5	1.175	20.171	2.206	26.518
E101	SO_2 heat exchanger	6	1.7	12.0	0.713	1.084	2.023	2.945
E102	Sec. III water heat exchanger	2	1.1	12.0	0.174	0.174	0.403	0.615
E103	Sec. II water heat exchanger	3	1.2	12.0	0.275	0.275	0.638	0.972
P101	Water feed pump	6+1	-	-	0.002	0.002	0.008	0.012
P103	Reactor feed pump from C101	6+1	-	-	0.009	0.017	0.031	0.042
P104	Iodine feed pump	6+1	-	-	0.018	0.036	0.065	0.090
P105	Reactor feed pump from C103	6+1	-	-	0.033	0.066	0.118	0.163
P106	Reactor feed pump from C104	6+1	-	-	0.046	0.092	0.169	0.233
TE101	O_2 power recovery turbine	1	-	-	0.971	0.971	2.095	3.157
TE103	Iodine power recovery turbine	1	-	-	0.057	0.165	0.244	0.321
Total Capital Cost					6.947	37.350	51.253	65.958

[a] Based on a hydrogen plant producing 4900 moles per second.
[b] Adder includes the field installation of liner.
[c] Adders include field installation of liner.

The Heat Exchanger Reactor is unique because of the material involved, niobium. The $220/kg cost of the niobium tubing dominates the reactor cost. Added to the $15.8M cost of the tubing is an appropriate amount for installation of the tubing ($3.2M), plus the FOB cost of the equivalent mild steel heat exchangers ($1.2M), giving and FOB cost of $20.2M. Installation cost was estimated from the cost of the equivalent mild steel heat exchanger since niobium is required only for the heat transfer surfaces.

The Guthrie method allows specification of the piping materials separate from the specification of the materials of construction of the equipment. Either mild steel or standard fluorocarbon lined mild steel piping was specified as appropriate. Pumps are either cast iron for water, or cast iron with a molded fluorocarbon liner for corrosive solutions.

Since Section I operates essentially as six systems in parallel, 83% of production capacity may be maintained if any one system is down for repairs. Pumps are cross-connected such that one installed spare backs up the active six. The power recovery turbines are not spared except by a by-pass valve.

The column labeled "Total Plant Investment Basis" is Table 11.3-1 indicates that the major unit costs of Section I are associated with the Heat Exchanger Reactor (R-101). The cost of R-101 may be decreased if more of the heat load is shifted to water-based heat exchangers. If the power bottoming cycle were eliminated the cost of R-101 would be significantly decreased due to the much larger differential temperatures across the exchanger.

11.3.2 H_2SO_4 Processing Step (Section II))

The simplified schematics for the Joule Boosted Decomposer were presented in Figures 9.4-1 and 9.4-2. Detailed lists of the equipment required for H_2SO_4 concentration and decomposition together with cost data are presented in Tables 11.3-2 and 11.3-3 for these two cases. All cost estimates were made using Guthrie's techniques[5,6] except for the decomposers. Details of the decomposer cost assumptions were presented in last year's report[4].

The major costs in Section II are associated with heat transfer equipment. Silicon carbide is the material of choice for heat transfer surfaces where liquid-gas interfaces occur. Silicon carbide is used for all heat transfer involving concetrated sulfuric acid except in the Recuperator/Decomposer Preheater. Incoloy-800H is used in the Recuperator/Decomposer Preheater as only gases exist at the temperatures encountered.

Vessels are fabricated from Fluorocarbon-lined mild steel, with this lining thermally insulated from the process via acid brick linings. At the higher acid concentrations, steel is passivated; and the fluorocarbon linings are unnecessary.

Costs of silicon carbide and vessel liners are treated as adders to the base carbon steel equipment costs. Silicon carbide U-tube costs are estimated to be \$32.7/M[8] for the 5 cm diameter tubes specified for the H_2SO_4 vaporizer, and this cost was used in estimating the rest of the silicon carbon heat exchangers.

11.3.3 HI Concentration Step (Section III)

Capital costs for Section III are presented in Table 11.3-4. The simplified flow diagram for this section was presented in Figure 9.7-1.

Table 11.3-2 Preliminary Capital Cost for Section II[a] Based on the Joule Boosted Decomposer - M$ July 1980

Item No.		Parallel Units	Diameter Meters	Length Meters	Equivalent Mild Steel FOB Cost	Actual FOB Cost Plus Adders	Installed Direct Capital Cost	Total Plant Investment Basis
C201	Atmospheric Distillation Column	1	6.3	11.0	.110	5.424	5.840	6.831
S201	Intermediate Flash Drum	2	3.6	9.0	.114	.391	.820	1.242
S202	Acid Separator #2	2	3.8	9.0	.127	.434	.911	1.380
S203	Acid Separator #2	2	3.8	9.0	.127	.434	.911	1.380
E201	Vaporizer Preheater	10	3.0	9.0	.976	4.388[b]	7.366	8.937
E202	Sulfuric Acid Vaporizer	20	3.0	10.0	2.333	11.305[b]	18.424	23.077
E203	Recuperator/Decomposer Preheater	25	5.6	10.0	3.125	15.524[b]	25.161	31.466
E204	Joule Boosted Decomposer	8	3.0	4.0	1.500	20.000	21.000	24.150
E208	Reboilers on C201	20	2.1	10.7	1.976	8.814[b]	14.898	18.733
E209	Steam Condenser on C201	5	2.5	6.0	.900	.900	2.052	3.088
E210	Concentrator Pretreater	25	3.0	9.0	3.252	16.525[b]	26.461	33.064
E211	Isobaric Flash Concentrator	50	3.0	9.0	6.341	31.804[b]	51.159	63.968
P201	Vaporizer Feed Pump	5+1	-	-	.124	.373	.690	.897
P202	Quench Feed Pump	5+1	-	-	.016	.049	.091	.118
P203	Condensate Feed Pump	5+1	-	-	.023	.023	.054	.082
P204	Concentrator Feed Pump	5+1	-	-	.372	1.119	2.070	2.691
TE201	Power Recovery Turbine	1	-	-	.053	.161	.265	.349
TE202	Power Recovery Turbine	1	-	-	.180	.180	.427	.642
Total	Capital Cost				21.522	117.958	178.600	222.095

[a] Based on a hydrogen plant producing 4900 moles per second.
[b] Adders include installation of silicon carbide tubing, acid brick and fluorocarbon.

Table 11.3-3 Preliminary Capital Cost for Section II[a] Based on the Fluid Bed Decomposer - M$, July 1980

Item No.		Parallel Units	Diameter Meters	Length Meters	Equivalent Mild Steel FOB Cost	Actual FOB Cost Plus Adders	Installed Direct Capital Cost	Total Plant Investment Basis
C201	Atmospheric Distillation Column	1	7.0	11.0	0.147	7.882	7.732	9.044
S201	Intermediate Flash Drum	2	3.6	9.0	.114	.391	.820	1.242
S202	Acid Separator #1	2	4.4	9.0	.168	.575	1.206	1.827
S203	Acid Separator #2	2	4.4	9.0	.168	.575	1.206	1.827
S204	Acid Separator #3	2	4.4	9.0	.168	.575	1.206	1.827
E201	Vaporizer Pretreater	10	3.0	10.0	1.142	5.134[b]	8.618	10.456
E202	Sulfuric Acid Vaporizer	20	3.2	10.0	2.	13.227[b]	21.556	27.000
E203	Recuperator/Decomposer Preheater	25	5.6	10.0	3.125	15.624	25.161	31.466
E204	Fluid Bed Decomposer	7	6.0	10.0	10.000	45.000	50.000	57.500
E208	Reboilers on C201	20	2.3	10.7	2.312	10.312[b]	17.431	21.918
E209	Steam Condenser on C201	5	2.5	6.0	.900	.900	2.052	3.088
E210	Concentrator Preheater	25	3.0	9.0	3.252	16.535[b]	26.461	33.064
E211	Isobaric Flash Concentrator	50	3.3	9.0	6.341	31.804	51.159	63.968
P201	Vaporizer Feed Pump	5+1	-	-	.124	.373	.690	.897
P203	Condensate Feed Pump	5+1	-	-	.023	.023	.054	.082
P204	Concentrator Feed Pump	5+1	-	-	.372	1.119	2.070	2.691
TE201	Liquid Expander-Condensate from C202	1	-	-	.053	.161	.265	.349
TE202	Liquid Expander-Condensate from S201	1	-	-	.180	.180	.427	.642
Total	Capital Cost				31.335	119.489	218.205	269.006

[a] Based on a hydrogen plant producing 4900 moles per second.
[b] Adders include installation of silicon carbide tubing, acid brick and fluorocarbon.

Table 11.3-4 Preliminary Capital Costs for Section III[a] - M$, July 1980

Item No.		Parallel Units	Diameter Meters	Length Meters	Equivalent Mild Steel FOB Cost	Actual FOB Cost Plus Adders	Installed Direct Capital Cost	Total Plant Investment Basis
C301	Iodine wash column	3	4.5	18.0	0.339	2.700[bc]	3.263	4.036
C302	Iodine knockout column	10	7.7	24.0	3.059	28.537[bc]	33.618	41.220
C303	HI distillation	3	6.9	21.6	0.889	21.642[b]	24.394	28.745
S301	Surge drum - C303 reflux	3	2.7	10.2	0.125	0.413[b]	0.737	0.945
S303	Flash drum - 1st H_3PO_4 stage	6	6.0	9.0	0.487	1.619[c]	2.876	3.686
S304	Flash drum - 2nd H_3PO_4 stage	5	3.6	16.2	0.348	1.162[c]	2.061	2.641
S305	Flash drum - 3rd H_3PO_4 stage	4	6.6	10.7	0.451	3.156	5.653	6.852
S306	S-H_3PO_4 separator	3	5.9	22.2	0.544	3.810	6.620	8.037
E302	Intermediate condenser on C303	3	1.6	12.0	0.144	1.459	2.029	2.450
E303	Reboiler on C303	6	1.1	12.0	0.881	3.863	4.983	6.444
E304	Condenser on C303	6	1.6	12.0	0.800	3.962	5.344	6.794
E305	Iodine cooler	1	1.4	12.0	0.099	0.998	1.388	1.676
E306	Heater - 1st H_3PO_4 stage	65	1.5	12.0	3.246	25.057	34.105	41.852
E307	Heater - 2nd H_3PO_4 stage	50	1.5	12.0	2.573	20.884	28.534	34.899
E308	Heater - 3rd H_3PO_4 stage	49	1.5	12.0	1.730	12.758	17.279	21.269
E309	Concentrated H_3PO_4 cooler	6	1.8	12.0	2.095	21.161	29.418	35.528
E310	Water cooler - 1st H_3PO_4 stage	1	1.7	12.0	0.233	1.719	2.327	2.865
E311	Water cooler - 2nd H_3PO_4 stage	1	1.8	12.0	0.218	1.606	2.174	2.677
E312	Water cooler - 3rd H_3PO_4 stage	1	1.7	12.0	0.156	1.152	1.560	1.921
P301	Lower phase feed pump	10+1	-	-	0.207	0.414	0.794	1.084
P302	Iodine wash water pump	3+1	-	-	0.006	0.006	0.013	0.020
P304	Feed pump - C303	10+1	-	-	0.724	1.449	2.653	3.656
P305	Concentrated H_3PO_4 pump	10+1	-	-	0.456	0.932	1.706	2.346
TE302	1st H_3PO_4 stage PR turbine	1	-	-	0.388	0.388	0.723	1.055
TE303	2nd H_3PO_4 stage PR turbine	1	-	-	0.251	0.251	0.548	0.870
TE304	3rd H_3PO_4 stage PR turbine	1	-	-	0.234	0.234	0.503	0.738
TE305	Iodine power recovery turbine	1	-	-	0.085	0.167	0.284	0.386
TC301	1st H_3PO_4 stage steam comp.	6	-	-	16.890	16.890	36.448	59.938
TC302	2nd H_3PO_4 stage steam comp.	5	-	-	14.075	19.075	30.374	45.781
TC303	3rd H_3PO_4 stage steam comp.	4	-	-	11.260	11.260	24.299	36.625
Total Capital Cost					63.003	2[illegible].732	306.706	397.046

[a] Based on a hydrogen plant producing 4900 moles per second.
[b] Adder includes field installation of packing.
[c] Adder includes field installation of liner.

Materials of construction and costing techniques are similar to those of Section I. Where, because of thermal or mechanical limitations, fluorocarbon linings are not acceptable, we have used Hastelloy-C.

The hydrogen iodide concentration step is the most capital intensive portion of the chemical plant. Although significant costs are associated with iodine knockout and hydrogen iodide distillation, the largest costs are associated with phosphoric acid concentration.

The high cost components of the phosphoric acid concentration system are steam compressors and heat exchangers. The compressor costs are based on vendor estimates[9] and reduced to the 1980 base using the M&S[7] cost index. These compressor costs appear to be fixed unless future developments bring down the relative cost of turbine compressors. Flowsheet modifications have the potential for reducing the heat transfer costs, particularly if direct contact heat transfer is employed between immiscible streams in Sections I and III and between Sections III and IV. The large amount of rotating machinery in the phosphoric acid concentration system makes this part of the process a potential source of downtime. The compressors in the third evaporation stage were deliberately oversized to make them identical to the first and second stage units. If any one of the 15 units is down, intermediate pressures may be shifted to permit operation at 93% of capacity with only a slight overall efficiency loss.

11.3.4 HI Decomposition Step (Section IV)

The HI decomposition step has the lowest flow rates and lowest costs of the four chemical process steps. The costs are as high as given in Table 11.3-5 only because of the high pressures involved. The simplified flowsheet for Section IV was given in Figure 9.8-1.

Table 11.3-5 Preliminary Capital Costs for Section IV[a] - MS, July 1980

Item No.		Parallel Units	Diameter Meters	Length Meters	Equivalent Mild Steel FOB Cost	Actual FOB Cost Plus Adders	Installed Direct Capital Cost	Total Plant Investment Basis
C401	HI-I_2 Distillation column	1	4.7	15.0	0.170	1.749[b]	2.143	2.597
C402	HI Absorber	6	4.1	9.6	1.050	1.399[bc]	4.301	5.704
C403	H_2S Scrubber	2	3.8	27.3	0.700	1.023[bc]	2.828	3.981
S401	Reactor effluent V-L separator	1	2.9	13.2	0.162	0.293[c]	0.710	0.984
S402	H2-HI vapor liquid separator	1	2.4	9.6	0.121	0.201[c]	0.514	0.717
D401	Reflux surge drum - C401	1	3.3	15.0	0.075	0.248[c]	0.364	0.497
R401	HI decomposition reactor	4	4.5	27.0	1.750	3.688[bc]	8.202	11.245
E400	Misc. integrated heat exch.	13	-	-	1.300	6.461	9.222	11.799
E4XX[d]	Absorption refrigeration unit	1	-	-	1.689	1.689	2.819	4.562
P401	Reactor feed pump	4+1	-	-	0.638	1.845	2.906	3.876
P402	HI recycle feed pump	1+1	-	-	0.287	1.406	2.215	2.954
P403	Reflux pump - C401	1+1	-	-	0.013	0.037	0.058	0.075
P404	Make-up water feed pump	6+1	-	-	0.020	0.020	0.048	0.072
P405	Recycle pump - C402	6+1	-	-	0.024	0.069	0.109	0.145
P406	SO_2-H_2O pump to C403	6+1	-	-	0.018	0.018	0.042	0.063
P407	Recycle pump -C403	2+1	-	-	0.015	0.015	0.035	0.052
TE401	HI-I_2 power recovery turbine	1	-	-	0.348	1.007	1.483	1.997
TE402	Hydrogen power recovery turbine	1	-	-	1.625	1.625	3.507	5.286
Total Capital					10.005	22.695	41.506	56.606

a Based on a hydrogen plant producing 4900 moles per second.
b Adder includes field installation of packing.
c Adder includes field installation of lines.
d The absorption refrigerator includes heat exchangers E408, E410, and E411.

11.3.5 Power Systems Interface (Section V)

The cost basis for Section V includes all of the helium coolant pumping, heat exchange, heat recovery, and shaft or electric power generation, except for the blanket heat exhangers (as covered in Section 11.3.6) and the process side (tube side) of the heat exchangers which are located within the Chemical Plant. We cost, in Section V, the shell side of all of the in-process heat exchangers.

The results are shown in Table 11.3-6. The most significant costs are those for the helium gas turbine generator sets which are costed at \$189/kW_e or \$54.10/kW_t.[10] This cost compares closely with those quoted by Pratt and Whitney Co.[11] at \$137.81/kW_e (\$49.34/kW_t) for an installed bare turbine generator set, and \$174.61/kW_e (\$62.51/kW_t) for installed units in a complete power station with land, buildings, accessory electric and power plant equipment and other minor expenses. Since we are not including land and power plant buildings, etc., the GA cost of \$54.10/kW_t appears a very reasonable compromise for our July 1980 dollar cost. Our application was discussed with Westinghouse[12] and Brown-Boveri[13], and they confirm our choice of \$54/kW_t as a good estimate for July 1980 dollar costs.

The next most significant item is the steam generator. Using a quotation to GA by United Engineers and Constructors[10], we take a value of \$76.80/kW_t in July 1980 dollars for a fabricated and installed steam generator unit including some indirect costs. Thus, a 2293MW_t unit would cost \$38.56M for the Heat Pipe Blanket, and a 1853 MW_t unit would cost \$31.13M for the Two-Zone Blanket.

Helium piping in both blanket designs is simple and inexpensive. We use a mild steel outer pipe which is from 100 to 200 K cooler than the helium. A 580 K stainless steel inner liner is perforated and spaced away from the cool,

TABLE 11.3-6

Power Systems Section V Capital Costs (Fabricated, Installed and Indirect Costs) - M$, July 1980

	Joule Boosted Decomposer System	Fluid Bed Decomposer System
STEAM RANKINE SYSTEM		
Steam Generators (3780/2810 MWt)[a]	75.6	56.2
Steam Power Plant (866/358 MW_e)[a]	173.2	71.6
Cooling Tower	26.0	10.7
Electric Plantard Instrumentation	34.6	14.3
Freon Botoming Power Plant (137/247 MW_e)[a]	54.8	98.8
DIRECT CONVERTER DC TO AC		
Main HV Transformer Station	3.44	3.44
Inverter Banks	1.72	1.72
Secondary Transformer Station	4.24	4.24
Electrical Distribution System	0.39	0.39
HELIUM PIPING		
Main Blanket:		
Mild Steel Outer Pipe	2.61	2.61
Perforated 304-S.S. Liner	0.52	0.52
Kao-Wool Insulation (Installed)	0.46	0.46
Direct Converter Heat Recovery:		
Total (Similar to Main Blanket)	0.61	0.61
To Fluidized Bed Decomposer	0	3.62
WATER TREATMENT PLANT	5.75	5.75
Total Direct Plus Indirect Capital Cost	383.94	274.960

[a] The first number refers to the JBD System and the second number to the FBD System.

mild steel outer wall by 5 cm, and the space is insulated with Babcock and Wilcox "Kao-Wool" spun mineral insulation.

A water treatment plant has been added to recondition the recirculated process water and to a minor extent precondition the make-up feed water. Water treatment consists of softening with ion-exchange and demineralization with reverse osmosis units, organic removal by carbon adsorption, and other standard waste treatment operations. The plant is sized for a total recirculated water flowrate of 2.0×10^4 moles H_2O/s (8 million gallons per day), and costed at $5.00M.

11.3.6 Fusion-Driven Nuclear Island

For the Tandem Mirror Reactor, we have adopted the capital costs of W. Neff[2] as indicated in Table 11.3-7. We applied a 1.5 factor to the two-zone blanket to account for the higher temperatures and additional complexity. We have not included any tubo-generator and electrical distibution equipment as part of the TMR costs, since they are included in Section V.

11.3.7 Summary of Capital Costs

Table 11.3-8 summarizes the capital costs developed above for the Thermochemical Plant and for the TMR Fusion Driver. The Thermochemical Plant estimates included the appropriate installation and indirect charges plus a contingency (usually 15%) to cover items not specified at this level of design effort. A 3% contactor's fee has been added, and a 5%/y interest charge has been carried over a 3-year construction period which the amount of increases uniformly. We have assumed a 30-year chemical plant life. Chemical plant costs have been scaled from the standard plant size of 4900 mole H_2/sec to the actual size of 3942 mole H_2/sec for the JBD plant and 5670 mole H_2/sec for the FBD plant. We have added a 35% direct charge and contingency as expected for utility industries[3] to construct the TMR Fusion Driver. We have carried a

TABLE 11.3-7

Capital Cost Estimate for 3500 MWt TMR[2] - M$, July 1980

	Single Zone Blanket	Two-Zone Blanket
CENTRAL CELL		
Magnets (1.5M$/meter)	225	225
Blanket (1.5M$/meter)[a]	225	338
TWO-END PLUGS		
Magnets	556	556
Cryo Pump	20	20
Direct Converter	100	100
Direct Converter Services	20	20
Neutral Beam Injectors	220	220
ECR Hardware ($4/watt)	260	260
Direct Capital Cost	1626	1739

[a] 1.5 complexity factor for Two-Zone Blanket.

TABLE 11.3-8

Summary of Capital Costs for the Thermochemical Plant and TMR Fusion Driven - M$, July 1980

	JBD LiO_2 Blanket	FBD Two-Zone Blanket
THERMOCHEMICAL PLANT		
Direct Plus Indirect Capital Costs:[a]		
Section I	53.1	76.3
Section II	178.7	311.3
Section III	319.4	459.4
Section IV	45.5	65.5
Section V	383.9	275.0
Total	980.6	1187.5
Total Capital Cost:[b]		
Public Utility (100% Debt)	1066.8	1291.9
Private Utility (50% Debt, 50% Equity)	1038.5	1257.6
Chemical Industry (100% Equity)	1010.0	1223.1
TMR FUSION DRIVER		
Direct Capital Cost	1626.0	1739.0
Direct Plus Indirect Capital Cost[c]	2195.1	2347.7
Total Capital Cost:[d]		
Public Utility (100% Debt)	2568.3	2746.8
Private Utility (50% Debt, 50% Equity)	2381.8	2547.3
Chemical Industry (100% Equity)	2195.1	2347.7

[a] Includes installation, indirect charges, and contingencies, scaled to thermochemical hydrogen plant operating rate of 3942 mole/sec for the JBD and 5670 mole/sec for FBD case.

[b] Adds contractor's fee of 3% and interest during construction for 3 y investment at 5%/y interest on debt capital only.

[c] Adds indirect costs of 15% for construction facilities, 15% for engineering, and 5% for owner's costs for a total of 35% indirect costs according to Battelle.[3]

[d] Adds interest during construction for 8 y investment at 5%/y interest on debt capital only.[3]

5%/y interest charge over an 8-year period where the amount of investment increases uniformly over the period on the construction. These interest charges vary depending on whether the utility is public (100% debt) or private (50% debt, 50% equity); and for the chemical industry, there is no interest charge since at 100% equity the investment is carried by the chemical firm. We have assumed a 30-year fusion plant life as recommended by Battelle[3].

11.4 HYDROGEN PRODUCTION COSTS

11.4.1 Plant Availability

We assume the operating personnel of the Thermochemical Plant to consist of a day crew of three chemical engineers, one electrical engineer, five plant operators, one electronics technician, one computer systems-programmer, and one analytical process chemist; and four shift crews with 16 plant operators with the professional staff on call for four hour shifts or longer if required. Staffing of the TMR follows the guidelines set up by Battelle for costing purposes.(3)

We have taken a 90% stream factor for the Chemical Plant, which takes into account 5% unscheduled and 5% scheduled downtimes. We have assumed that owing to the process unit redundancies that we have designed into the Thermochemical Plant that plant failures can only reduce the stream factor to 80%. This results from the fact that there are at least 5 parallel process trains that are configured in a redundant fashion. One of the redundant trains could be shutdown 50% of the time, without reducing availability below the stated 90% level.

We have taken a 77% TMR fusion plant availability as given by the Battelle report,[3] and assumed that this availability results from an 11% fraction of unscheduled shutdowns and 12% of scheduled shutdowns.

The combined overall system availability, therefore, can be calculated from the above information as follows: The unscheduled availability is 1.00-0.11 or 0.89, for the TMR Driver and 1.00-0.05, or 0.95, for the Chemical Plant, producing a combined availability arising from random shutdowns as the product, which is 0.89 x 0.95 = 0.846. The scheduled fraction shutdown must be the larger of that for the TMR Driver or the Chemical Plant; thus, 0.12 for the TMR Driver. The total availability is, therefore, the product of the scheduled availability times the unscheduled availability, i.e.:

$$A = (1.00-0.12) \times 0.846 \approx 0.744 \text{ (or 74.4\%)}.$$

11.4.2 Estimates of Hydrogen Production Costs

The purpose of this section is to obtain the hydrogen production costs ($/GJ) from the estimated capital costs in Table 11.3.8, the chemical Plant operating costs in Table 11.4-1, and the Battelle methods[3] for the TMR and electrical power systems. This will involve three different analyses: one based on public utility financing, one on private utility financing, and one on chemical industry financing. Table 11.4-2 summarizes for the Heat Pipe Blanket the computation of H_2 production costs utilizing the three different financing methods, while Table 11.4-3 summarizes the same information for the Two-Zone Blanket.

The computational procedure for both tables is identical. First, we need to separate the capital costs from Table 11.3-6 into the appropriate debt capital and equity capital portions depending upon how these capital cost expenditures are financed. Since the public utility is all debt financed either though prepayments of the rate payers under the justification of "future expansion" or under a utility bond, the capital costs are 100% debt financed. The private utility divides its capital between debt and equity capital (we assume 50% debt and 50% equity), while our model chemical industry takes it as entirely internally (100% equity) financed.

TABLE 11.4-1

Estimated Operating Cost of the Chemical Plant Sections I-IV Operating Costs Are Based on the Capital Cost of an Equivalent Chemical Plant Constructed of Mild Steel - M$, July 1980

	JBD Case	FBD Case
DIRECT CAPITAL COST (MILD STEEL)[a]		
Section I	5.6	8.0
Section II	25.2	24.9
Section III	50.7	72.9
Section IV	8.0	11.6
Total	81.5	117.4
DIRECT PLUS INDIRECT CAPITAL COST FOR SECTIONS I-IV (GUTHRIE, 248.2% OF ABOVE)	202.3	291.4
ANNUAL OPERATING COST FOR SECTIONS I-IV GUTHRIE, 20%/y OF DIRECT + INDIRECT CAPITAL COST	40.5	58.3

[a] The mild steel capital costs for the chemical plant are from Tables 11.3-1 through 11.3-5 scaled to 3942 mole/sec for the JBD case and 5670 moles/sec for the FBD case.

TABLE 11.4-2

Estimates of Operating Costs and Hydrogen Production Costs of a TMR Driven Thermochemical Plant Based on the Joule Boosted Decomposer - M$, July 1980

	PUBLIC UTILITY (100% debt)	PRIVATE UTILITY (50% debt) (50% equity)	CHEMICAL INDUSTRY (100% equity)
TOTAL CAPITAL COST[a]			
T/C Plant	1066.8	1038.5	1010.0
TMR	2568.3	2381.8	2195.1
ANNUAL OPERATING COST			
Financing Cost:			
T/C Plant (5%/y, 30y)	66.7	36.0	0
TMR (5%/y, 30y)	165.3	82.6	0
Production Cost:[b]			
T/C Sec. I-IV	40.5	40.5	40.5
T/C Sec. V	7.7	7.7	7.7
TMR	43.9	43.9	43.9
Other Fixed Costs:			
T/C Sec V and TMR[c]	82.5	170.2	170.2
Gross Profit (before taxes):			
10% Profit	0	171.0	320.5
20% Profit	0	342.0	641.0
Total Annual Operating Cost:			
10% Profit	406.6	551.9	582.8
20% Profit	406.6	722.9	908.3
HYDROGEN PRODUCTION COST[d]			
$/GJ, 10% Profit	14.84	20.14	21.27
$/GJ, 20% Profit	14.84	26.38	32.97

[a] Total capital costs are taken from Table 11.3-8.

[b] Annual production costs for Section I-IV are from Table 11.4-1. Operating and maintenance for the TMR and Section V use the Battelle[3] estimate of 2%/y of the direct plus indirect capital cost obtained from Table 11.3-8.

[c] Following Battelle[3], the other fixed costs are estimated from the Total Capital Cost (Table 11.3-8): depreciation 1.3%, interim replacement 0.3%, property insurance 0.2%, Federal income tax 2.0%, state and local taxes 2.8%. For the public utility case income taxes are eliminated and a 1.4% property tax equivalent is assumed.

[d] These costs are based on 74.4% plant availability and 27.4×10^6 GJ of H_2/y.

TABLE 11.4-3

Estimates of Operating Costs and Hydrogen Production Costs of a TMR Driven Thermochemical Plant Based on the Fluid Bed Decomposer - M$, July 1980

	PUBLIC UTILITY (100% debt)	PRIVATE UTILITY (50% debt) (50% equity)	CHEMICAL INDUSTRY (100% equity)
TOTAL CAPITAL COST[a]			
T/C Plant	1291.9	1257.6	1223.1
TMR	2746.8	2547.3	2347.7
ANNUAL OPERATING COST			
Financing Cost:			
T/C Plant (5%/y, 20y)	83.2	43.6	0
TMR (5%/y, 30y)	176.8	88.4	0
Production Cost:[d]			
T/C Sec. I-IV	58.3	58.3	58.3
T/C Sec. V	5.5	5.5	5.5
TMR	47.0	47.0	47.0
Other Fixed Costs:			
T/C Sec. V and TMR[c]	83.9	173.1	173.1
Gross Profit (before taxes):			
10% Profit	0	190.2	357.0
20% Profit	0	380.4	714.2
Total Annual Operating Cost:			
10% Profit	454.7	606.1	641.0
20% Profit	454.7	796.3	998.1
HYDROGEN PRODUCTION COST[d]			
$/GJ, 10% Profit	11.57	15.42	16.3
$/GJ, 20% Profit	11.57	20.26	25.40

[a] Total capital costs are taken from Table 11.3-8.

[b] Annual production costs for Sections I-IV are from Table 11.4-1. Operating and maintenance for the TMR and Section V use the Battelle[3] estimate of 2%/y of the direct plus indirect capital cost obtained from Table 11.3-8.

[c] Following Battelle[3], the other fixed costs are estimated from the Total Capital Cost (Table 11.3-8): depreciation 1.3%, interim replacement 0.3%, property insurance 0.2%, Federal income tax 2.0%, state and local taxes 2.8%. For the public utility case, income taxes are eliminated and a 1.4% property tax equivalent is assumed.

[d] These cost are based on 74.4% plant availability and 39.3 x 10^6 GJ of H_2/y.

This interest rate is based on constant dollars and is taken from the recommendations of the Battelle report.[3] In an inflated economy as we have today the true interest rate is the 5%/y constant dollar interest rate over and above the current inflation rate.

The annual production cost for the Chemical Plant (Sections I-IV) is obtained directly from Table 11.4-1 based on a 20% fraction of the mild steel equivalent capital cost of the chemical plant. For the power systems (Section V) of the chemical plant and for the TMR, the methods outlined by Battelle[3] are followed as detailed in the footnotes to Tables 11.4-2 and 11.4-3. The gross profit is obtained as a simple percentage of the total equity capital.

From the above analyses, we can now obtain the hydrogen production cost. We use as our basis a plant production rate of 3942 moles H_2/sec for the JBD case and 5670 moles H_2/sec for the FBD case. At a total combined availability of 74.4% (from Section 11.4-1) for the TMR/Thermochemical Plant, we obtain an energy production rate of 27.4 and 39.3 x 10^6 GJ/y for the two cases. This energy equivalence of the H_2 is obtained by using 285.77 kJ/mol H_2 as the higher heating value of H_2 plus an added compressive value of energy of RT ln P (9.70 kJ/mol H_2) associated with the 50 atm pressure of the hydrogen product, to obtain a total energy value of 295.47 KJ/mol H_2. The hydrogen product cost in \$/GJ is obtained by dividing the total annual operating costs (\$/y) by the yearly hydrogen energy production rate (GJ/y).

11.5 CONCLUSIONS ON PRELIMINARY COST ESTIMATES

1. Using conventional costing methods established by the fusion community and chemical industry, we obtain a hydrogen production cost of \$12-15/GJ in July 1980 dollars for the FBD/Two-Zone Blanket approach and the JBD/Single-Zone Blanket concept assuming public utility financing. Private utility and chemial industry financing give higher costs.

2. The $12-15/GJ hydrogen cost obtained here is very favorable and indicates that fusion synfuels will be competitive in the timeframe for emergence of fusion in approximately 2030.

References for Section 11.0

1. M. S. Peters and K. D. Timmerhaus, "Plant Design and Economics for Chemical Engineers," McGraw-Hill, New York, 1980.

2. W. Neff, LLNL, private communication to R. W. Werner, September, 1982.

3. S. C. Schulte, T. L. Willke, and J. R. Young, Fusion Reactor Design Studies Standard Accounts for Cost Estimates, Pacific Northwest Laboratory, Battelle Memorial Institute, Richland WA, Rept. PNL-2648 (May 1978).

4. R. W. Werner, et al, "Conceptual Design Study FY 1981, Synfuels from Fusion-Using the Tandem Mirror Reactor and a Thermochemical Cycle to Produce Hydrogen," Lawrence Livermore National Laboratory Report UCID-19311.

5. K. M. Guthrie, "Capital Cost Estimating," Chemical Engineering 76, (6), 114-142 (1969).

6. K. M. Guthrie, "Capital and Operating Costs for 54 Chemical Processes," Chemical Engineering 77, (13), 140-156 (1970).

7. Marshall and Swift, Los Angeles, Equipment Cost Index, compiled quarterly, for 47 different industries reported regularly in Chemical Engineering, McGraw Hill, New York.

8. J. Smelko, Union Carbide Company, Cleveland, OH, private communication to T. Galloway of LLNL, June, 1981.

9. D. Stanwich, Ingersol Rand Company, Philipsburg, MA, private communication, August, 1982.

10. K. Schultz, Cost quotation for a 2240 MW_t HTGR by United Engineers and Constructors Inc., private communication from . Schultz of General Atomic Company to T. Galloway of LLNL, March 2, 1981.

11. Pratt & Whitney Co., "Advanced Nonthermally Polluting Gas Turbines and Utility Applications," U.S. EPA Report 16130 DNE 0371, March, 1971.

12. R. Foster-Pegg, Westinghouse Electric Company, private communication to T. Galloway of LLNL, July 30, 1981.

13. J. Parsoneault, Brown-Boveri Corp., St. Cloud, MN, and R. Davis Brown-Boveri Corp., Pasadena, CA, private communication to T. Galloway of LLNL, August, 1981.

SECTION 12

SYNFUELS BEYOND HYDROGEN

Contributor:

R. G. Hickman

TABLE OF CONTENTS

LIST OF FIGURES

12.0 SYNFUELS BEYOND HYDROGEN

Large amounts of hydrogen are used to upgrade hydrocarbon feedstocks for use as transportation fuels. At present, the hydrogen is produced from fossil fuel resources, particularly natural gas. If a renewable hydrogen source were used, the fossil resources would not be depleted so rapidly. Also, the additional CO_2 produced during hydrogen production would not be exhausted to the atmosphere. Feedstock upgrading is the first expected large-scale use of hydrogen produced, according to the Ontario Electrolytic Hydrogen Study.[1]

12.1 METHANOL

Other than upgrading existing feedstocks, the simplist convenient liquid fuel that can be produced synthetically is probably methanol. This is a commercial process that uses catalysts in a one-step synthesis to make methanol according to the reaction

$$CO + 2H_2 \rightarrow CH_3OH \qquad (12.1)$$

The two companies' processes that dominate the world market are Imperial Chemical Industries (British) and Lurgi (German).[2] Both use fixed beds of catalysts based principally on mixtures of copper, zinc, and chromium. The specificity of these catalysts is remarkably good, and few byproducts are produced.

The equilibrium constant is not favorable as may be seen in Fig. 12.1. At low temperatures, the kinetics are too slow to be useful, even with a catalyst, so the reaction is normally operated between 250 ^{o}C and 350 ^{o}C. The higher temperature operation requires pressures of around 300 atm to give the same yield as the lower temperature process that runs around 100 atm. Even so, the unfavorable equilibrium allows only a few percent conversion per pass, so extensive recycle with chemical separation processing is required.

The synthesis reaction is highly exothermic (about 24 K cal/mole of

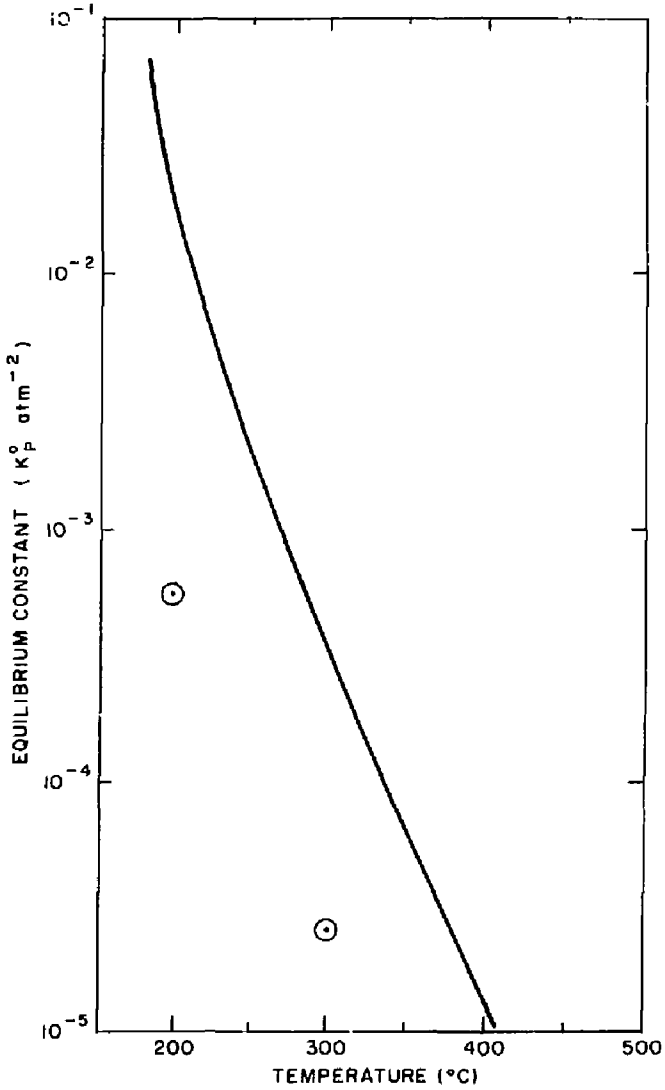

Fig. 12.1 Reaction equilibrium constant K_p^o for $CO + 2H_2 \rightleftharpoons CH_3OH$

methanol) so cooling of the reactor is required. The heat produced is recovered and is just adequate to supply the energy requirements of the compressors and distillation equipment.

An attractive long-term possibility would be to develop a fusion-produced liquid fuel from completely renewable resources. From reaction (12.1) it can be seen that a source of carbon monoxide is needed. At the very least a source of carbon must be available. Depending on the location and demand, this could be municipal waste, agricultural waste, or energy crops. In each of these cases the original carbon source is CO_2 in the air, and photosynthesis combined with other processes has separated it from the air and converted it to a solid or liquid hydrocarbon form. It is possible with today's technology to extract CO_2 directly from the air on a commercial scale. Liquid CO_2 sells for about $100 per tonne.

The synthesis of CH_3OH can be done with CO_2 directly rather than with CO. The reaction is then written

$$CO_2 + 3H_2 \rightarrow CH_3OH + H_2O \qquad (12.2)$$

Chemical kinetics are comparable with those of reaction (12.1) but the equilibrium constant drops by more than a factor of 10. This drop is depicted by the two circles on Fig. 12.1, and it is a very unattractive feature. It is readily observed that reaction (12.2) uses half again as much H_2 as reaction (12.1) to produce the same amount of CH_3OH. That, too, is unattractive as is the fact that reaction (12.2) is only about half as exothermic, even though the energy requirements for compression and chemical separation are increased.

In Fig. 12.2, the equilibria of some simple chemical reactions are shown. Some could be used to produce CO from CO_2 by reacting with H_2 or C. The C could come from either a renewable or a nonrenewable source. One common feature is that to show a favorable equilibrium, they all must operate near 1000 K, and they all are endothermic. This would have a substantial

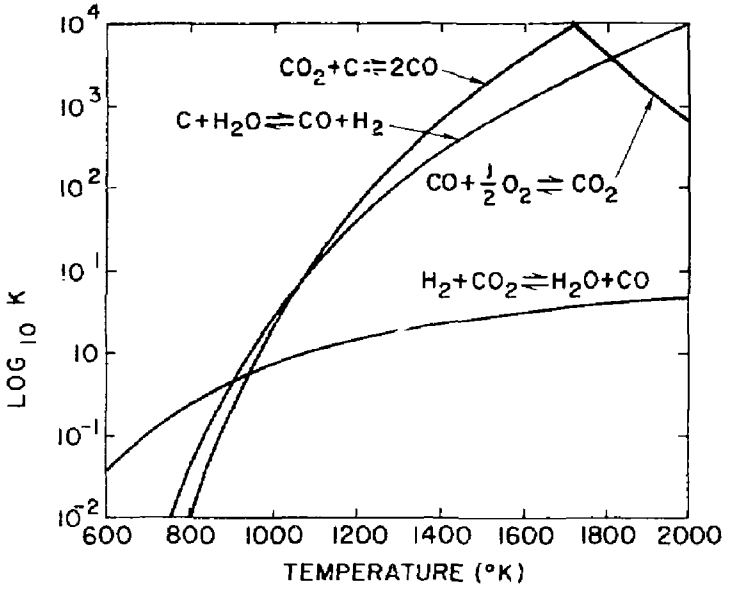

Fig. 12.2 Equilibrium constants of chemical reactions

influence on the final methanol cost. A reaction not shown but worthy of consideration is the partial oxidation of biomass char with surplus oxygen produced during hydrogen manufacturing. This oxidation is exothermic and the heat at the reaction temperature could produce the char in a conventional pyrolysis step. Regardless of the final choices made, many routes to synthetic liquid fuels are available once the H_2 can be produced in abundance at low enough costs.

A closing comment might be made here. With a two-step catalytic dehydration process known as Mobil M, methanol can be converted to high octane gasoline at about 90% efficiency.

References for Section 12.0

1. "Hydrogen, A Challenging Opportunity," Report of the Ontario Hydrogen Energy Task Force, Vol. 1, September 1981.

2. R. Salmon, M. Edwards, and R. Wham, "Production of Methanol and Methanol Related Fuels from Coal," Oak Ridge National Laboratory, Rpt. ORNL-5564.

SECTION 13

SIMULATION OF SECTION II OF GENERAL ATOMIC THERMOCHEMICAL CYCLE AND THE THERMODYNAMICS OF THE H_2SO_4-H_2O SYSTEM

Contributors:
M. E. Abhold, J. Oelund and A. L. Babb

TABLE OF CONTENTS

SECTION 13

List of Figures

List of Tables

13.0 SIMULATION OF SECTION II OF GENERAL ATOMIC THERMOCHEMICAL CYCLE AND THE THERMODYNAMICS OF THE H_2SO_4-H_2O SYSTEM

As pointed out in Section 9.4, the mass and energy balances in Section II of the General Atomic Sulfur-Iodine thermochemical process is especially crucial to interfacing the thermochemical plant to the fusion driver. As stated in Section 9.3 of this report, the primary design criterion of Section II is to increase the thermal energy recovery of the H_2SO_4 concentration step while maintaining a good match to the thermal heat source.

Determining the mass and energy balances for Section II involves calulating multiple recycle streams. Optimization of a process with multiple recycle streams requires iteration over input parameters. Due to the complexity of Section II this can only be accomplished by computer simulation.

This section (13.0) describes the development of a structured approach to the computer simulation of Section II of the process. As noted in Section 8.1 the present thermodynamic data for the H_2SO_4-H_2O system as published in the literature is not adequate for determining accurate mass and energy balances.

13.1 CHESS: THE U.W. PROCESS SIMULATION CODE

13.1.1 Description of CHESS

The process simulator available at the University of Washington is CHESS (Chemical Engineering Simulation System). CHESS is based on a computer program written at the University of Houston which was made available for academic users. CHESS is designed primarily to simulate a large chemical process with multiple recycle streams.

To simulate Section II of the General Atomic Sulfur-Iodine cycle, a process simulator must be capable of modeling two phase equilibria. There are three thermodynamic functions that must be calculated:

1. Vapor phase fugacity

   $$f_i^V = \phi_i P y_i$$

2. Liquid phase fugacity

   $$f_i^l = \gamma_i f_i^0 x_i$$

3. Enthalpy

   $$H(T,P,\{x_i\})$$

where:

ϕ_i = fugacity coefficient

P = total pressure

y_i = mole fraction of i^{th} species in the vapor phase

γ_i = activity coefficient

f_i^0 = fugacity of the pure liquid at it's vapor pressure for that temperature

x_i = mole fraction of the i^{th} species in the liquid phase

H = total enthalpy

The prediction method used by CHESS for enthalpy and fugacity coefficients is the Redlich-Kwong-Suave equation of state. This method was chosen because of the ability to select the constants appearing in the equation with a minimum of data (critical pressure, critical temperature, and an accentric factor for each chemical species). Because of it's simplicity, the Redlich-Kwong equation could not be expected to be sufficiently accurate to be used in precision calculations. It has, however, been used frequently for mixture calculations and phase equilibrium correlations with reasonably good success.

The liquid activity coefficient is much more difficult to determine since it depends on liquid-liquid interactions which vary greatly depending on whether the molecules are polar, electrolytic, or neither. The simplest situation is an ideal solution where the activity coefficients are one. The next most complicated, is the regular solution theory used by CHESS. The regular solution theory applies to solutions whose excess entropy of mixing is zero. This approach is suitable for non-polar of very weakly polar compounds. The liquid phase fugacity is based upon an empirical curve which includes a correction for the Pitzer-Curl acentric factor. Liquid activity coefficients are based on the

Hildebrand solubility parameter method with coefficients provided by Chao and Seader.

The CHESS system requires that the user supply information on (1) the feed streams to the process, (2) the process topology, and (3) designation of the type of process equipment and its parameters (i.e. a heat exchanger, number of shells, area, heat transfer coefficient etc.). CHESS then completes the mass and energy balances and provides a summary of (1) each stream, vapor fraction, temperature, pressure, enthalpy, and composition, and (2) each process unit: cooling required, work required. Although CHESS has some capability for design it is primarily suited for simulation.

The process units included in CHESS offer the capability of doing the following kinds of calculations (all multicomponent):

Absorber/Stripper	-- separation using several theoretical stages
Flash	-- isothermal or adiabatic
Distillation	-- plate to plate
	-- short cut
Heat exchangers	
Reactor	-- calculates stoichiometry only, no equilibrium constraints
Pumps	
Valves	
Fired Heators	

The restrictions on the system are:

(1) $\leq$ 100 streams
(2) $\leq$ 50 pieces of equipment
(3) $\leq$ 20 components
(4) regular liquid solutions
(5) ideal vapor solutions (i.e. vapor activity coefficients are one)

13.1.2 Modifications to CHESS for Electrolyte Systems

In order to simulate Section II of the General Atomic Sulfur-Iodine cycle, CHESS must be able to predict the vapor phase fugacity, liquid phase fugacity, and enthalpy for the $H_2SO_4 \cdot H_2O \cdot SO_3$ system. The prediction methods used by CHESS assume regular solutions and therefore are incapable of accurate predictions for the components in question.

It is necessary to add unit computation modules to CHESS to model the vapor liquid equilibrium of $H_2SO_4 \cdot H_2O$. The modules will utilize the thermodynamic data discussed in Section 13.2 empirically.

The CHESS input Schematic for Section II is shown in Fig. 13.1-1. As the Redlich-Kwong-Soave equation of state is adequate to predict vapor phase enthalpys, the standard CHESS unit calculation modules will be used in the vapor phase. For units which calculate vapor-liquid equilibrium modules will be added.

13.1.3 Example Add-On Module for the Multi-Effect H_2SO_4 Evaporators

The ADD1 module is an additional module added to the CHESS program to carry out isothermal flashes. Fig. 13.1-2 shows a schematic of the ADD1 module. With the equilibrium data discussed in Section 13.1, the ADD1 module will solve an isothermal flash with known K-values.

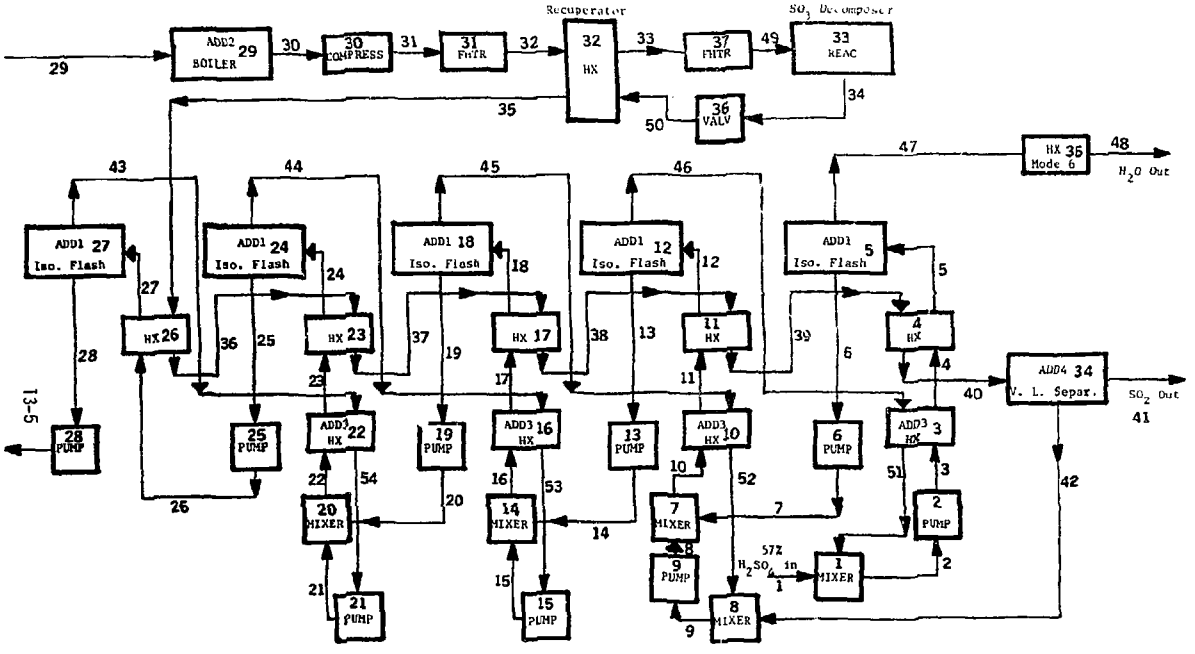

Fig. 13.1-1 CHESS Input Schematic for Section II.

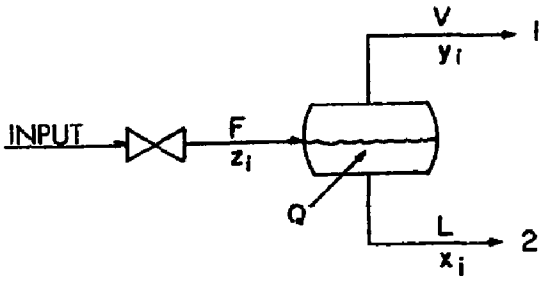

Fig. 13.1-2 Isothermal Flash Module

The variables are defined as follows:

- F = total moles fed to process
- V = total moles vapor
- L = total moles liquid
- z_i = mole fraction of component i in feed
- y_i = mole fraction of component i in vapor
- x_i = mole fraction of component i in liquid
- K_i = equilibrium constant of component i
- Q = energy into process
- H_x = enthalpy of x-stream
- T = temperature

The equations are:

Mass balance: $z_i F = x_i L + y_i V$

Energy balance: $H_F + Q = H_L + H_V$

Equilibrium: $T_F = T_L = T_V \qquad y_i = K_i x_i = \dfrac{x_i f_i^0 \gamma_i}{\phi_i P}$

Definition: $\Sigma y_i = 1.0$, $\Sigma x_i = 1.0$

The mass balance can be rearranged as follows:

$$z_i = y_i v + (1-v)x_i, \text{ where } v = V/F$$

$$= K_i x_i v + (1-v)x_i$$

$$= [(K_i-1)v + 1]x_i$$

Thus:

$$x_i = \frac{z_i}{(K_i-1)v + 1}$$

However

$$\Sigma y_i - \Sigma x_i = 1 - 1 = 0 \text{ or } \Sigma K_i x_i = \Sigma x_i = 0$$

or

$$\sum \frac{K_i z_i}{(K_i - 1)v + 1} - \sum \frac{z_i}{(K_i - 1)v + 1} = 0$$

define:

$$F(v) = \sum \frac{(K_i - 1)z_i}{(K_i - 1)v + 1} = 0$$

We can solve this equation with any of a number of unimodal search techniques. Given z_i and K_i we must find v such that $F(v) = 0$. Once v is found we can solve for x_i and y_i through the equilibrium relations.

13.2 REVIEW OF RELEVANT DATA AND ITS DEFICIENCIES

To provide an accurate result for the enthalpy requirement of Section II of the General Atomic water splitting cycle, accurate thermodynamic data for the H_2SO_4-H_2O-SO_3-SO_2 system is needed. The need for accurate data prompted a review of the relevant thermodynamic data. The data for SO_2 was consistent with the JANAF tables.[1] Calculations based on the integration of recent C_p data for SO_3 were inconsistant. Table 1 shows SO_3 enthalpys calculated[2], compared with the JANAF values. The values differ substantially at temperatures above 1000°K. The differences have a significant impact on K_P for SO_3 and thus influence the calculations of the composition of the vapor phase.

Table 13.2-1

SO_3 Enthalpy Data

T (°K)	JANAF Tables	CALCULATED
300	0.022	0.024
400	1.322	1.29
500	2.768	2.74
600	4.328	4.32
700	5.975	5.99
800	7.687	7.73
900	9.448	9.54
1000	11.248	11.40
1100	13.077	13.32
1200	14.930	15.29
1300	16.802	17.29
1400	18.688	19.34

Also of importance for separations operations are data on the vapor liquid equilibrium of the H_2O-H_2SO_4 system, over the complete range of concentrations and at elevated temperatures. To date the best estimation of the properties of aqueous sulfuric acid have been made by Gmitro and Vermeulen[3] They used an iterative procedure, normalizing to the azeotrope, to calculate the partial pressures over sulfuric acid over the complete range of dilution and up to temperatures of 400° C. Their calculations were essentially extrapolations of room temperature data, the estimate of the properties of aqueous sulfuric acid not being of sufficient reliability for the calculation of separations operations at high temperatures.

Excellent measurements of the vapor-liquid equilibrium of aqueous sulfuric acid have recently been made by Lennartz[4] They include both P-T-x and T-x-y data. The P-T-x measurements span the range of concentrations from 20-100% mole fraction H_2SO_4, with a temperature range of 110-500°C. The results are shown in Fig. 13.2-1. The T-x-y measurements also covered a wide range and are shown in Fig. 13.2-2. The azeotrope was determined from both P-T-x and T-x-y measurements and is shown in Fig. 13.2-3.

Currently, no analysis of Lennartz's data has been published. Nonetheless, rough comparison between Gmitros' calculations and Lennartzs' data can be made using the data as presented in figs. 13.2-1 to 13.2-3.

The comparison between total pressures as measured by Lennartz and calculated by Gmitro is shown in Fig. 13.2-4. The largest discrepancy in total pressures lies in the region near the azeotrope. Calculations made at the azeotrope as measured by Lennartz show that this is due to significant errors in the partial pressures of SO_3 and H_2SO_4. These errors have a significant impact on the distribution coefficients between the liquid and gaseous phases at equilibrium. The discrepancy is demonstrated by comparison of the partial pressures at the azeotrope as shown in Figs. 13.2-5 to 13.2-8. (At the azeotrope the partial pressures above the solution can easily be found with the published data.) While such a limited comparison cannot indicate the extent of error over the whole range of solutions, it shows that there are points at which the discrepancy is on the order of 100% for both SO_3 and H_2SO_4. Again, the implication is that the distribution coefficients are off by a significant amount. Also note that the total pressure temperature dependence is significantly different from that measured at the azeotrope

(see Fig. 13.2-4). This implies a large percentage error in the enthalpy of vaporization near the azeotrope.

Note that (see Fig. 13.2-6) the difference between the partial pressures for H_2O is minor in relation to the errors in the partial pressures of SO_3 and H_2SO_4 (Figs. 13.2-7 and 13.2-8). This explains the excellent agreement between the two sets of total pressure data at lower mole fractions of H_2SO_4 where the partial pressures of H_2SO_4 and SO_3 are negligible (see Fig. 13.2-4). Thus the error in Gmitros' calculations is almost solely due to errors in the partial pressures of H_2SO_4 and SO_3.

In view of the fact that the efficiency of the entire synfuel plant is strongly impacted by the efficiency of the separations operations the current thermochemical data being used for engineering analysis is inadequate for process optimization. In light of this situation the measurements made by Lennartz are currently being reduced to provide the relevant thermodynamic data for the H_2O-H_2SO_4 system.

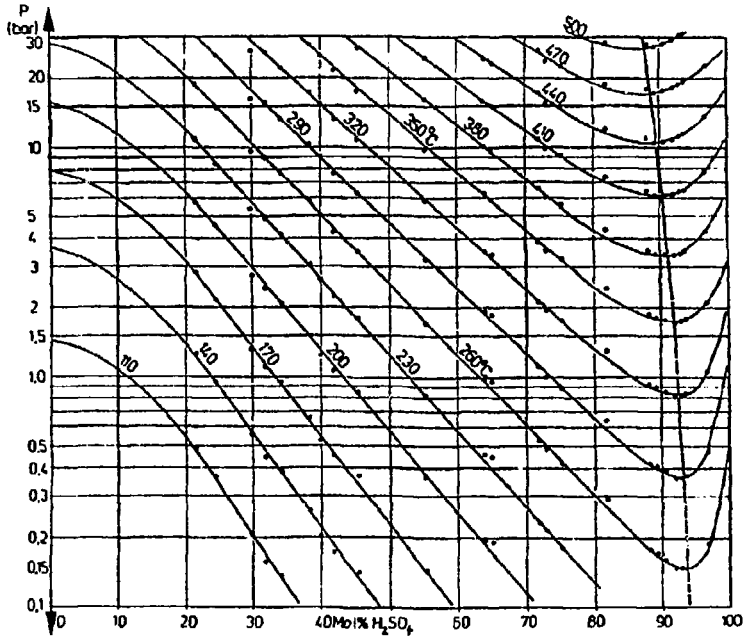

Fig. 13.2-1 Total pressures above aqueous sulfuric acid as measured by Lennartz[4]

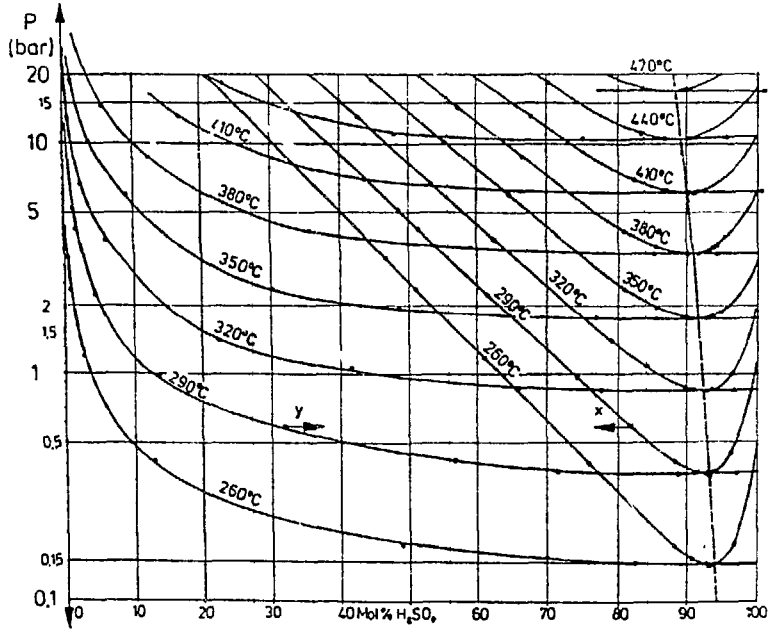

Fig. 13.2-2 Boiling (x) and condensation points (y) above aqueous sulfuric acid as measured by Lennartz[4].

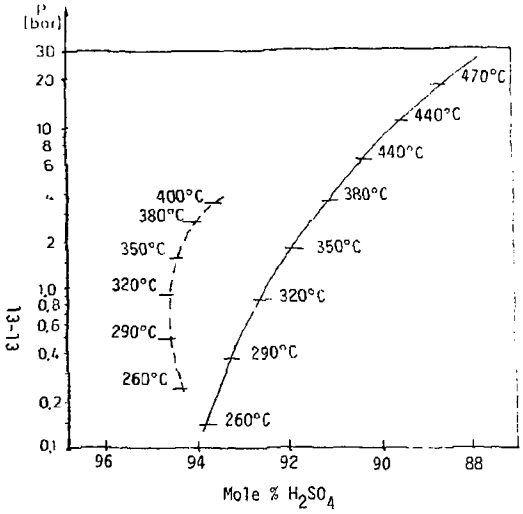

Fig. 13.2-3 Comparison of calculated with measured azeotrope for aqueous sulfuric acid.

-- Gmitro[3]

— Lennartz[4]

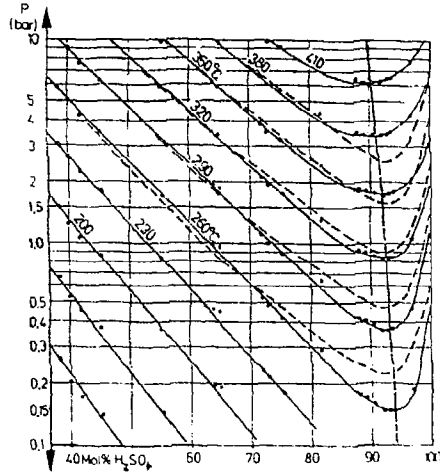

Fig. 13.2-4 Comparison of calculated with measured pressures above aqueous sulfuric acid.

--- Gmitro[3]

___ Lennartz[4]

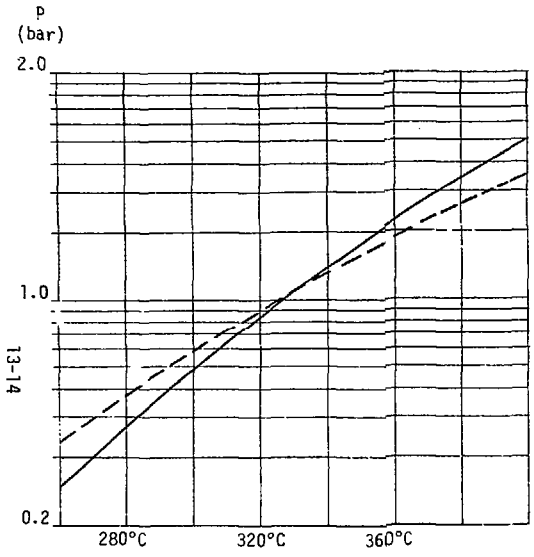

Fig. 13.2-5 Total pressure for aq. H_2SO_4

-- Gmitro[3] (calc'd)
— Lennartz[4] (meas'd)

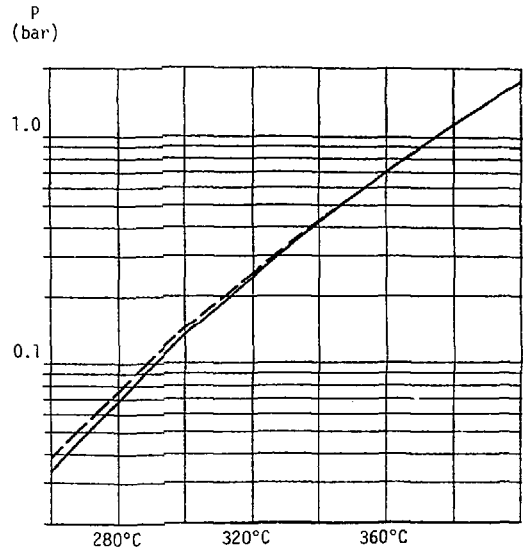

Fig. 13.2-6 Partial pressure for H_2O over aq. H_2SO_4 (at measured azeotrope)

-- Gmitro[3] (calc'd)
— Lennartz[4] (meas'd)

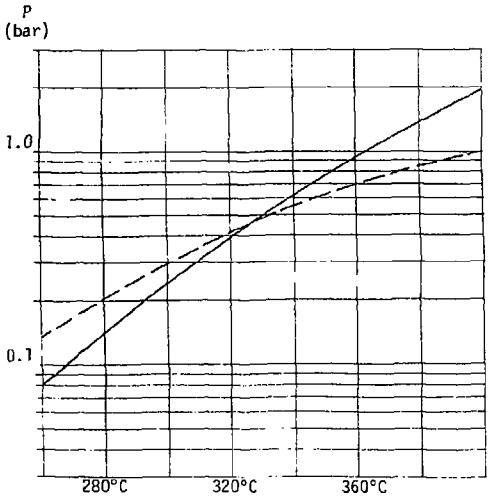

Fig. 13.2-7 Partial pressure of H_2SO_4 over aq. H_2SO_4 (at measured azeotrope)
-- Gmitro[3] (calc'd)
— Lennartz[4] (meas'd)

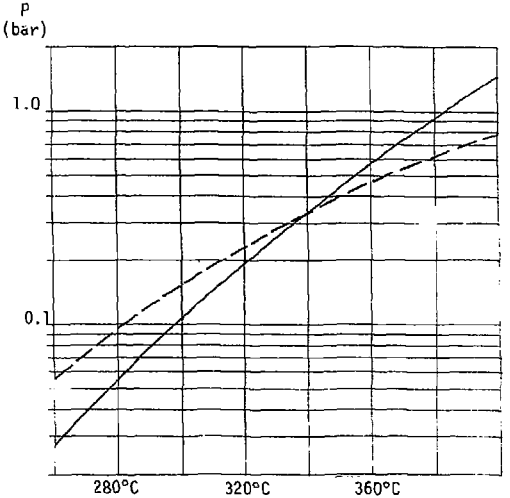

Fig. 13.2-8 Partial pressure of SO_3 over aq. H_2SO_4 (at measured azeotrope)
-- Gmitro[3] (calc'd)
— Lennartz[4] (meas'd)

REFERENCES

1. D. R. Stull and H. Prophet, "JANAF Thermodynamic Tables", 2nd ed., U.S. National Bureau of Standards, (1971), Washington D.C., with Supplements through March 31, 1979.

2. C. L. Yaws, K. Y. Li, C. H. Kvo, "Sulfur Oxides SO_2, SO_3", Chem. Eng. July 8, 1974 pp. 87.

3. J. I. Gemitro, and T. Vermeulen, T., "Vapor-Liquid Equilibria for Aqueous Sulfuric Acid", University of California, Ernest O. Lawrence Radiation Laboratory, Berkeley, CA, Report No. UCRL-10886, June 24, 1963.

4. A. A. Strub and G. Imarisio, Eds., In: Proc. Int. Seminar, "Hydrogen as an Energy Vector", Brussels, Belgium, February 1980. Published by Durdrecht, Holland, 1980.

GPO 687 -922/P9041